

SEISMICA

JUNE 2023 | VOL 2 | NO 1



ISSN 2816-9387



McGill

Library
Bibliothèque

Issue 2, Volume 1, 2023

Aims and Scope

Seismica publishes original, novel, peer-reviewed research in the fields of seismology, earthquake science, and related disciplines. Seismica is a community-driven, diamond open-access journal. Articles are free to publish and free to read without a subscription, and authors retain full copyright.

Seismica strives to be **accessible, transparent, respectful, credible, and progressive.**

Seismica's scope includes a wide range of topics in seismological and earthquake sciences. A non-exhaustive list of topics that fall within the scope of Seismica includes: Fault-slip and earthquake source phenomena, Earthquake records, Imaging the Earth, Theoretical and computational seismology, Beyond Earth-tectonic applications, Techniques and instrumentation, Earthquake engineering and engineering seismology, Community engagement, communication and outreach.

For submission instructions, subscription and all other information visit: <https://seismica.library.mcgill.ca/>.

For editorial questions or issues, please contact info@seismica.org.

For technical assistance, please contact info@seismica.org.



For appeals, please contact appeals@seismica.org.














About the cover









Cover Caption Installation of a weather station and self-sufficient seismic box on a Greenlandic outlet glacier. The glacier is called Sermeq Kujalleq in the Kangia icefjord (also known as Jakobshavn isbræ). The photo was taken at the fast ice stream approximately 60 km from the calving front. Installation of instruments at such locations can only be achieved by helicopter. The installation of the stations was part of the 2021 field campaign within the COEBELI project from the University of Zürich. The COEBELI project aims at investigating short-term ice flow dynamics with a combination of various field measurements. The total field campaign consisted of the installation of eight self-sufficient seismic box stations, two weather stations, two GPS stations, terrestrial radar measurements, and time-lapse cameras. More field campaigns with a larger number of sensors were done in 2022 and are planned for the summer of 2023. Credit: Ana Nap (photographer) and Adrien Wehrlé (in the picture)



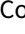

Editorial Board

We warmly thank the following volunteers of the Editorial Board that have been involved in the issue.

Production Editors Kiran Kumar Thingbaijam , Gareth Funning 

Handling Editors Tiegan Hobbs , Ryo Okuwaki , Yen Joe Tan , Stephen Hicks , Samantha Teplitzky , Pathikrit Bhattacharya , Atalay Ayele Wondem , Mathilde Radiguet , Carmine Galasso , Nicola Piana Agostinetti , Paula Koelemeijer , Vitor Silva , Randolph Williams 

Copy/layout Editors Oliver Lamb , Théa Ragon , Hannah Mark , Cláudia Reis , Ethan Williams , Kirsty Bayliss , Abhineet Gupta , Keyla Ramirez 

Media & Branding Adam Pascale , Daniel Corona , Jaime Convers , Ezgi Karasozen 

Volunteers

We warmly thank the following volunteers that have been involved in the issue.

Signed Reviewers Tiegan Hobbs , Yen Joe Tan , Daniel Trugman , Daniel Nüst , Wynn Tranfield , Edwin Nissen , Jonathan Griffin 

Issue 2, Volume 1, 2023

Table of Contents

Articles

Major California faults are smooth across multiple scales at seismogenic depth

Lomax et al.

Interacting Seismic Waveguides: Multimode Surface Waves and Leaking Modes

Kennett

How reproducible and reliable is geophysical research? A review of the availability and accessibility of data and software for research published in journals

Ireland et al.

Estimates of earthquake temperature rise and frictional energy

Coffey et al.

Co-seismic slip of the 18 April 2021 Mw 5.9 Genaveh earthquake in the South Dezful Embayment of Zagros (Iran) and its aftershock sequence

Jamalreyhani et al.

When are Non-Double-Couple Components of Seismic Moment Tensors Reliable?

Rösler et al.

Deep learning for denoising High-Rate Global Navigation Satellite System data

Thomas et al.

Validation of Peak Ground Velocities Recorded on Very-high rate GNSS Against NGA-West2 Ground Motion Models

Crowell et al.

PyRaysum: Software for Modeling Ray-theoretical Plane Body-wave Propagation in Dipping Anisotropic Media

Bloch et al.

Ocean Surface Gravity Wave Excitation of Flexural Gravity and Extensional Lamb Waves in Ice Shelves

Abrahams et al.

Exploring the Effect of Minimum Magnitude on California Seismic Hazard Maps

Gallahue et al.

3D Paleoseismology from iOS Lidar and Structure from Motion Photogrammetry: a case study on the Dog Valley fault, California

Pierce et al.

Fast Reports

Imaging the Western Edge of the Aegean Shear Zone: The South Evia 2022-2023 Seismic Sequence

Evangelidis et al.

Could planet/sun conjunctions be used to predict large (moment magnitude ≥ 7) earthquakes?

Romanet

Reports (excl. Fast Reports)

Curated Pacific Northwest AI-ready Seismic Dataset

Ni et al.

Self-sufficient seismic boxes for monitoring glacier seismology

Nap et al.

Major California faults are smooth across multiple scales at seismogenic depth

Anthony Lomax  * ¹, Pierre Henry  ²

¹ALomax Scientific, Mouans-Sartoux, France, ²Aix Marseille Univ, CNRS, IRD, INRAE, Coll France, CEREGE, Aix-en-Provence, France

Author contributions: *Conceptualization:* A. Lomax, P. Henry. *Methodology:* A. Lomax. *Software:* A. Lomax. *Formal Analysis:* A. Lomax, P. Henry. *Writing - original draft:* A. Lomax. *Writing - Review & Editing:* A. Lomax, P. Henry.

Abstract Surface traces of earthquake faults are complex and segmented on multiple scales. At seismogenic depth the detailed geometry of faults and earthquake rupture is mainly constrained by earthquake locations. Standard earthquake locations are usually too diffuse to constrain multi-scale fault geometry, while differential-timing relocation mainly improves finest scale precision. NLL-SSST-coherence, an enhanced, absolute-timing earthquake location procedure, iteratively generates traveltime corrections to improve multi-scale precision and uses waveform similarity to improve fine-scale precision. Here we apply NLL-SSST-coherence to large-earthquake sequences and background seismicity along strike-slip faults in California. Our relocated seismicity at seismogenic depth along major fault segments and around large-earthquake ruptures often defines smooth, planar or arcuate, near-vertical surfaces across the sub-km to 10's of km scales. These results show that multi-scale smooth fault segments are characteristic of major, strike-slip fault zones and may be essential to large earthquake rupture. Our results suggest that smoothness and curvature of faults influences earthquake initiation, rupture, rupture direction and arrest, and can define earthquake hazard. The results corroborate that surface traces of strike-slip fault zones reflect complex, shallow deformation and not directly simpler, main slip surfaces at depth, and support use of planar or smoothly curved faults for modeling primary earthquake rupture.

Non-technical summary Surface traces of earthquake faults, like many features of the natural landscape, are irregular and complex across many scales, from microscopic to many kilometers. However, there are conflicting views on the geometrical complexity and smoothness of earthquake faults deeper in the Earth at seismogenic depth, where most earthquakes occur - about 4 to 15 km for many large faults in California. But knowing fault geometry at seismogenic depth is key to understanding earthquakes, including the initiation, growth, and hazard of large earthquakes. The detailed geometry of earthquake faulting at seismogenic depth is mainly constrained by seismicity—earthquake locations derived from earthquake waves on seismograms. But the precision of earthquake locations from routine seismic network monitoring is insufficient for imaging the detailed geometry of faults, while modern, high-precision location procedures mainly improve locations on only the finest, sub-kilometer scales. Here we apply a new, multi-scale, high-precision earthquake location procedure to earthquake activity along major strike-slip faults in California. Our relocations reveal main fault zones at seismogenic depth as smooth, planar or arcuate, near-vertical surfaces across the sub-km to 10's of km scales. These results suggest that multi-scale smooth faulting is characteristic of major strike-slip fault zones, likely influences earthquake initiation, rupture, rupture direction and arrest, and may even be necessary for large earthquake to occur. The results can aid in mapping earthquake hazard, and underline that surface fault traces mainly reflect complex, secondary, shallow deformation and not directly simpler, large earthquake slip surfaces at depth.

1 Introduction

The geometry, complexity and smoothness of faults are related to maturity of fault zones, rupture physics and earthquake hazard (Okubo and Dieterich, 1984; Ben-Zion and Sammis, 2003; Dieterich and Smith, 2010; Fang and Dunham, 2013; Scholz, 2019). Surface traces of major, strike-slip earthquake faults are typically complex and segmented, and it is often considered that these shallow features reflect the fault geometry at seismogenic depth and control the size, initiation, arrest,

and recurrence intervals of large earthquake rupture (Bakun, 1980; Bakun et al., 1980; King and Nábělek, 1985; Wesnousky, 2006; Manighetti et al., 2007; Wesnousky, 2008; Klinger, 2010).

The roughness of natural faults has been idealized as fractal or self-affine (Aviles et al., 1987; Power et al., 1988; Scholz, 2019). Fault surfaces on smaller scales (e.g., up to ~100 m) are often close to statistically self-similar but acquire scale dependence as a result of wear, at least along the direction of slip (Power et al., 1988; Reardon et al., 2006; Sagy et al., 2007). However, the magnitude and sense of any roughness scaling depends on the definition of roughness, how it is measured, and if re-

Production Editor:
Gareth Funning
Handling Editor:
Stephen Hicks
Copy & Layout Editor:
Cláudia Reis
Hannah F. Mark

Signed reviewer(s):
Daniel Trugman

Received:
20 January 2023

Accepted:
4 May 2023

Published:
15 June 2023

*Corresponding author: anthony@alomax.net

ferring to single or multiple fault strands (Beeler, 2023). Surface mapping and exhumed faults suggest faults are rough or corrugated at all scales, from sub-millimeter to hundreds of km, but with a scale dependence (Candela et al., 2012; Renard and Candela, 2017; Beeler, 2023). On scales of up to ~100 m the roughness of exposed fault surfaces is found to decrease with total slip (Sagy et al., 2007). Larger scale surface mapping implies a reduction in fault system complexity with increasing geologic offset (Wesnousky, 1988; Stirling et al., 1996; Perrin et al., 2016; Manighetti et al., 2021). And fractal analysis of the main San Andreas, California fault trace indicates it is simple or planar at scales larger than about 1-2 km (Aviles et al., 1987).

The seismogenic depth, a brittle zone where most co-seismic slip and energy release occurs, is from 4 km or less to 10-15 km for many large faults in California (Sibson, 1982; Marone and Scholz, 1988). At these depths, standard, arrival-time relocations of background seismicity and aftershock sequences are usually too diffuse to constrain multi-scale and detailed fault geometry. For the ~60 km Parkfield segment of the strike-slip, San Andreas fault in California, various high-precision, differential-timing relocations image a twisting (Thurber et al., 2006; Kim et al., 2016; Perrin et al., 2019), straight (Simpson et al., 2006) or predominantly planar (Thurber et al., 2006) surface, and, on the km scale, as multiple active fault patches offset by tens to hundreds of meters perpendicular to the overall fault surface (Nadeau et al., 1994; Waldhauser et al., 2004). However, the geometry of faults segments and the main rupture zones of larger earthquakes are usually modeled as (Savran and Olsen, 2020; Ramos et al., 2022), and often imaged as (Cockerham and Eaton, 1984; Schaff et al., 2002; Graymer et al., 2007; Waldhauser and Schaff, 2008; Lomax, 2020a) smooth, near-planar surfaces.

Thus, current understanding of the multi-scale geometrical complexity and smoothness of faults and earthquake rupture zones at seismogenic depth is based on conflicting results (see also Goebel et al., 2014). This shortcoming hinders better understanding of earthquake rupture physics and of the relations between faulting at seismogenic depth and surface traces, with important ramifications for earthquake hazard assessment.

Seismicity, the distribution of earthquakes in space, time, and size, is fundamental for understanding earthquakes and for earthquake hazard assessment and forecasting (e.g. Scholz, 2019). Seismicity can show the geometry and activity of faults, the stages of earthquake initiation, and the extent of large earthquake rupture. In particular, seismicity can provide detailed information on fault geometry at seismogenic depth, including on and around surfaces of main, co-seismic slip and energy release. However, relative to the needs of modern seismological study, standard, arrival-time based earthquake locations often have low accuracy and precision, where accuracy is closeness to a usually unknown ground-truth, and precision is relative location accuracy—the correctness of the relative positions of nearby hypocenters. Useful and unbiased determination of the

geometry, complexity and smoothness of faults from seismicity requires earthquake location with uniformly high precision over multiple scales.

NLL-SSST-coherence (Lomax and Savvaidis, 2022), a recently developed, arrival-time earthquake location procedure, iteratively generates traveltime corrections to improve precision over many scales (e.g., from the size of a study area to ~1 km) and then uses waveform similarity to further improve precision on the finest scales (e.g. sub-km). NLL-SSST-coherence provides multi-scale, high-precision earthquake location.

Here, extending the work of (Lomax and Henry, 2022), we apply NLL-SSST-coherence to relocate recent large-earthquake sequences and background seismicity on major strike-slip faults in and around California. The relocated seismicity at depth surrounding high-slip patches of large earthquakes and on long stretches of major fault zones generally defines planar or arcuate, near-vertical surfaces that are multi-scale smooth (i.e., have fractal or Hausdorff dimension ~2.0 over a specified range of length scales). These results have implications for understanding of earthquake rupture physics, fault zone maturity, hazard, and maximum size, for the relationship of surface traces and paleo-seismic results to faulting at seismogenic depth, and for earthquake rupture modeling.

2 The NLL-SSST-coherence procedure for high-precision earthquake location

There are many means for improving the accuracy and precision of standard, arrival-time based earthquake locations. These include use of seismographic stations close to and above the source zone (Pavlis, 1986; Gomberg et al., 1990; Billings et al., 1994; Hardebeck and Husen, 2010; Buehler and Shearer, 2016), 3D (Aki and Lee, 1976; Crosson, 1976; Thurber, 1983; Micheli and McEvilly, 1991) and geology-based, seismic velocity models (e.g. Ryaboy et al., 2001; Wagner et al., 2013; Darold et al., 2014; Latorre et al., 2016), station traveltime corrections (Pavlis and Hokanson, 1985a; Myers, 2000; Richards-Dinger and Shearer, 2000; Lin and Shearer, 2005; Lomax, 2008; Nicholson et al., 2008; Nooshiri et al., 2017; Lomax, 2020a), ground-truth calibration (Ritzwoller et al., 2003; Bondár and McLaughlin, 2009; Lomax and Savvaidis, 2019), and location algorithms robust to error in the velocity models or earthquake arrival-time data (Stauder and Ryall, 1967; Shearer, 1997; Lomax, 2008; Lomax et al., 2014; Ishida and Kanamori, 1978).

High-precision, multi-event, relative location methods (Nakamura, 1978; Poupinet et al., 1982; Frémont and Malone, 1987; Got et al., 1994; Shearer, 1997; Fehler et al., 2000; Rowe et al., 2002; Lin et al., 2007; Landro et al., 2015), including the widely used HypoDD (Waldhauser and Ellsworth, 2000) and GrowClust (Trugman and Shearer, 2017), require and build upon initial, standard, arrival-time locations. Relative location methods use waveform similarity and precise, cross-

correlation, differential timing between events at individual stations to refine fine-scale, inter-event spatial relations. These methods can image seismicity in remarkable detail on the finest scales, showing narrow streaks, highly localized fault planes and sets of faulting structures (Got et al., 1994; Rubin et al., 1999; Waldhauser et al., 2004; Michele et al., 2020). However, these procedures depend on high-quality initial locations, good station and ray coverage, and a high-quality velocity model which produces accurate travel-times and gradients of travel-time (Michellini and Lomax, 2004; Richards et al., 2006; Matoza et al., 2013; Landro et al., 2015; Gibbons et al., 2017). These procedures may fail to resolve meaningful, larger and multi-scale differences between events in epicenter and especially depth (Schoenball and Ellsworth, 2017; Hauksson et al., 2020), perhaps because of poor station distribution and consequent poor ray coverage around the sources, or because of low accuracy and precision in the underlying, arrival-time locations.

We obtain multi-scale high-precision earthquake relocations through the combined use of source-specific, station traveltimes corrections (SSST) and stacking of probabilistic locations for nearby events based on inter-event waveform coherence (Lomax and Savvaidis, 2022). We use the NonLinLoc location algorithm (Lomax et al., 2000, 2014, NLL hereafter), which performs efficient, global sampling to obtain an estimate of the posterior probability density function (PDF) in 3D space for hypocenter location. This PDF provides a comprehensive description of likely hypocentral locations and their uncertainty, and enables application of the waveform coherence relocation. Within NLL, we use the equal differential-timing (EDT) likelihood function (Zhou, 1994; Font et al., 2004; Lomax, 2005, 2008; Lomax et al., 2014), which is highly robust in the presence of outlier data caused by large error in phase identification, measured arrival-times or predicted traveltimes. We use a finite-differences, eikonal-equation algorithm (Podvin and Lecomte, 1991) to calculate gridded P and S traveltimes for initial NLL locations.

2.1 Source-specific station term corrections

In a first relocation stage, NLL-SSST-coherence iteratively develops SSST corrections on collapsing length scales (Richards-Dinger and Shearer, 2000; Lomax and Savvaidis, 2022), which can greatly improve, multi-scale, relative location accuracy and clustering of events (Pavlis and Hokanson, 1985b; Richards-Dinger and Shearer, 2000; Lin and Shearer, 2005; Nooshiri et al., 2017). In contrast to station static corrections (Tucker et al., 1968; Ellsworth, 1975; Frohlich, 1979; Lomax, 2005, 2008), which give a unique time correction for each station and phase type, SSST corrections vary smoothly throughout a 3D volume to specify a source-position dependent correction for each station and phase type. These corrections account for 3D variations in velocity structure and corresponding distortion in source-receiver ray paths. NLL-SSST uses smooth, Gaussian distance kernels for accumulating SSST cor-

rections, while Richards-Dinger and Shearer (2000) use a fixed number of neighboring events, and Lin and Shearer (2005) use fixed distance and shrinking-box approaches.

Spatial-varying, SSST corrections are most effective for improving relative locations on all scales when the ray paths between stations and events differ greatly across the studied seismicity, including when stations are inside the seismicity distribution, the extent of seismicity is large relative to the distance to the stations, or the depth range of events is large. SSST corrections can improve multi-scale precision when epistemic error in the velocity model is large, such as when a 1D, laterally homogeneous model or a large-wavelength, smooth model is used in an area with sharp, lateral velocity contrasts or smaller scale, 3D heterogeneities.

2.2 Waveform coherency relocation method

In a second relocation stage, NLL-SSST-coherence reduces aleatoric location error by consolidating information across event locations based on waveform coherency between the events (Lomax and Savvaidis, 2022). This coherency relocation, NLL-coherence, is based on the concept that if the waveforms at a station for two events are very similar (e.g. have high coherency) up to a given dominant frequency, then the distance separating these events is small relative to the seismic wavelength at that frequency (e.g. Geller and Mueller, 1980; Poupinet et al., 1984), perhaps less than about a quarter of this wavelength (Geller and Mueller, 1980; Thorbjarnardottir and Pechmann, 1987). A pair of similar events is a doublet and a set of similar events may be called a cluster, multiplet or family; these events all likely occur on a small patch of a fault with similar magnitude and source mechanism (Gedney, 1967; Hamaguchi and Hasegawa, 1975; Ishida and Kanamori, 1978; Geller and Mueller, 1980; Poupinet et al., 1982; Nadeau et al., 1994; Cattaneo et al., 1997; Ferretti, 2005). In a high-precision, microseismic study Goertz-Allmann et al. (2017) show for waveform windows spanning both P and S waves that correlation coefficients greater than about 0.7 indicate event multiplets locate within about 0.1 km, which is about a quarter wavelength for the typical dominant waveform frequency ~20 Hz and wave velocity of ~2.5 km/s shown in their study. The results of Goertz-Allmann et al. (2017) (their figs. 4 and 6) also show lack of clustering and large separation of event pairs for correlation coefficients less than about 0.5.

For detailed seismicity analysis, the precise hypocenter locations of events in multiplets can be assigned to a unique centroid point or coalesced in space through some statistical combination of the initial hypocenter locations (Jones and Stewart, 1997; Kamer et al., 2015). Alternatively, precise, differential times between like-phases (e.g., P and S) for doublet events can be measured using time- or frequency-domain, waveform correlation methods. Differential times from a sufficient number of stations for pairs of doublet events allows high-precision, relative location between the events, usually maintaining the initial centroid of the event po-

sitions (Nakamura, 1978; Poupinet et al., 1982, 1984; Ito, 1985; Got et al., 1994; Nadeau et al., 1994; Waldhauser and Ellsworth, 2000; Matoza et al., 2013; Trugman and Shearer, 2017).

NLL-coherence uses waveform similarity directly to improve relative location accuracy without the need for differential time measurements or many stations with waveform data. The method assumes that high coherency between waveforms for two events implies the events are nearly co-located, and that all of the information in the event locations, when corrected for true origin-time shifts, should be nearly identical in the absence of noise. Then, stacking over probabilistic locations for nearby events can be used to reduce the noise in this information and improve the location precision for individual, target events. We measure coherency as the maximum, normalized cross-correlation between waveforms from one or more stations for pairs of events within a specified distance after NLL-SSST relocation (5-10 km in this study). We take the maximum station coherence between the target event and each other event as a proxy for true inter-event distances and thus as stacking weights to combine NLL-SSST location probability density functions (PDF's) over the events. In effect, this stack directly improves the hypocenter location for each target event by combining and completing arrival-time data over nearby events and reducing aleatoric error in this data such as noise, outliers, and missing arrivals. For a ground-truth test of NLL-SSST-coherence using controlled-source, explosion data from Finland, Lomax and Savvaidis (2022) estimated a relative horizontal location error of about 75 m. See Lomax and Savvaidis (2022) for more discussion and details, and Supplementary File S1 for NLL-SSST-coherence processing parameters used in this study.

A representation through analogy of the improvement of location precision given by NLL-SSST-coherence and by cross-correlation based, differential-timing methods is shown in Figure 1. Relative to a set of true locations, standard catalog locations using arrival-time based location methods contain multi-scale distortion primarily due to epistemic error in the velocity model, and smaller scale blurring primarily due to aleatoric error in the arrival-time data. NLL-SSST corrections remove epistemic error to improve multi-scale precision, and NLL-coherence removes aleatoric error to improve smaller scale precision. Differential-timing methods remove mainly aleatoric error in the arrival-time data to improve smaller and finest-scale precision, while, in practice (Waldhauser and Schaff, 2008; Trugman and Shearer, 2017), their time-difference formulation explicitly ignores and does not correct for larger scale, epistemic, velocity model error. These methods thus produce high, finest-scale precision, but do not remove larger, multi-scale distortion introduced in underlying, standard catalog locations. No methods can directly improve absolute epicenter and depth shifts and distortions on the largest scale (e.g., the full study area), for which accurate velocity models and calibration with ground truth information is needed.

3 NLL-SSST-coherence relocations along strike-slip faults in California

We present and discuss NLL-SSST-coherence relocations for well recorded, recent, moderate to large earthquake sequences and background seismicity on major strike-slip faults in and around California (Figure 2). We do not analyze sequences for very large, California strike-slip earthquakes such as 1993 Mw 7.3 Landers (Hauksson et al., 1993), 1999 Mw 7.1 Hector Mine (Hauksson, 2002) or 2019 Mw 7.1 Ridgecrest (Ross et al., 2019) primarily because aftershock seismicity for such large earthquakes occurs mainly away from main rupture surfaces (e.g. Das and Henry, 2003; Liu et al., 2003), but also, for the earlier Landers and Hector Mine events, due to sparsity of station distribution and lack of available digital waveform recordings.

In most cases we compare the results with high-precision, cross-correlation based, differential-timing relocations for the same time period and magnitude ranges, as available in the Northern California Seismic System HypoDD catalog (NCSS-DD Waldhauser and Ellsworth, 2000; Waldhauser and Schaff, 2008; Waldhauser, 2009). The number of available NCSS-DD events is always less than the number of NLL-SSST-coherence events since HypoDD relocates only events having a minimum number of high cross-correlation connections to nearby events. We analyze the results with a focus on the geometry and smoothness of apparent faulting as imaged or inferred by the multi-scale, NLL-SSST-coherence seismicity. It is important to note that even small heterogeneities in fault geometry, including roughness, kinks, bends, or offsets, can have a large effect on rupture physics (King and Nábělek, 1985; King, 1986; Dieterich and Smith, 2010; Fang and Dunham, 2013).

In the following relocations, we apply NLL-SSST with a smallest, Gaussian kernel smoothing length of 4 km or 2 km and apply NLL-coherence using waveforms up to 10 Hz or 20 Hz frequency (Supplementary File S1). We obtain formal NLL-SSST-coherence epicenter (errH) and depth (errZ) uncertainties as low as 100-200 m (Supplementary Table S1 and Datasets S1-5). This uncertainty range represents the relative locations accuracy (precision) of the NLL-SSST-coherence relocations, but not the absolute location accuracy which may be much larger. As with other location procedures, NLL-SSST-coherence does not directly improve absolute epicenter and depth accuracy on the largest scale (e.g., the full study area), for which accurate velocity models and calibration with ground truth information is needed. Thus, in the following, “multi-scale” precision ranges from approximately sub-km (as low as 100-200 m) to the extent of each study area.

3.1 Smooth, planar faulting: the Parkfield segment of the central San Andreas fault

We first examine the 2004 Mw 6.0 Parkfield sequence and background seismicity along the Parkfield segment of the central San Andreas fault (Figure 2). The Parkfield segment is at the southeastern end of an over 100

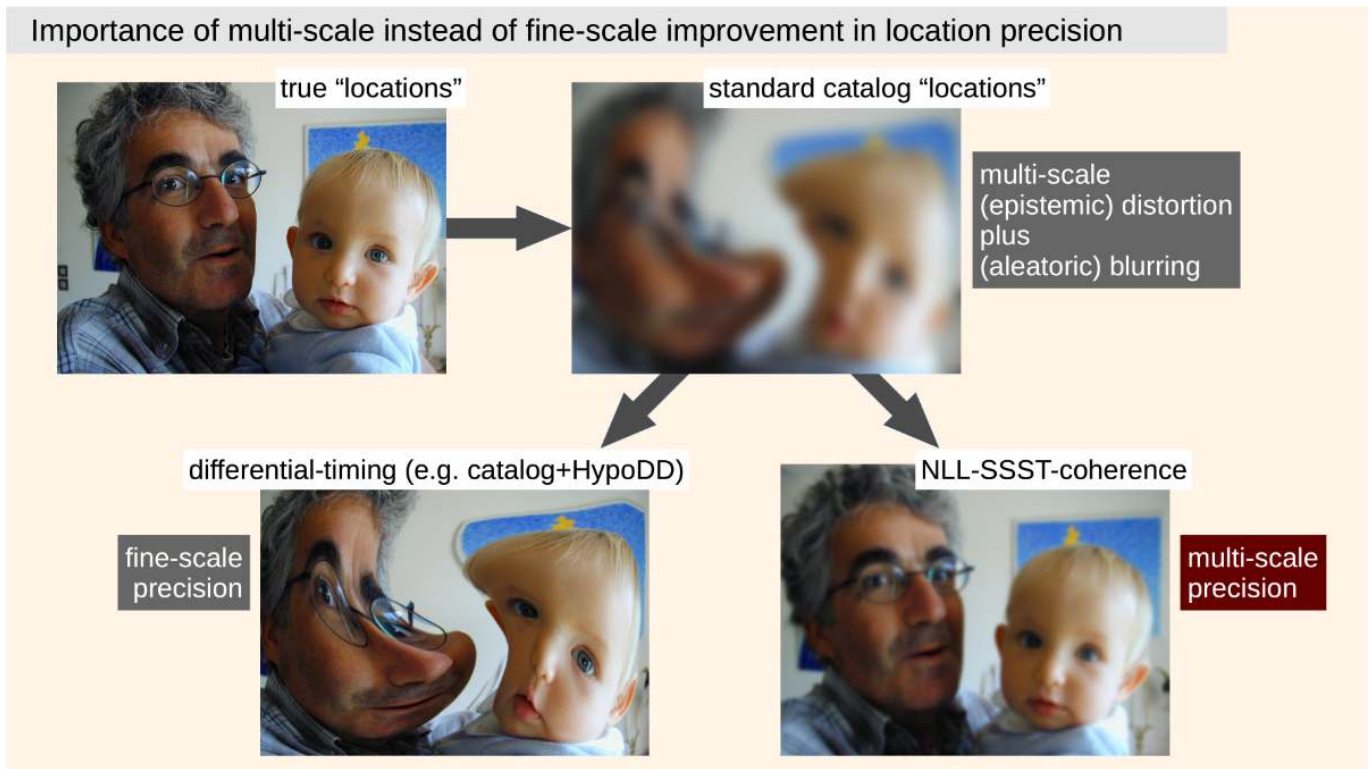


Figure 1 A photo analogy representing the multi-scale improvement in location precision of NLL-SSST-coherence versus the fine-scale improvement of differential-timing methods. NLL-SSST-coherence may not achieve the same precision at finest scales as differential-timing methods such as HypoDD or GrowClust, but can give a better representation of the true geometry of locations across other scales.

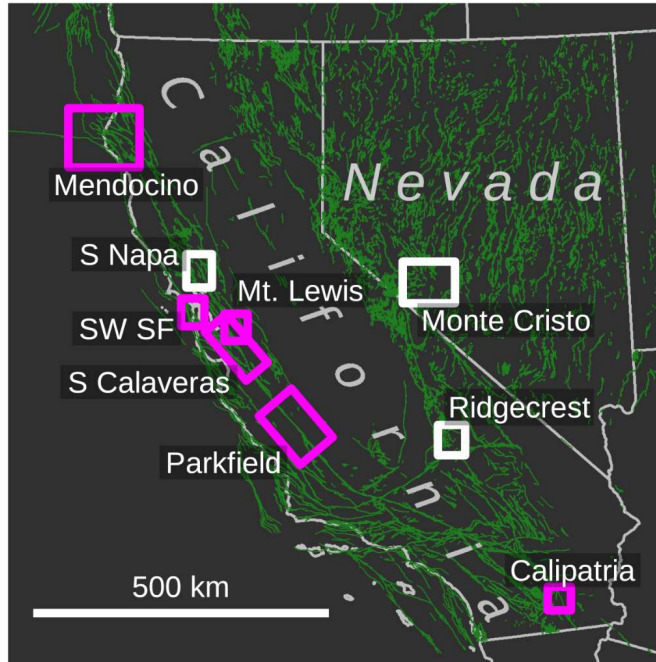


Figure 2 Study areas. Study areas in California and Nevada for NLL-SSST-coherence relocations presented (magenta) and discussed (white) in this work. Green lines show faults from the USGS Quaternary fault and fold database for the United States.

km long, near-straight stretch of the San Andreas fault which exhibits surface creep, and just northwest of a long, locked stretch of the fault that hosted the 1857 M

7.9 Fort Tejon earthquake (Bakun et al., 2005; Langbein et al., 2005). It is generally accepted (e.g. Simpson et al., 2006; Thurber et al., 2006) that there is a single main fault surface at seismogenic depth for the 2004 rupture, and that this rupture falls not along the curved, main San Andreas surface trace, but instead along and under the straighter, Southwest Fracture zone (Figure 3).

For the Parkfield area, NCSS-DD HypoDD relocations (NCSS-DD Waldhauser and Schaff, 2008; Waldhauser, 2009) show a fault geometry that is kinked and small-scale segmented (Figure 3ac Waldhauser et al., 2004), a common result for high-precision, differential-timing relocation. In contrast, NLL-SSST-coherence relocations (Figure 3bd) show a much smoother, near-planar fault surface across scales from sub-km to the ~50 km study extent. The difference in geometry for the two sets of relocations is emphasized by a singular value decomposition (SVD) fit of a single plane to each of the respective hypocenter sets (Figure 3cd); the mean absolute deviation of NLL-SSST-coherence hypocenters from their SVD plane (140 m) is 54% of that for NCSS-DD (260 m). These characteristics and differences between the two sets of relocations are accentuated in stretched views of the seismicity (Supplementary Figure S1) and in animated, rotating views along the San Andreas fault zone (Supplementary Movies S1 and S2).

The near-planar surface defined by the NLL-SSST-coherence relocation follows the overall trend of surface faults on the largest scales, but not the smaller scale segmentation and complexity of these faults. At seismogenic depth the NLL-SSST-coherence relocations show

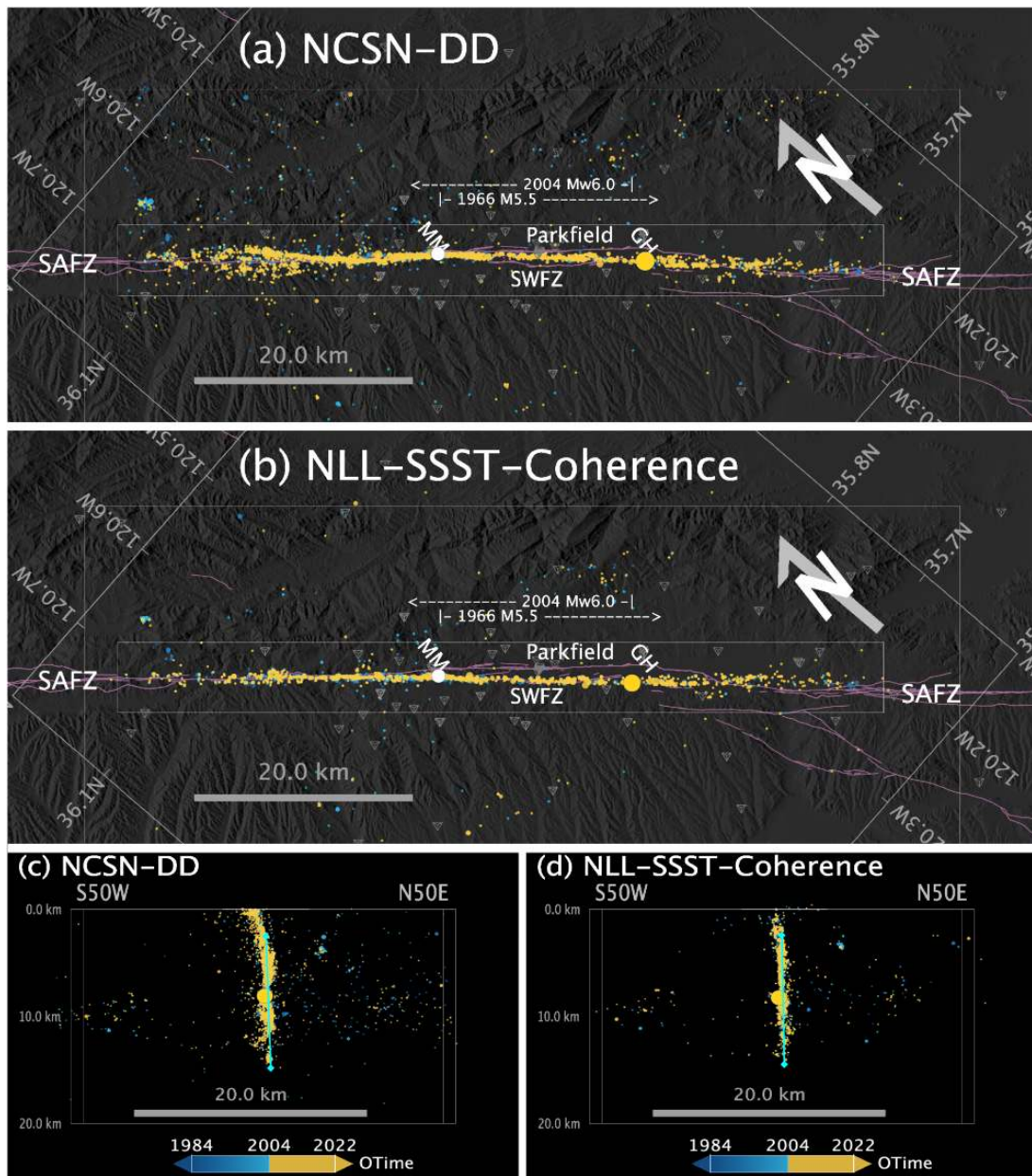


Figure 3 Seismicity along the central San Andreas fault zone around Parkfield. $M \geq 1.0$ hypocenters from 1984-01-01 to 2022-02-22 in map view for (a) 10384 NCSN-DD and (b) 11314 NLL-SSST-coherence event relocations; inner gray box shows area used for SVD fit of plane to hypocenters from 2.5 to 15 km depth. Lateral views from $\sim S40^\circ E$ along best fit SVD plane (near vertical, cyan line) for each catalog shown for (c) NCSN-DD and (d) NLL-SSST-coherence. Hypocenter color shows origin time (yellow events after the 2004 Mw 6.0 mainshock), symbol size is proportional to magnitude; larger yellow and white dots show 2004 Mw 6.0 hypocenter and approximate 1966 M 5.5 epicenter, respectively. Inverted pyramids show nearby seismic stations used for relocation. Light purple lines show faults from the USGS Quaternary fault and fold database for the United States, SAFZ – San Andreas fault zone, SWFZ – Southwest Fracture zone, MM – Middle Mountain, GH – Gold Hill. Background topography from OpenTopography.org. See also Supplementary Movies S1 and S2.

no offsets or bends below the epicenters of the 1966 M ~ 6 or 2004 Mw 6.0 Parkfield earthquakes. These two events ruptured nearly the same fault area but initiated at opposite ends of this area and propagated in opposing directions (Bakun et al., 2005); such differences in initiation point and rupture direction may be possible due to the planarity and smoothness of the fault at depth, i.e., fault complexity was not a controlling factor for initiation and other rupture characteristics (Bakun et al., 2005).

3.2 Smooth, arcuate faulting: the southern Calaveras fault zone

We next examine the 1984 Mw 6.2 Morgan Hill, California sequence and background seismicity along a 90 km stretch of the southern Calaveras fault zone (Figure 4).

The southern Calaveras fault zone, which exhibits shallow creep, branches towards the north from the north end of the creeping section of the San Andreas fault (Watt et al., 2014). Since the installation of dense seismometer networks in the 1970’s along this stretch of the Calaveras fault zone there has been abundant micro-

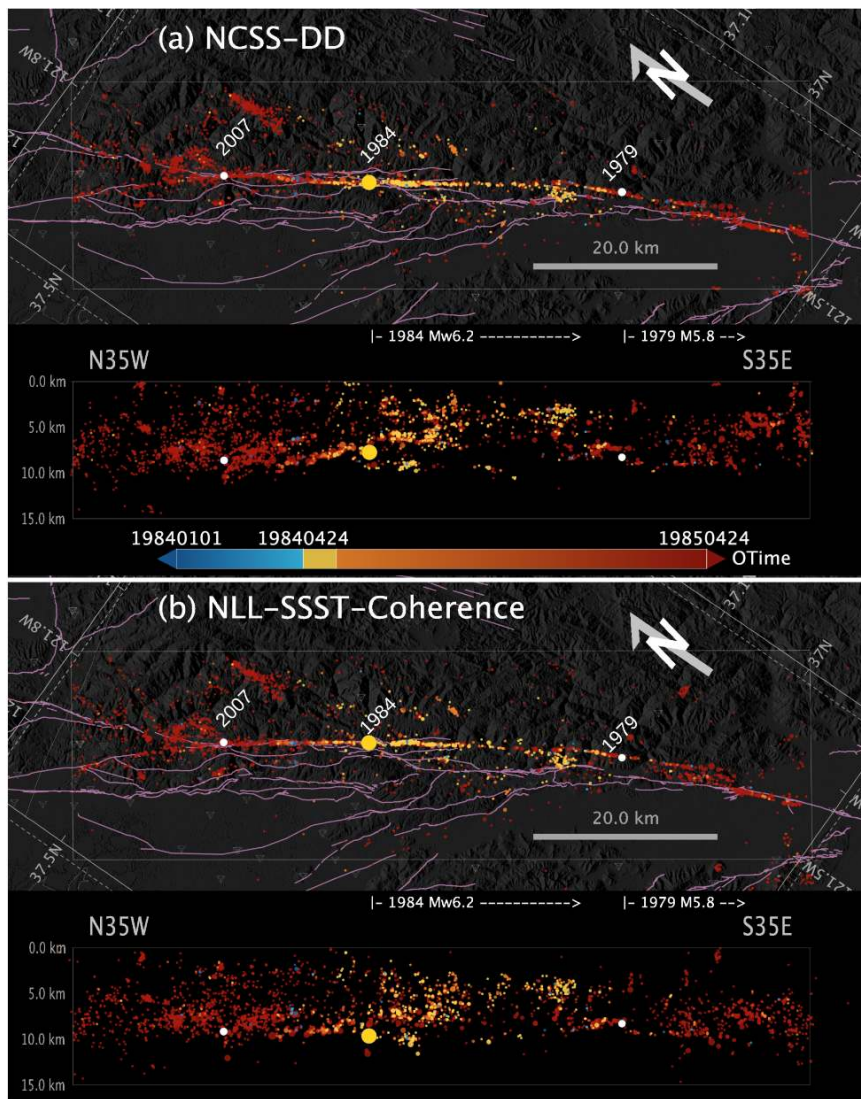


Figure 4 Seismicity along the southern Calaveras fault zone. $M \geq 1.5$ hypocenters from 1984-01-01 to 2022-10-26 in map and lateral view from $S55^\circ W$ of (a) 6138 NCSS-DD and (b) 6419 NLL-SSST-coherence event relocations. Hypocenter color shows origin time (yellow events within first month after the 1984 Mw 6.2 mainshock), symbol size is proportional to magnitude; larger white dots show the 1979 M 5.8 and 2007 M 5.4 hypocenters, and large yellow dot the 1984 Mw 6.2 hypocenter. Map views are tilted to best align along the near-vertical plane of Mw 6.2 aftershocks around its hypocenter: NCSS-DD view plunges 81° NE; NLL-SSST-coherence view plunges 84° NE. Dashed arrows show approximate main rupture direction and extent for the 1979 M 5.8 (Reasenber and Ellsworth, 1982) and 1984 Mw 6.2 (Cockerham and Eaton, 1984) events. Inverted pyramids show nearby seismic stations used for relocation. Light purple lines show faults from the USGS Quaternary fault and fold database for the United States. Background topography from OpenTopography.org. See also Supplementary Movie S3.

seismicity and several moderate earthquakes, including the 1979 M 5.8 Coyote Lake and the 1984 Mw 6.2 events (Oppenheimer et al., 1990), and the 2007 M 5.4 Alum Rock earthquake. For this area, high-precision, NCSS-DD differential-timing relocations (Figure 4a; see also Schaff et al., 2002) again show a kinked and segmented character for the main lineation of seismicity. In contrast, NLL-SSST-coherence relocations (Figure 4b) form a smoother, arcuate lineation on intermediate and larger scales, especially along and around the 1984 Mw 6.2 aftershock zone (yellow events in figure). This arcuate lineation follows closely the circumference of a circle of radius 428 km centered to the south-southwest (Supplementary Figure S2), the significance of which we discuss later.

Neither set of relocations shows a clear relation of

seismicity to the complex multitude of surface mapped faults, beyond similar, largest scale trends. And neither set shows a bend in the fault at seismogenic depth near the 1979 M 5.8 or 1984 Mw 6.2 hypocenters; such bends on surface fault traces have been proposed as related to the rupture initiation point for these and other earthquakes (Bakun, 1980; King and Nábělek, 1985). Both events ruptured to the southeast (Figure 4), with the 1984 Mw 6.2 rupture terminating to the southeast where both sets of relocations show clustered, shallow, off-fault aftershock seismicity and a possible small offset or kink at depth, while the 1979 M 5.8 main rupture likely terminated at a right step in fault segments, with later aftershocks along the segment further to the southeast (Reasenber and Ellsworth, 1982; Oppenheimer et al., 1990). The 2007 M 5.4 event also ruptured to the south-

east (Oppenheimer et al., 2010).

3.3 Smooth faulting in oceanic crust: Mendocino triple-junction, California

Next, we consider seismicity from 1995-2022 around the Mendocino triple-junction, Northern California (Figure 2). This area hosts a fault-fault-trench triple junction with complex, 3D plate interactions: dextral Pacific – Gorda plate motion across the Mendocino fault zone (MFZ), oblique subduction of the east-dipping Gorda plate under the North American plate along the Cascadia subduction zone, and dextral North American – Pacific plate motion across the San Andreas fault (Smith et al., 1993).

For the Mendocino triple-junction area, high-precision, differential-timing NCSS-DD relocations (Figure 5a) show diffuse lineations of seismicity offshore along the MFZ and in the underlying, subducting Gorda plate. In contrast, NLL-SSST-coherence relocations (Figure 5b) show a smooth, narrow, gently curved distribution of hypocenters along the MFZ around 20 km depth (yellow events in figure) and, within the Gorda plate, show several narrow, ~20-30km deep, NW-SE lineations of events suggesting smooth or linear sets of parallel fractures (Gong and McGuire, 2021; Lomax and Henry, 2022). For these relocations, NLL-SSST-coherence precision may only be 500 m to 1 km in some areas due to poor station coverage (Supplementary Table S1).

3.4 Smaller scale, smooth, planar faulting: the 1986 M 5.7 Mount Lewis sequence

We next examine on a smaller scale the 1986 M 5.7 Mount Lewis sequence and surrounding, 1984-1999 background seismicity (Figure 2). This sequence occurred just to the north of our southern Calaveras fault zone study in an ~25 km, north-south area with no mapped surface faults. The 1986 M 5.7 mainshock had a north-south oriented, right-lateral strike-slip mechanism and a highly productive aftershock sequence within in a distinctive, north-south oriented “hourglass” shaped volume (Zhou et al., 1993; Dodge et al., 1996; Kilb and Rubin, 2002).

For the Mount Lewis sequence, high-precision, differential-timing NCSS-DD relocations (Figure 6a), more clustered and organized, NLL-SSST-coherence relocations (Figure 6b) and the results of Kilb and Rubin (2002) all define well the extensive, volumetric, hourglass form of seismicity to the north and south of the mainshock hypocenter. All sets of relocations also show a narrow, central, ~2 km long (NCSS-DD) to ~3 km long (NLL-SSST-coherence; see Supplementary Movie S5) north-south, tabular trend of foreshocks (blue) and early aftershocks (yellow) around the mainshock hypocenter, extending from about 2 km above to 1 km below the hypocenter (large yellow dot). Kilb and Rubin (2002) interpret this trend as a kinked mainshock rupture surface. Here, SVD analyses of events within a 1.2 km wide rectangular prism centered on the tabular trends shows that near vertical planes fit well (mean

absolute deviation 66 m for NCSS-DD, 35 m for NLL-SSST-coherence) all foreshocks, mainshock and early aftershocks while covering an area similar to that inferred through teleseismic waveform analysis for the mainshock rupture (Zhou et al., 1993). For the NLL-SSST-coherence relocations, the aftershocks just north and south of the SVD plane are mainly offset east and west, respectively, from the strike of the plane, as expected for aftershocks concentrating in the extensional quadrant of a right-lateral, strike-slip event (Kim et al., 2004). These results suggest a simple, smooth, planar surface for the main M 5.7 rupture, while most aftershocks occur outside this surface on extended, complex secondary structures, including fault sets perpendicular to main rupture, indicating an immature fault system (Kilb and Rubin, 2002).

3.5 Indirect indication of smooth, planar faulting: southwest of San Francisco

We next consider background seismicity along ~50 km of the San Andreas fault zone (SAFZ) to the south and west of San Francisco (Figure 2). The SAFZ to the west of San Francisco likely hosts the hypocenter of the M 7.9 1906 California earthquake (Lomax, 2008). NLL-SSST-coherence relocations from Feb 1981 to April 2021 for this area are shown in Figure 7.

A major part of the seismicity forms an ~35 km long zone at about 5-11 km depth which is rotated about 5° clockwise to and crosses under the surface expression of the SAFZ. This seismicity has predominantly extensional focal mechanisms and is associated with an extensional, right stepover between the onshore San Andreas fault and the offshore Golden Gate fault (Zoback et al., 1999; Parsons, 2002; Lomax, 2008).

To the south of San Francisco, the onshore surface trace of the San Andreas fault (SAFZ and cyan line in Figure 2a) is nearly linear and exhibited up to 4.5 m of rupture during the M7.9 1906 earthquake (Reid and Lawson, 1908). These relations and evidence from seismicity (Zoback et al., 1999) and reflection seismics (Hole et al., 1996) suggest that the active fault surface that hosted 1906 rupture at seismogenic depth may be represented by a vertical plane under and along the surface trace. Such a plane delimits well the northeastern boundary of the extensional seismicity along this segment (Figure 7ab), as also found by Zoback et al. (1999) and Lomax (2008). The truncation of ongoing extensional seismicity along a vertical fault may indicate a strong contrast in geologic structure across the fault (e.g. Liu et al., 2003) such that present-day background stress leads to, in this case, distributed, normal faulting to the southwest while the northwest side remain mainly aseismic.

Along and below the northeast boundary of the extensional seismicity there is a 30 km long set of seismicity clusters at around 11–13 km depth (Figure 7ac) with mainly strike-slip focal mechanisms (Lomax, 2008). This set of deep clusters is well fit by a linear trend rotated about 5° clockwise to the SAFZ (white rectangle in Figure 7c) and which appears to connect the San Andreas and Golden Gate faults below and across the ex-

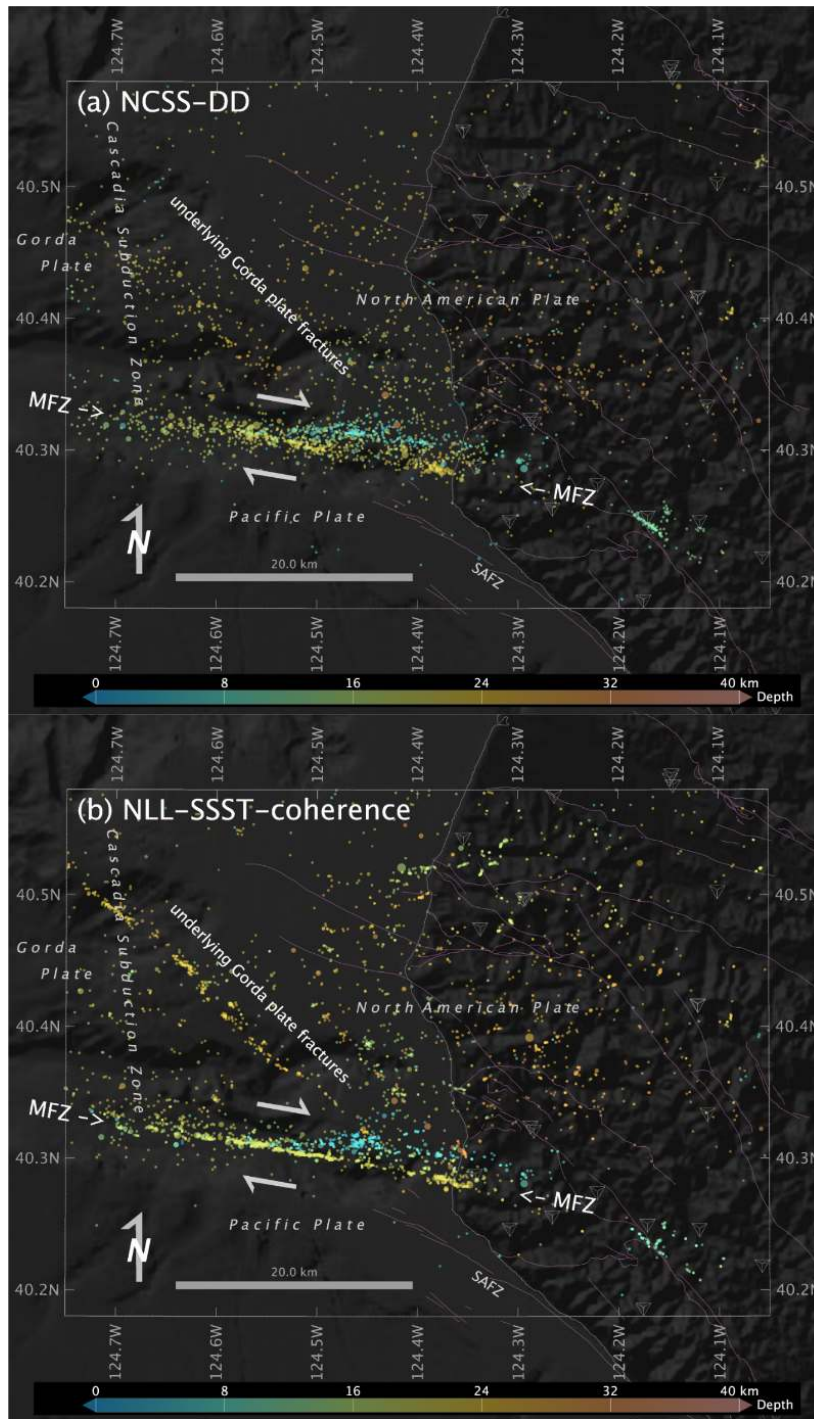


Figure 5 1995-2024 Mendocino triple-junction relocations. Map view of $M \geq 2.0$, 1995-01-01 to 2024-04-01 hypocenters for (a) 2585 NCSS-DD and (b) 3645 NLL-SSST-coherence event relocations. Hypocenter color shows depth, symbol size is proportional to magnitude. Inverted pyramids show nearby seismic stations used for relocation. Light purple lines show onshore faults from the USGS Quaternary fault and fold database for the United States; MFZ – Mendocino fault zone; SAFZ – San Andreas fault zone. Background topography image from www.ncei.noaa.gov. See also Supplementary Movie S4.

tensional stepover. This linear trend of deep seismicity suggests either a linear, strike-slip fault structure around 12 km depth, or localized, synthetic, or antithetic faulting at the base of a brittle crust in response to dextral shear across an underlying, linear ductile zone (Lomax, 2008). An upwards extension of the linear trend of deep seismicity appears to delimit the northeastern boundary of shallower extensional seismicity (Figure 7a), but examination of the geometrical relations in 3D and structural considerations favor that this

boundary is right-stepping with segments parallel to the main SAFZ.

4 Discussion

4.1 NLL-SSST-coherence methodology

NLL-SSST and NLL-coherence together greatly increase precision (relative location accuracy) on multiple scales within a standard, arrival-time location framework (Fig-

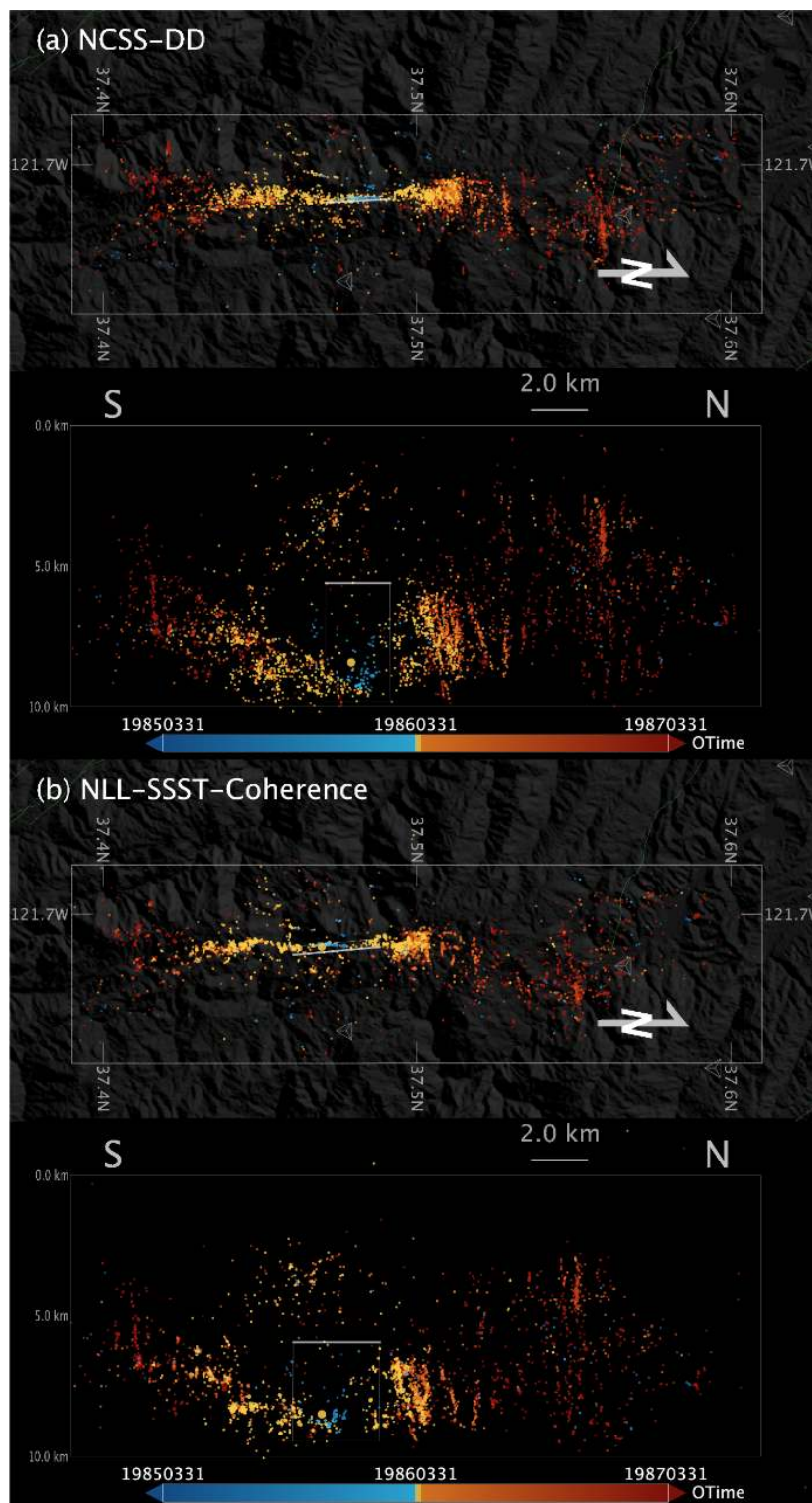


Figure 6 1984-1999 Mount Lewis sequence relocations. $M \geq 1.0$ hypocenters from 1984-01-01 to 1999-12-31 for (a) 3343 NCSS-DD and (b) 3503 NLL-SSST-coherence event relocations in map view (upper panels) and lateral view from east (lower panels). Hypocenter color shows origin time (cyan events show foreshocks before the M 5.7 mainshock (large yellow dot), yellow events the first 7 days of aftershocks), symbol size is proportional to magnitude. Inverted pyramids show nearby seismic stations used for relocation. White rectangles show plane of best SVD fit to hypocenters in a 0.6 km wide zone around the rectangle, heavy line indicates top of the plane. Background topography image from OpenTopography.org. See also Supplementary Movie S5.

ure 1; Lomax and Savvaidis, 2022). Building on and making use of the thorough, probabilistic global sampling and robust, EDT likelihood function of NLL, NLL-SSST improves multi-scale precision by iteratively removing common-mode traveltime residuals at available

stations as a function of hypocentral position. This procedure reduces epistemic model errors and location bias between nearby events located with differing sets of stations or phase types. NLL-coherence location improves smaller scale precision by stacking probabilis-

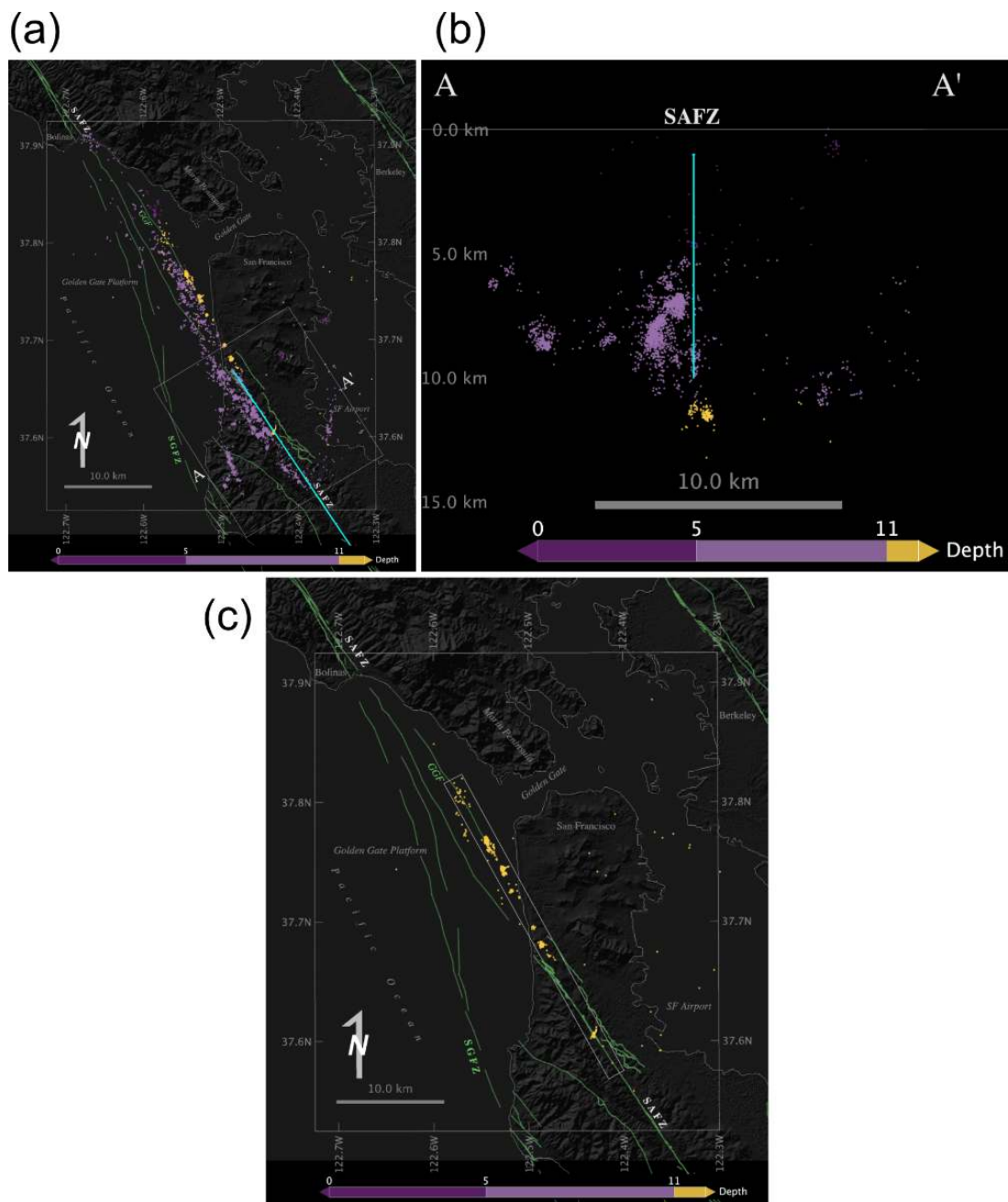


Figure 7 1981-2021 relocations southwest of San Francisco. NLL-SSST-coherence relocations of available NCSS events 1981-01-01 to 2022-11-30. 3170 events with 68% confidence ellipsoid semi-axis ≤ 2 km shown in a) map view, b) in section view from the southeast (from N146E) along the SAFZ and including only events within the white box in panel a), and c) in map view with only events deeper than 11 km plotted to emphasize the trend of deep clusters (white rectangle). Hypocenters are shifted randomly 0.2 km to avoid overlapping symbols. Green lines show faults from the USGS Quaternary fault and fold database for the United States and from Parsons (2002), SAFZ – San Andreas fault zone, SGFZ – San Gregorio Fault zone, GGF – Golden Gate Fault. The cyan line in panel a) shows a vertical plane from 1 to 10 km depth aligned to the nearly linear segment of the SAFZ south of San Francisco; the SAFZ and 1906 rupture are coincident with the cyan line. Background topography image from OpenTopography.org. See also Supplementary Movie S6.

tic, NLL-SSST location PDF’s of nearly co-located, multiplet events, as measured by waveform similarity. This stacking of PDF’s effectively reduces aleatoric data error and suppresses outliers in the underlying arrival times, while filling in missing arrival time data across multiplet events, resulting in a data-driven, spatial coalescence of location for events with similar waveforms. In the following, as explained earlier, “multi-scale” precision ranges from approximately sub-km (as low as 100-200m) to the extent of each study area.

In contrast to the coherence-weighted stacking of PDFs for nearby events in NLL-coherence, cross-correlation based, differential-timing methods such as HypoDD or GrowClust achieve high to very high, fine-scale precision through explicit, inter-event, differential location. This location involves over nearby event pairs of differences in distance along event-station ray directions, as constrained by all available arrival-time differences and the used velocity model. For relocation studies with good station coverage, and thus good ray

coverage around the events, these differential-timing methods should achieve higher, finest-scale precision than NLL-SSST-coherence. However, for cases of poor station and ray coverage, NLL-SSST-coherence may retain higher relative location accuracy and better depth control than do cross-correlation based, differential-timing methods, as indicated by our results for Mendocino triple-junction and Mount Lewis seismicity and previous results for the 2020 Mw 5.8 Lone Pine, California sequence (Lomax and Savvaidis, 2022). Furthermore, differential-timing methods such as HypoDD or GrowClust usually preserve or allow only slight change in the centroid of the starting locations for individual clusters of high similarity events (Waldhauser and Ellsworth, 2000; Waldhauser and Schaff, 2008; Trugman and Shearer, 2017) and thus, in general, will not improve larger, multi-scale precision beyond that of the starting locations (Figure 1). It is possible that applying cross-correlation based, differential-timing methods after NLL-SSST relocation would produce optimal multi- and finest-scale location precision. And applying these methods after NLL-SSST-coherence may also have advantages, as NLL-coherence can collect noisy, outlier locations back into their correct clusters. The XCORLOC method (Neves et al., 2022) precedes cross-correlation based, differential-timing relocation with L1 and L2 norm SSST and so can improve multi-scale precision in a manner analogous to NLL-SSST-coherence.

There is no evident reason why the NLL-SSST-coherence methodology might smooth hypocenters locations over larger distances as an artifact. Indeed, the iterative, multi-scale NLL-SSST procedure generates smaller-scale traveltime corrections that are independent over larger distances; this independence should preserve true roughness or offsets in alignments of seismicity. For the case of large error in the arrival-time data, the independence of NLL-SSST corrections over larger distances would more likely produce artifact error and offset between clusters of hypocenters than artifact smoothing. For Mount Lewis, the NLL-SSST-coherence relocations match well detailed features of the high-precision NCSS-DD (Figure 6) and Kilb and Rubin (2002) relocations, including definition of the main rupture surface, complex secondary structures and fault sets perpendicular to the main rupture, without exhibiting additional smoothing or smearing of these features that might be artifacts of the NLL-SSST-coherence methodology.

To further illustrate this point, we compare NLL-SSST-coherence with high-precision, differential-timing relocations based on a precursor to GrowClust (HYS Hauksson et al., 2012) for the complex, 2021 Mw 5.3 Calipatria sequence (Supplementary Figure S3). This sequence, in the Brawley Seismic zone at the southern end of the San Andreas fault system, ruptured 3 larger, near-orthogonal segments over scales of ~2-10 km and numerous smaller scale features over about 7 days (Hauksson et al., 2022). NLL-SSST-coherence and HYS relocations of the Calipatria seismicity (Supplementary Figure S3) closely reproduce the same features over all scales, including the larger scale, near-orthogonal planes, and smaller scale splay and

clustered seismicity, while both set of relocations show similar depth distribution of these features, including shallowing of a sharp base of seismicity towards the north. These results show that, besides larger scale distortion due to different velocity models and station correction procedures, NLL-SSST-coherence does not oversimplify or smooth distributed, multi-scale, multi-fault ruptures compared to high-precision, differential-timing relocations.

Similar to NLL-SSST, 3D, tomographic, velocity model inversions implicitly generate station and source dependent traveltime corrections, and may involve collapsing scale lengths. However, differential-timing relocation in 3D tomographic models for Parkfield relocations (Thurber et al., 2006) do not show as smooth, vertical, or planar a surface as does NLL-SSST-coherence (Figure 3b). This difference may be related to the mapping in tomographic inversion of all traveltime residuals to unique, 3D, V_p and V_s velocity grids, while SSST maps the residuals to a large set of 3D, station V_p and V_s traveltime grids; this latter procedure retains many more degrees of freedom and so can preserve a greater amount of information from the residuals that may be useful for precise location.

4.2 Relocation results

With relocation of earthquake sequences and background seismicity along the San Andreas (Parkfield) and southern Calaveras strike-slip faults in California, we have shown that NLL-SSST-coherence relocated seismicity at seismogenic depth along major faults and surrounding large-earthquake ruptures often defines narrow, multi-scale smooth, planar (e.g., Parkfield) or arcuate (e.g. southern Calaveras), near-vertical surfaces across multiple scales. For Parkfield, the high-precision relocations of Thurber et al. (2006) (see interpretation of Simpson et al., 2006), and the XCORLOC relocations of Neves et al. (2022) also suggests, on the intermediate and largest scales, smooth, near-vertical faulting.

NLL-SSST-coherence relocations for the Mendocino triple-junction area show that such multi-scale smooth faulting also occurs for strike-slip faulting in oceanic crust, as found in other areas (e.g. Schlaphorst et al., 2023). NLL-SSST-coherence relocations to the southwest of San Francisco suggests a deep, linear fault or response to a deeper, linear shear zone over ~30 km. For the 2019 Mw 7.1 Ridgecrest, California, sequence high-precision (e.g. Ross et al., 2019; Shelly, 2020) and standard NLL locations (Lomax, 2020a) define two planar, orthogonal faulting surfaces for main rupture of the Mw 6.4 foreshock, while Lomax (2020b) additionally determines that these planes are at different depths and non-intersecting.

On a smaller scale, for NLL-SSST-coherence relocations of the 1986 M 5.7 Mount Lewis sequence (Figure 6b), a near vertical, ~4x4 km plane fits well the foreshocks, mainshock and early aftershock hypocenters and covers an area similar to that of mainshock rupture as inferred through teleseismic waveform analysis. An hourglass form of aftershocks to the north and south of this simple, planar mainshock rupture surface, sug-

gest complex splay and cross faulting which falls mainly within the dilatational quadrants of right-lateral mainshock rupture as delimited by the $\sim 4 \times 4$ km plane.

The 2020 Mw 6.5 Monte Cristo Range, Nevada sequence occurred along an immature, strike-slip fault zone, with no clear surface traces related to primary rupture (Koehler et al., 2021). At seismogenic depth, NLL-SSST-coherence relocations for this sequence (Lomax, 2020a) define two, en-echelon, smooth, planar faulting segments corresponding in size and orientation to expected and modeled mainshock rupture, as well as lateral and shallow secondary and splay faulting forming an extensive damage zone, in similarity to the Mount Lewis results.

For NLL-SSST-coherence relocations to the south of San Francisco, the northeast limit of diffuse, extensional seismicity corresponds to a multi-scale smooth, vertical, planar fault along the SAFZ. In this case, the seismicity does not directly fall on and define an active surface of faulting, but instead delimits the edge and depth limits of the likely 1906 faulting surface that is currently mainly aseismic. Preliminary analysis of NLL-SSST-coherence relocations for the 2014 M 6.0 South of Napa, California sequence and background seismicity shows similar, though less clear, indirect indications of planar faulting for the M 6.0 mainshock rupture.

These NLL-SSST-coherence relocations define multi-scale smooth faulting over at least 10's of km for segments of mature, strike-slip fault zones, and over the likely rupture zones of large and moderate earthquakes along these faults and on less mature faults. These results suggest that multi-scale smooth (down to sub-km lengths), planar and arcuate faulting is characteristic of strike-slip fault zones at seismogenic depth and perhaps necessary for larger earthquake rupture. We next consider some important implications of these results.

4.3 Rupture physics

The smoothness and curvature of fault segments at seismogenic depth likely influences earthquake rupture physics—initiation, rupture, and arrest (Okubo and Dieterich, 1984; Ben-Zion and Sammis, 2003; Dieterich and Smith, 2010; Fang and Dunham, 2013), and perhaps enables the occurrence of larger earthquakes (Goebel et al., 2017, 2023). Earthquake initiation may be possible anywhere within smooth fault segments, though most likely at non-geometrical asperities—areas of stress concentration either within the segments due to previous rupture history or material heterogeneities and perhaps indicated by concentrations of microseismicity, or at limits of the segments including at kinks or stepovers (Das and Henry, 2003; Aki, 1979; King, 1986; Scholz, 2019). The arrest of earthquake rupture is likely favored at barriers such as kinks, steps, or other fault complexities at the limits of smooth segments at seismogenic depth, as well as within smooth segments at areas of stress relaxation due to previous rupture history (Sibson, 1985; King, 1986; Scholz, 2019). Laboratory experiments indicate that smooth faults have larger coseismic slip, lower residual stress and fewer aftershocks

compared to rough faults (Goebel et al., 2023).

Most importantly, for faults that are smooth and planar or horizontally arcuate (especially when following closely the circumference of a circle, as is the case for the southern Calaveras; Supplementary Figure S2), there may be negligible geometrical interactions and resulting backstresses (Dieterich and Smith, 2010) impeding strike-slip rupture displacement. In this case, minimal energy is absorbed by off-fault inelastic deformation as fracture energy (Cocco et al., 2023), and a maximum of strain energy released during rupture would be available to further drive the rupture. Thus, sustained earthquake rupture, and perhaps even the occurrence of larger earthquakes, would be more likely over a smooth fault surface than a rough or fine-scale segmented surface (e.g. Dieterich and Smith, 2010; Fang and Dunham, 2013; Perrin et al., 2016).

Multi-scale smooth faults are also considered most likely to support sustained supershear rupture propagation (Bouchon et al., 2010; Bruhat et al., 2016), and should radiate relatively less high-frequency energy than rough faults (Madariaga, 1977; Shi and Day, 2013; Trugman and Dunham, 2014). For planar faulting, the relative displacement between crustal blocks would be planar shear, while the displacement of blocks across arcuate faults would include a rotational component.

In addition, for a multi-scale smooth, curved fault, there may be a preferred direction for rupture (Rubin and Gillard, 2000), perhaps due to the position of the curved fault surface forward of rupture relative to the dilatational and extensional quadrants of the rupture (Fliss et al., 2005). This is suggested by our results for the southern Calaveras fault zone where the 1984 Mw 6.2, 1979 M 5.8 and 2007 M 5.4 events all ruptured to the southeast (Figure 4b). Given the sense of curvature of NLL-SSST-coherence seismicity and right-lateral slip, for southeastward rupture the fault forward of the rupture front is in the dilatational quadrant of strain from the current and previous rupture. This dilatational strain would decrease normal stress across the fault, producing dynamic “unclamping” in front of the rupture and facilitating further slip, in a manner analogous to a continuum of infinitesimal, extensional bends or stepovers (Poliakov et al., 2002; Oglesby, 2005; Oglesby and Mai, 2012; Parsons and Minasian, 2015). Under this mechanism, rupture in the opposite direction, northwest in this case, would be impeded, as with infinitesimal, compressional bends or stepovers, which may explain why 1979 M 5.8 rupture did not propagate or trigger slip to the northwest into the presumably well loaded, future rupture zone of the 1984 Mw 6.2 event. A general rule would be that rupture is promoted in the direction along which the fault is concave to the right for right-lateral slip and concave to the left for left-lateral slip. This mechanism could explain sense of rupture for other large earthquakes on smoothly curving segments of strike-slip faults, including for southeastwards rupture for the 2002 Mw 7.9 Denali fault, Alaska-Canada earthquake (Eberhart-Phillips et al., 2003), for primarily eastwards rupture of the 1943 Ms 7.7 Tosya, Turkey earthquake along the North Anatolian fault (Dewey, 1976; Barka and Kadinsky-Cade, 1988; Stein et al., 1997)

and perhaps for at least the first half of westward rupture for the 1939 Ms 7.9 Erzincan, Turkey earthquake (Emre et al., 2021) where the North Anatolian fault appears mildly concave to the north (Emre et al., 2018). A preferred, eastward rupture direction due to fault curvature for the 1943 Tosya earthquake could in part explain why it ruptured in the opposite direction to that of other major events along the North Anatolian fault in the past century and why its epicenter is, anomalously, not in an area of increased stress from previous events (Stein et al., 1997). For a planar fault, this mechanism is not active and gives no preferred rupture direction, which is consistent with the 1966 M 5.5 and 2004 Mw 6.0 Parkfield earthquakes rupturing in opposing directions from opposite ends of a segment of the San Andreas fault that our NLL-SSST-coherence results show is smooth and planar (Figure 3b).

Most of these relations between rupture physics and smooth faulting may apply to individual fault segments of any size in a self-similar manner, so that, for example, the smaller is a segment of smooth faulting, the smaller is the largest rupture that can occur on that segment. Thus, while seismicity on secondary, splay and damage zone faulting, such as around the apparently smooth main rupture segments for the Mount Lewis and Monte Cristo (Lomax, 2020b) sequences, and aftershock seismicity in general may not exhibit larger scale patterns suggesting fault smoothness, individual events and localized clusters could follow these relations on the (small) scale of their rupture segments.

On larger scales, many complex and very large earthquakes involve rupture on a number of separate fault segments, each of which may be multi-scale smooth, as is the case for Monte Cristo, and possibly the case for the 2016 Mw 7.8 Kaikōura, New Zealand earthquake (Hamling et al., 2017), and for the 1993 Mw 7.3 Landers (Hauksson et al., 1993) and 1999 Mw 7.1 Hector Mine (Hauksson et al., 2022) earthquakes in California. However, aftershock seismicity for large earthquakes occurs mainly or almost entirely off of main rupture surfaces (e.g. Das and Henry, 2003; Liu et al., 2003; Goebel et al., 2023) making it difficult to define precisely the geometry of main rupture surfaces for very large earthquakes.

It is possible that on the largest scales, e.g., for the 1857 M 7.9 and 1906 M 7.9 rupture zones along the San Andreas fault, main rupture may occur on one or few long, smooth segments. In this case features of rupture physics of smooth faults discussed above combined with a possible strong locking of smooth faults due, for example, to efficient healing by cementation or other processes on thin, smooth fault surface (Muhuri et al., 2003; Williams and Fagereng, 2022), may be explanations for potentially long recurrence intervals and resulting large size of these events. Additionally, the seismicity patterns southwest of San Francisco, where upper crustal seismicity occurs mostly off the SAF with dominantly extensional focal mechanisms, is consistent with near complete release of shear stress after the 1906 earthquake. Thus, for a given length scale, a smooth segment may be expected to take more time than a rough segment to reload back to a critical state after rupture.

This self-similarity likely extends to the concept of fault maturity, characterized by increased simplification including smoothing and reduced extent of lateral damage zones (Naylor et al., 1986; Wesnousky, 1988; Scholz, 2019). We find that sequences on immature fault systems such as Mount Lewis and Monte Cristo, though terminated by extensive damage and splay faulting, contain core segments of main rupture which may be planar, multi-scale smooth surfaces with little, lateral damage zone seismicity. Such main rupture surfaces may be mature, on their smaller length and age scales, in the same sense as are much longer segments of major fault systems such as the San Andreas on much larger scales. Such a scale invariance is found by Evans et al. (2000) for faults exhumed from seismogenic depth, which show similarity of shear-induced microstructures and deformation mechanisms for faults 10 m to 10 km long starting from an early age as inferred from total slip.

4.4 Earthquake hazard and maximum size

Our overall results suggest identification of stretches of smooth faulting would help identify zones of earthquake hazard and possibly help quantify maximum earthquake size. This identification might be made directly from background seismicity or aftershocks falling on smooth surfaces, or indirectly by the distribution and geometry of clustered, diffuse, or other seismicity which may delimit stretches of aseismic, smooth faulting, as suggested in our analysis of seismicity south of San Francisco. Difficulties arise due to the possibility that future large earthquakes may occur in areas of current seismic quiescence, including gaps or locked patches, for example as indicated by the sparsity of recent seismicity along the 1857 M 7.9 and 1906 M 7.9 rupture zones on the San Andreas fault (Jiang and Lapusta, 2016; Scholz, 2019). In this case, if delimited by stretches of smooth faulting at seismogenic depth, near-silent segments of known or inferred fault zones might be identified as having elevated hazard. Also, surface mapped fault traces that are rough, multi-stranded or offset, but smooth on average over large length scales may be generated by smooth faulting at seismogenic depth, as is found with analogue fault modeling and interpreted for shallow natural faulting (Naylor et al., 1986; Klinger, 2010; Dooley and Schreurs, 2012), such surface features can therefore indicate elevated hazard.

4.5 Faulting at shallow versus seismogenic depth

Our NLL-SSST-coherence relocations along major strike-slip faults mainly concentrate on a single, smooth surface at more than a few km depth below zones with a multitude of surface traces, sometimes offset from these traces. These relations provide further evidence that surface traces and offsets of strike-slip fault zones reflect complex, shallow deformation, perhaps involving braided and upwards diverging fault structures (e.g. Christie-Blick and Biddle, 1985; Richard et al., 1995; Graymer et al., 2007), and not directly simpler and hidden slip surfaces at seismogenic depth (e.g.

Michael, 1988; Oppenheimer et al., 1990; Schaff et al., 2002; Ponce et al., 2004; Graymer et al., 2007; Watt et al., 2014; Chaussard et al., 2015), where most co-seismic slip and energy release occurs. Furthermore, NLL-SSST-coherence relocations for the Mount Lewis and Monte Cristo (Lomax, 2020b) sequences, along smaller and immature strike-faults, also define at seismogenic depth one or more smooth faulting surfaces which correspond to probable mainshock rupture surfaces. However, for these cases there are either no mapped surface faults (Mount Lewis) or complex, mapped surface fractures showing little relation to the deeper mainshock rupture (Monte Cristo), again emphasizing an indirect relation of surface features to main rupture surfaces at seismogenic depth.

In general, shallow deformation associated with earthquake ruptures involves significant diffuse anelastic deformation (e.g. Antoine et al., 2023). Several processes may contribute to explain a broadening of the zone of deformation around faults from the seismogenic zone to the surface, forming, for instance, flower structures above strike-slip faults (e.g. Harding, 1985). These include transition from unstable to stable sliding, which limits co-seismic slip on fault surfaces toward the surface (Scholz, 1998), and increasingly distributed damage due to relatively weaker shallow materials and the geometrical effect of the free surface, as shown in numerical and analog models (e.g. McClay and Bonora, 2001; Finzi et al., 2009; Wu et al., 2009; Ma and Andrews, 2010). For basic understanding of large earthquake faulting and hazard it is important to better define the geometrical transitions and physical connections between complex shallow faulting and potentially simpler and smoother fault segments at seismogenic depth.

4.6 Earthquake rupture modeling

The occurrence of earthquake rupture on multi-scale smooth faults justifies and would require the use of planar or smoothly curved fault segments for kinematic or dynamic numerical modeling (Ramos et al., 2022) of primary rupture and energy release of an earthquake at seismogenic depth. However, modeling of secondary, splay and damage zone faulting, such as is apparent around the main ruptures for the Mount Lewis and Monte Cristo sequences, likely requires use of complicated and rough model fault geometries (Ramos et al., 2022) or may be better represented by continuum mechanics-based numerical modeling (Preuss et al., 2020) across 3D volumes. Additionally, an indirect relation of surface fault traces to main rupture surfaces at seismogenic depth may preclude simple, downward projection of these shallow traces for rupture modeling; available information from aftershock or background seismicity, and geophysical and geologic studies should always be considered for constructing fault segments at seismogenic depth.

5 Conclusions

Our NLL-SSST-coherence relocations for California along major, strike-slip faults and surrounding large-earthquake ruptures show narrow, planar, or arcuate, near-vertical, multi-scale smooth faulting at seismogenic depth across the sub-km to 10's of km scales. These results suggest that multi-scale smooth faulting may be a characteristic of segments of major, strike-slip fault zones, of large earthquake rupture within individual fault segments, and, in a self-similar manner, of earthquake ruptures of smaller sizes.

The smoothness and curvature of faults likely influences large earthquake initiation (possible anywhere within or at the limits of smooth fault segments), rupture (multi-scale smooth faults facilitate, and may be required, for large earthquake rupture; if the fault is curved, there may be a preferred direction for rupture), and arrest (favored at kinks, steps, or other non-smooth fault complexities). Consequently, zones of earthquake hazard can be identified directly from planar and smooth alignments of seismicity and indirectly from patterns in clustered or diffuse seismicity.

Our findings provide further evidence that surface traces and offsets of strike-slip fault zones reflect complex, shallow deformation, and not may not correspond directly to simpler, smoother slip surfaces at depth where most co-seismic slip and energy release occurs. This relation has important implications for earthquake hazard assessment, and supports use of planar or smoothly curved surfaces, but not necessarily the complexity of surface rupture traces, for earthquake rupture modeling.

Acknowledgements

We gratefully thank Daniel Trugman, an anonymous reviewer and the editor Stephen Hicks for extensive comments that greatly improved this work. We thank Alberto Michelini and Clément Perrin for helpful comment and discussion, and Egill Hauksson for assistance with the high-precision, HYS catalog for the 2021 Calipatria sequence. Special thanks to the analysts, technicians and scientists who formed the high-quality, NCEDC and SCEDC arrival-time and event catalogs which made the precision of this work possible. We use LibreOffice (<https://www.libreoffice.org>, last accessed April 2023) for word processing, spreadsheet calculations and drawings, and Zotero (<https://www.zotero.org>, last accessed April 2023) for citation management. This work was performed outside any specific funding or grant.

Data and code availability

The supplementary information for this article includes Table S1 and Figure S1-3, and, in a repository (Lomax and Henry, 2023), Movies S1-7 showing animated views of NLL-SSST-coherence relocations presented in the main paper, Datasets S1-6 containing CSV format catalogs of NLL-SSST-coherence relocation results, and

File S1 containing run scripts and related set-up, configuration and other meta-data files for locations cases presented in this paper.

Earthquake catalogs and corresponding phase arrival times, waveforms and metadata were accessed through the Northern California Earthquake Data Center (NCEDC, 2014, last accessed April 2023), through the Southern California Earthquake Data Center SCEDC (2013, <http://service.scedc.caltech.edu/fdsnws/event/1/>, last accessed April 2023) from and through USGS-earthquake hazards available at <https://www.usgs.gov> and <https://earthquake.usgs.gov/earthquakes/search> (last accessed April 2023). The USGS Quaternary fault and fold database for the United States is available at: <https://www.usgs.gov/natural-hazards/earthquake-hazards/faults> (last accessed April 2023).

Earthquake relocations were performed with NonLinLoc (Lomax et al., 2000, 2014, <http://www.alomax.net/nlloc>; <https://github.com/alomax/NonLinLoc>; last accessed April 2023) following the workflow presented in Lomax and Savvaidis (2022) and using configuration metadata available in File S1. SeismicityViewer (<http://www.alomax.net/software>, last accessed April 2023) was used for 3D seismicity analysis and plotting. ObsPy (Beyreuther et al., 2010; Krischer et al., 2015, <http://obspy.org>, last accessed April 2023) was used for reading and processing seismicity catalogs and for coherence calculations.

Competing interests

The authors declare no competing interests.

References

- Aki, K. Characterization of barriers on an earthquake fault. *Journal of Geophysical Research: Solid Earth*, 84:6140–6148, 1979. doi: 10.1029/JB084iB11p06140.
- Aki, K. and Lee, W. Determination of three-dimensional velocity anomalies under a seismic array using first P arrival times from local earthquakes: 1. A homogeneous initial model. *Journal of Geophysical Research*, 81:4381–4399, 1976. doi: 10.1029/JB081i023p04381.
- Antoine, S., Klinger, Y., Wang, K., and Burgmann, R. Diffuse deformation explains the magnitude-dependent coseismic shallow slip deficit, 2023. doi: 10.21203/rs.3.rs-2536085/v1. Preprint.
- Aviles, C., Scholz, C., and Boatwright, J. Fractal Analysis Applied to Characteristic Segments of the San Andreas Fault. *Journal of Geophysical Research*, 92, 1987. doi: 10.1029/JB092iB01p00331.
- Bakun, W. Seismic activity on the southern Calaveras Fault in central California. *Bulletin of the Seismological Society of America*, 70:1181–1197, 1980. doi: 10.1785/BSSA0700041181.
- Bakun, W., Stewart, R., Bufe, C., and Marks, S. Implication of seismicity for failure of a section of the San Andreas Fault. *Bulletin of the Seismological Society of America*, 70:185–201, 1980. doi: 10.1785/BSSA0700010185.
- Bakun, W., Aagaard, B., Dost, B., Ellsworth, W., Hardebeck, J., Harris, R., and Ji, C. Implications for prediction and hazard assessment from the 2004 Parkfield earthquake. *Nature*, 437:969–974, 2005. doi: 10.1038/nature04067.
- Barka, A. and Kadinsky-Cade, K. Strike-slip fault geometry in Turkey and its influence on earthquake activity. *Tectonics*, 7: 663–684, 1988. doi: 10.1029/TC007i003p00663.
- Beeler, N. On the scale-dependence of fault surface roughness. *Journal of Geophysical Research: Solid Earth*, 2023. doi: 10.1029/2022JB024856.
- Ben-Zion, Y. and Sammis, C. Characterization of Fault Zones. *Pure and Applied Geophysics*, 160:677–715, 2003. doi: 10.1007/PL00012554.
- Beyreuther, M., Barsch, R., Krischer, L., Megies, T., Behr, Y., and Wassermann, J. ObsPy: A Python Toolbox for Seismology. *Seismological Research Letters*, 81:530–533, 2010. doi: 10.1785/gssrl.81.3.530.
- Billings, S., Sambridge, M., and Kennett, B. Errors in hypocenter location: Picking, model, and magnitude dependence. *Bulletin of the Seismological Society of America*, 84:1978–1990, 1994.
- Bondár, I. and McLaughlin, K. A New Ground Truth Data Set For Seismic Studies. *Seismological Research Letters*, 80:465–472, 2009. doi: 10.1785/gssrl.80.3.465.
- Bouchon, M., Karabulut, H., Bouin, M.-P., Schmittbuhl, J., Vallée, M., Archuleta, R., and Das, S. Faulting characteristics of super-shear earthquakes. *Tectonophysics*, 493:244–253, 2010. doi: 10.1016/j.tecto.2010.06.011.
- Bruhat, L., Fang, Z., and Dunham, E. Rupture complexity and the supershear transition on rough faults. *Journal of Geophysical Research: Solid Earth*, 121:210–224, 2016. doi: 10.1002/2015JB012512.
- Buehler, J. and Shearer, P. Characterizing Earthquake Location Uncertainty in North America Using Source–Receiver Reciprocity and USArrayShort. *Bulletin of the Seismological Society of America*, 106:2395–2401, 2016. doi: 10.1785/0120150173.
- Candela, T., Renard, F., Klinger, Y., Mair, K., Schmittbuhl, J., and Brodsky, E. Roughness of fault surfaces over nine decades of length scales. *Journal of Geophysical Research: Solid Earth*, 117, 2012. doi: 10.1029/2011JB009041.
- Cattaneo, M., Augliera, P., Spallarossa, D., and Eva, C. Reconstruction of seismogenetic structures by multiplet analysis: An example of Western Liguria, Italy. *Bulletin of the Seismological Society of America*, 87:971–986, 1997. doi: 10.1785/BSSA0870040971.
- Chaussard, E., Bürgmann, R., Fattahi, H., Nadeau, R., Taira, T., Johnson, C., and Johanson, I. Potential for larger earthquakes in the East San Francisco Bay Area due to the direct connection between the Hayward and Calaveras Faults. *Geophysical Research Letters*, 42:2734–2741, 2015. doi: 10.1002/2015GL063575.
- Christie-Blick, N. and Biddle, K. Deformation and Basin Formation along Strike-Slip Faults. In Biddle, K. and Christie-Blick, N., editors, *Strike-Slip Deformation, Basin Formation, and Sedimentation*, volume 37. SEPM Society for Sedimentary Geology, 1985. doi: 10.2110/pec.85.37.0001.
- Cocco, M., Aretusini, S., Cornelio, C., Nielsen, S., Spagnuolo, E., Tinti, E., and Toro, G. Fracture Energy and Breakdown Work During Earthquakes. *Annual Review of Earth and Planetary Sciences*, 51, 2023. doi: 10.1146/annurev-earth-071822-100304.
- Cockerham, R. and Eaton, J. Morgan Hill earthquake and its aftershocks: April 24 through September 30. In *The Morgan Hill, California, Earthquake*. California Department of Conservation, Division of Mines and Geology, 1984.
- Crosson, R. Crustal structure modeling of earthquake data: 1. Simultaneous least squares estimation of hypocenter and velocity parameters. *Journal of Geophysical Research*, 81:3036–3046, 1976. doi: 10.1029/JB081i017p03036.
- Darold, A., Holland, A., Chen, C., and Youngblood, A. Preliminary Analysis of Seismicity Near Eagleton 1-29, Carter County.

- Technical report, Oklahoma Geological Survey, 2014. <http://ogs.ou.edu/docs/openfile/OF2-2014.pdf>. Open-File Report No. OF2-2014.
- Das, S. and Henry, C. Spatial relation between main earthquake slip and its aftershock distribution. *Reviews of Geophysics*, 41, 2003. doi: 10.1029/2002RG000119.
- Dewey, J. Seismicity of Northern Anatolia. *Bulletin of the Seismological Society of America*, 66:843–868, 1976. doi: 10.1785/BSSA0660030843.
- Dieterich, J. and Smith, D. Nonplanar Faults: Mechanics of Slip and Off-fault Damage. In Ben-Zion, Y. and Sammis, C., editors, *Mechanics, Structure and Evolution of Fault Zones*, page 1799–1815. Pageoph Topical Volumes, 2010. doi: 10.1007/978-3-0346-0138-2_12.
- Dodge, D., Beroza, G., and Ellsworth, W. Detailed observations of California foreshock sequences: Implications for the earthquake initiation process. *Journal of Geophysical Research*, 101: 22371–22392, 1996. doi: 10.1029/96JB02269.
- Dooley, T. and Schreurs, G. Analogue modelling of intraplate strike-slip tectonics: A review and new experimental results. *Tectonophysics*, 574–575:1–71, 2012. doi: 10.1016/j.tecto.2012.05.030.
- Eberhart-Phillips, D., Haeussler, P., Freymueller, J., Frankel, A., Rubin, C., Craw, P., and Ratchkovski, N. The 2002 Denali Fault Earthquake, Alaska: A Large Magnitude, Slip-Partitioned Event. *Science*, 300:1113–1118, 2003. doi: 10.1126/science.1082703.
- Ellsworth, W. Bear Valley, California, earthquake sequence of February-March 1972. *Bulletin of the Seismological Society of America*, 65:483–506, 1975. doi: 10.1785/BSSA0650020483.
- Emre, O., Duman, T., Ozalp, S., Şaroğlu, F., Olgun, S., Elmacı, H., and Can, T. Active fault database of Turkey. *Bulletin of Earthquake Engineering*, 16:3229–3275, 2018. doi: 10.1007/s10518-016-0041-2.
- Emre, O., Kondo, H., Ozalp, S., and Elmacı, H. Fault geometry, segmentation and slip distribution associated with the 1939 Erzincan earthquake rupture along the North Anatolian fault, Turkey. *Geological Society of London, Special Publications*, 501:23–70, 2021. doi: 10.1144/SP501-2019-141.
- Evans, J., Shipton, Z., Pachell, L., S., and Robeson, K. The structure and composition of exhumed faults, and their implications for seismic processes. In *Proceedings of the 3rd Conference on Tectonic problems of the San Andreas system*. Stanford University, 2000. <http://eprints.gla.ac.uk/938/1/Evansetal2000.pdf>.
- Fang, Z. and Dunham, E. Additional shear resistance from fault roughness and stress levels on geometrically complex faults. *Journal of Geophysical Research: Solid Earth*, 118:3642–3654, 2013. doi: 10.1002/jgrb.50262.
- Fehler, M., Phillips, W., House, L., Jones, R., Aster, R., and Rowe, C. Improved Relative Locations of Clustered Earthquakes Using Constrained Multiple Event Location. *Bulletin of the Seismological Society of America*, 90:775–780, 2000. doi: 10.1785/0119990095.
- Ferretti, G. An Improved Method for the Recognition of Seismic Families: Application to the Garfagnana-Lunigiana Area, Italy. *Bulletin of the Seismological Society of America*, 95:1903–1915, 2005. doi: 10.1785/0120040078.
- Finzi, Y., Hearn, E., Ben-Zion, Y., and Lyakhovskiy, V. Structural Properties and Deformation Patterns of Evolving Strike-slip Faults: Numerical Simulations Incorporating Damage Rheology. *Pure and Applied Geophysics*, 166:1537–1573, 2009. doi: 10.1007/s00024-009-0522-1.
- Fliss, S., Bhat, H., Dmowska, R., and Rice, J. Fault branching and rupture directivity. *Journal of Geophysical Research: Solid Earth*, 110, 2005. doi: 10.1029/2004JB003368.
- Font, Y., Kao, H., Lallemand, S., Liu, C.-S., and Chiao, L.-Y. Hypocentre determination offshore of eastern Taiwan using the Maximum Intersection method. *Geophysical Journal International*, 158:655–675, 2004. doi: 10.1111/j.1365-246X.2004.02317.x.
- Frolich, C. An efficient method for joint hypocenter determination for large groups of earthquakes. *Computers and Geosciences*, 5:387–389, 1979. doi: 10.1016/0098-3004(79)90034-7.
- Frémont, M.-J. and Malone, S. High precision relative locations of earthquakes at Mount St Helens, Washington. *Journal of Geophysical Research: Solid Earth*, 92:10223–10236, 1987. doi: 10.1029/JB092iB10p10223.
- Gedney, L. A preliminary study of focal mechanisms of small earthquakes in the central Nevada region. Master's thesis, University of Nevada, Reno, 1967. <https://scholarworks.unr.edu/handle/11714/1307>.
- Geller, R. and Mueller, C. Four similar earthquakes in central California. *Geophysical Research Letters*, 7:821–824, 1980. doi: 10.1029/GL007i010p00821.
- Gibbons, S., Pabian, F., Näsholm, S., Kværna, T., and Mykkeltveit, S. Accurate relative location estimates for the North Korean nuclear tests using empirical slowness corrections. *Geophysical Journal International*, 208:101–117, 2017. doi: 10.1093/gji/ggw379.
- Goebel, T., Becker, T., Sammis, C., Dresen, G., and Schorlemmer, D. Off-fault damage and acoustic emission distributions during the evolution of structurally complex faults over series of stick-slip events. *Geophysical Journal International*, 197:1705–1718, 2014. doi: 10.1093/gji/ggu074.
- Goebel, T., Kwiatek, G., Becker, T., Brodsky, E., and Dresen, G. What allows seismic events to grow big?: Insights from b-value and fault roughness analysis in laboratory stick-slip experiments. *Geology*, 45:815–818, 2017. doi: 10.1130/G39147.1.
- Goebel, T., Brodsky, E., and Dresen, G. Fault Roughness Promotes Earthquake-Like Aftershock Clustering in the Lab. *Geophysical Research Letters*, 50:2022 101241, 2023. doi: 10.1029/2022GL101241.
- Goertz-Allmann, B., Gibbons, S., Oye, V., Bauer, R., and Will, R. Characterization of induced seismicity patterns derived from internal structure in event clusters. *Journal of Geophysical Research: Solid Earth*, 122:3875–3894, 2017. doi: 10.1002/2016JB013731.
- Gomberg, J., Shedlock, K., and Roecker, S. The effect of S-wave arrival times on the accuracy of hypocenter estimation. *Bulletin of the Seismological Society of America*, 80:1605–1628, 1990. doi: 10.1785/BSSA08006A1605.
- Gong, J. and McGuire, J. Constraints on the Geometry of the Subducted Gorda Plate From Converted Phases Generated by Local Earthquakes. *Journal of Geophysical Research: Solid Earth*, 126, 2021. doi: 10.1029/2020JB019962.
- Got, J.-L., Fréchet, J., and Klein, F. Deep fault plane geometry inferred from multiplet relative relocation beneath the south flank of Kilauea. *Journal of Geophysical Research*, 99:15375, 1994. doi: 10.1029/94JB00577.
- Graymer, R., Langenheim, V., Simpson, R., Jachens, R., and Ponce, D. Relatively simple through-going fault planes at large-earthquake depth may be concealed by the surface complexity of strike-slip faults. *Geological Society of London, Special Publications*, 290:189–201, 2007. doi: 10.1144/SP290.5.
- Hamaguchi, H. and Hasegawa, A. Recurrent Occurrence of the Earthquakes with Similar Wave Forms and Its Related Problems. *Zisin1*, 28:153–169, 1975. doi: 10.4294/zisin1948.28.2_153.
- Hamling, I., Hreinsdóttir, S., Clark, K., Elliott, J., Liang, C., Fielding, E., and Litchfield, N. Complex multifault rupture during the 2016

- M w 7.8 Kaikōura earthquake, New Zealand. *Science*, 356:7194, 2017. doi: 10.1126/science.aam7194.
- Hardebeck, J. and Husen, S. Earthquake location accuracy, Community Online Resource for Statistical Seismicity Analysis, 2010. doi: 10.5078/CORSSA-55815573.
- Harding, T. Seismic Characteristics and Identification of Negative Flower Structures, Positive Flower Structures, and Positive Structural Inversion1. *AAPG Bulletin*, 69:582–600, 1985. doi: 10.1306/AD462538-16F7-11D7-8645000102C1865D.
- Hauksson, E. The 1999 Mw 7.1 Hector Mine, California, Earthquake Sequence: Complex Conjugate Strike-Slip Faulting. *Bulletin of the Seismological Society of America*, 92:1154–1170, 2002. doi: 10.1785/0120000920.
- Hauksson, E., Jones, L., Hutton, K., and Eberhart-Phillips, D. The 1992 Landers Earthquake Sequence: Seismological observations. *Journal of Geophysical Research*, 98:19835–19858, 1993. doi: 10.1029/93JB02384.
- Hauksson, E., Yang, W., and Shearer, P. Waveform Relocated Earthquake Catalog for Southern California. *Bulletin of the Seismological Society of America*, 102:2239–2244, 2012. doi: 10.1785/0120120010.
- Hauksson, E., Olson, B., Grant, A., Andrews, J., Chung, A., Hough, S., and Kanamori, H. The Normal-Faulting 2020 Mw 5.8 Lone Pine, Eastern California, Earthquake Sequence. *Seismological Research Letters*, 2020. doi: 10.1785/0220200324.
- Hauksson, E., Stock, J., and Husker, A. Seismicity in a weak crust: the transtensional tectonics of the Brawley Seismic Zone section of the Pacific–North America Plate Boundary in Southern California, USA. *Geophysical Journal International*, 231:717–735, 2022. doi: 10.1093/gji/ggac205.
- Hole, J., Thybo, H., and Klemperer, S. Seismic reflections from the near-vertical San Andreas Fault. *Geophysical Research Letters*, 23:237–240, 1996. doi: 10.1029/96GL00019.
- Ishida, M. and Kanamori, H. The foreshock activity of the 1971 San Fernando earthquake, California. *Bulletin of the Seismological Society of America*, 68:1265–1279, 1978. doi: 10.1785/BSSA0680051265.
- Ito, A. High Resolution Relative Hypocenters of Similar Earthquakes by Cross-Spectral Analysis Method. *Journal of Physics of the Earth*, 33:279–294, 1985. doi: 10.4294/jpe1952.33.279.
- Jiang, J. and Lapusta, N. Deeper penetration of large earthquakes on seismically quiescent faults. *Science*, 352:1293–1297, 2016. doi: 10.1126/science.aaf1496.
- Jones, R. and Stewart, R. A method for determining significant structures in a cloud of earthquakes. *Journal of Geophysical Research*, 102:8245–8254, 1997. doi: 10.1029/96JB03739.
- Kamer, Y., Ouillon, G., Sornette, D., and Wössner, J. Condensation of earthquake location distributions: Optimal spatial information encoding and application to multifractal analysis of south Californian seismicity. *Physical Review E*, 92, 2015. doi: 10.1103/PhysRevE.92.022808.
- Kilb, D. and Rubin, A. Implications of diverse fault orientations imaged in relocated aftershocks of the Mount Lewis, ML 5.7, California, earthquake. *Journal of Geophysical Research: Solid Earth*, 107, 2002. doi: 10.1029/2001JB000149.
- Kim, W., Hong, T.-K., Lee, J., and Taira, T. Seismicity and fault geometry of the San Andreas fault around Parkfield, California and their implications. *Tectonophysics*, 677–678:34–44, 2016. doi: 10.1016/j.tecto.2016.03.038.
- Kim, Y.-S., Peacock, D., and Sanderson, D. Fault damage zones. *Journal of Structural Geology*, 26:503–517, 2004. doi: 10.1016/j.jsg.2003.08.002.
- King, G. Speculations on the geometry of the initiation and termination processes of earthquake rupture and its relation to morphology and geological structure. *Pure and Applied Geophysics*, 124:567–585, 1986. doi: 10.1007/BF00877216.
- King, G. and Nábělek, J. Role of Fault Bends in the Initiation and Termination of Earthquake Rupture. *Science*, 228:984–987, 1985. doi: 10.1126/science.228.4702.984.
- Klinger, Y. Relation between continental strike-slip earthquake segmentation and thickness of the crust. *Journal of Geophysical Research: Solid Earth*, 115, 2010. doi: 10.1029/2009JB006550.
- Koehler, R., Dee, S., Elliott, A., Hatem, A., Pickering, A., Pierce, I., and Seitz, G. Field Response and Surface-Rupture Characteristics of the 2020 M 6.5 Monte Cristo Range Earthquake, Central Walker Lane, Nevada. *Seismological Research Letters*, 92:823–839, 2021. doi: 10.1785/0220200371.
- Krischer, L., Megies, T., Barsch, R., Beyreuther, M., Lecocq, T., Caudron, C., and Wassermann, J. ObsPy: a bridge for seismology into the scientific Python ecosystem. *Computational Science and Discovery*, 8, 2015. doi: 10.1088/1749-4699/8/1/014003.
- Landro, G., Amoroso, O., Stabile, T., Matrullo, E., Lomax, A., and Zollo, A. High-precision differential earthquake location in 3-D models: evidence for a rheological barrier controlling the microseismicity at the Irpinia fault zone in southern Apennines. *Geophysical Journal International*, 203:1821–1831, 2015. doi: 10.1093/gji/ggv397.
- Langbein, J., Borchardt, R., Dreger, D., Fletcher, J., Hardebeck, J., Hellweg, M., and Ji, C. Preliminary Report on the M 6.0 Parkfield, California Earthquake. *Seismological Research Letters*, 76:10–26, 2005. doi: 10.1785/gssrl.76.1.10.
- Latorre, D., Mirabella, F., Chiaraluce, L., Trippetta, F., and Lomax, A. Assessment of earthquake locations in 3-D deterministic velocity models: A case study from the Altotiberina Near Fault Observatory (Italy). *Journal of Geophysical Research: Solid Earth*, 121:8113–8135, 2016. doi: 10.1002/2016JB013170.
- Lin, G. and Shearer, P. Tests of relative earthquake location techniques using synthetic data. *Journal of Geophysical Research: Solid Earth*, 110, 2005. doi: 10.1029/2004JB003380.
- Lin, G., Shearer, P., and Hauksson, E. Applying a three-dimensional velocity model, waveform cross correlation, and cluster analysis to locate southern California seismicity from 1981 to 2005. *Journal of Geophysical Research*, 112:12309, 2007. doi: 10.1029/2007JB004986.
- Liu, J., Sieh, K., and Hauksson, E. A Structural Interpretation of the Aftershock “Cloud” of the 1992 Mw 7.3 Landers Earthquake. *Bulletin of the Seismological Society of America*, 93:1333–1344, 2003. doi: 10.1785/0120020060.
- Lomax, A. A Reanalysis of the Hypocentral Location and Related Observations for the Great 1906 California Earthquake. *Bulletin of the Seismological Society of America*, 95:861–877, 2005. doi: 10.1785/0120040141.
- Lomax, A. Location of the Focus and Tectonics of the Focal Region of the California Earthquake of 18 April 1906. *Bulletin of the Seismological Society of America*, 98:846–860, 2008. doi: 10.1785/0120060405.
- Lomax, A. Absolute Location of 2019 Ridgecrest Seismicity Reveals a Shallow Mw 7.1 Hypocenter, Migrating and Pulsing Mw 7.1 Foreshocks, and Duplex Mw 6.4 Ruptures. *Bulletin of the Seismological Society of America*, 110:1845–1858, 2020a. doi: 10.1785/0120200006.
- Lomax, A. The 2020 Mw 6.5 Monte Cristo Range, Nevada earthquake: relocated seismicity shows rupture of a complete shear-crack system, 2020b. doi: 10.31223/X5X015. Preprint, Earth-ArXiv.
- Lomax, A. and Henry, P. Major California faults are smooth across

- multiple scales at seismogenic depth. In Baize, S. and Rizza, M., editors, *Proceedings of the 11th International INQUA Workshop on Paleoseismology, Active Tectonics and Archaeoseismology*, Aix-En-Provence, FRANCE, 2022. doi: 10.5281/zenodo.7736476.
- Lomax, A. and Henry, P. Supplementary Datasets and Movies for the Paper "Major California faults are smooth across multiple scales at seismogenic depth", 2023. doi: 10.5281/zenodo.7802679.
- Lomax, A. and Savvaidis, A. Improving Absolute Earthquake Location in West Texas Using Probabilistic Proxy Ground-Truth Station Corrections. *Journal of Geophysical Research: Solid Earth*, 124:11447–11465, 2019. doi: 10.1029/2019JB017727.
- Lomax, A. and Savvaidis, A. High-Precision Earthquake Location Using Source-Specific Station Terms and Inter-Event Waveform Similarity. *Journal of Geophysical Research: Solid Earth*, 127, 2022. doi: 10.1029/2021JB023190.
- Lomax, A., Virieux, J., Volant, P., and Berge-Thierry, C. Probabilistic Earthquake Location in 3D and Layered Models. In Thurber, H., C., and Rabinowitz, N., editors, *Advances in Seismic Event Location Modern Approaches in Geophysics*, volume 18, pages 101–134., Springer Netherlands, 2000. doi: 10.1007/978-94-015-9536-0_5.
- Lomax, A., Michelini, A., and Curtis, A. Earthquake Location, Direct, Global-Search Methods. In Meyers, R. A., editor, *Encyclopedia of Complexity and Systems Science*, page 1–33. Springer New York, 2014. doi: 10.1007/978-3-642-27737-5_150-2.
- Ma, S. and Andrews, D. Inelastic off-fault response and three-dimensional dynamics of earthquake rupture on a strike-slip fault. *Journal of Geophysical Research: Solid Earth*, 115, 2010. doi: 10.1029/2009JB006382.
- Madariaga, R. High-frequency radiation from crack (stress drop) models of earthquake faulting. *Geophysical Journal International*, 51:625–651, 1977. doi: 10.1111/j.1365-246X.1977.tb04211.x.
- Manighetti, I., Campillo, M., Bouley, S., and Cotton, F. Earthquake scaling, fault segmentation, and structural maturity. *Earth and Planetary Science Letters*, 253:429–438, 2007. doi: 10.1016/j.epsl.2006.11.004.
- Manighetti, I., Mercier, A., and Barros, L. Fault Trace Corrugation and Segmentation as a Measure of Fault Structural Maturity. *Geophysical Research Letters*, 48, 2021. doi: 10.1029/2021GL095372.
- Marone, C. and Scholz, C. The depth of seismic faulting and the upper transition from stable to unstable slip regimes. *Geophysical Research Letters*, 15:621–624, 1988. doi: 10.1029/GL015i006p00621.
- Matoza, R., Shearer, P., Lin, G., Wolfe, C., and Okubo, P. Systematic relocation of seismicity on Hawaii Island from 1992 to 2009 using waveform cross correlation and cluster analysis. *Journal of Geophysical Research: Solid Earth*, 118:2275–2288, 2013. doi: 10.1002/jgrb.50189.
- McClay, K. and Bonora, M. Analog models of restraining stepovers in strike-slip fault systems. *AAPG Bulletin*, 85:233–260, 2001.
- Michael, A. Effects of three-dimensional velocity structure on the seismicity of the 1984 Morgan Hill, California, aftershock sequence. *Bulletin of the Seismological Society of America*, 78: 1199–1221, 1988. doi: 10.1785/BSSA0780031199.
- Michele, M., Chiaraluce, L., Stefano, R., and Waldhauser, F. Fine-Scale Structure of the 2016–2017 Central Italy Seismic Sequence From Data Recorded at the Italian National Network. *Journal of Geophysical Research: Solid Earth*, 125, 2020. doi: 10.1029/2019JB018440.
- Michelini, A. and Lomax, A. The effect of velocity structure errors on double-difference earthquake location. *Geophysical Research Letters*, 31, 2004. doi: 10.1029/2004GL019682.
- Michelini, A. and McEvelly, T. Seismological studies at Parkfield. I. Simultaneous inversion for velocity structure and hypocenters using cubic B-splines parameterization. *Bulletin of the Seismological Society of America*, 81:524–552, 1991. doi: 10.1785/BSSA0810020524.
- Muhuri, S., Dewers, T., Scott, Jr., T., and Reches, Z. Interseismic fault strengthening and earthquake-slip instability: Friction or cohesion? *Geology*, 31:881–884, 2003. doi: 10.1130/G19601.1.
- Myers, S. Improving Sparse Network Seismic Location with Bayesian Kriging and Teleseismically Constrained Calibration Events. *Bulletin of the Seismological Society of America*, 90: 199–211, 2000. doi: 10.1785/0119980171.
- Nadeau, R., Antolik, M., Johnson, P., Foxall, W., and McEvelly, T. Seismological studies at Parkfield III: microearthquake clusters in the study of fault-zone dynamics. *International Journal of Rock Mechanics and Mining Sciences and Geomechanics Abstracts*, 31:271, 1994. doi: 10.1016/0148-9062(94)90077-9.
- Nakamura, Y. A1 moonquakes: source distribution and mechanism. In *Proceedings of the Lunar and Planetary Science Conference*, page 3589–3607, 1978. <https://ci.nii.ac.jp/naid/10006236523/en/>.
- Naylor, M., Mandl, G., and Supesteijn, C. Fault geometries in basement-induced wrench faulting under different initial stress states. *Journal of Structural Geology*, 8:737–752, 1986. doi: 10.1016/0191-8141(86)90022-2.
- NCEDC. Northern California Earthquake Data Center, 2014. doi: 10.7932/NCEDC.
- Neves, M., Peng, Z., and Lin, G. A High-Resolution Earthquake Catalog for the 2004 Mw 6 Parkfield Earthquake Sequence Using a Matched Filter Technique. *Seismological Research Letters*, 2022. doi: 10.1785/0220220206.
- Nicholson, T., Clarke, D., and Townend, J. Regional earthquake location using empirical traveltimes in a region of strong lateral velocity heterogeneity. *Geophysical Journal International*, 175: 560–570, 2008. doi: 10.1111/j.1365-246X.2008.03858.x.
- Nooshiri, N., Saul, J., Heimann, S., Tilmann, F., and Dahm, T. Revision of earthquake hypocentre locations in global bulletin data sets using source-specific station terms. *Geophysical Journal International*, 208:589–602, 2017. doi: 10.1093/gji/ggw405.
- Oglesby, D. The Dynamics of Strike-Slip Step-Overs with Linking Dip-Slip Faults. *Bulletin of the Seismological Society of America*, 95:1604–1622, 2005. doi: 10.1785/0120050058.
- Oglesby, D. and Mai, P. Fault geometry, rupture dynamics and ground motion from potential earthquakes on the North Anatolian Fault under the Sea of Marmara. *Geophysical Journal International*, 188:1071–1087, 2012. doi: 10.1111/j.1365-246X.2011.05289.x.
- Okubo, P. and Dieterich, J. Effects of physical fault properties on frictional instabilities produced on simulated faults. *Journal of Geophysical Research: Solid Earth*, 89:5817–5827, 1984. doi: 10.1029/JB089iB07p05817.
- Oppenheimer, D., Bakun, W., and Lindh, A. Slip partitioning of the Calaveras Fault, California, and prospects for future earthquakes. *Journal of Geophysical Research: Solid Earth*, 95: 8483–8498, 1990. doi: 10.1029/JB095iB06p08483.
- Oppenheimer, D., Bakun, W., Parsons, T., Simpson, R., Boatwright, J., and Uhrhammer, R. The 2007 M5.4 Alum Rock, California, earthquake: Implications for future earthquakes on the central and southern Calaveras Fault. *Journal of Geophysical Research: Solid Earth*, 115, 2010. doi: 10.1029/2009JB006683.
- Parsons, T. Crustal Structure of the Coastal and Marine San Fran-

- cisco Bay Region, California. Technical report, U.S. Geological Survey, 2002. <https://pubs.usgs.gov/pp/1658/>. Professional Paper 1658.
- Parsons, T. and Minasian, D. Earthquake rupture process recreated from a natural fault surface. *Journal of Geophysical Research: Solid Earth*, 120:7852–7862, 2015. doi: 10.1002/2015JB012448.
- Pavlis, G. Appraising earthquake hypocenter location errors: A complete, practical approach for single-event locations. *Bulletin of the Seismological Society of America*, 76:1699–1717, 1986.
- Pavlis, G. and Hokanson, N. Separated earthquake location. *Journal of Geophysical Research: Solid Earth*, 90:12777–12789, 1985a. doi: 10.1029/JB090iB14p12777.
- Pavlis, G. and Hokanson, N. Separated earthquake location. *Journal of Geophysical Research: Solid Earth*, 90:12777–12789, 1985b. doi: 10.1029/JB090iB14p12777.
- Perrin, C., Manighetti, I., Ampuero, J.-P., Cappa, F., and Gaedemmer, Y. Location of largest earthquake slip and fast rupture controlled by along-strike change in fault structural maturity due to fault growth. *Journal of Geophysical Research: Solid Earth*, 121:3666–3685, 2016. doi: 10.1002/2015JB012671.
- Perrin, C., Waldhauser, F., Choi, E., and Scholz, C. Persistent fine-scale fault structure and rupture development: A new twist in the Parkfield, California, story. *Earth and Planetary Science Letters*, 521:128–138, 2019. doi: 10.1016/j.epsl.2019.06.010.
- Podvin, P. and Lecomte, I. Finite difference computation of traveltimes in very contrasted velocity models: a massively parallel approach and its associated tools. *Geophysical Journal International*, 105:271–284, 1991. doi: 10.1111/j.1365-246X.1991.tb03461.x.
- Poliakov, A., Dmowska, R., and Rice, J. Dynamic shear rupture interactions with fault bends and off-axis secondary faulting. *Journal of Geophysical Research: Solid Earth*, 107, 2002. doi: 10.1029/2001JB000572.
- Ponce, D., Simpson, R., Graymer, R., and Jachens, R. Gravity, magnetic, and high-precision relocated seismicity profiles suggest a connection between the Hayward and Calaveras Faults, northern California. *Geochemistry, Geophysics, Geosystems*, 5, 2004. doi: 10.1029/2003GC000684.
- Poupinet, G., Glangeaud, F., and Cote, P. P-Time delay measurement of a doublet of microearthquakes. In *Proceedings of ICASSP 1982: IEEE International Conference on Acoustics, Speech, and Signal Processing*, volume 7, pages 1516–1519. Institute of Electrical and Electronics Engineers, 1982. doi: 10.1109/ICASSP.1982.1171796.
- Poupinet, G., Ellsworth, W., and Frechet, J. Monitoring velocity variations in the crust using earthquake doublets: An application to the Calaveras Fault, California. *Journal of Geophysical Research*, 89:5719–5731, 1984. doi: 10.1029/JB089iB07p05719.
- Power, W., Tullis, T., and Weeks, J. Roughness and wear during brittle faulting. *Journal of Geophysical Research: Solid Earth*, 93:15268–15278, 1988. doi: 10.1029/JB093iB12p15268.
- Preuss, S., Ampuero, J., Gerya, T., and Dinther, Y. Characteristics of earthquake ruptures and dynamic off-fault deformation on propagating faults. *Solid Earth*, 11:1333–1360, 2020. doi: 10.5194/se-11-1333-2020.
- Ramos, M., Thakur, P., Huang, Y., Harris, R., and Ryan, K. Working with Dynamic Earthquake Rupture Models: A Practical Guide. *Seismological Research Letters*, 93:2096–2110, 2022. doi: 10.1785/0220220022.
- Reasenber, P. and Ellsworth, W. Aftershocks of the Coyote Lake. *Journal of Geophysical Research*, 87:10637–10655, 1982. doi: 10.1029/JB087iB13p10637.
- Reid, H. and Lawson, A. *The California earthquake of April 18, 1906: report of the State Earthquake Investigation Commission, in two volumes and atlas*. Carnegie Institution of Washington publication, 1908.
- Renard, F. and Candela, T. Scaling of Fault Roughness and Implications for Earthquake Mechanics. In *Fault Zone Dynamic Processes*, page 195–215. American Geophysical Union, 2017. doi: 10.1002/9781119156895.ch10.
- Renard, F., Voisin, C., Marsan, D., and Schmittbuhl, J. High resolution 3D laser scanner measurements of a strike-slip fault quantify its morphological anisotropy at all scales. *Geophysical Research Letters*, 33, 2006. doi: 10.1029/2005GL025038.
- Richard, P., Naylor, M., and Koopman, A. Experimental models of strike-slip tectonics. *Petroleum Geoscience*, 1995. doi: 10.1144/petgeo.1.1.71.
- Richards, P., Waldhauser, F., Schaff, D., and Kim, W.-Y. The Applicability of Modern Methods of Earthquake Location. *Pure and Applied Geophysics*, 163:351–372, 2006. doi: 10.1007/s00024-005-0019-5.
- Richards-Dinger, K. and Shearer, P. Earthquake locations in southern California obtained using source-specific station terms. *Journal of Geophysical Research*, 105:10939–10960, 2000. doi: 10.1029/2000JB900014.
- Ritzwoller, M., Shapiro, N., Levshin, A., Bergman, E., and Engdahl, E. Ability of a global three-dimensional model to locate regional events. *Journal of Geophysical Research*, 108, 2003. doi: 10.1029/2002JB002167.
- Ross, Z., Idini, B., Jia, Z., Stephenson, O., Zhong, M., Wang, X., and Zhan, Z. Hierarchical interlocked orthogonal faulting in the 2019 Ridgecrest earthquake sequence. *Science*, 366:346–351, 2019. doi: 10.1126/science.aaz0109.
- Rowe, C., Aster, R., Phillips, W., Jones, R., Borchers, B., and Fehler, M. Using Automated, High-precision Repicking to Improve Delineation of Microseismic Structures at the Soultz Geothermal Reservoir. *Pure and Applied Geophysics*, 159:34, 2002. doi: 10.1007/978-3-0348-8179-1_24.
- Rubin, A. and Gillard, D. Aftershock asymmetry/rupture directivity among central San Andreas fault microearthquakes. *Journal of Geophysical Research: Solid Earth*, 105:19095–19109, 2000. doi: 10.1029/2000JB900129.
- Rubin, A., Gillard, D., and Got, J.-L. Streaks of microearthquakes along creeping faults. *Nature*, 400:635–641, 1999. doi: 10.1038/23196.
- Ryaboy, V., Baumgardt, D., Firbas, P., and Dainty, A. Application of 3-D Crustal and Upper Mantle Velocity Model of North America for Location of Regional Seismic Events. *Pure and Applied Geophysics*, 158:79–103, 2001. doi: 10.1007/PL00001169.
- Sagy, A., Brodsky, E., and Axen, G. Evolution of fault-surface roughness with slip. *Geology*, 35:283–286, 2007. doi: 10.1130/G23235A.1.
- Savran, W. and Olsen, K. Kinematic Rupture Generator Based on 3-D Spontaneous Rupture Simulations Along Geometrically Rough Faults. *Journal of Geophysical Research: Solid Earth*, 125:2020 019464, 2020. doi: 10.1029/2020JB019464.
- SCEDC. Southern California Earthquake Data Center, 2013. doi: 10.7914/SN/CI.
- Schaff, D., Bokelmann, G., Beroza, G., Waldhauser, F., and Ellsworth, W. High-resolution image of Calaveras Fault seismicity. *Journal of Geophysical Research: Solid Earth*, 107, 2002. doi: 10.1029/2001JB000633.
- Schlaphorst, D., Rychert, C., Harmon, N., Hicks, S., Bogiatzis, P., Kendall, J.-M., and Abercrombie, R. Local seismicity around the Chain Transform Fault at the Mid-Atlantic Ridge from OBS ob-

- servations. *Geophysical Journal International*, page 124, 2023. doi: 10.1093/gji/ggad124.
- Schoenball, M. and Ellsworth, W. Waveform-Relocated Earthquake Catalog for Oklahoma and Southern Kansas Illuminates the Regional Fault Network. *Seismological Research Letters*, 88: 1252–1258, 2017. doi: 10.1785/0220170083.
- Scholz, C. Earthquakes and friction laws. *Nature*, 391:37–42, 1998. doi: 10.1038/34097.
- Scholz, C. *The Mechanics of Earthquakes and Faulting*. Cambridge University Press, 2019. doi: 10.1017/9781316681473.
- Shearer, P. Improving local earthquake locations using the L1 norm and waveform cross correlation: Application to the Whittier Narrows, California, aftershock sequence. *Journal of Geophysical Research*, 102:8269–8283, 1997. doi: 10.1029/96JB03228.
- Shelly, D. A High-Resolution Seismic Catalog for the Initial 2019 Ridgecrest Earthquake Sequence: Foreshocks, Aftershocks, and Faulting Complexity. *Seismological Research Letters*, 91: 1971–1978, 2020. doi: 10.1785/0220190309.
- Shi, Z. and Day, S. Rupture dynamics and ground motion from 3-D rough-fault simulations. *Journal of Geophysical Research: Solid Earth*, 118:1122–1141, 2013. doi: 10.1002/jgrb.50094.
- Sibson, R. Fault zone models, heat flow, and the depth distribution of earthquakes in the continental crust of the United States. *Bulletin of the Seismological Society of America*, 72:151–163, 1982. doi: 10.1785/BSSA0720010151.
- Sibson, R. Stopping of earthquake ruptures at dilational fault jogs. *Nature*, 316:248–251, 1985. doi: 10.1038/316248a0.
- Simpson, R., Barall, M., Langbein, J., Murray, J., and Rymer, M. San Andreas Fault Geometry in the Parkfield, California, Region. *Bulletin of the Seismological Society of America*, 96:28–37, 2006. doi: 10.1785/0120050824.
- Smith, S., Knapp, J., and McPherson, R. Seismicity of the Gorda Plate, structure of the continental margin, and an eastward jump of the Mendocino Triple Junction. *Journal of Geophysical Research: Solid Earth*, 98:8153–8171, 1993. doi: 10.1029/93JB00026.
- Stauder, W. and Ryall, A. Spatial distribution and source mechanism of microearthquakes in Central Nevada. *Bulletin of the Seismological Society of America*, 57:1317–1345, 1967.
- Stein, R., Barka, A., and Dieterich, J. Progressive failure on the North Anatolian fault since 1939 by earthquake stress triggering. *Geophysical Journal International*, 128:594–604, 1997. doi: 10.1111/j.1365-246X.1997.tb05321.x.
- Stirling, M., Wesnousky, S., and Shimazaki, K. Fault trace complexity, cumulative slip, and the shape of the magnitude-frequency distribution for strike-slip faults: a global survey. *Geophysical Journal International*, 124:833–868, 1996. doi: 10.1111/j.1365-246X.1996.tb05641.x.
- Thorbjarnardottir, B. and Pechmann, J. Constraints on relative earthquake locations from cross-correlation of waveforms. *Bulletin of the Seismological Society of America*, 77:1626–1634, 1987. doi: 10.1785/BSSA0770051626.
- Thurber, C. Earthquake locations and three-dimensional crustal structure in the Coyote Lake Area, central California. *Journal of Geophysical Research: Solid Earth*, 88:8226–8236, 1983. doi: 10.1029/JB088iB10p08226.
- Thurber, C., Zhang, H., Waldhauser, F., Hardebeck, J., Michael, A., and Eberhart-Phillips, D. Three-Dimensional Compressional Wavespeed Model, Earthquake Relocations, and Focal Mechanisms for the Parkfield, California, Region. *Bulletin of the Seismological Society of America*, 96:38–49, 2006. doi: 10.1785/0120050825.
- Trugman, D. and Dunham, E. A 2D Pseudodynamic Rupture Model Generator for Earthquakes on Geometrically Complex Faults. *Bulletin of the Seismological Society of America*, 104:95–112, 2014. doi: 10.1785/0120130138.
- Trugman, D. and Shearer, P. GrowClust: A Hierarchical Clustering Algorithm for Relative Earthquake Relocation, with Application to the Spanish Springs and Sheldon, Nevada, Earthquake Sequences. *Seismological Research Letters*, 88:379–391, 2017. doi: 10.1785/0220160188.
- Tucker, W., Herrin, E., and Freedman, H. Some statistical aspects of the estimation of seismic travel times. *Bulletin of the Seismological Society of America*, 58:1243–1260, 1968. doi: 10.1785/BSSA0580041243.
- Wagner, M., Husen, S., Lomax, A., Kissling, E., and Giardini, D. High-precision earthquake locations in Switzerland using regional secondary arrivals in a 3-D velocity model. *Geophysical Journal International*, 193:1589–1607, 2013. doi: 10.1093/gji/ggt052.
- Waldhauser, F. Near-Real-Time Double-Difference Event Location Using Long-Term Seismic Archives, with Application to Northern California. *Bulletin of the Seismological Society of America*, 99: 2736–2748, 2009. doi: 10.1785/0120080294.
- Waldhauser, F. and Ellsworth, W. A Double-Difference Earthquake Location Algorithm: Method and Application to the Northern Hayward Fault, California. *Bulletin of the Seismological Society of America*, 90:1353–1368, 2000. doi: 10.1785/0120000006.
- Waldhauser, F. and Schaff, D. Large-scale relocation of two decades of Northern California seismicity using cross-correlation and double-difference methods. *Journal of Geophysical Research: Solid Earth*, 113, 2008. doi: 10.1029/2007JB005479.
- Waldhauser, F., Ellsworth, W., Schaff, D., and Cole, A. Streaks, multiplets, and holes: High-resolution spatio-temporal behavior of Parkfield seismicity. *Geophysical Research Letters*, 31, 2004. doi: 10.1029/2004GL020649.
- Watt, J., Ponce, D., Graymer, R., Jachens, R., and Simpson, R. Sub-surface geometry of the San Andreas-Calaveras fault junction: Influence of serpentinite and the Coast Range Ophiolite. *Tectonics*, 33:2025–2044, 2014. doi: 10.1002/2014TC003561.
- Wesnousky, S. Seismological and structural evolution of strike-slip faults. *Nature*, 335:340–343, 1988. doi: 10.1038/335340a0.
- Wesnousky, S. Predicting the endpoints of earthquake ruptures. *Nature*, 444:358–360, 2006. doi: 10.1038/nature05275.
- Wesnousky, S. Displacement and Geometrical Characteristics of Earthquake Surface Ruptures: Issues and Implications for Seismic-Hazard Analysis and the Process of Earthquake Rupture. *Bulletin of the Seismological Society of America*, 98: 1609–1632, 2008. doi: 10.1785/0120070111.
- Williams, R. and Fagereng, A. The Role of Quartz Cementation in the Seismic Cycle: A Critical Review. *Reviews of Geophysics*, 60, 2022. doi: 10.1029/2021RG000768.
- Wu, J., McClay, K., Whitehouse, P., and Dooley, T. 4D analogue modelling of transtensional pull-apart basins. *Marine and Petroleum Geology*, 26:1608–1623, 2009. doi: 10.1016/j.marpetgeo.2008.06.007.
- Zhou, H. Rapid three-dimensional hypocentral determination using a master station method. *Journal of Geophysical Research*, 99, 1994. doi: 10.1029/94JB00934.
- Zhou, Y., McNally, K., and Lay, T. Analysis of the 1986 Mt. Lewis, California, earthquake: preshock sequence-mainshock-aftershock sequence. *Physics of the Earth and Planetary Interiors*, 75: 267–288, 1993. doi: 10.1016/0031-9201(93)90005-T.
- Zoback, M., Jachens, R., and Olson, J. Abrupt along-strike change in tectonic style: San Andreas Fault zone, San Francisco Peninsula. *Journal of Geophysical Research*, 104:10719–10742, 1999.

doi: 10.1029/1998JB900059.

The article *Major California faults are smooth across multiple scales at seismogenic depth* © 2023 by Anthony Lomax is licensed under CC BY 4.0.

Interacting Seismic Waveguides: Multimode Surface Waves and Leaking Modes

Brian L.N. Kennett  * 1

¹Research School of Earth Sciences, Australian National University, Canberra, Australia

Author contributions: *Conceptualization*: B.L.N. Kennett. *Formal Analysis*: B.L.N. Kennett. *Writing - original draft*: B.L.N. Kennett.

Abstract Recent developments in seismic recording provide dense sampling of the seismic wavefield that allows the extraction of higher surface wave modes as well as the fundamental, and in some circumstances also *P*-dominated modes. The character of the modal branches and their dispersion with frequency and phase speed depends on interactions between different aspects of the seismic structure and between wavetypes. The influence of *P* waves becomes quite strong in the very near surface when there are strong wavespeed gradients. An effective tool for understanding the nature of the modal interactions due to structure is provided by the seismic response in frequency–phase speed space, the kernel for seismogram calculation. Such displays for all three-components of the surface response extract the full modal response for Rayleigh and Love waves, including leaking mode effects, and an indication of the way that the modes are excited.

Non-technical summary Seismic energy trapped between the free surface and the rapid increase in seismic wavespeeds with depth can propagate to substantial distances. With increasing density of seismic observations the full character of such guided waves can be revealed, with strong dependencies on interaction between different parts of the structure and wavetypes. In favourable circumstances, *P*-wave dominated features can be tracked in addition to the more commonly studied *S* dominated modes. Understanding the nature of such modes aids improved rendering of structure at depth.

Production Editor:
Gareth Funning
Handling Editor:
Stephen Hicks
Copy & Layout Editor:
Hannah F. Mark

Received:
November 30, 2022
Accepted:
March 8, 2023
Published:
March 31, 2023

1 Introduction

Surface waves have received increased attention in recent years, in part because of the success in exploiting ambient noise (see, e.g., Nakata et al., 2019, and references therein). With increasing station density and careful processing it has proved possible to extract the dispersion of both the fundamental mode and two or three higher modes from broad scale deployments of seismometers, at frequencies up to 0.5 Hz (e.g., Chen et al., 2022). Such *S*-dominated modes are fully trapped between the free surface and the increasing wavespeeds at depth. With very high density observations, as in the LASSO deployment of 1800 seismic nodes in Oklahoma, USA, the dispersion characteristics of partially trapped *P*-dominated modes have also been imaged in frequency–phase speed space (Li et al., 2022). Other classes of high-density sampling of the seismic wavefield such as the use of distributed acoustic sensing (DAS) also can allow the extraction of multi-mode dispersion including *P* modes in favourable circumstances (e.g., Fichtner et al., submitted 2023).

Although the concepts of surface wave dispersion are well established, the complexities of modal interaction at high frequency are rarely considered. Sediments, the crust, and the upper mantle each have the capacity to trap seismic energy and interactions between these different waveguides produce complexity in the charac-

ter of surface wave modes. The dispersion curves for modes with different character apparently cross. Likewise, although Rayleigh waves are dominantly linked to the behaviour of the *SV* wavespeed with depth, where low *P* wavespeeds occur near surface there can be significant interaction between *SV*- and *P*-dominated modes. The nature of the waveguide interactions can be understood in terms of the controls on modal dispersion.

In a full three-dimensional body, such as the Earth, all deformations can be completely described by a superposition of the set of normal modes of the structure. However, when we consider a truncated portion of the structure in cartesian geometry, the properties at depth set a limit on the range of phase speeds for which surface wave modes are fully trapped. Waves with higher phase speed lose energy as they propagate horizontally by radiation into the lower halfspace, but can sometimes be recognised as ‘leaking’ modes. For a fully elastic medium, the trapped modes correspond to poles of the response lying in the real frequency–slowness plane. When leakage occurs, the singularities for the leaking modes occur on lower sheets in complex slowness at each frequency (e.g., Haddon, 1984). In the presence of attenuation all poles are shifted into the complex plane. However, for typical levels of seismic attenuation the trajectories of the poles in frequency–slowness space can be retrieved with a purely elastic approximation.

For a realistic seismic structure, including attenua-

*Corresponding author: brian.kennett@anu.edu.au

tion, the character of the modal field can be extracted by direct calculation in the frequency-slowness domain with modal branches defined by localised increases in amplitude reflecting the presence of poles off the top slowness sheet. In this way both trapped modes and leaking modes can be visualised, and the effects associated with the interactions of multiple seismic waveguides analysed.

Commonly the near-surface has sediment cover with lower wavespeeds than the basement. Wavespeeds increase steadily through the crust, and then jump again on entry to the upper mantle at the Moho. The wavespeed increases again through the mantle punctuated by the upper-mantle discontinuities near 410 and 600 km depth. Wavespeed gradients are generally not strong, but are sufficient to turn back energy to the surface. When a cartesian geometry is used, earth-flattening transformations increase the gradients to compensate for the decrease in horizontal distance scale with depth due to sphericity (e.g., [Chapman, 1973](#)).

The sediment, crustal, and mantle structures are each linked to a set of reverberations whose interference controls the associated surface wave dispersion. But, such multiple reflections with the same slowness (phase speed) can also span multiple zones so that dispersion behaviour is linked. An individual mode will then partake mostly of the character of the multiple guides in different segments with link points where mode branches nearly meet. The presence of low velocity channels within the structures produces further opportunities for guided waves with further classes of modal interaction ([Kerry, 1981](#)).

I here bring together a range of results based on the reflection properties of the free surface and the structure at depth to provide physical insight into the nature of surface wave dispersion and the way in which different modes of propagation interact to produce the nature of the different modes. Following a presentation of the nature of coupling between different types of wave guiding, I show how the properties of the full modal field can be readily examined by constructing and displaying the response of the full structure as a function of frequency and phase speed (slowness).

2 The character of the modal field

Consider an stratified elastic medium with surface P and S wavespeeds α_0, β_0 , underlain by a uniform half-space with properties α_L, β_L . The response of the medium to a surface source in the frequency-slowness ($\omega - p$) domain is ([Kennett, 1983](#)):

$$\mathbf{w}_0 = \mathbf{W}_F [\mathbf{I} - \mathbf{R}_D^{0L} \mathbf{R}_F]^{-1} \mathbf{R}_D^{0L} \quad (1)$$

where \mathbf{R}_D^{0L} is the response of the entire structure below the surface, \mathbf{R}_F the matrix of free-surface reflection coefficients, \mathbf{W}_F the displacement response including free-surface effects and \mathbf{I} the identity matrix. Here the source has been left arbitrary. Different aspects of the seismic wave field can be isolated by selecting the components of \mathbf{R}_D^{0L} to be modulated by the reverberations in the structure (the inverse term) and the free surface response \mathbf{W}_F .

For isotropic, and transversely isotropic, media the response (Eq. 1) breaks into two separate parts. SH waves propagate independently and the characteristics of the medium are expressed through the SH reflection coefficient $[\mathbf{R}_D^{0L}]_{HH}$. The P and SV components are coupled so that we need to treat 2×2 matrices of reflection coefficients and free-surface terms

$$\begin{aligned} \mathbf{R}_D^{0L} &= \begin{pmatrix} \mathbf{R}_D^{PP} & \mathbf{R}_D^{PS} \\ \mathbf{R}_D^{SP} & \mathbf{R}_D^{SS} \end{pmatrix}, \\ \mathbf{R}_F &= \begin{pmatrix} \mathbf{R}_F^{PP} & \mathbf{R}_F^{PS} \\ \mathbf{R}_F^{SP} & \mathbf{R}_F^{SS} \end{pmatrix}, \\ \mathbf{W}_F &= \begin{pmatrix} \mathbf{W}_F^{ZP} & \mathbf{W}_F^{ZS} \\ \mathbf{W}_F^{RP} & \mathbf{W}_F^{RS} \end{pmatrix}, \end{aligned} \quad (2)$$

where we have used a compressed notation so that

$$\begin{aligned} \mathbf{R}_F^{PP} &= [\mathbf{R}_F]_{PP}, \\ \mathbf{R}_D^{PS} &= [\mathbf{R}_D^{0L}]_{PS}, \\ \mathbf{W}_F^{ZP} &= [\mathbf{W}_F]_{ZP}, \text{ etc.} \end{aligned} \quad (3)$$

Here Z is the vertical and R the radial component. The P wave response of the structure can be emphasised by selecting just the PP and PS elements of the matrix \mathbf{R}_D^{0L} in Eq. 1 and the SV response by selecting the SS and SP elements.

The response of the medium specified by Eq. 1 will be singular when the determinant of the reverberation term vanishes, i.e., $\det[\mathbf{I} - \mathbf{R}_D^{0L} \mathbf{R}_F] = 0$. The locus of such values in frequency-slowness space determines the trajectory of the dispersion branches for seismic modes. We will concentrate on the response directly in the frequency-slowness domain. Seismograms may be constructed by introducing the source spectrum and relevant horizontal phase terms followed by integration over both slowness and frequency.

The dispersion relation for the entire structure takes a relatively simple form for Love waves, involving only the SH (tangential) component:

$$(1 - [\mathbf{R}_D^{0L}(p, \omega)]_{HH}) = 0, \quad (4)$$

since SH waves do not couple to P and the free-surface reflection coefficient for SH waves is unity. This means that the dispersion condition requires the SH reflection coefficient for the entire structure has to be equal to unity and so its phase $\chi_D(p, \omega)$ must be a multiple of 2π :

$$\begin{aligned} \chi_D(p, \omega) &= 2n\pi, \\ n &= 0, 1, 2, \dots \end{aligned} \quad (5)$$

This property can be used to set up an efficient recursive system for models without localised low velocity zones ([Kennett and Clarke, 1983](#)).

For the P - SV case the dispersion relation for Rayleigh waves takes the form

$$\det(\mathbf{I} - \mathbf{R}_D^{0L}(p, \omega) \mathbf{R}_F(p)) = 0, \quad (6)$$

where $\mathbf{R}_F(p)$ is the free-surface reflection matrix that depends on slowness p alone and $\mathbf{R}_D^{0L}(p, \omega)$ is the reflection matrix from the full stratification. Other equivalent representations exist where the structure is broken at different levels ([Kerry, 1981](#); [Chen, 1993](#)).

In terms of the components of the free surface reflection matrix R_F and the reflection matrix R_D^{0L} from the structure beneath the surface, the dispersion relation (Eq. 6) can be written as

$$\begin{aligned} & [1 - R_D^{SS}R_F^{SS} - R_D^{SP}R_F^{PS}] \\ & [1 - R_D^{PP}R_F^{PP} - R_D^{PS}R_F^{SP}] \\ & - [R_D^{SP}R_F^{PP} + R_D^{SS}R_F^{SP}] \\ & [R_D^{PP}R_F^{PS} + R_D^{PS}R_F^{SS}] = 0. \end{aligned} \quad (7)$$

With the aid of Eq. 7 we can identify different propagation regimes in terms of slowness p or its reciprocal phase speed $c = 1/p$.

Both P and S evanescent

($p > \beta_0^{-1}$; $c < \beta_0$)

In this regime there is only a single possible Rayleigh mode, the fundamental. At moderate to high frequencies only the coefficient R_D^{SS} has significant amplitude and R_D^{PP} , R_D^{PS} , R_D^{SP} are negligible. The dispersion relation for the fundamental mode (Eq. 7) then reduces to

$$1 - R_D^{SS}(p, \omega)R_F^{SS}(p) = 0, \quad (8)$$

so that the small amplitude of R_D^{SS} has to be compensated by the growth of $R_F^{SS}(p)$ in this evanescent regime. With increasing frequency R_D^{SS} tends to zero, and the dispersion relation for the fundamental mode tends to that for a Rayleigh wave on a half space with the surface properties (see, e.g., Kennett, 2001).

S propagating, P evanescent

($\alpha_0^{-1} < p < \beta_0^{-1}$, $\alpha_0 > c > \beta_0$)

Now, in principle there is an infinite sequence of Rayleigh modes, and the higher modes have the asymptotic limit $p = \beta_0^{-1}$, so their phase speed is always greater than the surface S wavespeed β_0 . For this slowness range S waves have travelling wave character at the surface and a turning level at depth. P waves are still evanescent throughout the structure. The spacing of the modal branches at fixed slowness p (phase speed c) is primarily controlled by the inverse of the delay time $\tau(p)$, so that the interval between successive modes decreases as the slowness decreases and phase speed increases (see, e.g., Kennett, 1983).

For high frequency propagation, the decay of evanescent P means that R_D^{PP} , R_D^{SP} , R_D^{PS} are small compared to R_D^{SS} . We neglect all terms involving R_D^{PP} , and all processes involving more than a single conversion of wavetype in the structure at depth. Then, at moderate frequencies we can reduce the dispersion relation (Eq. 7) to the approximate form

$$\begin{aligned} & 1 - R_D^{SS}R_F^{SS} [1 - \{R_D^{SP}R_F^{PS} + R_D^{PS}R_F^{SP}\}] \\ & - \{R_D^{SP}R_F^{PS}\} = 0. \end{aligned} \quad (9)$$

The single conversions from depth will be weak because of the evanescence of the P wave legs. At high frequencies these conversion terms in braces in Eq. 9 can be neglected.

Equation 9 applies to the full set of Rayleigh modes, so that for fixed slowness p there will be a sequence of modes with increasing frequency and mode number, with similar spacing in frequency dictated by the phase of the $R_D^{SS}R_F^{SS}$ combination.

P and S both trapped

($\beta_L^{-1} < p < \alpha_0^{-1}$, $\beta_L > c > \alpha_0$)

In this regime both P and S waves are trapped in the structure, and the full form of the dispersion relation (Eq. 7) needs to be used. The principal term comes from the product of two elements

$$[1 - R_D^{SS}R_F^{SS} - R_D^{SP}R_F^{PS}][1 - R_D^{PP}R_F^{PP} - R_D^{PS}R_F^{SP}] \quad (10)$$

that correspond to dominant S or P propagation. The condition for the first bracket to vanish is a direct continuation of the surface wave branches from Eq. 9 corresponding to trapped S waves. The vanishing of the second bracket represents a suite of modes associated with multiple P -wave reverberations between the surface and structure at depth, which will be most evident when there is a rapid increase in P wavespeed in the near surface.

Thus, the dispersion relation (Eq. 7) can be read as the interaction of two separate dispersion systems for SV and P waves linked by the conversion terms

$$[R_D^{SP}R_F^{PP} + R_D^{SS}R_F^{SP}][R_D^{PP}R_F^{PS} + R_D^{PS}R_F^{SS}] \quad (11)$$

with a double surface interaction. The conversions R_D^{PS} , R_D^{SP} will have a strong dependence on the V_p/V_s ratio through the structure.

The modes with dominantly S character continue from the previous regime. For phase speeds c just greater than the surface P wave speed α_0 the free-surface reflection coefficient R_F^{SS} is quite small whilst R_F^{SP} is close to unity. This means that the near-surface conversions between P and S play an important role in controlling the modal dispersion.

Through this regime the main Rayleigh mode branches are controlled by the influence of S -wave structure. Even when P dominated branches are not directly evident their existence modulates the structure of the other mode branches by influencing their spacing (see, e.g., Figure 11.3 of Kennett, 1983; Sun et al., 2021). As noted above the spacing of branches at a given slowness is approximately proportional to the inverse of the delay time. This means that the spacing for the P -dominated modes with small delay is much larger than that for the S -dominated modes.

The full dispersion relation (Eq. 7) can be thought of as comprising the product of terms that would represent specifically S or P dispersion coupled by inter-conversions between wavetypes. A mode branch will switch character according to which dispersion relation is most closely satisfied. There will be a rapid switch in slope near where both dispersion relations approach zero. At such zones mode branches nearly touch ('osculation' points).

P propagating, S not trapped

$$(\alpha_L^{-1} < p < \beta_L^{-1}, \alpha_L > c > \beta_L)$$

Once the phase speed is larger than the shear wavespeed at the base of the structure, S waves leak into the underlying halfspace by radiation, and the S -dominated branches head into the leaking mode regime on lower sheets in the complex slowness plane at each frequency. Just beyond the cut off at $c = \beta_L$ such modes can still have a muted effect on the top sheet from the proximity of the poles.

Even so partial trapping is possible for P waves and the the response is singular when

$$1 - \mathbf{R}_D^{PP} \mathbf{R}_F^{PP} - \mathbf{R}_D^{PS} \mathbf{R}_F^{SP} = 0. \quad (12)$$

but this only occurs for complex p at real frequency. The dominant conversions will occur at the free surface. For a smooth wavespeed profile with gentle gradients with depth, internal conversion from P to S will be negligible, so the dispersion relation reduces to a direct analogue of the condition for acoustic modes in a layered fluid

$$1 - \mathbf{R}_D^{PP} \mathbf{R}_F^{PP} = 0, \quad (13)$$

but still $|\mathbf{R}_F^{PP}| < 0$ and so there are no real p roots for real frequency. With strong wavespeed gradients, such as in the near-surface zone in the presence of sediments, inter-conversions between P and S become significant and such P -dominated modes still have a dependence on the S wavespeed structure.

P and S not trapped

$$(p < \alpha_L^{-1}, c > \alpha_L)$$

Now the phase speed exceeds the P wavespeed at the base of the layering so that P waves radiate into the underlying half space and a modal treatment is no longer very useful. Only leaking modes are left well onto the underlying complex slowness sheets that have little influence on the real frequency-slowness response.

3 Interacting waveguides

The dependence of the seismic response for a surface source on structure at depth comes through the combination

$$[\mathbf{I} - \mathbf{R}_D^{0J}(p, \omega) \mathbf{R}_F(p)]^{-1} \mathbf{R}_D^{0L}(p, \omega) \quad (14)$$

in Equation 1. In the case of a structure containing two distinct parts separated by a level J we can expand the reflection term \mathbf{R}_D^{0L} into contributions associated with shallow ($0J$) and deep structure (JL):

$$\begin{aligned} \mathbf{R}_D^{0L} &= \mathbf{R}_D^{0J} + \mathbf{T}_U^{0J} [\mathbf{I} - \mathbf{R}_D^{JL} \mathbf{R}_U^{0J}]^{-1} \mathbf{R}_D^{JL} \mathbf{T}_D^{0J} \\ &= \mathbf{R}_D^{0J} + \hat{\mathbf{R}}_D^{JL}. \end{aligned} \quad (15)$$

We can think of these two parts of the structure as representing separate waveguides linked to surface reflections, with waves always having to pass through the shallower zone to get to the deeper. In consequence, there will be interaction between the surface wave propagation in the two waveguides.

With the split (Eq. 15) of the reflection response, the matrix inverse in Eq. 14 can be expanded as

$$\begin{aligned} [\mathbf{I} - \mathbf{R}_D^{0J} \mathbf{R}_F - \hat{\mathbf{R}}_D^{JL} \mathbf{R}_F]^{-1} &= [\mathbf{I} - \mathbf{R}_D^{0J} \mathbf{R}_F]^{-1} + \\ &[\mathbf{I} - \mathbf{R}_D^{0L} \mathbf{R}_F]^{-1} \hat{\mathbf{R}}_D^{JL} \mathbf{R}_F [\mathbf{I} - \mathbf{R}_D^{0L} \mathbf{R}_F]^{-1} + \dots, \end{aligned} \quad (16)$$

so that each reflection from the deeper part of the structure is accompanied by multiple reverberations in the shallow structure. Although Eq. 16 provides some insight into the wave processes at work it is not directly useful for assessing dispersion.

Using the decomposition (Eq. 15), the dispersion relation (Eq. 6) takes the form

$$\det(\mathbf{I} - \mathbf{R}_D^{0J}(p, \omega) \mathbf{R}_F(p) - \hat{\mathbf{R}}_D^{JL}(p, \omega) \mathbf{R}_F(p)) = 0. \quad (17)$$

We can rearrange this singular term as

$$\begin{aligned} \det([\mathbf{I} - \mathbf{R}_D^{0J}(p, \omega) \mathbf{R}_F(p)] \\ [\mathbf{I} - \hat{\mathbf{R}}_D^{JL}(p, \omega) \mathbf{R}_F(p)] \\ - \mathbf{R}_D^{0J}(p, \omega) \mathbf{R}_F(p) \hat{\mathbf{R}}_D^{JL}(p, \omega) \mathbf{R}_F(p)) = 0, \end{aligned} \quad (18)$$

where we extract the product of two components that have the form of dispersion elements for the shallower and deeper parts of the structure, together with a coupling term that involves both elements of the reflection response and the free surface reflections.

For a 2×2 matrix of the form $(\mathbf{I} - \mathbf{A} - \mathbf{B})$ the determinant can be expressed as

$$\begin{aligned} \det(\mathbf{I} - \mathbf{A} - \mathbf{B}) &= \det(\mathbf{I} - \mathbf{A}) \det(\mathbf{I} - \mathbf{B}) \\ &- \left\{ \det(\mathbf{A}\mathbf{B}) + \text{tr}(\mathbf{I} - \mathbf{A}) \text{tr}(\mathbf{I} - \mathbf{B}) \text{tr}(\mathbf{A}\mathbf{B}) \right. \\ &\quad \left. - \text{tr}[(\mathbf{I} - \mathbf{A})(\mathbf{I} - \mathbf{B})\mathbf{A}\mathbf{B}] \right\}. \end{aligned} \quad (19)$$

Thus if we identify $\mathbf{A} = \mathbf{R}_D^{0J} \mathbf{R}_F$ and $\mathbf{B} = \hat{\mathbf{R}}_D^{JL} \mathbf{R}_F$ our dispersion relation can be cast into the form

$$\det(\mathbf{I} - \mathbf{R}_D^{0J} \mathbf{R}_F) \det(\mathbf{I} - \hat{\mathbf{R}}_D^{JL} \mathbf{R}_F) - C_J = 0 \quad (20)$$

where the coupling term C_J involves a minimum of two surface reflection terms and propagation in both parts of the structure. This is a comparable scenario to that encountered above for the coupling of SV - and P -dominated modes.

Consider then the general coupled dispersion system

$$\det(\mathbf{I} - \mathbf{A}) \det(\mathbf{I} - \mathbf{B}) - C = 0, \quad (21)$$

at fixed slowness p and consider the neighbourhood of a root of $\det(\mathbf{I} - \mathbf{A}) = 0$ at frequency ω_A . Set $\omega = \omega_A + \delta\omega$ and then $\det(\mathbf{I} - \mathbf{A}) \approx \delta\omega \partial[\det(\mathbf{I} - \mathbf{A})]/\partial\omega|_{\omega_A}$. From Eq. 21 we then find

$$\delta\omega \approx \left[\frac{C}{(\det(\mathbf{I} - \mathbf{B}) \partial[\det(\mathbf{I} - \mathbf{A})]/\partial\omega + \partial C/\partial\omega)} \right]_{\omega_A}. \quad (22)$$

Unless $\det(\mathbf{I} - \mathbf{B})$ itself approaches zero, the frequency shift $\delta\omega$ will be small. Hence the dispersion characteristics will be close to that for the \mathbf{A} system alone. A

comparable effect arises near frequencies that satisfy $\det(\mathbf{I} - \mathbf{B}) = 0$, but now involving the frequency derivative for the \mathbf{B} relation. For such a coupling scenario we therefore have two sets of largely independent mode segments satisfying the separate dispersion relations, with strong interaction only where both dispersion relations are close to being satisfied.

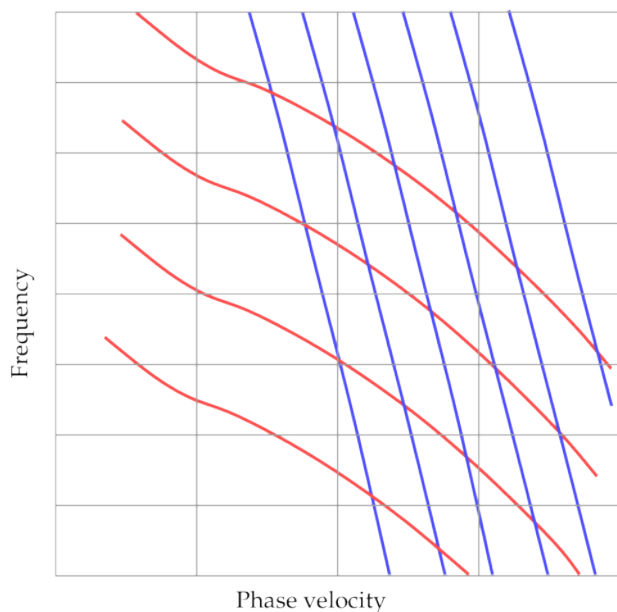


Figure 1 Schematic representation of multiple modes associated with a shallow low speed waveguide (red), crossing the modal curves for a deeper guide with higher wavespeeds (blue). The spacing of modes is inversely proportional to delay time and so larger for the lower wavespeed guide.

For our situation with a separation into shallower and deeper parts of the structure, we therefore have a mode branch suite with relatively wide spacing associated with the shallow component where the delay time is small, these will appear to cross the modes linked to the deeper structure with longer delay times and closer spacing. This situation is schematically rendered in Figure 1. There are no actual crossing points, though the various branches come close to touching. In the neighbourhood of these osculation points there is strong curvature as an individual mode branch switches character between shallow and steeper slopes. Even with just a separation into two parts we see that a formal description of the behaviour becomes quite complex, but we are able to recognise the main characteristics. With the addition of additional component of structure with depth, we will get a similar situation with suites of apparently distinct modes associated with each part of the structure that interact strongly locally.

For Rayleigh waves, the decomposition of the dispersion relation for each part of the structure will have a strong variation with slowness, as discussed above, because of the presence of both S - and P -dominated modes. Thus, superimposed on the basic mode structure controlled primarily by the S wavespeed distribution, we have further effects linked to the (partial) trap-

ping of P waves.

For Love waves in an isotropic model, the situation is simpler because we no longer have wavetype coupling and there is no slowness variation of the free-surface reflection coefficient. Nevertheless, there is still the potential for interaction between waves dominantly propagating in different parts of the stratification.

Each discontinuity in wavespeed structure or zone of strong wavespeed gradients will have a modest influence on the modal structure, but the largest effects are associated with significant jumps in physical properties, as in models comprised of a few uniform layers. In frequency-phase speed space the presence of a discontinuity induces an inflection in the slope of the modal trajectory around the wavespeed associated with the faster layer, even when modal branches do not approach closely. In effect, at each discontinuity we are seeing the interaction of the waveguides above and below the interface.

Strong effects on modal dispersion arise in the presence of pronounced zones of lowered seismic wavespeeds within the structure that act as strong waveguides, particularly at high frequencies. Channelled waves can be trapped in such waveguides, with only weak linkage to the external structure via evanescent waves (Kerry, 1981). The transition between the regular surface wave modes and the channel waves is very abrupt as a function of slowness (or phase speed) and can cause substantial difficulties in tracking individual mode branches.

4 Illustration of multi-mode surface waves and leaking modes

In the discussion above I have focussed on the dispersion of surface waves and the way that this is affected by coupling between different components of the waveguide and between wavetypes. The tracking of dispersion for complex models for even a few mode branches can become a tricky exercise in numerical root finding, particularly when it involves leaking modes where the singular points are no longer on the top sheet.

However, when seeking to understand the structure of the wavefield it is more effective to look directly at the response in the frequency–slowness or frequency–phase speed domain, since this will capture all the different mode branches and their relative excitation (e.g., Kennett, 2001; Dal Moro, 2020). All modes, including leaking ones, that make an effective contribution to the wavefield can thereby be captured. A number of authors have constructed such diagrams, principally in context of analysing models with a few uniform layers. For example, Li et al. (2022) have constructed ‘theoretical dispersion spectra’ as an aid to the interpretation of dispersion diagrams constructed from very dense LASSO array in Oklahoma, with attention to the difference in characteristics seen on the vertical and radial components.

A similar approach is adopted here to examine the separate behaviour of the SH and P - SV systems and the way in which the different components of the wavefield separate modes with dominant SV or P character. I con-

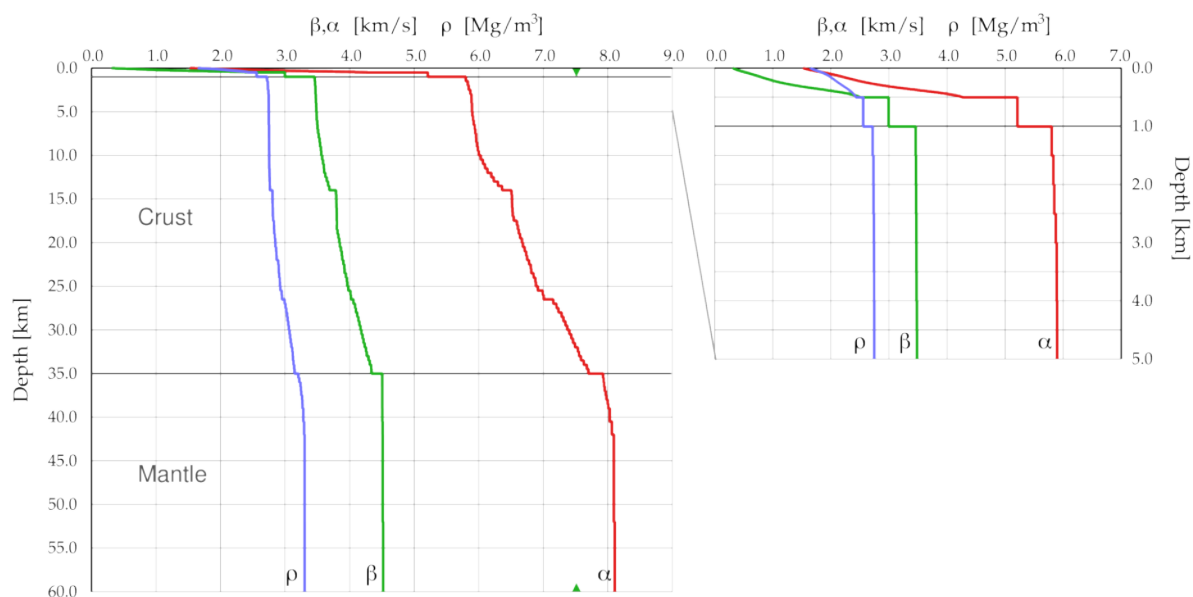


Figure 2 Seismic wavespeeds and density as a function of depth for a structure with sediments above a continental crust and mantle. The upper 60 km are shown, but the full model continues to 1000 km depth. The solid green triangles indicate the S wavespeed at the base of the model and thus the span of wavespeeds for which modes are fully trapped.

struct the three components of the seismic response from Eq. 1 for a surface source evaluated on a pre-assigned grid with even sampling in frequency and slowness or phase speed. The use of phase speed provides greater separation of the different aspects of the modal field and a more direct relation to the wavespeed structure and so is adopted in the figures below.

To illustrate the interaction of different waveguides, I have built a composite model with horizontal stratification combining realistic sedimentary, crustal and upper mantle structures (Figure 2). The shallow structure was derived from an ambient noise study on a dry lake bed to the north of Canberra in southeastern Australia (C. Jiang - personal communication, 2022). The crustal structure is derived from receiver function studies of stations in eastern Australia on Phanerozoic fold belts. The mantle structure below 45 km depth comes from *ak135* (Kennett et al., 1995) and is continued to 1000 km depth. Earth flattening is applied to compensate for the sphericity of the Earth. The S wavespeed at the base of the flattened model is 7.513 km/s, and only modes with phase speed higher than this will lie in the true leaking mode domain. At smaller phase speeds the extension of the structure to depth allows S waves lost from the crust to be returned to the surface by refraction and so ensure full trapping of energy, described by modes on the top slowness sheet.

This model has strong gradients in seismic wavespeed at the surface with a high ratio of P to S wavespeeds. The rapid changes in seismic wavespeed with depth allow strong trapping of both S and P energy above the basement structure. The wavespeed gradients are more muted in the crust down to 35 km depth, and then a modest jump in wavespeed at the Moho ties into the upper mantle structure. Fine discretisation with 5 m thick uniform layers was used to 0.5 km depth, and then for the crust layers 0.5 km thick were

employed. In the mantle below 45 km, layer thickness increases from 10 to 14 km with increasing depth. Weak attenuation has been applied throughout the model with $Q_{\alpha}^{-1} = 0.001$ and $Q_{\beta}^{-1} = 0.002$. The presence of attenuation means that no surface wave poles actually reside on the real phase speed axis.

In Figures 3 and 4 I show the frequency–phase speed response for the composite model, with 257 layers, for SV and SH excitation via a grey-tone display. The responses were calculated using recursive construction of the reflection matrix \mathbf{R}_D^{OL} for the entire structure for each phase speed and frequency. I have used 200 frequencies and 400 phase speeds for these displays and have set a common threshold for the transition to black. The various modes appear directly through the elevated amplitude associated with the trajectories of the modal dispersion. The first few modal dispersion curves are labelled for Rayleigh waves in Figure 3 and Love waves in Figure 4. In each case the width of the band around each mode provides a measure of the relative excitation.

A comparison of the response of the full model and that for just the sediment zone is made in Appendix A. The dispersion curves for both Rayleigh waves and Love waves out to 5.3 km/s, for the full model are displayed in Appendix B.

There is a notable difference between the SV and SH scenarios. The gradient zones in the sediments have a stronger effect on the Rayleigh modes than the Love modes, in part because of the rather low P wavespeeds at the surface. In each case the multiple mode branches associated with crustal trapping of S waves appear once the phase speed exceeds 3.5 km/s. For the Rayleigh modes the transition between the continuation of the sediment mode branches and the crustal modes is so sharp that the first higher mode branch appears to be dissected into several pieces. For the second higher mode it is more difficult to track the continuation of the

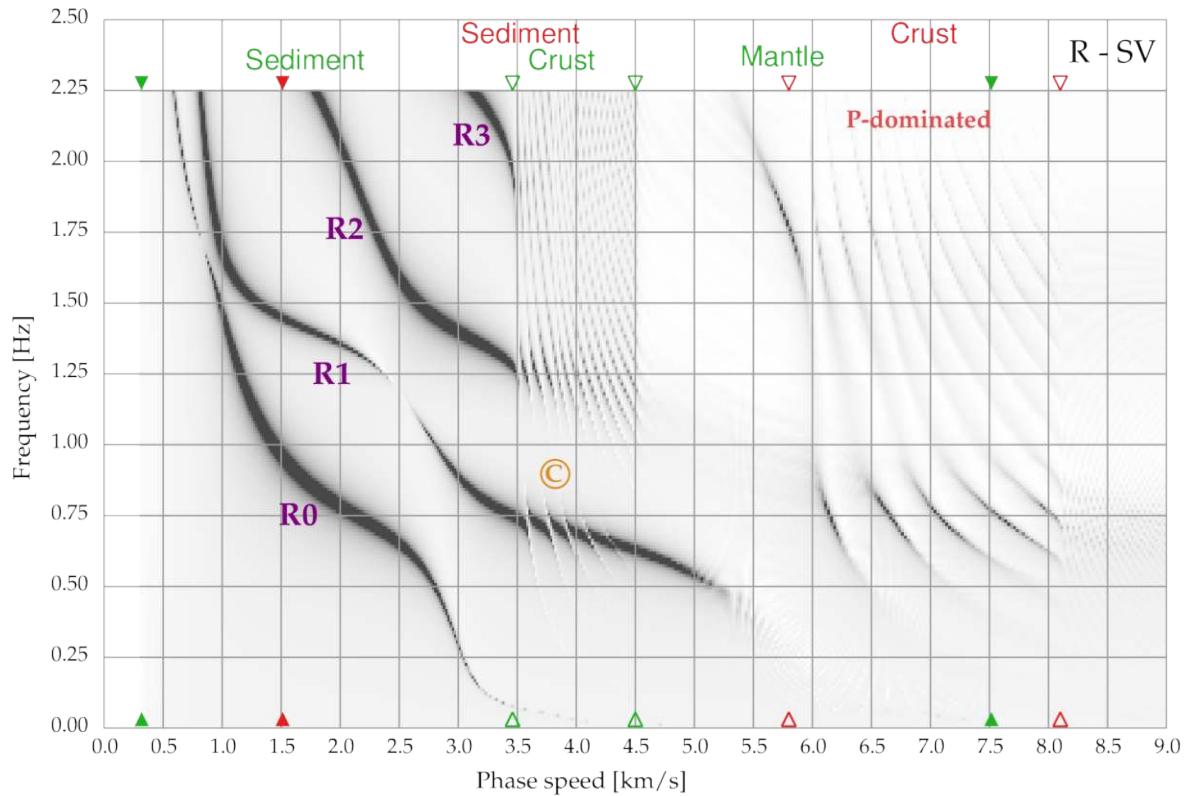


Figure 3 The radial component of the surface response in frequency–phase speed for the composite model, corresponding to SV excitation. The radial component emphasises Rayleigh modes for lower phase speeds, but still displays noticeable contributions from *P*-dominated modes for the interval of crustal *P* wavespeeds. The markers indicate the wave speeds associated with the different segments of the model (Figure 2) with *S* structure in green and *P* in red. The solid symbols mark the wave speeds at the surface and the base of the full model.

mode branch but its presence is apparent from the enhanced visibility of the crustal modes. A similar effect is seen for the Love modes, where the crustal modes appear more distinctly in the zone where the extension of the sediment branches occurs, even though the continuation of such branches cannot be tracked directly. These features associated with interaction between waveguides are marked with a circled C in both Figures 3 and 4. Such complications will not be readily picked up by conventional dispersion calculations unless they are accompanied by detailed assessments of relative amplitudes (Sun et al., 2021), but this involves much more work than the direct approach employed here.

With the threshold employed for the plots in Figures 3 and 4, the modal branches associated with mantle propagation are very difficult to discern for either Rayleigh or Love waves. Such modes are much more effectively excited for sources at depth, and can be handled with a similar frequency–phase speed approach with a source set at some depth. The trajectories of the modal branches are unaffected by such a change of reference level, but the amplitudes will be modified.

To the right of Figure 3, for wavespeeds greater than 5.0 km/s, we see a group of mode branches associated with *P* wave propagation in the crust that extend into the leaking mode zone and even begin to pick up mantle effects, though finer sampling in frequency would be needed to see the details. It is intriguing to find

that these *P*-dominated modes are most visible along the general location of the extension of the SV sedimentary branches. The delay times for *P* waves in the crust are around 1.8 times smaller than those for *S* waves so the spacing between the mode branches in frequency is greater.

In the frequency range displayed in Figure 3 there is no direct interaction between *P*- and SV-dominated modes. To see such effects we need to look at somewhat higher frequencies. In Figure 5 I have confined attention to phase speeds between 2.0 and 6.0 km/s for frequencies up to 10 Hz. This figure compares the vertical component for *P* excitation with the radial component for SV excitation. The two images of the frequency–phase speed response strikingly separate the *P*-dominated modes on the vertical component from their SV-dominated counterparts on the radial component.

The complementary character of the *P*-dominated and SV-dominated modes is well illustrated in Figure 5. The *P*-dominated trajectories are comprised of segments of many different mode branches. The net effect is to cut across the SV-dominated modes with just short intervals in phase speed where character is indeterminate, as expected from Eq. 22. In the neighbourhood of the close approach between mode branches with different physical character, the modes are visible in both displays. However, away from such locations the modes tend to be more distinct in one or other of

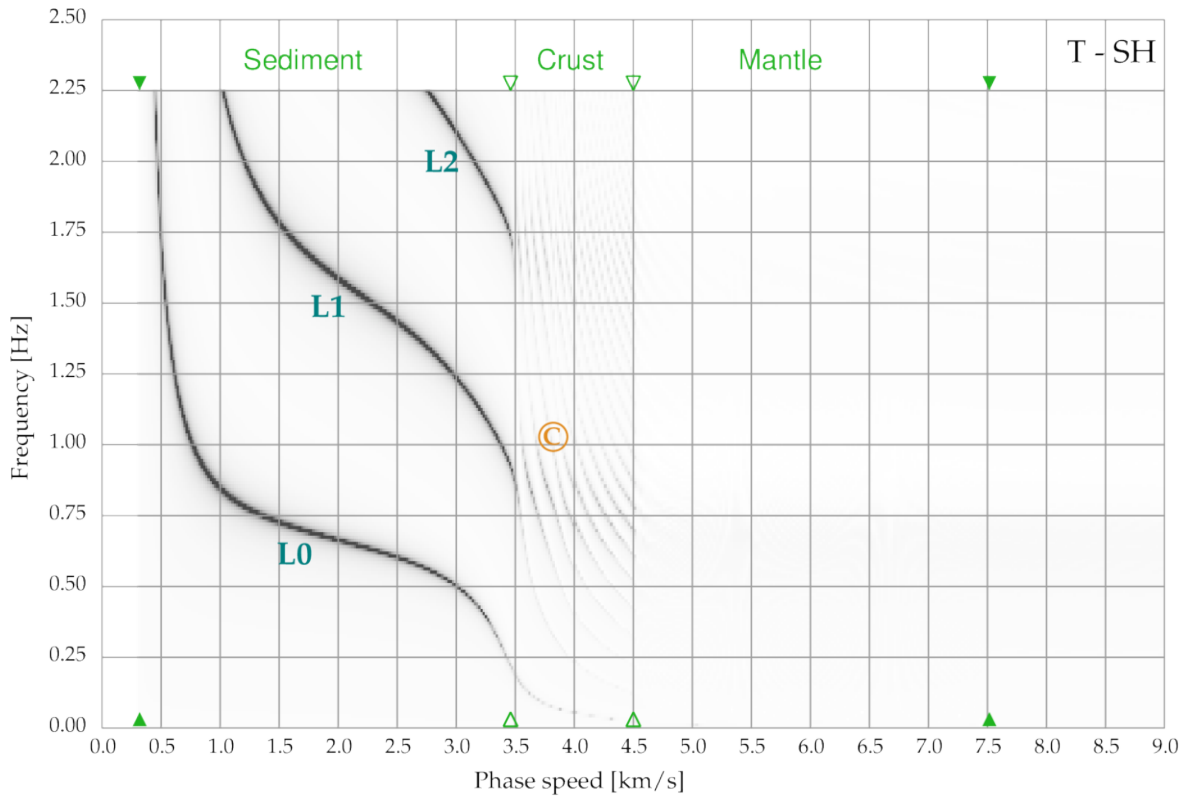


Figure 4 The tangential component of the surface response in frequency–phase speed corresponding to *SH* excitation displaying the Love modes in the sediment and crust. The markers indicate the S wave speeds associated with the different segments of the model (Figure 2). The solid symbols mark the wave speeds at the surface and the base of the full model.

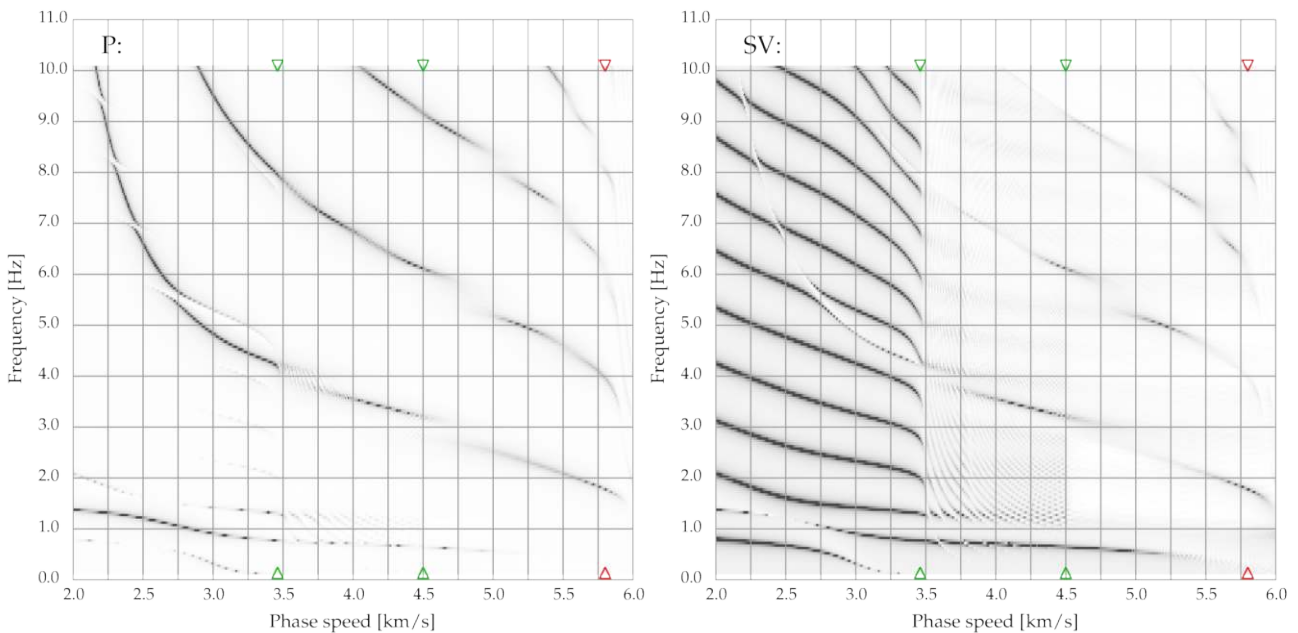


Figure 5 Comparison of the frequency–phase speed response for the vertical and radial components in the composite model. The left-hand panel shows the vertical component emphasising modes that have *P*-dominated behaviour, and the right-hand panel shows the radial component with *SV*-dominated modes. The markers follow the same convention as in Figure 3.

the panels. We have noted before the way in which the crustal modes apparently cut the extension of the sedimentary *SV* branches; a similar effect can be seen for the *P* mode branches. The blurring of the *P*-dominated

mode branches beyond 4.5 km/s arises from the influence of the upper mantle on the higher branches of the *SV*-dominated modes.

In this complex near-surface structure the first higher

mode has a higher P wave content than the fundamental mode. Such behaviour has been found for other models with strong near-surface gradients and would not be expected from studies that employ relatively thick uniform layers.

5 Discussion and Conclusions

Modern developments in seismic recording open up the possibility of a full rendering of the wavefield, and this needs to be complemented by holistic methods that can present the full character of the seismic response of a medium. As the higher modes of surface waves become more readily accessible, the full character of seismic structures can be revealed rather than the muted versions derived from just the dispersion of the fundamental mode.

The direct use of frequency–phase speed as presented here enables effective analysis of complex structures, without any of the issues associated with the presence of, e.g., low velocity channels, in dispersion calculations. All modes are present and can be examined in detail by appropriate choice of frequency and phase speed ranges. On even a modest computer a 200×200 frequency–phase speed array can be calculated for a 400 layer model in a few seconds to visualise the full suite of modes and their interactions.

The effect of sediment compaction means that the near-surface frequently contains quite strong wavespeed gradients, and such structures contribute strongly to the trapping of both S and P waves that can be recognised as surface wave branches. For shallow structure it is tempting to make an approximation with a few uniform layers to simplify inversion, but this approach runs the risk of an inadequate representation of the physical processes.

The modulation of SV -dominated dispersion curves by the influence of the P wavespeed structure so clearly seen in Figure 5 has been suggested as a diagnostic for estimating shallow P wavespeeds (Li et al., 2021). For such studies it is important that a full elastic treatment be made, because the acoustic approximation will tend to under-estimate the modal frequencies, though the discrepancy is reduced for very low shear wavespeeds compared to those for P waves (Roth et al., 1998). With considerable effort it is possible to track leaking modes on the other sheets (Shi et al., 2021), but it is preferable to work with an extension of structure to depth so that only propagating modes need be considered. As noted in Appendix A, such an extension also means that the low-frequency parts of the dispersion characteristics can be correctly captured.

The use of the frequency–phase speed diagrams enables an improved understanding of the characteristics of the interactions of surface wave modes due to the presence of waveguides formed by different parts of the structure or the effects of the structure associated with different wavetypes. Where fine sampling of the seismic wavefield has been achieved, observed seismograms can be transformed into the frequency–phase speed domain using, e.g., the F-J transform (Li et al., 2021). It is then possible to contemplate direct compar-

ison of the theoretical and observed response in this transform domain, as the basis for a nonlinear inversion using an exploration of a suitable parameter space. Where specific dispersion results are needed, the techniques developed for handling observed spectra (e.g., Dong et al., 2021) can be used to extract the trajectories of mode branches in frequency–phase speed space.

The results we have derived are for a stratified model with no horizontal variation in seismic wavespeeds within each layer, for which the various surface wave modes propagate independently. The influence of lateral heterogeneity can be described by introducing coupling between mode branches, which will have most effect when modal branches are tightly spaced. Thus, although variations in the near surface are stronger than at depth, the broad spacing of the modal branches mean that their general character will be maintained. In general, the strongest features seen in the frequency – phase speed response diagrams in Figure 3 and 4 can be expected to be robust under the influence of moderate horizontal changes in wavespeed.

Acknowledgements

Emeritus support from the Research School of Earth Sciences, Australian National University is gratefully acknowledged. Discussions with Chengxin Jian and Andreas Fichtner have encouraged the development of the material presented here.

Data and code availability

Fortran codes for frequency-slowness (phase speed) synthesis and display are made available at Zenodo (Kennett, 2022, doi: 10.5281/zenodo.7384357).

Competing interests

None

References

- Chapman, C. H. The Earth flattening approximation in body wave theory, *Geophys. J. R. Astr. Soc.*, 35, 1973. doi: 10.1111/j.1365-246X.1973.tb02414.x.
- Chen, J., Pan, L., Li, Z., and Chen, X. Continental reworking in the eastern South China Block and its adjacent areas revealed by F-J multimodal ambient noise tomography. *J. Geophys. Res.: Solid Earth*, 127, 2022. doi: 10.1029/2022JB024776.
- Chen, X. A systematic and efficient method of computing normal modes for multilayered half-space. *Geophys. J. Int.*, 115(2), 1993. doi: 10.1111/j.1365-246X.1993.tb01194.x.
- Dal Moro, G. The magnifying effect of a thin shallow stiff layer on Love waves as revealed by multi-component analysis of surface waves. *Sci. Rep.*, 10, 2020. doi: 10.1038/s41598-020-66070-1.
- Dong, S., Li, Z., Chen, X., and Fu, L. DisperNet: An effective method of extracting and classifying the dispersion curves in the frequency–Bessel dispersion spectrum, *Bull. Seismol. Soc. Am.*, 111, 2021. doi: 10.1785/0120210033.
- Fichtner, A., Hofstede, C., Kennett, B. L. N., Nymand, N. F., Lauritzen, M. L., and Eisen, O. Fiber-optic airplane seismology on the northeast Greenland ice stream, submitted 2023.

- Haddon, R. A. W. Computation of synthetic seismograms in layered earth models using leaking modes. *Bull. Seism. Soc. Am.*, 74(4), 1984. doi: 10.1785/bssa0740041225.
- Kennett, B. L. N. *Seismic Wave Propagation in Stratified Media*. Cambridge University Press, 1983.
- Kennett, B. L. N. *The Seismic Wavefield I: Introduction and Theoretical Development*. Cambridge University Press, 2001.
- Kennett, B. L. N. Construction of Frequency-Slowness and Frequency-Phase speed diagrams. doi: 10.5281/zenodo.7384357.
- Kennett, B. L. N. and Clarke, T. J. Rapid surface wave dispersion calculations, *Geophys. J. R. Astr. Soc.*, 72, 1983. doi: 10.1111/j.1365-246x.1983.tb02823.x.
- Kennett, B. L. N., Engdahl, E. R., and Buland, R. Constraints on seismic velocities in the Earth from travel times, *Geophys. J. Int.*, 122, 1995. doi: 10.1111/j.1365-246x.1995.tb03540.x.
- Kerry, N. J. Synthesis of seismic surface waves, *Geophys. J. R. Astr. Soc.*, 64, 1981. doi: 10.1111/j.1365-246x.1981.tb02675.x.
- Li, Z., Shi, C., and Chen, X. Constraints on crustal P wave structure with leaking mode dispersion curves. *Geophysical Research Letters*, 48, 2021. doi: 10.1029/2020GL091782.
- Li, Z., Shi, C., Ren, H., and Chen, X. Multiple leaking mode dispersion observations and applications from ambient noise cross-correlation in Oklahoma. *Geophysical Research Letters*, 49, 2022. doi: 10.1029/2021GL096032.
- Nakata, N., Gualtieri, L., and Fichtner, A. *Seismic Ambient Noise*. Cambridge University Press, Cambridge, 2019.
- Roth, M., Holliger, K., and Green, A. G. Guided waves in near-surface seismic surveys. *Geophysical Research Letters*, 25, 1998. doi: 10.1029/98gl00549.
- Shi, C., Ren, H., Li, Z., and Chen, X. Calculation of normal and leaky modes in planar waveguides based on a semi-analytical spectral element method. *Geophys. J. Int.*, 230, 2021. doi: 10.1093/gji/ggac163.
- Sun, C., Wang, Z., Wu, D., Cai, R., and Wu, H. A unified description of surface waves and guided waves with relative amplitude dispersion maps. *Geophys. J. Int.*, 227, 2021. doi: 10.1093/gji/ggab284.

Appendix A: Comparison of coupled and single waveguide results

In Section 4 I have shown the dispersion characteristics for the composite model, where there are three major divisions of seismic structure that each act as a waveguide. How then does the response compare with the situation where the sediment zone is considered on its own? The sedimentary structure is taken down to 1 km depth (as indicated in the right hand panel in Figure 1) and then extended to a half space with no contrast in physical properties, rather than the further jump as in the case where the full crust and mantle are included.

In Figure 6 I show a comparison of the frequency-phase speed response for the two cases for frequencies up to 5 Hz and phase speeds out to 6 km/s. The modes for the sediment-only case are superimposed in magenta on the grey tone for the full model. The underlying half-space for the sediment-only model now has S wavespeed of 3.0 km/s and P wavespeed of 5.2 km/s, so that everything with phase speeds greater than 3 km/s represents leaking modes for this case. However, in the

full model this regime will still contain trapped modes.

For phase speeds below 2.2 km/s there is a complete correspondence between the Rayleigh modes for the sediment-only and full cases. This regime represents trapping by the strong near-surface S wavespeed gradients. The change in structure at depth between the two models manifests itself in a change in the character of the fundamental mode and the first higher mode with frequency. The first higher mode shows a distinct sensitivity to P wave structure and extends well into the leaking mode domain. There is slight P dependence for the second higher mode that only just nudges into the leaking mode field. The other higher modes for the sediment-only case effectively truncate at the 3.0 km/s cut off associated with the underlying half space. It is interesting to note that the extension of these branches in the full model to the entry into the main crustal waveguide at 3.5 km/s shows weak P wavespeed dependence.

In the frequency range up to 5 Hz, only the lowest frequency mode for P-dominated propagation is visible. For the phase speed range less than 4.5 km/s where the P waves interact with the wavespeed gradient in the sediment, the leaking mode for the sediment-only case and the trapped mode for the full model coincide apart from the interruptions by the crustal modes. The behaviour near the P cut off for the sediment only case, as near the S cut off, is modified by the absence of the deeper structure.

The changes in the dispersion behaviour imposed by the truncation of the model in the sediment-only case present a warning for sensitivity to the assumptions made about the extent of the model. As noted earlier it is preferable for models to be allowed to extend to substantial depth, so that the evanescent behaviour of the modes is well represented, rather than to force a specific, shallow, depth for the range of the structure. Inversion of the true dispersion curves with a truncated model is liable to produce a distortion of structure, particularly if only the first couple of modes are available. The dispersion curves for slower phase speeds should be reliable, and discrepancies will only occur as the assumed S wavespeed for the uniform underlying half space is approached.

In many studies the choice of the depth at which a transition is made into a uniform half space is made based on *a priori* assumptions about the nature of structure. Thus it would be common to make a truncation at the expected base of sediments and often to use a model composed of a few uniform layers. Strong gradient zones, such as in compacting sediments, require fine layering for an accurate description of the wave behaviour and there is the potential for an over-simplified model to be very misleading. Complications will ensue if there is a significant interface in the actual scenario below the level of truncation. This can be seen in Figure 6 in the behaviour of the fundamental and first higher Rayleigh modes.

Appendix B: Dispersion Curves

In Section 4 we have demonstrated the interaction of multiple wave guide effects by examining the re-

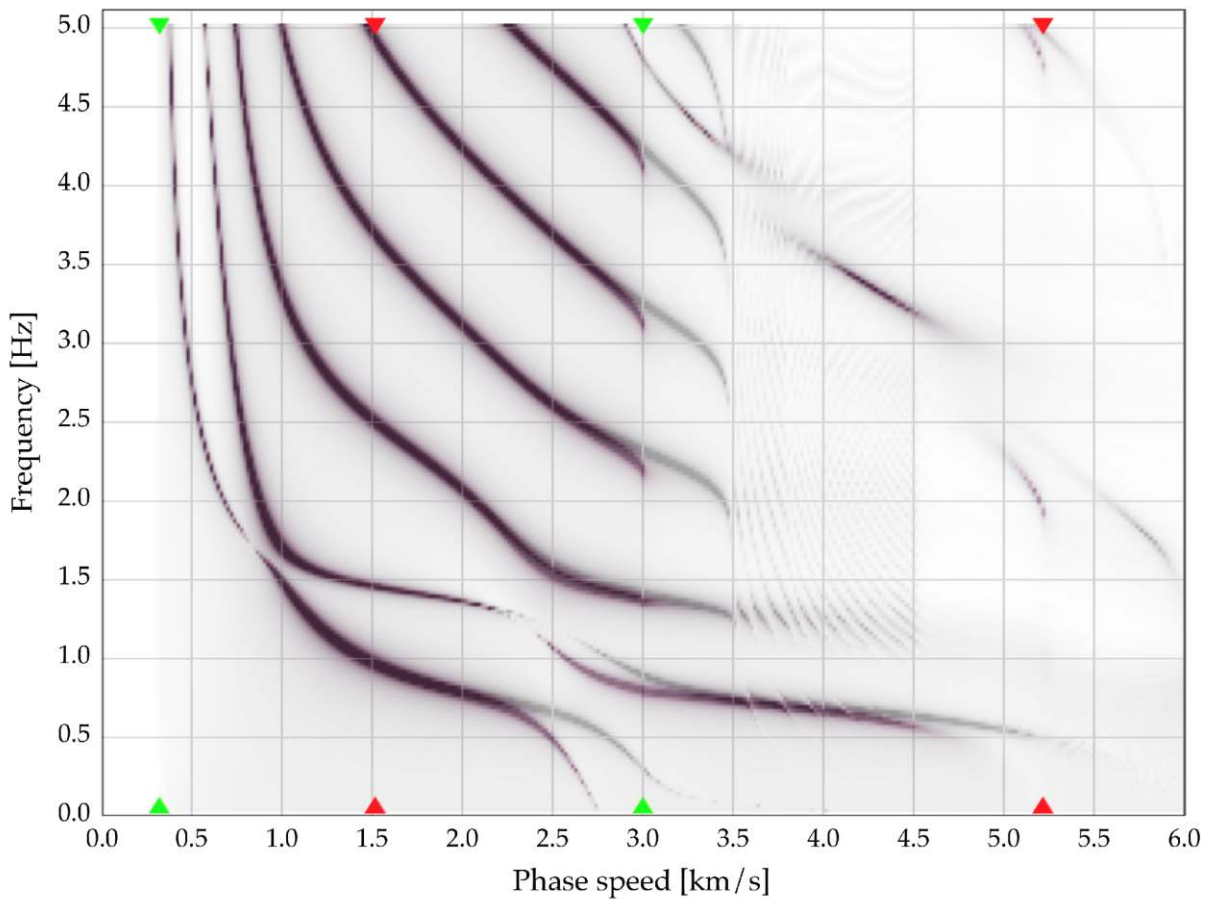


Figure 6 Comparison of the frequency–phase speed response for the full composite model (Figure 2) in grey and just the sediment component (model truncated at 1 km depth) in magenta. The markers indicate the wave speeds associated with the sediment component of the model with S structure in green and P in red. The solid symbols mark the wave speeds at the surface and the base of the sediments.

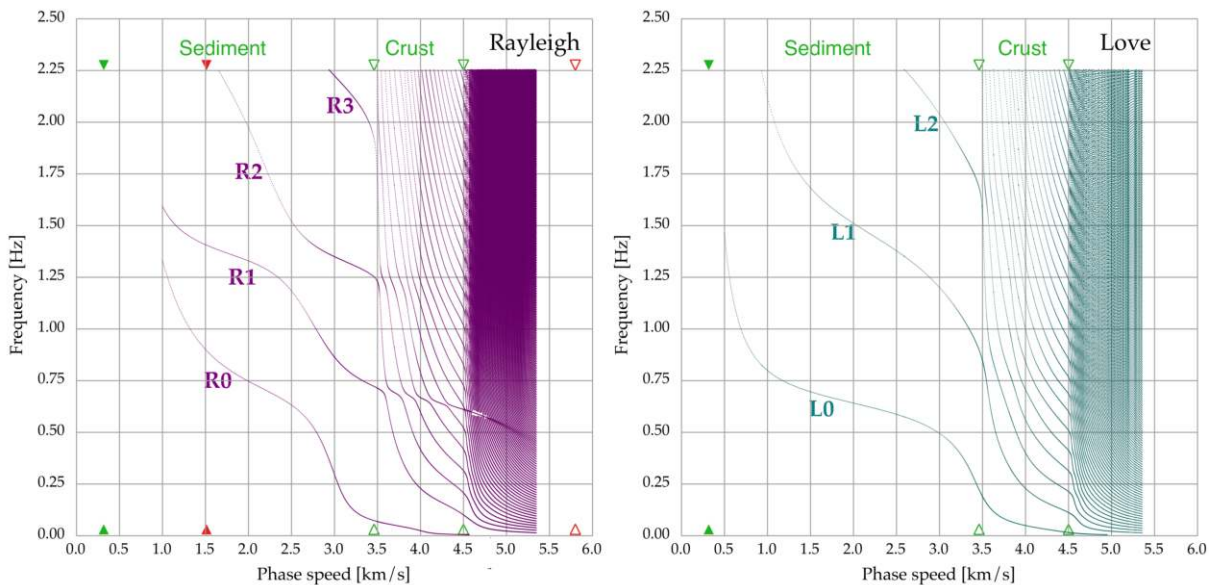


Figure 7 Dispersion curves for both Rayleigh and Love waves for phase speeds out to 5.3 km/s, for the same frequency band as used in Figures 3 and 4. The markers follow the same convention as in the earlier figures.

sponse in frequency – phase speed space, rather than the more conventional approach of working with dispersion curves. In Figure 7 we show the dispersion curves for both Rayleigh and Love wave modes for

phase speeds out to 5.3 km/s, for the same frequency band as in Figures 3 and 4. A slightly simplified model has been used with 100 layers extending down to 410 km depth. For higher phase speeds more than 200 modes

occur in the frequency interval up to 2.25 Hz and it is no longer at all easy to track features that depend on subtle modulation of the spacing of the modal branches.

This portion of frequency – phase speed space was computed for Figures 3 and 4 with 200×200 evaluations of the response, i.e., 40,000. Whereas, for the dispersion behaviour the roots of the secular equation have to be found for each mode. The dispersion results in Figure 7 were computed with the scheme of Kerry (1981) which uses fixed phase speed and then searches for successive modes in frequency. The choice of phase speed step is adaptive so that the changes in slope of the mode branches can be followed. More than 50,000 roots need to be found for the Love wave diagram and over 200,000 for the Rayleigh case. For each root the frequency has to be bracketed and refined. This means that many response evaluations are required and so computation times are typically several orders of magnitude greater than for the direct approach used in Figures 3 and 4. Very high precision is needed to disentangle the modal branches and their changes of slope.

We can see a direct correspondence between the visible features in Figures 3 and 4 and the structure of the dispersion branches for the span of phase speeds covered in Figure 7. Where apparent extensions of modal branches from the sediments to higher wavespeeds occur we can see that they are related to the fine structure of the dispersion curves and, notably, tight osculation points. This is very distinctive for the projection of the mode R1 through the crustal and mantle branches. The switches between branches occur on such a fine scale that some roots were missed or misidentified, producing a small blank zone for phase speeds between 4.6 and 4.7 km/s associated with the depth range between 120 and 210 km in the mantle.

The article *Interacting Seismic Waveguides: Multimode Surface Waves and Leaking Modes* © 2023 by Brian L.N. Kennett is licensed under CC BY 4.0.

How reproducible and reliable is geophysical research? A review of the availability and accessibility of data and software for research published in journals

Mark T. Ireland ^{*1}, Guillermo Algarabel², Michael J. Steventon ³, Marcus R. Munafò ⁴

¹Newcastle University, School of Natural and Environmental Sciences, Drummond Building, Newcastle Upon Tyne, NE1 7RU, ²Department of Physics, Durham University, Durham University, Stockton Road, Durham, DH1 3LE, ³Shell Research Ltd., Shell Centre, London, United Kingdom, ⁴School of Psychological Science, University of Bristol, Bristol, United Kingdom

Author contributions: *Conceptualization:* M. T. Ireland. *Conceptualization Supporting:* M. J. Steventon, M. R. Munafò. *Data Curation:* G. Algarabel, M. T. Ireland. *Formal Analysis:* G. Algarabel, M. T. Ireland. *Investigation:* M. T. Ireland, G. Algarabel, M. J. Steventon, M. R. Munafò. *Writing – original draft:* M. T. Ireland. *Writing – review & editing:* M. T. Ireland, M. J. Steventon, M. R. Munafò, G. Algarabel.

Abstract Geophysical research frequently makes use of agreed-upon methodologies, formally published software, and bespoke code to process and analyse data. The reliability and repeatability of these methods is vital in maintaining the integrity of research findings and thereby avoiding the dissemination of unreliable results. In recent years there has been increased attention on aspects of reproducibility, which includes data availability, across scientific disciplines. This review considers aspects of reproducibility of geophysical studies relating to their publication in peer reviewed journals. For 100 geophysics journals it considers the extent to which reproducibility in geophysics is the focus of published literature. For 20 geophysical journals it considers a) journal policies on the requirements for providing code, software, and data for submission; and b) the availability of data and software associated for 200 published journal articles. The findings show that: 1) between 1991 and 2021 there were 72 articles with reproducibility in the title and 417 with reliability, with an overall increase in the number of articles with reproducibility or reliability as the subject over the same period; 2) while 60% of journals have a definition of research data, only 20% of journals have a requirement for a data availability statement; and 3) despite ~86% of sampled journal articles including a data availability statement, only 54% of articles have the original data accessible via data repositories or web servers, and only 49% of articles name software used. It is suggested that despite journals and authors working towards improving the availability of data and software, frequently they are not identified, or easily accessible, therefore limiting the possibility of reproducing studies.

Non-technical summary In studies of the Earth, other planets, oceans and atmospheres, scientists often carry out quantitative analysis of measurements from specialist instruments or create numerical models to represent complex natural systems. These approaches are useful for understanding important processes such as plate tectonics and patterns of ocean circulation, and often have wider societal importance, such as understanding natural hazards or the distribution of economically significant natural resources. When scientists present the findings of their work in scientific publications, the focus is primarily on the written narrative. However, a cornerstone of the scientific method should be the ability to replicate an experiment or study. To enable this the input data and details of the methodology, for example the computer code used, are essential. This work reviewed how reproducible the published work in the field of geophysics has been to date. The findings show that despite most publications now requiring the underlying data to be made available, most of the time these data are not easily accessible, and therefore limit the opportunity for scientists to verify existing findings.

1 Introduction

Geophysics is perhaps best described as the application of physics to study the Earth, oceans, atmosphere, and near-Earth space, including other planets ([British Geophysical Association, 2014](#)). Geophysical methods, which typically either take raw records from instrumentation and process the recorded signals or carry out numerical modelling, rely on quantitative analysis to make robust interpretations of these systems. Frequently,

geophysical methods use processing flows with numerous (often iterative) steps to accomplish tasks such as, for example, distinguishing signal from noise ([Robinson and Treitel, 2000](#)), or modelling complex processes such as mantle convection ([Hager and Clayton, 1989](#)). The reproducibility and reliability of these methods is vital to ensure that the scientific community can verify previous findings and avoid the dissemination, or misinterpretation, of results which are unreliable or ambiguous ([Steventon et al., 2022](#)). Computer analysis has long been vital to geophysical methods (cf. [Reese, 1965](#)),

Production Editor:
Gareth Funning
Handling Editor:
Samantha Teplitzky
Copy & Layout Editor:
Hannah F. Mark

Reviewed by:
Daniel Nüst
Wynn Tranfield

Received:
16 November 2022
Accepted:
10 May 2023
Published:
30 May 2023

*Corresponding author: mark.ireland@newcastle.ac.uk

and this continues to be true today, where most methods involve the use of code or software to process and analyze data sets of ever increasing volume.

Different scientific disciplines often use reproducibility and replicability inconsistently (National Academies of Sciences, 2019). In geophysics, and Earth Sciences more broadly, definitions and terminology used for reproducibility, replicability and reliability in research have not been examined to the same extent that they have been in, for example, medical sciences (e.g., Goodman et al., 2016). The Turing Way project defines reproducible research as “work that can be independently recreated from the same data and the same code that the original team used” (Arnold et al., 2019). It is useful to expand this definition by classifying how reproducible research is different from robust, replicable, and generalisable research (Figure 1). The Turing Way definitions for each of are as follows:

- **Reproducible:** when the same analysis steps performed on the same dataset consistently produces the same answer.
- **Replicable:** when the same analysis performed on different datasets produces qualitatively similar answers.
- **Robust:** when the same dataset is subjected to different analysis workflows to answer the same research question and a qualitatively similar or identical answer is produced. Robust results show that the work is not dependent on the specifics of the programming language/equipment/methodology chosen to perform the analysis.
- **Generalisable:** Combining replicable and robust findings allow us to form generalisable results. Generalisation is an important step towards understanding that the result is not dependent on a particular dataset nor a particular version of the analysis pipeline.

To date the existing published literature on the topic of reproducibility in geophysics can broadly be grouped into four areas: 1) the benefits of specific open-source software for improved repeatability (e.g. Oren and Nowack, 2018); 2) the repeatability of surveying techniques (e.g. Waage et al., 2018); 3) the reproducibility of individual studies (e.g. Walker et al., 2021); and 4) improving the repeatability of specific workflows (e.g. Jun and Cho, 2022). There has been some limited examination of reproducibility in geosciences more broadly (e.g., Konkol et al., 2019; Nüst and Pebesma, 2021; Steventon et al., 2022). Specifically in the field of geophysics, however, to date there has been no empirical consideration of the extent to which the existing publications and published work are reproducible.

The role of journals has been described as a way to provide a source of information and knowledge that can easily be located and read (Childe, 2006). This includes specifically: 1) registration of the author’s claim to the work; 2) certification, usually by peer review,

that the research was conducted properly; 3) dissemination; and 4) archiving, providing a permanent public record of the work that can be found and cited (Rallison, 2015). Preserving the data and methods that underpin research has become an increasingly important part of the publication process. In some subjects journals have acknowledged the need to strengthen approaches to reproducibility (Nature, 2014) and some even adopt specific policies with regards to verification of results (e.g., American Journal of Political Science, 2019). Similarly, the Transparency and Openness Promotion (TOP) guidelines were introduced by the Centre for Open Science to review the extent to which the research that journals support improves reproducibility through increasing the transparency of the research process (Nosek et al., 2015).

This work attempts to quantify the ways in which existing journals that publish geophysical research have to date made data and software available and accessible, in turn promoting reproducibility and repeatability.

2 Reproducibility, repeatability, and data availability

In recent years there has been increased attention on aspects of reproducibility, including data availability, across many scientific disciplines (e.g. Tedersoo et al., 2021); however, there has been limited focus on this topic in areas of Earth Sciences (Wildman and Lewis, 2022). At the 2016 G20 Summit, the G20 leaders formally endorsed the application of FAIR principles to research data (European Commission, 2016). The FAIR principles set out the importance of research data being Findable, Accessible, Interoperable and Reusable to improve and accelerate scientific research (Hodson et al., 2018) and were set out by a diverse set of stakeholders across academia, industry, funding agencies, and scholarly publishers. Contemporaneous to this, computational approaches have become increasingly important as more and more scientists are now able to adopt computational methods due to the improved ease and availability of both hardware and software (cf. Mesirov, 2010). Indeed, software is now a ubiquitous, if often invisible, component of research in most scientific disciplines, and for research to be reproducible requires understanding the software used by the original research (e.g., National Academies of Sciences, 2016). With this, the availability and support for large scale data sharing has led to increased attention and resources to enable scientists to share data (Tenopir et al., 2011). Despite computational and storage infrastructure being in place, there are still perceived barriers to effectively making both data (Tenopir et al., 2011) and software (Gomes et al., 2022) available and accessible. In a survey of >1300 scientists on data sharing practices, Tenopir et al. (2011) found that one third of the respondents chose not to answer whether they make their data available to others, and of those that did respond 46% reported they do not make their data electronically available to others. In exploring why researchers chose not to make their data available Tenopir et al. (2011) found

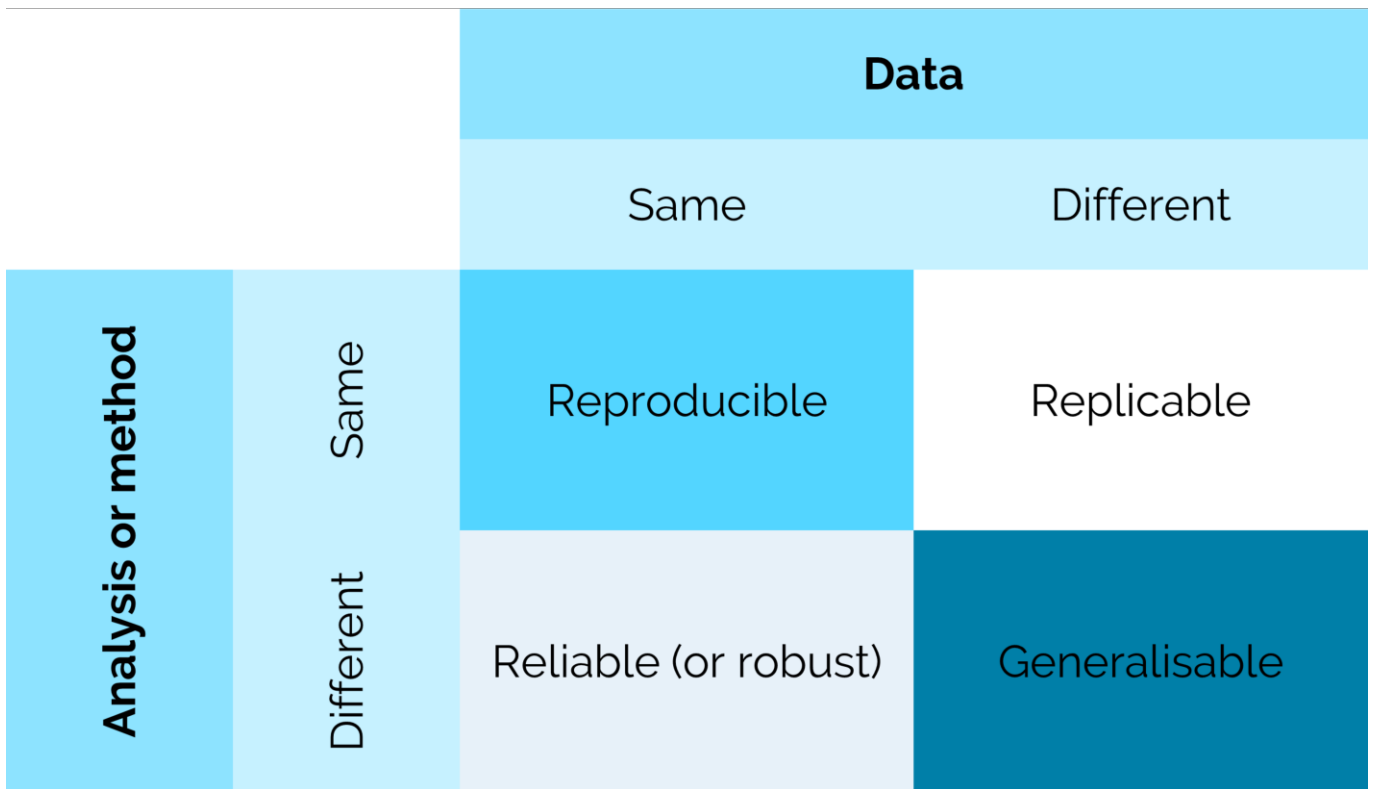


Figure 1 Definitions of reproducible, replicable, reliable, and generalisable, mapped against data and methods. Modified after Arnold et al. (2019).

the leading reason is insufficient time (54%), followed by lack of funding (40%), having no place to put the data (24%), lack of standards (20%), and “sponsor does not require” (17%), with only 14% of respondents stating their data “should not be available”. For code sharing, Gomes et al. (2022) identified reasons why code sharing is not more common in biological sciences, including perceived barriers such as: unclear process, complex workflows, data too large, lack of incentives, and concerns on re-use of data. These barriers are also identified in other disciplines, for example psychology (Houtkoop et al., 2018), and more broadly across the science community (Borgman, 2010).

3 Review Methodology

This study considers the reproducibility of geophysical studies which have been published in peer reviewed journals. It does not include any consideration of the reproducibility of geophysical studies outside of this, for example unpublished work from the private sector, or non-peer reviewed published reports. The analysis consists of three parts: 1) a mapping review of the extent to which reproducibility in geophysics is explored in the literature; 2) a review of journals’ policies on the requirements for providing code, software, and data for submission; and 3) a sample of articles examining the availability of code, software, and data.

Each part of the analysis is based on geophysical journals as identified by SCImago Journal Rank (see Supplemental Table 1 in Ireland, 2022). SCImago Journal Rank (SJR) is a numeric value representing the average number of weighted citations received during a selected

year per document published in that journal during the previous three years, as indexed by Scopus (SCImago). While journal metrics are frequently misused to assess the influence of individual papers (Pendlebury, 2009), here the list is simply used as a mechanism to firstly identify journals by subject area. Each journal in the list is assigned a subject area and subject category. We include journals where either the first or second subject category is “geophysics”. The journals identified using SCImago are a broad representation of journals which may be widely read and used by the geophysics community, or they frequently publish articles where geophysics is the dominant discipline. Journals whose exclusive focus are review articles are excluded from the analysis. The review does not use the SJR as a measure of the ‘prestige’ of any individual journal, nor to make any comparison or interpretations between individual journals.

3.1 Mapping Review Protocol

This study used a basic mapping review, designed to identify primary studies relating reproducibility and reliability in geophysics without manually selecting which articles to include. The aim was to enable a semi-quantified assessment of the extent to which studies focus on the topic of reproducibility (or reliability) in geophysics and determine how frequently the primary focus of studies is to investigate reproducibility or reliability. To do this, search strings were constructed based on the terms “reproducibility”, “reliability” and “replicable”. The search strings used are as shown in Table 1.

We restricted the search to the journals ranked in the

Definition theme	Search terms
Reproducibility	reproducibility OR reproduce OR reproducible OR reproduction
Reliability	reliability OR reliable OR reliably OR reliabilities

Table 1 Search strings used in the literature mapping review.

top 100 by SCImago (see Supplemental Table 1 in Ireland, 2022). The searches are conducted using Publish or Perish software (Harzing, 2010, 2007), using a single search for each journal. The searches used Google Scholar and while there is still no consensus on the use of Google Scholar in systematic literatures reviews (Boeker et al., 2013), it is adopted here as it is free-to-use, and therefore allows anyone to repeat the searches carried out in the future, regardless of access to subscription services. For each search the date range and title of the journal was specified. The terms in Table 1 were used for title word searches only. The data presented are accurate as of 3 April 2023.

3.2 Review of Journal Policies

To evaluate journals' existing policies relating to the inclusion of code, software, and data, we use the top 20 entries on the list of geophysical journals identified using SCImago Journal Rank. For each of these journals the requirements for code, software, and data, as per the 'instructions for authors' and the publishers' policies, were compiled. Table 2 shows the criteria for which we reviewed journals' policies. As the criteria outlined in Table 2 are rarely a clear binary yes/no, scoring criteria were used. The scoring criteria used are shown in Table 3. The score for each journal was assessed by author Algarabel and then reviewed by author Ireland. It is acknowledged that using scoring criteria like this could be considered subjective; however, by using descriptors of the criteria it is anticipated that aspects of bias are minimized.

3.3 Review of Journal Submissions

To evaluate the extent to which published, peer-reviewed articles make data and code available, the same list of the top 20 geophysical journals identified using SCImago Journal Rank was used (see Supplemental Table 1 in Ireland, 2022). As journals do not currently include search filters to discern which articles make data available, a sample of individual publications was selected to evaluate the extent to which they meet the criteria set out by a journal's policy. Two hundred articles were selected from a 3-year period (2020-2022). Again Publish or Perish software (Harzing, 2010, 2007) was used, and Google Scholar used as for the search. The date range was set to 2020-2022¹ and the "Maximum number of results" was set to 10. This search was car-

¹The search was done on 29 July 2022, and therefore covers articles published and index over 31 months.

ried out for each of the 20 journals in Supplemental Data Table 1 (Ireland, 2022)².

Each article is noted as either open access or paywalled. This is on a per article basis, rather than by journal, since authors may opt to make an article in a subscription access journal available open access by paying a journal an Article Publication Charge (APC). Again, as the availability and accessibility rarely be described using binary yes/no, scoring criteria are used, shown in Table 4. To assess the availability and accessibility of software we used the same sample of 200 articles as for data and reviewed if an article named any software used in the research. We searched the main text, availability statements, acknowledgements, and supplementary materials (where present). We also, where possible, report the license of the software that was used (e.g. open source or commercial). Throughout the article the word software is used as an inclusive term covering applications with graphical user interfaces (GUIs), code for interpreted programming languages (e.g. Python), and code for general-purpose programming languages (C++).

Included in policy/guidance	Category
Has definition of 'research data'	Policy
Includes separate 'data policy' section	Policy
Requirement to include data availability statement	Data
Requirement to include citations for data	Data
Requirement to make data available	Data
Guidance to include data in dedicated data repository	Data
Requirement to include software/code availability statement	Software
Requirement to include citations for software/-code	Software
Requirement to make software/code available	Software
Guidance to include software in dedicated repository	Software
Guidance to include data in supplementary materials	Data

Table 2 Criteria which journal policies and guidelines were reviewed against.

We made the decision to anonymise the data as we considered that this review was centered on the field of geophysics rather than highlighting the reproducibility of any individual published piece of work. Although the articles were anonymised we maintained a key to enable us to link the anonymised list back to the original sources.

In the 100 journals which publish geophysical research searched there were, between 1991 and 2022, 72 articles with "reproducibility", "reproduce", "reproducible" or "reproduction" in the title and 417 with "reliability", "reliable", "reliably", or "reliabilities" in the title (see Figure 2). From 1990 to 1999 there were 64 publications with "reliability", "reliable", "reliably", or "re-

²Despite having introduced those dates, some articles date from 2019.

Score	Summary	Descriptions
1	Required	Required, (e.g., must) with very limited exceptions (for example to preserve confidentiality of human participants)
2	Partial requirement	Partial requirement with flexibility around inclusion method.
3	Encouraged	Encouraged, with wording proactively encouraging (e.g., <i>should</i>) authors to include
4	Mentioned	Mentioned or implied but not proactively encouraged
5	Not mentioned	No mention in guidance to authors
6	Not allowed	Inclusion of data or content not permitted.

Table 3 Scoring criteria used to evaluate the extent to which journals proactively support improving the availability of data and code.

Score	Summary	Descriptions
1	Data available and accessible via dedicated data repository	Data available and is hosted on a repository which provides a DOI for the data. Includes where data is provided in tables within article.
2	Data available via website / webserver	Data available but no DOI.
3	Data source linked	Includes cases where article provides link to a web-hosted database but the specifics of the dataset (for example time periods, filters) are not clear.
4	Data provided in supplementary information or data	Includes where data are included under ‘supplementary information’. The lack of consistency in use of supplementary information makes data frequently harder to access.
5	Data listed as available but not accessible	Includes when authors state ‘data available on request’.
6	Data not available or no mention of data availability	Includes when authors explicitly state that data is confidential and not available or accessible.
X	Data linked but link no longer valid	

Table 4 Scoring criteria used to evaluate the availability and accessibility of data in published articles.

liabilities” in the title. Compare this with 2000 to 2009, when there were 114, and 2010 to 2019 when there were 181. This represents an increase of 77% and 59% respectively. From 1990 to 1999 there were 8 publications with “reproducibility”, “reproduce”, “reproducible”, or “reproduction” in the title, between 2000 to 2009 there were 13 and between 2010 to 2019 there were 34. These represent an increase of 63% and 161% respectively.

Of the 100 journals, 32 (32%) have published articles with “reproducibility”, “reproduce”, “reproducible”, or “reproduction” in the title, and 64 (64%) have published articles with “reliability”, “reliable”, “reliably”, or “reliabilities” in the title. The Bulletin of Earthquake Engineering has published the most articles with “reliability” “reliable”, “reliably”, or “reliabilities” in the title (63). Geophysical Research Letters has published the most articles with “reproducibility”, “reproduce”, “reproducible”, or “reproduction” in the title (11). A full breakdown of the number of publications with keywords in the title is provided in Supplementary Data Tables 2 and 3 (Ireland, 2022).

3.4 Journal Policies

From reviewing journal policies, it was found that 12 out of 20 (60%) journals have a definition of research data, while eight out of 20 (40%) do not have a definition (see Figure 4); 17 out of 20 (85%) of journals have

a discrete ‘data’ section within the journal policies and guidance. Despite 18 of the 20 journals either requiring or mentioning making data available, eight of these are from a single publisher, the American Geophysical Union (AGU), which applies the same requirements across all its Earth science publications. Only four out of 20 (20%) have a requirement for a data availability statement and only one journal, The Journal of Petrology, has an explicit requirement for both inclusion of data and a data availability statement. Information for authors is found within dedicated data policy sections for 17 out of 20 (85%), with three (15%) embedding the information within other sections. These results are summarized in Figure 5.

It is found that only one of the 20 journals (5%) reviewed required any code used to be made available and only one out of 20 journals (5%) require a code availability statement. There are 12 out of 20 (60%) journals that encourage making code available, while seven out of 20 make no mention of making code available. No journals have a requirement to make data or code available through repositories, or to include DOIs. However, 15 of the 20 journals (75%) encourage the use of data repositories and 14 of the 20 journals (70%) encourage the use of DOIs. Two of the 20 journals (10%) mention the use of repositories, and four of the 20 (20%) mention the use of DOIs. Two of the journals (10%) make no mention of the use of repositories and one journal makes no mention

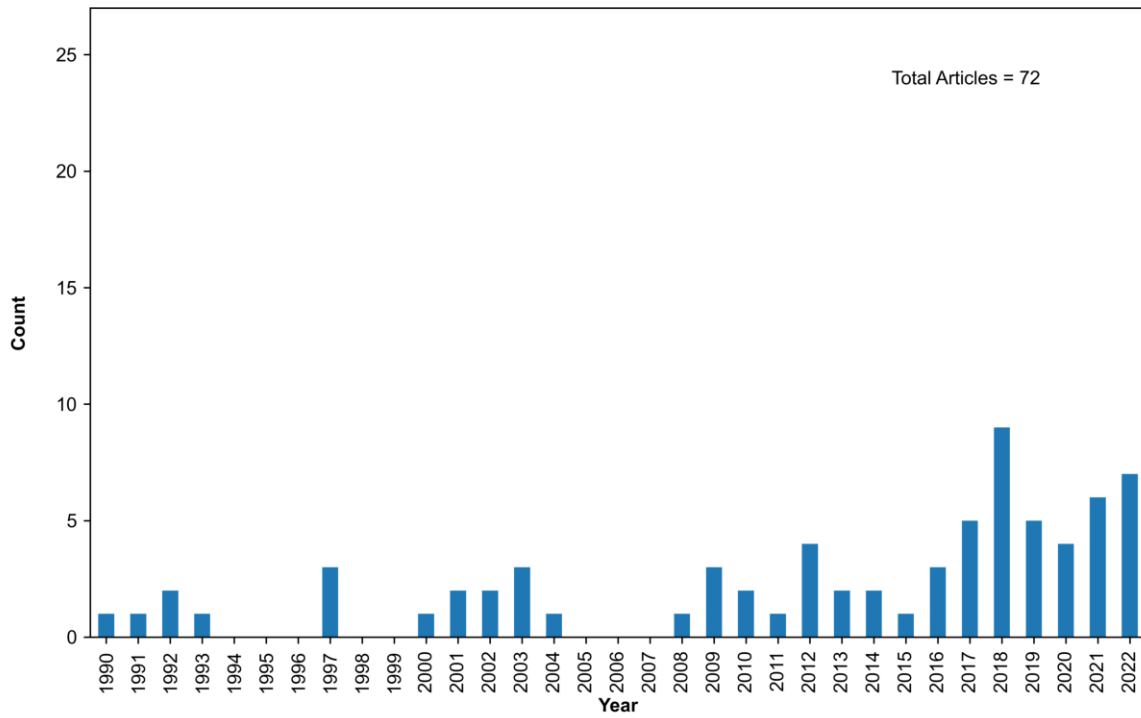


Figure 2 Number of publications with the keywords “reproducibility”, “reproduce”, “reproducible” or “reproduction” in the article title, by year.

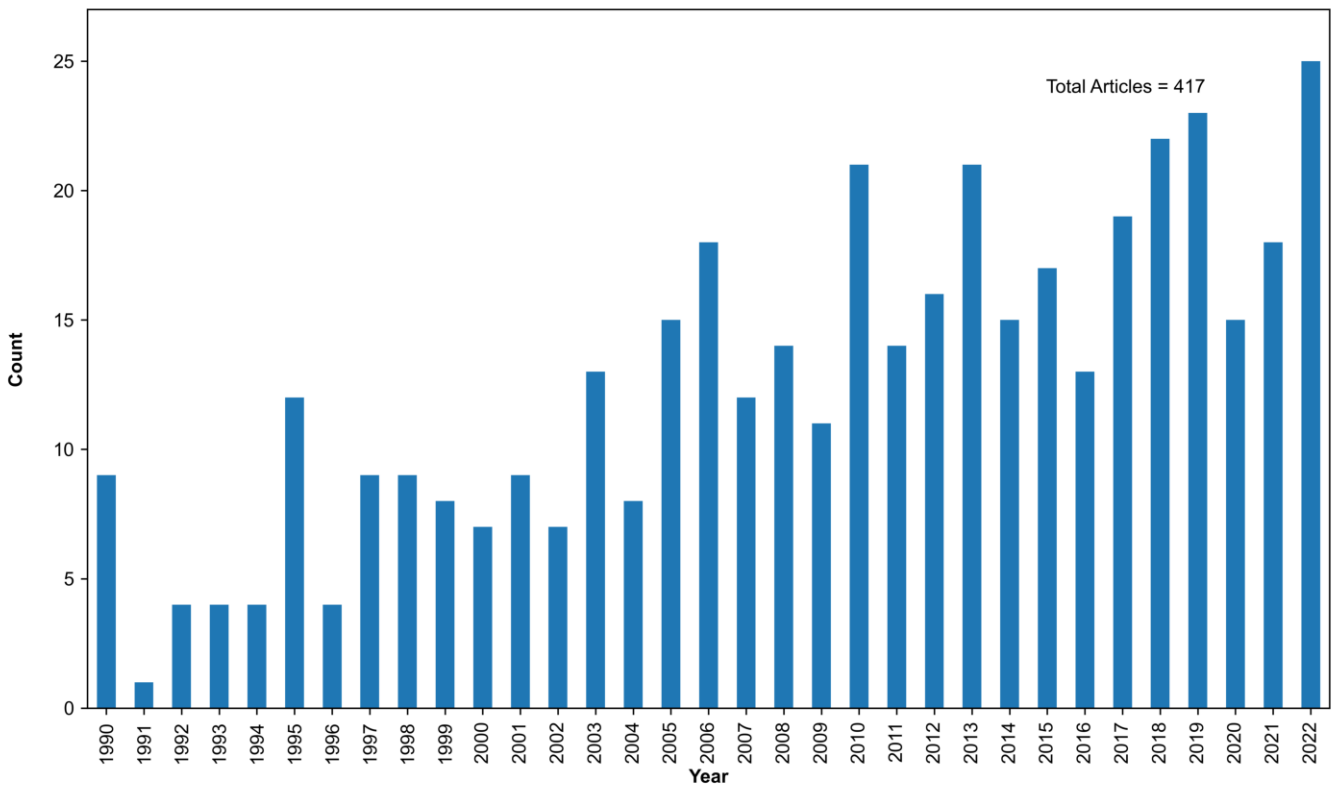


Figure 3 Number of publications with the keywords “reliability”, “reliable”, “reliably” or “reliabilities in the article title, by year.

of the use of DOIs.

Qualitative analysis of journals policies and guidance

suggests that different publishers are adopting different approaches to encouraging making data and code

available. Some are clear that they now require the inclusion of available data. For example, the AGU author resources explicitly refer to the FAIR principles and include the following regarding data availability statements:

“It is not sufficient to write that your data will be available upon request and to archive and make your data available in the supplementary information of your manuscript.” (AGU)

In contrast, the Society of Exploration Geophysicists (SEG)'s Geophysics makes no direct reference in the author instructions to the FAIR principles, although the SEG is a signatory to the Coalition on Publishing Data in the Earth and Space Sciences (COPDESS) Statement of Commitment. In their instructions to authors, they state:

“... papers from industry authors and academic researchers whose work is built on unshareable industry-owned data are invited, encouraged, and welcome.” (Geophysics)

The guidance for authors across journals frequently allows for authors to self-select from a range of options relating to data availability; however, only in the case of two publishers, AGU and Springer, was there any text indicating that the deposition of data was checked as part of the publishing process.

3.5 Journal Submissions

Of the articles with accessible information, it is identified that 165 of the 191 (~86%) articles have data availability statements and 26 (~14%) do not have data availability statements. A breakdown of data availability statements by journal is shown in Table 5. All sampled articles (n=100) published across the 10 AGU journals included data availability statements. In contrast, of the eight sampled articles accessible to us published in Economic Geology, only one had a data availability statement, and seven had no data availability statement.

Of the 191 articles sampled, 90 (~47%) make available original data from their research and a further nine (~4%) provide information to available secondary data sources. Four articles state that the original data is available on request and four articles state that secondary data is available on request. Four articles provide no information of the availability of original data, and 38 articles provide no information on the availability of secondary data. 41 of the 191 (~21%) articles have the data available via repositories and 63 of the 191 articles provide weblinks to data sources. Zenodo, FigShare and Mendeley are the most used repositories for data sharing (~75%). Examples of data sources for which articles provide weblinks to include NASA's Planetary Data System, Incorporated Research Institutions for Seismology, and the National Oceanic and Atmospheric Administration data portal. In most instances the exact details of the dataset or search criteria used to return a dataset are not included. For articles sampled from Geophysics, Marine and Petroleum Geology, and Economic Geology, none of the articles reviewed had made the original data accessible or available.

Of the 200 articles, 132 were open-access (e.g., acces-

sible through the publishers' site without subscription access) and 68 were paywalled access (e.g., required a subscription to access the full article). Of the 132 open access articles it was found that 46% made the data available (scores 1 to 4 in Table 3). and 54% did not make the data available via a data repository (scores 5 and 6 in Table 3). Of the 68 paywalled articles, we found that just 14% of these made their data available via a data repository or web server (Figure 6).

There is, at least qualitatively, a difference in the data availability between geophysical research which has a basis in resource or economic applications, and those with either a fundamental or global seismological focus. For example in SEG's Geophysics, which publishes research focused on geophysical method applied to extractive or resource industries (Geophysics), it was found that none of the ten articles reviewed made the underlying data available. In contrast in the Seismological Society of America's Seismological Research Letters, whose scope covers topics of broad interest across seismology and related disciplines, it was found that seven of the ten provided links to underlying data, and the three which did not, did not use original data. It is also found that for paywalled articles, publishers take different approaches as to what information to provide in the public domain. For example, in both Tectonophysics and Earth and Planetary Science Letters published by Elsevier, in some instances the data availability statement is not behind the paywall even if the full article is, whereas Geophysics, published by SEG, does not make this information available without paid access to the article.

Of the 200 articles it was found that 49% (98 articles) named software used in the research and 30% (60 articles) did not name any software used in the research (Figure 7). Of the 200 articles, we were unable to review the software used for 13.5% (27) of them due to articles being paywalled. For 6% (12) software could be considered not applicable due to articles being review papers and 1.5% (3) used large scale numerical models, where it was not possible to identify the software environment. Of the 98 articles which did name the software, 63% exclusively or partly used open source software and 38% exclusively or partly used commercial software (these do not total 100% due to some publications using a combination of open source and commercial software) (Figure 8). There were 100 unique software items identified in the 98 articles that named the software used. Of the software named those with more than five occurrences were: Python (17), Matlab (8), Generic Mapping Tools (7) and ImageJ (5).

4 Discussions

The identification of 489 articles that examine aspects of reproducibility and reliability since 1990 qualitatively suggests that both are topics of interest for geophysics research. It is worth noting that, as has long been recognized (e.g., Carr et al., 1997), the digitization of journal formats has resulted in an increase in the number of publications. Therefore, the observed increasing number of articles examining reproducibility and reliabil-

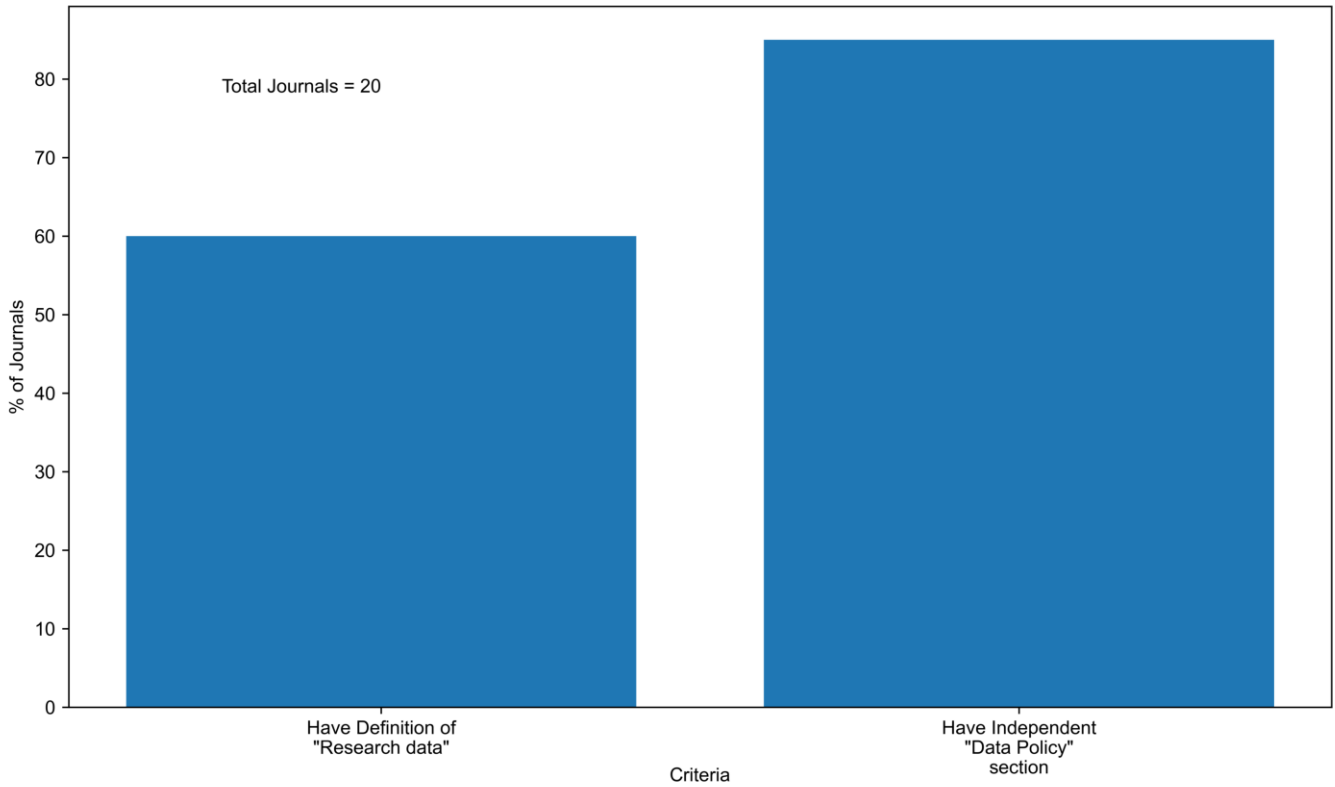


Figure 4 Percentage of journals which have a definition of “research data” and percentage of journals which have an independent “data policy” section.

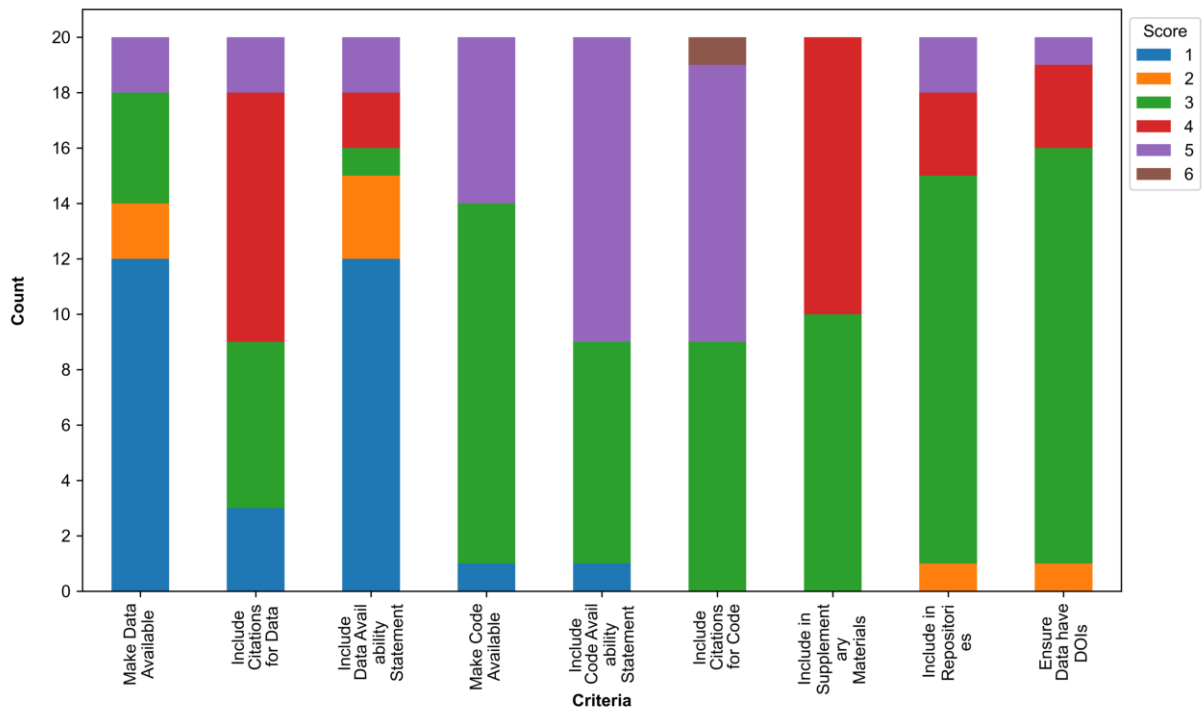


Figure 5 Stacked bar charts showing the requirements set out by journals relating to data and software. All based on the data provided in Data Table 4.

ity may not only be the result of increased attention by researchers. Of the 100 journals reviewed 32 (32%) have published articles with “reproducibility”, “reproduce”, “reproducible”, or “reproduction” in the title, and 64 (64%) with “reliability”, “reliable”, “reliably”, or “re-

liabilities” in the title, suggesting that the theme of reliability has been of greater focus than reproducibility. This would seem to support the hypothesis of [Stevenson et al. \(2022\)](#) who suggested that studies focused on reproducibility or replication are less likely to be

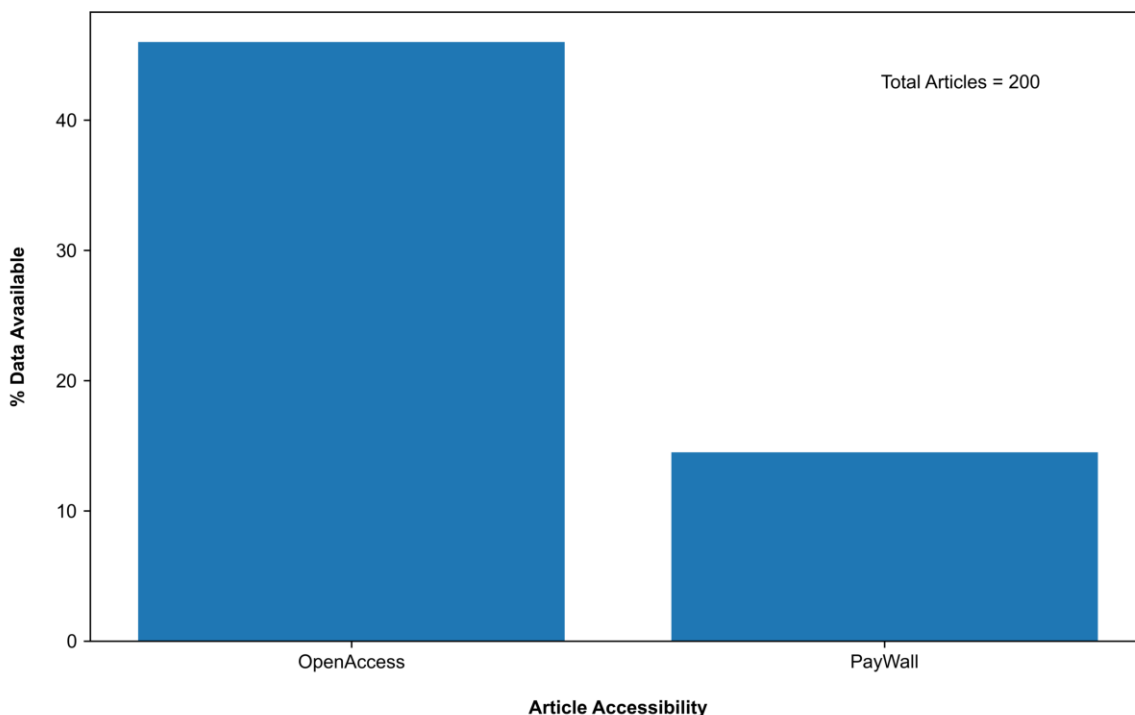


Figure 6 Chart showing the difference in data availability between open access articles and paywalled articles.

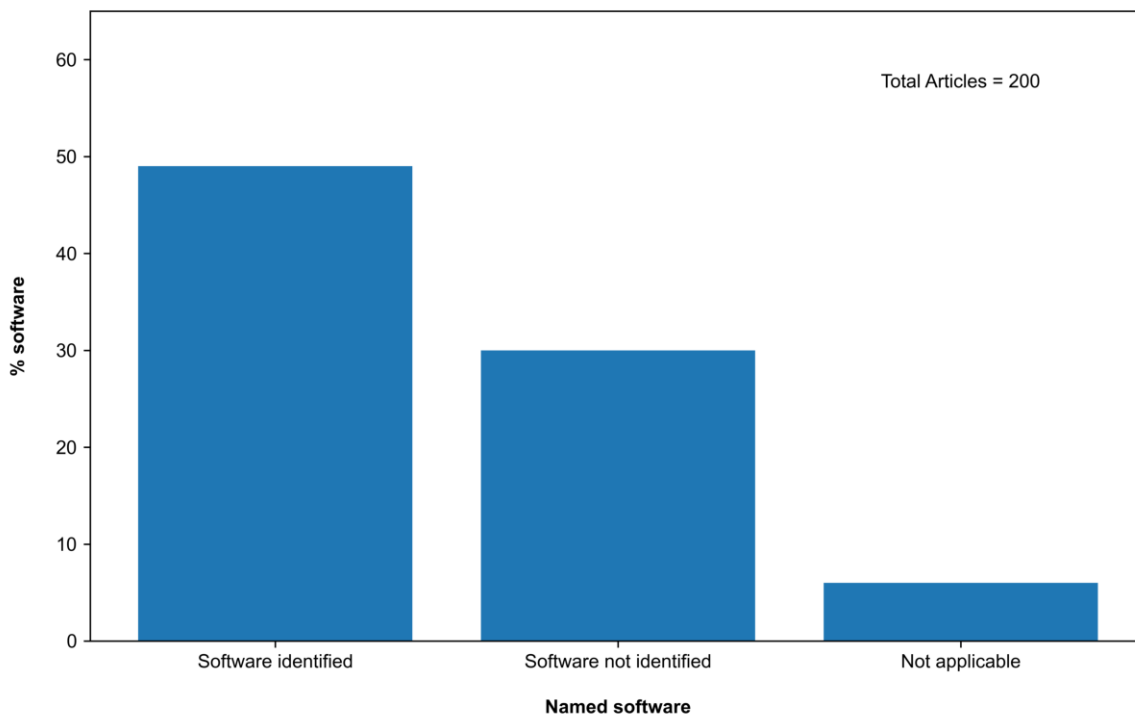


Figure 7 Chart showing the percentage of total number of articles that either identify or do not identify the software used in the research, or where the software is potentially not applicable (e.g. review articles).

published than “novel” or “ground-breaking” work. It therefore may be that this publication bias has led to published articles focusing on new methods and new

datasets, rather than exploring the reproducibility and replicability of previously published research.

Journal	Data Availability Statement		Original Data Accessible	
	Yes	No	Yes	No
Tectonics (10)	10	0	8	2
Geochemistry, Geophysics, Geosystems (10)	10	0	10	0
Geophysical Research Letters (10)	10	0	2	0
Journal of Geophysical Research D: Atmosphere (10)	10	0	10	0
Journal of Geophysical Research B: Solid Earth (10)	10	0	9	0
Journal of Geophysical Research E: Planets (10)	10	0	6	0
Journal of Geophysical Research C: Oceans (10)	10	0	1	1
Journal of Geophysical Research F: Earth Surface (10)	10	0	4	2
Earth and Planetary Science Letters (10)	10	0	10	0
Tectonophysics (10)	5	5	5	4
Geophysics (8)	7	3	0	9
Journal of Petrology (10)	10	0	9	0
Seismological Research Letters (5)	7	3	7	0
Contributions to Mineralogy and Petrology (10)	10	0	10	0
Journal of Geodesy (10)	8	2	2	3
Mineralium Deposita (10)	9	1	8	1
Economic Geology (8)	1	7	3	5
Earthquake Spectra (10)	5	5	5	2
Marine and Petroleum Geology (10)	8	2	1	5
Geophysics Journal International (10)	7	3	3	5

Table 5 Summary data for articles examined, showing the number of articles that 1) provided a data availability statement and 2) whether they made the original data available. For both criteria scores 1 to 4 count as ‘yes’ and scores 5 and 6 counted as ‘no’ (see Table 3 for details on scoring). As not all articles used original data, or some were solely modelling studies, the total of yes/no for *original data* does not always match the total count.

4.1 Subjective interpretation of journal policies

The findings indicate that journals have a mixed approach to the wording used in policies relating to the provision of data and code (see Figure 5). While the TOP Factor (<https://topfactor.org/>) provides a score of how journal policies align scientific ideals with practices, no geophysical journals have been scored to date (as of 17 April, 2023). We found that journals repeatedly used ambiguous language in their policies when referring to data and code availability. While 60% of journals had a policy which stated that the submission of data was a requirement, the statements used in the other 40% of journals were frequently ambiguous, using terms such as encourages, where possible, where applicable. Clearly those journals without a clear definition of data will likely result in more subjective interpretation of the guidelines by authors, reviewers, and editors. From the publisher’s side, from a marketing and commercial perspective it could make sense to have submission guidelines and policies that clearly define data and code access. A counter view could be that ambiguity in the policies and guidelines may be beneficial from a commercial perspective as it may encourage submis-

sions and consequently facilitate the journal to publish more articles than if there were tighter restrictions on data and software requirements. However, where data and code are easily identifiable and accessible, there is empirical evidence to suggest that the sharing of research data may can be associated with an increase in citations (Christensen et al., 2019; Piwowar et al., 2007). When it comes to the use of supplementary information, it is worth highlighting, as in the AGU’s data availability statement, that this section of a manuscript is still indicated as a suitable place to accommodate data. There are however issues with this as highlighted by previous studies (Pop and Salzberg, 2015). Most notably there is often a lack of guidance on how supplementary information should be used to include data (e.g. Pop and Salzberg, 2015), which means that often data or metadata provided in supplementary information is inaccessible. Supplementary files are for the most part not considered to be a part of the formal record of an article, and therefore the integrity of these materials is frequently poorly maintained. In the case of internet hosted materials, this is evidenced by other studies (e.g., Evangelou et al., 2005) which have shown that the percentage of inactive links to supplementary informa-

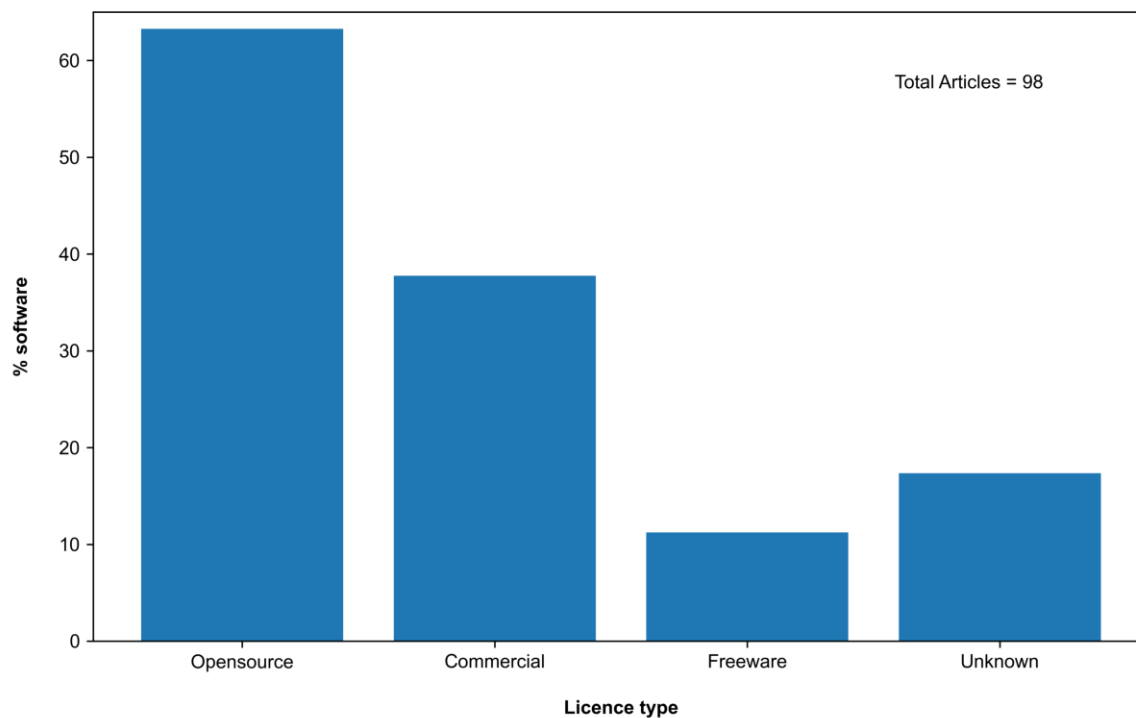


Figure 8 Chart showing, for the articles which did identify software, the percentage that make use of open source, commercial, and freeware, as well as the percent where the license was not easily identifiable or traceable. The percentages here do not total 100% as some articles used multiple pieces of software.

tion increased with time since publication,

4.2 Availability vs accessibility

We found that, where journal articles used original data, in general the availability of data was improved over journal articles which used existing data or data derived from third party sources. Frequently where articles used non-original data, while articles provided information on the data in the data availability statements, they provided insufficient information to identify specific datasets, or in several cases the weblinks no longer worked. This suggests that it is not only data availability that is important, but also data accessibility. [Starr et al. \(2015\)](#) list eight core principles of data citation which have been endorsed by 87 scholarly societies, publishers and other institutions. Of relevance to the findings here are the unique identification and specificity and verifiability. For the majority of the articles sampled, there was insufficient information for the dataset to be identified without human search input, in contrast to the recommendation that data identification should be machine actionable ([Starr et al., 2015](#)). Commonly it was difficult to identify the specific dataset used in the research: for example, it was possible to follow a weblink to website which hosts data, but not to identify the data on which the analysis was based. While many articles (>30%) provide weblinks or the names of the organizations which host the data, they frequently provided insufficient information for readers to identify and verify that the data is the same as that which was used by

the authors. Frequent issues include, for example, the data linked consisting of multiple files with no explicit statement of what files from that dataset the authors used. Another persistent issue is the use of non-static weblinks for data sets.

4.3 Role of Journals, Editors and Reviewers

The contributions of editors and reviewers for journals, whether they are for-profit or not-for-profit, are invaluable in ensuring the continued and timely publication of scientific findings. In most cases, those scientists that undertake the role do so without remuneration. The role of a journal editor could be summarized as to sustain integrity in published research and enforce the policies and the standards for the journal, both for authors and reviewers ([Caellegh, 1993](#)). The role of reviewers could be summarized as "evaluat[ing] whether or not there is a meaningful...contribution, whether the constructs are adequately defined,...and whether the underlying mechanisms/process...are explained" ([Lepak, 2009](#)). Based on journal (and publisher) policies it is unclear as to whether reviewers are expected to evaluate the suitability of data and software availability statements. It could be suggested that there should be a clear distinction then between the role which editors and reviewers have in determining whether an article's approach to data and software availability (and accessibility) is suitable or not. In practice, clarification by journals over the role of reviewers and editors could improve the situation. For example, one

possibility could be for reviewers to have the responsibility for ensuring that the data and software is suitable to demonstrate the scientific findings, and that the editorial board and office has the responsibility to ensure that authors have included a data and software availability statement and adhered to the requirements for making data and software accessible and available. Indeed, this is how AGU handles the availability of data, as indicated on their information to authors where it clearly states, “AGU now checks to see if data/software has been properly cited vs simply linking to a DOI, website, platform” (AGU).

It is worth noting that while it was found that fewer journals had dedicated requirements for software, sometimes they are mentioned within the policies, guidelines, and definitions of data. This can lead to some ambiguity when the guidance is interpreted by authors. Further, while not all studies use bespoke software (e.g. customized code), there are very few aspects of geophysical research which do not have some reliance on computer-based analysis. Therefore, journals could perhaps consider a simplified approach when it comes to more commonly used software (e.g., for statistical analysis), whereby authors simply choose from a list.

In the review of existing journal submissions, it became clear that it is currently not possible to identify which articles have accessible data and software quickly and efficiently. For the most part, journals use data availability statements, with only 10% of the 20 journals examined not mentioning including a data availability statement. However, it is not possible to filter or search articles by the information in these statements. In chemistry it has been suggested that one solution to this challenge would be to completely recast data-rich scientific journal articles into two components, a narrative and separate data component, each of which is assigned a persistent digital object identifier (Harvey et al., 2014). However, perhaps a simpler solution could be the requirement for authors to choose from pre-defined categories of data availability, with authors' assertions checked for accuracy as part of the editorial process. Journals could then implement a search criterion based upon if the data is available and accessible.

4.4 Software Availability and Accessibility

In the review of existing journal submissions approximately half the articles reported the software used in the research (49%). Where identified, the software is not consistently reported in the same location in different journals, or even within different articles in the same journal. For example, some articles reported software in the ‘methods’ section of the article, others referenced the software used in the acknowledgements, and some only mentioned the software within supplementary materials. The 51% of articles which did not report the software used all frequently included quantitative or statistical analysis, and while articles commonly detail the theory, they do not report on the implementation of this. In other science disciplines, studies have highlighted the need for consistently specifying

the analytical software used in, as different software packages could produce varying results (Dembe et al., 2011). It is postulated that where software, both commercial and open source, are widely available, accessible, and used, such as Microsoft Excel, authors may unintentionally omit them from inclusion from the methods. However, the accuracy of statistical methods in such packages has been the focus of repeated studies (e.g., McCullough and Heiser, 2008; McCullough and Wilson, 2002, 2005; Mélard, 2014). The data indicate that open source and freeware software, sometimes referred to as free and open-source software (FOSS) was used in 63% of the articles which identified the software they used. While there has been a widespread adoption of FOSS documented (e.g., Glynn et al., 2005; Hauge et al., 2010; van Rooij, 2011), there has been very limited focus on the extent to which FOSS is adopted with Earth sciences and geophysics specifically. The findings in this study suggest that commercial software still is important within in research, where 38% of the articles which identified their software made use of it. Some authors (e.g., de Groot and Bril, 2005) have speculated that FOSS has rarely been used for larger scale, high end-user applications and software is frequently closed source or proprietary. However, increasingly open source interpreted programming languages such as Python through the wide variety of packages available are increasingly capable of handling large and complex datasets such as N-dimensional arrays (e.g., Hamman, 2017). Anecdotally, the number of downloads for dedicated geophysics Python packages, suggests that open-source software is growing in usage. For example Obspy (Beyreuther et al., 2010) has, according to PePy (<https://pepy.tech/>) been downloaded 1,783,753 (as of 8 April 2023). Proprietary software may offer benefits, such as well-developed GUIs that do not require as high a level of computer literacy (e.g., Muenchow et al., 2019). As noted by Nüst and Pebesma (2021), in some instances, such as where software are linked to hardware, proprietary software may be unavoidable. This could include, for example, software linked to specific seismic acquisition systems.

4.5 Perceived Barriers

Data and code sharing are often perceived as being limited by digital infrastructure (Gomes et al., 2022). However, while making data and code available may have been previously limited by such restrictions, there now exists the underlying digital architecture to, for example, host individual files typically up to 20GB in size on data repositories such as Figshare and Zenodo. Repositories have added the functionality to archive code, for example from GitHub to Zenodo, and assign a DOI. Indeed, many of the perceived barriers, for example challenges in handling large data files, are not unique to geophysics and these concerns have mostly been shown to be relatively straightforward to manage in terms of absolute volume. For example, a study in neurosciences by Poldrack and Gorgolewski (2014) described how the sharing of raw MRI data from 1,000 authors would consist of ~2.7 terabytes, a relative modest volume by current stor-

age infrastructure solutions (e.g., Behnke et al., 2019); however, there are major challenges in ensuring that data sets are curated to make them accessible and useful to researchers. Indeed, the common occurrence of big data within nearly all subjects has served to identify that discussing absolute data volume as a barrier in any context is limiting, as computing hardware and software advances at such a rate that any absolute numbers are soon superseded (Oguntimilehin and Ademola, 2014).

4.6 Limitations of study

The findings presented in this review are not exhaustive. There exist several limitations to the study that should be highlighted. Firstly, there are alternative ways in which the choice of journals to include could be made. The approach here, as far as possible, was designed to avoid user bias in the selection of journals, but it is recognized that the breadth of journals included covers some topics that may be considered outside of the immediate subject area of geophysics. Secondly, and related to this, the choice of search tools could impact the results. In this study searches were undertaken using tools and databases which did not require paid subscription access. Alternative subscription-only search services may result in different results, for the review of existing literature. Thirdly, when reviewing journal policies, there is a component of subjectivity in the categorization of a journal's requirements. As discussed above this is itself one of the issues which publishers and journals need to tackle to avoid any ambiguity in the requirements. Fourthly, when categorizing the availability of data for an individual article, while in some cases it is very clear if data is available and accessible (e.g., DOI linked data) or not (e.g., data is confidential) there are examples where, for example the availability of the data is insufficiently described to easily assess if the data is accessible. Examples of this include where a link to a website which hosts data is provided, but there are no specifics of the data used (for example, not specifying the exact time series). Overcoming this uncertainty in future studies would require attempting to download the exact dataset used in each case, which would be significant undertaking, not least as it would require some subject matter expertise across a diverse range of geophysical subjects. It is worth noting that data repositories do provide application programming interfaces (API) for the datasets which enables programmatic access to items (Figshare). In this work, both a score of 1 or 2 could enable scripted access to data, however for data that score 2 the lack of DOI ultimately means that there is no persistent record. Finally, while the institutional subscriptions that were available to Algarabel and Ireland who undertook the principal data collection provided access to a high proportion of the individual articles reviewed, there were still 27 of 200 articles for which the full text was not accessible.

5 Conclusions

Reproducibility and repeatability are important themes for the geophysics community as evidenced by the in-

creasing number of publications identified in this review. Through examining the current policies of multiple journals which publish geophysical articles, it is identified that all too often the wording used is ambiguous and open to interpretation. If journals want to publish truly reproducible works, it will require not just a shift to using concise wording, but also for journals to enforce stricter policies. Despite this, the empirical evidence is that journals are making a concerted efforts to provide guidance on the provision of data and software. For published articles there are stark differences in the availability and accessibility of both data and software. However, there is still a long way to go for geophysical research (as a whole) to be reproducible, as shown by the findings which indicate that less than 30% of articles over the past 5 years provide enough information on the source of data, and less than 50% of articles identify the software used, both of which are required to reproduce results.

Acknowledgements

The work was enabled by funding from the IAPETUS2 DTP for Guillermo Algarebel to undertake a Research Experience Placement at Newcastle University in the summer of 2022. The authors are grateful for reviews by Daniel Nüst and Wynn Tranfield. Thanks also to Chris Jackson and Matt Hall which stimulated some of the themes discussed in this review.

6 Data and software availability

The data used in this study are available in a repository (Ireland, 2022). There are 5 data tables included, and the description of each is provided below.

- DataTable1_JournalListSciMargo – List of 100 geophysics journals used as starting point for review
- DataTable2_ExistingLiteratureReliability – Number of journal articles published, by year, with the word 'reliability' in the title.
- DataTable3_ExistingLiteratureReproducibility – Number of journal articles published, by year, with the word 'reproducibility' in the title.
- DataTable4_JournalRequirements – Summary of journal requirements categorized.
- DataTable5_PublishedArticles_Anon – Summary of availability of data and software for individual publications. We have removed any identifiable details relating to the individual articles sampled in this study.

The study used the free Publish or Perish software (Harzing, 2007).

All plots were created in Python and the scripts are available (Ireland, 2022). Users will need to download the data dables and add file path locations to the scripts to replicate the plots as they appear in the paper.

Competing interests

The authors have no competing interests.

References

- AGU. Data and Software for Authors. <https://www.agu.org/Publish-with-AGU/Publish/Author-Resources/Data-and-Software-for-Authors#availability>. Retrieved 23 October 2022.
- American Journal of Political Science. A.J.P.S. Verification Policy, 2019. <https://ajps.org/ajps-verification-policy/>.
- Arnold, B., Bowler, L., Gibson, S., Herterich, P., Higman, R., Krystalli, A., Morley, A., O'Reilly, M., and Whitaker, K. *The Turing Way: A handbook for reproducible data science*. Zenodo, 2019. doi: 10.5281/zenodo.3233853.
- Behnke, J., Mitchell, A., and Ramapriyan, H. NASA's Earth Observing Data and Information System – Near-Term Challenges. 18:1, 2019. doi: 10.5334/dsj-2019-040.
- Beyreuther, M., Barsch, R., Krischer, L., Megies, T., Behr, Y., and Wassermann, J. ObsPy: A Python Toolbox for Seismology. *Seismological Research Letters*, 81(3):530–533, 2010. doi: 10.1785/gssrl.81.3.530.
- Boeker, M., Vach, W., and Motschall, E. Google Scholar as replacement for systematic literature searches: Good relative recall and precision are not enough. *BMC Medical Research Methodology*, 13(1):131, 2013. doi: 10.1186/1471-2288-13-131.
- Borgman, C. L. Research Data: Who Will Share What, with Whom, When, and Why? *SSRN Electronic Journal*, 2010. doi: 10.2139/ssrn.1714427.
- British Geophysical Association. What is geophysics?, 2014. <https://geophysics.org.uk/what-is-geophysics/>.
- Caelleigh, A. S. Role of the journal editor in sustaining integrity in research. *Academic Medicine*, 68(9):23–29, 1993. doi: 10.1097/00001888-199309000-00030.
- Carr, T. R., Buchanan, R. C., Adkins-Heljeson, D., Mettelle, T. D., and Sorensen, J. The future of scientific communication in the earth sciences: The impact of the internet. *Computers & Geosciences*, 23(5):503–512, 1997. doi: 10.1016/S0098-3004(97)00032-0.
- Childe, S. J. What is the role of a research journal? *Production Planning & Control*, 17(5):439–439, 2006. doi: 10.1080/09537280600888862.
- Christensen, G., Dafoe, A., Miguel, E., Moore, D. A., and Rose, A. K. A study of the impact of data sharing on article citations using journal policies as a natural experiment. *PLOS ONE*, 14(12): 0225883, 2019. doi: 10.1371/journal.pone.0225883.
- de Groot, P. and Bril, B. The open source model in geosciences and OpendTect in particular. In *SEG Technical Program Expanded Abstracts 2005*, page 802–805. Society of Exploration Geophysicists, 2005. doi: 10.1190/1.2148280.
- Dembe, A. E., Partridge, J. S., and Geist, L. C. Statistical software applications used in health services research: Analysis of published studies in the U.S. *BMC Health Services Research*, 11(1): 252, 2011. doi: 10.1186/1472-6963-11-252.
- European Commission. G20 Leaders' Communique Hangzhou Summit, 2016. https://ec.europa.eu/commission/presscorner/detail/en/STATEMENT_16_2967.
- Evangelou, E., Trikalinos, T. A., and Ioannidis, J. P. Unavailability of online supplementary scientific information from articles published in major journals. *The FASEB Journal*, 19(14):1943–1944, 2005. doi: 10.1096/fj.05-4784lsf.
- Figshare. Figshare API User Documentation. doi: 10.6084/m9.figshare.4880372.v2.
- Geophysics. GEOPHYSICS instructions to authors. <https://library.seg.org/page/gpysa7/ifa/instructions>. Retrieved 23 October 2022.
- Glynn, E., Fitzgerald, B., and Exton, C. Commercial adoption of open source software: an empirical study. In *2005 International Symposium on Empirical Software Engineering, 2005*, pages 10 pp.–, 2005. doi: 10.1109/ISESE.2005.1541831.
- Gomes, D. G. E., Pottier, P., Crystal-Ornelas, R., Hudgins, E. J., Foroughirad, V., Sánchez-Reyes, L. L., Turba, R., Martinez, P. A., Moreau, D., Bertram, M., Smout, C., and Gaynor, K. Why don't we share data and code? *MetaArXiv*, 2022. doi: 10.31222/osf.io/gaj43.
- Goodman, S. N., Fanelli, D., and Ioannidis, J. P. What does research reproducibility mean? *Science Translational Medicine*, 8(341): 341 12–341 12, 2016. doi: 10.1126/scitranslmed.aaf5027.
- Hager, B. H. and Clayton, R. W. Constraints on the structure of mantle convection using seismic observations, flow models, and the geoid, 1989. <https://resolver.caltech.edu/CaltechAUTHORS:20121002-141328164>.
- Hamman, J. xarray: N-D labeled Arrays and Datasets in Python, 2017. doi: 10.5334/jors.148.
- Harvey, M. J., Mason, N. J., and Rzepa, H. S. Digital Data Repositories in Chemistry and Their Integration with Journals and Electronic Notebooks, 2014. doi: 10.1021/ci500302p.
- Harzing, A. W. Publish or Perish. <https://harzing.com/resources/publish-or-perish>.
- Harzing, A. W. *The publish or perish book*. Tarma Software Research Pty Limited Melbourne, Australia, 2010.
- Hauge, Ø., Ayala, C., and Conradi, R. Adoption of open source software in software-intensive organizations – A systematic literature review. *Information and Software Technology*, 52(11): 1133–1154, 2010. doi: 10.1016/j.infsof.2010.05.008.
- Hodson, S., Jones, S., Collins, S., Genova, F., Harrower, N., Laaksonen, L., Mietchen, D., Petrauskaitė, R., and Wittenburg, P. Turning FAIR data into reality. Technical report, 2018. doi: 10.2777/1524. Interim report from the European Commission Expert Group on FAIR data.
- Houtkoop, B. L., Chambers, C., Macleod, M., Bishop, D. V., Nichols, T. E., and Wagenmakers, E. J. Data sharing in psychology: A survey on barriers and preconditions. *Advances in Methods and Practices in Psychological Science*, 1(1):70–85, 2018. doi: 10.1177/2515245917751886.
- Ireland, M. Reproducibility in Geophysics, 2022. doi: 10.25405/data.ncl.21564381.v1.
- Jun, H. and Cho, Y. Repeatability enhancement of time-lapse seismic data via a convolutional autoencoder. *Geophysical Journal International*, 228(2):1150–1170, 2022. doi: 10.1093/gji/ggab397.
- Konkol, M., Kray, C., and Pfeiffer, M. Computational reproducibility in geoscientific papers: Insights from a series of studies with geoscientists and a reproduction study. *International Journal of Geographical Information Science*, 33(2):408–429, 2019. doi: 10.1080/13658816.2018.1508687.
- Lepak, D. Editor's Comments: What is Good Reviewing? *Academy of Management Review*, 34(3):375–381, 2009. doi: 10.5465/amr.2009.40631320.
- McCullough, B. D. and Heiser, D. A. On the accuracy of statistical procedures in Microsoft Excel 2007. *Computational Statistics & Data Analysis*, 52(10):4570–4578, 2008. doi: 10.1016/j.csda.2008.03.004.
- McCullough, B. D. and Wilson, B. On the accuracy of statistical procedures in Microsoft Excel 2000 and Excel XP. *Computational Statistics & Data Analysis*, 40(4):713–721, 2002. doi:

- 10.1016/S0167-9473(02)00095-6.
- McCullough, B. D. and Wilson, B. On the accuracy of statistical procedures in Microsoft Excel 2003. *Computational Statistics & Data Analysis*, 49(4):1244–1252, 2005. doi: 10.1016/j.csda.2004.06.016.
- Mesirov, J. P. Accessible Reproducible Research. *Science*, 327(5964):415–416, 2010. doi: 10.1126/science.1179653.
- Muenchow, J., Schäfer, S., and Krüger, E. Reviewing qualitative GIS research—Toward a wider usage of open-source GIS and reproducible research practices. *Geography Compass*, 13(6):12441, 2019. doi: 10.1111/gec3.12441.
- Mélar, G. On the accuracy of statistical procedures in Microsoft Excel 2010. *Computational Statistics*, 29(5):1095–1128, 2014. doi: 10.1007/s00180-014-0482-5.
- National Academies of Sciences. Statistical challenges in assessing and fostering the reproducibility of scientific results: Summary of a workshop, 2016. doi: 10.17226/21915.
- National Academies of Sciences. Understanding Reproducibility and Replicability. In *Reproducibility and Replicability in Science*. 2019. <https://www.ncbi.nlm.nih.gov/books/NBK547546/>. National Academies Press (US).
- Nature. Journals unite for reproducibility. *Nature*, 515(7525), 2014. doi: 10.1038/515007a.
- Nosek, B. A., Alter, G., Banks, G. C., Borsboom, D., Bowman, S. D., Breckler, S. J., Buck, S., Chambers, C. D., Chin, G., and Christensen, G. Promoting an open research culture. *Science*, 348(6242):1422–1425, 2015. doi: 10.1126/science.aab2374.
- Nüst, D. and Pebesma, E. Practical Reproducibility in Geography and Geosciences. *Annals of the American Association of Geographers*, 111(5):1300–1310, 2021. doi: 10.1080/24694452.2020.1806028.
- Oguntimilehin, A. and Ademola, E. O. A Review of Big Data Management, Benefits and Challenges. *A Review of Big Data Management, Benefits and Challenges*, 5(6):6, 2014.
- Oren, C. and Nowack, R. L. An overview of reproducible 3D seismic data processing and imaging using Madagascar. *Geophysics*, 83(2):9–20, 2018. doi: 10.1190/geo2016-0603.1.
- Pendlebury, D. A. The use and misuse of journal metrics and other citation indicators. *Archivum Immunologiae et Therapiae Experimentalis*, 57(1):1–11, 2009. doi: 10.1007/s00005-009-0008-y.
- Piwowar, H. A., Day, R. S., and Fridsma, D. B. Sharing Detailed Research Data Is Associated with Increased Citation Rate. *PLOS ONE*, 2(3):308, 2007. doi: 10.1371/journal.pone.0000308.
- Poldrack, R. A. and Gorgolewski, K. J. Making big data open: Data sharing in neuroimaging. *Nature Neuroscience*, 17(11):11, 2014. doi: 10.1038/nn.3818.
- Pop, M. and Salzberg, S. L. Use and mis-use of supplementary material in science publications. *BMC Bioinformatics*, 16(1):237, 2015. doi: 10.1186/s12859-015-0668-z.
- Rallison, S. What are Journals for? *Annals of The Royal College of Surgeons of England*, 97(2):89–91, 2015. doi: 10.1308/003588414X14055925061397.
- Reese, R. J. Recent Applications of Digital Computers to Geophysical Problems. *AAPG Bulletin*, 49(7):1089–1089, 1965. doi: 10.1306/A66336EE-16C0-11D7-8645000102C1865D.
- Robinson, E. A. and Treitel, S. *Geophysical signal analysis*. Society of Exploration Geophysicists, 2000.
- SCImago. SCImago Journal & Country Rank. <https://www.scimagojr.com/aboutus.php>. Retrieved 25 August 2022.
- Starr, J., Castro, E., Crosas, M., Dumontier, M., Downs, R., Duerr, R., Haak, L. L., Haendel, M., Herman, I., Hodson, S., Hourclé, J., Kratz, J. E., Lin, J., Nielsen, L. H., Nurnberger, A., Proell, S., Rauber, A., Sacchi, S., Smith, A., and Clark, T. Achieving human and machine accessibility of cited data in scholarly publications. *PeerJ Computer Science*, 1:1, 2015. doi: 10.7717/peerj.cs.1.
- Steventon, M. J., Jackson, C. A., Hall, M., Ireland, M. T., Munafa, M., and Roberts, K. J. Reproducibility in subsurface geoscience. *Earth Science, Systems and Society*, 12, 2022. doi: 10.3389/esss.2022.10051.
- Tedersoo, L., Küngas, R., Oras, E., Köster, K., Eenmaa, H., Leijen, Ä., Pedaste, M., Raju, M., Astapova, A., Lukner, H., Kogermann, K., and Sepp, T. Data sharing practices and data availability upon request differ across scientific disciplines. *Scientific Data*, 8(1), 2021. doi: 10.1038/s41597-021-00981-0.
- Tenopir, C., Allard, S., Douglass, K., Aydinoglu, A. U., Wu, L., Read, E., Manoff, M., and Frame, M. Data Sharing by Scientists: Practices and Perceptions. *PLOS ONE*, 6(6):21101, 2011. doi: 10.1371/journal.pone.0021101.
- van Rooij, S. W. Higher education sub-cultures and open source adoption. *Computers & Education*, 57(1):1171–1183, 2011. doi: 10.1016/j.compedu.2011.01.006.
- Waage, M., Bünz, S., Landrø, M., Plaza-Faverola, A., and Waghorn, K. A. Repeatability of high-resolution 3D seismic data. *Geophysics*, 84(1):75–94, 2018. doi: 10.1190/geo2018-0099.1.
- Walker, R., Gill, S. P., Greenfield, C., McCaffrey, K., and Stephens, T. L. No demonstrated link between sea-level and eruption history at Santorini., 2021. <https://eartharxiv.org/repository/view/2638/>.
- Wildman, G. and Lewis, E. Value of open data: A geoscience perspective. *Geoscience Data Journal*, 2022. doi: 10.1002/gdj3.138.

The article *How reproducible and reliable is geophysical research? A review of the availability and accessibility of data and software for research published in journals* © 2023 by Mark T. Ireland is licensed under CC BY 4.0.

Estimates of earthquake temperature rise, frictional energy, and implications to earthquake energy budgets

G. L. Coffey  *¹, H. M. Savage  ², P. J. Polissar  ³

¹Department of Earth Structure and Processes, GNS Science, Lower Hutt, New Zealand, ²Department of Earth and Planetary Science, University of California Santa Cruz, Santa Cruz, United States, ³Department of Ocean Sciences, University of California Santa Cruz, Santa Cruz, United States

Author contributions: *Conceptualization:* G. Coffey, H. Savage. *Data Curation:* G. Coffey. *Formal Analysis:* G. Coffey. *Funding Acquisition:* G. Coffey, H. Savage, P. Polissar. *Investigation:* G. Coffey, H. Savage, P. Polissar. *Methodology:* G. Coffey, H. Savage, P. Polissar. *Project Administration:* G. Coffey. *Resources:* G. Coffey, H. Savage, P. Polissar. *Supervision:* H. Savage, P. Polissar. *Visualization:* G. Coffey, H. Savage. *Writing – original draft:* G. Coffey. *Writing – review & editing:* G. Coffey, H. Savage, P. Polissar.

Abstract Coseismic temperature rise is a fundamental state variable that changes dramatically during earthquakes due to frictional heating, however in situ temperatures are notoriously hard to measure. The development of multiple paleotemperature proxies over the last twenty years has led to an increasing number of coseismic temperature measurements collected across a variety of faults. Here we present the first compilation of coseismic temperature rise measurements and frictional energy estimates to investigate the contribution of frictional heating to the earthquake energy budget and how this varies over different fault and earthquake properties. This compilation demonstrates that coseismic temperature rise increases with the depth of faulting until ~5 km, and below this depth remains relatively constant. Frictional energy, similarly, increases with depth until ~5 km. However, frictional energy is remarkably similar across the faults studied here, with most falling below 45 MJ/m². Our results suggest that dynamic weakening mechanisms may limit frictional energy during coseismic slip. We also demonstrate a basic difference between small and large earthquakes by comparing frictional energy to other components of the earthquake energy budget. The energy budget for small earthquakes (<1-10 m of displacement) is dominated by frictional energy, while in large events (>1-10 m of displacement), frictional, radiated, and fracture energy contribute somewhat equally to the earthquake energy budget.

Non-technical summary During an earthquake, frictional resistance can lead to generation of very high temperatures as both sides of the fault slide past each other rapidly. Understanding these temperatures and the energy that is dissipated as heat (the frictional energy) provides insight into how earthquakes start, propagate, and what leads to their arrest. Recently, more and more methods to address this have been developed, leading to a growing database of earthquake temperature measurements and frictional energy estimates. In this study we present the first compilation of these data. We find that earthquake temperature rise increases with the depth of faulting to ~5 km, and below this depth it remains fairly constant. We also find that frictional energy is remarkably similar across the faults studied here with most falling below 45 MJ/m² (for reference, 0.08 MJ is required to heat a single cup of coffee). This suggests that faults become very weak and slide more easily during earthquake slip, limiting the energy that is dissipated as heat. Our results demonstrate a basic difference between small earthquakes (<1-10 m of slip), where the earthquake energy budget is dominated by frictional heating, and large earthquakes (>1-10 m of slip) where energy is more equally split between frictional heating, radiating seismic waves, and damage (fractures).

1 Introduction

Temperature exerts a fundamental control on both the chemical and mechanical behavior of faults. During earthquakes, rapid frictional heating from fault slip can lead to a large increase in the in-situ near-fault temperature. These temperature spikes can have a profound effect on fault rheology, chemical disequilibria, and the rates of chemical reactions, leading to changes in fault strength, structure, and mineralogy (Reches and Lockner, 2010; Di Toro et al., 2011; Noda and Lapusta, 2013; Collettini et al., 2014). Although geologically brief, co-

seismic temperature rise is effectively a metamorphic process, however, very few observational estimates of coseismic temperature rise exist.

In addition to shedding light on chemo-mechanical processes during earthquakes, quantifying temperature rise during earthquake slip also allows us to place constraints on the earthquake energy budget. This is a key component in understanding earthquake physics as it controls a rupture's ability to grow and provides information on what processes facilitate rupture propagation or lead to its arrest. The earthquake energy budget comprises dissipative (frictional and fracture energy) and radiated energy (Figure 1; Kanamori and Heaton,

Production Editor:
Gareth Funning
Handling Editor:
Pathikrit Bhattacharya
Copy & Layout Editor:
Ethan Williams

Received:
October 10, 2022
Accepted:
May 16, 2023
Published:
June 5, 2023

*Corresponding author: g.coffey@gns.cri.nz

2000). Portions of the earthquake budget that are related to stress drop can be measured or inferred from seismology, however the frictional energy depends on the absolute shear stress level during the earthquake. As seismology does not measure absolute stresses, we rely on measurements of coseismic temperature rise from frictional resistance to quantify frictional energy (Kanamori and Heaton, 2000). With the development of paleotemperature proxies and the installation of borehole observatories, a number of frictional energy estimates for different faults have been made (Pittarello et al., 2008; Fulton et al., 2013; Savage and Polissar, 2019; Coffey et al., 2021, 2022).

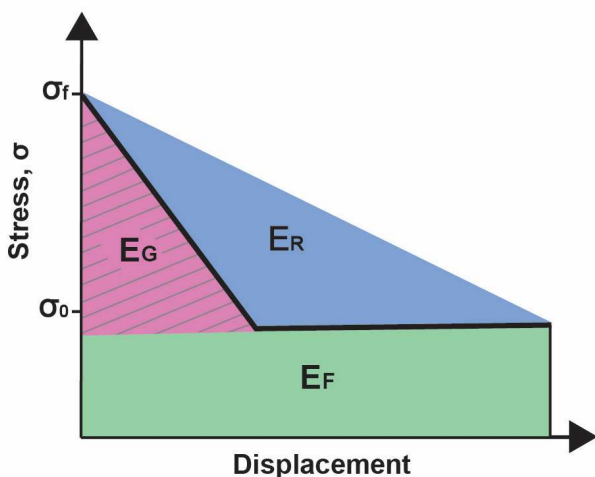


Figure 1 Simplified example of the earthquake energy budget based upon Kanamori and Heaton (2000) including frictional energy (E_F), fracture energy (E_G), and the energy radiated as seismic waves (E_R). The hatched area is the breakdown energy (Cocco and Tinti 2005), here it is depicted as equal to fracture energy, but it may also include frictional energy.

Here, we present a compilation of earthquake temperature and frictional energy estimates from a suite of fault types. The data are from a variety of paleotemperature proxies, but rely heavily on biomarker thermal maturity (Polissar et al., 2011; Savage et al., 2014; Shepard et al., 2015; Savage and Polissar, 2019; Coffey et al., 2019; Rabinowitz et al., 2020; Coffey et al., 2021, 2022). This compilation is the first attempt to understand the frictional energy component of the earthquake energy budget from an observational perspective and enables exploration of how energy is partitioned into different sinks depending upon earthquake depth and other parameters.

2 Coseismic temperature rise and earthquake paleothermometry

During an earthquake, frictional resistance along a fault can lead to the generation of very high temperatures. The temperature rise (ΔT) that occurs during an event

depends on various fault and earthquake properties:

$$\Delta T \propto \frac{\tau \cdot vt}{\rho c_p 2a} \quad (1)$$

where τ is shear stress (the product of normal stress and friction minus pore pressure), ρ is density, c_p is heat capacity, t is time, v is slip velocity, and a is the half width of the slipping layer. Equation 1 illustrates the essential parameters that relate temperature rise to faulting and earthquake slip. The absolute temperature rise is also influenced by heat diffusion away from the slipping surface (Lachenbruch, 1986) and the full equations that include heat diffusion can be found in Supplementary Material S1.

When solving Equation 1 for depths below a couple of kilometers and for pore pressures that follow an assumed regular hydrostat, heat generation for even moderate-size earthquakes can easily create temperatures that melt all or some of the minerals present. Evidence of this melt is preserved in the rock record as pseudotachylyte, crystallized frictional melt that has long been considered a robust recorder of coseismic slip (Sibson, 1973, 1975). However, pseudotachylyte is famously underrepresented in outcrop (Kirkpatrick et al., 2009) and absent on faults shallower than ~3 km depth (Sibson and Toy, 2006). This dearth of pseudotachylyte has been attributed to alternative dynamic-weakening mechanisms, such as thermal pressurization, that can make faults so weak during earthquakes that they did not achieve significant temperatures (Rice, 2006). Theoretical analyses of dynamic weakening have been supported by dozens of high-speed friction experiments, which demonstrated that faults weaken dramatically at fast slip rates (Di Toro et al., 2011). Although it is very likely that faults are weak during earthquakes, more recent studies have also suggested that evidence of pseudotachylyte can be difficult to observe in outcrop, especially when the pseudotachylyte itself has undergone retrograde reaction to other minerals (Kirkpatrick and Rowe, 2013). Whether faults lack pseudotachylyte or it is obscured in outcrop, it is clear that developing additional thermal proxies for faults would shed light on earthquake mechanics. Recently, a greater range of techniques has been applied to study coseismic temperature rise (Rowe and Griffith, 2015). In addition to pseudotachylyte these include thermal decomposition of calcite, vitrinite reflectance, (U-Th)/He of hematite and other minerals, and mineralogic/textural zoning (Pittarello et al., 2008; Sakaguchi et al., 2011a; Kirkpatrick et al., 2012; Collettini et al., 2013; Ault et al., 2015; Rowe and Griffith, 2015). For example, microstructural evidence of carbonate dissociation has been used to argue that temperatures greater than ~750 °C were achieved during earthquakes (Rodríguez-Navarro et al., 2009; Collettini et al., 2013). Vitrinite, a type of kerogen found in bituminous coal, has been widely applied in the hydrocarbon industry as its reflectance increases with increasing thermal maturity, which is a function of time and temperature. Vitrinite reflectance has also been shown to be sensitive to shorter, earthquake-duration heating and has been applied to quantify coseismic temperature rise in settings

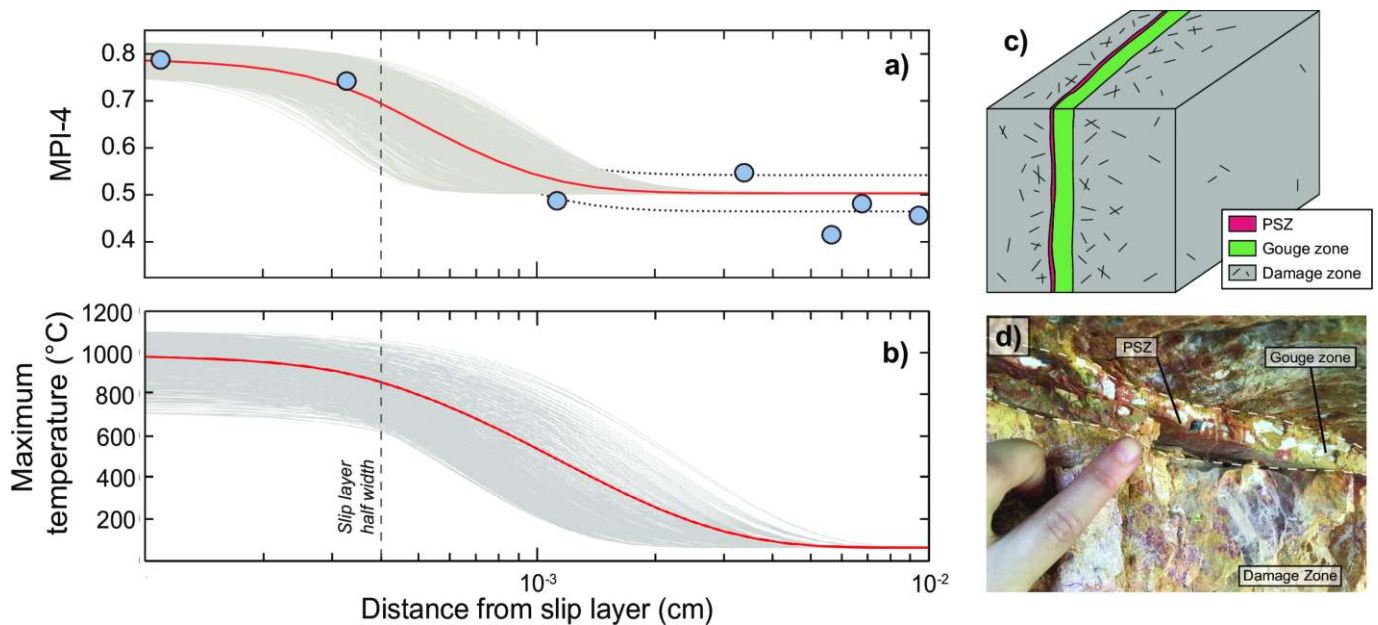


Figure 2 Examples of a) thermal maturity and b) maximum temperature from Coffey et al. (2019) as a function of the distance from the slipping layer. Profiles are modeled to fit measured biomarker (MPI-4) data shown by the blue points in a). Gray lines are 10,000 Monte Carlo iterations of the modeled thermal maturity and temperature profiles, and the red line is the mean. c) A simplified fault zone schematic showing the Principal Slip Zone (PSZ), gouge zone, and damage zone. d) photograph of a fault zone from the Muddy Mountain thrust in Nevada, USA.

such as the Nankai trough (Sakaguchi et al., 2011b). (U-Th)/He dating of hematite along fault surfaces has demonstrated that the thermal conditions occurring during earthquake slip are sufficient to reset U-Th/He ages along very localized surfaces (hundreds of μm thick) and that these reset ages can be used to model and constrain coseismic temperatures (Ault et al., 2015; McDermott et al., 2017; Ault et al., 2019; Armstrong et al., 2022).

In addition to these paleotemperature proxies, biomarkers have been increasingly used over recent years to investigate frictional heating, and they provide us with a robust and widely-applicable tool to explore coseismic temperature rise. Biomarkers are the molecular remains of past organisms that accumulate in sedimentary rocks over time. When heated, their abundance and molecular structure is systematically altered to achieve more thermally-stable configurations or products. This alteration can occur under earthquake temperatures and durations (Savage et al., 2018). While burial heating will also increase biomarker thermal maturity, comparing the difference in thermal maturity between fault zone and off-fault background samples reflects how much of the thermal maturity of the fault zone is due to temperature rise during the earthquake (Polissar et al., 2011; Savage et al., 2014; Savage and Polissar, 2019). Temperature can be calculated from biomarker thermal maturity because the kinetics for numerous biomarker reactions have been established from heating experiments (Sheppard et al., 2015; Rabinowitz et al., 2017). As a result, we can forward model temperature rise and biomarker reaction for a range of appropriate earthquake and fault parameters (Equation 1, Supplementary Material S1) to best fit the thermal maturity signal measured within a localized

slip layer. For example, Figure 2 shows the best-fitting temperature model for one biomarker thermal maturity parameter, MPI-4 (methylphenanthrene index), for the Muddy Mountain thrust (Figure 2c). Biomarker thermal maturation is strongly temperature dependent, and larger events with the greatest temperature rise will dominate the maturity signal (Coffey et al., 2019). Because of this relationship and field observations of variability in displacement across different earthquakes on the same fault patch (Nicol et al., 2016), we assume that any biomarker heating signal present is a result of the largest earthquake the fault has experienced. As a result, estimates from biomarkers on the faults compiled here are likely upper bounds on temperature and frictional energy.

Three biomarker thermal maturity ratios are utilized in the dataset compiled here: the methylphenanthrene index (MPI-4) calculated from methylphenanthrene isomers (Coffey et al., 2019; Polissar et al., 2011; Savage et al., 2014), the Carbon Preference Index (CPI) calculated over C₂₆-C₃₅ *n*-alkanes (Rabinowitz et al., 2017; Coffey et al., 2021; Rabinowitz et al., 2020), as well as the alkenone unsaturation ratio (U₃₇^{k'}) and concentrations from long-chain alkenones (Rabinowitz et al., 2017, 2020). More detailed information on the relevant thermal maturity parameters can be found in Supplementary Material S2.

Uncertainties in temperature estimates from biomarkers relate to uncertainties in the biomarker reaction kinetics, as well as the slip velocity, principal slip zone (PSZ) thickness, displacement, and shear stress during the event. The temperatures required for measurable biomarker reaction require seismic slip speeds, which limits the possible sliding velocity range (Savage et al., 2018). Slip zone thickness is measured

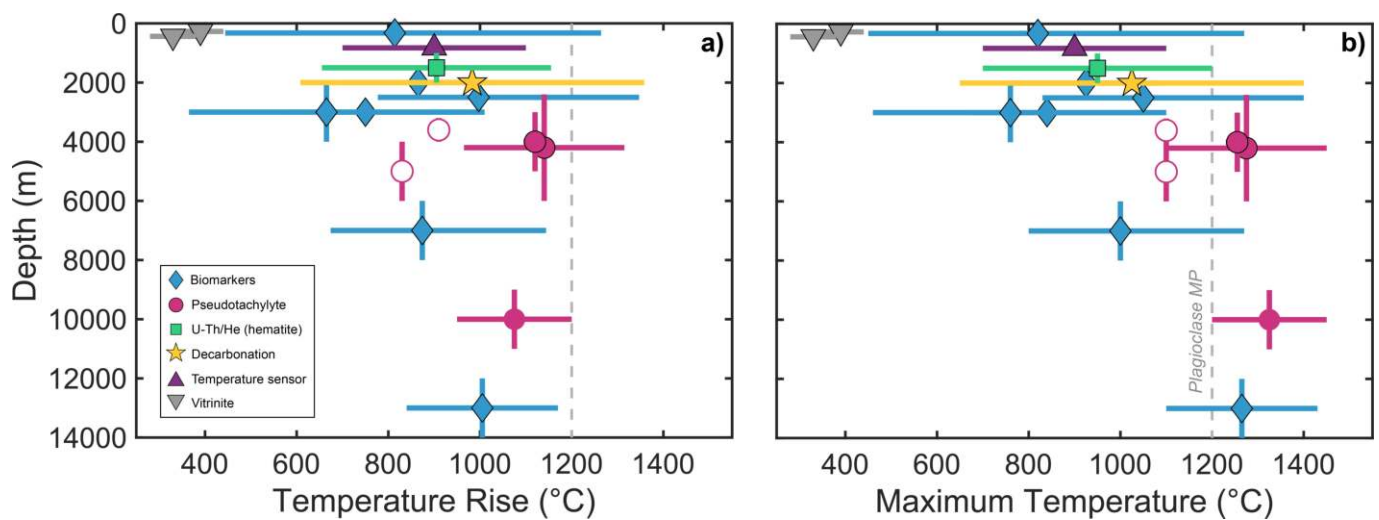


Figure 3 Compilation of earthquake temperatures with depth color-coded by proxy type. Symbols are mean and error bars are the 95% confidence intervals a) Earthquake temperature rise above background (i.e., does not include ambient temperature). b) Maximum temperature (temperature rise plus ambient temperature). Temperature rise during earthquakes is higher on more deeply buried faults because of increasing shear strength from increasing normal stress with depth. Open symbols are minimum bounds on temperature rise and maximum temperature.

in the field (Figure 2c); however, thickness may vary along a fault, and where possible we couple each temperature estimate with a measured thickness from the specific point along the fault that was sampled. Finally, although we typically do not know shear stress or displacement, we can place broad constraints on shear stress using in situ regional stress estimates and lab estimates of frictional weakening (e.g. Colletini et al., 2009; Jeppson et al., 2010). Observational, experimental, and theoretical work of the last two decades has found that shear strength on large faults is most likely low during earthquake slip (Di Toro et al., 2011; Fulton et al., 2013; Rice et al., 2014). Simple models of earthquake slip based on Equation 1 (also in Equations 1 and 2 in Supplementary Material S1) demonstrate that if slip indeed localizes onto very thin layers as is often observed in the field (millimeter-scale or thinner; Figure 2c) and friction values were constant at ~ 0.6 as found in static friction experiments (e.g. Byerlee 1978), faults would reach unrealistically high temperature even during moderate earthquakes (Rice, 2006). High-velocity friction experiments confirmed that after a run-in phase of high friction, fault strength should drop dramatically for most rock types (Di Toro et al., 2011; Chang et al., 2012; Rubino et al., 2017). This drop in friction is a function of the thermal weakening displacement, D_{th} (Di Toro et al., 2011):

$$D_{th} = a\sigma_n^{-b} \quad (2)$$

where a and b are experimentally derived coefficients. As a result, the shear stress (τ) will evolve during sliding according to (Seyler et al., 2020):

$$\tau = \tau_{ss} + (\tau_p - \tau_{ss})e^{-\frac{\delta}{D_{th}}} \quad (3)$$

where τ_{ss} is the steady-state shear stress, τ_p is the peak shear stress, and δ is the slip accumulated after the peak shear stress. Because of this, the average shear stress during sliding will be lower for larger displacements as

D_{th} is a lower fraction of total slip in these events, and more slip occurs at lower friction. In our models, we assume that shear stress evolves following Equation 3 and that normal stress is equal to overburden less hydrostatic pore pressure. We can then iterate the average friction as displacement increases and use this in our thermal models to define a shear stress range (Coffey et al., 2022).

3 Frictional Energy and the Earthquake Energy Budget

The energy expended during an earthquake is a function of the stress drop, $\Delta\sigma$, residual (dynamic) stress and total displacement, D , during the event. The available potential energy related to the stress drop due to the displacement, ΔW , is:

$$\Delta W = 1/2(\Delta\sigma D) \quad (4)$$

A simplified schematic of this is shown in Figure 1. Progress of the earthquake is delineated by the bold line and begins at some initial stress, σ_0 . As the earthquake proceeds, stress drops to a final value, σ_f , over some displacement, D . During this time elastic strain energy in the volume around the slip surface is broadly converted into dissipative and radiated energy (Kanamori and Heaton, 2000). Radiated energy goes into the propagation of seismic waves, while dissipated energy includes fracture energy, which encompasses plastic deformation at the rupture tip and off-fault damage, as well as frictional energy, which is required to overcome frictional resistance (Kanamori and Brodsky, 2004; Kanamori and Rivera, 2006; Lambert et al., 2021; Viesca and Garagash, 2015).

Determining all components of the earthquake energy budget is difficult, as each component is estimated through different analyses. Radiated energy can in principle be determined from analysis of seismic waves.

The available energy, ΔW , depends on calculation of stress drop. The portion of the energy budget that is available energy less the radiated energy is often considered to go to fracture energy, but some of this energy can go to the dissipation of heat. As a result, some authors use the term breakdown energy as a more agnostic term because it is impossible to determine the amount of heat dissipation from seismological measurements (Cocco and Tinti, 2008; Lambert and Lapusta, 2020; Cocco et al., 2023). This distinction is important to note here because some of the temperature rise we measure could have in fact been part of the breakdown energy.

Coseismic temperature rise can be used to quantify the frictional energy dissipated during slip. We use the temperature proxies outlined above to identify seismic layers and quantify coseismic temperature rise. Frictional energy, E_F , is an integration of the product of velocity and shear stress, which is the total displacement during the earthquake, D :

$$E_F = \tau D \quad (5)$$

When referring to the frictional energy throughout the results of this study we are reporting frictional energy density (MJ/m^2) and emphasize that this will include any heat dissipated as part of the breakdown energy. Once the temperature rise, thickness of the fault, and the rock thermal and material properties have been established, the only unknown from Equation 1 is the product of the shear stress and displacement. We do not need to solve for shear stress and displacement to estimate temperature and frictional energy as their product is the important parameter. However, our estimate of shear stress from depth of faulting and frictional weakening across many rock types allows us to evaluate frictional energy as a function of displacement, and therefore earthquake size.

4 Thermal evidence of coseismic slip in faults

We compile estimates of coseismic temperature rise to synthesize what has been learned from investigations into coseismic temperature rise to date. We also compile estimates of frictional energy for the same faults where available, and for those faults where frictional energy has not been reported, we establish our own constraints based on our forward modeling described above. This compilation was made using a variety of thermal proxies, fault types, and tectonic settings and is presented in Table 1. New temperature estimates from biomarker thermal maturity are measured on the: Hundalee fault, Spoleto fault, Monte Maggio fault, and a thrust within the Marin Headlands (Supplementary Figure 1). We compare the temperature rise and frictional energy from these studies to fault and earthquake properties to explore any relationships that exist and the implications that some of these properties may have on earthquake rupture.

We estimate both absolute temperature and temperature rise (absolute temperature less the ambi-

ent temperature when independently calculated) during earthquake slip. We find that temperature rise ranges between 280 - 1350°C and the maximum temperature achieved by the fault ranges from ~280°C to 1450°C (Table 1; Figure 3). The lowest measurable temperatures (besides null results, which for the biomarker proxy depends on background thermal maturity but is usually less than ~500°C) were found in the Nankai frontal thrust using vitrinite reflectance (Sakaguchi et al., 2011b), while the highest temperatures occurred along the Pasagshak megathrust (Alaska) from biomarker measurements and the presence of pseudotachylyte (Rowe et al., 2005; Savage et al., 2014). The Pasagshak megathrust is unique in this dataset as it was exhumed from 12 - 14 km depth and has developed at least six pseudotachylyte layers, making it the deepest fault with the most evidence of frictional melt of the faults analyzed here.

We expect that fault strength increases with depth as a function of normal stress and frictional strength (Sibson, 1977; Byerlee, 1978), which would lead to an increase in both maximum temperature and temperature rise with increasing depth. Figure 3 demonstrates that both temperature rise and maximum temperature increase with depth down to ~5 km, below which temperature is more or less constant. This relationship between temperature and depth is apparent even though we are likely comparing earthquakes with different displacements (Supplementary Figure 2). Sibson and Toy (2006) showed a similar relationship between depth and temperature by demonstrating that pseudotachylyte is nearly absent in faults that were active at burial depths above ~3 km. If all other parameters except depth are held constant, a continued increase in temperature with depth is expected due to increasing normal stress and hence, shear strength. The observed nearly constant (or only subtly increasing) temperatures at depths below ~5 km may reflect that the faults in our database are mostly pseudotachylyte bearing at these depths. Once melting temperatures are achieved, melt lubrication may prevent further temperature rise (Ujii et al., 2007; Kirkpatrick et al., 2012).

5 Earthquake Energy Budget

We combine frictional energy estimates from our biomarker studies with previous estimates from the literature and these are plotted in Figure 4. Frictional energy across all of the faults in this study varies from 0.9 - 228 MJ/m^2 (this range includes the 95% confidence interval limits of these estimates). This is generally higher than frictional energy estimates from laboratory experiments which range from 500 J/m^2 - 5 MJ/m^2 but involve displacements orders of magnitude lower than those considered in this compilation (Passelègue et al., 2016; Aubry et al., 2018; McBeck et al., 2019). The lowest frictional energy in our study occurs along faults of the frontal thrust of the Nankai subduction zone, which has a mean frictional energy of 2.5 MJ/m^2 , (95% confidence interval: 0.9 - 3.8 MJ/m^2), while the highest occurs along the Pasagshak megathrust with a range of 105 - 228 MJ/m^2 . The Pasagshak megathrust is a clear outlier,

Fault	PSZ thickness (mm)	Displacement (m)	Depth (m)	Burial T (°C)	Maximum T (°C)	T rise (°C)	Frictional energy (MJ/m ²)	Proxy	Source
Nankai megasplay	10	12.0 (7.7 - 19.9)	271	<20	340-440	340-440	16.2 (13.4 - 18.4)	Vitrinite reflectance	Sakaguchi et al. (2011a)
Papaku	0.1 - 2	11-15	300	10	820 (450-1270)	810 (440-1260)	8-13	Biomarkers	Saffer et al. (2019); Coffey et al. (2021)
Nankai frontal thrust	2	6.7 (1 - 19.1)	438	<20	280-380	280-380	6.5 (3.1 - 10.1)	Vitrinite reflectance	Sakaguchi et al. (2011b)
Japan trench	2.6-4.8	50	820-835	0	700-1100	700-1100	20-86	Biomarkers, borehole measurement	Brodsky et al. (2020); Fulton et al. (2013); Rabinowitz et al. (2020); Sun et al. (2017)
Wasatch damage zone	<2	0.1-0.5	1000-2000	45	700-1200	650-1150	3.8 (2-7.4)	Hematite (U-Th)/He	Ault et al. (2015); McDermott et al. (2017)
Muddy Mountain	0.8 - 20	0.3-5	2000	60	760-1090	700-1030	6.7 (3.5-10.7)	Biomarkers	Brock and Engelder (1977); Coffey et al. (2019)
Monte Maggio	0.1 - 1	1.8 (0.1 - 4.7)	2000	42	650-1400	508-1358	8.8 (1.6-18)	Biomarkers, carbonate decomposition	Colletini et al. (2014); Kaneko et al. (2016); Carpenter et al. (2014)
Spoletto	0.3 - 1	0.9 (0.06-2.0)	2000-3000	50	650-1300	600-1250	6.6 (1.2-10.6)	Biomarkers, decarbonation	Colletini et al. (2013)
Punchbowl	0.3 - 20	1-4	2000-4000	95	460-1060	365-955	2-25	Biomarkers	Chester et al. (2005); Savage and Polissar (2019)
Skeeter	0.25 - 10	1 (0.01-1.5)	2400-6000	110-160	1100-1450	940-1340	7.8 (2.5-11.7)	Pseudotachylyte	Kirkpatrick et al. (2012), this study
Central San Andreas	0.1 - 18	0.3-5	3000	90	840 (670-1100)	750 (580-1010)	8.2 (2.8-15.2)	Biomarkers	Coffey et al. (2022)
Nojima	1 - 3	2	3000-5000	110-160	1230-1280	1090-1140	17.4 (6.6-26.2)	Pseudotachylyte	Otsuki et al. (2003), this study
Marin Headlands	1 - 4	0.2 (0.1-0.5)	6000-8000	126	1000 (800-1270)	874 (674-1044)	6.3 (4.2-7.0)	Biomarkers	Regalia et al. (2018), this study
Hundalee	10 - 30	1.6 (0.9-2.2)	-	10	640 (500-900)	630 (490-890)	14.2 (1.3-19.7)	Biomarkers	Williams et al. (2018)
Larghe	6	0.3-2	9000-11000	250	1200-1450	950-1200	27 (22.8-32.9)	Pseudotachylyte	Di Toro and Pennacchioni (2005); Pittarello et al. (2008)
Pasagshak	30 - 50	1-8	12000-14000	260	1100-1430	840-1170	105-228	Biomarkers, Pseudotachylyte	Meneghini and Moore (2007); Rowe et al. (2011); Savage et al. (2014)
Shimanto [†] (Mugi)	>0.6-1.5	-	3200-4000	170-190	> 1100	>910-930	-	Pseudotachylyte	Ujije et al. (2007)
Shimanto [†] (Okitsu)	>0.6-1.5	-	4000-6000	230-270	> 1100	>830-870	-	Pseudotachylyte	Ujije et al. (2007)

Table 1 Thickness and number of PSZs observed as well as lithologies of each fault compiled here. Values reflect what was reported in the source for that data and are either a single value, which likely has considerable uncertainties, or a range that incorporates uncertainties. Values in brackets are 95% confidence intervals.

[†]Temperature and thickness data from Ujije et al. (2007) for the two localities in the Shimanto accretionary complex are minimum bounds and no upper limit is given. We do not model displacement or frictional work here as a result of this uncertainty.

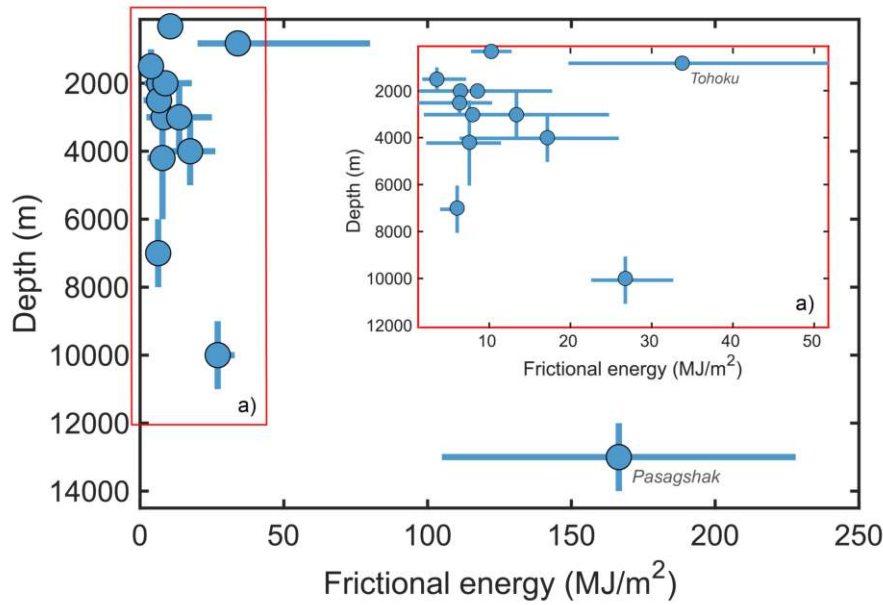


Figure 4 Depth plotted against frictional energy for faults in this compilation. Inset a), as outlined by the red box, shows frictional energy as a function of depth but only for those faults with a frictional energy ≤ 50 MJ/m². This only excludes the Pasagshak megathrust and highlights a slight trend in frictional energy at shallower depths ($\leq \sim 5$ km).

and as described above, it is unique in this dataset due to the thickness of pseudotachylyte that formed. The rest of the faults in this dataset have frictional energy that falls below 45 MJ/m², with most below 26 MJ/m², suggesting a tendency for frictional energy to remain within a narrow range despite differences in displacement, depth, fault type, lithology, or ambient temperature. While frictional energy varies over a relatively narrow range, we see a weak relationship between frictional energy and depth, similar to coseismic temperature rise, frictional energy increases slightly with depth until ~ 5 km (Figure 4). The exception to this trend is the Tohoku earthquake, where rapid fault zone drilling captured the temperature decay after that earthquake (Fulton et al., 2013).

By estimating the average shear stress during the earthquake (Equation 3), we can also estimate the earthquake displacement and compare frictional energy to values of fracture and radiated energy calculated from other studies. We used estimates from (Ye et al., 2016), which are included in their supplement. Radiated energy is estimated from the ground velocity spectra according to (Venkataraman and Kanamori, 2004). G' , a proxy for fracture energy, which we refer to as breakdown energy, that is calculated as follows:

$$G' = 0.5(1 - \eta_R)\Delta\sigma_E D \quad (6)$$

where η_R is the radiation efficiency estimated from the ratio of measured radiated energy to available potential energy, $\Delta\sigma_E$ is the energy-related stress drop, and D is the average slip.

All components of the energy budget increase with displacement, however the frictional energy increase is subtle compared to the other components (Figure 5). Radiated energy is generally slightly lower than breakdown energy for a given displacement and can reach

values of up to 20 MJ/m² when normalized by the rupture area. The breakdown energy on the other hand reaches values as large as 140 MJ/m² but generally falls below 100 MJ/m². Frictional energy (0.9 – 228 MJ/m²) tends to locate toward the higher end of both the breakdown and radiated energy at a given displacement, although at high displacements frictional and breakdown energy become more similar.

The limited range of frictional energy values compared to breakdown and radiated energy may reflect a self-limiting process due to temperature-driven changes in fault strength. As sliding occurs at earthquake slip rates, friction evolves to a lower steady-state value over some thermal weakening distance, D_{th} (Di Toro et al., 2011; Paola et al., 2011). Accordingly, a large fraction of the total frictional energy should be released during the initial period of sliding before D_{th} is reached. Sliding after this distance dissipates little energy because the fault is weak, so that the total frictional energy increases only slightly for larger earthquakes (if at all). Weakening also explains the lack of relationship observed between frictional energy and depth for faults below ~ 5 km (Figure 4), because D_{th} is smaller at higher normal stresses, and low friction is achieved with less total slip (Seyler et al., 2020). We acknowledge that fault weakening was assumed in our displacement estimates from biomarkers, however the consistency in frictional energy estimates in our field data require that frictional energy is not strongly dependent on displacement (e.g. if friction was at a constant level throughout the earthquake, frictional energy should increase linearly with displacement).

Using the values of breakdown, radiated, and frictional energy from Figure 5, we have put together a representative complete earthquake energy budget for small (< 1 -10 m of displacement) and large (> 1 -10 m of

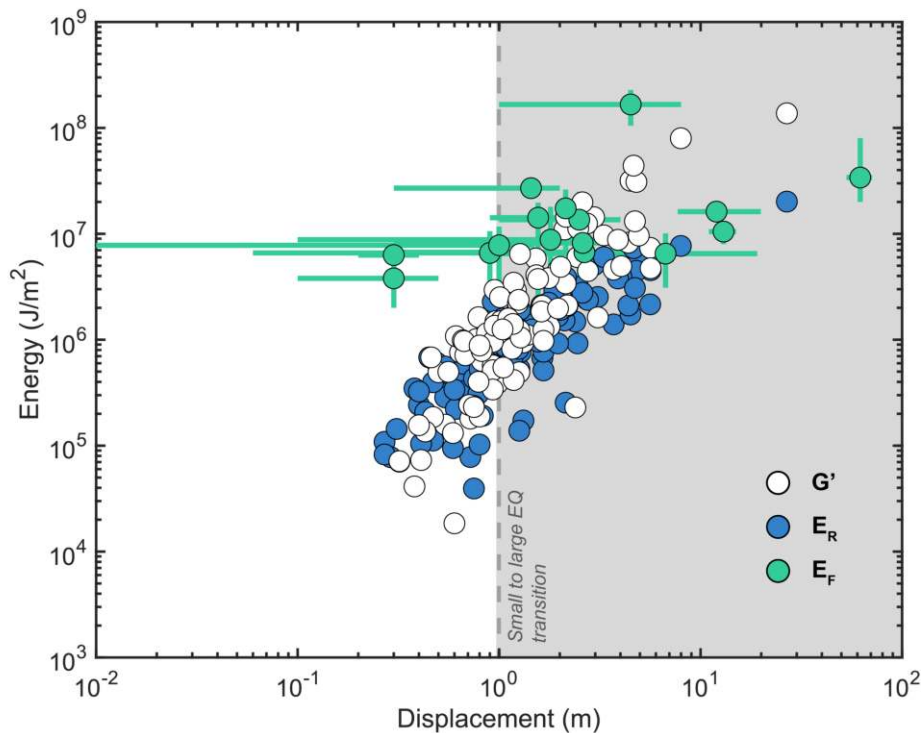


Figure 5 G' is breakdown energy and consists of fracture energy and some unknown component of frictional energy (Abercrombie and Rice, 2005), E_R is the radiated energy, and E_F is the frictional energy. E_R and G' are from Ye et al. (2016). E_F is compiled from previous studies or calculated here from temperature data (Table 1). Bars on frictional energy represent the range of displacement and E_F for each event. The dashed line and gray shaded region reflect the approximate transition from small (<1-10 m of displacement) to large earthquakes (>1-10 m of displacement)

displacement) events (Figure 6). The distinction at 1-10 m displacement, i.e., between small and large events, corresponds to the displacement where frictional energy is no longer the dominant energy sink (Figure 5). We suggest that as earthquakes get large and friction is low, a greater fraction of the total energy can go towards radiating seismic waves and towards deformation such as plastic deformation at the rupture tip and off-fault damage. Dedicating less energy to frictional resistance might allow earthquakes to keep propagating. Although our frictional energy dataset is small, it covers a range of depths, lithologies, fault thicknesses, and slip distances, suggesting that the basic relationships observed are fundamental and not the result of biases in the faults sampled. This observation of low friction at large displacements is what has been proposed from high velocity friction experiments and the efficacy of dynamic weakening mechanisms (Di Toro et al., 2011; Viesca and Garagash, 2015; Lambert et al., 2021), however the results from this study are the first that show this from field data. Our results provide insight into fundamental differences between small and large earthquakes, contributing to an integrated view of the earthquake energy budget and improving our overall understanding of how energy is partitioned during earthquakes.

6 Conclusions

Temperature rise and frictional energy have been compiled for newly analyzed and previously studied faults that reflect a range of different tectonic settings, depths,

and earthquake sizes. This dataset has been used to better understand the role of frictional heating during earthquakes and place the first broad constraints on the total earthquake energy budget. Temperature rise increases with depth of faulting, which is likely a consequence of increasing normal stress. However, below ~5 km depth, temperature rise no longer increases, suggesting a temperature limit through thermal weakening mechanisms. While frictional energy increases somewhat with displacement, the increase is remarkably small across different faults, suggesting that dynamic weakening limits the frictional work along most faults to values below 45 MJ/m². Along with frictional energy estimates, we have aggregated radiated and breakdown energy estimates and created an integrated view of the earthquake energy budget as a whole. In doing this, we demonstrate a fundamental difference in the way energy is partitioned between small and large earthquakes. For small earthquakes, the energy budget is dominated by frictional energy, whereas for large earthquakes, frictional, breakdown, and radiated energy contribute more equally to the total budget as a consequence of rapid frictional strength reduction with accumulating slip. These findings are an important advancement in understanding the energy required for earthquake rupture.

Acknowledgements

Early versions of this manuscript were greatly improved by comments from Jamie Kirkpatrick, Thorne Lay,

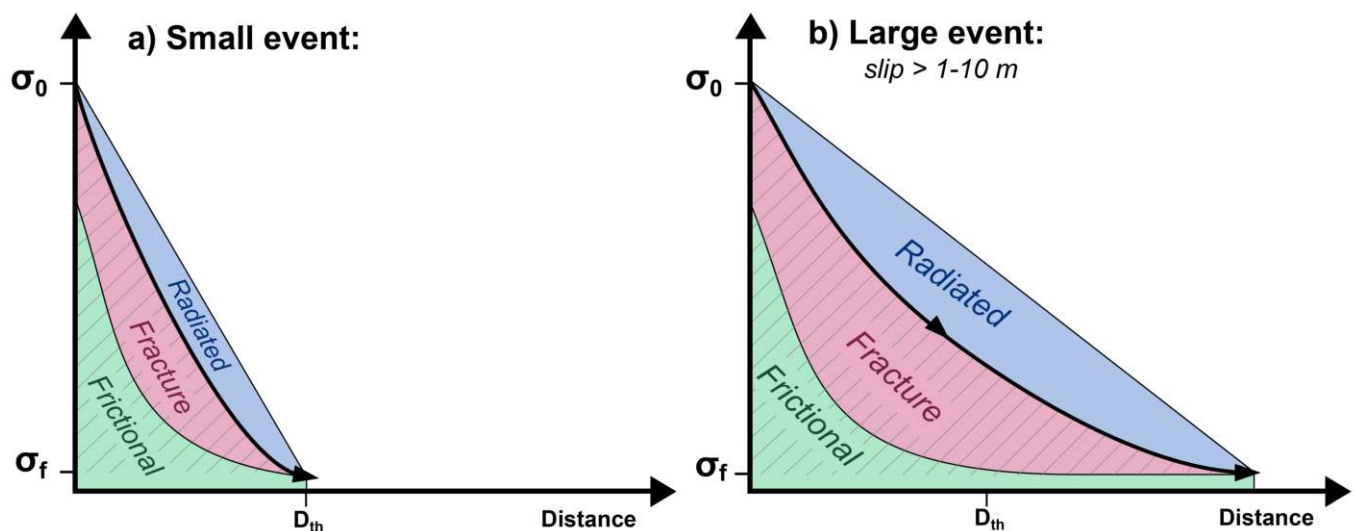


Figure 6 Schematic of the earthquake energy budget for small and large events with ranges for each component added. The bold line indicates stress drop as a function of slip and the colored areas represent the partitioning of energy into radiated (E_R), fracture (E_G), and frictional energy (E_F). The dashed region indicates the potential breakdown energy (G') and consists of fracture energy and some amount of frictional energy.

Christie Rowe, Rob Skarbak, and Nick Beeler. Conversations with Valere Lambert on earthquake energy budget helped us understand how best to compare different energy sinks and greatly improved the paper. Jack Williams graciously donated samples from the Hundalee fault. This work was partially supported by NSF Earthscope EAR1358585, DOE grant DE-SC0022360, and the Brinson Foundation (Chicago, IL). Heather Savage was partially supported by a UC Santa Cruz EVC Writing Fellowship program. We thank Pathikrit Bhattacharya and an anonymous reviewer for the comments and suggestions, which improved the quality of this manuscript.

Data and code availability

Data used in this study can be found in the manuscript and supplementary material. Code for biomarker and thermal modelling can be found at [10.6084/m9.figshare.21308343](https://doi.org/10.6084/m9.figshare.21308343)

References

- Abercrombie, R. and Rice, J. Can observations of earthquake scaling constrain slip weakening? *Geophysical Journal International*, 162(2):406–424, 2005. doi: [10.1111/j.1365-246X.2005.02579.x](https://doi.org/10.1111/j.1365-246X.2005.02579.x).
- Armstrong, E., Ault, A., Bradbury, K., Savage, H., Polissar, P., and Thomson, S. A multi-proxy approach using zircon (U-Th)/He thermochronometry and biomarker thermal maturity to robustly capture earthquake temperature rise along the punchbowl fault, California. *Geochemistry, Geophysics, Geosystems*, 23(4), 2022. doi: [10.1029/2021gc010291](https://doi.org/10.1029/2021gc010291).
- Aubry, J., Passelègue, F., Deldicque, D., Girault, F., Marty, S., Lahfid, A., and Schubnel, A. Frictional heating processes and energy budget during laboratory earthquakes. *Geophysical Research Letters*, 45(22):12–274, 2018. doi: [10.1029/2018GL079263](https://doi.org/10.1029/2018GL079263).
- Ault, A., Reiners, P., Evans, J., and Thomson, S. Linking hematite (U-Th)/He dating with the microtextural record of seismicity in the Wasatch fault damage zone. *Geology*, 43(9):771–774, 2015. doi: [//doi.org/10.1130/G36897.1](https://doi.org/10.1130/G36897.1).
- Ault, A., Jensen, J., Mcdermott, R., Shen, F., and Devener, B. Nanoscale evidence for temperature-induced transient rheology and postseismic fault healing. *Geology*, 48:1–5, 2019. doi: [10.1130/G46317.1](https://doi.org/10.1130/G46317.1).
- Brock, W. and Engelder, T. Deformation associated with the movement of the Muddy Mountain overthrust in the Buffington window, southeastern Nevada. *Geological Society of America Bulletin*, 88:1667–1677, 1977.
- Brodsky, E., Mori, J., Anderson, L., Chester, F., Conin, M., Dunham, E., Eguchi, N., Fulton, P., Hino, R., Hirose, T., and Others. The state of stress on the fault before, during, and after a major earthquake. *Annual Review of Earth and Planetary Sciences*, 48(1):49–74, 2020. doi: [10.1146/annurev-earth-053018-060507](https://doi.org/10.1146/annurev-earth-053018-060507).
- Byerlee, J. Friction of Rocks. In Byerlee, J. and Wyss, M., editors, *Rock Friction and Earthquake Prediction*, page 615–626. Birkhäuser Basel, 1978. doi: [10.1007/978-3-0348-7182-2_4](https://doi.org/10.1007/978-3-0348-7182-2_4).
- Carpenter, B., Scuderi, M., Collettini, C., and Marone, C. Frictional heterogeneities on carbonate-bearing normal faults: Insights from the Monte Maggio Fault, Italy. *Journal of Geophysical Research: Solid Earth*, 119(12):9062–9076, 2014. doi: [10.1002/2014JB011337](https://doi.org/10.1002/2014JB011337).
- Chang, J., Lockner, D., and Reches, Z. Rapid acceleration leads to rapid weakening in earthquake-like laboratory experiments. *Science*, 338(6103):101–105, 2012. doi: [10.1126/science.1221195](https://doi.org/10.1126/science.1221195).
- Chester, J., Chester, F., and Kronenberg, A. Fracture surface energy of the Punchbowl fault, San Andreas system. *Nature*, 437(7055):133–136, 2005. doi: [10.1038/nature03942](https://doi.org/10.1038/nature03942).
- Cocco, M. and Tinti, E. Scale dependence in the dynamics of earthquake propagation: Evidence from seismological and geological observations. *Earth and Planetary Science Letters*, 273(1–2):123–131, 2008. doi: doi.org/10.1016/j.epsl.2008.06.025.
- Cocco, M., Aretusini, S., Cornelio, C., Nielsen, S., Spagnuolo, E., Tinti, E., and Toro, G. Fracture Energy and Breakdown Work During Earthquakes. *Annual Review of Earth and Planetary Sciences*, 51, 2023. doi: [10.1146/annurev-earth-071822-100304](https://doi.org/10.1146/annurev-earth-071822-100304).
- Coffey, G., Savage, H., Polissar, P., Rowe, C., and Rabinowitz, H. Hot

- on the trail: Coseismic heating on a localized structure along the Muddy Mountain fault, Nevada. *Journal of Structural Geology*, 120:67–79, 2019. doi: 10.1016/j.jsg.2018.12.012.
- Coffey, G., Savage, H., Polissar, P., Meneghini, F., Ikari, M., Fagereng, A., Morgan, J., and Wang, M. Evidence of seismic slip on a large splay fault in the hikurangi subduction zone. *Geochemistry, Geophysics, Geosystems*, 22(8), 2021. doi: 10.1029/2021gc009638.
- Coffey, G., Savage, H., Polissar, P., Cox, S., Hemming, S., Winckler, G., and Bradbury, K. History of earthquakes along the creeping section of the San Andreas fault. *Geology*, 50(4):516–521, 2022. doi: 10.1130/G49451.1.
- Collettini, C., Niemeijer, A., Viti, C., and Marone, C. Fault zone fabric and fault weakness. *Nature*, 462(7275):907–910, 2009. doi: 10.1038/nature08585.
- Collettini, C., Viti, C., Tesei, T., and Mollo, S. Thermal decomposition along natural carbonate faults during earthquakes. *Geology*, 41:927–930, 2013. doi: 10.1130/G34421.1.
- Collettini, C., Carpenter, B., Viti, C., Cruciani, F., Mollo, S., and Tesei, T. Fault structure and slip localization in carbonate-bearing normal faults: An example from the Northern Apennines of Italy. *Journal of Structural Geology*, 67:154–166, 2014. doi: 10.1016/j.jsg.2014.07.017.
- Di Toro, G. and Pennacchioni, G. Fault plane processes and mesoscopic structure of a strong-type seismogenic fault in tonalites, Adamello batholith, Southern Alps. *Tectonophysics*, 402(1-4 SPEC. ISS.):55–80, 2005. doi: 10.1016/j.tecto.2004.12.036.
- Di Toro, G., Han, R., Hirose, T., Paola, N., Nielsen, S., Mizoguchi, K., Ferri, F., Cocco, M., and Shimamoto, T. Fault lubrication during earthquakes. *Nature*, 471(7339):494–498, 2011. doi: 10.1038/nature09838.
- Fulton, P., Brodsky, E., Kano, Y., Mori, J., Chester, F., Ishikawa, T., Harris, R., Lin, W., Eguchi, N., and Toczko, S. Low Coseismic Friction on the Tohoku-Oki Fault Determined from Temperature Measurements. *Science*, 6153:1214–1217, 2013. doi: 10.1126/science.1243641.
- Jeppson, T., Bradbury, K., and Evans, J. Geophysical properties within the San Andreas Fault Zone at the San Andreas Fault Observatory at Depth and their relationships to rock properties and fault zone structure. *Journal of Geophysical Research: Solid Earth*, 115(12):1–20, 2010. doi: 10.1029/2010JB007563.
- Kanamori, H. and Brodsky, E. The physics of earthquakes. *Reports on Progress in Physics*, 67(8):1429–1496, 2004. doi: 10.1088/0034-4885/67/8/R03.
- Kanamori, H. and Heaton, T. Microscopic and macroscopic physics of earthquakes. *Geophysical Monograph Series*, 120:147–163, 2000. doi: 10.1029/GM120.
- Kanamori, H. and Rivera, L. Energy partitioning during an earthquake. *Geophysical Monograph Series*, 170:3–13, 2006. doi: 10.1029/170GM03.
- Kaneko, Y., Nielsen, S., and Carpenter, B. The onset of laboratory earthquakes explained by nucleating rupture on a rate-and-state fault. *Journal of Geophysical Research: Solid Earth*, 121(8):6071–6091, 2016. doi: 10.1002/2016JB013143.
- Kirkpatrick, J. and Rowe, C. Disappearing ink: How pseudotachylytes are lost from the rock record. *Journal of Structural Geology*, 52:183–198, 2013. doi: 10.1016/j.jsg.2013.03.003.
- Kirkpatrick, J., Shipton, Z., and Persano, C. Pseudotachylytes: Rarely generated, rarely preserved, or rarely reported? *Bulletin of the Seismological Society of America*, 99(1):382–388, 2009. doi: 10.1785/0120080114.
- Kirkpatrick, J., Dobson, K., Mark, D., Shipton, Z., Brodsky, E., and Stuart, F. The depth of pseudotachylyte formation from detailed thermochronology and constraints on coseismic stress drop variability. *Journal of Geophysical Research: Solid Earth*, 117(6):1–13, 2012. doi: 10.1029/2011JB008846.
- Lachenbruch, A. Simple models for the estimation and measurement of frictional heating by an earthquake, 1986.
- Lambert, V. and Lapusta, N. Rupture-dependent breakdown energy in fault models with thermo-hydro-mechanical processes. *Solid Earth*, 11(6):2283–2302, 2020. doi: 10.5194/se-11-2283-2020.
- Lambert, V., Lapusta, N., and Perry, S. Propagation of large earthquakes as self-healing pulses or mild cracks. *Nature*, 591(7849):252–258, 2021. doi: 10.1038/s41586-021-03248-1.
- McBeck, J., Cordonnier, B., Mair, K., and Renard, F. The evolving energy budget of experimental faults within continental crust: Insights from in situ dynamic X-ray microtomography. *Journal of Structural Geology*, 123:42–53, 2019. doi: 10.1016/j.jsg.2019.03.005.
- McDermott, R., Ault, A., Evans, J., and Reiners, P. Thermochronometric and textural evidence for seismicity via asperity flash heating on exhumed hematite fault mirrors, Wasatch fault zone, UT, USA. *Earth and Planetary Science Letters*, 471:85–93, 2017. doi: 10.1016/j.epsl.2017.04.020.
- Meneghini, F. and Moore, J. Deformation and hydrofracture in a subduction thrust at seismogenic depths: The Rodeo Cove thrust zone, Marin Headlands, California. *Bulletin of the Geological Society of America*, 119(1-2):174–183, 2007. doi: 10.1130/B25807.1.
- Nicol, A., Robinson, R., Dissen, R., and Harvison, A. Variability of recurrence interval and single-event slip for surface-rupturing earthquakes in New Zealand. *New Zealand Journal of Geology and Geophysics*, 59(1):97–116, 2016. doi: 10.1080/00288306.2015.1127822.
- Noda, H. and Lapusta, N. Stable creeping fault segments can become destructive as a result of dynamic weakening. *Nature*, 493(7433):518–521, 2013. doi: 10.1038/nature11703.
- Otsuki, K., Monzawa, N., and Nagase, T. Fluidization and melting of fault gouge during seismic slip: Identification in the Nojima fault zone and implications for focal earthquake mechanisms. *Journal of Geophysical Research: Solid Earth*, 108(B4), 2003. doi: 10.1029/2001JB001711.
- Paola, N., Hirose, T., Mitchell, T., Toro, G., Viti, C., Shimamoto, T., and Laterina, V. Fault lubrication and earthquake propagation in thermally unstable rocks. *Geology*, 39(1):35–38, 2011. doi: 10.1130/G31398.1.
- Passelègue, F., Schubnel, A., Nielsen, S., Bhat, H., Deldicque, D., and Madariaga, R. Dynamic rupture processes inferred from laboratory microearthquakes. *Journal of Geophysical Research: Solid Earth*, 121(6):4343–4365, 2016. doi: 10.1002/2015JB012694.
- Pittarello, L., Di Toro, G., Bizzarri, A., Pennacchioni, G., Hadizadeh, J., and Cocco, M. Energy partitioning during seismic slip in pseudotachylyte-bearing faults, Gole Larghe Fault, Adamello, Italy. *Earth and Planetary Science Letters*, 269(1-2):131–139, 2008. doi: 10.1016/j.epsl.2008.01.052.
- Polissar, P., Savage, H., and Brodsky, E. Extractable organic material in fault zones as a tool to investigate frictional stress. *Earth and Planetary Science Letters*, 311(3-4):439–447, 2011. doi: 10.1016/j.epsl.2011.09.004.
- Rabinowitz, H., Polissar, P., and Savage, H. Reaction kinetics of alkenone and n-alkane thermal alteration at seismic timescales. *Geochemistry, Geophysics, Geosystems*, 18(1):204–219, 2017. doi: 10.1002/2016GC006553.
- Rabinowitz, H., Kirkpatrick, J., Savage, H., Polissar, P., and Rowe, C. Earthquake slip surfaces identified by biomarker thermal matu-

- riety within the 2011 Tohoku-Oki earthquake fault zone. *Nature Communications*, 11(533):1–9, 2020. doi: 10.1038/s41467-020-14447-1.
- Reches, Z. and Lockner, D. Fault weakening and earthquake instability by powder lubrication. *Nature*, 467(7314):452–455, 2010. doi: 10.1038/nature09348.
- Regalla, C., Rowe, C., Harrichhausen, N., Tarling, M., and Singh, J. Styles of underplating in the Marin Headlands terrane, Franciscan complex, California. *Special paper of the Geological Society of America*, 534:155–173, 2018. doi: 10.1130/2018.2534(10).
- Rice, J. Heating and weakening of faults during earthquake slip. *Journal of Geophysical Research*, 111:1–29, 2006. doi: 10.1029/2005JB004006.
- Rice, J., Rudnicki, J., and Platt, J. Stability and localization of rapid shear in fluid-saturated fault gouge: 1. Linearized stability analysis. *Journal of Geophysical Research: Solid Earth*, 119(5):4311–4333, 2014. doi: 10.1002/2013JB010710.
- Rodriguez-Navarro, C., Ruiz-Agudo, E., Luque, A., Rodriguez-Navarro, A., and Ortega-Huertas, M. Thermal decomposition of calcite: Mechanisms of formation and textural evolution of CaO nanocrystals. *The American Mineralogist*, 94(4):578–593, 2009. doi: 10.2138/am.2009.3021.
- Rowe, C. and Griffith, W. Do faults preserve a record of seismic slip: A second opinion. *Journal of Structural Geology*, 78:1–26, 2015. doi: 10.1016/j.jsg.2015.06.006.
- Rowe, C., Moore, J., Meneghini, F., and McKeirnan, A. Large-scale pseudotachylytes and fluidized cataclasites from an ancient subduction thrust fault. *Geology*, 33(12):937–940, 2005. doi: 10.1130/G21856.1.
- Rowe, C., Meneghini, F., and Casey Moore, J. Textural record of the seismic cycle: Strain-rate variation in an ancient subduction thrust. *Geological Society Special Publication*, 359(1):77–95, 2011. doi: 10.1144/SP359.5.
- Rubino, V., Rosakis, A., and Lapusta, N. Understanding dynamic friction through spontaneously evolving laboratory earthquakes. *Nature Communications*, 8:15991, 2017. doi: 10.1038/ncomms15991.
- Saffer, D., Wallace, L., Barnes, P., Pecher, I., Petronotis, K., Levay, L., Bell, R., Crundwell, M., Fagereng, A., Fulton, P., Greve, A., Harris, R., Hashimoto, Y., Ikari, M., Ito, Y., Kitajima, H., Kutterolf, S., Lee, H., Li, X., and Wang, X. Site U1518. In *Proceedings of the International Ocean Discovery Program*, volume 372B/375, page 1–63, 2019. doi: 10.14379/iodp.proc.372B375.101.2019.
- Sakaguchi, A., Chester, F., Curewitz, D., Fabbri, O., Goldsby, D., Kimura, G., Li, C., Masaki, Y., Sreaton, E., Tsutsumi, A., Ujiie, K., and Yamaguchi, A. Seismic slip propagation to the updip end of plate boundary subduction interface faults: Vitronite reflectance geothermometry on integrated ocean drilling program nantro SEIZE cores. *Geology*, 39(4):395–398, 2011a. doi: 10.1130/G31642.1.
- Sakaguchi, A., Kimura, G., Strasser, M., Sreaton, E., Curewitz, D., and Murayama, M. Episodic seafloor mud brecciation due to great subduction zone earthquakes. *Geology*, 39(10):919–922, 2011b. doi: 10.1130/G32043.1.
- Savage, H. and Polissar, P. Biomarker Thermal Maturity Reveals Localized Temperature Rise from Paleoseismic Slip along the Punchbowl Fault, CA, USA. *Geochemistry, Geophysics, Geosystems*, 20:3201–3215, 2019. doi: 10.1029/2019GC008225.
- Savage, H., Polissar, P., Sheppard, R., Rowe, C., and Brodsky, E. Biomarkers heat up during earthquakes: New evidence of seismic slip in the rock record. *Geology*, 42(2):99–102, 2014. doi: 10.1130/G34901.1.
- Savage, H., Rabinowitz, H., Spagnuolo, E., Aretusini, S., Polissar, P., and Di, G. Biomarker thermal maturity experiments at earthquake slip rates. *Earth and Planetary Science Letters*, 502:253–261, 2018. doi: 10.1016/j.epsl.2018.08.038.
- Seyler, C., Kirkpatrick, J., Savage, H., Hirose, T., and Faulkner, D. Rupture to the trench? Frictional properties and fracture energy of incoming sediments at the Cascadia subduction zone. *Earth and Planetary Science Letters*, 546:116413, 2020. doi: 10.1016/j.epsl.2020.116413.
- Sheppard, R., Polissar, P., and Savage, H. Organic thermal maturity as a proxy for frictional fault heating: Experimental constraints on methylphenanthrene kinetics at earthquake timescales. *Geochimica et Cosmochimica Acta*, 151:103–116, 2015. doi: 10.1016/j.gca.2014.11.020.
- Sibson, R. Interactions between Temperature and Pore-Fluid Pressure during Earthquake Faulting and a Mechanism for Partial or Total Stress Relief. *Nature*, 243:66–68, 1973. doi: 10.1038/physci243066a0.
- Sibson, R. Generation of Pseudotachylyte by Ancient Seismic Faulting. *Geophysical Journal of the Royal Astronomical Society*, 43:775–794, 1975. doi: 10.1111/j.1365-246X.1975.tb06195.x.
- Sibson, R. Fault rocks and fault mechanisms. *Journal of the Geological Society*, 133(3):191–213, 1977. doi: 10.1144/gsjgs.133.3.0191.
- Sibson, R. and Toy, V. The habitat of fault-generated pseudotachylyte: Presence vs. absence of friction-melt. *Geophysical Monograph Series*, 170:153–166, 2006. doi: 10.1029/170GM16.
- Sun, T., Wang, K., Fujiwara, T., Kodaira, S., and He, J. Large fault slip peaking at trench in the 2011 Tohoku-oki earthquake. *Nature Communications*, 8:4–11, 2017. doi: 10.1038/ncomms14044.
- Ujiie, K., Yamaguchi, H., Sakaguchi, A., and Toh, S. Pseudotachylytes in an ancient accretionary complex and implications for melt lubrication during subduction zone earthquakes. *Journal of Structural Geology*, 29(4):599–613, 2007. doi: 10.1016/j.jsg.2006.10.012.
- Venkataraman, A. and Kanamori, H. Observational constraints on the fracture energy of subduction zone earthquakes. *Journal of Geophysical Research: Solid Earth*, 109:1–20, 2004. doi: 10.1029/2003JB002549.
- Viesca, R. and Garagash, D. Ubiquitous weakening of faults due to thermal pressurization. *Nature Geoscience*, 8(11):875–879, 2015. doi: 10.1038/ngeo2554.
- Williams, J., Barrell, D., Stirling, M., Sauer, K., Duke, G., and Hao, K. Surface rupture of the Hundalee fault during the 2016 Mw 7.8 Kaikōura earthquake. *Bulletin of the Seismological Society of America*, 108(3B):1540–1555, 2018. doi: 10.1785/0120170291.
- Ye, L., Lay, T., Kanamori, H., and Rivera, L. Rupture characteristics of major and great (Mw≥7.0) megathrust earthquakes from 1990–2015: 1. Source parameter scaling relationships. *Journal of Geophysical Research: Solid Earth*, 121:3782–3803, 2016. doi: 10.1002/2015JB012426.

The article *Estimates of earthquake temperature rise, frictional energy, and implications to earthquake energy budgets* © 2023 by G. L. Coffey is licensed under CC BY 4.0.

Co-seismic slip of the 18 April 2021 M_w 5.9 Genaveh earthquake in the South Dezful Embayment of Zagros (Iran) and its aftershock sequence

M. Jamalreyhani  ^{*1,7}, L. Pousse-Beltran  ², M. A. Hassanzadeh  ³, S. Sadat-Arabi  ⁴, E. A. Bergman  ⁵, A. Shamszadeh  ⁶, S. Arvin  ³, N. Fariborzi  ³, A. Songhori  ⁷

¹GFZ German Research Center for Geosciences, Potsdam, Germany., ²University Grenoble Alpes, University Savoie Mont Blanc, CNRS, IRD, UGE, ISTerre, Grenoble, France., ³Department of Earth Sciences, Institute for Advanced Studies in Basic Sciences, Zanjan, Iran., ⁴Science and Research Branch of Islamic Azad University (SRBIAU), Tehran, Iran, ⁵Global Seismological Services, Golden, CO, USA, ⁶Department of Earth Sciences, College of Sciences, Shiraz University, Shiraz, Iran, ⁷Institute of Geophysics, University of Tehran, Tehran, Iran.

Author contributions: *Conceptualization:* M. Jamalreyhani, L. Pousse-Beltran, M. A. Hassanzadeh. *Visualization:* M. Jamalreyhani, L. Pousse-Beltran, M. A. Hassanzadeh, S. Sadat-Arabi, E. A. Bergman, A. Shamszadeh. *Formal Analysis:* M. Jamalreyhani, L. Pousse-Beltran, M. A. Hassanzadeh, S. Sadat-Arabi, E. A. Bergman, A. Shamszadeh, Sh. Arvin, N. Fariborzi, A. Songhori. *Software:* M. Jamalreyhani, L. Pousse-Beltran, M. A. Hassanzadeh, S. Sadat-Arabi, E. A. Bergman. *Validation:* M. Jamalreyhani, L. Pousse-Beltran. *Supervision:* M. Jamalreyhani. *Investigation:* M. Jamalreyhani, L. Pousse-Beltran, E. A. Bergman. *Writing:* M. Jamalreyhani, L. Pousse-Beltran, E. A. Bergman, A. Shamszadeh.

Abstract On 2021 April 18, an M_w 5.9 earthquake struck the Genaveh region in the south Dezful embayment of the Zagros, Iran. Here, we investigate the active tectonics of the region, the geometry and slip distribution of the causative fault plane, and its aftershock behavior. We applied a combination of different geodetic and seismological methods (slip distribution inversion of the mainshock using Sentinel-1 Interferometric Synthetic Aperture Radar (InSAR), relocation, and moment tensor inversion of aftershocks and background seismicity of the region). Co-seismic InSAR modeling shows that the slip is confined to the sedimentary cover at depths of 4-7 km with a maximum slip of 1 m and highlights the influence of lithology in the rupture propagation. Moment tensors and centroid depths of aftershocks down to M_w 4 show that the distributed aftershocks sequence is dominated by reverse faulting at centroid depths of 4-10 km. The causative fault is compatible and parallel to the trend of the Gulkhari anticline and the coseismic uplift of the Genaveh earthquake implies that the growth of this particular fold is linked to the fault(s). However, still, due to the absence of surface rupture, the clear relationship between buried faulting and surface folding remains unclear.

Non-technical summary We investigate the M_w 5.9 Genaveh earthquake that occurred on 2021 April 18 near the Genaveh harbor in the Persian Gulf, located in the Zagros mountains of Iran. We assess this seismic activity using seismology and space geodetic measurements and models. We discuss the connection between faulting and folding in the region and the causative fault of the Genaveh earthquake. Our results show this earthquake involved a gently NE-dipping fault plane. We found that the mainshock was restricted to depths of between 4-7 with a maximum slip of 1 m within the sedimentary cover. Our results are helpful for hazard and risk assessment of the Genaveh harbor which is an important economic spot in Iran.

Production Editor:
Gareth Funning
Handling Editor:
Yen Joe Tan
Copy & Layout Editor:
Kirsty Bayliss

Reviewed by:
Edwin Nissen and
anonymous reviewer

Received:
September 27, 2022
Accepted:
April 18, 2023
Published:
May 18, 2023

1 Introduction

The Zagros Fold-and-Thrust Belt (ZFTB) is a seismically active region of Iran, formed during the collision of the Afro-Arabian continent and the Iranian microcontinent (e.g. [Stöcklin, 1968](#); [McQuarrie, 2004](#); [Mouthereau et al., 2012](#)). The region presents one of the youngest continental collision zones on Earth and hosts frequent episodes of moderate to large shallow seismicity (e.g. [Talebian and Jackson, 2004](#); [Nissen et al., 2019](#); [Jamalreyhani et al., 2022](#)) (Figure 1). The Zagros changes morphology along and across strike, likely reflecting differences in the sedimentary cover — in particular its overall thickness and the spatial extents of weak, detachment-forming evaporitic layers. However, it's not well understood whether these morphological

changes are reflected in (or perhaps even governed by) differences in the style of earthquake faulting. The advent of InSAR and recent improvements in seismic station coverage have allowed focused studies of major earthquake sequences that can shed light on these questions. A long-standing question in the ZFTB is the extent to which the Precambrian basement and the thick Phanerozoic sedimentary layer participate in the observed seismicity ([McQuarrie, 2004](#); [Mouthereau et al., 2007](#); [Talebian and Jackson, 2004](#); [Jamalreyhani et al., 2022](#)). [Nissen et al. \(2011\)](#) suggested a vertical separation of the seismicity in the Zagros, implying that most of the moderately-sized events (M_w 5-6), especially those in the ZSFB, happen in the competent segment of the sedimentary layer and most the aftershocks in the basement, mostly triggered by stress perturbations. Recent studies show the variety of deformation styles

*Corresponding author: m.jamalreyhani@gmail.com

and seismicity in different parts of the ZFTB (e.g. Nissen et al., 2019; Jamalreyhani et al., 2019, 2022, 2021b). The outer part of the ZFTB, named Zagros Foreland Folded Belt (ZFFB), is subdivided into four tectono-stratigraphy domains (Figure 1): from SE to NW, the Fars Arc, the Dezful Embayment, the Lurestan Arc, and the Kirkuk Embayment. Recent studies of earthquakes in the SE Zagros (Qeshm (Nissen et al., 2010), Fin (Roustaei et al., 2010), Khaki-Shonbe (Elliott et al., 2015), Khalili (Jamalreyhani et al., 2021a)) and in the NW Zagros (Ezgeleh and Sarpolzahab (Nissen et al., 2019; Jamalreyhani et al., 2022), Mandali (Nissen et al., 2019), Murmuri (Copley et al., 2015)) have illuminated the structural style in those regions, but so far there has been an absence of large events in the central Zagros. The M_w 5.9 Genaveh earthquake on 2021 April 18, therefore, fills an important gap and provides an opportunity to study the characteristics of observed seismicity in the Dezful Embayment.

The Dezful Embayment, known as the lower-lying area in Zagros ZFFB (Allen and Talebian, 2011), is the ~500 km-long segment situated in the outer part of the central Zagros and covers an area of 75000 km² (Allen and Talebian, 2011) (Figure 1). It contains a > 5 km thick of the Fars Group sediments (Figure S1; Gachsaran, Mishan, Aghajari, and Bakhtiyari formations) (Abdullahie Fard et al., 2011; Shamszadeh et al., 2022a). This region is co-located with 45 natural oil fields, equal to ~8% of Earth's total (Najafi et al., 2014; Seraj et al., 2020; Najafi and Lajmorak, 2020; Shamszadeh et al., 2022a) (Figure 1). It is formed from the west of the Kazerun fault zone to the Balarud fault zone in the northwest and in the footwall of the Mountain Front Flexure (MFF) (Berberian, 1995; Allen and Talebian, 2011; Shamszadeh et al., 2022a). Most of the Dezful Embayment arc's seismicity occurs on ~30°-50° dipping blind reverse faults and some on strike-slip mechanisms (Figure 1). In the Dezful Embayment, layer-parallel shortening resulting from the Zagros orogeny is accommodated by several symmetric and asymmetric mostly NW-SE trending anticlines and synclines (Figure 1) (e.g. Sherkati et al., 2006; Seraj et al., 2020).

Almost 7-12 km of the Phanerozoic sedimentary succession including alternative competent and incompetent layers, is folding and faulting in response to the continental collision in the ZFTB (Alavi, 2008; Irandoust et al., 2022). The Precambrian-Cambrian Hormuz salt layer is located between the basement and sediments in ZFFB. Despite some outcrops of Hormuz salt being observed in the adjacent area of the Dezful Embayment, the fold style and geometry suggest a decollement layer at the base of the sedimentary cover in the South Dezful Embayment (SDE) (Shamszadeh et al., 2022a,b, and references therein). Nonetheless, the surface salt diapirs are lacking in the Dezful Embayment (Jahani et al., 2009; Sherkati and Letouzey, 2004; Najafi and Lajmorak, 2020). This challenges the clear exposure of the Hormuz salt layer in the Dezful Embayment (Sherkati and Letouzey, 2004; Jahani et al., 2017) but the lower Paleozoic Shale at depth of ~3-4 km has been reported (Sherkati and Letouzey, 2004; Farahzadi et al., 2019; Najafi and Lajmorak, 2020). The estimated thickness of

the sedimentary cover from subsurface investigations shows ~8-12 km of sediment in the SDE (Sherkati et al., 2006; Najafi and Lajmorak, 2020; Shamszadeh et al., 2022a). This is suggested by the construction of some longitudinal sections along the strike of anticlinal structures and across the NNE-SSW trending, e.g. Kharg-Mish Paleo High (KMPH) (Sherkati et al., 2006; Shamszadeh et al., 2022a). Above the Precambrian crystalline basement, a 4–6 km thick sequence which has been named as 'Competent Group' is composed (Vergés et al., 2011; Najafi and Lajmorak, 2020). Mainly two sets of faults with the NW-SE Zagros trend and the NNE-SSW Afro-Arabian trend have been developed and involved in the deformation of the SDE (e.g. Sepehr and Cosgrove, 2004; Shamszadeh et al., 2022b). In addition to several NW-SE pre-existing basement faults in the ZFTB (e.g. the MFF), most of the SDE's anticlinal structures (e.g. Gulkhari and Gachsaran anticlines) with steeper SW forelimbs are developed over an NW-SE trending emergent or blind thrust faults dipping NE (e.g. McQuarrie, 2004; Carruba et al., 2006). Furthermore, several NNE-SSW trending basement-involved faults, e.g. Kharg-Mish and Hendijan-Bahregansar-Norooz, affected the tectono-stratigraphy evolution of the SDE during the Phanerozoic (Figure 1) (Sherkati and Letouzey, 2004; Abdullahie Fard et al., 2011; Shamszadeh et al., 2022a).

On 2021 April 18, at 6:41 UTC the M_w 5.9 Genaveh earthquake (named after a nearby famous harbor in the Persian Gulf) occurred in the southern portion of the SDE (Figure 1). It was followed by 370 aftershocks larger than M_n 2.5 and 21 aftershocks larger than M_n 4 (Iranian Seismological Center (IRSC) bulletin). This earthquake is an excellent case study of buried thrust faulting in the sedimentary cover of the SDE that could provide valuable information on the subsurface structure of the area. The Genaveh earthquake and its aftershock activity affected the Bushehr province (Tourani et al., 2021) but there are no reports of death due to this event (Tourani et al., 2021). There are no historical and instrumental records of any earthquake unambiguously linked to faults within Bushehr province (Ambraseys and Melville, 1982; Berberian, 1995). The Genaveh seismic cluster partially filled the data gap in the Karasözen et al. (2019) study, in which they relocate the 70-year instrumentally recorded seismicity in the entire Zagros, but there was no report of relocated events in our study area. Nevertheless, the IRSC catalog indicates 3 events larger than M_w 5, co-located with the Gulkhari anticline, and in this study considered as the background seismicity.

Thanks to high-quality satellite data before and after the mainshock, and co- and post-seismic waveform records (both for mainshock and aftershocks), we focus on understanding whether the growth of the Gulkhari anticline is controlled by a fault directly beneath it or not. We probe links between faulting and folding and investigate the robustness of the vertical separation idea, suggested by Nissen et al. (2011). Another important question to answer is which fault or faults are responsible for the shaking. Furthermore, the Genaveh earthquake co-located with the major active Gulkhari

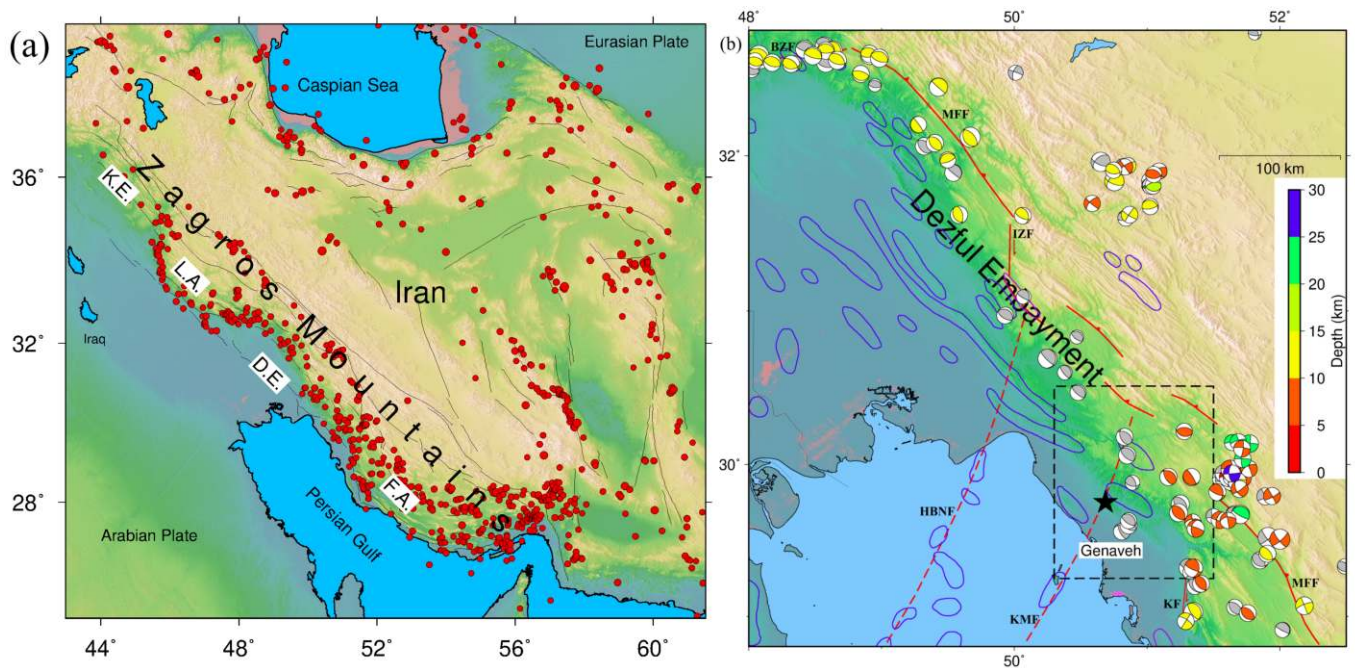


Figure 1 a) Seismicity of Iran and the location of the Zagros Mountains. Red circles are $M_w > 5.0$ earthquakes from 1900 to 2020 from the USGS catalog. The black lines represent the major active faults of Iran. Four tectono-stratigraphy domains: from SE to NW, the Fars Arc (F.A.), the Dezful Embayment (D.E.), the Lurestan Arc (L.A.), and the Kirkuk Embayment (K.E.). b) A zoom-in of the Dezful Embayment. The oil fields are shown by blue polygons in this area (Najafi and Lajmorak, 2020). Red lines show major mapped active faults, including the Mountain Front Flexure (MFF) (Berberian, 1995), Kharg-Mish Fault (KMF), Hendijan-Bahregansar Nowrooz Fault (HBNF), Izeh Fault Zone (IFZ), BalaRud Fault Zone (BFZ), and Kazerun Fault (KF). Focal mechanisms from published waveform modeling studies are plotted at relocated epicenters and colored according to focal depth (Karasözen et al., 2019). Those with gray color are from Yaghoubi et al. (2021) without showing depth. The black rectangle shows our study area and the black star shows the location of the 5.9 M_w 2021 Genaveh earthquake (Figure 2).

oil field, raising the possibility that this earthquake is induced by human activity. We check the feasible relationship between the exploitation of oil reservoirs with this earthquake. The coseismic slip distribution of the Genaveh earthquake has been investigated by Golshadi et al. (2022) and Jafari et al. (2023) based on Interferometric Synthetic Aperture Radar (InSAR) modeling and they only discuss the mainshock causative fault plane. In this study, we applied a combination of different seismological methods, including relocation of aftershocks using phase readings of local and regional seismic stations, moment tensor inversion of the mainshock, and aftershocks down to M_n 4 using regional waveform records of Iran seismic networks, and slip distribution of the mainshock using Sentinel-1 data.

Our results reveal a close relationship between coseismic uplift and the growth of Gulkhari anticline. We show the seismicity and causative fault are parallel to the trend of the Gulkhari anticline with complex fault zone architecture. Because of the absence of surface rupture, the clear relationship between buried faulting and surface folding remains debated. Our results are helpful for hazard and risk assessment of the Genaveh harbor and surrounding area—one of the important economic spots of Iran.

2 The 2021 Genaveh earthquake sequence

2.1 Relocation of the sequence

To refine the seismicity patterns we applied the multiple-relocation method “mloc” which is specialized to provide (given suitable data) hypocenters with minimal bias from unknown Earth structures, and realistic uncertainties (Bergman et al., 2022). This technique has been used in relocating many earthquakes in the Zagros and other regions of Iran (e.g., Nissen et al., 2019; Walker et al., 2011; Karasözen et al., 2019; Jamalreyhani et al., 2021a). Thanks to the local and regional seismic networks of the IRSC and the International Institute of Earthquake Engineering and Seismology (IIEES) (Figure 2), we were able to improve the relative locations of the Genaveh seismic sequence and calibrate the absolute location of the cluster with an epicentral uncertainty of 3.1–3.5 km (Figure 2). The relocated cluster includes 117 earthquakes (Table S1), from early 2015 to January 2022, selected on the basis of the number of phase readings and the azimuthal gap. The minimum number of readings for events that are connected to other events, and thus used to estimate relative locations, is 24. The minimum and maximum azimuthal gaps are 19.5° and 163.7°, respectively. There are 69 relocated events soon after the mainshock but some of them are spatially away from the mainshock and likely represent background seismicity. Due to the lack of perma-

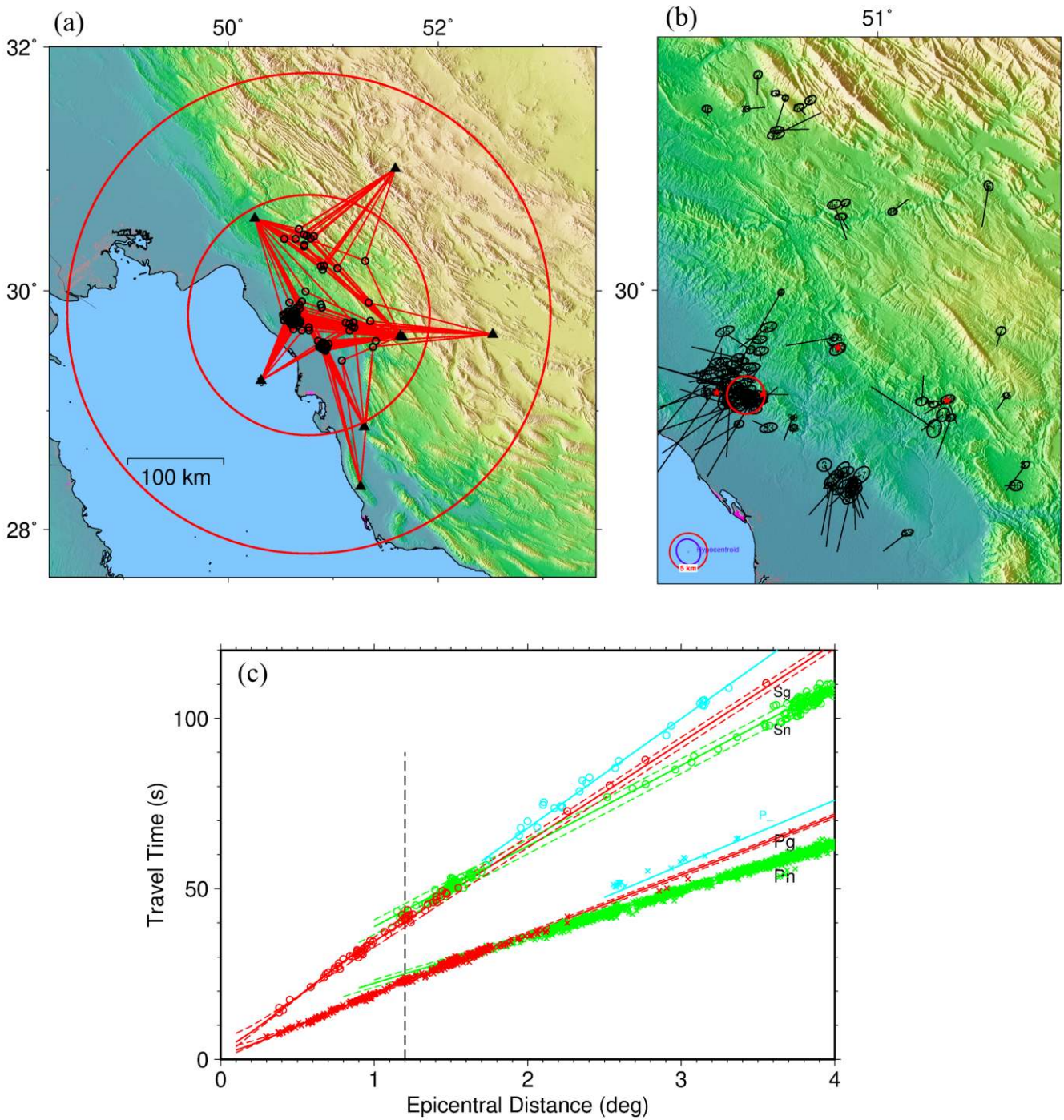


Figure 2 (a) Station distribution (black triangles) and ray paths (red straight lines) used to determine the calibrated hypocentroid (i.e., absolute location) of the Genaveh cluster. Only observations within 1.2° are used for this purpose. All events in the cluster are plotted, including the 13 events that do not have any readings in that distance range. Large red circles show radii of 1.0° and 2.0° from the cluster hypocentroid. (b) Relocated earthquake hypocenters with 90% confidence ellipses for relative location. The 90% confidence ellipse for the absolute location of hypocentroid is shown as a blue ellipse on the left bottom corner of the figure. The red ellipse represents a reference circle of 5 km radius. The full epicentral uncertainty of any given event requires the addition of relative uncertainty to the hypocentroidal uncertainty. Red stars denote events with a magnitude larger than 5. Black vectors for each event show the change in location from the epicenter given in the arrival time data file, which varies from event to event. (c) Fit between observed phase arrivals (Pg: red crosses, Sg: red circles, Pn: green crosses, Sn: green circles) and theoretical travel times (red and green lines) calculated from the simple flat-layered velocity model determined for this dataset, for epicentral distances of up to 4° . The vertical dashed line at 1.2° indicates the cut-off distance used in the calibrated location of the hypocentroid (228 readings).

ment seismic stations in this region, no near-source data is available for this cluster; the nearest readings are ~30

km away. Focal depths of most events in the cluster are set manually and fixed in the relocation according to the

fit of local distance data (first-arriving Pg and Sg) and a crustal model typical of the Zagros region from other relocation studies, a method with poorer resolving power than near-source readings, but still useful. Due to the lack of appropriate data, we fix the depth of three events at the centroid depth obtained from waveform modeling (see Section 2.2) and in nine cases the focal depths were fixed at 12 km, the median of constrained focal depths for this cluster, and very typical of Zagros earthquakes (e.g. Karasözen et al., 2019). To predict theoretical travel times (Figure 2a), we use a 2 layered crustal model (Moho depth 47 km), in combination with the AK135 model (Table S2). Figure 2 shows the station distribution and ray paths used to relocate the Genaveh seismic sequence and background seismicity, and the pattern and uncertainty of the relative locations. Both Pg and Sg phases have near-zero mean and there is no evidence of a slope with distance to the residuals. The scatter is typical in a region that certainly has some heterogeneity in crustal velocities. The only drawback is the lack of really close-in data, which hampers depth constraints. The 90% confidence ellipse of the hypocenter has semi-axis lengths of 3.1 and 3.5 km and the relative locations, as seen in Figure 2b, are very well constrained.

2.2 Moment tensor inversion of the sequence

The temporal evolution of the Genaveh earthquake sequence depicts a mainshock aftershock behavior, including 22 aftershocks larger than 4 within 5 months (Figure 3). During 2015-2020 and before the Genaveh earthquake mainshock, there are 3 events larger than M_w 5 in the southeast of Gulkhari anticline considered as the background seismicity (Figure 3). Seismic records of the Genaveh earthquake sequence and background seismicity were recorded with a good signal-to-noise ratio by broadband sensors at regional distances. Thus, we estimate the centroid Moment Tensor (MT), based on the inversion of regional data. In this distance, modeling has been performed in the frequency band 0.02-0.05 Hz, representing dominant periods of the Rayleigh and Love waves. The MT inversion is based on broadband data of IRSC and IIEES and simultaneously fitting 3-component waveforms in the time and in frequency domains (Figure S2). The observations have been revised manually to exclude noisy records and have been restituted to displacement. To perform centroid MT inversions of the Genaveh earthquake, its aftershocks down to M_w 4, and background seismicity down to M_w 5, we use a probabilistic Bayesian bootstrap optimization nonlinear inversion method (Heimann et al., 2017), which provides ensembles of best-fitting MTs, and estimates the uncertainties and trade-offs for all inverted source parameters. This technique previously has been successfully applied to other earthquakes in the Zagros (Jamalreyhani et al., 2021a, 2022) as well as in other regions (Jamalreyhani et al., 2020; Büyükakpinar et al., 2021; Wang et al., 2022).

Synthetic seismograms are computed using pre-calculated Green's functions (Heimann et al., 2019). The pre-calculated Green's functions were calculated

on a grid for combinations of source depth and source-receiver surface distance based on the regional velocity model "Karbaas" by Karasözen et al. (2019).

Our results for the focal mechanism of the mainshock show that the causative fault plane has a either strike of $306^\circ \pm 5^\circ$, a dip of $28^\circ \pm 9^\circ$, with a reverse mechanism (rake $86^\circ \pm 10^\circ$), or strike of $131^\circ \pm 5^\circ$, a dip of $62^\circ \pm 4^\circ$, and rake of $92^\circ \pm 5^\circ$, within 68% of confidence (Table S3, Figure S3). All fault plane angles are very well resolved with uncertainties not exceeding 10° . We also determined a shallow centroid depth of 6 ± 2 km and a moment magnitude of M_w 5.9. The obtained focal mechanisms for the mainshock are in good agreement with the Global Centroid Moment Tensor (GCMT) and other available solutions (Table S3). For the smaller magnitude aftershocks, no solution is available to compare. All obtained source parameters for the studied events, together with their uncertainties (68% confidence intervals) are listed in Table S4. We observe almost the same types of focal mechanisms for the aftershocks; the reverse/thrust mechanisms which are located on both sides of the Gulkhari anticline (Figure 3). A combination of seismic section and focal mechanism solutions manifests the faulting and folding at the sedimentary cover (Figure 3).

Figure 4 shows the full moment tensor inversion result of the M_w 5.9 Genaveh earthquake and its decomposition into ISOtropic (ISO), Compensated Linear Vector Dipole (CLVD), and Double Couple (DC) parts. A relatively large CLVD component, similar to that resolved independently by GCMT is observed for the mainshock. Resolving non-DC components in MT inversion is challenging (e.g., Zahradnik et al., 2008; Wang et al., 2018; Jamalreyhani et al., 2021b). To exclude that the non-DC is not a result of mismodeling, we evaluate the influence of frequency bands, input data types, and Green functions on non-DC components, and we find the stable non-DC components of the mainshock. However, the accurate resolving of non-DC requires a more detailed 3D-velocity model (Donner et al., 2018; Jamalreyhani et al., 2021b), which is not available for the region. For aftershocks, that are smaller, the double-couple approach is used.

2.3 Slip distribution of the 18 April 2021 M_w 5.9 Genaveh earthquake by InSAR modeling

To estimate the slip distribution and fault geometry of the Genaveh earthquake, we rely on near-field geodetic data. The coseismic surface displacement field of the Genaveh mainshock was recorded by the Sentinel-1 from European Space Agency (ESA) in both descending and ascending orbits. We calculated two twelve-day interferograms capturing the mainshock and a few days of post-seismic (8 days on the ascending track A101 and 4 days on the descending track D35, see detail in Table 1). Both interferograms recorded 8 events of $4 < M_n < 4.6$ after the mainshock. We applied the same methodology as described in Pousse-Beltran et al. (2020) and Jamalreyhani et al. (2021a) for interferograms. The wrapped interferograms were processed with GDM-SAR online service and then were unwrapped using the branch

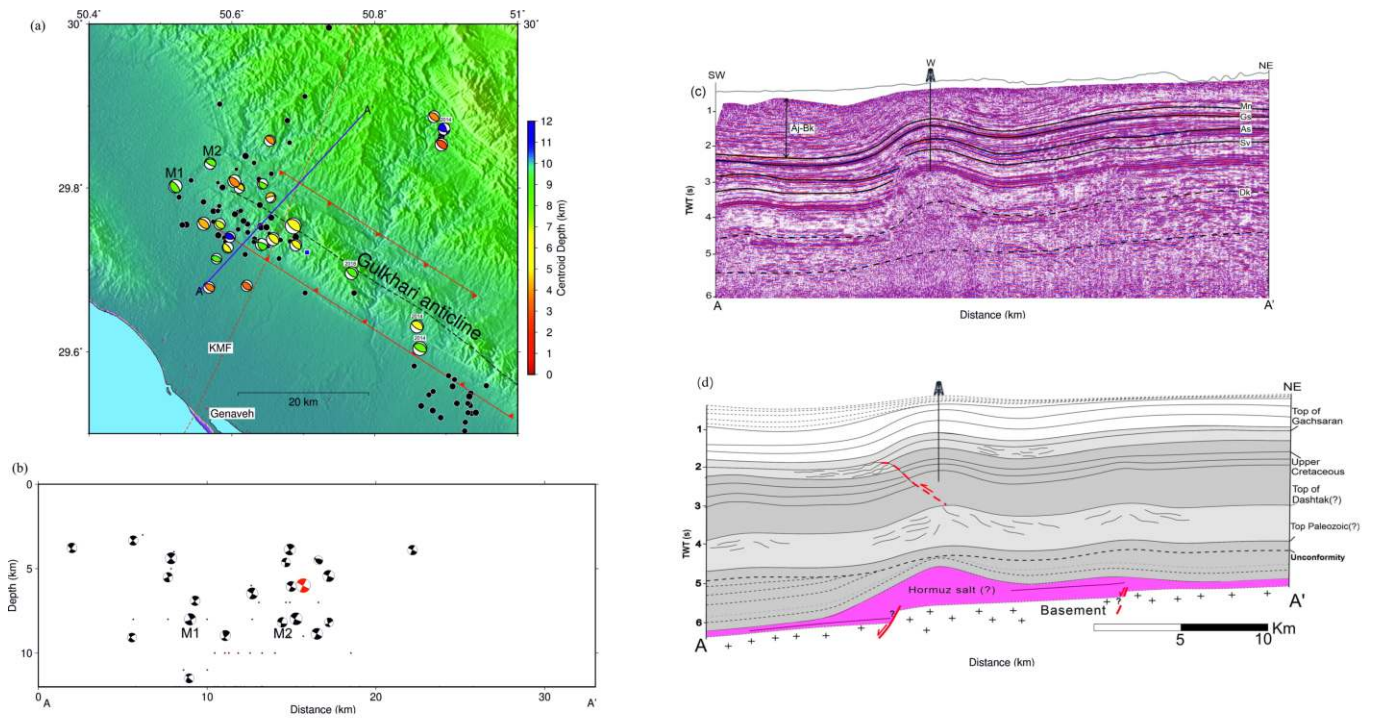


Figure 3 a) Relocated epicenters (Black circles) of $M_w \geq 3.0$ events and focal mechanisms of $M_n \geq 4.0$ events colored by centroid depth. Four earthquake mechanisms labelled with years (2014, 2018) are background events and every other mechanism is an aftershock of the April 18, M_w 5.9 Genaveh earthquake. The blue square shows the closest oil well to the seismic cluster. The Kharg-Mish Fault (KMF) and NW-SE trending blind thrust faults dipping NE and SW are shown by red lines. b) Cross section across the Gulkhari anticlines (A–A’ profile) with our calculated focal mechanisms at their centroid depths. The red mechanism presents the Genaveh mainshock. c) Interpreted seismic reflection profile (AA’ in panel a) across the Gulkhari anticline (Shamszadeh et al., 2022a). The y-axis is two-way travel time (TWT). Aj-Bk: Aghajari-Bakhtiyari formations, Mn: Mishan Formation, Gs: Gachsaran Formation, As: Asmari Formation, Sv: Sarvak Formation, and Dk: Dashtak Formation (for more information see figure S1). d) The interpreted 2D seismic profile of the Gulkhari anticline (after Shamszadeh et al., 2022a). The interpreted approximately NE-dipping reverse fault has an associated fold. The A–A’ seismic sections is presented in panel a. Panels (b),(c) and (d) are designed such that they have roughly equivalent vertical scales.

cut algorithm, unwrapping errors were then manually fixed. The fringes patterns obtained from InSAR consist of 4-5 fringes (Figure 5) that could be produced with a single fault plane either by a gently NE-dipping thrust fault or by a steeper SW-dipping one. To invert the ground displacements observed we followed routine elastic dislocation modeling procedures (Okada, 1985; Funning et al., 2005; Pousse-Beltran et al., 2020) in a half-space with elastic Lamé parameters $\lambda = \mu = 2.5 \times 10^{10}$ Pa, to represent the sedimentary cover in which the fault is embedded (e.g. Nissen et al., 2010; Elliott et al., 2015; Jamalreyhani et al., 2021a). We derive the coseismic slip model in two steps: first, a uniform slip inversion with multiple Monte Carlo restarts (Wright et al., 1999), to search for the best fault geometry (position, strike, rake, dip, see Text S1, Figures S4, and S5), and secondly, we use this geometry to perform a slip distribution inversion. For the slip distribution inversion, we extended the model fault planes along the strike and up- and down-dip obtained in the first step, and we subdivided the extended fault plane into 1 km square patches (Figure 5). We also applied a Laplacian smoothing operator and assessed misfits using the L-curve criterion in order to determine the appropriate degree of smoothing (Funning et al., 2005; Wright et al., 2003). Ascending and descending data were weighted equally in the

inversion. We observe more residuals in the descending track, those positive residuals reaching 9.4 mm can be due to post-seismic displacements inverted as being recorded in the ascending track. Indeed the ascending interferogram spans 4 days more of the post-seismic period than the descending track.

The dip direction of the causative fault is ambiguous from the interferograms and both NE-dipping and SW-dipping model faults could reproduce the overall InSAR deformation pattern. But based on the mainshock and aftershock hypocentral locations, as well as the wide aftershock cloud (Figure 3), our preferred dip is the lower angle NE-dipping plane. This model also fits the InSAR data better than the other (RMS of 5.8×10^{-3} m here vs 6.3×10^{-3} m). The alternative SW-dipping model and a side-by-side comparison of the two models are shown in figures S6 and S7. Furthermore, the possible trade-off between parameters during the uniform inversion in both models is presented in figures S8 and S9. To consider the usual trade-off between slip and width, we repeat the inversion with slip fixed to an appropriate value for the M_w 5.9 earthquake (e.g. 0.5 meters). We observed the high value of RMS and M_w for the SW-dipping model (Table S5 and Figure S10). In addition, when the slip is fixed, for the SW-dipping model, the dip is 7° higher (66°) and the fault plane is wider (Figure S10). Meanwhile, for

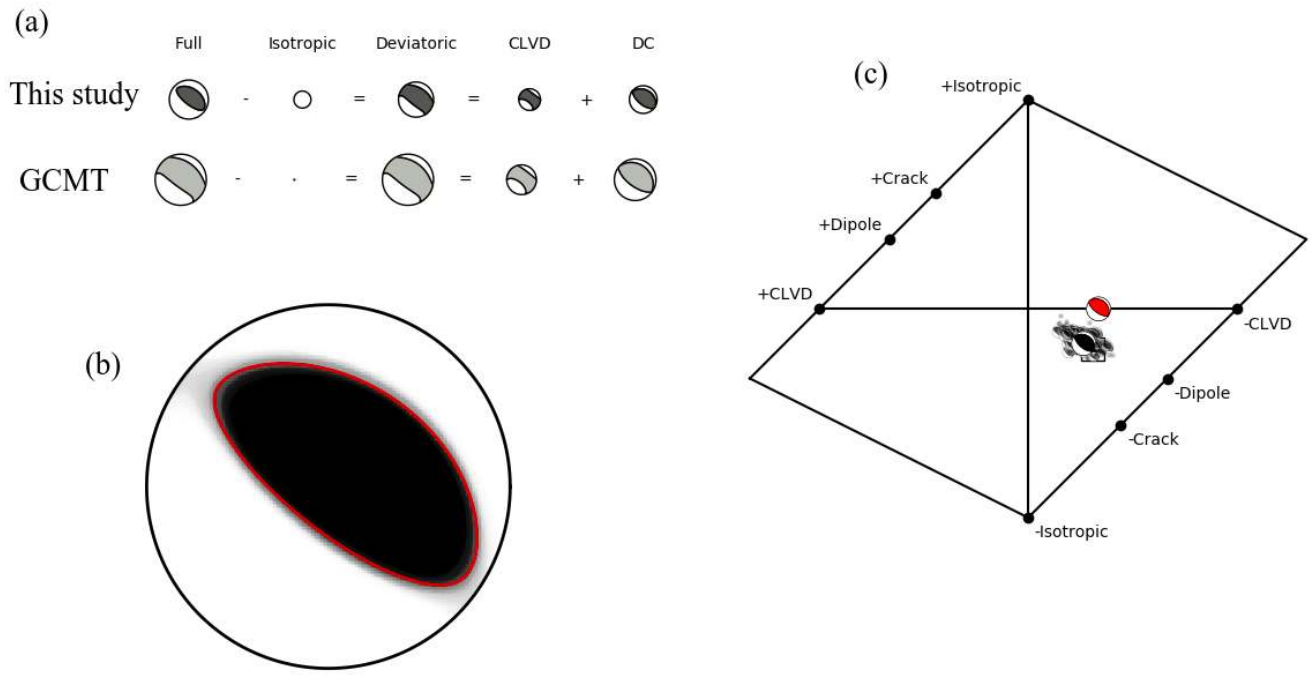


Figure 4 a) Solution of full moment tensor inversion for the M_w 5.9 Genaveh earthquake and decomposition of it in ISO, CLVD, and DC parts. The symbol size indicates the relative strength of the components. The Global Centroid Moment Tensor (GCMT) solution is shown for comparison. (b) The fuzzy full MT solution illustrates the uncertainty of the solution. (c) Hudson's source type plot with the ensemble of bootstrap solutions. The red mechanism shows the GCMT solution in the Hudson plot.

the NW-dipping fault model, solutions are similar.

The slip distribution model of the NE-dipping plane shows a slip mainly concentrated at depths of 5-6 km reaching 1m of slip. This distribution and amplitude depend on the degree of smoothing chosen according to the [Funning et al. \(2005\)](#) methodology. The InSAR model moment reaches 1.104×10^{18} Nm (M_w 6.0) and yields an RMS of 0.00316 m. The hypocenter is located at the eastward limit and closer to the bottom of the slipping areas, likely indicating up-dip lateral rupture propagation toward NW.

3 Discussion

The M_w 5.9 Genaveh earthquake occurred on 2021 April 18 in the SDE of ZFFB. The coseismic slip distribution of the Genaveh earthquake has been investigated by [Golshadi et al. \(2022\)](#) and [Jafari et al. \(2023\)](#) based on satellite data (see Table 2). [Golshadi et al. \(2022\)](#) suggested $5.0 \times 9.5 \text{ km}^2$ for the fault plane and the fault top-edge depth at 4 km. Our obtained source geometry based on InSAR data conforms to their finding although we use a different downsampling methodology. There are differences between the results of [Golshadi et al. \(2022\)](#) and our study concerning slip depth, and the amount of maximum slip. [Golshadi et al. \(2022\)](#) obtained a maximum slip around 4.5 km depth, whereas we obtained a maximum slip at depths of 5-6 km. The localization of the [Golshadi et al. \(2022\)](#) fault is not clearly specified enough to compare. In addition, they obtained higher residuals above 10 mm. Furthermore, [Golshadi et al. 2020](#) and [Jafari et al., 2023](#) suggest the NE-dipping Zagros foredeep fault ([Berberian, 1995](#)) as a causative fault

for the Genaveh earthquake, however, our results show the shallow, N^{W} -trending, NE and SW dipping faults, located at both crest of the Gulkhari anticline and parallel to the trend of it, control the growth of this particular fold (Figure 3, e.g. M1, M2). Thus, we suggest the causative fault for the Genaveh earthquake mainshock is the gently NE-dipping Gulkhari fault, modeled through the InSAR technique and seismological observations. Our NE-dipping model fault has a strike of 311° , dips of 20° , and rake of 96° , conforming to the focal mechanism solution from waveform modeling (306° , 28° , and 86° for the strike, dip, and rake, respectively). The InSAR model moment is higher than the seismic moment (M_w 5.9), though it is possible that our InSAR models also include a small amount of postseismic afterslip. This solution is also coherent with other published source models (see Table 2). Our results show minimum RMS with a top depth around 4-5 km and a bottom depth around 5.5-6.5 km (Figure S8). This supports the slip localization around 5-6 km depth in our slip distributed inversion and at the same depth range determined by moment tensor inversion (Figure S3).

We additionally assess the aftershock sequence and calculate their focal mechanisms by waveform modeling. Locations and mechanisms of the aftershock sequence are very useful to understand the on/off fault seismicity, the process of mainshock rupture, and post-seismic deformation ([Das and Henry, 2003](#)). The relocation of the Genaveh earthquake sequence, which was recorded by newly installed stations by the IRSC network, helped to partly complement the existing data gap in the South Dezful Embayment in [Karasözen et al. \(2019\)](#) study which was due to poor station coverage.

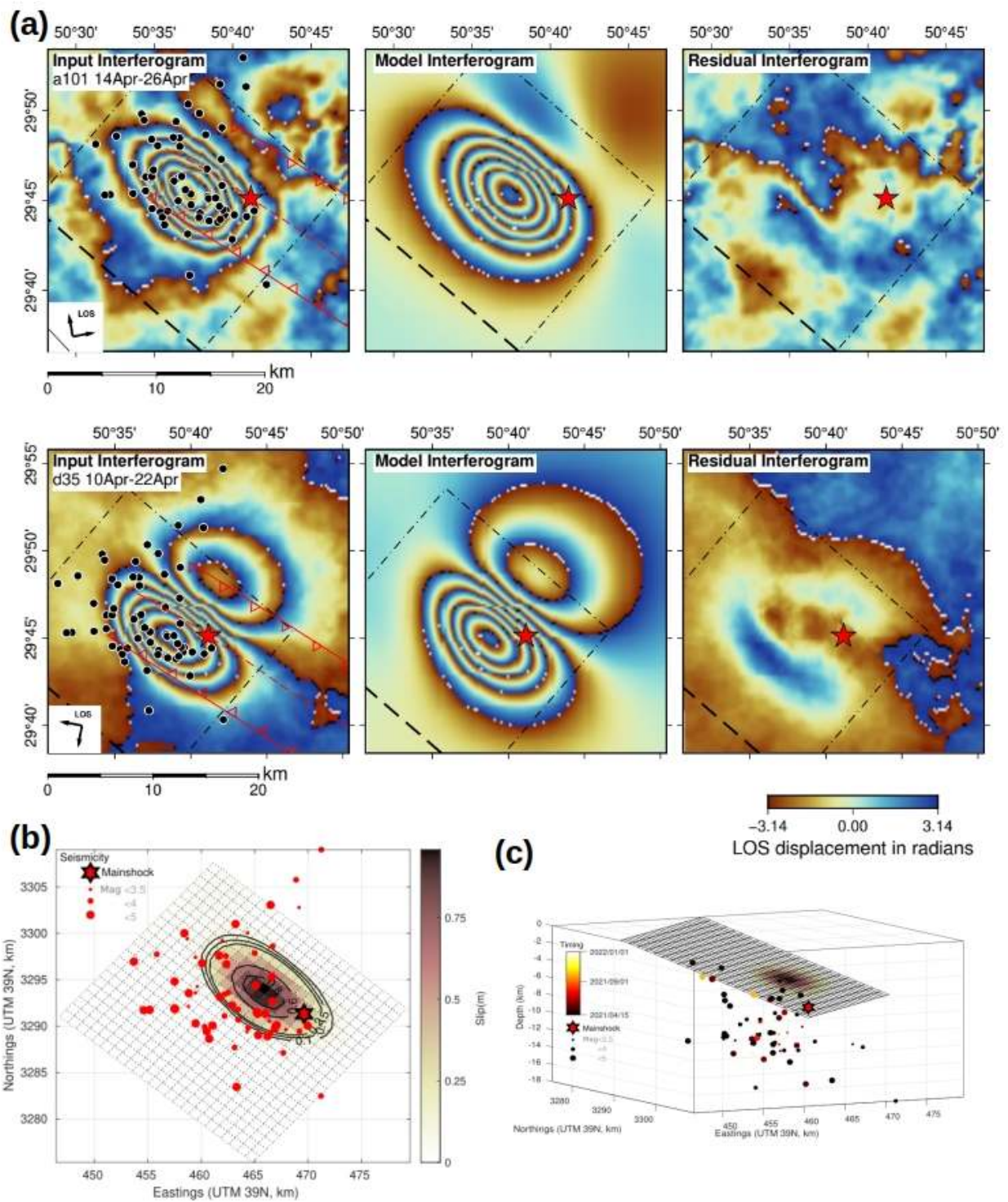


Figure 5 Coseismic slip distribution inversion results. (a) The first and second rows correspond, respectively, to the ascending track A101 and the descending track D35. From left to right columns: observed, model, and residual interferograms. Results are shown re-wrapped. The red star is the relocated epicenter of the mainshock. Black dots are the relocated aftershocks. The bold black dashed line corresponds to the surface projection of the modeled faults. The black dashed dotted rectangle corresponds to the projection of the modeled fault plane. The Kharg-Mish Fault (KMF) and NW-SE trending blind thrust faults dipping NE and SW are shown by red lines. (b) Coseismic slip distribution in map view, the model fault is divided by a 1 km^2 patch. The red star is the relocated epicenter, dots show the relocated aftershocks. (c) Coseismic slip distribution in 3D, dots shows the relocated aftershocks colored according to time.

The aftershock focal mechanisms and their distribution suggest that some of the aftershocks take place on the same fault plane as the Genaveh mainshock, but some are also distributed along the ~NW-trending, SW dip-

ping fault, located at the northern crest of the Gulkhari anticline (Figure 3), likely the consequence of mainshock and bending stresses within the layers of the fold, which highlights the role of fault structure and rheology

Track	Date 1	Date 2	LOS incidence (°)	LOS azimuth (°)
A101	14 Apr. 2021	26 Apr. 2021	42	77
D035	10 Apr. 2021	22 Apr. 2021	35	-77

Table 1 InSAR interferogram characteristic used in this study (A: Ascending, D: Descending, LOS: Line of Sight). Incidence and azimuth angles are measured at the epicenter.

Method	Source	Magnitude (M_w)	Strike (°)	Dip (°)	Rake (°)	Depth (km)	Max Slip (m)
InSAR	Golshadi et al., (2022)	5.9	313	20	100	4	1
InSAR	Jafari et al., (2023)	5.8	306	23	89	6	0.95
InSAR	This study	6	311	20	96	4-7	1
Waveform modeling	This study	5.9	306 ± 5	28 ± 9	86 ± 10	6.0 ± 2.0	-

Table 2 Source parameters of the 2021 Genaveh earthquake obtained in this study, Golshadi et al. (2022) and Jafari et al. (2023) based on InSAR and seismological models.

in controlling the distribution of seismicity (e.g. Colletini et al., 2022). Furthermore, this displays the correlation between the Gulkhari anticline and the seismogenic thrust and reverse faults beneath it.

The focal solution and location of the background seismicity which are spatially away from the mainshock and localized in the southern part of the Gulkhari anticline (Figures 2 and 3), demonstrate that the southern part of the NE dipping Gulkhari fault was seismically active (Two events occurred on 21 April 2014 within the magnitude of M_w 5.3 and 5.1, and an event in March 2018, M_w 5.0). The Genaveh earthquake is spatially localized in the northern part of the Gulkhari anticline.

The MT inversion of the mainshock shows a centroid depth of 6 ± 2 km. Focal mechanisms represent a regional transpressional tectonic regime (maximum horizontal stress, σ_1) oriented axis at $\sim N45E$ (Heidbach et al., 2018), and are compatible with the principal stress axis of the region. From InSAR modeling, we obtained the depth of a large slip area of about 5 km. Considering the low dip angle of the modeled fault (from both focal mechanism and finite fault modeling), the rupture occurred in the competent group (Sherkati et al., 2005; Nissen et al., 2011) of sedimentary cover. It is probable that the incompetent layers limit the rupture to propagate and generate large magnitudes (M_w 6+) of shock. Likely, the rupture deepest part is affected by the Paleozoic Shale layer, which makes the rupture fail to propagate and highlights the influence of lithology in the rupture propagation. Furthermore, the top depth of the ruptured area confines at the depth of $\sim 3-4$ km, corresponding to the depth of the upper mobile group. Moreover, the presence of an NE dipping fault is clear in the seismic section and it has grown in between Gachsaran and Dashtak layers (Figure 3). This explains top and bottom depths corresponding to detachments in weak evaporitic layers that act to limit up- and down-dip rupture propagation and thus, restrict the magnitude. Also, none of the aftershock centroid depths are less than ~ 3 km. There are no large instrumental earthquakes exceeding M_w 6 in the Dezful Embayment, showing that the seismogenic layer is segmented by weak evaporitic within the sedimentary cover, and controls the propagation of earthquake rupture, similar to the Fars arc (Nissen et al., 2010; Jamalreyhani et al., 2021a).

There are very few thrust-faulting earthquakes in the Fars arc of ZFFB with significantly large magnitudes (Nissen et al., 2011). Clearly, at the base of the cover, the Hormuz salt plays a role and barriers the rupture propagation in the Fars arc. The most moderate-sized event ($5 < M_w < 6$) in the ZFFB occurs within the mid-lower sedimentary cover (Nissen et al., 2007, 2010; Roustaei et al., 2010; Copley et al., 2015; Motagh et al., 2015). In the Dezful Embayment, the presence of the Hormuz salt layer is debated. Nonetheless, in the Gulkhari anticline, the seismic profile displays a salt-cored structure within slight vergence to the SW, which is detached from the Hormuz salt layers (Shamszadeh et al., 2022a). Therefore, this may be controlled by other weak evaporitic or shale horizons within the cover and also reflect the narrow (small width-to-length ratio) dimensions, as observed in the Genaveh coseismic slip. In the middle and upper parts of the cover, there are for example Gurpi marls and Gachsaran evaporites to play a barrier role. Aftershocks of the Genaveh earthquake lie within the sedimentary cover too, there is no observation of vertical separation for this cluster. Meanwhile, a detailed micro-aftershocks study would be required to discuss this, which is beyond the data resolution of this study.

The Genaveh earthquake is co-located with the major Gulkhari oil reservoir at the Asmari-Jahrum formation and raised the question about the possible involvement of the oil extraction in the field and this earthquake. However, human actions only affect the uppermost several kilometers of the crust, and the induced earthquakes are expected to occur at shallow depths (Dahm et al., 2015; Cesca et al., 2021). Hence, depth is a particularly important discriminator between anthropogenic and natural seismicity in the Zagros (Jamalreyhani et al., 2021a). The depth of the Genaveh seismic sequence is in the typical earthquake depth range in the Zagros and does not support an induced earthquake related to the oil field (oil extraction starting in 1987 with 15,000 barrels per day), which is deeper than the oil reservoir's depth (~ 4 km). Although, the full moment tensor of the mainshock, suggests a notable non-DC component (Figure 4) and may reflect the source complexity (Dahm et al., 2015; Wang et al., 2018). The sequence also depicts typical mainshock-aftershock patterns and focal mechanisms represent-

ing reverse/thrust faulting, compatible with regional tectonic stresses and corresponding to the previously known fault(s). Furthermore, the Genaveh earthquake is spatially localized in the northern part of the Gulkhari anticline, which is outward of the location of extraction/injection wells (Figure 3). Therefore, detailed sophisticated production data in the Gulkhari oil field is required to track the relationship between oil extraction and seismic activity in the past and future.

4 Conclusion

We present a detailed analysis of the M_w 5.9 Genaveh earthquake on 2021 April 18 as a well-recorded example of seismic activity in the South Dezful Embayment of Zagros foreland folded belt. We analyzed the Genaveh earthquake sequence using local and regional seismic data and constrained the co-seismic slip of the mainshock with InSAR modeling. Coseismic uplift in the Gulkhari anticline shows the surface configuration of this fold, reflecting subsurface structural conditions. This earthquake involved a gently ($\sim 20^\circ$) NE-dipping fault plane (named Gulkhari fault). The main slip of the mainshock was restricted to depths of between 4–7 with a maximum slip of 1 m within the sedimentary cover which highlights the influence of lithology in the rupture propagation. Aftershocks of the Genaveh earthquake are widely distributed and dominated by reverse faulting at centroid depths of 4–10 km.

Although the Genaveh earthquake is co-located with the major Gulkhari oil reservoir, the detailed relationship between the oil extraction in the field and this earthquake needs sophisticated data to investigate, though, our results support the essence of a tectonic earthquake.

Acknowledgements

We thank all data research centers for providing the data used in this study. We thank Isapron Sethanant for sharing the plotting codes. We appreciate the Seismica community that supports open-access publishing in seismology and earthquake science. We would like to thank E. Nissen and an anonymous reviewer for their careful reviews, the associate editor G. Funning, and editor Y.J. Tan for their comments and for handling the manuscript.

Data and code availability

All data used in this study is freely available. The seismic catalog and waveforms of the Iran network were downloaded from the Iranian Seismological Center (IRSC) available at <http://irsc.ut.ac.ir/>. InSAR interferograms were made using Copernicus Sentinel data (<https://scihub.copernicus.eu/>).

The nonlinear inversion code of moment tensors is all provided by the Pyrocko (Heimann et al., 2017) seismology toolbox and library (<https://pyrocko.org>). The relocation software (The MLOC program Bergman

et al., 2022) is available at <https://seismo.com/mloc/>. InSAR data were processed using the online service GDM-SAR (<https://www.poleterresolide.>) supported by Formater (<https://www.poleterresolide.>), CNES (<https://cnes.fr/fr>) and the European Union's Copernicus User Framework Partnership Agreement on Copernicus User Uptake under grant agreement No FPA 275/G/GRO-COPE/17/10042, project FPCUP (Framework Partnership Agreement on Copernicus User Uptake), Action 2019-1-39 "Promote the use of COPERNICUS Sentinel-1 data and valorize a prototype of an on-demand service for radar interferometry processing". For the InSAR inversion, we used the codes developed by the Centre for the Observation and Modelling of Earthquakes, Volcanoes, and Tectonics (COMET) group (<https://comet.nerc.ac.uk/>) (Wright et al., 1999; Funning et al., 2005) available from request.

The InSAR unwrapped data, the result of the quadtree sampling, and the two slip distribution models are stored in this link: <https://zenodo.org/record/7148513> and can be downloaded anonymously.

Competing interests

The authors declare that they have no known competing financial interests or personal relationships that could have appeared to influence the work reported in this paper.

References

- Abdollahie Fard, I., Sepehr, M., and Sherkati, S. Neogene salt in SW Iran and its interaction with Zagros folding. *Geological Magazine*, 148(5-6):854–867,, 2011. doi: 10.1017/S0016756811000343.
- Alavi, M. Structures of the Zagros Fold-Thrust Belt in Iran. *American Journal of Science*, 308(1):104–104, 2008. doi: 10.2475/01.2008.05.
- Allen, M. and Talebian, M. Structural variation along the Zagros and the nature of the Dezful Embayment. *Geological Magazine*, 148:911–924,, 2011. doi: 10.1017/S0016756811000318.
- Ambraseys, N. and Melville, C. *A history of Persian earthquakes*. Cambridge University Press, 1982.
- Berberian, M. Master "blind" thrust faults hidden under the Zagros folds: Active basement tectonics and surface morphotectonics. *Tectonophysics*, 241(3):193–224,, 1995. doi: 10.1016/0040-1951(94)00185-C.
- Bergman, E., Benz, H., Yeck, W., Karasözen, E., Engdahl, E., Ghods, A., Hayes, G., and Earle, P. A Global Catalog of Calibrated Earthquake Locations. *Seismological Research Letters*, 2022. doi: 10.1785/0220220217.
- Büyükkapınar, P., Cesca, S., Hainzl, S., Jamalreyhani, M., Heimann, S., and Dahm, T. Reservoir-Triggered Earthquakes Around the Atatürk Dam (Southeastern Turkey). *Frontiers in Earth Sciences*, 9, 2021. doi: 10.3389/feart.2021.663385.
- Carruba, S., Perotti, C., Buonaguro, R., Calabrò, R., Carpi, R., and Naini, M. Structural pattern of the Zagros fold-and-thrust belt in the Dezful Embayment (SW Iran). In Mazzoli, S. and Butler, R., editors, *Styles of Continental Contraction: Geological Society of America Special Paper 414*, pages 11–32,, 2006. doi: 10.1130/2006.2414(02).

- Cesca, S., Stich, D., Grigoli, F., Vuan, A., López-Comino, J., Niemi, P., Blanch, E., Dahm, T., and Ellsworth, W. Seismicity at the Castor gas reservoir driven by pore pressure diffusion and asperities loading. *Nature communications*, 12:4783, 2021. doi: 10.1038/s41467-021-24949-1.
- Collettini, C., Barchi, M., Paola, N., Trippetta, F., and Tinti, E. Rock and fault rheology explain differences between on fault and distributed seismicity. *Nature communications*, 13:5627, 2022. doi: 10.1038/s41467-022-33373-y.
- Copley, A., Karasozen, E., Oveisi, B., Elliott, J., Samsonov, S., and Nissen, E. Seismogenic faulting of the sedimentary sequence and laterally variable material properties in the Zagros Mountains (Iran) revealed by the August 2014 Murmuri (E. Dehloran) earthquake sequence. *Dehloran earthquake sequence. Geophysical Journal International*, 203:1436–1459, 2015. doi: 10.1093/gji/ggv365.
- Dahm, T., Cesca, S., Hainzl, S., Braun, T., and Krüger, F. Discrimination between induced, triggered, and natural earthquakes close to hydrocarbon reservoirs: A probabilistic approach based on the modeling of depletion-induced stress changes and seismological source parameters. *Journal of Geophysical Research: Solid Earth*, 120:2491–2509, 2015. doi: 10.1002/2014JB011778.
- Das, S. and Henry, C. Spatial relation between main earthquake slip and its aftershock distribution. *Reviews of Geophysics*, 41, 2003. doi: 10.1029/2002RG000119.
- Donner, S., Igel, H., Hadziioannou, C., and the Romy group. Retrieval of the Seismic Moment Tensor from Joint Measurements of Translational and Rotational Ground Motions: Sparse Networks and Single Stations. In D'Amico, S., editor, *Moment Tensor Solutions: A Useful Tool for Seismotectonics*, pages 263–280, Springer Natural Hazards. Springer International Publishing, Cham, 2018. doi: https://doi.org/10.1007/978-3-319-77359-9_12.
- Elliott, J., Bergman, E., Copley, A., Ghods, A., Nissen, E., Oveisi, B., Tatar, M., Walters, R., and Yamini-Fard, F. The 2013 Mw 6.2 Khaki-Shonbe (Iran) Earthquake: Insights into seismic and aseismic shortening of the Zagros sedimentary cover. *Earth and Space Science*, 2:435–471, 2015. doi: 10.1002/2015EA000098.
- Farahzadi, E., Alavi, S., Sherkat, S., and Ghassemi, M. Variation of subsidence in the Dezful Embayment, SW Iran: influence of reactivated basement structures. *Arabian Journal of Geosciences*, 12:616, 2019. doi: 10.1007/s12517-019-4758-5.
- Funning, G., Parsons, B., Wright, T., Jackson, J., and Fielding, E. Surface displacements and source parameters of the 2003 Bam (Iran) earthquake from Envisat advanced synthetic aperture radar imagery. *Journal of Geophysical Research: Solid Earth*, 110(B9), 2005. doi: 10.1029/2004JB003338.
- Golshadi, Z., Famiglietti, N., Atzori, S., and Vicari, A. Surface Displacement and Source Parameters of the 2021 Bandar-e Genaveh, Iran, Earthquake Determined from InSAR Observations. *Applied Sciences*, 12:4223, 2022. doi: 10.3390/app12094223.
- Heidbach, O., Rajabi, M., Cui, X., Fuchs, K., Müller, B., Reinecker, J., Reiter, K., Tingay, M., Wenzel, F., Xie, F., Ziegler, M., Zoback, M.-L., and Zoback, M. The World Stress Map database release 2016: Crustal stress pattern across scales. *Tectonophysics*, 744: 484–498, 2018. doi: 10.1016/j.tecto.2018.07.007.
- Heimann, S., Kriegerowski, M., Isken, M., Cesca, S., Daout, S., Grigoli, F., Juretzek, C., Megies, T., Nooshiri, N., Steinberg, A., Sudhaus, H., Vasyura-Bathke, H., Willey, T., and Dahm, T. Pyrocko - An open-source seismology toolbox and library, 2017. doi: 10.5880/GFZ.2.1.2017.001, GFZ Data Services.
- Heimann, S., Vasyura-Bathke, H., Sudhaus, H., Isken, M., Kriegerowski, M., Steinberg, A., and Dahm, T. A Python framework for efficient use of pre-computed Green's functions in seismological and other physical forward and inverse source problems. *Solid Earth*, 10:1921–1935, 2019. doi: 10.5194/se-10-1921-2019.
- Irandoost, M., Priestley, K., and Sobouti, F. High-Resolution Lithospheric Structure of the Zagros Collision Zone and Iranian Plateau. *Journal of Geophysical Research: Solid Earth*, 127, 2022. doi: 10.1029/2022JB025009.
- Jafari, M., Aflaki, M., Mousavi, Z., Walpersdorf, A., and Motaghi, K. Coseismic and postseismic characteristics of the 2021 Ganaveh earthquake along the Zagros foredeep fault based on InSAR data. *Geophysical Journal International*, 2023. doi: 10.1093/gji/ggad127.
- Jahani, S., Callot, J., Letouzey, J., and Lamotte, D. The eastern termination of the Zagros Fold-and-Thrust Belt, Iran: Structures, evolution, and relationships between salt plugs, folding, and faulting. *Tectonics*, 28(6), 2009. doi: 10.1029/2008TC002418.
- Jahani, S., Hassanpour, J., Mohammadi-Firouz, S., Letouzey, J., Lamotte, D., Alavi, S., and Soleimany, B. Salt tectonics and tear faulting in the central part of the Zagros Fold-Thrust Belt, Iran. *Marine and Petroleum Geology*, 86:426–446, 2017. doi: 10.1016/j.marpetgeo.2017.06.003.
- Jamalreyhani, M., Rezapour, M., Cesca, S., Heimann, S., Vasyura-Bathke, H., Sudhaus, H., Isken, M., and Dahm, T. The 2017 November 12 Mw 7.3 Sarpol-Zahab (Iran-Iraq border region) earthquake: source model, aftershock sequence and earthquakes triggering. EGU2020 Copernicus Meetings, EGU2020-759, 2019. doi: 10.5194/egusphere-egu2020-759.
- Jamalreyhani, M., Büyükkakpınar, P., Cesca, S., Dahm, T., Sudhaus, H., Rezapour, M., Isken, M. P., Maleki Asayesh, B., and Heimann, S. Seismicity related to the eastern sector of Anatolian escape tectonic: the example of the 24 January 2020 Mw 6.77 Elazığ-Sivrice earthquake. *Solid Earth Discussions*, 2020:1–22, 2020. doi: 10.5194/se-2020-55.
- Jamalreyhani, M., Pousse-Beltran, L., Büyükkakpınar, P., Cesca, S., Nissen, E., Ghods, A., López-Comino, J., Rezapour, M., and Najafi, M. The 2019–2020 Khalili (Iran) Earthquake Sequence—Anthropogenic Seismicity in the Zagros Simply Folded Belt? *Journal of Geophysical Research: Solid Earth*, 126, 2021a. doi: 10.1029/2021JB022797.
- Jamalreyhani, M., Rezapour, M., and Büyükkakpınar, P. Evaluation of seismic sensor orientations in the full moment tensor inversion results, 2021b. doi: 10.5194/egusphere-egu21-459, EGU21 Copernicus Meetings, EGU21-459.
- Jamalreyhani, M., Rezapour, M., Cesca, S., Dahm, T., Heimann, S., Sudhaus, H., and Isken, M. Insight into the 2017–2019 Lurestan arc seismic sequence (Zagros, Iran); complex earthquake interaction in the basement and sediments. *Geophysical Journal International*, 2022. doi: 10.1093/gji/ggac057.
- Karasözen, E., Nissen, E., Bergman, E., and Ghods, A. Seismotectonics of the Zagros (Iran) From Orogen-Wide, Calibrated Earthquake Relocations. *Journal of Geophysical Research: Solid Earth*, 124:9109–9129, 2019. doi: 10.1029/2019JB017336.
- McQuarrie, N. Crustal scale geometry of the Zagros fold-thrust belt. *Iran, Journal of Structural Geology*, 26:519–535, 2004. doi: 10.1016/j.jsg.2003.08.009.
- Motagh, M., Bahroudi, A., Haghghi, M. H., Samsonov, S., Fielding, E., and Wetzel, H. The 18 August 2014 Mw 6.2 Mormori, Iran, Earthquake: A Thin-Skinned Faulting in the Zagros Mountain Inferred from InSAR Measurements. *Seismological Research Letters*, 86(3):775–782, 04 2015. doi: 10.1785/0220140222.
- Mouthereau, F., Tensi, J., Bellahsen, N., Lacombe, O., De Boissgrolier, T., and Kargar, S. Tertiary sequence of deformation in a thin-skinned/thick-skinned collision belt: The Zagros

- Folded Belt (Fars, Iran). *Tectonics*, 26(5), 2007. doi: <https://doi.org/10.1029/2007TC002098>.
- Mouthereau, F., Lacombe, O., and Vergés, J. Building the Zagros collisional orogen: Timing, strain distribution and the dynamics of Arabia/Eurasia plate convergence. *Tectonophysics*, 532–535: 27–60,, 2012. doi: [10.1016/j.tecto.2012.01.022](https://doi.org/10.1016/j.tecto.2012.01.022).
- Najafi, M. and Lajmorak, S. Contractional salt-tectonic system in the south Dezful embayment, Zagros. *Journal of Structural Geology*, 141:104204,, 2020. doi: [10.1016/j.jsg.2020.104204](https://doi.org/10.1016/j.jsg.2020.104204).
- Najafi, M., Yassaghi, A., Bahroudi, A., Vergés, J., and Sherkati, S. Impact of the Late Triassic Dashtak intermediate detachment horizon on anticline geometry in the Central Frontal Fars, SE Zagros fold belt, Iran. *Marine and Petroleum Geology*, 54:23–36,, 2014. doi: [10.1016/j.marpetgeo.2014.02.010](https://doi.org/10.1016/j.marpetgeo.2014.02.010).
- Nissen, E., Ghorashi, M., Jackson, J., Parsons, B., and Talebian, M. The 2005 Qeshm Island earthquake (Iran)—a link between buried reverse faulting and surface folding in the Zagros Simply Folded Belt? *Geophysical Journal International*, 171(1):326–338, 10 2007. doi: [10.1111/j.1365-246X.2007.03514.x](https://doi.org/10.1111/j.1365-246X.2007.03514.x).
- Nissen, E., Yamini-Fard, F., Tatar, M., Gholamzadeh, A., Bergman, E., Elliott, J., Jackson, J., and Parsons, B. The vertical separation of mainshock rupture and microseismicity at Qeshm island in the Zagros fold-and-thrust belt, Iran. *Earth and Planetary Science Letters*, 296(3):181–194, 2010. doi: <https://doi.org/10.1016/j.epsl.2010.04.049>.
- Nissen, E., Tatar, M., Jackson, J., and Allen, M. New views on earthquake faulting in the Zagros fold-and-thrust belt of Iran. *Geophysical Journal International*, 186(3):928–944,, 2011. doi: [10.1111/j.1365-246X.2011.05119.x](https://doi.org/10.1111/j.1365-246X.2011.05119.x).
- Nissen, E., Ghods, A., Karasözen, E., Elliott, J., Barnhart, W., Bergman, E., Hayes, G., Jamal-Reyhani, M., Nemati, M., Tan, F., Abdalnaby, W., Benz, H., Shahvar, M., Talebian, M., and Chen, L. The 12 November 2017 M_w 7.3 Ezgeleh-Sarpolzahab (Iran. *Earthquake and Active Tectonics of the Lurestan Arc. Journal of Geophysical Research: Solid Earth*, 124:2124–2152,, 2019. doi: [10.1029/2018JB016221](https://doi.org/10.1029/2018JB016221).
- Okada, Y. Surface deformation due to shear and tensile faults in a half-space. *Bulletin of the seismological society of America*, 75 (4):1135–1154,, 1985. doi: [10.1785/BSSA0750041135](https://doi.org/10.1785/BSSA0750041135).
- Pousse-Beltran, L., Nissen, E., Bergman, E., Cambaz, M., Gaudreau, E., Karasözen, E., and Tan, F. The 2020 M_w 6.8 Elazığ (Turkey) earthquake reveals rupture behavior of the East Anatolian Fault. *Geophysical Research Letters*, 47(13), 2020. doi: [10.1029/2020GL088136](https://doi.org/10.1029/2020GL088136).
- Roustaei, M., Nissen, E., Abbassi, M., Gholamzadeh, A., Ghorashi, M., Tatar, M., Yamini-Fard, F., Bergman, E., Jackson, J., and Parsons, B. The 2006 March 25 Fin earthquakes (Iran)—insights into the vertical extents of faulting in the Zagros Simply Folded Belt. *Geophysical Journal International*, 181:1275–1291,, 2010. doi: [10.1111/j.1365-246X.2010.04601.x](https://doi.org/10.1111/j.1365-246X.2010.04601.x).
- Sepehr, M. and Cosgrove, J. Structural framework of the Zagros Fold–Thrust Belt, Iran. *Marine and Petroleum Geology*, 21(7):829–843, 2004. doi: <https://doi.org/10.1016/j.marpetgeo.2003.07.006>.
- Seraj, M., Faghih, A., Motamedi, H., and Soleimany, B. Major Tectonic Lineaments Influencing the Oilfields of the Zagros Fold-Thrust Belt, SW Iran: Insights from Integration of Surface and Subsurface Data. *Journal of Earth Science*, 31:596–610,, 2020. doi: [10.1007/s12583-020-1303-0](https://doi.org/10.1007/s12583-020-1303-0).
- Shamszadeh, A., Sarkarinejad, K., Ferrer, O., Mukherjee, S., and Seraj, M. Effect of inherited structural highs on the structure and kinematics of the South Dezful Embayment, SW Iran. *Geological Magazine*, pages 1–23,, 2022a. doi: [10.1017/S0016756822000541](https://doi.org/10.1017/S0016756822000541).
- Shamszadeh, A., Sarkarinejad, K., Ferrer, O., Mukherjee, S., and Seraj, M. Interaction of inherited structures and contractional deformation in the South Dezful Embayment: Insights from the Gachsaran oilfield, SW Iran. *Marine and Petroleum Geology*, 145: 105871,, 2022b. doi: [10.1016/j.marpetgeo.2022.105871](https://doi.org/10.1016/j.marpetgeo.2022.105871).
- Sherkati, S. and Letouzey, J. Variation of structural style and basin evolution in the central Zagros (Izeh zone and Dezful Embayment. *Iran. Marine and Petroleum Geology*, 21:535–554,, 2004. doi: [10.1016/j.marpetgeo.2004.01.007](https://doi.org/10.1016/j.marpetgeo.2004.01.007).
- Sherkati, S., Molinaro, M., Lamotte, D., and Letouzey, J. Detachment folding in the Central and Eastern Zagros fold-belt (Iran): salt mobility, multiple detachments and late basement control. *Journal of Structural Geology*, 27:1680–1696,, 2005. doi: [10.1016/j.jsg.2005.05.010](https://doi.org/10.1016/j.jsg.2005.05.010).
- Sherkati, S., Letouzey, J., and Frizon de Lamotte, D. Central Zagros fold-thrust belt (Iran): New insights from seismic data, field observation, and sandbox modeling. *Tectonics*, 25(4), 2006. doi: <https://doi.org/10.1029/2004TC001766>.
- Stöcklin, J. Structural History and Tectonics of Iran1: A Review. *AAPG Bulletin*, 52:1229–1258,, 1968. doi: [10.1306/5D25C4A5-16C1-11D7-8645000102C1865D](https://doi.org/10.1306/5D25C4A5-16C1-11D7-8645000102C1865D).
- Talebian, M. and Jackson, J. A reappraisal of earthquake focal mechanisms and active shortening in the Zagros mountains of Iran. *Geophysical Journal International*, 156(3):506–526,, 2004. doi: [10.1111/j.1365-246X.2004.02092.x](https://doi.org/10.1111/j.1365-246X.2004.02092.x).
- Tourani, M., Isik, V., Saber, R., and Caglayan, A. Radar Interferometric Assessment of April 18, 2021 Bandar Ganaveh Earthquake (m_w : 5.8. In *Southern Iran. Presented at the 11th Congress of the Balkan Geophysical Society, European Association of Geoscientists and Engineers*, pages 1–5,, 2021. doi: [10.3997/2214-4609.202149BGS89](https://doi.org/10.3997/2214-4609.202149BGS89).
- Vergés, J., Saura, E., Casciello, E., Fernández, M., Villaseñor, A., Jiménez-Munt, I., and García-Castellanos, D. Crustal-scale cross-sections across the NW Zagros belt: implications for the Arabian margin reconstruction. *Geological Magazine*, 148: 739–761,, 2011. doi: [10.1017/S0016756811000331](https://doi.org/10.1017/S0016756811000331).
- Walker, R., Bergman, E., Szeliga, W., and Fielding, E. Insights into the 1968–1997 Dasht-e-Bayaz and Zirkuh earthquake sequences, eastern Iran, from calibrated relocations, InSAR and high-resolution satellite imagery. *Geophysical Journal International*, 187:1577–1603,, 2011. doi: [10.1111/j.1365-246X.2011.05213.x](https://doi.org/10.1111/j.1365-246X.2011.05213.x).
- Wang, R., Gu, Y., Schultz, R., and Chen, Y. Faults and Non-Double-Couple Components for Induced Earthquakes. *Geophysical Research Letters*, 45:8966–8975,, 2018. doi: [10.1029/2018GL079027](https://doi.org/10.1029/2018GL079027).
- Wang, S., Nissen, E., Pousse-Beltran, L., Craig, T., Jiao, R., and Bergman, E. Structural controls on coseismic rupture revealed by the 2020 M_w 6.0 Jiashi earthquake (Kepingtag belt, SW Tian Shan, China. *Geophysical Journal International*, 2022. doi: [10.1093/gji/ggac159](https://doi.org/10.1093/gji/ggac159).
- Wright, T., Parsons, B., Jackson, J., Haynes, M., Fielding, E., England, P., and Clarke, P. Source parameters of the 1 October 1995 Dinar (Turkey) earthquake from SAR interferometry and seismic bodywave modelling. *Earth and Planetary Science Letters*, 172: 23–37,, 1999. doi: [10.1016/S0012-821X\(99\)00186-7](https://doi.org/10.1016/S0012-821X(99)00186-7).
- Wright, T., Lu, Z., and Wicks, C. Source model for the M_w 6.7, 23 October 2002, Nenana Mountain Earthquake (Alaska) from InSAR. *Geophysical Research Letters*, 30(18), 2003. doi: [10.1029/2003GL018014](https://doi.org/10.1029/2003GL018014).
- Yaghoubi, A., Mahbaz, S., Dusseault, M. B., and Leonenko, Y. Seismicity and the State of Stress in the Dezful Embayment, Zagros Fold and Thrust Belt. *Geosciences*, 11(6), 2021. doi: [10.3390/geosciences11060254](https://doi.org/10.3390/geosciences11060254).

Zahradnik, J., Jansky, J., and Plicka, V. Detailed Waveform Inversion for Moment Tensors of $M \sim 4$ Events: Examples from the Corinth Gulf, Greece. *Bulletin of the Seismological Society of America*, 98:2756–2771, 2008. doi: 10.1785/0120080124.

The article *Co-seismic slip of the 18 April 2021 M_w 5.9 Genaveh earthquake in the South Dezful Embayment of Zagros (Iran) and its aftershock sequence* © 2023 by M. Jamalreyhani is licensed under CC BY 4.0.

When are Non-Double-Couple Components of Seismic Moment Tensors Reliable?

Boris Rösler  *¹, Seth Stein ^{1,2}, Bruce D. Spencer ^{2,3}

¹Department of Earth and Planetary Sciences, Northwestern University, Evanston, Illinois, U.S.A., ²Institute for Policy Research, Northwestern University, Evanston, Illinois, U.S.A., ³Department of Statistics and Data Science, Northwestern University, Evanston, Illinois, U.S.A.

Abstract There has been considerable discussion as to how to assess when non-double-couple (NDC) components of seismic moment tensors represent real source processes. We explore this question by comparing moment tensors (MTs) of earthquakes in three global catalogs, which use different inversion procedures. Their NDC components are only weakly correlated between catalogs, suggesting that they are largely artifacts of the inversion. A monotonic decrease in the NDC components' standard deviation with magnitude indicates increased reliability of the NDC components for larger earthquakes. The standard deviation begins to decrease for large NDC components exceeding 60 %, suggesting that they represent real source processes. Randomly generated NDC components with the same mean and standard deviation as in the MT catalogs only reproduce some of this decrease. Thus NDC components of large earthquakes and NDC components that exceed 60 % are likely to represent real source processes.

Production Editor:
Gareth Funning
Handling Editor:
Atalay Ayele Woldem
Copy & Layout Editor:
Abhineet Gupta

Received:
September 15, 2022
Accepted:
January 30, 2023
Published:
March 10, 2023

1 Introduction

Moment tensors provide a general description of seismic sources which may include components that differ from slip on planar faults, represented by double-couple (DC) force systems. Non-double-couple (NDC) components include isotropic components and compensated linear vector dipoles (CLVDs). CLVD components describe three force dipoles with one twice the magnitude of the others, yielding no volume change. Following the deployment of large digital seismic networks and the automatic derivation of moment tensors (MTs) after an earthquake, it was observed that many MTs had NDC components (Frohlich, 1994) whose geologic meaning has been debated (Sipkin, 1986; Miller et al., 1998).

Vavryčuk (2001, 2011) showed that the ratio of isotropic and CLVD components arising during the inversion depends on the ratio of the seismic velocities of P and S waves at the source. Thus, constraining the isotropic component also reduces the appearance of spurious CLVD components.

Additionally, the isotropic components of earthquake MTs are generally small (Kawakatsu, 1991; Okal et al., 2018). Therefore, catalogs usually constrain the isotropic component during the inversion to be zero and report only deviatoric MTs (Dziewonski and Woodhouse, 1983; Ekström et al., 2012). Because CLVD components are the only possible NDC components in deviatoric MT catalogs, we use the terms interchangeably.

Some earthquakes in specific geologic environments, notably volcanic ones, have NDC components that have been interpreted to represent real source processes (Kanamori and Given, 1982; Ross et al., 1996; Nettles

and Ekström, 1998; Shuler et al., 2013a,b; Gudmundsson et al., 2016; Sandanbata et al., 2021; Rodríguez-Cardozo et al., 2021). Other NDC components reflect near-simultaneous rupture on nearby faults with different geometry (Hayes et al., 2010; Hamling et al., 2017; Scognamiglio et al., 2018; Yang et al., 2021; Ruhl et al., 2021) or a rupture with changes in geometry (Wald and Heaton, 1994; Cohee and Beroza, 1994; Pang et al., 2020). However, NDC components can also be artifacts of the MT inversion without geologic meaning (Ammon et al., 1994; Chapman, 2013).

Determining the origin of NDC components of earthquakes reported by MT inversions without additional information about the geologic setting of the earthquake is challenging. Rösler and Stein (2022) examined a large moment tensor dataset to assess how NDC components vary between earthquakes. Their general consistency with magnitude and faulting type and hence geologic environment suggests that most NDC components are artifacts of the inversion procedures used in compiling different catalogs.

However, several studies argue that there exists a threshold above which NDC components represent real source processes. Vavryčuk's 2002 study of $M < 3$ events in Bohemia placed this threshold between 20 % and 40 %. Stierle et al.'s 2014 analysis of $M < 4.1$ aftershocks of the 1999 Izmit earthquake found that spurious NDC components can reach 15 %, and Adamová and Šílený's 2010 modeling study determined that spurious components can exceed 20 %. In this study, we consider earthquakes worldwide with $4.4 \leq M_w \leq 8.6$ and use the differences between NDC components in different catalogs to assess their reliability and thus the issue of a possible threshold to derive criteria for the distinction between artifacts of the inversion and real source pro-

*Corresponding author: boris@earth.northwestern.edu

cesses.

2 Methodology

The Global CMT (GCMT) Project (Ekström et al., 2012), German Research Centre for Geosciences (GFZ), and U.S. Geological Survey (USGS, Hayes et al., 2009) catalogs report deviatoric moment tensors for a global distribution of earthquakes. We compile a dataset of 5000 earthquakes common to all three catalogs from July 2011 to December 2021 (Fig. 1), and identify MTs describing the same event by similar source times (± 60 s), locations (difference less than 1°), and magnitudes ($M_w \pm 0.5$). We use the USGS catalog's definition of the scalar moment as the Euclidean norm of the moment tensor (Silver and Jordan, 1982)

$$M_0 = \sqrt{\frac{1}{2} \sum_{i=1}^3 \sum_{j=i}^3 M_{ij}^2}, \quad (1)$$

where M_{ij} represent the six independent moment tensor components. This definition is equivalent to using the square root of the sums of the squares of the eigenvalues of the deviatoric moment tensor, λ'_i . This definition differs from that in the GCMT catalog, which uses the scalar moment of the best-fitting DC. From the scalar moment, we calculate the earthquake's moment magnitude following Kanamori (1977) as

$$M_w = \frac{2}{3} (\log_{10} M_0 - 9.1), \quad (2)$$

where M_0 is in $N \cdot m$.

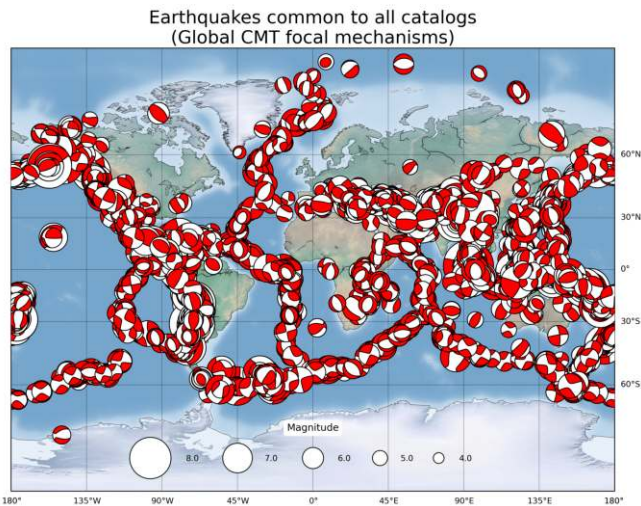


Figure 1 Location and focal mechanisms of the 5000 earthquakes used in this study. The earthquakes occurred between July 2011 and December 2021. Shown are the focal mechanisms in the Global CMT Project catalog.

For each earthquake, the NDC component in each catalog is obtained as the ratio of the absolutely smallest and absolutely largest eigenvalues of the MT (Giardini, 1984),

$$\epsilon = \frac{\lambda'_3}{\max(|\lambda'_1|, |\lambda'_2|)}, \quad (3)$$

where $\lambda'_1 > \lambda'_3 > \lambda'_2$ (Hudson et al., 1989). The NDC component is usually reported in moment tensor catalogs as 2ϵ with values from -100% to 100% (Jost and Herrmann, 1989). The mean NDC component for an earthquake is calculated as the mean of the NDC components in the three catalogs

$$\bar{\epsilon} = \frac{1}{3} \sum_{i=1}^3 \epsilon_i, \quad (4)$$

where the index i represents the three different catalogs. The NDC's standard deviation is

$$\sigma_{2\epsilon} = \sqrt{\frac{4}{3} \sum_{i=1}^3 (\epsilon_i - \bar{\epsilon})^2}. \quad (5)$$

To classify earthquakes by faulting type, we calculate the plunge of the P-, N- (also called B-), and T-axes from the eigenvectors of the moment tensors (Frohlich, 1992). An earthquake is considered a normal faulting earthquake if the plunge of its P-axis satisfies $\sin^2 \delta_P \geq 2/3$ ($\delta_P \geq 54.75^\circ$), strike-slip if its N-axis plunge exceeds 54.75° , and a thrust fault if its T-axis plunge exceeds 54.75° (Saloor and Okal, 2018). If the plunge of none of the axes exceeds the threshold, we consider an earthquake to have oblique faulting.

3 Results

The NDC components in our dataset $2|\bar{\epsilon}|$ have a similar distribution with magnitude in all three catalogs (Fig. 2). The decrease with magnitude has been observed by Rösler and Stein (2022), who, using a large dataset compiled from multiple global and regional MT catalogs, found an average NDC component of 23.2% that varies only slightly with magnitude.

However, the values of the NDC components 2ϵ for earthquakes in the three catalogs are only weakly correlated between catalogs (Fig. 3), consistent with findings by Frohlich and Davis (1999). The correlation coefficients vary between 0.49 for the NDC components reported in the GCMT and USGS catalogs, and 0.39 for the GFZ and USGS catalogs. Hence the standard deviation of the NDC components for each earthquake in the catalogs is a measure of the NDC component's consistency and can be used to assess the reliability of its determination. Fig. 4a shows that the standard deviation among the three catalogs $\sigma_{2\epsilon}$ decreases significantly with the magnitude of an earthquake, suggesting a more consistent determination of NDC components for larger earthquakes.

Rösler et al. (2021) found that the source processes of large earthquakes are more reliably determined, which is consistent with our dataset. Because the size of the NDC components varies only slightly for earthquakes of different magnitudes (Fig. 2), the decrease in their standard deviation cannot be due to their size, and we attribute it to the magnitude of the earthquakes. Thus, NDC components of large earthquakes are more reliably determined than the ones of small earthquakes, possibly due to moment tensor inversions for larger

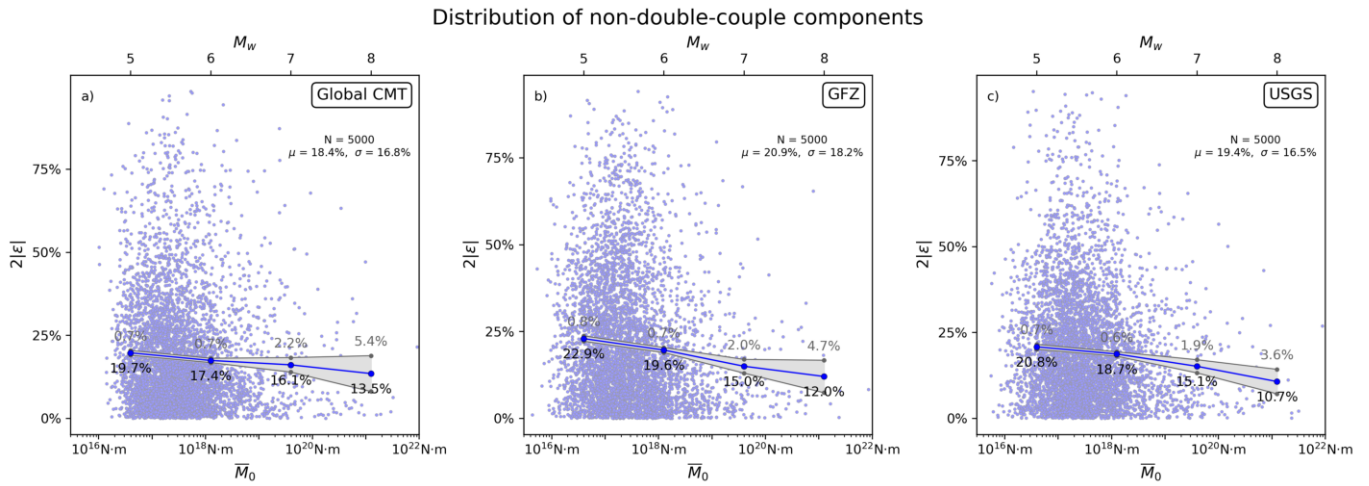


Figure 2 Distribution of NDC components with magnitude in the three MT catalogs. Also shown are the mean NDC component and the 95 % confidence intervals, calculated as twice the standard deviation of the mean. The distribution in all catalogs is similar, with NDC components decreasing with magnitude.

Correlation of non-double-couple components

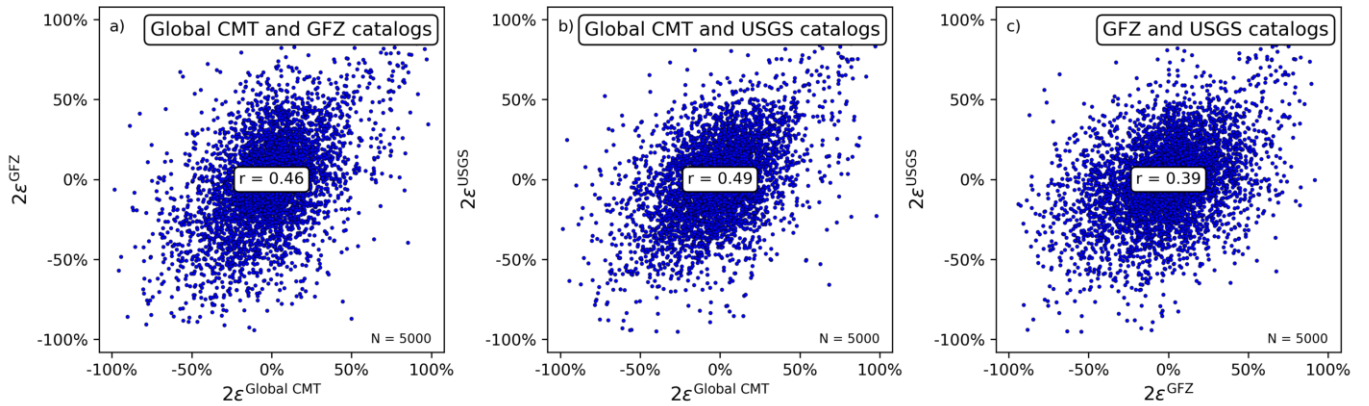


Figure 3 Correlation of NDC components between each two of the three catalogs. Despite slight variations, the correlation between NDC components in different catalogs is weak, hinting at large uncertainties in their determination.

earthquakes being carried out using longer period seismic waves for which the velocity models agree better than for the shorter period seismic waves used for smaller earthquakes.

Similarly, Fig. 4b shows a decrease of the standard deviation for NDC components larger than 60 %. This observation may support the existence of a threshold above which NDC components represent real source processes. However, a complexity arises for large NDC components because, by definition, these cannot exceed 100 %. When the mean of the NDC components from the three catalogs is large in absolute value, the individual measurements tend to be closer than average. An extreme example illustrates this effect: If the NDC component has an average (among the three catalogs) of 99 %, the largest variation that could occur among the three individual values is for 100 %, 100 %, and 97 %, and for these values the standard deviation is below 1.75 %. A related phenomenon is found in the binomial distribution in statistics, where the standard deviation decreases as the probability parameter increases beyond 50 %.

To explore the possible impact of this ceiling effect, we conducted a simulation in which we randomly generated NDC components with the same mean as the observed triple from the three catalogs and the same standard deviation as the entire dataset. To do this, we first generated three sets of 5000 random values x , y , and z independently from a Gaussian distribution with zero mean and the standard deviation as in our dataset ($\sigma = 13.3 %$). We then set $X_i = \bar{\epsilon}_i + ax_i - by_i - bz_i$, $Y_i = \bar{\epsilon}_i - bx_i + ay_i - bz_i$, and $Z_i = \bar{\epsilon}_i - bx_i - by_i + az_i$ for all $i = 1, 2, \dots, 5000$ with $a = (2/3)^{1/2}$, $b = (1/6)^{1/2}$, and $\bar{\epsilon}_i$ being the mean NDC component for each earthquake among the three catalogs. The resulting X , Y , and Z each have mean $\bar{\epsilon}_i$, standard deviation σ , and equal correlations so that the variance of their sum equals zero, i.e., $V(X + Y + Z) = 0$. The triples provide a set of three catalogs whose NDC components have the same mean and standard deviation as the observed datasets.

Fig. 5a shows that the standard deviation $\sigma_{2\epsilon}$ of these randomly generated NDC components does not vary with the size of the NDC components. However, this dataset contains values for which individual NDC com-

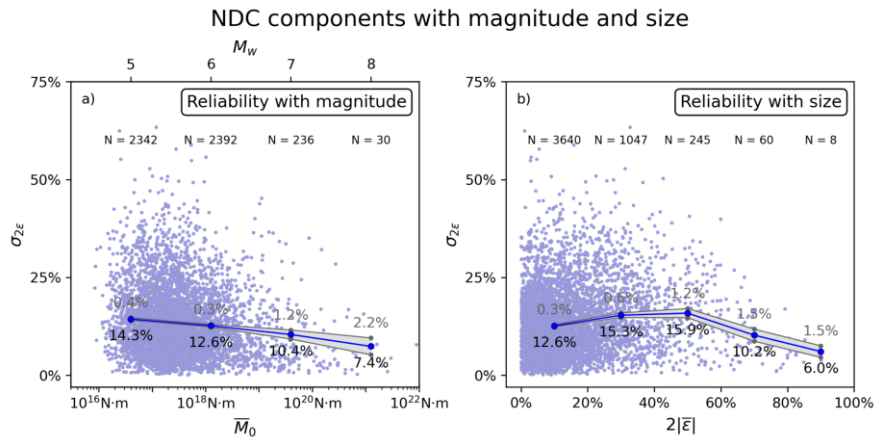


Figure 4 Standard deviation among NDC components in different catalogs with a) magnitude of the earthquake and b) size of the NDC component, and 95 % confidence intervals for mean standard deviations. The standard deviation, a measure of their reproducibility, decreases significantly with magnitude, suggesting more reliable determination of NDC components for large earthquakes. The standard deviation decreases similarly for the largest NDC components.

ponents exceed $2|\epsilon| > 100\%$, which violates the definition of NDC components. Recall that the NDC component depends on the size of the absolutely smallest eigenvalue λ'_3 . If λ'_3 becomes larger in absolute value than one of the other eigenvalues λ'_1 or λ'_2 where $2|\epsilon| > 100\%$, the eigenvalues switch order and the NDC component decreases in size and approaches a DC source again.

Discarding earthquakes for which individual NDC components X_i , Y_i , or Z_i exceed the ceiling of 100 % truncates the random dataset to values which are physically possible. Because individual NDC components of $2|\epsilon| > 100\%$ are more likely for large mean NDC components, the bin of largest NDC components with $2|\epsilon| > 80\%$ is expected to be the most affected by this truncation. Fig. 5b shows that this process eliminates the triples of random NDC components with the largest standard deviation, leading to a decrease in standard deviation for the bin of largest NDC components while leaving other bins practically unchanged. This decrease is similar to that in the observed dataset (Fig. 4b). Repeating this experiment 10 000 times results in an average decrease in standard deviation of 3.3 % for this bin (Fig. 5c), which is smaller than in the observed dataset. Instead of discarding earthquakes with NDC components larger than 100 %, it is also possible to include them with smaller NDC components in this experiment. This can be done in different ways: if we limit the largest NDC components to 100 %, we increase the smallest NDC component by the same amount by which the largest NDC component exceeded 100 %, to preserve the mean of each triple. Repeating this experiment 10 000 times results in an average decrease in standard deviation of 2.0 % in the largest size bin after modification of the NDC components exceeding 100 %. Reducing the largest NDC components to values below 100 % by an amount corresponding to which those NDC components exceeded 100 % is equivalent to a decrease in NDC components when the smallest eigenvalue λ'_3 continues to increase and switches order with another eigenvalue. To preserve the mean of each triple of NDC components

in this case, we increase the smallest NDC component by twice the amount by which the largest NDC component exceeded 100 %. Repeating this experiment 10 000 times results in a decrease in standard deviation of 3.1 % for the bin of largest NDC components, comparable in size to discarding triples where individual values exceed values allowed by their definition, which resulted in a decrease of 3.3 % in standard deviation. The standard deviation can be minimized when also modifying the intermediate NDC component: Assuming $|X_i| \geq |Y_i| \geq |Z_i|$, we calculate $d = \text{sgn}(X_i)(|X_i| - 100\%)$ and replace X_i by $X_i - 2d$, Y_i by $Y_i + gd$, and Z_i by $Z_i + (2 - g)d$, where $g = 1 - (Y_i - Z_i)/(2d)$. If the new value of Y_i exceeds 100 %, we reduce it to 100 % and increase X_i accordingly. In this case, the standard deviation decreases by 4.0 % after 10 000 repetitions in the largest NDC components bin.

Therefore, this ceiling effect produces a distribution of standard deviation $\sigma_{2\epsilon}$ with size of the NDC component similar to that in the MT catalogs, but with a smaller decrease in the bin of largest NDC components. The observed dataset shows a standard deviation of 6.0 % for NDC components larger than 80 %, 7.3 % smaller than the standard deviation for the complete dataset of 13.3 %. Moreover, the ceiling effect does not reproduce the observed decrease in standard deviation for the bin of second largest NDC components between 60 % and 80 %, where the random NDC components only show an insignificant change. We hence conclude that the largest NDC components are, on average, more reliably determined. However, the threshold above which NDC components can be considered reliable, based on the significant decrease in standard deviation among NDC components in different catalogs lies at around 60 %. This value is much larger than proposed in earlier studies.

Rösler and Stein (2022) noticed small differences in the size of NDC components of earthquakes with different faulting types. Consistent with their observation, thrust-faulting earthquakes have the smallest NDC components on average of all different faulting types

Reliability of synthetic NDC components with size

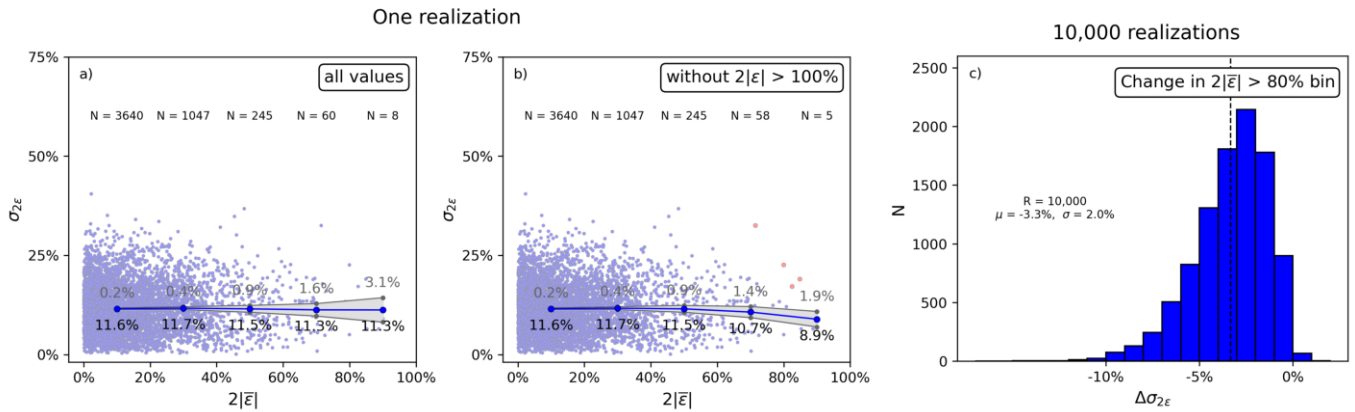


Figure 5 a) Standard deviation of randomly generated NDC components from a Gaussian distribution with the same mean and standard deviation as the MTs in our dataset. The standard deviation is constant over the range of sizes of NDC components. b) Some randomly generated NDC components exceed 100 % (marked in red). Discarding these values decreases the standard deviation for the largest NDC component bin ($2|\epsilon| > 80\%$). c) Repeating this experiment 10 000 times yields a 3.3 % average decrease, smaller than for the observed NDC components.

in our dataset (Fig. 6a). Their standard deviation $\sigma_{2\epsilon}$ between catalogs varies as well, with that for thrust-faulting earthquakes being the smallest (Fig. 6b). This is expected because the standard deviation of a Gaussian distribution with zero mean determines the mean of the absolute values. Therefore, it is unsurprising that the standard deviation of the different faulting types $\sigma_{2\epsilon}$ reflects the average size of NDC components $2|\epsilon|$, which suggests that the reliability between NDC components does not vary between faulting types.

4 Discussion and Conclusions

The moment tensors in global MT catalogs result from different inversion procedures. These procedures may vary in the stations used for the inversion, the individual weights given to the stations, the frequency of seismic waves analyzed, the processing of waveforms, and the inversion algorithm. Although the inversion results are also influenced by the Earth models used for the generation of Green’s functions, the moment tensors in the three catalogs in this study were all calculated using Earth model PREM. The standard deviation between the NDC components in different catalogs is therefore a measure of their consistency and thus, presumably, their reliability. In this study, we use a dataset of 5000 MTs of earthquakes common to the catalogs of the Global CMT Project, the GFZ, and the USGS to assess the reliability of their NDC components.

The standard deviation of observed NDC components decreases for NDC components that are larger than 60 %. Generating random NDC components with the same mean and standard deviation as the observed dataset shows that the decrease in standard deviation for the largest NDC components can be only partially explained by the constraint that NDC components must satisfy $2|\epsilon| < 100\%$ rather than a higher reliability of large NDC components. We therefore conclude that the largest NDC components are generally more reliably determined, and the threshold above which NDC components in global MT catalogs likely represent real source processes is about three times larger the observed average of NDC components of around 20 %. Hence our sense is that an NDC component greater than 60 % is likely to reflect a real source process, although different moment tensor inversions may yield different results. Smaller NDC components are likely to be artifacts, and thus need further investigation before they can be considered real source processes.

The standard deviation between NDC components in different catalogs decreases monotonically with the

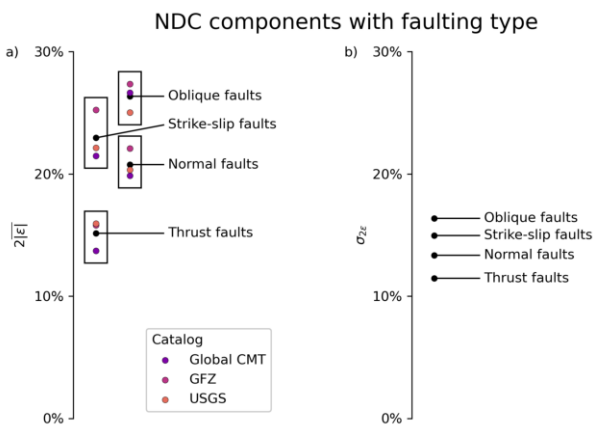


Figure 6 a) Mean NDC components of earthquakes with different faulting types in the three catalogs and their mean for each faulting type. The 95 % confidence interval is too small to be shown in the plot. b) Standard deviation of NDC components between catalogs for earthquakes with different faulting types. The standard deviation reflects the average size of the NDC components because the standard deviation of a Gaussian distribution with zero mean determines the mean of the absolute values. Therefore, the variation in standard deviation between faulting types does not reflect varying reliability.

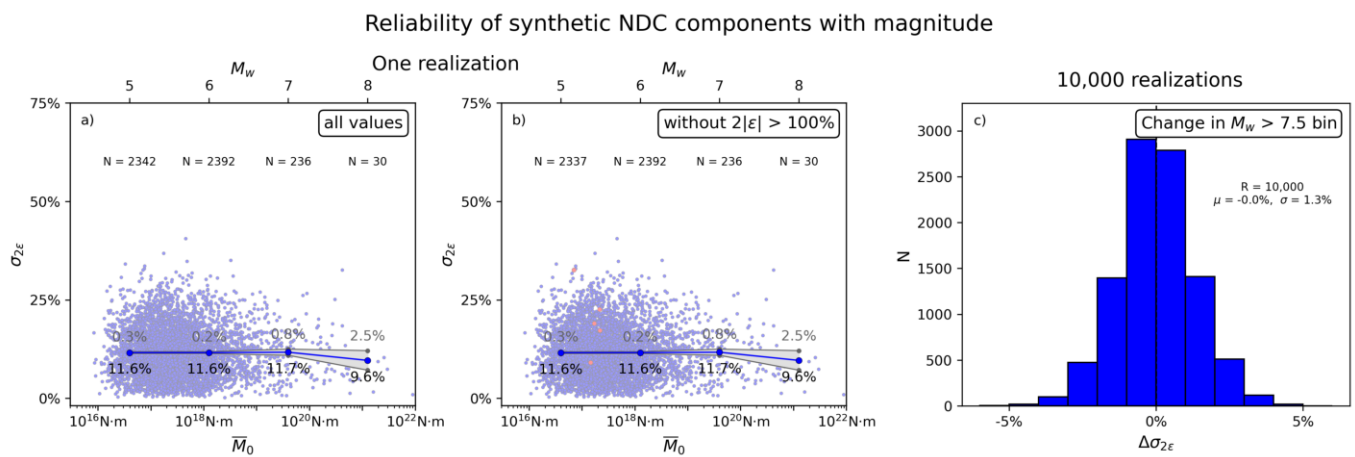


Figure 7 a) Standard deviation of the randomly generated NDC components in Fig. 3 with magnitude. The standard deviation is constant over all magnitudes. b) Discarding values for which individual NDC components exceed $2|\epsilon| > 100\%$ does not have influence on the standard deviation in any magnitude bin. c) Repeating this experiment 10 000 times shows that deleting large NDC components does not affect the standard deviation in the largest magnitude bin. Therefore, randomly generated NDC components cannot reproduce the observed decrease in standard deviation for the largest earthquakes, which suggests an increased reliability of NDC components for large earthquakes.

magnitude of an earthquake (Fig. 4a). Figs 7a and 7b show that the randomly generated NDC components exceeding 100% are distributed arbitrarily among the magnitude bins. They are most likely to fall into the magnitude bins with the most earthquakes and hence the smallest magnitude bins. In contrast to the distribution with size, the distribution of random NDC components with magnitude does not create a ceiling effect. Additionally, large earthquakes have, on average, smaller NDC components (Fig. 2). As a consequence, the largest magnitude bin is, in most cases, unaffected by NDC components exceeding a size of 100% and deleting them from the dataset or modifying them has no influence on the standard deviation in any magnitude bin. Repeating the experiment 10 000 times shows no difference in standard deviation in the largest magnitude bin. Therefore, in the absence of ceiling constraints, the observed decrease in standard deviation for NDC components of large earthquakes reflects the magnitude of an earthquake. As a consequence, the better agreement between catalogs suggests a higher reliability of NDC components of large earthquakes.

The variation of the NDC's standard deviation between faulting types does not reflect a variation in reliability, and is a consequence of the varying size of NDC components between faulting types. Therefore, only the variation of NDC components with earthquake magnitude and size appears to indicate a variation in reliability of the NDC component.

Acknowledgements

We thank Emile Okal and Craig Bina for helpful discussions.

Data and code availability

The moment tensors used in this study were compiled from publicly available data sets. GCMT solutions

are from <https://www.globalcmt.org> (last accessed June 2022). The USGS and GFZ catalogs were downloaded using the Python package ObsPy (Beyreuther et al., 2010) and its International Federation of Digital Seismograph Networks webservice client (June 2022). A list of the earthquakes used in this study including their moment tensors in different catalogs is available by request from the authors.

Competing interests

The authors declare no competing interests.

References

- Adamová, P. and Šílený, J. Non-double-couple earthquake mechanism as an artifact of the point-source approach applied to a finite-extent focus. *Bulletin of the Seismological Society of America*, 100(2):447–457, 2010. doi: 10.1785/0120090097.
- Ammon, C. J., Lay, T., Velasco, A. A., and Vidale, J. E. Routine estimation of earthquake source complexity: The 18 October 1992 Colombian earthquake. *Bulletin of the Seismological Society of America*, 84(4):1266–1271, 1994. doi: 10.1785/BSSA0840041266.
- Beyreuther, M., Barsch, R., Krischer, L., Megies, T., Behr, Y., and Wassermann, J. ObsPy: A Python toolbox for seismology. *Seismological Research Letters*, 81(3):530–533, 2010. doi: 10.1785/gssrl.81.3.530.
- Chapman, M. C. On the rupture process of the 23 August 2011 Virginia earthquake. *Bulletin of the Seismological Society of America*, 103(2A):613–628, 2013. doi: 10.1785/0120120229.
- Cohee, B. P. and Beroza, G. C. Slip distribution of the 1992 Landers earthquake and its implications for earthquake source mechanics. *Bulletin of the Seismological Society of America*, 84(3):692–712, 1994. doi: 10.1785/BSSA0840030692.
- Dziewonski, A. M. and Woodhouse, J. An experiment in systematic study of global seismicity: centroid-moment tensor solutions for 201 moderate and large earthquakes of 1981. *Journal of Geophysical Research*, 88(B4):3247–3271, 1983. doi: 10.1029/JB088iB04p03247.

- Ekström, G., Nettles, M., and Dziewonski, A. The global CMT project 2004-2010: Centroid-moment tensors for 13,017 earthquakes. *Physics of the Earth and Planetary Interiors*, 200-201:1-9, 2012. doi: 10.1016/j.pepi.2012.04.002.
- Frohlich, C. Triangle diagrams: ternary graphs to display similarity and diversity of earthquake focal mechanisms. *Physics of the Earth and Planetary Interiors*, 75(1-3):193-198, 1992. doi: 10.1016/0031-9201(92)90130-N.
- Frohlich, C. Earthquakes with non-double-couple mechanisms. *Science*, 264(5160):804-809, 1994. doi: 10.1126/science.264.5160.804.
- Frohlich, C. and Davis, S. D. How well constrained are well-constrained T, B, and P axes in moment tensor catalogs? *Journal of Geophysical Research*, 104(B3):4901-4910, 1999. doi: 10.1029/1998JB900071.
- Giardini, D. Systematic analysis of deep seismicity: 200 centroid-moment tensor solutions for earthquakes between 1977 and 1980. *Geophysical Journal International*, 77(3):883-914, 1984. doi: 10.1111/j.1365-246X.1984.tb02228.x.
- Gudmundsson, M. T., Jónsdóttir, K., Hooper, A., Holohan, E. P., Halldórsson, S. A., Ófeigsson, B. G., Cesca, S., Vogfjörð, K. S., Sigmundsson, F., Högnadóttir, T., Einarsson, P., Sigmarsson, O., Jarosch, A. H., Jónasson, K., Magnússon, E., Hreinsdóttir, S., Bagnardi, M., Parks, M. M., Hjörleifsdóttir, V., Pálsson, F., Walter, T. R., Schöpfer, M. P. J., Heimann, S., Reynolds, H. I., Dumont, S., Bali, E., Gudfinnsson, G. H., Dahm, T., Roberts, M. J., Hensch, M., Belart, J. M. C., Spaans, K., Jakobsson, S., Gudmundsson, G. B., Fridriksdóttir, H. M., Drouin, V., Dürig, T., Aðalgeirsdóttir, G., Riishuus, M. S., Pedersen, G. B. M., Van Boeckel, T., Oddsson, B., Pfeffer, M. A., Barsotti, S., Bergsson, B., Donovan, A., Burton, M. R., and Aiuppa, A. Gradual caldera collapse at Bárðarbunga volcano, Iceland, regulated by lateral magma outflow. *Science*, 353(6296), 2016. doi: 10.1126/science.aaf8988.
- Hamling, I. J., Hreinsdóttir, S., Clark, K., Elliott, J., Liang, C., Fielding, E., Litchfield, N., Villamor, P., Wallace, L., Wright, T. J., d'Anastasio, E., Bannister, S., Burbridge, D., Denys, P., Gentle, P., Howarth, J., Mueller, C., Palmer, N., Pearson, C., Power, W., Barnes, P., Barrell, D. J. A., van Dissen, R., Langridge, R., Little, T., Nicol, A., Pettinga, J., Rowland, J., and Stirling, M. Complex multifault rupture during the M_w 7.8 Kaikōura earthquake, New Zealand. *Science*, 356(6334), 2017. doi: 10.1126/science.aam7194.
- Hayes, G. P., Rivera, L., and Kanamori, H. Source inversion of the W-Phase: real-time implementation and extension to low magnitudes. *Seismological Research Letters*, 80(5):817-822, 2009. doi: 10.1785/gssrl.80.5.817.
- Hayes, G. P., Briggs, R. W., Sladen, A., Fielding, E. J., Prentice, C., Hudnut, K., Mann, P., Taylor, F. W., Crone, A. J., Gold, R., Ito, T., and Simons, M. Complex rupture during the 12 January 2010 Haiti earthquake. *Nature Geoscience*, 3(11):800-805, 2010. doi: 10.1038/ngeo977.
- Hudson, J. A., Pearce, R. G., and Rogers, R. M. Source type plot for inversion of the moment tensor. *Journal of Geophysical Research: Solid Earth*, 94(B1):765-774, 1989. doi: 10.1029/JB094iB01p00765.
- Jost, M. U. and Herrmann, R. B. A student's guide to and review of moment tensors. *Seismological Research Letters*, 60(2):37-57, 1989. doi: 10.1785/gssrl.60.2.37.
- Kanamori, H. The energy release in great earthquakes. *Journal of Geophysical Research*, 82(20):2981-2987, 1977. doi: 10.1029/JB082i020p02981.
- Kanamori, H. and Given, J. W. Analysis of long-period seismic waves excited by the May 18, 1980, eruption of Mount St. Helens - A terrestrial monopole? *Journal of Geophysical Research*, 87(B7):5422-5432, 1982. doi: 10.1029/JB087iB07p05422.
- Kawakatsu, H. Insignificant isotropic component in the moment tensor of deep earthquakes. *Nature*, 351(6321):50-53, 1991. doi: 10.1038/351050a0.
- Miller, A. D., Foulger, G. R., and Julian, B. R. Non-double-couple earthquakes 2. Observations. *Reviews of Geophysics*, 36(4):551-568, 1998. doi: 10.1029/98RG00717.
- Nettles, M. and Ekström, G. Faulting mechanism of anomalous earthquakes near Bárðarbunga Volcano, Iceland. *Journal of Geophysical Research: Solid Earth*, 103(B8):17973-17983, 1998. doi: 10.1029/98JB01392.
- Okal, E. A., Saloor, N., Kirby, S. H., and Nettles, M. An implosive component to the source of the deep Sea of Okhotsk earthquake of 24 May 2013: Evidence from radial modes and CMT inversion. *Physics of the Earth and Planetary Interiors*, 281:68-78, 2018. doi: 10.1016/j.pepi.2017.10.006.
- Pang, G., Koper, K. D., Mesimeri, M., Pankow, K. L., Baker, B., Farrell, J., Holt, J., Hale, J. M., Roberson, P., Burlacu, R., Pechmann, J. C., Whidden, K., Holt, M. M., Allam, A., and DuRoss, C. Seismic analysis of the 2020 Magna, Utah, earthquake sequence: Evidence for a listric Wasatch fault. *Geophysical Research Letters*, 47(18), 2020. doi: 10.1029/2020GL089798.
- Rodríguez-Cardozo, F., Hjörleifsdóttir, V., K., J., Iglesias, A., Franco, S. I., Geirsson, H., Trujillo-Castrillón, N., and M., H. The 2014-2015 complex collapse of the Bárðarbunga caldera, Iceland, revealed by seismic moment tensors. *Journal of Volcanology and Geothermal Research*, 416, 2021. doi: 10.1016/j.jvolgeores.2021.107275.
- Rösler, B. and Stein, S. Consistency of Non-Double-Couple Components of Seismic Moment Tensors with Earthquake Magnitude and Mechanism. *Seismological Research Letters*, 93(3):1510-1523, 2022. doi: 10.1785/0220210188.
- Rösler, B., Stein, S., and Spencer, B. D. Uncertainties in Seismic Moment Tensors Inferred from Differences Between Global Catalogs. *Seismological Research Letters*, 92(6):3698-3711, 2021. doi: 10.1785/0220210066.
- Ross, A., Foulger, G. R., and Julian, B. R. Non-double-couple earthquake mechanisms at the Geysers geothermal area, California. *Geophysical Research Letters*, 23(8):877-880, 1996. doi: 10.1029/96GL00590.
- Ruhl, C. J., Morton, E. A., Bormann, J. M., Hatch-Ibarra, R., Ichinose, G., and Smith, K. D. Complex Fault Geometry of the 2020 M_w 6.5 Monte Cristo Range, Nevada, Earthquake Sequence. *Seismological Research Letters*, 92(3):1876-1890, 2021. doi: 10.1785/0220200345.
- Saloor, N. and Okal, E. A. Extension of the energy-to-moment parameter Θ to intermediate and deep earthquakes. *Physics of the Earth and Planetary Interiors*, 274:37-48, 2018. doi: 10.1016/j.pepi.2017.10.006.
- Sandanbata, O., Kanamori, H., Rivera, L., Zhan, Z., Watada, S., and Satake, K. Moment tensors of ring-faulting at active volcanoes: Insights into vertical-CLVD earthquakes at the Sierra Negra caldera, Galápagos Islands. *Journal of Geophysical Research: Solid Earth*, 126(6), 2021. doi: 10.1029/2021JB021693.
- Scognamiglio, L., Tinti, E., Casarotti, E., Pucci, S., Villani, F., Cocco, M., Magnoni, F., Michelini, A., and Dreger, D. Complex fault geometry and rupture dynamics of the M_w 6.5, 30 October 2016, Central Italy earthquake. *Journal of Geophysical Research*, 123(4):2943-2964, 2018. doi: 10.1002/2018JB015603.
- Shuler, A., Ekström, G., and Nettles, M. Physical mechanisms for vertical-CLVD earthquakes at active volcanoes. *Journal of Geophysical Research: Solid Earth*, 118(4):1569-1586, 2013a. doi: 10.1002/jgrb.50131.

- Shuler, A., Nettles, M., and Ekström, G. Global observation of vertical-CLVD earthquakes at active volcanoes. *Journal of Geophysical Research: Solid Earth*, 118(1):138–164, 2013b. doi: 10.1029/2012JB009721.
- Silver, P. G. and Jordan, T. H. Optimal estimation of scalar seismic moment. *Geophysical Journal International*, 70(3):755–787, 1982. doi: 10.1111/j.1365-246X.1982.tb05982.x.
- Sipkin, S. A. Interpretation of non-double-couple earthquake mechanisms derived from moment tensor inversion. *Journal of Geophysical Research: Solid Earth*, 91(B1):531–547, 1986. doi: 10.1029/JB091iB01p00531.
- Stierle, E., Bohnhoff, M., and Vavryčuk, V. Resolution of non-double-couple components in the seismic moment tensor using regional networks - II: application to aftershocks of the 1999 M_w 7.4 Izmit earthquake. *Journal of Geophysical Research: Solid Earth*, 119(3):1878–1888, 2014. doi: 10.1093/gji/ggt503.
- Vavryčuk, V. Inversion for parameters of tensile earthquakes. *Journal of Geophysical Research: Solid Earth*, 106(B8):16339–16355, 2001. doi: 10.1029/2001JB000372.
- Vavryčuk, V. Non-double-couple earthquakes of 1997 January in West Bohemia, Czech Republic: evidence of tensile faulting. *Geophysical Journal International*, 149(2):364–373, 2002. doi: 10.1046/j.1365-246X.2002.01654.x.
- Vavryčuk, V. Tensile earthquakes: theory, modeling, and inversion. *Journal of Geophysical Research: Solid Earth*, 116(B12), 2011. doi: 10.1029/2011JB008770.
- Wald, D. J. and Heaton, T. H. Spatial and temporal distribution of slip for the 1992 Landers, California, earthquake. *Bulletin of the Seismological Society of America*, 84(3):668–691, 1994. doi: 10.1785/BSSA0840030668.
- Yang, J., Zhu, H., Lay, T., Niu, Y., Ye, L., Lu, Z., Luo, B., Kanamori, H., Huang, J., and Li, Z. Multi-fault opposing-dip strike-slip and normal-fault rupture during the 2020 M_w 6.5 Stanley, Idaho earthquake. *Geophysical Research Letters*, 48(10), 2021. doi: 10.1029/2021GL092510.

The article *When are Non-Double-Couple Components of Seismic Moment Tensors Reliable?* © 2023 by Boris Rösler is licensed under CC BY 4.0.

Deep learning for denoising High-Rate Global Navigation Satellite System data

A. M. Thomas *¹, D. Melgar ¹, S. N. Dybing ¹, J. R. Searcy ²

¹Department of Earth Sciences, University of Oregon, Eugene, Oregon, USA, ²Data Science Initiative, University of Oregon, Eugene, Oregon, USA

Author contributions: *Conceptualization:* A. M. Thomas, D. Melgar. *Methodology:* A. M. Thomas, J. R. Searcy. *Formal Analysis:* A. M. Thomas, D. Melgar. *Software:* A. M. Thomas, D. Melgar, J. R. Searcy. *Resources:* D. Melgar, S. N. Dybing. *Data Curation:* D. Melgar, S. N. Dybing. *Writing - original draft:* A. M. Thomas, D. Melgar. *Writing - review and editing:* A. M. Thomas, D. Melgar, S. N. Dybing, J. R. Searcy. *Project Administration:* A. M. Thomas, D. Melgar. *Funding acquisition:* D. Melgar, A. M. Thomas.

Abstract High-rate global navigation satellite system (HR-GNSS) data records ground displacements and can be used to identify earthquakes and slow slip events. One limitation of such data is the high amplitude, cm-level noise which makes it difficult to identify processes that produce surface displacements smaller than these values. Deep learning has proven adept at performing many useful tasks in seismology and geophysics. Here we explore using deep learning to denoise HR-GNSS data. We develop three different convolutional neural networks with similar architectures but different targets. Training data are synthetic HR-GNSS records and actual noise recordings that are superimposed to generate noisy signals. We train each of the three models to output masks that can be used to reconstruct the true signal. We use a set of performance metrics that quantify the models' ability to denoise the testing data and find that denoising significantly improves the signal-to-noise ratio and the ability to identify first arrivals. Finally, we test the models on HR-GNSS records from the Ridgecrest earthquakes recorded at stations that have nearly colocated strong-motion sites that can be used as ground-truth for the denoising results. We find that the models greatly improve the signal-to-noise ratios in these records and make the P-wave onset clearly identifiable.

Production Editor:
Gareth Funning
Handling Editor:
Mathilde Radiguet
Copy & Layout Editor:
Abhineet Gupta

Received:
September 13, 2022
Accepted:
March 07, 2023
Published:
May 04, 2023

1 Introduction

High-rate Global Navigation Satellite System (HR-GNSS) data record ground displacements at increments of ≥ 1 Hz and are a type of geophysical measurement commonly used to identify and characterize earthquakes and slip transients (Bock and Melgar, 2016; Larson, 2019). GNSS data can augment traditional seismic data and are superior for some applications. For example, long-period recordings of earthquakes contain diagnostic information about earthquake magnitude (e.g., Melgar et al., 2015). This property of GNSS is used extensively for down-stream applications such as earthquake early warning (e.g., Murray et al., 2018) and tsunami early warning (e.g., Williamson et al., 2020). Inertial recordings of earthquakes suffer from a well-known magnitude saturation problem; recordings of the first arriving seismic waves cannot distinguish between large and very large magnitude earthquakes (e.g., Trugman et al., 2019). In contrast, GNSS faithfully record ground motions at long-periods, including zero-frequency static offsets, and do not suffer from this limitation (e.g., Crowell et al., 2013). Additionally, for modeling finite faults for the largest events it has become commonplace to include HR-GNSS in post-processing (e.g., Goldberg et al., 2020). The data provide fundamental constraints on total moment and on the spatial distribution of slip. For large events it is expected that

a credible rupture model will be capable of reproducing these kinds of observations (e.g., Satake and Heidarzadeh, 2017; Lay, 2018). As a final example, some types of crustal deformations such as slow earthquakes and fault creep have long duration source processes and do not effectively generate seismic waves (e.g., Thomas et al., 2016). These slow deformation processes are often identified by a gradual displacement of the Earth's surface, hence characterization of these events relies on GNSS data.

One of the main limitations of HR-GNSS data is the high noise level of ~ 1 – 2 cm both in post-processing and in real-time (Geng et al., 2018; Melgar et al., 2020). This limits the utility of HR-GNSS recordings to situations where ground displacements are in excess of these amplitudes such as moderate to large earthquakes at local to regional distances. Several factors contribute to the high noise level of HR-GNSS data. This includes measurement noise, the number and location of satellites, model estimates of orbital errors, satellite and receiver clocks, atmospheric delays, antenna effects, and multipath errors (Melbourne et al., 2021). Several methods have been proposed to eliminate particular forms of noise. For example, sidereal filtering leverages repeating satellite-receiver geometries to correct for noise resulting from multipath errors (i.e., when a transmitted signal arrives at a receiver via an indirect path). Simply stated this technique involves taking displacements recorded during the previous orbital repeat pe-

*Corresponding author: amt.seismo@gmail.com

riod (the time since the satellite constellation was last in the same configuration), applying a low pass filter (e.g. 11 s corner frequency), and subtracting the filtered displacement record from the displacement recorded at the present time (e.g., Choi et al., 2004). Spatial filtering targets common-mode noise that is highly correlated across GNSS stations in close spatial proximity (Wdowinski et al., 1997). This technique simply averages detrended records on many nearby stations and the resulting average is subtracted from each station. Principal component analysis (e.g., Dong et al., 2006; He et al., 2015) has been employed to remove long period noise (0.2–0.1 cycles/year) and various match-filtering approaches have also been employed to reduce noise levels (Frank, 2016; Rousset et al., 2019). With respect to HR-GNSS, there are a dearth of denoising techniques that are both applicable to high rate data and are efficient. For example, sidereal filtering is one of the most commonly employed techniques but because of the low-pass filtering, it does not apply to frequencies higher than the chosen corner frequency. Additionally, Geng et al. (2017) noted that sidereal filtering can also increase noise levels for periods between 20 and 33 s (those authors used a 10 s corner frequency). While data-driven denoising strategies are capable of mitigating high-frequency noise (e.g., Li et al., 2018), as proposed, they involve multiple decompositions using techniques such as empirical mode decomposition, which is known to be computationally time consuming.

Machine learning is adept at many commonly performed tasks in seismology and crustal deformation. For example, deep learning (DL) can identify and make phase picks on small magnitude earthquakes (e.g., Zhu and Beroza, 2019; Thomas et al., 2021). DL can recognize crustal deformation patterns measured with HR-GNSS data and accurately estimate the earthquake moment in real time (Lin et al., 2021). Additionally, and of particular interest for the present study, DL methods have been applied to denoise various types of geophysical data. For example, Zhu et al. (2019) developed an algorithm known as Deep Denoiser which they showed drastically improved the signal-to-noise ratio (SNR) in earthquake seismograms. We discuss this method in more detail in Section 2. Additionally, Ende et al. (2021) developed a methodology to denoise distributed acoustic sensing data. Since GNSS measures position and the decomposition into components is arbitrary, noise is often correlated across components on the same station similar to seismic noise. This suggests that deep learning may also be adept at denoising GNSS records.

Motivated by these recent results, here we explore using DL to denoise HR-GNSS records. In Section 2 we discuss the methodology including the generation of training and testing data, network architectures, and the training procedure. In Section 3 we discuss the results of the methodologies including performance on both the training data and real records from the 2019 Ridgecrest, California earthquake sequence. In Section 4 we discuss the successes and limitations of the methods, potential applications, and future directions. Overall, DL appears to be a promising path forward to increasing the utility of HR-GNSS data in rapidly identifying and as-

sessing source properties of intermediate to large magnitude earthquakes and lowering the noise threshold of HR-GNSS data for detecting small magnitude transient slip events.

2 Methods

2.1 Training data for denoising

As a testbed for our proposed approach we focus on the recent Ridgecrest, California earthquake sequence that commenced in July, 2019. This energetic set of earthquakes included an M6.4 foreshock on a NE striking fault plane, followed 34 hours later by an M7.2 mainshock on an adjacent, conjugate fault striking NW (e.g., Ross et al., 2019; Goldberg et al., 2020). The GNSS network surrounding Ridgecrest, shown in Fig. 1A and B, includes multiple near-field stations close enough to record static offsets in both the M6.2 and M7.2 events. Both events were followed by energetic aftershock sequences that included four M5+ events (Fig. 1A and B; Shelly, 2020).

To create an algorithm capable of separating signal from noise we need many thousands of examples of both signal (i.e., HR-GNSS displacement time series from real earthquakes) and noise waveforms. For the noise recordings, we use three-component timeseries of real noise recorded on the 278 GNSS stations closest to the Ridgecrest events, shown in Fig. 1A. These data are from the Network of the Americas (NOTA) sites operated by UNAVCO and the positions are true real-time solutions produced and archived by UNAVCO (Hodgkinson et al., 2020). The timing of the noise waveforms was selected at random times from days between June 1, 2019 to July 31, 2020 that did not have an earthquake above M4.3. This magnitude is a conservative lower bound for the size of an earthquake that one may expect to generate an observable signal in the GNSS data.

Obtaining a similar number of real “signal” waveforms over a range of magnitudes is challenging for two reasons. First, unlike seismic data, which can have SNRs of many orders of magnitude, the high noise floor of GNSS data makes it such that even the largest amplitude displacements have relatively modest SNR and still contain appreciable noise. Second, only large magnitude earthquakes recorded in the near-field generate signals of sufficient magnitude to exceed the noise floor. This is problematic because we would like to include signals that are at or below the noise level (i.e., $\text{SNR} \leq 1$) to train an algorithm capable of detecting small amplitude displacements. These limitations prohibit using real signals for training, and so we turn to generating realistic, synthetic displacements.

The *FakeQuakes* code (Melgar et al., 2016) generates stochastic ruptures using the assumption that slip on a fault is distributed like a random field (Mai and Beroza, 2002). If the statistics of this field are known then random draws can be made to generate arbitrarily large numbers of ruptures. This approach is common in strong motion seismology (e.g., Graves and Pitarka, 2010; Goulet et al., 2015). As is typical, we assume a VonKarman correlation function (VKCF). The along-

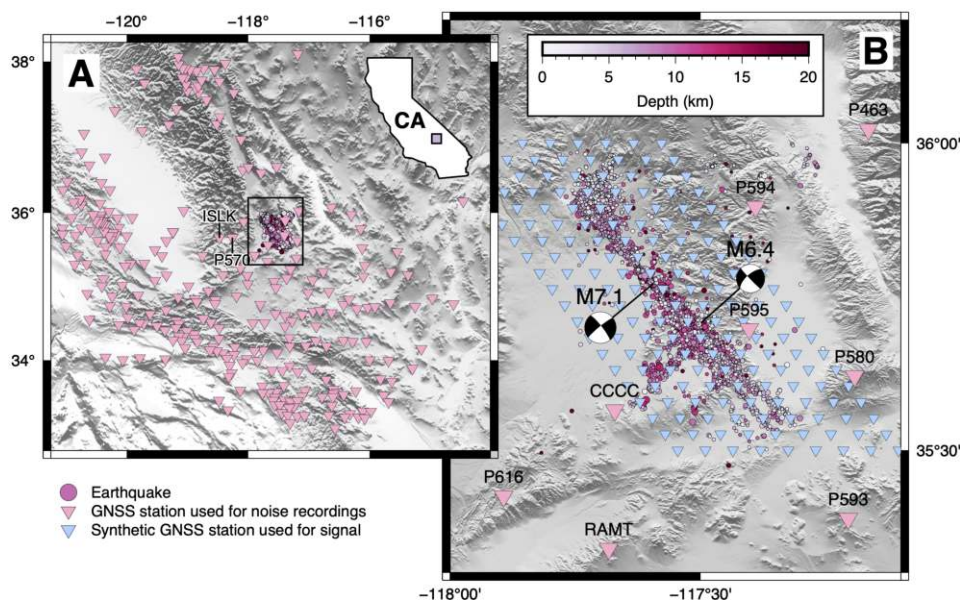


Figure 1 Maps of the Ridgecrest area. Panel A shows a regional map with GNSS stations used for noise recordings (pink) and synthetic signal recordings (blue) shown as inverted triangles. Ridgecrest earthquakes are outlined by the black square. The locations of stations P570 (Fig. 14) and ISLK (Fig. 15) are annotated. Inset shows an outline of the state of California with the region location indicated by the purple square. Panel B shows a closeup of the Ridgecrest earthquake sequence. Events are color coded according to their depth and scaled by magnitude. Focal mechanisms for the M7.1 and M6.4 are also shown.

strike and along-dip correlation lengths of the VKCF control the predominant sizes and aspect ratios of asperities in the slip patterns. Meanwhile the Hurst exponent, H , of the VKCF determines the amount of short-wavelength structure in between them. Mai and Beroza (2002) proposed scaling laws for the correlation lengths which depend on fault dimension, and fixed $H = 0.7$. Here we use updated scaling laws from an analysis of the U.S. Geological Survey’s database of finite faults (Melgar and Hayes, 2019) and we use $H = 0.4$. A full description of the stochastic approach can be found in Melgar et al. (2016). Once the slip patterns are created, kinematic rupture properties such as rise time, rupture velocities, etc., are set following Graves and Pitarka (2015). We assume a 1D layered Earth model for Eastern California used in the Southern California Earthquake Center’s Broadband Platform (Goulet et al., 2015) and produce the waveforms using a frequency-wavenumber approach to generating elastodynamic Green’s functions (GFs; Zhu and Rivera, 2002). For this work we introduce an additional modification. After comparing our kinematic rupture waveforms with HR-GNSS data from the Ridgecrest earthquakes we noticed that many waveforms from the Ridgecrest earthquakes had significant “ringing” or long duration coda that was not present in the synthetic waveforms. We hypothesized that these waveforms were affected by either site or basin effects. Since we are not using fully 3D GFs in order to produce waveforms with long durations we created an extra family of “soft layer” waveforms. We varied the thickness of the soft layer between 100 and 900 m and allowed shear wave speeds as slow as 100 m s^{-1} and as fast as 900 m s^{-1} . These two families of waveforms, the ones without and the ones with the soft layers, are then used for training.

The *FakeQuakes* output is then three-component

ground displacement timeseries from earthquakes with magnitudes ranging from 4 to 7.2 that rupture the 3D fault geometry of Goldberg et al. (2020). The displacement timeseries from each earthquake are calculated at the 180 synthetic GNSS station locations shown in blue in Fig. 1B. The station distribution shown in Fig. 1B and magnitude range were initially chosen so that the resulting displacement timeseries are not dominated by very small amplitude displacements and instead represent more uniform sampling of peak ground displacement. At each station, displacement waveforms are calculated at 1 sample/s for a 256 s window centered on the P-wave arrival expected from ray-tracing through the velocity model. North, east, and vertical displacements for 20 example “fakequakes” are shown in Fig. 2A, B, and C respectively. Despite this selection of magnitudes and station locations, small magnitude peak ground displacements (PGD) still dominate the dataset so we implemented a culling procedure such that we have a nearly uniform distribution of PGD up to 1 m and then exponentially decreasing numbers of events with $\text{PGD} > 1 \text{ m}$. Overall our dataset includes 822 256 three-component signal records and 729 303 three-component noise records.

2.2 Network architecture

Convolutional neural networks (CNNs) are a deep learning architecture capable of efficiently extracting diagnostic information from multidimensional images. The essential component of any CNN is one or more convolutional layers. In these layers, the user defines both the number of filters and the filter size. The network then convolves these filters with the layer input to create a feature map which is further manipulated in subsequent network layers. Filters can be defined a-priori

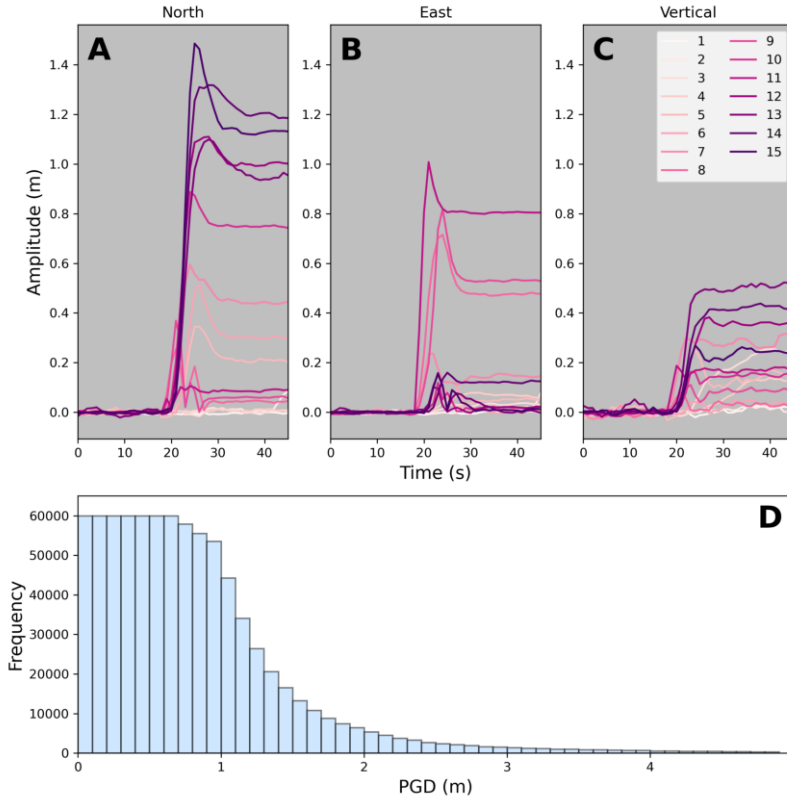


Figure 2 GNSS displacement timeseries and PGD distribution. Panels A, B, and C show north, east, and vertical displacements for 15 different simulated earthquakes, color coded by the example number. Panel D shows PGD distributions for all “fakequake” displacement records in the dataset.

but most often they are learned during training. A U-Net is a special case of a CNN with symmetric contracting and expanding branches (Ronneberger et al., 2015). The contracting branch includes repeated convolutions with a 3x3 filter, rectified linear unit activation functions (Agarap, 2018), and batch normalization. In the contracting branch, each successive convolutional layer has a stride of two and double the number of filters in the previous layer. This results in feature maps that decrease in size but increase in number as network depth increases. In the expanding branch, the filter number is halved while the convolutions upsample their respective feature maps resulting in larger maps after each successive convolutional layer. Skip connections also feed outputs from the contracting branch to inputs of the expanding branch at the same depth in the network, skipping the deeper layers.

Zhu et al. (2019) employed a U-Net called Deep Denoiser to denoise single channel seismic data. In their denoising approach, the noisy signal, $Y(t)$ is the sum of a known signal, $S(t)$, and known noise, $N(t)$, or

$$Y(t) = S(t) + N(t) \quad (1)$$

In the frequency domain, the short-time Fourier Transform (STFT) of the noise, $N(t, f)$, and the STFT of the signal, $S(t, f)$, are summed to represent the STFT of the noisy signal

$$Y(t, f) = S(t, f) + N(t, f) \quad (2)$$

Then the signal mask is defined as

$$M_S(t, f) = \frac{1}{1 + \frac{|N(t, f)|}{|S(t, f)|}} \quad (3)$$

And the noise mask is defined as

$$M_N(t, f) = \frac{\frac{|N(t, f)|}{|S(t, f)|}}{1 + \frac{|N(t, f)|}{|S(t, f)|}} \quad (4)$$

Each mask has the same dimensions as the input STFTs and takes on values between 0 and 1. The network is trained to output an estimate of the signal and noise masks, $\hat{M}_S(t, f)$ and $\hat{M}_N(t, f)$. From these, the estimated signal, $\hat{S}(t, f)$ can be obtained by multiplying $Y(t, f)$ by the respective mask and inverse transforming

$$\hat{S}(t) = STFT^{-1} \left\{ Y(t, f) \hat{M}_S(t, f) \right\} \quad (5)$$

Similarly, the estimated noise, $\hat{N}(t, f)$ can be obtained by multiplying $Y(t, f)$ by the noise mask and inverse transforming

$$\hat{N}(t) = STFT^{-1} \left\{ Y(t, f) \hat{M}_N(t, f) \right\} \quad (6)$$

Zhu et al. (2019) showed that Deep Denoiser could reliably denoise seismic signals, resulting in significant increases in SNR in the denoised waveforms thereby improving earthquake detection capabilities.

Motivated by the results of Zhu et al. (2019), we develop a similar U-Net, which can be accessed in the

repository linked in the Data Availability section, with some noteworthy modifications. First, Deep Denoiser operated on single channel seismic data. For accurate denoising of HR-GNSS data, we anticipate that using all three channels as network input will significantly improve the results given the higher noise levels on the vertical channels and the fact that noise is very highly correlated across channels. As such, each network we present here has inputs derived from three component HR-GNSS data. Second, a notable attribute of Deep Denoiser is that it can distort signal amplitudes during the denoising process, reducing their true amplitudes (Tibi et al., 2021). For some applications, such as earthquake detection and arrival time picking, this amplitude distortion is not a limitation. However, if denoising of HR-GNSS were to be used for early-warning or source studies, amplitude distortion could underpredict early earthquake magnitude estimates. As such we explore three different model variations, described in the next section.

2.3 Inputs, outputs, and model variations

The inputs to each of our networks are generated in the following way. The HR-GNSS data we employ here is sampled at 1 Hz. The noise and signal records described above are 256 s long originally. Leaving the training data in the original form, with the P-wave pick in the middle, would bias the resulting CNN to assign noise prior to the middle of each window and signal thereafter. As such, we use a data generator during training which applies the following modifications to the data prior to input to the network. First, we randomly select a set of N signal timeseries and N noise timeseries, where N is the batch size. These timeseries are added to simulate noisy signals. Second, we randomly select a start-time in the first half of each trace and include only 128 s of data beginning at that time. This has the effect of randomly shifting the earthquake onset in time such that it can occur at any point during the window. The signal can also be shifted such that the window is mostly or entirely noise. The combinations of signal and noise and the time-shifting are data augmentation strategies that significantly increase the size of the training dataset. Third, we compute the STFT of the signal timeseries, the noise timeseries, and the noisy signal timeseries which results in complex, 2D time-frequency representations of the timeseries for each component. To compute the STFT we use a segment length of 31 and 30 points of overlap between segments. The real and imaginary parts of the noisy signal are normalized by dividing the STFTs for each component by the maximum of their absolute value. This accounts for the differences in amplitude of the input data which can vary over several orders of magnitude. The final input to the CNN is six channels (the real and complex parts of the STFT for the north, east, and vertical components), each with dimension 16×128 .

We train three different model versions to denoise the HR-GNSS data. In the first model, which we will call Model 1, we adopt an approach very similar to Deep Denoiser (Zhu et al., 2019) The only modifications are that

the network ingests six channels of data and we predict only one signal mask for each channel. The noise mask can be determined by taking the complement of the signal mask. For Model 1, the activations on the final layer are sigmoids to accommodate the three channel mask outputs (in the one-component version of Deep Denoiser, the final layer activations were softmax functions). To determine the estimated signal from the input signal, we simply use equation 5.

Model 2 is motivated by Model 1's limitations. Namely that by using a real-valued mask, we cannot account for phase differences between signal and noise which can result in amplitude distortion. As such, in the final layer we use linear activation functions and the model predicts the real and imaginary parts of the complex valued $S(t, f)$ normalized by the maximum absolute value of $Y(t, f)$. We can obtain the signal estimate by multiplying the output by the maximum absolute value of $Y(t, f)$, which can be calculated from the input data, and inverse transforming.

Finally, in Model 3, we explore predicting the ratio $S(t, f)/Y(t, f)$. Model 3 was also motivated by the desire to account for phase differences and minimize amplitude distortion but employs a similar masking technique as Deep Denoiser. Because this ratio can be infinite, we convert the complex representation of the STFT to amplitude and phase and train the network to output the scaled amplitude and phase ratios. Specifically the first output is defined as

$$A(S(t, f), N(t, f)) = \ln(|S(t, f)/Y(t, f)| + \epsilon) \quad (7)$$

where ϵ is a small magnitude constant added to ensure that the target is never infinite; we set $\epsilon = 10^{-9}$. Direct prediction of the phase is challenging in machine learning because of the modular property of angular measurements. To address this modularity, we use targets for phase prediction defined as

$$\phi_1(S(t, f), N(t, f)) = \cos(\theta) \quad (8)$$

and

$$\phi_2(S(t, f), N(t, f)) = \sin(\theta) \quad (9)$$

where

$$\theta = \tan^{-1} \left(\frac{\text{Im}(S(t, f)/Y(t, f))}{\text{Re}(S(t, f)/Y(t, f))} \right) \quad (10)$$

The functions A , ϕ_1 , and ϕ_2 are the targets for each component resulting in nine total predictions for the third model. Like Model 2, Model 3 employs linear activation functions and the estimated signal can be determined using equations 7-10.

Finally, to explore how variations in network size affect performance we vary slightly the network architecture by increasing the number of filters in the convolutional layers by a factor of two.

2.4 Training

We train the three different models for 50 epochs each using Tensorflow (Abadi et al., 2016). In all cases we set aside 10% of the signal and noise waveforms for testing

and train using the remaining 90 %. For all networks, we use the Adam optimization algorithm (Kingma and Ba, 2014) with a learning rate of 0.0001, we also use a drop rate of 0.2. All models used a mean-squared error loss function on all targets.

2.5 Performance metrics

We use three different metrics to quantify model performance. First, we employ the normalized cross-correlation coefficient to measure the similarity between the signal and the model predicted signal, denoted as CC. CC varies between +1 when two signals are exactly correlated and -1 when they are exactly anticorrelated. We note that the normalized cross-correlation does not account for amplitude differences between signals. This choice was deliberate such that the inherent amplitude distortion does not bias the result. Second, we compute the SNR using

$$\text{SNR} = \frac{\max(|\text{signal}|)}{2 * \sigma_{\text{noise}}} \quad (11)$$

Here $\max(|\text{signal}|)$ is the maximum absolute value of the signal waveform and σ_{noise} is the standard deviation of the noise evaluated on the time window prior to the P-wave arrival. This metric has a value of ~ 1 when the signal and noise amplitudes are equal, and is greater (or less) than one when the signal amplitude exceeds (or is less than) the noise amplitude. We note that some other common measures of SNR utilized on seismic data often employ the standard deviation in both the numerator and denominator but this metric does not properly account for the static offsets that represent signal in GNSS data. We also note that the SNR metric can become infinite if the σ_{noise} approaches zero. When we use SNR to quantify general attributes of the waveforms prior to denoising, the numerator of equation 11 is evaluated on the signal waveforms alone while the denominator is evaluated on the noise. We also quantify the change in SNR, ΔSNR , between noisy and denoised waveforms. We evaluate ΔSNR by computing SNR on the noisy signal (i.e., signal + noise) and on the denoised signal and subtracting the two. For all SNR calculations, we require that signal and noise be at least 10 s in duration. Third, we use the Euclidean or L^2 distance as a measure of the difference between the signal and the noisy signal or the denoised signal. The L^2 distance between two vectors \mathbf{x} and \mathbf{y} , with components x_i and y_i respectively, is defined as

$$L^2(\mathbf{x}, \mathbf{y}) = \sqrt{\sum_i (x_i - y_i)^2} \quad (12)$$

As an additional test of applying our simulated training data to real HR-GNSS records, we compare the original HR-GNSS records, denoised HR-GNSS records, and displacements derived from strong motion accelerograms recorded during the Ridgecrest, California earthquake sequence. These GNSS and strong motion stations are the only closely located pairs in proximity to the Ridgecrest earthquakes. For small to moderate ground motions, the strong-motion accelerograms

can be used to estimate the three-component ground displacements. For extremely strong ground motions, baseline offsets make the displacement records inaccurate, sometimes by widely large amounts, at periods longer than ~ 10 s (e.g., Melgar et al., 2013).

We focus our analysis on two site pairs: P570 and WOR, which are separated by 3.5 km and are 59 km from the M7.1 mainshock, and ISA and ISLK, which are 62 m apart and 80.5 km from the mainshock. We take strong motion records from WOR and ISA, integrate twice and correct for gain. We then bandpass filter the strong motion data, raw HR-GNSS, and denoised HR-GNSS between 3 and 15 s for comparison. The results of this analysis are described further in Section 3.

3 Results

3.1 Denoising examples

For each model we select from the testing dataset as denoising examples two records with peak signal amplitudes below 4 cm, since the denoising process will be most useful for these low amplitude signals, and one higher amplitude signal with peak amplitude above 4 cm. As such, the low and higher amplitude signals have different characteristics. For example, the low amplitude signals are typically dominated by transient seismic wave arrivals and have low-amplitude or zero static offset, whereas the higher amplitude signals contain transient features in addition to large amplitude permanent offsets. We also selected examples to showcase model performance on different types of noise, targeting samples with varying amplitude and frequency content.

Example denoising results are shown in Figs 3-11. Figs 3-4 show a low-amplitude example from Model 1. Each row in the figures correspond to a different component: north, east, and vertical. The first column shows the signal waveform in blue and the summed signal and noise in gray. The annotation indicates the SNR of the noisy signal. The second column shows the target signal mask, $M_S(t, f)$, while the third column shows the model predicted mask, $\hat{M}_S(t, f)$. The fourth column is identical to the first but includes the denoised waveform in magenta with the CC and ΔSNR .

Figs 3-5 show the performance of Model 1 for multiple examples. In Fig. 3, the SNR has comparable values of 2.4 and 1.9 on the north and east components, and lower value of 0.4 on the vertical. After applying Model 1 to denoise, the resulting waveforms have a high CC with the known signal on the horizontals and denoising also recovering much of the signal character for the vertical component, which has $\text{CC} = 0.674$ between the true and denoised vertical components. All components have significant improvements in SNR. Fig. 4 shows another low-amplitude example similar to Fig. 3 but with more complex signal character. The model still recovers much of it, i.e., arrival time, amplitudes, and frequency content, on all three components. Such low amplitudes, like that on the vertical, are sometimes not recoverable (i.e., the model predicts noise) however the model can utilize higher amplitude signals on the

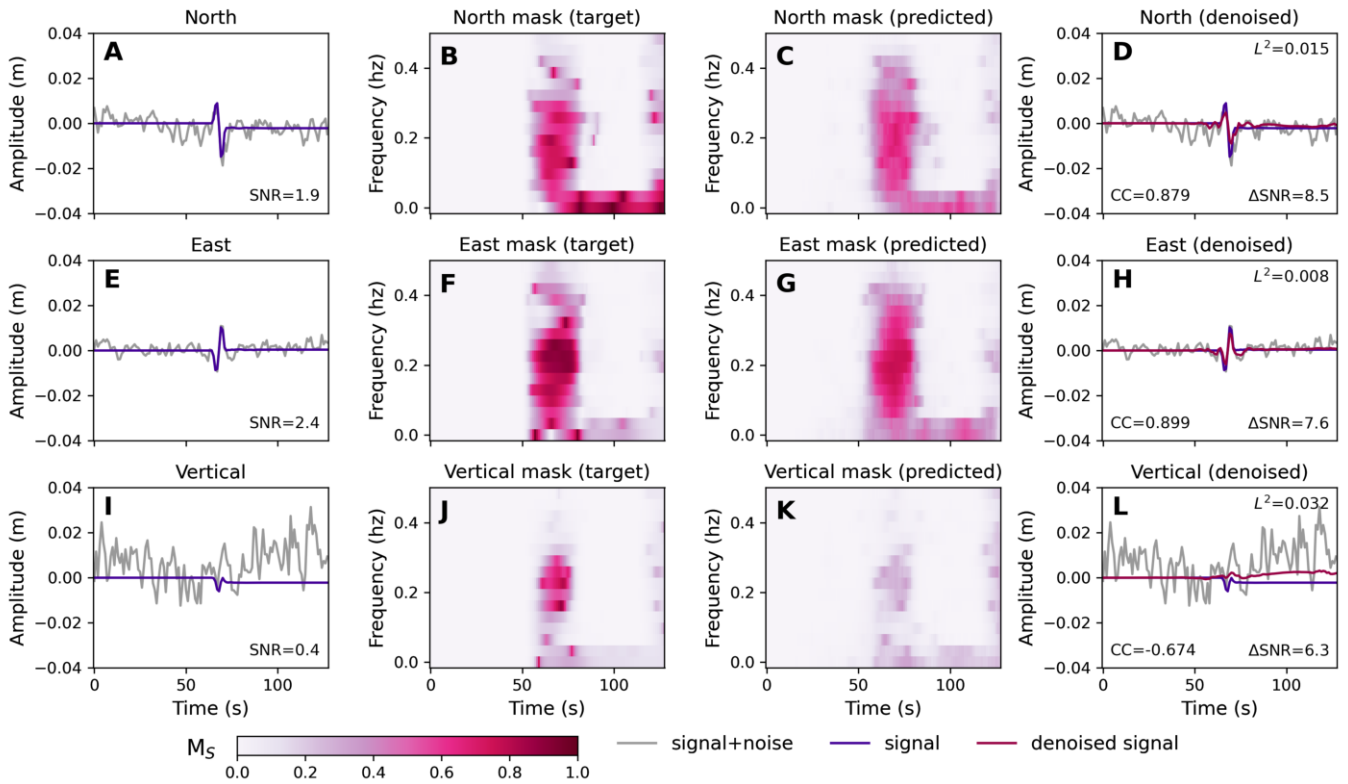


Figure 3 Example denoising using Model 1. Panels A-D, E-H, and I-L correspond to the north, east, and vertical components respectively. The first column shows the signal timeseries (blue) and the noisy signal timeseries (i.e., signal+noise) in gray. The SNR and L^2 distance from equations 11 and 12 respectively are annotated. The second column is the target mask, M_S , for each component. The third column shows the predicted mask for each component. The fourth column shows the signal (blue), noisy signal (gray), and denoised signal (magenta) along with the CC between the signal and denoised signal and the Δ SNR between the noisy and denoised signals.

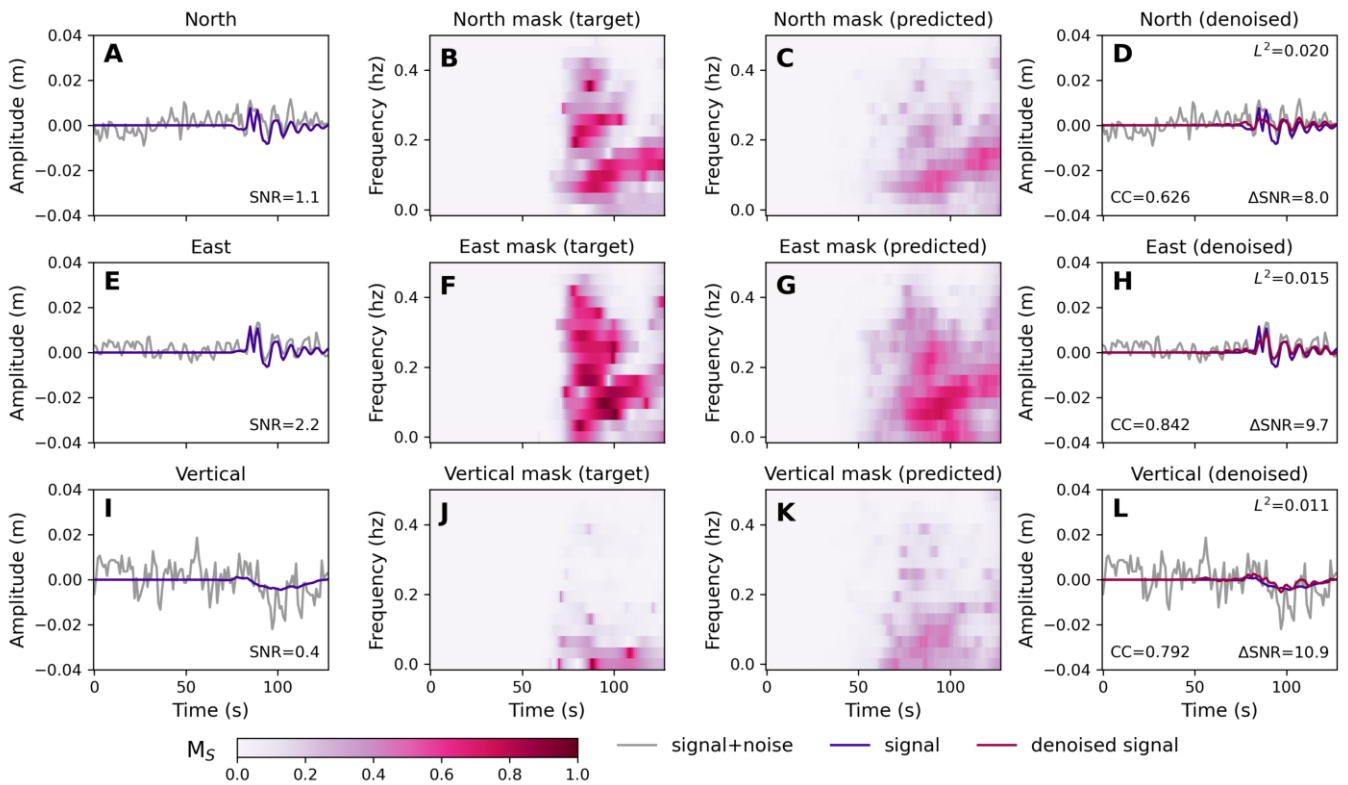


Figure 4 Example denoising using Model 1. Panels are the same as those in Fig. 3.

higher amplitude components to recover some signal character on the components with lower amplitude signals (this is also apparent in Fig. 5). Figs 3 and 4 contain two noteworthy features. First, the signal amplitudes are sometimes underpredicted by Model 1 (see Fig. 3D, H and L and Fig. 4D and H). Second, sometimes the static offset is not well predicted by the model but instead fluctuates with the amplitude of the noisy signal (Panel L in Fig. 3). We discuss these properties more in Section 4. Finally, Fig. 5 shows a higher amplitude demonstration of Model 1 (note the difference in scale between Figs 3-4 and Fig. 5). Denoising essentially does not modify the large amplitude signals on the horizontal components. The main benefit of denoising is to both reduce the amplitude of the noise prior to the first arrivals and to increase the SNR on components with lower signal.

Since the masks predicted by Models 2 and 3 are complex valued, in Figs 6-11 we only show the time domain representations of the noisy signal, signal, and estimated signal (panels D, H, and L of Figs 3-5). Figs 6 and 7 show low amplitude denoising examples using Model 2. In Fig. 6, the three components have SNRs of 0.46, 1.22, and 0.95. Despite low SNR, denoising successfully recovers signal on all components with high CC between all original and estimated signals. Fig. 7 is similar to Fig. 6 showing another example of retrieval of the signal when SNR is low. In particular, the vertical component is well recovered in Fig. 7 despite the high-amplitude and low frequency character of the noise (Fig. 7C). Also note that on the horizontal components, there is constructive interference between the signal and noise (Fig. 7B). In some cases, such as the later arrivals on the north component and the east component, Model 2 is able to successfully partition signal and noise and predicts the true signal amplitude (Fig. 6A and B). In other cases, such as the vertical component in this same example (Fig. 6C), Model 2 can underpredict the signal amplitudes and long term signal character, such as static offset can be influenced by noise. Fig. 8 is a high amplitude example with complex signal character. Model 2 performs well, particularly in predicting the low amplitude vertical component.

Figs 9-11 show examples of denoising using Model 3. Figs 9 and 10 show significant improvements in horizontal SNR even given the relatively low amplitude of the signals. Additionally both examples have high correlations between the true and predicted signals on the horizontal components. While Model 3 generally succeeds on the east component in Fig. 11, the model fails to predict the static offset in the denoised north and vertical signals causing them to deviate from the true static offset. This is commonly observed in Model 3. Figs S1-S10 show the performance of all three models on some common examples.

3.2 Model performance on the testing data

To evaluate the overall performance of each model on the testing dataset ($N = 82\,226$) we compute the CC between the true and denoised signals as a function of the SNR. We then bin the data by SNR and compute the 10th,

50th, and 90th percentiles of the CCs for the signals contained in each bin. We also compute the median CC between the noisy and true signals as a function of SNR. The results are shown in Fig. 12 which includes panels for individual components and all signals combined. While many horizontal components have $\text{SNR} > 6$, we chose this particular cutoff to highlight model behavior at lower amplitudes. As expected, model performance improves significantly with SNR. At very low SNR, there is a large spread in CC for all models. For SNRs of 0.5 to 2, the models have significantly larger CCs than the noisy data with the true signal. As SNR increases further, this difference diminishes as the noise becomes a smaller fraction of the overall signal and CCs become high approaching 1 at very large SNR. For all components, Models 1 and 3 have median CCs of 0.51 and 0.41 for an SNR of 0.5. These values increase to 0.78 and 0.74 at an SNR of 1. Model 2 has better performance with a $\text{CC} = 0.70$ at $\text{SNR} = 0.5$ and $\text{CC} = 0.89$ at $\text{SNR} = 1$. For the horizontal components alone, we note that the percentiles are determined from a smaller numbers of events. This is because the horizontal components typically have larger amplitudes for the strike-slip geometry that we considered in this study and lower noise levels than the vertical components, hence there are fewer horizontal records that satisfy the $\text{SNR} < 6$ criterion. Additionally, we note that at very low SNR (i.e., those < 1), the vertical components typically have higher CC than the horizontal components. This is due to two factors. First, the models can use higher amplitude information recorded on the horizontal components to make predictions about content on the vertical component despite the higher amplitude noise. These predictions often result in higher CC than that between the true and noisy waveforms. Second, the high amplitude noise in the noisy waveforms can result in lower CC with the true signal than does a prediction with a near zero value prior to the first arrival and a low amplitude signal, even if the predicted signal departs significantly from the true signal.

Similar to Fig. 12, Fig. 13 shows the L^2 distances between the true and denoised signals as a function of the SNR. The data are binned by SNR and we compute the 10th, 50th, and 90th percentiles of the L^2 distances for the signals contained in each bin. The black line shows the distribution of L^2 distances between the noisy signal and true signal, while the colored lines show the distances between the true signal and those estimated using Models 1, 2, and 3. For all models and components, denoising results in smaller L^2 distances between the true signal and denoised signal than the noisy data independent of SNR. On the horizontal components, the distances between denoised and true signals are small at low SNR because the denoising algorithm generally predicts noise (i.e., zero amplitude true signal) in these scenarios. As the SNR increases and the models make more non-zero signal predictions the L^2 distances increase until, at intermediate to high SNR they plateau. In this region, model distances are still less than the original distances likely due to the zero amplitude prediction of the models prior to the first arrivals. The overall larger distances on the vertical result from the higher

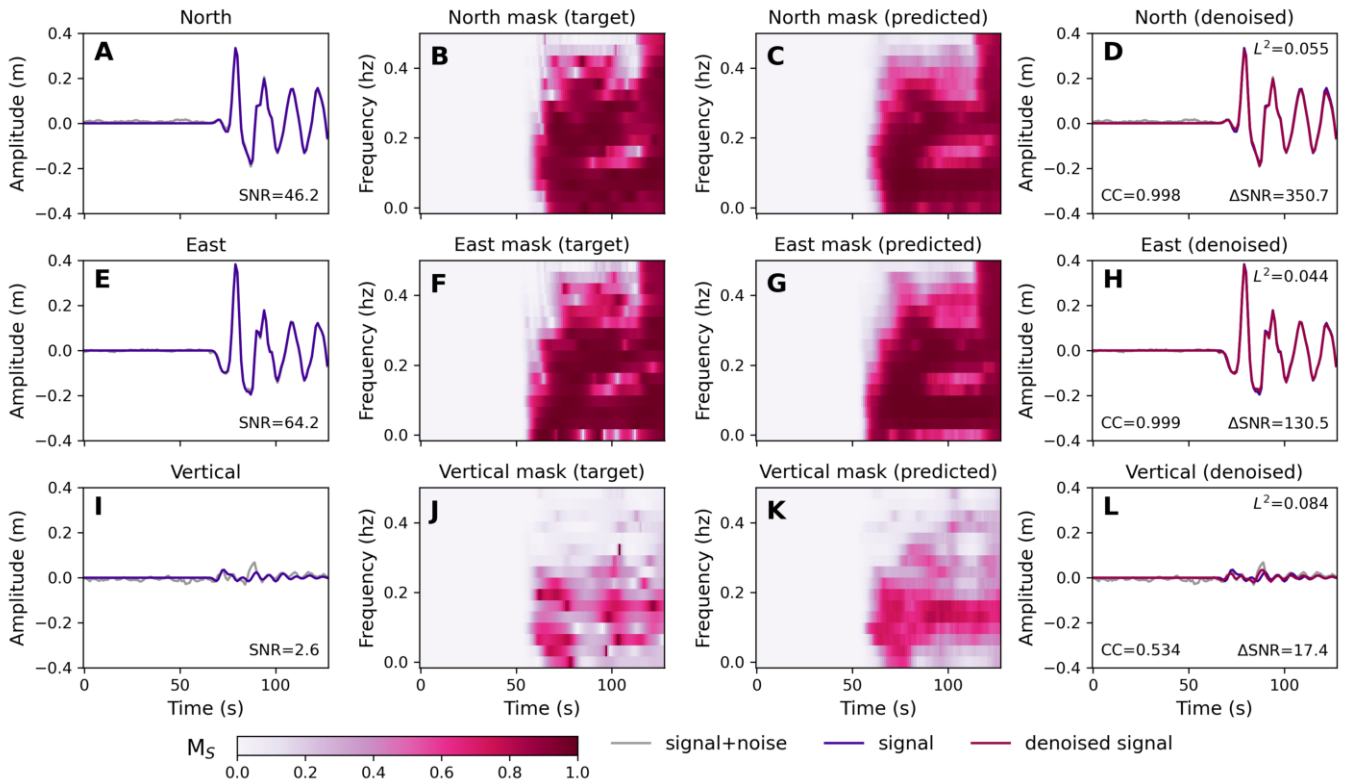


Figure 5 Higher amplitude example denoising using Model 1. Panels are the same as those in Fig. 3.

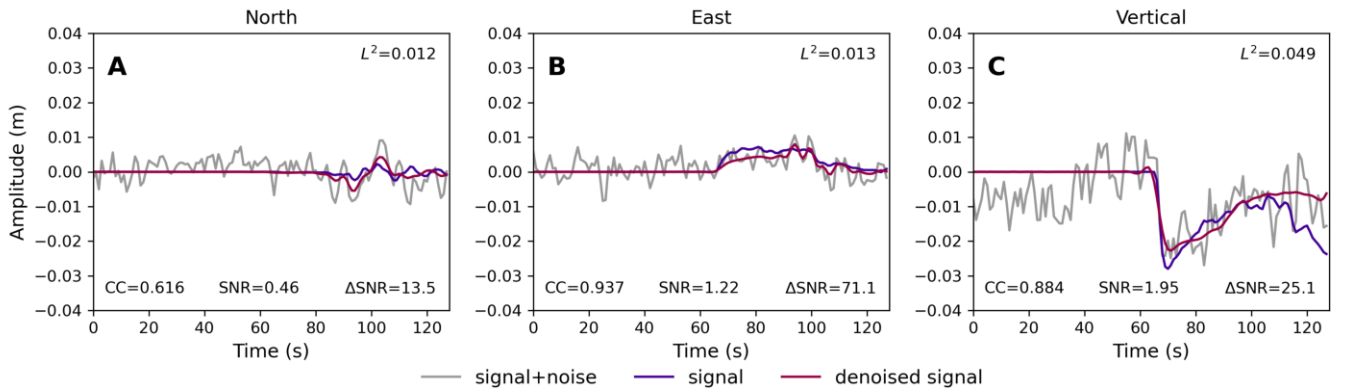


Figure 6 Example denoising using Model 2. Panels A-C correspond to the north, east, and vertical components respectively. Each panel shows the signal timeseries (blue), the noisy signal timeseries (i.e. signal+noise) in gray, and the denoised signal in pink. The SNR (equation 11), CC, L^2 distance (equation 12), and Δ SNR between the noisy and denoised signals are annotated.

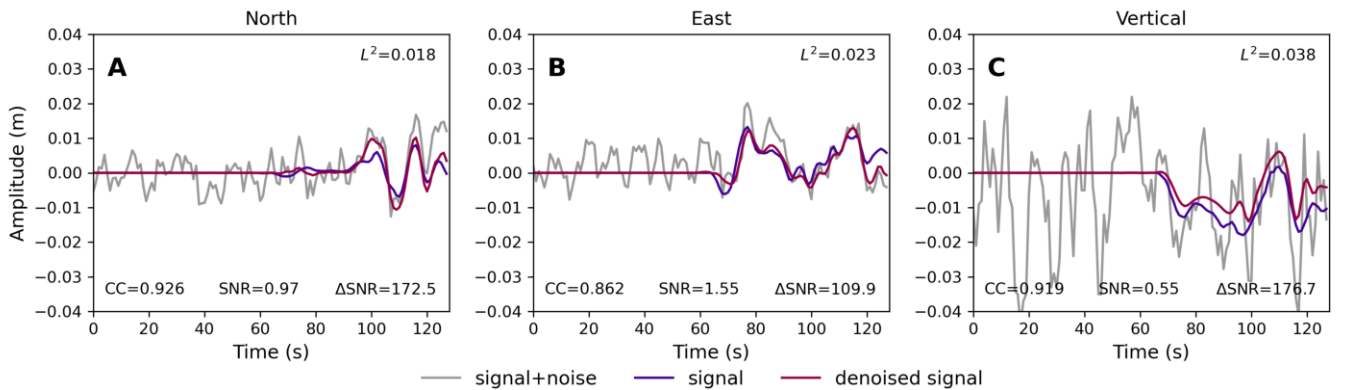


Figure 7 Example denoising using Model 2. Panels are the same as those in Fig. 6.

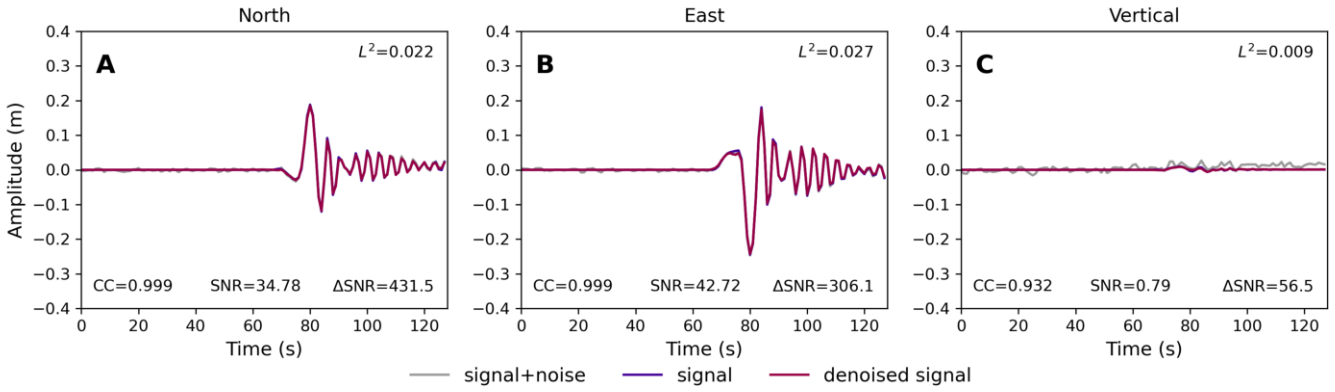


Figure 8 Higher amplitude example denoising using Model 2. Panels are the same as those in Fig. 6.

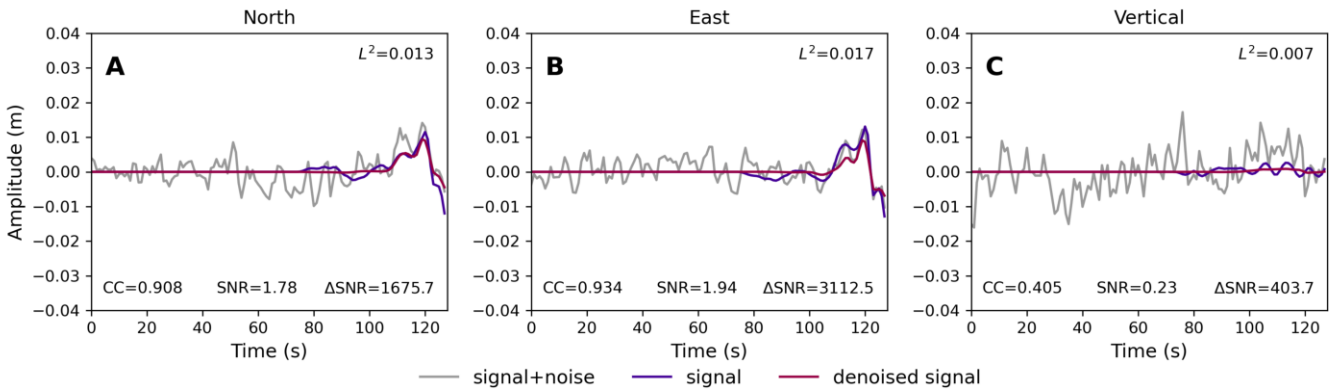


Figure 9 Example denoising using Model 3. Panels A-C correspond to the north, east, and vertical components respectively. Each panel shows the signal timeseries (blue), the noisy signal timeseries (i.e. signal+noise) in gray, and the denoised signal in pink. The SNR (equation 11), CC, L^2 distance (equation 12), and Δ SNR between the noisy and denoised signals are annotated.

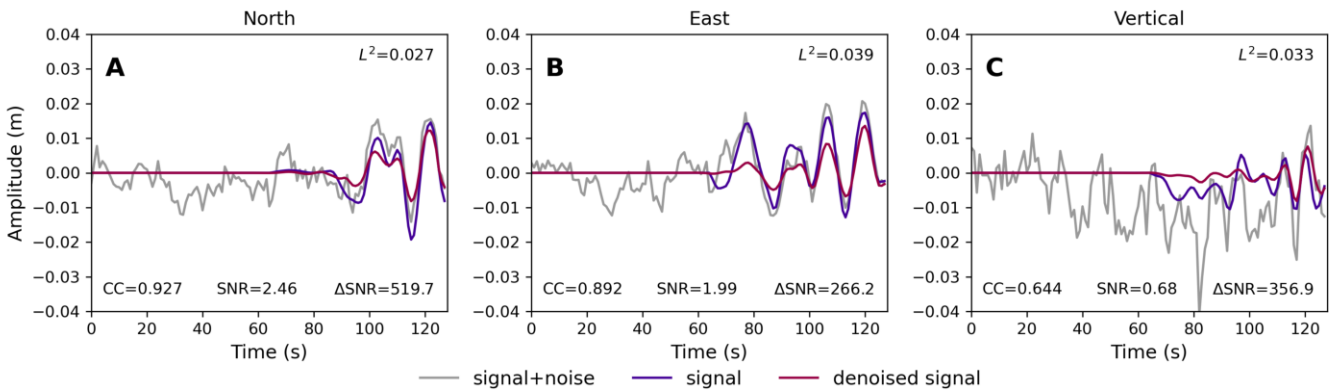


Figure 10 Example denoising using Model 3. Panels are the same as those in Fig. 9.

amplitude noise that is generally present in HR-GNSS data and the lower amplitude signals that result from the choice to simulate earthquakes on strike-slip fault systems.

3.3 Application to the 2019 Ridgecrest earthquakes

As a performance test of our trained models, we apply the denoising algorithms to the Ridgecrest earthquake sequence. While the aftershocks of these events included a number of intermediate magnitude earthquakes, determining how well the denoising models

perform is hampered by lack of knowledge of what the true signal is. GNSS sites with nearby strong motion stations obviate this issue; the strong-motion data can be used to estimate true ground motions.

Denoising results at P570 and WOR are shown in Fig. 14. The model successfully identifies the arrival time (vertical black line) and suppresses noise prior to the first arrivals (SNRs are shown in bottom right of each panel). All models also successfully predict signal amplitudes, particularly on the vertical component. The SNR is significantly improved in the denoised versions of all components. The models generally do well

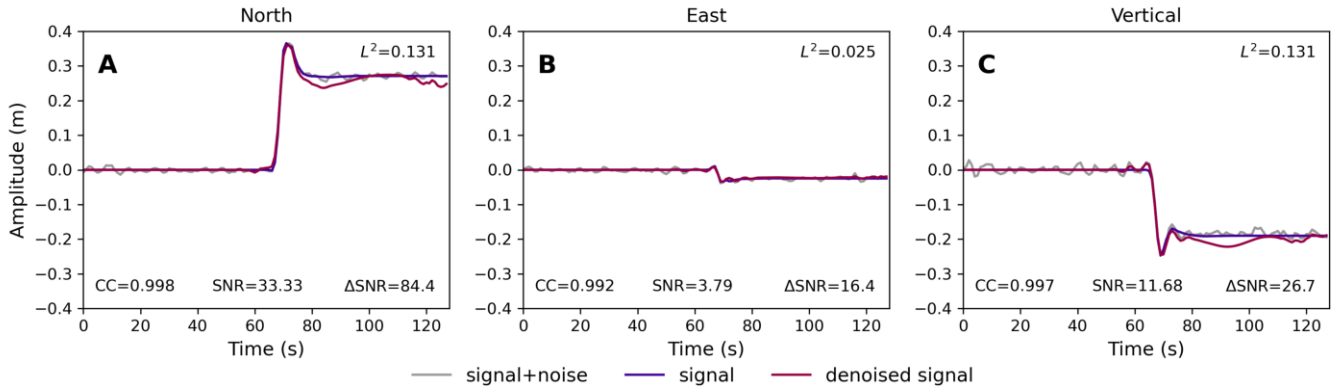


Figure 11 Example denoising using Model 3. Panels are the same as those in Fig. 9.

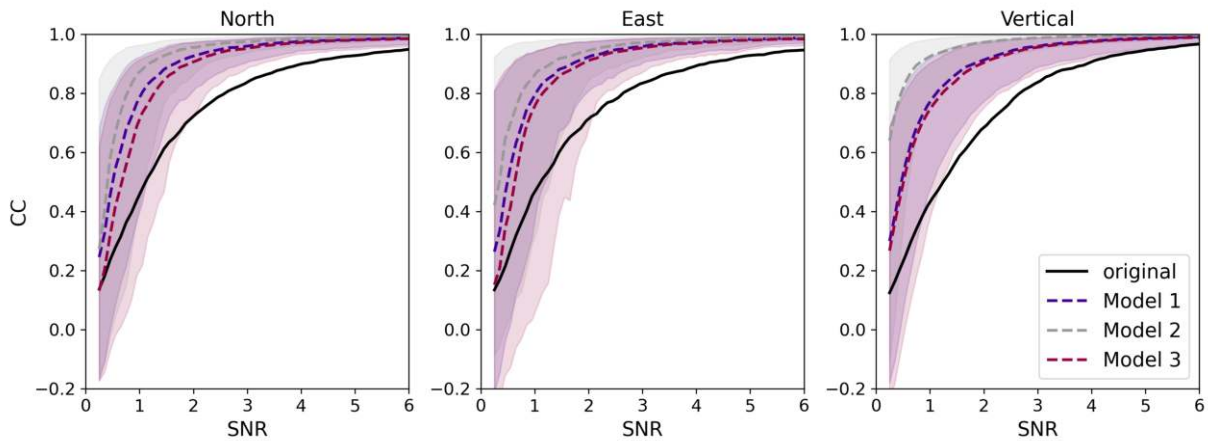


Figure 12 CC as a function of SNR. The median value of the CC between the true signal and noisy signal is shown in black. Median CC values between the true signal and signals denoised by Models 1, 2, and 3 are indicated by the blue, grey, and pink lines respectively. The shaded areas represent the region between the 10th and 90th percentiles that contain 80 % of the testing data and have the same color coding as the median CC.

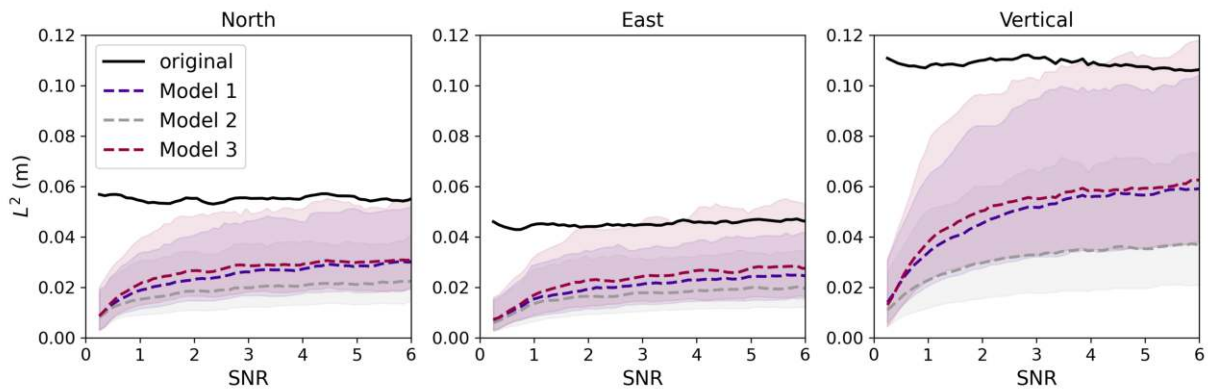


Figure 13 L^2 distances as a function of SNR. The median value of the L^2 distance between the true signal and noisy signal is shown in black. Median L^2 values between the true signal and signals denoised by Models 1, 2, and 3 are indicated by the blue, grey, and pink lines respectively. The blue, grey, and pink shaded areas represent the region between the 10th and 9-th percentiles that contain 80 % of the testing data for Models 1, 2, and 3 respectively.

early on (~35–60 s) however the coda is not well predicted i.e., the noisy GNSS better predicts these later arrivals (~60–80 s). Performance is similar for the ISA and ISLK station pair shown in Fig. 15. The models suppress noise prior to the first arrivals, predict phase and amplitude well early in the wave train, and then trend toward zero amplitude prediction for the later coda ar-

rivals. Results for the M6.4 are shown in Figs S11 and S12. We will discuss this more in the following section.

Finally, as denoising may be applied to HR-GNSS in real time, we explored the false positive rate of Models 1, 2, and 3 on additional 10 000 noise waveforms. The results of this exercise is shown in Fig. S13. The false positive rate at a decision threshold of 1 cm PGD

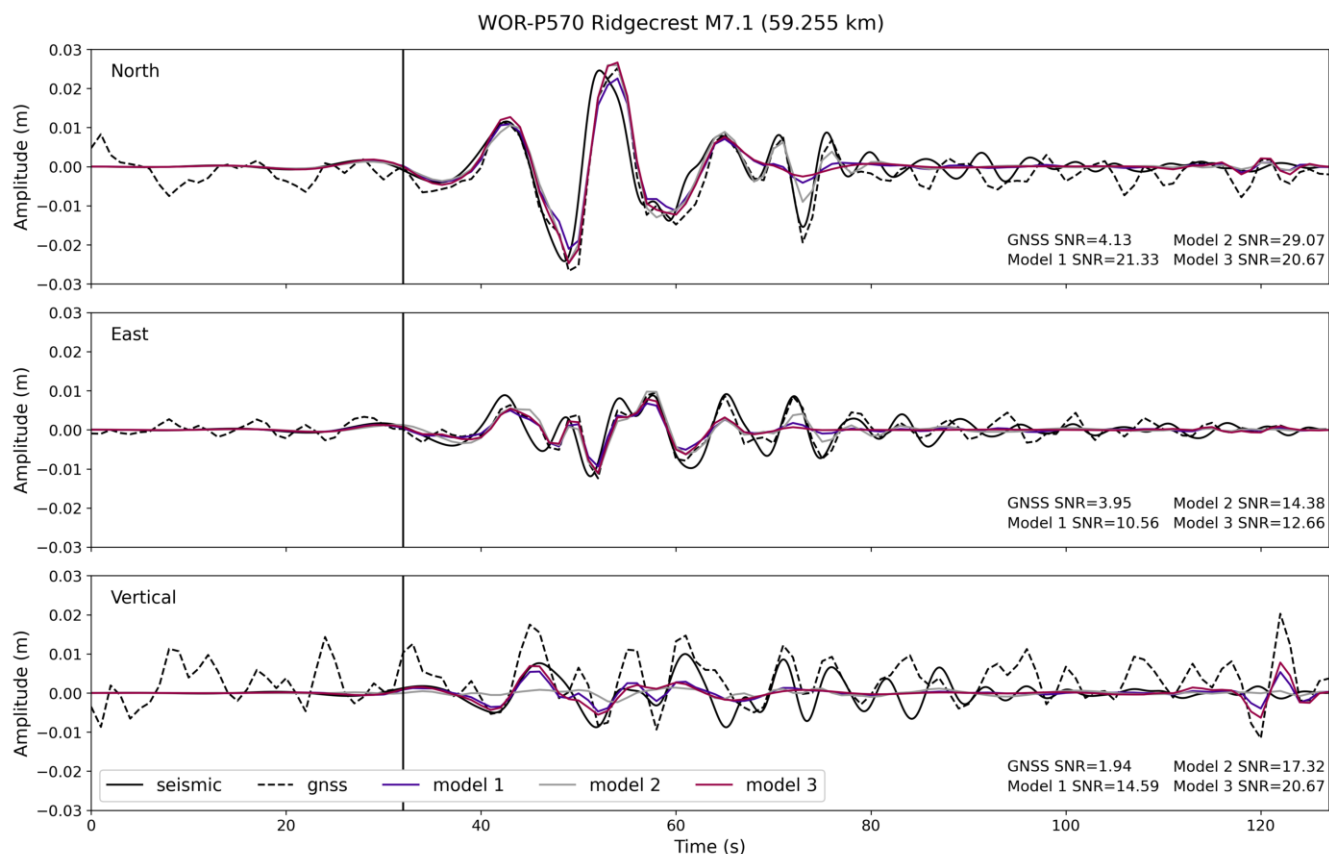


Figure 14 Comparison of recordings of the M7.1 Ridgecrest earthquake at strong motion station WOR and GNSS station P570. GNSS and integrated strong motion data are shown as dashed and solid black lines respectively. GNSS records denoised by Models 1, 2, and 3 are shown in blue, grey, and pink respectively. Vertical black line shows the theoretical P-wave arrival time. SNRs of the original HR-GNSS data, Models 1, 2, and 3 are shown in the bottom right.

is 2.05%, 2.51%, and 0.16% for Models 1, 2, and 3 respectively. The false positive rate at a decision threshold of 2 cm PGD is 0.4%, 0.53%, and 0.06% for Models 1, 2, and 3 respectively. These values are far smaller than the PGD of the noise waveforms themselves. Additionally, they could be further reduced by considering waveform character at multiple stations as all earthquake early warning algorithms do.

4 Discussion

As is evident in Figs 12 and 13, denoising HR-GNSS data offers significant improvements over utilizing noisy records. On all components, the median performance of Model 1, Model 2, and Model 3 exceeds that of the noisy records for all SNRs for both the CC and distance based performance metrics. Generally the models are excellent at suppressing noise prior to the first arrivals making identification of earthquake onsets more apparent. P-waves are almost always well below the GNSS noise, and, as shown in Figs 14 and 15, the P-wave arrival is clear in the denoised GNSS waveforms. Additionally, models can recover signals with amplitudes between 5 mm and 1 cm, i.e., with $\text{SNR} < 1$. Because of our choice to model strike-slip motion on vertical faults, the horizontal components are typically larger than the vertical. Additionally the vertical component generally has higher noise levels. Despite this, the models often

predict well the timing and amplitude on the vertical component by utilizing information on the horizontal components to inform its character. The greatest improvements in CC are between SNRs of slightly below 1 to 3. At high SNR, applying denoising does not result in significant improvements as expected. At low SNR, amplitudes on all three components diminish, the model generally predicts zero amplitude signal on all components.

Models 2 and 3 were motivated by the amplitude distortion inherent in Model 1 which was originally developed for seismic data (Zhu et al., 2019). After assessing the performance of all models we find that Model 2, simple direct amplitude prediction, generally performs better than Models 1 and 3. It does not suffer from the amplitude distortion and is better at predicting both ringing and static offsets than the other models. By both performance metrics utilized here, it performs better at all SNRs than Model 1 and Model 3.

The main shortcoming of the models are the mispredictions of static offsets apparent in Figs 3L, 6C, 11A, and 11C. These mispredictions in some cases result from the noise character; the model predicts the average noise level as the static offset so noise with complex character in the presence of a static offset can result in a nonstationary prediction (e.g., Fig. 6C). In other cases these mispredictions appear to result from the frequency decomposition as is apparent from the oscillations.

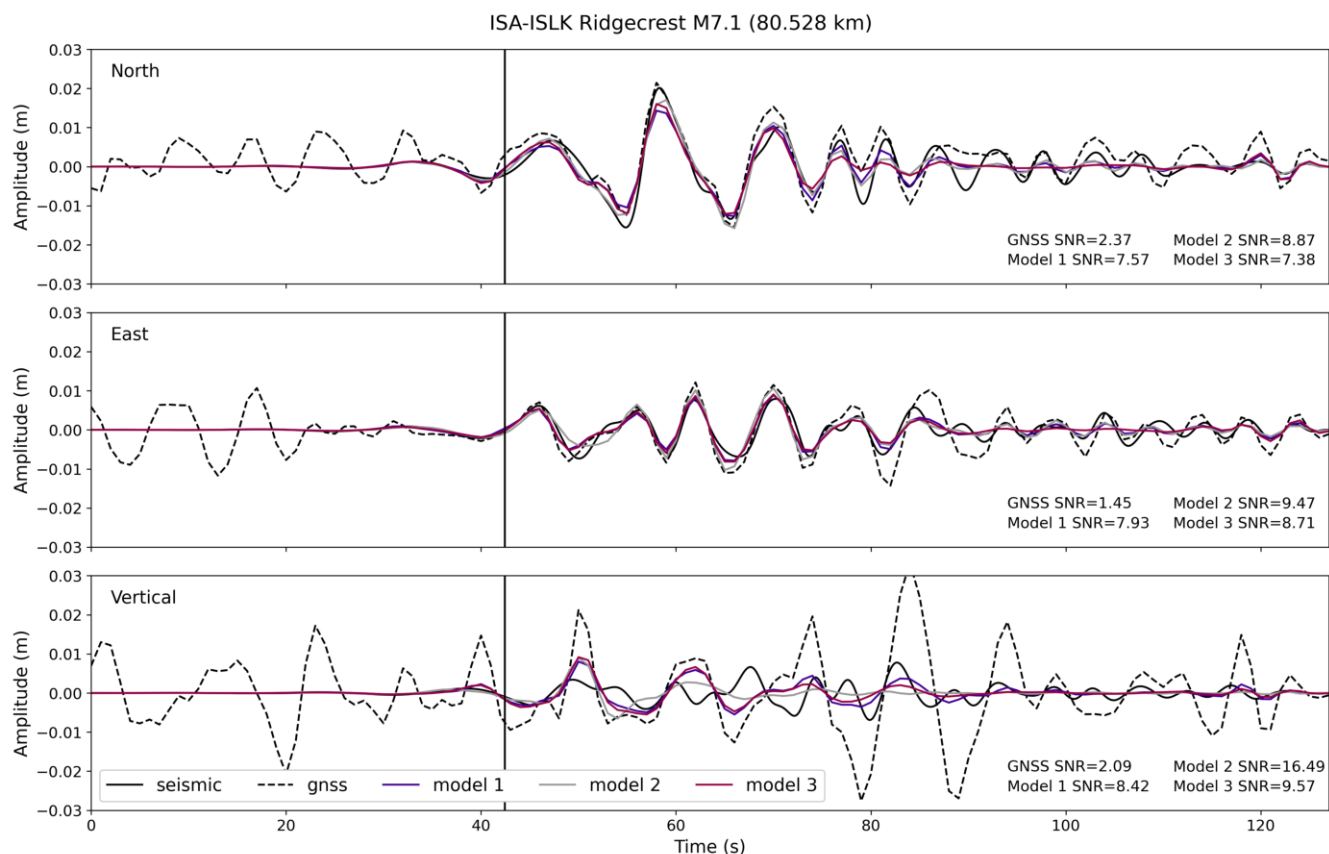


Figure 15 Comparison of recordings of the M7.1 Ridgecrest earthquake at strong motion station ISA and GNSS station ISLK. GNSS and integrated strong motion data are shown as dashed and solid black lines respectively. GNSS records denoised by Models 1, 2, and 3 are shown in blue, grey, and pink respectively. Vertical black line shows the theoretical P-wave arrival time. SNRs of the original HR-GNSS data, Models 1, 2, and 3 are shown in the bottom right.

tions in Fig. 11A and C that are unrelated to noise character and the overshoot in Fig. 11A that is reminiscent of Gibbs phenomenon. In the application of the models to the Ridgecrest data, the main shortcoming of the model was the misprediction of the lower amplitude, later arriving coda. We note that the amplitudes of these arrivals were < 1 cm measured on the horizontal components. This may simply be too low SNR for the model to detect these arrivals. Incorporating more long duration low amplitude data may improve denoising in this scenario.

The single station algorithms we have developed here show promise for denoising HR-GNSS data. However, we made a number of decisions in the process of developing the models that might not make them more generally applicable. First, we utilized noise data from NOTA sites closest to the Ridgecrest earthquakes processed by UNAVCO. GNSS noise is network and processing algorithm dependent. Application to a different location or to a different processing algorithm will require re-training. Second, we simulated earthquakes on predominantly vertically dipping strike-slip faults. The resulting crustal deformation patterns are clearly not representative of earthquakes in other tectonic environments and simulation of such events would be needed for an all-purpose denoiser. Third, by utilizing “Fakequakes” to generate our synthetic earthquake database we make the assumption that the parameterizations and

design choices therein are representative of real earthquakes. Fourth, by utilizing a 1D velocity structure we neglect 3D wave propagation effects. We have attempted to obviate this by including some simulations with soft layers that mimic basin resonance apparent in the two Ridgecrest examples we showed but this is a shortcut that could be improved upon with fully 3D GFs. Finally, we made a number of design choices in the deep learning implementation of denoising that could be improved upon. For example, the frequency decomposition technique may not be the best approach, other architectures may work better than the traditional CNN we employed here, etc.

While we have demonstrated that the models we developed are capable of denoising HR-GNSS data, their main limitation in our opinion, is that they are single station algorithms that do not utilize information from multiple stations. Certain types of GNSS noise, such as common mode errors, are highly correlated on nearby stations. For example, Fig. 16 shows normalized cross-correlations of noise windows prior to the M6.4 Ridgecrest earthquake. The 120s of noise recorded on station P811 prior to the start of the event is cross-correlated with the same time window recorded on nearby stations. CC values between P811 and CCCC (55.5 km) are 0.81. CC values decrease to smaller values of 0.52–0.53 on stations P091 (168 km), ISLK (70.2 km), P595 (82.3 km), and P570 (73.9 km). Developing other

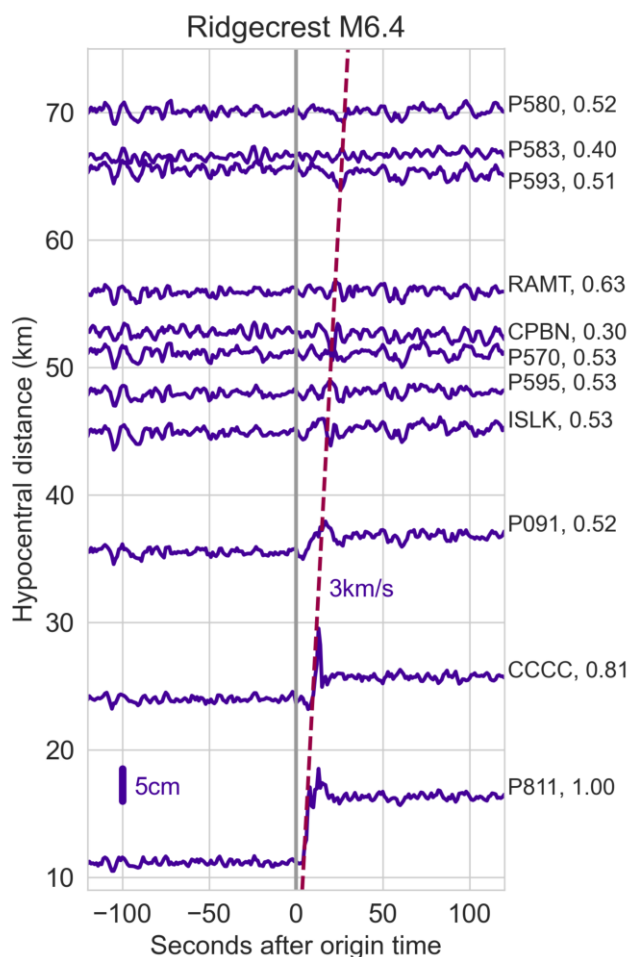


Figure 16 Comparison of recordings of the M6.4 Ridgecrest earthquake (blue timeseries) on stations with hypocentral distances up to 70 km. Noise windows in the 120 s prior to the start time of the M6.4 Ridgecrest earthquake (start time is vertical grey line, moveout is dashed pink line) are cross-correlated with noise recorded on P811. Station names and CC values are annotated on the right.

GNSS denoising algorithms that are network based, include information from many stations, and can leverage the similarity of noise character on nearby stations will undoubtedly be more successful than the single station approach developed here. Such an algorithm would have a number of applications. For example, the identification of small magnitude slip transients that are typically challenging to detect in GNSS data but have limited to no seismic expression (e.g., Rousset et al., 2019), first arrivals of large magnitude earthquakes that, if rapidly identified, decrease the latency of early warning systems (e.g., Lin et al., 2021), and the incorporation of far-field, lower SNR GNSS data to constrain earthquake slip inversions.

5 Conclusions

The goal of this work was to explore the performance of single station, three component denoising algorithms on high-rate GNSS data. Single station denoising algo-

rithms have been developed for seismic records, but their application to GNSS data has not been explored. To this end, we adapted frameworks proposed for denoising seismic data to perform on GNSS data by modifying such algorithms to work on three component data and proposing two additional slightly modified approaches that attempt to overcome amplitude distortion inherent in seismic algorithms. Earthquake metrics derived from HR-GNSS such as PGD rely heavily on signal amplitudes so it's important for any denoising algorithm to preserve amplitude information. After training three machine learning models on synthetic data designed to simulate the 2019 Ridgecrest earthquake sequence, we find that denoising can significantly improve the SNR of HR-GNSS waveforms. The denoised waveforms effectively suppress noise prior to the first arrivals making them more apparent. Additionally, small amplitude signals with SNR at or lower than noise levels can be identified and characterized. Also, because the three models utilize all three components, we are often able to recover much of the signal character on components with low SNR (such as the vertical) by utilizing signal character on the horizontal components. Overall this approach to denoising is promising and if employed in real-time may reduce the latency and improve the accuracy of early warning algorithms.

Acknowledgements

This work used the Python programming language (Van Rossum and Drake Jr, 1995), the Obspy package (Beyreuther et al., 2010; Krischer et al., 2015), Tensorflow (Abadi et al., 2016), and Keras (Chollet, 2015). Figures were made with the Generic Mapping Tools software (Wessel et al., 2019), the matplotlib software package (Hunter, 2007), and Netron for model visualization (<https://github.com/lutzroeder/netron>). This work is supported by NASA Grants 80NSSC19K0360, 80NSSC19K0741, and 80NSSC22K0458.

Data and code availability

GNSS noise data are from NOTA stations, funded by the National Science Foundation and operated by UNAVCO, Inc. Data based on services provided by the GAGE Facility, operated by UNAVCO, Inc. with support from the National Science Foundation and the National Aeronautics and Space Administration under NSF Cooperative Agreement EAR-1724794.

The synthetic records calculated from fakequakes and noise data are available on Zenodo at <https://doi.org/10.5281/zenodo.7075919>. The code used to develop and train the models, and the trained models are available at https://github.com/amtseismo/hrgnss_denoising.

Competing interests

The authors have no competing interests.

References

- Abadi, M., Agarwal, A., Barham, P., Brevdo, E., Chen, Z., Citro, C., and Zheng, X. Tensorflow: Large-scale machine learning on heterogeneous distributed systems. *Preprint*, 2016. doi: 10.48550/arXiv.1603.04467.
- Agarap, A. Deep learning using rectified linear units (ReLU). *Preprint*, 2018. doi: 10.48550/arXiv.1803.08375.
- Beyreuther, M., Barsch, R., Krischer, L., Megies, T., Behr, Y., and Wassermann, J. ObsPy: A Python toolbox for seismology. *Seismological Research Letters*, 81(3):530–533, 2010. doi: 10.1785/gssrl.81.3.530.
- Bock, Y. and Melgar, D. Physical applications of GPS geodesy: A review. *Reports on Progress in Physics*, 79(10):10 1088 0034–4885 79 10 106801, 2016. doi: 10.1088/0034-4885/79/10/106801.
- Choi, K., Bilich, A., Larson, K., and Axelrad, P. Modified sidereal filtering: Implications for high-rate GPS positioning. *Geophysical research letters*, 31(22), 2004. doi: 10.1029/2004GL021621.
- Chollet, F. Keras. <https://github.com/keras-team/keras>. Retrieved from GitHub.
- Crowell, B., Melgar, D., Bock, Y., Haase, J., and Geng, J. Earthquake magnitude scaling using seismogeodetic data. *Geophysical Research Letters*, 40(23):6089–6094, 2013. doi: 10.1002/2013GL058391.
- Dong, D., Fang, P., Bock, Y., Webb, F., Prawirodirdjo, L., Kedar, S., and Jamason, P. Spatiotemporal filtering using principal component analysis and Karhunen-Loeve expansion approaches for regional GPS network analysis. *Journal of geophysical research: solid earth*, 111(B3), 2006. doi: 10.1029/2005JB003806.
- Ende, M., Lior, I., Ampuero, J., Sladen, A., Ferrari, A., and Richard, C. A self-supervised deep learning approach for blind denoising and waveform coherence enhancement in distributed acoustic sensing data. *IEEE Transactions on Neural Networks and Learning Systems*, 2021. doi: 10.1109/TNNLS.2021.3132832.
- Frank, W. Slow slip hidden in the noise: The intermittence of tectonic release. *Geophysical Research Letters*, 43(19):10–125, 2016. doi: 10.1002/2016GL069537.
- Geng, J., Jiang, P., and Liu, J. Integrating GPS with GLONASS for high-rate seismogeodesy. *Geophysical research letters*, 44(7): 3139–3146, 2017. doi: 10.1002/2017GL072808.
- Geng, J., Pan, Y., Li, X., Guo, J., Liu, J., Chen, X., and Zhang, Y. Noise characteristics of high-rate multi-GNSS for subdaily crustal deformation monitoring. *Journal of Geophysical Research: Solid Earth*, 123(2):1987–2002, 2018. doi: 10.1002/2018JB015527.
- Goldberg, D., Melgar, D., Sahakian, V., Thomas, A., Xu, X., Crowell, B., and Geng, J. Complex rupture of an immature fault zone: A simultaneous kinematic model of the 2019 Ridgecrest, CA earthquakes. *Geophysical Research Letters*, 47(3):2019 086382, 2020. doi: 10.1029/2019GL086382.
- Goulet, C., Abrahamson, N., Somerville, P., and Wooddell, K. The SCEC broadband platform validation exercise: Methodology for code validation in the context of seismic-hazard analyses. *Seismological Research Letters*, 86(1):17–26, 2015. doi: 10.1785/0220140104.
- Graves, R. and Pitarka, A. Broadband ground-motion simulation using a hybrid approach. *Bulletin of the Seismological Society of America*, 100(5A):2095–2123, 2010. doi: 10.1785/0120100057.
- Graves, R. and Pitarka, A. Refinements to the Graves and Pitarka (2010) broadband ground-motion simulation method. *Seismological Research Letters*, 86(1):75–80, 2015. doi: 10.1785/0220140101.
- He, X., Hua, X., Yu, K., Xuan, W., Lu, T., Zhang, W., and Chen, X. Accuracy enhancement of GPS time series using principal component analysis and block spatial filtering. *Advances in Space Research*, 55(5):1316–1327, 2015. doi: 10.1016/j.asr.2014.12.016.
- Hodgkinson, K., Mencin, D., Feaux, K., Sievers, C., and Mattioli, G. Evaluation of earthquake magnitude estimation and event detection thresholds for real-time GNSS networks: Examples from recent events captured by the network of the Americas. *Seismological Research Letters*, 91(3):1628–1645, 2020. doi: 10.1785/0220190269.
- Hunter, J. Matplotlib: A 2D Graphics Environment. *Computing in Science and Engineering*, 9(3):90–95,, 2007. doi: 10.1109/M-CSE.2007.55.
- Kingma, D. and Ba, J. Adam: A method for stochastic optimization. *Preprint*, 2014. doi: 10.48550/arXiv.1412.6980.
- Krischer, L., Megies, T., Barsch, R., Beyreuther, M., Lecocq, T., Caudron, C., and Wassermann, J. ObsPy: A bridge for seismology into the scientific Python ecosystem. *Computational Science and Discovery*, 8(1):014003, 2015. doi: 10.1088/1749-4699/8/1/014003.
- Larson, K. Unanticipated uses of the global positioning system. *Annual Review of Earth and Planetary Sciences*, 47:19–40, 2019. doi: 10.1146/annurev-earth-053018-060203.
- Lay, T. A review of the rupture characteristics of the 2011 Tohoku Mw 9.1 earthquake. *Tectonophysics*, 733:4–36, 2018. doi: 10.1016/j.tecto.2017.09.022.
- Li, Y., Xu, C., Yi, L., and Fang, R. A data-driven approach for denoising GNSS position time series. *Journal of Geodesy*, 92:905–922, 2018. doi: 10.1007/s00190-017-1102-2.
- Lin, J., Melgar, D., Thomas, A., and Searcy, J. Early warning for great earthquakes from characterization of crustal deformation patterns with deep learning. *Journal of Geophysical Research: Solid Earth*, 126(10), 2021. doi: 10.1029/2021JB022703.
- Mai, P. and Beroza, G. A spatial random field model to characterize complexity in earthquake slip. *Journal of Geophysical Research: Solid Earth*, 107(B11):–10, 2002. doi: 10.1029/2001JB000588.
- Melbourne, T., Szeliga, W., Marcelo Santillan, V., and Scrivner, C. Global Navigational Satellite System Seismic Monitoring. *Bulletin of the Seismological Society of America*, 111(3):1248–1262, 2021. doi: 10.1785/0120200356.
- Melgar, D. and Hayes, G. The Correlation Lengths and Hypocentral Positions of Great EarthquakesThe Correlation Lengths and Hypocentral Positions of Great Earthquakes. *Bulletin of the Seismological Society of America*, 109(6):2582–2593, 2019. doi: 10.1002/2016JB013314.
- Melgar, D., Bock, Y., Sanchez, D., and Crowell, B. On robust and reliable automated baseline corrections for strong motion seismology. *Journal of Geophysical Research: Solid Earth*, 118(3): 1177–1187, 2013. doi: 10.1002/jgrb.50135.
- Melgar, D., Crowell, B., Geng, J., Allen, R., Bock, Y., Riquelme, S., and Ganas, A. Earthquake magnitude calculation without saturation from the scaling of peak ground displacement. *Geophysical Research Letters*, 42(13):5197–5205, 2015. doi: 10.1002/2015GL064278.
- Melgar, D., LeVeque, R., Dreger, D., and Allen, R. Kinematic rupture scenarios and synthetic displacement data: An example application to the Cascadia subduction zone. *Journal of Geophysical Research: Solid Earth*, 121(9):6658–6674, 2016. doi: 10.1002/2016JB013314.
- Melgar, D., Crowell, B., Melbourne, T., Szeliga, W., Santillan, M., and Scrivner, C. Noise characteristics of operational real-time high-rate GNSS positions in a large aperture network. *Journal of Geophysical Research: Solid Earth*, 125(7):2019 019197, 2020. doi: 10.1029/2019JB019197.
- Murray, J., Crowell, B., Grapenthin, R., Hodgkinson, K., Langbein,

- J., Melbourne, T., and Schmidt, D. Development of a geodetic component for the US West Coast earthquake early warning system. *Seismological Research Letters*, 89(6):2322–2336, 2018. doi: 10.1785/0220180162.
- Ronneberger, O., Fischer, P., and Brox, T. U-Net: Convolutional networks for biomedical image segmentation. In *International Conference on Medical image computing and computer-assisted intervention*, page 234–241, Cham, 2015. Springer. doi: 10.1007/978-3-319-24574-4_28.
- Ross, Z., Idini, B., Jia, Z., Stephenson, O., Zhong, M., Wang, X., and Jung, J. Hierarchical interlocked orthogonal faulting in the 2019 Ridgecrest earthquake sequence. *Science*, 366(6463):346–351, 2019. doi: 10.1126/science.aaz0109.
- Rousset, B., Bürgmann, R., and Campillo, M. Slow slip events in the roots of the San Andreas fault. *Science advances*, 5(2), 2019. doi: 10.1126/sciadv.aav3274.
- Satake, K. and Heidarzadeh, M. A review of source models of the 2015 Illapel, Chile earthquake and insights from tsunami data. *Pure and Applied Geophysics*, 174(1):1–9, 2017. doi: 10.1007/978-3-319-57822-4_1.
- Shelly, D. A high-resolution seismic catalog for the initial 2019 Ridgecrest earthquake sequence: Foreshocks, aftershocks, and faulting complexity. *Seismological Research Letters*, 91(4):1971–1978, 2020. doi: 10.1785/0220190309.
- Thomas, A., Beroza, G., and Shelly, D. Constraints on the source parameters of low-frequency earthquakes on the San Andreas Fault. *Geophysical Research Letters*, 43(4):1464–1471, 2016. doi: 10.1002/2015GL067173.
- Thomas, A., Inbal, A., Searcy, J., Shelly, D., and Bürgmann, R. Identification of Low-Frequency Earthquakes on the San Andreas Fault With Deep Learning. *Geophysical Research Letters*, 48(13):2021093157, 2021. doi: 10.1029/2021GL093157.
- Tibi, R., Hammond, P., Brogan, R., Young, C., and Koper, K. Deep learning denoising applied to regional distance seismic data in Utah. *Bulletin of the Seismological Society of America*, 111(2):775–790, 2021. doi: 10.1785/0120200292.
- Trugman, D., Page, M., Minson, S., and Cochran, E. Peak ground displacement saturates exactly when expected: Implications for earthquake early warning. *Journal of Geophysical Research: Solid Earth*, 124(5):4642–4653, 2019. doi: 10.1029/2018JB017093.
- Van Rossum, G. and Drake Jr, F. L. *Python reference manual*. Centrum voor Wiskunde en Informatica Amsterdam, 1995. <https://www.narcis.nl/publication/RecordID/oai%3Acwi.nl%3A5008>.
- Wdowinski, S., Bock, Y., Zhang, J., Fang, P., and Genrich, J. Southern California permanent GPS geodetic array: Spatial filtering of daily positions for estimating coseismic and postseismic displacements induced by the 1992 Landers earthquake. *Journal of Geophysical Research: Solid Earth*, 102(B8):18057–18070, 1997. doi: 10.1029/97JB01378.
- Wessel, P., Luis, J., Uieda, L., Scharroo, R., Wobbe, F., Smith, W., and Tian, D. The Generic Mapping Tools version 6. *Geochimistry, Geophysics, Geosystems*, 20:5556–5564, 2019. doi: 10.1029/2019GC008515.
- Williamson, A., Melgar, D., Crowell, B., Arcas, D., Melbourne, T., Wei, Y., and Kwong, K. Toward near-field tsunami forecasting along the Cascadia subduction zone using rapid GNSS source models. *Journal of Geophysical Research: Solid Earth*, 125(8):202019636, 2020. doi: 10.1029/2020JB019636.
- Zhu, L. and Rivera, L. A note on the dynamic and static displacements from a point source in multilayered media. *Geophysical Journal International*, 148(3):619–627, 2002. doi: 10.1046/j.1365-246X.2002.01610.x.
- Zhu, W. and Beroza, G. PhaseNet: a deep-neural-network-based seismic arrival-time picking method. *Geophysical Journal International*, 216(1):261–273, 2019. doi: 10.1093/gji/ggy423.
- Zhu, W., Mousavi, S., and Beroza, G. Seismic signal denoising and decomposition using deep neural networks. *IEEE Transactions on Geoscience and Remote Sensing*, 57(11):9476–9488, 2019. doi: 10.1109/TGRS.2019.2926772.

The article **Deep learning for denoising High-Rate Global Navigation Satellite System data** © 2023 by A.is licensed under CC BY 4.0.

Validation of Peak Ground Velocities Recorded on Very-high rate GNSS Against NGA-West2 Ground Motion Models

Brendan W. Crowell  * ¹, Jensen V. DeGrande  ¹, Timothy Dittmann  ², Jessica N. Ghent  ¹

¹Department of Earth and Space Sciences, University of Washington, Seattle, USA, ²UNAVCO, Inc., Boulder, USA

Author contributions: *Conceptualization:* B. W. Crowell, J. V. DeGrande. *Methodology:* B. W. Crowell, J. V. DeGrande, T. Dittmann. *Software:* B. W. Crowell, T. Dittmann, J. N. Ghent. *Validation:* B. W. Crowell, J. V. DeGrande. *Formal Analysis:* B. W. Crowell, J. V. DeGrande, T. Dittmann. *Writing - original draft:* B. W. Crowell. *Writing - Review & Editing:* B. W. Crowell, J. V. DeGrande, T. Dittmann, J. N. Ghent. *Supervision:* B. W. Crowell. *Project administration:* B. W. Crowell. *Funding acquisition:* B. W. Crowell.

Abstract Observations of strong ground motion during large earthquakes are generally made with strong-motion accelerometers. These observations have a critical role in early warning systems, seismic engineering, source physics studies, basin and site amplification, and macroseismic intensity estimation. In this manuscript, we present a new observation of strong ground motion made with very high rate (≥ 5 Hz) Global Navigation Satellite System (GNSS) derived velocities. We demonstrate that velocity observations recorded on GNSS instruments are consistent with existing ground motion models and macroseismic intensity observations. We find that the ground motion predictions using existing NGA-West2 models match our observed peak ground velocities with a median log total residual of 0.03-0.33 and standard deviation of 0.72-0.79, and are statistically significant following normality testing. We finish by deriving a Ground Motion Model for peak ground velocity from GNSS and find a total residual standard deviation 0.58, which can be improved by $\sim 2\%$ when considering a simple correction for V_{s30} .

Non-technical summary Traditionally, scientists will study the shaking due to earthquakes using seismometers that record either acceleration or velocity. They will use recordings from real earthquakes to derive a relationship that predicts the amount of shaking one would expect at a location based on different properties of the earthquake such as the magnitude, distance to the event, and the types of rock or soil at a location. In this study, we determine the peak levels of shaking from Global Navigation Satellite System (GNSS) data, otherwise known as GPS. GNSS usually gives you the position or displacement at a given location, but we process this data slightly differently to give us observations of velocity. We compare the GNSS velocity observations to the well known relationships for ground motion prediction that were determined with only seismometers and find good agreement with our dataset. This is especially useful since GNSS can directly record the velocity of shaking, which is currently difficult with seismometers undergoing strong shaking.

1 Introduction

Ground motion models (GMMs), traditionally known as ground motion prediction equations (GMPEs), are empirical relationships between an earthquake source and the ground motion expected at a station. GMMs will commonly incorporate magnitude, distance attenuation, site amplification terms, and source terms to determine the peak ground accelerations, velocities, displacements, and spectral accelerations/displacements at different periods (PGA, PGV, PGD, and SA/SD, respectively). The coefficients in GMMs are determined empirically using observations from real earthquakes on strong-motion accelerometers or broadband seismometers if they are unclipped. GMMs are utilized in engineering seismology for building code design (Bommer et al., 2010; Katsanos et al., 2010), in ShakeMap and PAGER (Prompt Assessment of Global Earthquakes for Response) generation for rapid assessment of

impact and ground motions after large earthquakes (Wald et al., 1999; Allen et al., 2009), in paleoseismic studies (Rasanen et al., 2021), and in earthquake early warning systems (Allen and Melgar, 2019; Meier, 2017; Thakoor et al., 2019). Many GMMs are derived for specific regions where epistemic uncertainties may be consistent across the region, but some use generalized global datasets or only include one style of faulting. Each GMM will have a parametric specific range in which the model is valid, i.e. a distance or magnitude limit, and most generally do not include very large magnitude events or far-field observations. There is also a question of whether or not PGV observations for large ground motions recorded with inertial sensors are recording the true ground motions due to sensor rotations and tilts (Boore et al., 2002; Clinton, 2004). In this study, we provide a new observation which can faithfully record high PGV, Global Navigation Satellite System (GNSS) derived velocities.

Production Editor:
Gareth Funning
Handling Editor:
Carmine Galasso
Copy & Layout Editor:
Cláudia Reis

Received:
September 9, 2022
Accepted:
February 2, 2023
Published:
March 1, 2023

*Corresponding author: crowellb@uw.edu

For earthquake and tsunami early warning systems, the importance of GNSS displacements for large earthquake characterization has been demonstrated (Crowell et al., 2009, 2012, 2016; Blewitt et al., 2006; Grapenthin et al., 2014; Minson et al., 2014; Murray et al., 2018; Williamson et al., 2020). The addition of this data is critical to properly characterizing the impacts of large earthquakes ($M > 7$) where traditional seismic methods begin to saturate (Melgar et al., 2013a). GNSS displacements do not saturate since they are computed in a non-inertial reference frame, that of the fixed center of the Earth. The GNSS observations capture both the coseismic static offsets, important for understanding moment release and total slip, and dynamic motions, which can be leveraged for rapid magnitude determination and kinematic inversions. However, issues with phase ambiguity fixing, cycle slips, and loss of satellite lock can lead to large errors that obscure ground displacements when computing GNSS displacements in real-time. These processing issues can lead to displacement excursions of many meters, a major problem for real-time analysis in early warning systems. GNSS displacements are also noisier than seismic observations due to path errors between the satellites and receivers, most notably the tropospheric and ionospheric delays (Melgar et al., 2020). One potential solution is to compute velocities rather than displacements at the GNSS stations. This approach is commonly referred to as the ‘variometric approach’, and it consists of performing a single difference in time between satellite orbital positions and the raw GNSS phase observables (Colosimo et al., 2011; Benedetti et al., 2014; Geng et al., 2016; Grapenthin et al., 2018; Shu et al., 2018; Crowell, 2021). The variometric approach is more sensitive to smaller magnitude ground motions and when integrated into displacement, leads to lower noise than traditional positioning since the various errors in real-time positioning do not change appreciably over short time periods (Shu et al., 2018; Dittmann et al., 2022a); in this study, we will show that GNSS velocities can be resolved for earthquakes as low as M4.9 in the near-field (< 25 km), over a full magnitude unit less than what is possible with real-time GNSS displacements (Melgar et al., 2020; Goldberg et al., 2021).

In this manuscript, we first describe how the full GNSS velocity dataset, spanning a magnitude range from 4.9-9.1, is generated and provide statistics of the data. Next, we use 3 NGA-West2 GMMs and published finite fault models where available to predict ground motions for all station-event pairs and compare the predictions against our peak ground velocity observations. We also look at the statistics for specific earthquakes and conditions, and test for normality in the residuals using a Lilliefors test. Finally, we generate a GMM with magnitude and distance scaling terms and solve for the coefficients using two different distance measures.

2 Data and Processing Methods

The variometric approach for geophysical applications was first presented by Colosimo et al. (2011) for geo-

physical applications. In this method, a single time difference is performed on the GNSS phase observables and on the orbital positions. For a single frequency, L_1 , and satellite, s , the simplified variometric observation equation is at a receiver, r ,

$$\Delta L_{1,s,r} = \Delta \rho_{s,r} + c(\Delta \tau_r - \Delta \tau_s) + \Delta T_{s,r} - \Delta I_{1,s,r} + \Delta M_{s,r} + \Delta B_{1,s,r} + \Delta e_{1,s,r} \quad (1)$$

where $\rho_{s,r}$ is the range between satellite and receiver, c is the speed of light, τ_r and τ_s are the receiver and satellite clock biases respectively, $T_{s,r}$ is the tropospheric component between satellite and receiver, $I_{1,s,r}$ is the ionospheric delay on the L_1 frequency between satellite and receiver, $M_{1,s,r}$ is the L_1 multipath component for a given satellite and receiver, $B_{1,s,r}$ is the ambiguity term on the L_1 frequency for a given satellite and receiver, and $e_{1,s,r}$ are any uncharacterized noise sources at the L_1 frequency. The Δ indicates that we are taking a difference between the observations at the current time, t , and the observations at the prior time step, $t-1$. Within Equation 1, many of the terms drop out as they typically do not appreciably change over small time periods, notably the multipath, the satellite clock errors, the troposphere, the ionosphere, and the fractional cycle and integer ambiguities, assuming no cycle slips are present. Receiver clock drifts do need to be solved since the drift rate can exceed the nanosecond per second level, which would equate to tens of centimeters per second.

To solve for receiver velocities, we use the SNIVEL (Satellite Navigation derived Instantaneous Velocities; Crowell (2021)) software package, which currently only uses the Global Positioning System (GPS). SNIVEL forms the narrow-lane (NL) combination of L_1 and L_2 , which is defined as

$$NL = \frac{f_{L1}}{(f_{L1} + f_{L2})} L_1 + \frac{f_{L2}}{(f_{L1} + f_{L2})} L_2 \quad (2)$$

$$= 0.56 * L_1 + 0.44 * L_2$$

where f_{L1} and f_{L2} are the frequencies of the L_1 and L_2 bands, 1575.42 MHz and 1227.60 MHz, respectively. The narrow-lane combination has an effective wavelength of 10.7 cm, which is less than the wavelengths of L_1 (19.0 cm) or L_2 (24.4 cm) alone, which slightly reduces the noise on the derived velocities. For determining the orbital velocities, we use the GPS broadcast orbits, which are well modeled and readily available in real-time. To solve for receiver velocity, the basic observation equation in Equation 1 is Taylor expanded about the range, ρ , which allows for the generation of a design matrix based upon the direction cosines between satellite and receiver. We then set up the following linear observation model at a given receiver for n satellites:

$$\begin{bmatrix} \Delta NL_{s1} - \Delta \rho_{s1} + c\Delta \tau_{s1} - \Delta T_{s1} + \Delta I_{s1} \\ \vdots \\ \Delta NL_{sn} - \Delta \rho_{sn} + c\Delta \tau_{sn} - \Delta T_{sn} + \Delta I_{sn} \end{bmatrix} = \begin{bmatrix} \frac{x_{s1} - x_r}{\rho_{s1}} & \frac{y_{s1} - y_r}{\rho_{s1}} & \frac{z_{s1} - z_r}{\rho_{s1}} & 1 \\ \vdots & \vdots & \vdots & \vdots \\ \frac{x_{sn} - x_r}{\rho_{sn}} & \frac{y_{sn} - y_r}{\rho_{sn}} & \frac{z_{sn} - z_r}{\rho_{sn}} & 1 \end{bmatrix} \begin{bmatrix} v_x(t) \\ v_y(t) \\ v_z(t) \\ \Delta \tau_r(t) \end{bmatrix} \quad (3)$$

where $x_{s,r}$, $y_{s,r}$, and $z_{s,r}$ are the Cartesian coordinates of the satellite and receiver, and v is the velocity of the receiver. We make two simple phase corrections to account for subtle atmospheric signal path variations using the readily available in real-time hydrostatic tropospheric correction of Niell (Niell, 1996) and the Klobuchar ionospheric correction (Klobuchar, 1987). The velocities and clock drift rate can be solved through ordinary least squares. We additionally weight the least squares problem through a diagonal matrix of elevation angle between satellite and receiver since lower elevation observations will have more noise.

2.1 SNIVEL Dataset

The data that we used was recorded by six networks (number of earthquakes followed by observations in parentheses), the Plate Boundary Observatory (27; 178), COCONet (10; 46), TLALOCnet (5; 27), Geonet New Zealand (9; 158), the TU-CWU (Tribhuvan University - Central Washington University) network in Nepal (4; 29), and the Italian RING network (6; 71). A map view of the distribution of events is shown in Figure 1. The first three networks were historically separate, however, they now comprise the federated Network of the Americas (NOTA) and their data is archived at UNAVCO (Murray et al., 2019). Since 2007, the standard practice at UNAVCO has been to download any available 5 Hz GNSS data within a given radius after a significant event within North and Central America. The earliest NOTA-recorded earthquake we include in this study is the 2009 Mw 7.3 Honduras earthquake. Geonet, operated by the Institute of Geological and Nuclear Sciences (GNS), has downloaded 10 Hz raw GNSS data after significant events since 2013. The 2016 Mw 7.8 Kaikoura earthquake is the best recorded event in our dataset, with 122 observations and PGV values greater than 40 cm/s at 8 sites and greater than 95 cm/s at 2 sites. The TU-CWU network was able to record at 5 Hz the 2015 Mw 7.8 Gorkha earthquake in Nepal, the Mw 7.3 aftershock two weeks later and two additional aftershocks. Three of the sites during the Gorkha earthquake exceeded 50 cm/s. The RING network operated by Istituto Nazionale di Geofisica e Vulcanologia (INGV) consolidated data from several smaller networks within Italy (ISPRA, DPC, Regione Lazio, Regione Abruzzo, Leica ITALPOS, and Topcon NETGEO) and recorded most stations at 10 Hz and several at 20 Hz for events during the Amatrice-Norcia sequence in 2016 and the Emilia-Romagna sequence in 2012. A 20 Hz recording at station ARQT during the October 30, 2016 Mw 6.6 Amatrice earthquake exceeded 100 cm/s and 5 additional stations exceeded 30 cm/s. In total, we have 509 observations from 61 earthquakes ranging in magnitude from 4.9 to 8.2. Figure 2 shows the distribution of these observations as a function of rupture distance and an overview of all the events with the PGV values at every station is provided (see Data Availability).

We low pass filter all of the waveforms to one-quarter of the sampling rate, 1.25 Hz for the 5 Hz observations, 2.5 Hz for the 10 Hz observations, and 5 Hz for the 20 Hz observations using a 4-pole zero-phase Butterworth

filter. All waveforms are visually inspected to ensure the peak velocity is related to shaking rather than noise. We do find that for the lower magnitude events ($M < 6$), the low pass filtering of the waveforms does reduce the peak velocity values, which is predicted when looking at the corner frequency dependence on magnitude (e.g., Joyner, 1984). When using an average stress drop of 30 bars and a shear wave velocity of 3 km/s, the corner frequency of a M5 earthquake would be roughly 0.6 Hz. This value drops precipitously, and by M8, the corner frequency is roughly 0.02 Hz. For consistency, we retain the low pass filtering as we find it beneficial to reduce the high frequency noise within the GNSS velocities as they are plagued by higher order wet tropospheric, ionospheric, and multipath noise. The peak value of each component is taken separately and the station PGV value is the maximum of the three individual components (north, east, or vertical); note that this is the same approach taken by the GMMs. For smaller levels of shaking, the vertical component was unable to record any ground motion and these observations are excluded from our dataset (the vertical component is on average 3-5 times noisier than the horizontal components). Figure 2 shows the PGV values versus mean rupture distance for the entire dataset.

2.2 Seismogeodetic Dataset

In addition to the SNIVEL dataset, we include observations from two earthquakes that were processed through a multi-rate Kalman filter, the 2011 M9.1 Tohoku-oki and 2003 M8.2 Tokachi-oki earthquakes in Japan on the Geonet network operated by GSI (Crowell et al., 2009; Bock et al., 2011; Melgar et al., 2013b). For both of these earthquakes, 1-Hz GNSS displacements were computed and then Kalman filtered with collocated strong-motion accelerometer data from either K-NET or Kik-net. Since this dataset includes a combination of both seismic and geodetic data, it is termed 'seismogeodetic' herein. The Kalman filter effectively integrates the accelerometer under the displacement constraint of the GNSS and produces both velocity and displacement waveforms at the sampling rate of the accelerometer. Melgar et al. (2013a) showed that this method was better able to reconcile ground motions in the low frequency end than simply integrating accelerometer data. In total, 174 observations for the two Japanese events at 100 Hz are included. Similarly to the SNIVEL dataset, we low-pass filter the velocity observations to 25 Hz.

2.3 Ground Motion Models Used

We use three of the NGA-West2 (Next Generation Attenuation for Western United States, 2.0) ground motion models (GMM) to compare our observed PGV values: Chiou and Youngs (2014), Boore et al. (2014), and Campbell and Bozorgnia (2014), herein referred to as CY14, BSSA14, and CB14 respectively. The NGA-West2 database consists of events between magnitudes of 3 and 7.9, and most of its observations are between 0 and 400 km (Bozorgnia et al., 2014). The distance distribution between our dataset and NGA-West2 is comparable,

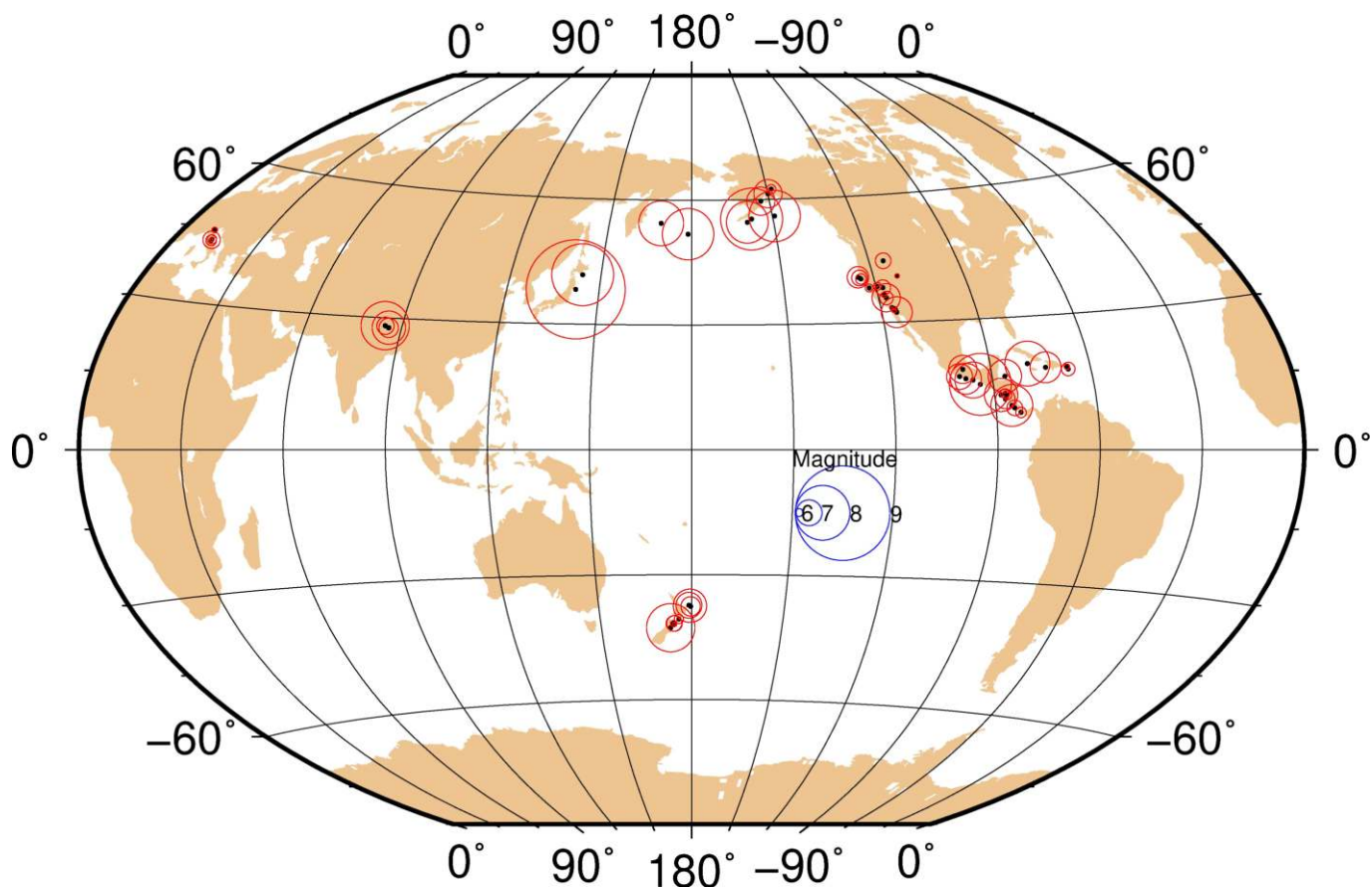


Figure 1 Map view of all earthquakes in this study. The solid black circles are the epicentral locations of the earthquakes and the red circles are sized by magnitude.

although we are more skewed towards the larger magnitude end since velocities cannot be recorded on GNSS instruments well below M5.5 (Figure 2). We include observations out to rupture distances of ~ 800 km.

For events that we do not have slip models for, we treat them as point sources, otherwise we use the complete distance descriptions within the GMMs. The slip models we use are the National Earthquake Information Center (NEIC) official finite fault models (e.g., Hayes, 2017) which we extract directly from the geoJSON files provided on the USGS event overview pages (e.g., <https://earthquake.usgs.gov/earthquakes/eventpage/ci38457511/finite-fault>). Between the different GMMs, there are 5 different distance measurements: Joyner-Boore distance (R_{jb}), rupture distance (R_{rup}), distance to the surface projection of the updip edge (R_x), depth to the updip edge of the rupture (Z_{tor}), and hypocentral depth. When treating the earthquake as a point source, R_{rup} is the hypocentral distance, R_{jb} and R_x are the epicentral distance, and Z_{tor} is the hypocentral depth. We also use the mean rupture distance (R_p) proposed by Thompson and Baltay (2018), which replaces the traditional rupture distance, R_{rup} , with a slip scaled distance to account for the heterogeneity in slip distributions. For R_p , we use a value of $p = -2.0$ for the power law weighting, which is the optimal value for PGV (Thompson and Baltay, 2018). While we make this correction, we do note that none of the GMMs were validated using mean rupture distance and we are simply using it as an additional comparison. We

use the USGS global VS30 database to approximate the shear wave velocity in the upper 30 meters (Heath et al., 2020). Also, for basin terms ($Z_{1.0}$ and $Z_{2.5}$), we use the equations within the GMMs that relate VS30 to the basin terms. We disregard any hanging wall, directivity, and dip dependent terms within all of the GMMs for simplicity.

3 Results

The log residual between the GMM prediction and the observed PGV values, $\ln(PGV_{GMM}) - \ln(PGV_{GNSS})$, are shown as a function of mean rupture distance, R_p , for the three GMMs in Figure 3. Table 1 shows the median and standard deviations for a number of scenarios using both R_p and R_{rup} (note that BSSA14 has the same performance for R_{rup} and R_p since it only uses R_{jb}). For comparison, the self-reported total residual standard deviation for the three NGA-West2 GMMs are 0.65, 0.54, and 0.58 for BSSA14, CY14, and CB14 respectively. For all three GMMs, the histograms of the log residuals are tightly distributed about zero. There are however differences between the three GMMs, mainly in the performance for the Kaikoura earthquake (grey shaded histograms on Figure 3). All three GMMs underestimate the observed PGV values for the Kaikoura earthquake, with BSSA14 performing the worst with a median residual of -1.29, and CY14 (median residual -0.45) performing slightly better than CB14 (median residual -0.73) when using R_{rup} . Part of the underesti-

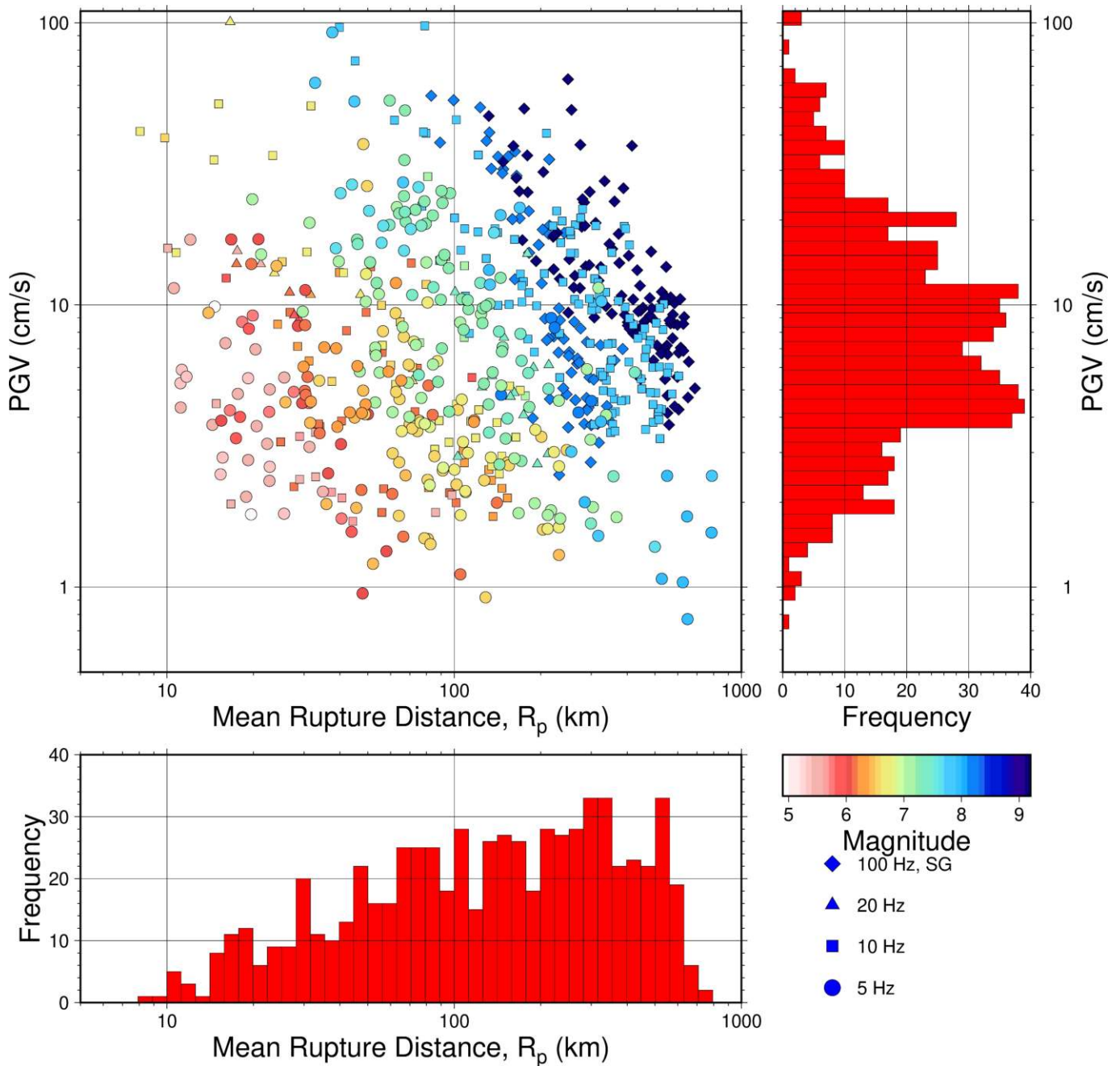


Figure 2 Distribution of GNSS velocity data used in this study. The upper left panel shows the PGV values versus the mean rupture distance, in log-log space. The mean rupture distance is defined in Thompson and Baltay (2018), and we use $p = -2$ here. The different symbols signify the sampling rate of the data. The histogram on the right shows the frequency of PGV observations. The histogram on the bottom shows the frequency of the mean rupture distance.

mate for the Kaikoura earthquake is due to the strong northward directivity and the complexity of the rupture onto more than a dozen crustal faults (Hamling et al., 2017). The log residual using R_{rup} for Kaikoura is better than R_p primarily due to the shorter rupture distances making up for the impacts of directivity and shallow slip. When the Kaikoura earthquake is removed from the dataset, the log residual standard deviation dropped considerably, down to 0.61-0.67 when using R_p . For BSSA14, the performance appreciably changes when removing Kaikoura, with it performing better than any of the other GMMs using R_{rup} , which is unsurprising given the wide distribution of residuals shown in Figure 3b. No other event in the dataset has such a strong negative

residual between the recorded ground motions and the GMMs. Surprisingly, all three GMMs model the Tohoku-oki earthquake well, with most stations showing a residual less than 1 log unit even though none of the GMMs used ground motion data for events greater than Mw 8. We postulate that the rather compact nature of the Tohoku-oki rupture coupled with the further distances to stations allows for the GMMs to predict PGV well.

For all three of the GMMs, there is a slight underestimation of ground motions at further distances (> 400 km). This is unsurprising as this distance is outside the specified distance range for the GMMs. When we exclude stations further than 400 km, there is an improvement for BSSA14 and CB14, but no change for

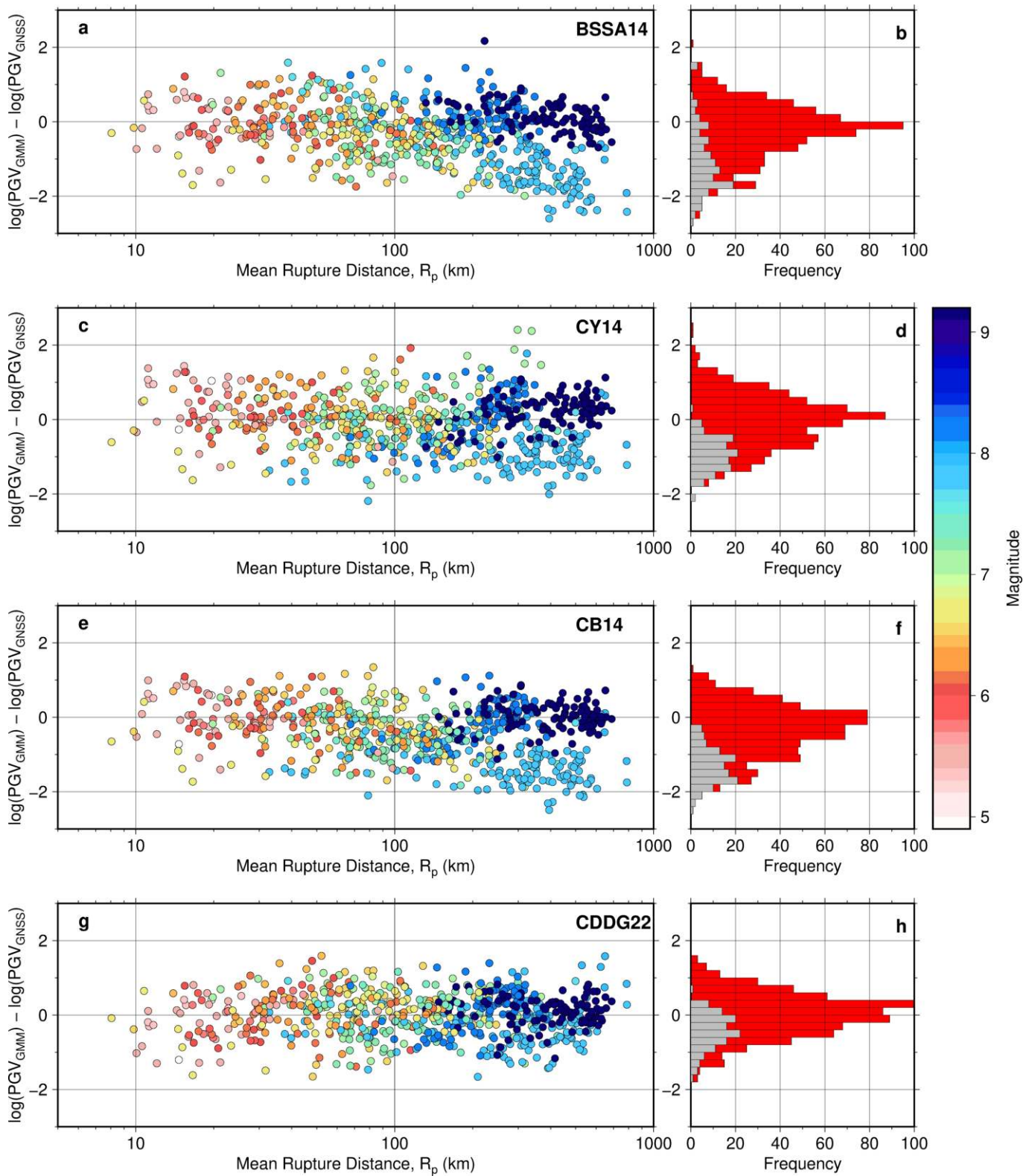


Figure 3 The log-residual between PGV from the GMMs and GNSS. Panels a, c, e, and g show the residuals as a function of mean rupture distance for GMMs BSSA14, CY14, CB14, and CDDG22 (this study) respectively. Panels b, d, f, and h show the histograms of the residuals for the GMMs to their left for all observations. On the histograms, the smaller grey bars in the foreground show the distribution for the 2016 Mw 7.8 Kaikoura earthquake.

CY14, indicating the CY14 is more sensitive to further rupture distances than the self-reported model limit of $R_{rup} < 300$ km. We also computed statistics for two additional event subsets: subduction zone events and non-subduction events (minus Kaikoura). None of the three GMMs were not directly developed for the subduc-

tion environment, so it is important to understand any systematic biases that may arise due to the tectonic environment. When discounting Kaikoura, there are 268 observations of subduction earthquakes and 293 observations from primarily strike-slip faults. When using R_p , the median residuals for the non-subduction events

were all negative, indicating the GMMs are underestimating ground motions. For the subduction events, the standard deviations were all lower than the non-subduction events, and the median residuals were better for BSSA14 and CB14. This result is somewhat paradoxical in that the GMMs we are comparing against in this study were developed primarily for upper-crustal faults, so a better fit for those events would be expected, however, the shallower events will have far more variability with regards to source terms, distance measurements, and directivity such that a greater variability in the ground motion residuals would be observed. For subduction events, the source distances are generally greater so much of the GMM complexity can be averaged out. We would expect even better fits by using subduction zone specific GMMs (e.g., Parker et al. (2022)).

3.1 Normality Testing

While the distribution of results and statistics shown in Figure 3 and Table 1 are indicative of reasonable model and observation agreement, we test the null hypothesis that the log residuals of the GMMs are drawn from a normal distribution. In order to do this, we perform a Lilliefors test, which is similar to a Kolmogorov-Smirnov test except the data is allowed to be from any generalized normal distribution and the test statistic is more stringent (Lilliefors, 1967). The null hypothesis for the test is the log residuals are drawn from a normal distribution. For this test we choose a significance level of 0.05, which the p-value needs to be larger than, and the test statistic needs to be smaller than the critical value for the number of data points in the test. While there is no requirement that our data residuals be normally distributed, it does lead to higher confidence that any variations between our data and the GMMs are due to random Gaussian noise and not due to biases in the observations or GMMs. For 683 observation points, the Lilliefors test statistic critical value is 0.035. Of the GMMs tested, only CY14 passes the Lilliefors test and cannot reject the null hypothesis, with a p-value of 0.14 and a test statistic of 0.032. This is further illustrated when looking at the Quantile-Quantile (Q-Q) plots in Figure 4, where the theoretical quantiles, those drawn from a normal distribution, are plotted against the data/sample quantiles. While near the centers of the theoretical quantiles, both CB14 and BSSA14 perform well, at the edges there are considerable outliers. The Q-Q plot for CY14 is good out to 2.5 quantiles. From these results, we can confidently say that the GNSS velocities can be represented well by CY14 at a random normal level.

3.2 Noise Characteristics of GNSS Velocities

To characterize the relative noise levels on the GNSS velocities, we processed 30 minutes of data at station ARQT in the Italian RING network at 1, 5, 10, and 20 Hz on day 300 of 2016, between the M5.5 and M6.1 Norcia earthquakes. Table 2 shows the standard deviations for the three components of motion at the 4 sampling rates. Along all three components of motion, the standard deviation increases with higher sample rates, which has

been shown in other studies (e.g., Shu et al., 2018), and the vertical component is roughly twice as large as the horizontal components; also, there is a strong autocorrelation of noise between the components and a regional correlation of noise due to the similar constellation geometries. The reason behind this is the errors in the orbits, multipath, and clocks are fairly constant at high frequency, but we are taking incrementally smaller and smaller time steps, which to first order, leads to an increase in noise. When looking at the power spectral content at these sample rates (Figure 5), we see that the noise behavior is more complex. We see between periods of 0.3 and 2 s that the power is progressively smaller for higher sample rates, however, there is an increase in power for smaller periods until the noise becomes roughly white below 0.25 s. Since for higher sampling rates, the data is in the higher frequency, higher noise part of the spectrum, the standard deviations are higher, but the higher sampling rates reduce the noise at given periods due to reducing the higher order noise in the GNSS observation model. This would indicate that it is beneficial to sample GNSS velocities at the highest possible sample rate, but then re-sample the data to 5-10 Hz, or wherever temporal aliasing will be minimized based upon the frequency content of the earthquake (e.g., Joyner, 1984). Indeed, Table 2 shows that when we re-sample the 20 Hz phase observations to 5 Hz and process through SNIVEL, we obtain a standard deviation of roughly half that obtained by processing the data directly at 5 Hz.

4 Ground Motion Model Development

We developed a preliminary GMM (herein referred to as CDDG22) using the same formalism as in Thompson and Baltay (2018) and Goldberg et al. (2021) where we only consider magnitude scaling (F_M) and distance-scaling (F_R) terms such that

$$\ln(PGV) = c_o + F_M + F_R \quad (4)$$

The distance-scaling term is separated into an anelastic attenuation term (c_{R2}) and a geometrical spreading/magnitude-dependent attenuation term ($c_{R0} + c_{R1}M$)

$$F_R = (c_{R0} + c_{R1}M)\ln(R) + c_{R2}R \quad (5)$$

The magnitude-scaling term roughly follows the form of Chiou and Youngs (2014), however we use the expression directly from Goldberg et al. (2021) that is simplified to ignore small magnitude terms

$$F_M = c_{M1}M + c_{M2}\ln(1 + \exp(-M)) \quad (6)$$

The coefficients in Equations 4-6 are solved through a least-squares regression and can be found in Table 3. We test two different distance measures for R: R_p and R_{rup} . Figure 3 shows the log-residual plots of our GMM using R_p and the observed GNSS PGV values. The standard deviation is 0.58 and 0.59 using R_p and R_{rup} respectively, and the residuals are much more tightly distributed about zero. We also do not see any appreciably anomalous earthquakes like Kaikoura when using the

GMM	Event Subset	Median Residual, R_p	σ , R_p	Median Residual, R_{rup}	σ , R_{rup}
BSSA14	All	-0.212	0.792	-0.212	0.792
CB14	All	-0.330	0.721	-0.029	0.794
CY14	All	-0.050	0.735	0.153	0.738
BSSA14	dist <= 400 km	-0.189	0.737	-0.189	0.737
CB14	dist <= 400 km	-0.342	0.696	-0.048	0.741
CY14	dist <= 400 km	-0.057	0.736	0.114	0.711
BSSA14	exclude Kaikoura	-0.110	0.674	-0.110	0.674
CB14	exclude Kaikoura	-0.147	0.605	0.168	0.755
CY14	exclude Kaikoura	0.109	0.653	0.345	0.710
BSSA	subduction	0.023	0.582	0.023	0.582
CB14	subduction	-0.045	0.514	0.632	0.637
CY14	subduction	0.218	0.588	0.693	0.611
BSSA	no sub, no Kaikoura	-0.303	0.697	-0.303	0.697
CB14	no sub, no Kaikoura	-0.302	0.657	-0.229	0.674
CY14	no sub, no Kaikoura	-0.007	0.692	0.049	0.699
CDDG22 (this study)	All	0.035	0.581	0.039	0.593
CDDG22 (this study)	dist <= 400 km	0.044	0.594	0.037	0.590
CDDG22 (this study)	exclude Kaikoura	0.148	0.562	0.126	0.589
CDDG22 (this study)	subduction	0.217	0.487	0.158	0.487
CDDG22 (this study)	no sub, no Kaikoura	0.080	0.619	0.053	0.668

Table 1 The median and standard deviation of the log residual between the GMM predictions and the GNSS velocities. Log residual is defined as $\ln(PGV_{GMM}) - \ln(PGV_{GNSS})$, with PGV in units of cm/s. Event Subset describes the filtering of events in the statistical analysis.

Sample Rate	σ_N	σ_E	σ_Z
1 Hz	0.17	0.12	0.31
5 Hz	0.70	0.47	1.22
10 Hz	1.49	0.98	2.56
20 Hz	2.73	1.83	4.69
20 Hz, 5 Hz resample	0.34	0.20	0.57

Table 2 Standard deviation for GNSS velocities at station ARQT processed at 4 different sampling rates. The time period covered is between 17:30 and 18:00 UTC on October 26, 2016. σ has units of cm/s.

Coefficient	Distance R_p	Distance R_{rup}
c_0	-13.485	0.588
c_{R0}	3.081	-0.939
c_{R1}	-0.782	-0.097
c_{R2}	0.0016	0.00025
c_{M1}	2.835	0.658
c_{M2}	206.078	-208.937
c_{S1}	0.000544	0.00064
c_{S2}	-0.258	-0.303

Table 3 The coefficients for the CDDG22 GMM using either R_p or R_{rup} . The coefficients are defined in Equations 4-7.

NGA-West2 GMMs (e.g., Figure 3). In CDDG22, we have not considered any site terms, such as Vs30. In Figure 6, we plotted the residual error for CDDG22 against Vs30 and see that there is a small trend that is linearly modeled as

$$\ln(PGV_{GMM}) - \ln(PGV_{GNSS}) = c_{s1} * Vs30 - c_{s2} \quad (7)$$

When we apply this site correction to our residuals, we reduce the standard deviations to 0.57 and 0.58 for R_p and R_{rup} respectively. While this is not an appreciable reduction ($\sim 2\%$), it does indicate that further investigation into site-specific corrections is warranted as we expand out our dataset in the future. Statistically, the residuals between our GMM and the data pass the Lilliefors test (p-value = 0.067, test statistic 0.034) and the Q-Q plot (Figure 4) shows excellent agreement out to 2.5 quantiles.

5 Discussion

The standard mode of GNSS displacement positioning today is to either process the raw observations at a central processing center that can accumulate corrections

for satellite orbits, clocks, fractional cycle biases, and tropospheric corrections or to perform the computations onsite while transmitting the corrections to the station. Within PPP computations, it is imperative to properly compute the integer cycle ambiguities before precise displacements can be obtained, which requires segregating the fractional cycle biases and integer ambiguities (e.g., Geng et al., 2012). This is generally an iterative process and requires many minutes for the solution to converge to its stable and precise estimate. Even after properly correcting for all sources of error, real-time displacement observations generally have a noise level of 1-2 cm in the horizontal components and 5 cm in the vertical (Melgar et al., 2020) over short time periods and long period drifts due to constellation geometry and multipath are evident at periods greater than 30 seconds. The GNSS velocity approach does not require any external corrections and can be easily deployed onboard GNSS receivers since it uses the broadcast orbital information from the satellites. The accuracy of our GNSS velocity estimates in the horizontal is roughly 0.6, 1.2, and 2.3 cm/s at 5, 10 and 20 Hz respectively, and

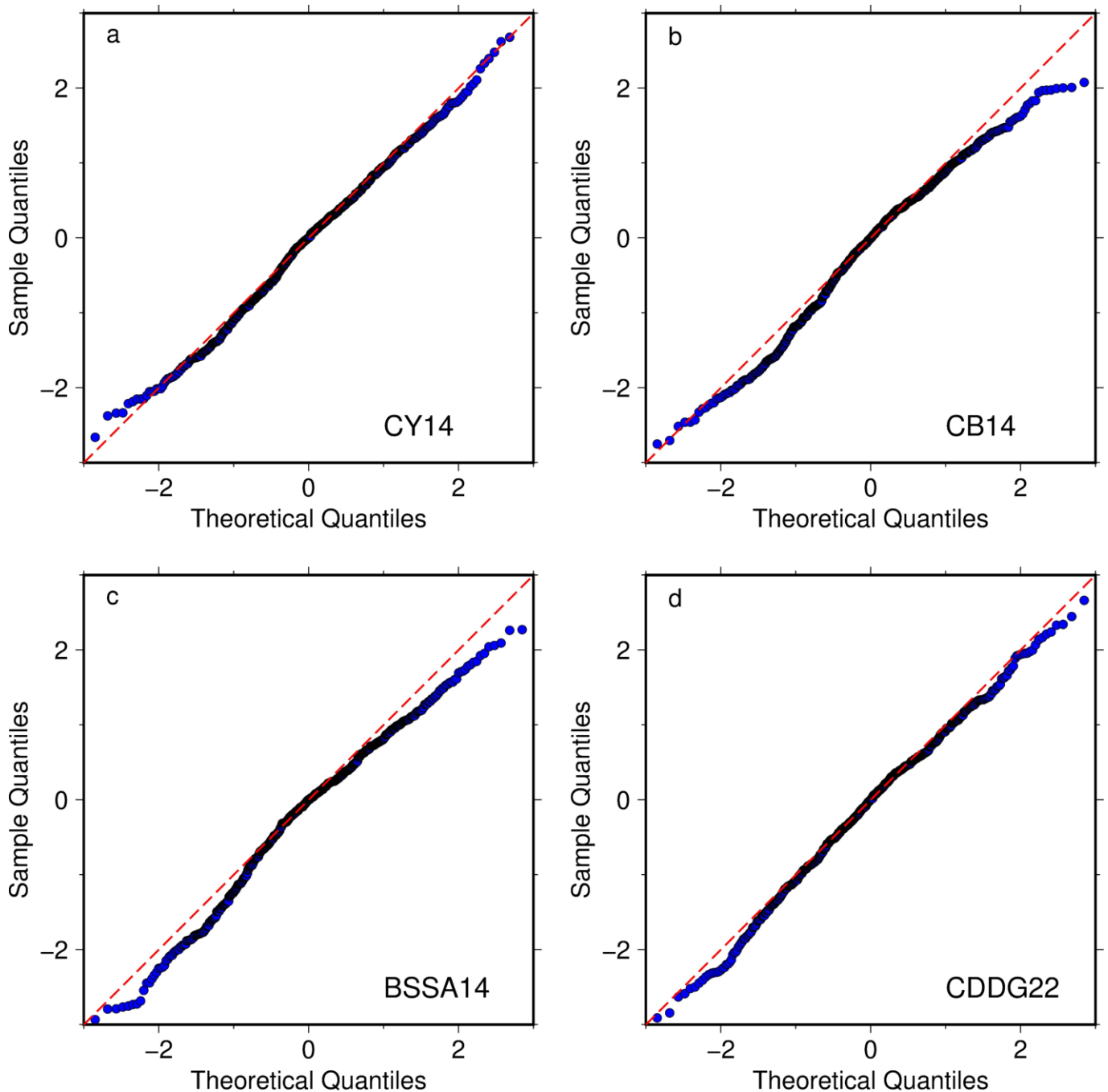


Figure 4 Quantile-quantile plots of the log residual between the GMM determined PGV and the GNSS derived PGV using R_p . The quantiles assume a normal distribution with the data corrected and normalized to a mean of 0 and standard deviation of 1. The red dashed lines indicate a 1-to-1 correspondence for perfectly normal data.

these values could be further improved by using International GNSS Service Ultra-Rapid orbits and clocks and temporal re-sampling from higher rates (e.g., [Shu et al., 2020](#)).

Given the accuracy of the GNSS velocity estimates with respect to the GMMs, their use in ShakeMap generation should be considered. ShakeMaps are a powerful post-earthquake evaluation tool that provides information on ground motion (peak ground acceleration, velocity, spectral accelerations) and shaking intensity (in the form of Modified Mercalli Intensity, MMI). These maps are generated from a combination of GMMs relating an earthquake source to ground motions, instrumental recordings of ground motions, and com-

munity intensity reports (i.e., Did You Feel It). The work presented here has demonstrated that GNSS velocities can be added to the instrumental recordings within ShakeMaps. This is important because the station distribution of seismic and GNSS networks are vastly different due to the motivating factors behind the installations. Indeed, [Grapenthin et al. \(2018\)](#) demonstrated for the 2017 Mw 7.1 Iniskin earthquake the enhanced value of GNSS derived velocities in a region with sparse seismic network coverage. Seismic networks were primarily installed either near well known seismic sources or near major population centers. GNSS networks were installed primarily to aid the surveying community and are thus more evenly distributed geo-

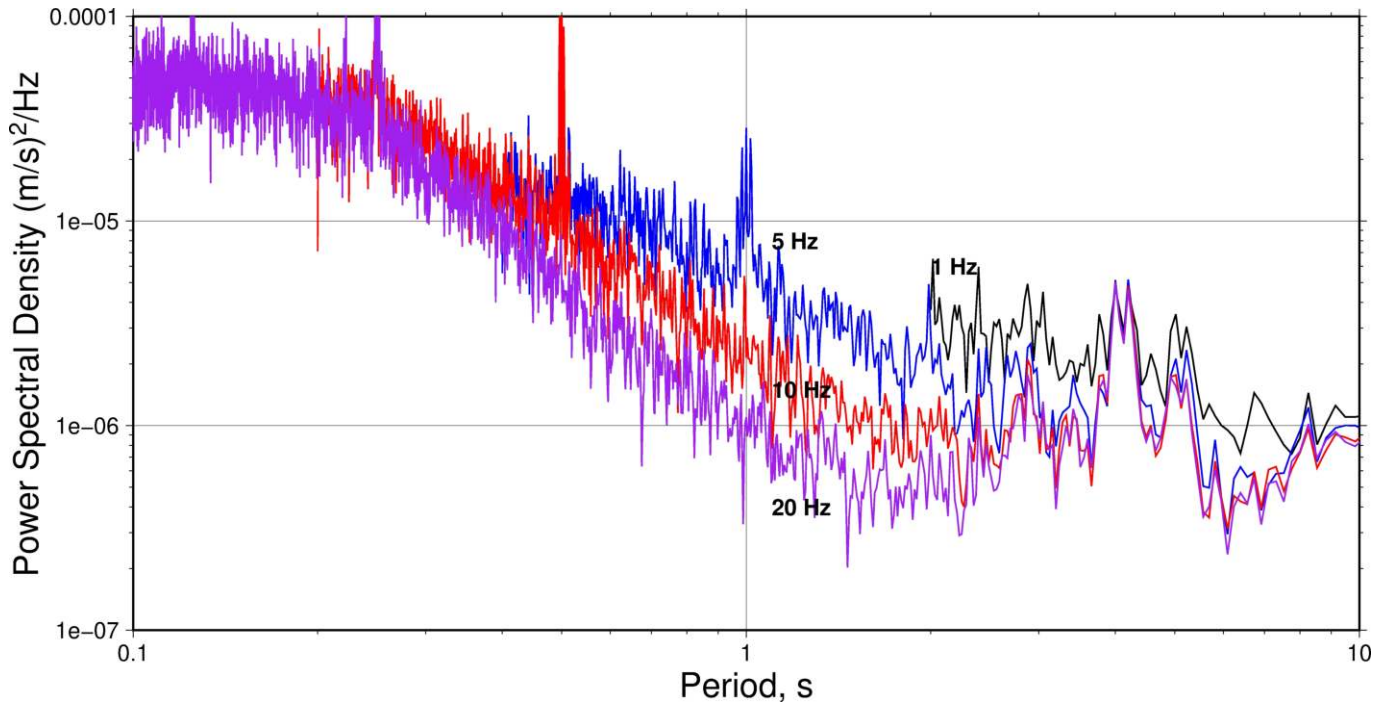


Figure 5 Power spectral density in the east direction for 30 minutes of noise recorded at station ARQT and processed at 4 sampling rates, 1, 5, 10, and 20 Hz. The time period covered is between 17:30 and 18:00 UTC on October 26, 2016.

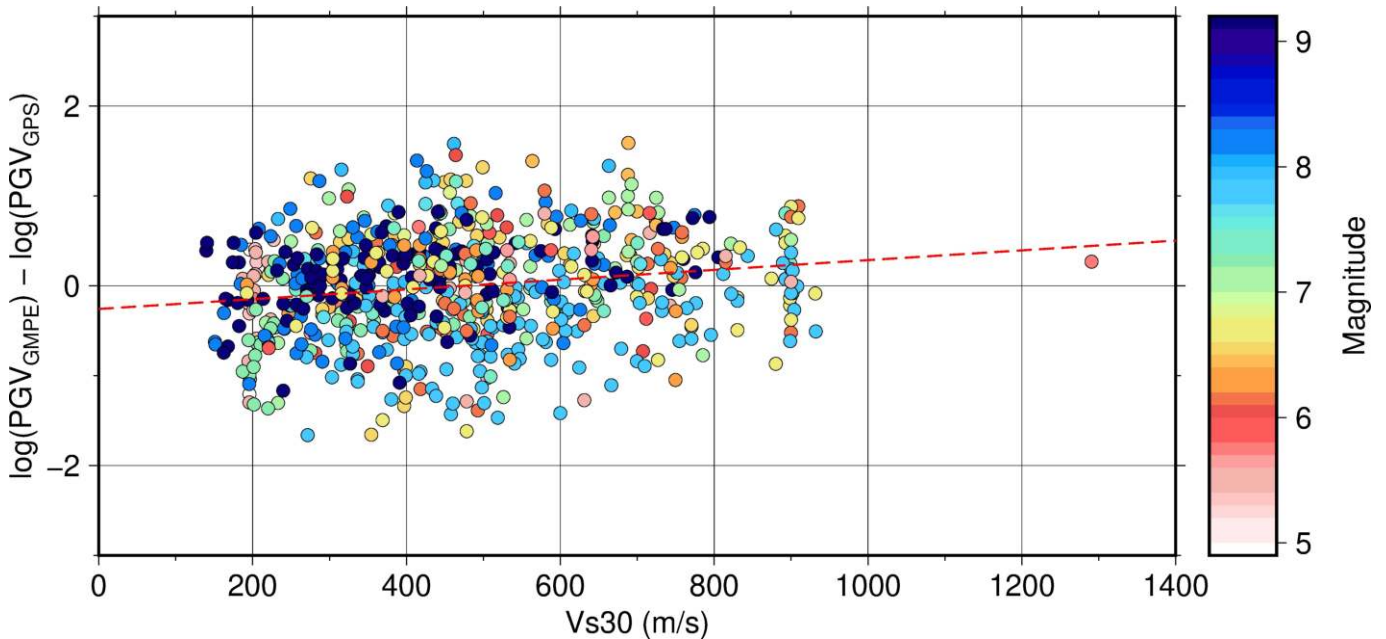


Figure 6 The log residual for CDDG22 versus Vs30, the shear wave velocity in the upper 30 meters. The red dashed line corresponds to Equation 7, with coefficients in Table 3.

graphically. GNSS networks have also been targeted at high strain accumulation regions. This is now somewhat changing with collocating of instruments and expansion of seismic networks, but the different station distributions allow for us to provide observations of PGV in new locations, further constraining the interpolation schemes used in ShakeMap. To show the efficacy of GNSS velocities within ShakeMaps, we computed several sets of ShakeMaps for the 2016 Mw 6.6 Norcia, which are shown in Figure 7. For this demonstration, we replaced the input instrumental data with the PGV values recorded at the GNSS stations (Figure

7a). We see in the near-field, there are considerably more GNSS stations than seismic stations (Figure 7b), which leads to considerably higher intensities. We also computed the ShakeMap using both the seismic observations and the GNSS velocities, which is shown in Figure 7c. This model is closer to the original ShakeMap, however, in the near-field, there is upwards of 0.8 MMI difference between the two models (Figure 7d). While there are many issues still to explore with the optimal ways to incorporate this data into ShakeMaps regarding the appropriate weighting schemes, this demonstration shows a promising potential improvement in near-real-

time intensity characterization.

While we have not explicitly shown the utility of GNSS derived velocities to earthquake early warning, there are several ways in which we envision these observations improving geodetic early warning. Many studies have shown the value of GNSS displacements to rapid magnitude and slip determination for large earthquakes, but the aforementioned issues with real-time positioning require clever logic within operational early warning systems. For example, the G-FAST system that is operating on ShakeAlert development servers, requires a gross outlier filter, a magnitude and time dependent uncertainty scheme, a time dependent minimum displacement filter (on 4 stations), and a minimum seismic magnitude filter (Murray et al., 2021). These logic filters built onto the back-end of G-FAST have the effect of throttling messages from the system from all events except those that we have the highest confidence in. Incorporating GNSS velocity streams into G-FAST could remove or reduce the levels of these filters by lending more confidence to the displacement streams. For example, ambiguity resolution issues on the displacement streams do not appear on the velocity streams, so we can use this stream to flag parts of the time series that there is no expected shaking. Moreover, the ground velocity observations can be used to appropriately window displacement time series or to select only those stations that should have a significant displacement signal and exclude those that are effectively noise, thus improving the precision and accuracy of the geodetic source models within G-FAST. For example, Dittmann et al. (2022b) trained a random forest classifier to select only parts of the GNSS velocity time series that had earthquake related ground shaking and showed a true positive rate of roughly 90% for earthquakes greater than M5 and out to hypocentral distances greater than 1000 km for larger events. Finally, GNSS derived velocities can be used directly in early warning systems either in existing seismic algorithms that rely on velocity observations or through magnitude scaling. Fang et al. (2020) showed a simple PGV scaling relationship, with a similar form to peak ground displacement scaling used in early warning (Crowell et al., 2013), to determine earthquake magnitude with uncertainty of 0.26 magnitude units.

6 Conclusions

We have demonstrated that GNSS derived velocities, recorded at 5 Hz or greater, are capable of characterizing strong ground motions for moderate to large earthquakes without going off scale. These observations agree well with the three NGA-West2 GMMs that we compared against, with the best agreement with Chiou and Youngs (2014) using R_{rup} and with Campbell and Bozorgnia (2014) using R_p . Deriving our own simple GMM directly from our PGV values and published USGS finite fault models yields roughly a 20% reduction in the log residual down to 0.58-0.59; this value is in line with the total residual reported by the three NGA-West2 GMMs using the seismic database, between 0.54 and 0.65 log units. Most importantly, our dataset includes

PGV records from many large earthquakes, with almost half the observations (333) coming from $M > 7.5$ earthquakes, and this study provides true unfiltered records of strong ground motion in a non-inertial reference frame.

Acknowledgements

This work is funded by the US Geological Survey External Grants Program, grant number G22AP00038 to University of Washington. Additional funding is provided by USGS Cooperative Agreement G21AC10529 to University of Washington. This material is based on services provided by the GAGE Facility, operated by UNAVCO, Inc., with support from the National Science Foundation, the National Aeronautics and Space Administration, and the U.S. Geological Survey under NSF Cooperative Agreement EAR-1724794. We acknowledge the New Zealand GeoNet project and its sponsors EQC, GNS Science, LINZ, NEMA and MBIE for providing data/images used in this study. We also acknowledge RING GPS data by Istituto Nazionale di Geofisica e Vulcanologia, which are licensed under a Creative Commons Attribution 4.0 International License and outlined in the following reference: INGV RING Working Group (2016), Rete integrata Nazionale GNSS, doi:10.13127/RING. We would like to thank three anonymous reviewers who helped improve the manuscript.

Data and code availability

The SNIVEL codebase, version 1.0, is available on Zenodo (<https://zenodo.org/record/7065801>). The GNSS velocity records in SAC format from SNIVEL, the seismogeodetic velocities in Matlab .mat format, and an spreadsheet of the events and peak ground motions is available on Zenodo (<https://doi.org/10.5281/zenodo.7065910>). GNSS data in Receiver Independent Exchange Format is available at UNAVCO (<https://data.unavco.org/archive/gnss/highrate/>), GNS (<https://data.geonet.org.nz/gnss/event.highrate/>), and INGV (<http://ring.gm.ingv.it/>).

Competing interests

The authors declare no competing interests.

References

- Allen, R. M. and Melgar, D. Earthquake Early Warning: Advances, Scientific Challenges, and Societal Needs. *Annual Review of Earth and Planetary Sciences*, 47(1):361–388, 2019. doi: 10.1146/annurev-earth-053018-060457.
- Allen, T. I., Wald, D. J., Earle, P. S., Marano, K. D., Hotovec, A. J., Lin, K., and Hearne, M. G. An Atlas of ShakeMaps and population exposure catalog for earthquake loss modeling. *Bulletin of Earthquake Engineering*, 7:701–708, 2009. doi: 10.1007/s10518-009-9120-y.
- Benedetti, E., Branzanti, M., Biagi, L., Colosimo, G., Mazzoni, A., and Crespi, M. Global Navigation Satellite Systems Seismology for the 2012 Mw 6.1 Emilia Earthquake: Exploiting the VADASE Algorithm. *Seismological Research Letters*, 85(3):649–656, 2014. doi: 10.1785/0220130094.

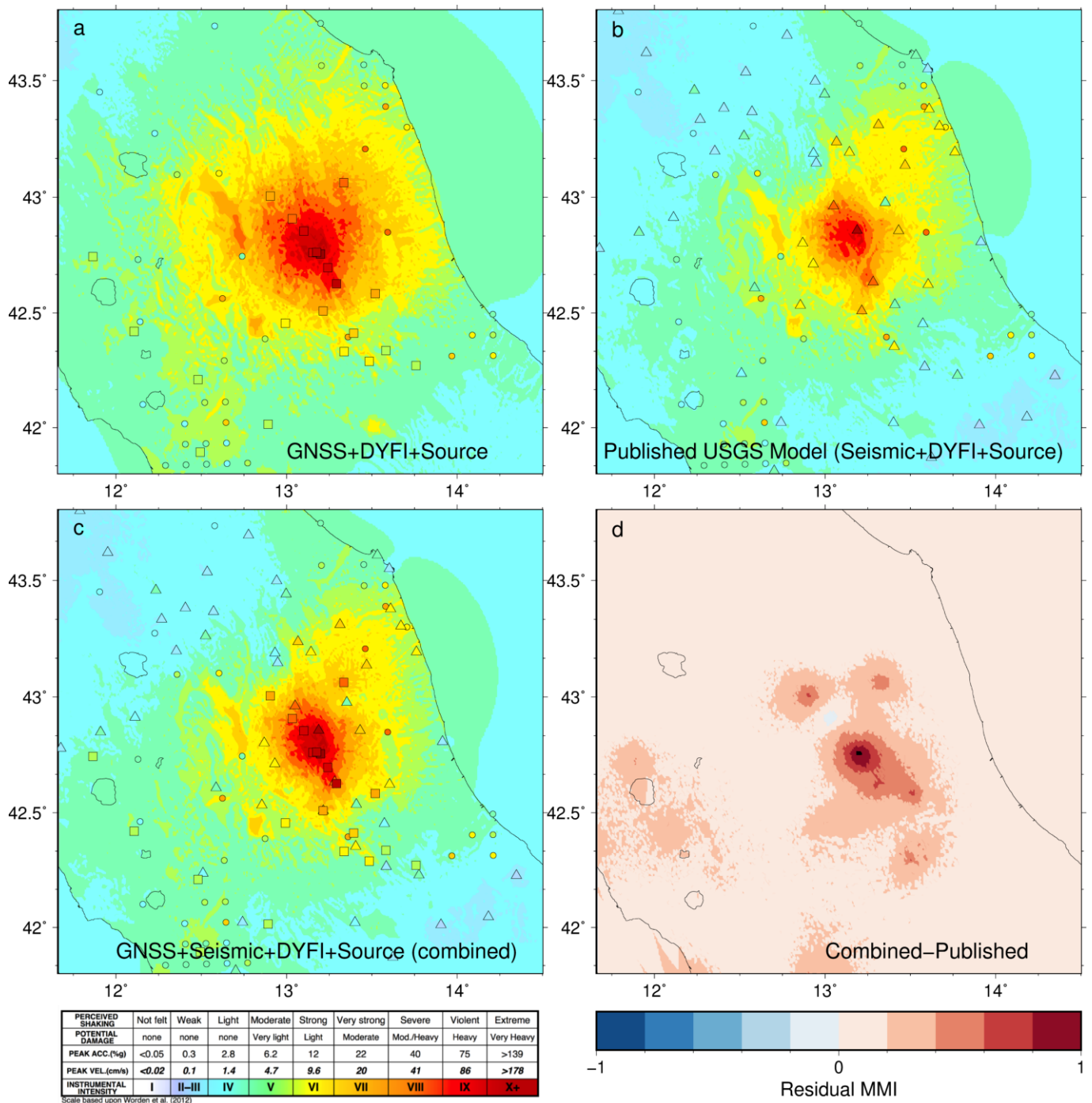


Figure 7 ShakeMaps for the Mw 6.6 Norcia earthquake on December 30, 2016. (a) A ShakeMap run with the default parameters and using only the GNSS velocities for instrumental data. The squares show the locations of the GNSS stations, colored by their Modified Mercalli Intensity (MMI). The circles are the Did You Feel It? (DYFI) reports. (b) The published USGS ShakeMap which uses only seismic data for instrumental data. The triangles show the locations of the seismic stations, colored by their MMI. (c) A ShakeMap run combining the GNSS and seismic instrumental data. Squares and triangles indicate the locations of GNSS and seismic stations respectively. (d) The MMI residual between panels (c) and (b). All models use the same DYFI, earthquake source, and GMM information.

Blewitt, G., Kreemer, C., Hammond, W. C., Plag, H.-P., Stein, S., and Okal, E. Rapid determination of earthquake magnitude using GPS for tsunami warning systems. *Geophysical Research Letters*, 33(11), 2006. doi: 10.1029/2006GL026145.

Bock, Y., Melgar, D., and Crowell, B. W. Real-Time Strong-Motion Broadband Displacements from Collocated GPS and Accelerometers. *Bulletin of the Seismological Society of America*, 101(6): 2904–2925, 2011. doi: 10.1785/0120110007.

Bommer, J. J., Stafford, P. J., and Akkar, S. Current empirical

ground-motion prediction equations for Europe and their application to Eurocode 8. *Bulletin of Earthquake Engineering*, 8:5, 2010. doi: 10.1007/s10518-009-9122-9.

Boore, D. M., Stephens, C. D., and Joyner, W. B. Comments on Baseline Correction of Digital Strong-Motion Data: Examples from the 1999 Hector Mine, California, Earthquake. *Bulletin of the Seismological Society of America*, 92(4):1543–1560, 2002. doi: 10.1785/0120000926.

Boore, D. M., Stewart, J. P., Seyhan, E., and Atkinson, G. M. NGA-



- West2 Equations for Predicting PGA, PGV, and 5% Damped PSA for Shallow Crustal Earthquakes. *Earthquake Spectra*, 30(3):1057–1085, 2014. doi: 10.1193/070113EQS184M.
- Bozorgnia, Y., Abrahamson, N. A., Atik, L. A., Ancheta, T. D., Atkinson, G. M., Baker, J. W., Baltay, A., Boore, D. M., Campbell, K. W., Chiou, B. S.-J., Darragh, R., Day, S., Donahue, J., Graves, R. W., Gregor, N., Hanks, T., Idriss, I. M., Kamai, R., Kishida, T., Kottke, A., Mahin, S. A., Rezaeian, S., Rowshandel, B., Seyhan, E., Shahi, S., Shantz, T., Silva, W., Spudich, P., Stewart, J. P., Watson-Lamprey, J., Wooddell, K., and Youngs, R. NGA-West2 Research Project. *Earthquake Spectra*, 30(3):973–987, 2014. doi: 10.1193/072113EQS209M.
- Campbell, K. W. and Bozorgnia, Y. NGA-West2 Ground Motion Model for the Average Horizontal Components of PGA, PGV, and 5% Damped Linear Acceleration Response Spectra. *Earthquake Spectra*, 30(3):1087–1115, 2014. doi: 10.1193/062913EQS175M.
- Chiou, B. S.-J. and Youngs, R. R. Update of the Chiou and Youngs NGA Model for the Average Horizontal Component of Peak Ground Motion and Response Spectra. *Earthquake Spectra*, 30(3):1117–1153, 2014. doi: 10.1193/072813EQS219M.
- Clinton, J. F. *Modern digital seismology: instrumentation, and small amplitude studies in the engineering world*. PhD thesis, California Institute of Technology, 2004.
- Colosimo, G., Crespi, M., and Mazzoni, A. Real-time GPS seismology with a stand-alone receiver: A preliminary feasibility demonstration. *Journal of Geophysical Research: Solid Earth*, 116(B11), 2011. doi: 10.1029/2010JB007941.
- Crowell, B. W. Near-Field Strong Ground Motions from GPS-Derived Velocities for 2020 Intermountain Western United States Earthquakes. *Seismological Research Letters*, 92(2A):840–848, 2021. doi: 10.1785/0220200325.
- Crowell, B. W., Bock, Y., and Squibb, M. B. Demonstration of Earthquake Early Warning Using Total Displacement Waveforms from Real-time GPS Networks. *Seismological Research Letters*, 80(5):772–782, 09 2009. doi: 10.1785/gssrl.80.5.772.
- Crowell, B. W., Bock, Y., and Melgar, D. Real-time inversion of GPS data for finite fault modeling and rapid hazard assessment. *Geophysical Research Letters*, 39(9), 2012. doi: 10.1029/2012GL051318.
- Crowell, B. W., Melgar, D., Bock, Y., Haase, J. S., and Geng, J. Earthquake magnitude scaling using seismogeodetic data. *Geophysical Research Letters*, 40(23):6089–6094, 2013. doi: 10.1002/2013GL058391.
- Crowell, B. W., Schmidt, D. A., Bodin, P., Vidale, J. E., Gomberg, J., Renate Hartog, J., Kress, V. C., Melbourne, T. I., Santillan, M., Minson, S. E., and Jamison, D. G. Demonstration of the Cascadia G-FAST Geodetic Earthquake Early Warning System for the Nisqually, Washington, Earthquake. *Seismological Research Letters*, 87(4):930–943, 2016. doi: 10.1785/0220150255.
- Dittmann, T., Hodgkinson, K., Morton, J., Mencin, D., and Mattioli, G. S. Comparing Sensitivities of Geodetic Processing Methods for Rapid Earthquake Magnitude Estimation. *Seismological Research Letters*, 93(3):1497–1509, 2022a. doi: 10.1785/0220210265.
- Dittmann, T., Liu, Y., Morton, Y., and Mencin, D. Supervised Machine Learning of High Rate GNSS Velocities for Earthquake Strong Motion Signals. *Journal of Geophysical Research: Solid Earth*, 127(11):e2022JB024854, 2022b. doi: 10.1029/2022JB024854.
- Fang, R., Zheng, J., Geng, J., Shu, Y., Shi, C., and Liu, J. Earthquake Magnitude Scaling Using Peak Ground Velocity Derived from High-Rate GNSS Observations. *Seismological Research Letters*, 92(1):227–237, 2020. doi: 10.1785/0220190347.
- Geng, J., Shi, C., Ge, M., Dodson, A. H., Lou, Y., Zhao, Q., and Liu, J. Improving the estimation of fractional-cycle biases for ambiguity resolution in precise point positioning. *Journal of Geodesy*, 86:579–589, 2012. doi: 10.1007/s00190-011-0537-0.
- Geng, T., Xie, X., Fang, R., Su, X., Zhao, Q., Liu, G., Li, H., Shi, C., and Liu, J. Real-time capture of seismic waves using high-rate multi-GNSS observations: Application to the 2015 Mw 7.8 Nepal earthquake. *Geophysical Research Letters*, 43(1):161–167, 2016. doi: 10.1002/2015GL067044.
- Goldberg, D. E., Melgar, D., Hayes, G. P., Crowell, B. W., and Sahakian, V. J. A Ground-Motion Model for GNSS Peak Ground Displacement. *Bulletin of the Seismological Society of America*, 111(5):2393–2407, 2021. doi: 10.1785/0120210042.
- Grapenthin, R., Johanson, I. A., and Allen, R. M. Operational real-time GPS-enhanced earthquake early warning. *Journal of Geophysical Research: Solid Earth*, 119(10):7944–7965, 2014. doi: 10.1002/2014JB011400.
- Grapenthin, R., West, M., Tape, C., Gardine, M., and Freymueller, J. Single-Frequency Instantaneous GNSS Velocities Resolve Dynamic Ground Motion of the 2016 Mw 7.1 Iniskin, Alaska, Earthquake. *Seismological Research Letters*, 89(3):1040–1048, 2018. doi: 10.1785/0220170235.
- Hamling, I. J., Hreinsdóttir, S., Clark, K., Elliott, J., Liang, C., Fielding, E., Litchfield, N., Villamor, P., Wallace, L., Wright, T. J., D’Anastasio, E., Bannister, S., Burbidge, D., Denys, P., Gentle, P., Howarth, J., Mueller, C., Palmer, N., Pearson, C., Power, W., Barnes, P., Barrell, D. J. A., Dissen, R. V., Langridge, R., Little, T., Nicol, A., Pettinga, J., Rowland, J., and Stirling, M. Complex multifault rupture during the 2016 Mw 7.8 Kaikōura earthquake, New Zealand. *Science*, 356(6334):eaam7194, 2017. doi: 10.1126/science.aam7194.
- Hayes, G. P. The finite, kinematic rupture properties of great-sized earthquakes since 1990. *Earth and Planetary Science Letters*, 468:94–100, 2017. doi: 10.1016/j.epsl.2017.04.003.
- Heath, D. C., Wald, D. J., Worden, C. B., Thompson, E. M., and Smoczyk, G. M. A global hybrid VS 30 map with a topographic slope-based default and regional map insets. *Earthquake Spectra*, 36(3):1570–1584, 2020. doi: 10.1177/8755293020911137.
- Joyner, W. B. A scaling law for the spectra of large earthquakes. *Bulletin of the Seismological Society of America*, 74(4):1167–1188, 1984. doi: 10.1785/BSSA0740041167.
- Katsanos, E. I., Sextos, A. G., and Manolis, G. D. Selection of earthquake ground motion records: A state-of-the-art review from a structural engineering perspective. *Soil Dynamics and Earthquake Engineering*, 30(4):157–169, 2010. doi: 10.1016/j.soildyn.2009.10.005.
- Klobuchar, J. A. Ionospheric Time-Delay Algorithm for Single-Frequency GPS Users. *IEEE Transactions on Aerospace and Electronic Systems*, AES-23(3):325–331, 1987. doi: 10.1109/TAES.1987.310829.
- Lilliefors, H. W. On the Kolmogorov-Smirnov Test for Normality with Mean and Variance Unknown. *Journal of the American Statistical Association*, 62(318):399–402, 1967. doi: 10.1080/01621459.1967.10482916.
- Meier, M.-A. How “good” are real-time ground motion predictions from Earthquake Early Warning systems? *Journal of Geophysical Research: Solid Earth*, 122(7):5561–5577, 2017. doi: 10.1002/2017JB014025.
- Melgar, D., Bock, Y., Sanchez, D., and Crowell, B. W. On robust and reliable automated baseline corrections for strong motion seismology. *Journal of Geophysical Research: Solid Earth*, 118(3):1177–1187, 2013a. doi: 10.1002/jgrb.50135.
- Melgar, D., Crowell, B. W., Bock, Y., and Haase, J. S. Rapid modeling of the 2011 Mw 9.0 Tohoku-oki earthquake with seismogeodesy. *Geophysical Research Letters*, 40(12):2963–2968, 2013b. doi: 10.1002/grl.50590.

- Melgar, D., Crowell, B. W., Melbourne, T. I., Szeliga, W., Santillan, M., and Scrivner, C. Noise Characteristics of Operational Real-Time High-Rate GNSS Positions in a Large Aperture Network. *Journal of Geophysical Research: Solid Earth*, 125(7), 2020. doi: 10.1029/2019JB019197.
- Minson, S. E., Murray, J. R., Langbein, J. O., and Gombert, J. S. Real-time inversions for finite fault slip models and rupture geometry based on high-rate GPS data. *Journal of Geophysical Research: Solid Earth*, 119(4):3201–3231, 2014. doi: 10.1002/2013JB010622.
- Murray, J., Crowell, B., Hagerty, M., Kress, V., Smith, D., Murray, M., Aranha, M., Hodgkinson, K., McGuire, J., Ulberg, C., et al. Toward inclusion of peak ground displacement magnitude estimates in ShakeAlert. In *AGU Fall Meeting Abstracts*, volume 2021, pages S13A–08, 2021.
- Murray, J. R., Crowell, B. W., Grapenthin, R., Hodgkinson, K., Langbein, J. O., Melbourne, T., Melgar, D., Minson, S. E., and Schmidt, D. A. Development of a Geodetic Component for the U.S. West Coast Earthquake Early Warning System. *Seismological Research Letters*, 89(6):2322–2336, 2018. doi: 10.1785/0220180162.
- Niell, A. E. Global mapping functions for the atmosphere delay at radio wavelengths. *Journal of Geophysical Research: Solid Earth*, 101(B2):3227–3246, 1996. doi: 10.1029/95JB03048.
- Parker, G. A., Stewart, J. P., Boore, D. M., Atkinson, G. M., and Hassani, B. NGA-subduction global ground motion models with regional adjustment factors. *Earthquake Spectra*, 38(1):456–493, 2022. doi: 10.1177/87552930211034889.
- Rasanen, R. A., Marafi, N. A., and Maurer, B. W. Compilation and forecasting of paleoliquefaction evidence for the strength of ground motions in the U.S. Pacific Northwest. *Engineering Geology*, 292:106253, 2021. doi: 10.1016/j.enggeo.2021.106253.
- Shu, Y., Fang, R., Li, M., Shi, C., Li, M., and Liu, J. Very high-rate GPS for measuring dynamic seismic displacements without aliasing: performance evaluation of the variometric approach. *GPS Solutions*, 22:121, 2018. doi: 10.1007/s10291-018-0785-z.
- Shu, Y., Fang, R., Liu, Y., Ding, D., Qiao, L., Li, G., and Liu, J. Precise coseismic displacements from the GPS variometric approach using different precise products: Application to the 2008 MW 7.9 Wenchuan earthquake. *Advances in Space Research*, 65(10): 2360–2371, 2020. doi: 10.1016/j.asr.2020.02.013.
- Thakoor, K., Andrews, J., Hauksson, E., and Heaton, T. From Earthquake Source Parameters to Ground-Motion Warnings near You: The ShakeAlert Earthquake Information to Ground-Motion (eqInfo2GM) Method. *Seismological Research Letters*, 90(3): 1243–1257, 2019. doi: 10.1785/0220180245.
- Thompson, E. M. and Baltay, A. S. The Case for Mean Rupture Distance in Ground-Motion Estimation. *Bulletin of the Seismological Society of America*, 108(5A):2462–2477, 2018. doi: 10.1785/0120170306.
- Wald, D. J., Quitoriano, V., Heaton, T. H., Kanamori, H., Scrivner, C. W., and Worden, C. B. TriNet “ShakeMaps”: Rapid Generation of Peak Ground Motion and Intensity Maps for Earthquakes in Southern California. *Earthquake Spectra*, 15(3):537–555, 1999. doi: 10.1193/1.1586057.
- Williamson, A. L., Melgar, D., Crowell, B. W., Arcas, D., Melbourne, T. I., Wei, Y., and Kwong, K. Toward Near-Field Tsunami Forecasting Along the Cascadia Subduction Zone Using Rapid GNSS Source Models. *Journal of Geophysical Research: Solid Earth*, 125(8):e2020JB019636, 2020. doi: 10.1029/2020JB019636.

4.0.

The article *Validation of Peak Ground Velocities Recorded on Very-high rate GNSS Against NGA-West2 Ground Motion Models* © 2023 by Brendan W. Crowell is licensed under CC BY

PyRaysum: Software for Modeling Ray-theoretical Plane Body-wave Propagation in Dipping Anisotropic Media

Wasja Bloch *¹, Pascal Audet ²

¹Department of Earth, Atmospheric and Ocean Sciences, University of British Columbia, Vancouver, BC, Canada, ²Department of Earth and Environmental Sciences, University of Ottawa, Ottawa, Ontario, Canada

Author contributions: *Writing, Software:* W. Bloch, P. Audet. *Visualization, Validation:* W. Bloch. *Conceptualization:* P. Audet.

Abstract This article introduces *PyRaysum*, a Python software for modeling ray-theoretical body-wave propagation in dipping and/or anisotropic layered media based on the popular Fortran code *Raysum*. We improve and expand upon *Raysum* in several ways: 1) we significantly reduce the overhead by avoiding input/output operations; 2) we implement automatic phase labeling to facilitate the interpretation of complex seismograms; 3) we provide the means to correct inaccuracies in the calculated amplitude of free surface reverberations. We take advantage of the modern, object-oriented Python environment to offer various classes and methods to perform receiver function calculation, filtering and plotting. *PyRaysum* is fully backward compatible with legacy *Raysum* files and integrates well with *NumPy* and *ObsPy*, two standard libraries for numerical computing and seismology. *PyRaysum* is built in Python version 3 and requires a Fortran compiler, but otherwise runs on all platforms. The software offers a high-level, ease-of-use user interface and is equipped with complete documentation and testing as well as tutorials to reproduce published examples from the literature. Time-optimized post-processing functions allow for the straightforward and efficient incorporation of *PyRaysum* synthetic data into optimization or probabilistic parametric search approaches.

Non-technical summary We introduce *PyRaysum*, an overhaul of the popular Fortran computer program *Raysum* for modeling receiver functions, wrapped in the Python programming language. *PyRaysum* computes synthetic seismograms for subsurface models that consist of a few layers with constant elastic properties. The layer properties may be anisotropic and the layers may be dipping. Compared to the original code, *PyRaysum* is faster, more intuitive to use, and can easily be combined with other programs written in the Python programming language. These enhancements facilitate its usage in the estimation of subsurface properties from seismograms.

1 Motivation

Modeling teleseismic body-wave propagation in complex media is an important component of passive seismological approaches that aim to decipher upper mantle and crustal seismic velocity structure on the receiver side (e.g., receiver functions and teleseismic shear-wave splitting analyses). Modeling wave propagation in highly heterogeneous and anisotropic 3D media can be performed using full-waveform approaches (e.g. spectral element or finite-difference methods). Most often, however, a simpler parameterization of the subsurface velocity structure is desirable, because Earth structure is dominantly 1D or 2D at the scale of the upper mantle and lithosphere, and faster modeling methods allow searching for a wider range of model parameters that fit the data. Among those approaches, matrix-propagation techniques (Kennett, 2009; Thomson, 1997) provide accurate wave field reconstructions from horizontally layered media, including anisotropy. However, heterogeneous seismic velocity structure, in

the form of layer dip (Figure 1), is not easily incorporated in such approaches. The most popular alternative for modeling layer dip (with or without layer anisotropy) is based on a ray-theoretical approximation that can model low-order scattering, but neglects higher order wave effects (Cassidy and Ellis, 1993; Frederiksen and Bostock, 2000). This approach is implemented in the software *Raysum* (Frederiksen and Bostock, 2000), which has been used in numerous receiver function studies to characterize seismic discontinuities such as the continental Moho (e.g., Lombardi et al., 2008), the lithosphere-asthenosphere boundary (e.g., Kumar et al., 2007), or the mid-lithosphere discontinuity (e.g., Selway et al., 2015), and has helped unravel the seismic velocity structure within subduction zones (e.g., Audet and Bürgmann, 2014; Nicholson et al., 2005), orogenic belts (e.g., Schulte-Pelkum et al., 2005; Sodoudi et al., 2009), and collisional settings (Schneider et al., 2013).

The original *Raysum* software is written in native Fortran for fast and efficient computations. The input and output to *Raysum* consist of formatted text files, and

Production Editor:
Gareth Funning
Handling Editor:
Nicola Piana Agostinetti
Copy & Layout Editor:
Keyla Ramirez
Théa Ragon

Received:
August 29, 2022
Accepted:
December 19, 2023
Published:
February 20, 2023

*Corresponding author: wbloch@eoas.ubc.ca

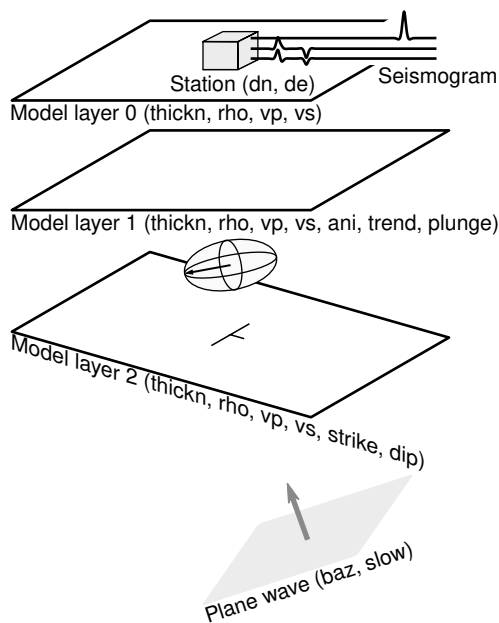


Figure 1 *PyRaysum* computes three-component synthetic seismograms for a plane wave that travels through a stack of dipping, anisotropic layers. This example shows a 2-layer over a half-space model, where the top and bottom layers are isotropic, and the middle layer is elastically anisotropic (represented by the anisotropic ellipsoid (*ani*) and orientation (*plunge* and *trend*) of the symmetry axis). The top interface of the half-space is inclined, as parameterized by the *strike* and *dip* angles. The ray geometry is defined by the back-azimuth and horizontal slowness of the incident plane wave ray vector and the location of the station relative to the origin.

users have to write their own scripts for reading, writing, processing and visualizing the synthetic data. This makes it challenging and cumbersome for beginners to quickly produce synthetic data, explore the parameter space efficiently, and combine synthetic with observed data in optimization problems. Furthermore, reading and writing files to disk represent a substantial performance bottleneck for repeated and automated program execution. *PyRaysum* was developed to remedy these shortcomings, by wrapping *Raysum* in a modern Python environment with classes and modules to facilitate its usage for beginners and to streamline the modeling approach in optimization or probabilistic search approaches. It employs *ObsPy* (Krischer et al., 2015) for handling seismic data, *NumPy* (Harris et al., 2020) for data processing, and *Matplotlib* (Hunter, 2007) for visualization. The installation, testing, full user interface and Jupyter notebook tutorials are described in the online documentation at <https://paudetseis.github.io/PyRaysum/index.html>. Here we give an overview of the user interface and provide examples that validate the results against published and synthetic examples. We provide timing benchmarks for various program execution options and suggest new applications that arise from the improved performance and transparency of results.

Listing 1 General structure of a *PyRaysum* setup. The parameters chosen here reproduce the synthetic data shown in Figure 2.

```
from pyraysum import Model, Geometry, Control
from pyraysum import run
from fraysum import run_bare

# Subsurface model
mod1 = Model(
    thickn=[32000, 0], # m
    rho=[2800, 3600], # kg/m^3
    vp=[6400, 8100], # m/s
    vs=[3600, 4650], # m/s
)

# Ray geometry
geom1 = Geometry(
    baz=97, # degree
    slow=0.07, # s/km
)

# Run-control parameters
ctrl1 = Control(
    mults=2, rot="ZNE", npts=1000, align=0
)

# Result with ObsPy Streams
res1 = run(mod1, geom1, ctrl1)

# NumPy Array
arr1 = run_bare(
    *mod1.parameters,
    *geom1.parameters,
    *ctrl1.parameters,
)
```

2 User Interface

Simulating seismic waveforms with *PyRaysum* is done by setting up: 1) a subsurface model; 2) the ray and station geometry; and 3) a suite of run-control parameters. With this setup, synthetic seismograms can either be generated as *ObsPy* Streams or *NumPy* arrays. In Listing 1, the *res1* and *arr1* objects both contain the same synthetic seismograms. They differ in that *res1* is a *Result* object that contains the synthetics as feature-rich *ObsPy* Streams with additional metadata, while *arr1* holds the bare synthetic samples as a *NumPy* Array. *PyRaysum* offers common methods for receiver function post-processing for both objects, where the *ObsPy*-based routines focus on exploratory data analysis, while the *NumPy*-based ones have an emphasis on computational efficiency.

PyRaysum provides two packages: *fraysum* and *pyraysum*. *fraysum* bundles access to the underlying Fortran routines, which are based on the original *Raysum* code (Frederiksen and Bostock, 2000). *pyraysum* provides the Python interface for computing, post-processing and plotting receiver functions. The object-oriented interface can be imported directly from *pyraysum*. Functions for advanced users are stored in three modules: *prs* allows users to create *PyRaysum* objects from files, including legacy *Raysum* files; *frs* exposes functions for fast, *NumPy*-based post-processing of *fraysum* output; *plot* provides plotting functionality.

2.1 fraysum

The `fraysum` package is generated during compilation of the *Raysum* code through the `NumPy f2py` interface generator. This package facilitates access to the `run_full()` and `run_bare()` functions, which are the low-level calls to the underlying Fortran code. `run_bare()` only returns the synthetic 3-component seismograms, while `run_full()` additionally returns arrays of times, amplitudes and identifiers of the converted and reflected seismic phases, at the cost of a longer run time. This module lacks any convenience and bookkeeping functionality.

2.2 pyraysum

The `pyraysum` package exposes the primary function `run()` to compute synthetic seismograms. It defines the three classes `Model`, `Geometry` and `Control` that organize the required input parameters and the `Result` class that holds the results.

run() Results are created through a call to `run()`, which requires an instance of each of the input parameter classes representing a subsurface model (`Model`), the ray- and station geometry (`Geometry`) and run control parameters (`Control`) as required positional arguments. The optional keyword arguments `rf` and `mode` provide switches to automatically compute receiver functions and skip automatic phase labelling.

Model The subsurface seismic velocity structure is parameterized as a stack of layers (Figure 1), where each layer is described by its vertical thickness (`thickn`, in *m*), density (`rho`, in *kg/m³*) and isotropic P- and S-wave velocities (`vp` and `vs`, in *m/s*), indexed from top to bottom. Optionally, the layer may be inclined (`strike` and `dip` angles in degrees with a right-hand-rule) and/or anisotropic (`ani` is percent anisotropy; Figure 1). Anisotropy is parameterized in a simplified hexagonal symmetry class as

$$\text{ani} = \frac{V_{\parallel} - V_{\perp}}{V} \cdot 100\%, \quad (1)$$

where V_{\parallel} and V_{\perp} are the seismic velocities parallel and perpendicular to the symmetry axis. P- and S-wave anisotropy are equal and pure elliptical anisotropy is assumed (Porter et al., 2011; Sherrington et al., 2004; Levin and Park, 1997). The orientation of the anisotropy axis is defined by `p_lunge` (degrees down from horizontal) and `trend` (degrees clockwise from north) angles. Positive anisotropy refers to a fast axis of symmetry, whereas negative anisotropy denotes a slow axis. We note that, unlike all other model parameters that apply to the entire layer properties, specifying layer strike and dip angles refers to the orientation of the top interface. To define a uniform-thickness dipping layer, the same strike and dip angles must be specified at the underlying layer.

The model layers can be accessed and manipulated by their index (see Section 3.2 for examples). Convenience methods for the manipulation of a `Model` instance include: parametrizing `vp` and `vs` in terms of V_P/V_S

(`vpvs`); changing model attributes interactively using brief command strings (`change()`); adding, splitting, removing and averaging of layers (`+`, `split_layer()`, `remove_layer()`, `average_layer()`); plotting the subsurface model as a staircase diagram or profile sketch (`plot()`); saving the model to file, including legacy *Raysum* model files (`save()`).

Geometry The ray and station geometry are parameterized in terms of the ray back-azimuth angle (`baz`, in degrees clockwise from north) and horizontal slowness (`slow`, in *s/km*), and station offset in north and east direction from the model origin (`dn` and `de`, in *m*). Ray parameters can be specified as either floats to model single-event waveforms, or iterables to simulate multiple event recordings. Each ray can be accessed and manipulated by index, where the ray indices are associated with those of the three-component synthetic waveforms in the `Result` object generated from a call to `run()` (see below).

Control The `Control` class controls the computation of the synthetic waveforms. Various options can be specified, namely: the number of samples (`npts`) and the sampling interval (`dt` in *s*) of the seismograms; the polarization of the incoming wave-field (`wvtype`); the order to which free surface reverberations are computed (`multiples`, `mults`); whether only specific phases should be computed (`set_phaselist`); the time-alignment (`align`) and time-shift (`shift`) of the seismograms; the rotation of seismogram components to left-handed geographical (Z-N-E) or right-handed ray (R-T-Z or P-V-H) coordinate systems (`rot`); and the verbosity of the program execution (`verbose`). Default options exist for each of these parameters.

Result The `Result` class holds the output synthetic seismograms, which can be accessed by ray index or as a list of 3-component `ObsPy Streams` with the `"stream"` or `"seismogram"` keyword. If the seismograms are computed in a ray coordinate system (`rot` equal to `"RTZ"` or `"PVH"`), synthetic receiver functions can be computed on the fly using the `calculate_rfs()` method. They are then stored as an additional list of 2-component (radial/vertical shear and transverse/horizontal shear) `ObsPy Stream` objects under the `"rf"` keyword and can be accessed as the second element of the returned tuple when indexing `Result`. All functionalities of the `ObsPy Stream` class are readily available. Convenience methods `plot()` and `filter()` allow plotting and filtering the `streams` or `rfs` attributes in a single command.

The arrival time, amplitude, phase descriptor, abbreviated phase name, and conversion name of each converted or reflected phase arrival are stored within the `stats` attribute for each trace within the seismogram streams. The `phase_descriptors` serve as unique phase identifiers throughout *PyRaysum*. They are strings that consist of paired indices and letters that fully describe the direction (up or down) and type of rays converted or reflected at specific interfaces. *P* in-

indicates a P-wave, *S* a (fast) S-wave and *T* a (slow) S-wave. Uppercase and lowercase letters indicate up-going and down-going rays, respectively. In the case of an isotropic medium, *S* and *T* arrive at the same time and may both carry some energy. Note that *S* and *T* do not imply a polarization, but are chosen as synonyms for *S1* and *S2* to avoid ambiguity with the layer indices. For instance, the phase descriptor of the P-to-S converted wave at the bottom of the top-most layer (index 0) in a 2-layer over half space model (Figure 1) would be *2P1POS*. The `conversion_names` attribute abbreviates the phase descriptors by omitting equal wave types in adjacent ray segments, only indicating the layer indices on top of which a conversion has occurred. The conversion name of the example phase would be *P1S*. Lastly, the `phase_names` attribute provides the shortest, yet ambiguous phase description, listing only the converted phase types, here *PS*. The unique set of all phases present can be retrieved with the `descriptors()` method.

2.2.1 prs

The `prs` module holds the object-oriented interface described above and additional functions to interact with it. Namely, `read_geometry()`, `read_control()`, and `read_model()` read saved input objects from file and allow the direct use of legacy *Raysum* files. `equivalent_phases()` returns the seismic phases that arrive at the same time as a given phase (see Section 4).

2.2.2 frs

The `frs` module holds the functions used to interpret `fraysum` output. Most importantly, `make_array()` allocates an array suitable for the repeated post-processing of similar waveform simulations. Post-processing can be done with `filtered_array()` and `filtered_rf_array()`, the *NumPy*-based, computationally-efficient functions to compute filtered synthetic seismograms and receiver functions from the output of `fraysum.run_bare()`.

2.2.3 plot

The `plot` module holds the plotting functions used by the `Result.plot()` method. The direct function calls expose more options to customize the plots. `stream_wiggles()` and `rf_wiggles()` create plots of multiple-event seismograms or receiver functions with either 3- or 2-component panels, respectively, ordered by either back-azimuth or slowness. The function `seis_wiggles()` creates a line plot of single-event seismograms.

3 Examples

In this section, we present three simple workflows that showcase usage of *PyRaysum*: In Section 3.1 we forward-model three-component waveforms through a simple layer-over-half-space model and compare them with observed data at station *G.HYB* in Hyderabad, India; in

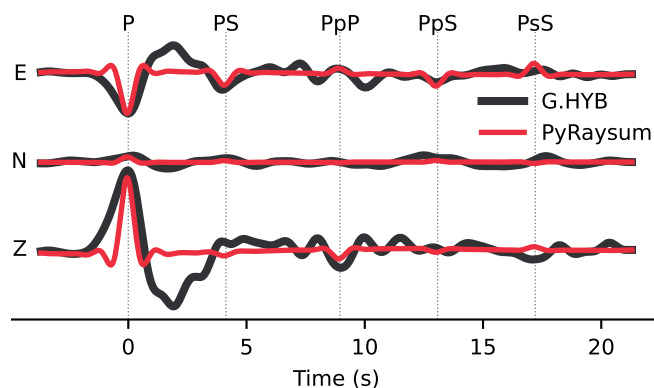


Figure 2 Modeling of the direct Moho conversion and multiples of a teleseismic seismogram recorded at station *G.HYB*. The code that generates the impulse response function is given in Listing 1. The P-to-S Moho conversion *PS*, as well as its free surface reverberations *PpP*, *PpS*, and *PsS* modeled on the basis of the subsurface model of [Saul et al. \(2000\)](#) are discernible in the seismogram. Model and Data traces were bandpass filtered between 1 and 20 s and scaled to the *P* amplitude on the east-component.

Section 3.2 we demonstrate how to interactively manipulate models and quickly examine the resulting receiver function signature; and in Section 3.3 we reproduce previously published synthetic receiver functions representative for coastal California, USA, where a strongly anisotropic layer underlies a crustal block.

3.1 Conversions and multiples in a Seismogram

Station *G.HYB* is located on a seismically transparent cratonic crust. It yields very clear receiver function data ([Saul et al., 2000](#)) that show the direct P-to-S Moho conversion (*PS*) and first-order free-surface reverberations (*PpS* and *PsS*) arriving ~ 4 s, ~ 12 s and ~ 16 s after the direct P-wave, respectively. These data are consistent with a 33 km-thick crust with an average S-wave velocity V_S of 3.7 km/s and a P-to-S wave velocity ratio V_P/V_S of 1.74 ([Saul et al., 2000](#)).

Here we use seismic data recorded at station *G.HYB* for a magnitude *M* 6.3 earthquake that occurred on January 1, 2002 in the Philippines, as a test case for waveform modeling. This wave front arrives due east at the station, and its direct P-waveform exhibits a relatively simple, Ricker-II-like shape due to the large earthquake focal depth (140 km; Figure 2). We model these three-component waveforms with *PyRaysum* (Listing 1) using the appropriate source-receiver geometry and the seismic velocity model proposed by [Saul et al. \(2000\)](#). In the `Control` parameters, no time alignment (`align=0`) is applied and we specify a geographic coordinate system (`rot="ZNE"`). The synthetic waveforms reproduce the main phase arrivals, although the convolved source wavelet distorts this comparison. The phase names, times and amplitudes are the `phase_names` output by *PyRaysum* and facilitate the understanding and description of seismograms. A more complete example is part of the online *PyRaysum* documentation.

3.2 Interactive exploration of receiver functions

We next demonstrate how the effect of changes in the subsurface structure on receiver functions can be explored. In Listing 2, we specify rays with evenly spaced back-azimuths and a constant horizontal slowness of 0.06 s km^{-1} . We set the rotation of the coordinate axes to the P-V-H system, which are oriented parallel to the P -, SH -, and SV polarization of the incoming wave field as predicted by the ray back-azimuth, slowness, and isotropic velocities of the topmost model layer (Kennett, 1991). This rotation ensures that as much converted energy as possible is mapped to the radial and transverse components and removes the constant-amplitude, zero-lag signal on the radial component. Receiver function calculation is straightforward with a simple argument `rf=True` in the call to `run()`. Figure 3a shows the receiver function signature of the isotropic crust modeled in the previous example with a horizontal Moho as the only interface. The PS -conversion is clearly visible on the radial component at 4 s.

To explore the effect of a possible dipping Moho, we next set a 30° eastward dip of the interface (Listing 2 and Figure 3b). The effect is an undulation of the Moho conversion in timing and amplitude with a period of 360° (so-called $1-\theta$ variations). Converted waves from the west arrive earlier and with a lower amplitude on the radial component, due to the relatively shorter ray path and lower layer-orthogonal incidence angle. Conversely, conversions from the east arrive later and with a higher amplitude. Energy from northerly and southerly directions gets converted into the dip direction, evident from the positive and negative amplitudes on the transverse component. The P -coordinate vector is not aligned with the actual ray polarization, because the dipping interface results in an apparent slowness of the ray that is different from the actual slowness of the layer. Therefore, some energy appears on the radial and transverse components at time 0 s.

Next we rotate the interface by 180° —so that it dips west—and increase its dip to 60° (Listing 2 and Figure 3c), thus producing an interface orthogonal to that in the previous example. The undulation pattern of the conversion is more pronounced between 2 and 3 s. The greater misalignment of the P -coordinate vector with the ray polarization leads to significant converted energy on the P -component that gets mapped to the receiver function as an artificial secondary pulse between 4 and 6 s through deconvolution.

To explore anisotropy in the topmost layer, we set the layer dip back to horizontal and instead vary the anisotropic parameters in the model (Listing 2 and Figure 3d and e). With a fast symmetry axis (orthogonal to the plane of the slow axes) trending northward and plunging 30° , the converted wave field gets separated into a fast $S1$ -wave—arriving earlier, N-S-polarized parallel to the fast anisotropy axis, with a strong move-out pattern—and a slow $S2$ -wave, arriving later, E-W-polarized, without a move-out pattern characterized by 180° periodicity (i.e., $2-\theta$ variations). Next we switch from fast- to slow-axis anisotropy and rotate the now

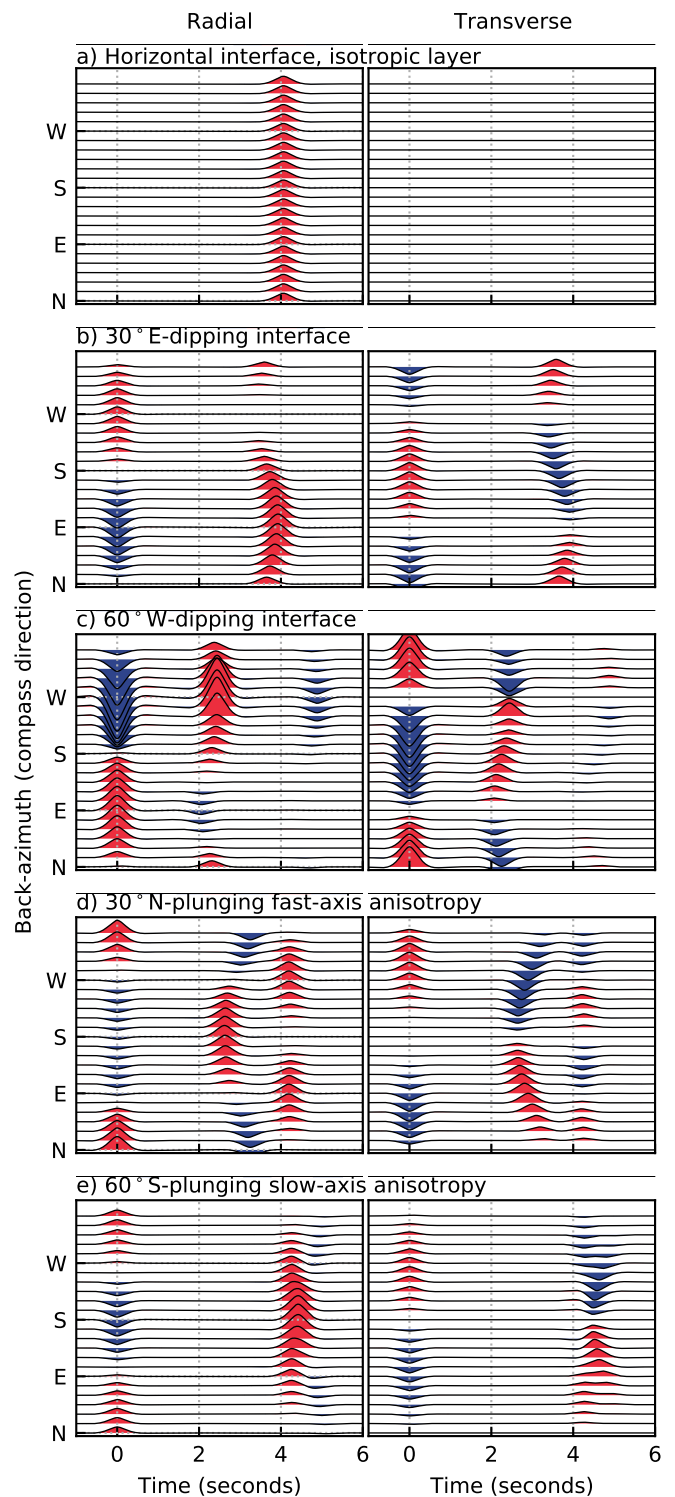


Figure 3 Interactive exploration of receiver functions. The sections correspond to simple layer-over-half-space subsurface models. An interpretation is given in Section 3.2. The code to produce the images is given in Listing 2.

unique slow anisotropy axis such that it is aligned with one of the inclined slow anisotropy axes from the previous example (Listing 2 and Figure 3e). The polarization of the $S1$ and $S2$ waves remains the same. Now the $S2$ -wave shows the move-out pattern, as the wave encounters azimuthally-varying velocities.

Listing 2 Exploration of simple layer-over-half-space models with either a dipping interface or anisotropy. Definitions of Listing 1 are assumed.

```
# Plotting parameters
scale = 4000
tmin = -1
tmax = 6

# Evenly spaced back-azimuths, fixed slowness
geom2 = Geometry(range(0, 360, 15), 0.06)

# Create a copy of mod1
model = mod1.copy()

# Direct conversions, PVH coordinate system
ctrl2 = Control(
    mults=0, rot="PVH", dt=0.01, npts=1200
)

# Calculate, filter and plot
# receiver functions
def run_plot():
    res = run(model, geom2, ctrl2, rf=True)
    res.filter(
        "rfs", "lowpass", freq=1,
        zerophase=True, corners=2
    )
    res.plot_rfs(scale, tmin, tmax)

# Figure 3a
run_plot()

# Figure 3b - 30 deg east-dipping interface
model[1, "dip"] = 30
run_plot()

# Figure 3c - 60 deg west-dipping interface
model[1, "strike"] = 180
model[1, "dip"] = 60
run_plot()

# Figure 3d - remove dip, add north-plunging
# fast axis with 20% anisotropy
model[1, "dip"] = 0
model[0, "ani"] = 20
model[0, "plunge"] = 30
run_plot()

# Figure 3e - south-plunging slow axis
model[0, "ani"] *= -1
model[0, "trend"] += 180
model[0, "plunge"] += 30
run_plot()
```

3.3 Reproduction of earlier work

To demonstrate the handling of layer dip and anisotropy in multi-layered models and show additional plotting functionality of *PyRaysum*, we reproduce figure 3 of Porter et al. (2011). In Listing 3, the definition of the dipping lower-crustal layer model `dipm` implies that the top of the half space and that of the lower layer are dipping 20°, striking east. The layers of the anisotropic model `anim` are flat. The bottom layer is characterized by 20% hexagonal anisotropy with a slow symmetry axis (`ani[1]=-20`) trending south, and plunging 45° down from horizontal. The layer configuration is visualized in Figure 4 a and b, which is a modified output of the call to `model.plot_interfaces()` shown in Listing 3. The corresponding radial and transverse receiver functions

are shown in Figure 4c and d, which are plotted using `res.plot('rfs')` with additional options. The complete example is included in the online *PyRaysum* documentation.

The receiver functions of the dipping and anisotropic lower crustal models shown in Figure 4c and d correspond to the ones shown in figure 3 of Porter et al. (2011). Specifically, both dipping and anisotropic layers are capable of converting seismic energy onto the transverse component, but the specific signature of amplitude variation with back-azimuth is distinct (although both show $1-\theta$ patterns). On the transverse component, the dipping layer causes a broader symmetry pattern with a lower amplitude (Figure 4c), while the anisotropic layer produces high-amplitude conversions in a relatively narrow back-azimuth range (Figure 4d).

Listing 3 Code to reproduce Figure 4 and figure 3 of Porter et al. (2011).

```
from pyraysum import Model, Geometry, Control
from pyraysum import run

# Lower-crustal dipping layer model
th = [20000, 5000, 0]
vp = [6400, 5800, 7800]
ps = [1.75, 1.74, 1.74]
dip = [0, 20, 20]
rho = 2800
st = 90

dipm = Model(
    th, rho, vp, vpvs=ps, strike=st, dip=dip
)

# Lower crustal anisotropy model
ani = [0, -20, 0]
tr = [0, 180, 0]
pl = [0, 45, 0]
fl = [1, 0, 1]

anim = Model(
    th, rho, vp, vpvs=ps,
    flag=fl, ani=ani, trend=tr, plunge=pl
)

# Evenly spaced back azimuths, fixed slowness
geom3 = Geometry(range(0, 360, 10), 0.06)

# Direct conversions, RTZ coordinate system
ctrl3 = Control(mults=0, rot="RTZ")

for model in [dipm, anim]:
    res = run(model, geom3, ctrl3, rf=True)
    res.filter(
        "rfs", "lowpass",
        freq=2., zerophase=True
    )

    model.plot_interfaces()
    res.plot("rfs", tmin=-0.5, tmax=4)
```

4 Validation

We validate the synthetic seismograms created with *PyRaysum* by comparing them with those obtained using the matrix propagator method (Kennett, 2009; Thomson, 1997), as implemented in the *Telewavesim* package for Python (Audet et al., 2019), for the same seismic ve-

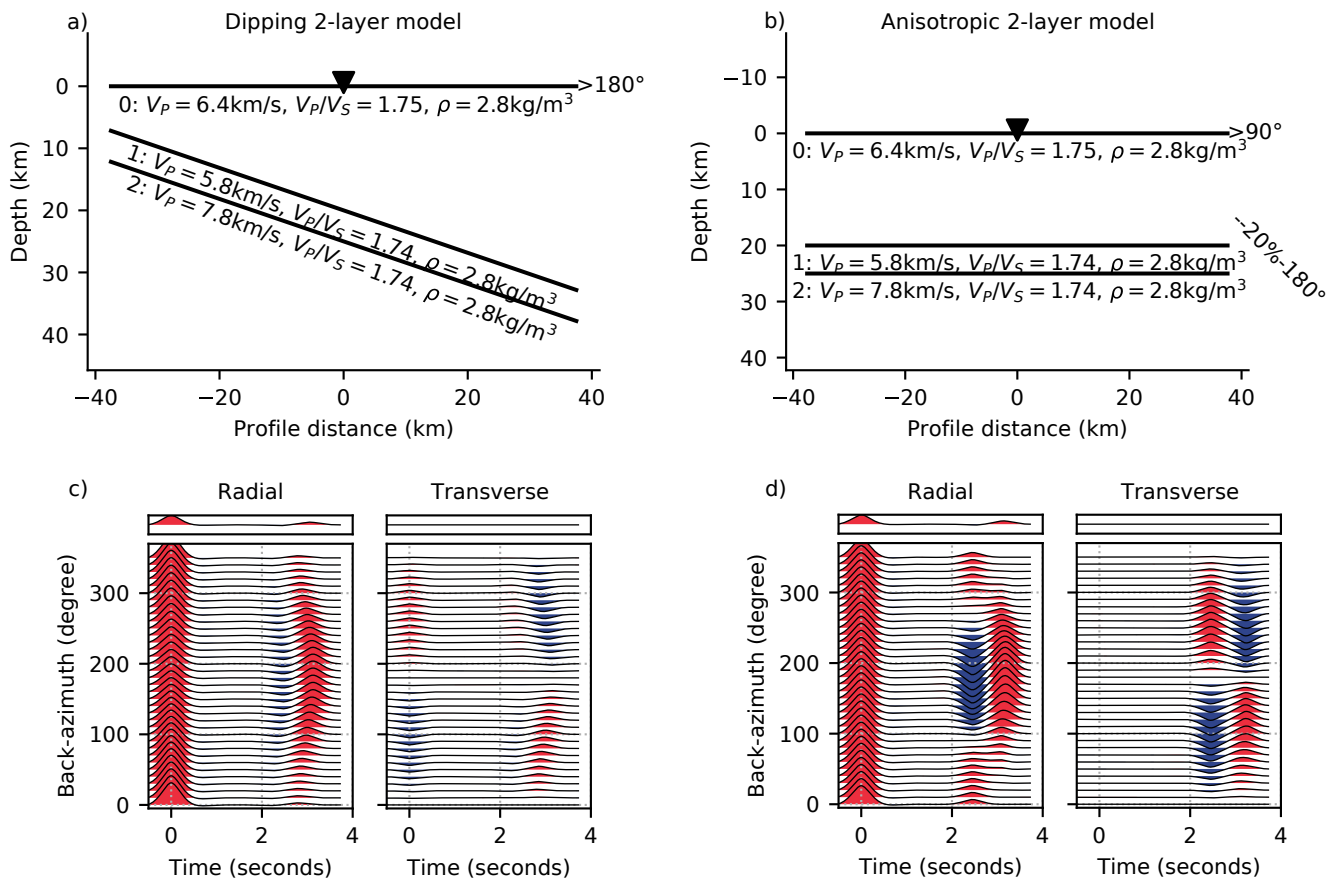


Figure 4 Reproduction of figure 3 of Porter et al. (2011). (a) and (b) Layer geometry and properties. (c) and (d) Resulting receiver functions. The code that reproduces this figure is given in Listing 3.

locity models. The two test cases are the isotropic 1-layer case with free surface reflections (mod1 in Listing 1; Figure 2) and the anisotropic lower crust case with direct conversions only (anim in Listing 3; Figure 4b and d). *Telewavesim* seismograms were generated using the code given in Listing 5. Note that *Telewavesim* lacks the capacity of synthesizing seismograms for dipping layers and inherently always includes all theoretical phase arrivals within the time window. Additionally, *Telewavesim* results do not provide a good infinite frequency approximation and therefore need to be filtered for comparison with *PyRaysum* results.

For the isotropic 1-layer model, the *Telewavesim* and *PyRaysum* traces agree with a cross-correlation coefficient of 0.9975, if multiples of the direct P-wave (first-order multiples) are considered (`mults=2`; Figure 5a). However, the amplitude of the *PpS* arrival differs noticeably. This is the case because, with the `mults=2` option, no second-order multiple is calculated. For instance, neither reflections of conversion (e.g., *PSpP*) nor conversions of reflections (e.g., *PsP*) are considered. As we will discuss below, this behaviour is deliberate, because the implicit inclusion of these phases results in a large overhead for multi-layered models, leading to long run times and eventually segmentation faults. The limitation of `mults=2` to first-order multiples ensures that the phase with the largest amplitude is present in the synthetic seismograms.

In the present case, the free-surface reflection of

the P-to-S Moho conversion *PSpP* contributes significantly to the amplitude of the *PpS* phase. Such equivalent phases can explicitly be included using the `Control.set_phaselist()` method. The unique set of phase descriptors present can be retrieved from a `Result` object and be used to compute the additional equivalent phases (Listing 4). With the inclusion of equivalent phases, the cross-correlation coefficient between the *Telewavesim* and *PyRaysum* seismograms improves to 0.9996 (Figure 5a).

For the anisotropic lower crust model (Figure 4, Listing 3), the *Telewavesim* and *PyRaysum* traces agree with a cross-correlation coefficient of 0.9996. Plotting of the `conversion_names` facilitates the interpretation of the complex converted wave forms in terms of conversions to fast and slow S-waves at the two subsurface interfaces (Figure 5b).

5 Performance

We compared the run times of typical calls to *Raysum* with comparable calls to *PyRaysum*, as well as different processing options of *PyRaysum*, using an AMD EPYC™3 GHz Central Processing Unit.

We first tested the run time of the current *Raysum* version 1.2 with input models consisting of 1 to 7 layers over a half-space, for 24 rays, calculating all first order multiples (`mults=2`). The model, geometry and parameter files were read from disk; seismic traces, arrival times

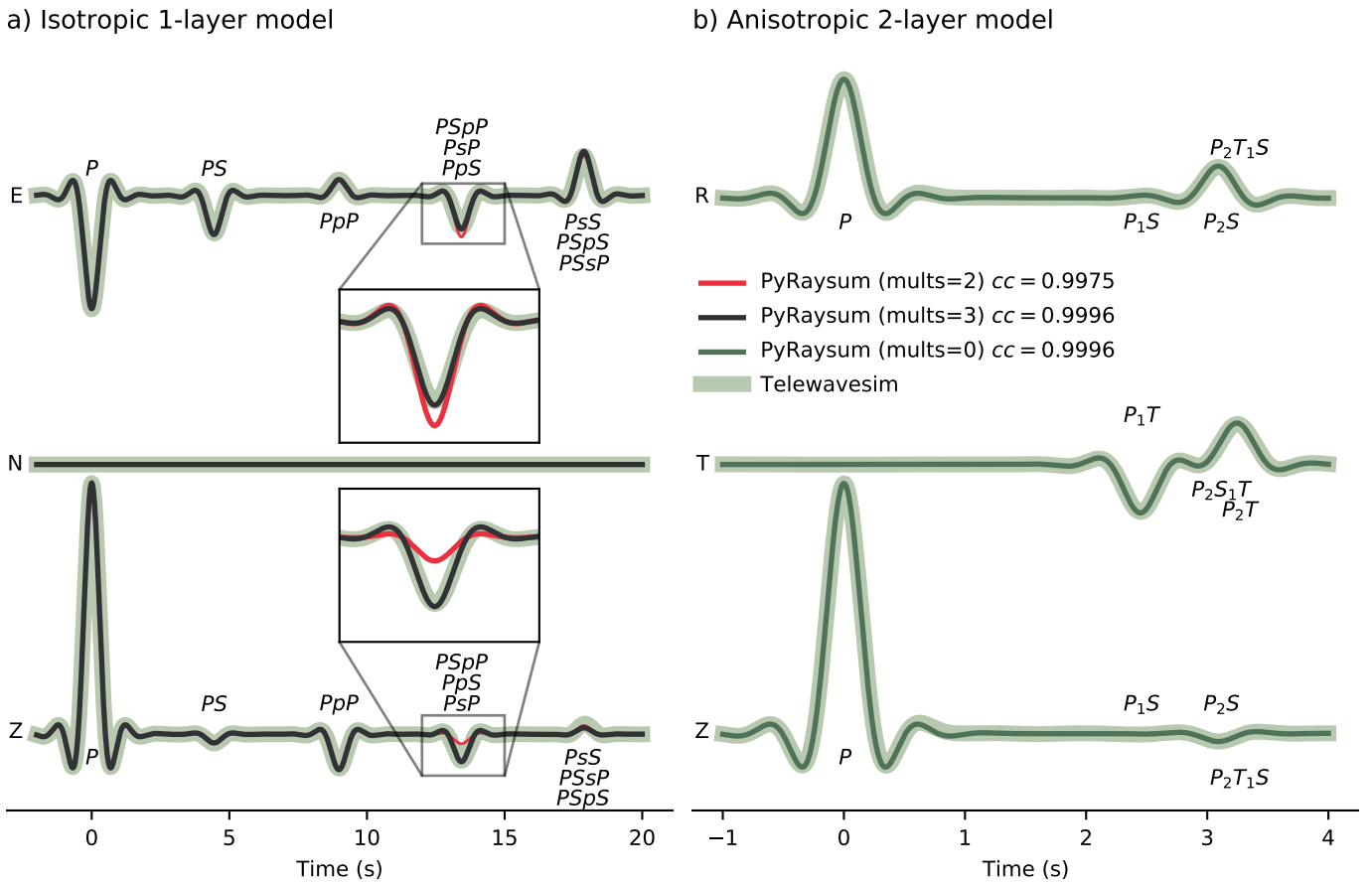


Figure 5 Validation of the timing and amplitude of direct, converted and reflected seismic phases of *PyRaysum* (thin lines) against *Telewavesim* (thick lines). (a) Conversions and multiples in an isotropic 1-layer model (Figure 2, Listing 1); 1 Hz low-pass filter applied. (b) Direct conversions in an anisotropic lower crust model (Figure 4b and d, Listing 3). Phase nomenclature as in Section 2.2. ENZ: East, North, Vertical seismogram components. RTZ: Radial, Transverse, Vertical seismogram components.

and phase descriptor files were written to disk. The computation completed in about 800 ms for the single layer model with a factorial increase to about 5 s for the 7 layer model (blue line in Figure 6). At 8 layers, *Raysum* encountered a segmentation fault, because the number of computed phases exceeded the maximum `maxph`, which is defined during compilation. Using *PyRaysum*, the same results can be obtained faster. With *NumPy* array output and an otherwise identical configuration, the

Listing 4 Code illustrating the use of equivalent phases. Definitions of Listing 1 are assumed.

```
# Get descriptors from seismogram
descriptors = res1.descriptors()

# Add equivalent phases
# Implicitly sets Control.mults=3
ctrl1.set_phaselist(
    descriptors, equivalent=True
)

# Due east incidence
geom4 = Geometry(90, 0.06)

# Black seismogram of Figure 5a
res4 = run(mod1, geom4, ctrl1)
```

1 layer model completed in 70 ms and the 7 layer model in 2.1 s (teal line in Figure 6). These numbers convert to a 2- to 11-fold decrease in computation time, primarily because the in-/output overhead is avoided.

We now illustrate the computational cost of the treatment of phase combinations (setting of `Control.mults`) and the overhead of handling the metadata-rich *ObsPy* objects against the bare *NumPy* array. We use the *ObsPy*-based receiver function computation and filtering provisions as given in Listing 6 and measure the run time of Listing 6 with different options for `Control.mults`:

Obs-M2-F-RF Compute all conversions and first order multiples: `ctrl6 = Control(mults=2)`

Obs-M0-F-RF Only compute direct conversions: `ctrl6 = Control(mults=0)`

Obs-M3-F-RF Only compute two explicit phases: the direct P wave and one P-to-S conversion: `ctrl6.set_phaselist(["1P0P", "1P0S"])` (for the 1-layer case). This implicitly sets `ctrl6.mults=3`.

The pink-shaded lines in Figure 6 illustrate the run time of Listing 6 with increasing number of layers in the model. When all conversions and multiples of all layers

are computed (*Obs-M2-F-RF*), the run time increases factorially from about 200 ms for a one-layer model to 6.3 seconds for 7 layers. When only forward conversions are considered (*Obs-M0-F-RF*), the factorial increase is less steep. Explicitly fixing the number of rays to be computed (*Obs-M3-F-RF*) yields a constant run time, as expected. The likely small increase due to increased number of ray segments is smaller than the precision of our time measurement.

Run times on the order of a second are usually acceptable when executing code a few times manually. For frequent and automatic calls that do not require bookkeeping of metadata, results can be obtained faster by directly calling the Fortran routine `run_bare()`. We next illustrate the computational cost of three *NumPy*-based post-processing options, keeping the number of phases constant as in the last case examined above. The post processing steps timed are (Listing 7):

Num-M3-F-RF Compute seismograms. Then compute receiver functions through spectral division and filter them using `filtered_rf_array()`.

Num-M3-F Compute seismograms. Filter them using `filtered_array()`.

Num-M3 Only compute synthetic seismograms.

In Listing 7, `rffarray` holds the processed data. It is allocated once before the (possibly subsequent) calls to `filtered_rf_array` or `filtered_array`.

For all three cases, the run time is constant with respect to the number of model layers (green-shaded lines in Figure 6). Compared to the *ObsPy*-based post processing, time spent for filtering and spectral division (*Num-M3-F-RF*) is approximately halved, with only 100 instead of 200 ms, implying that as much time is required for bookkeeping. Sparing spectral division (*Num-M3-F*) saves about 1/5th of run time, or 20 ms in the present example. Filtering is computationally cheap, taking only about 1/25th of time, or 5 ms (*Num-M3*).

6 Outlook and Future Work

With the time-efficient, *NumPy*-based post-processing, *PyRaysum* can be used as a forward code in parameter estimation problems. For example, the common problem of finding the optimal crustal thickness and bulk V_P/V_S ratio from the time and amplitude of the Moho conversion and reverberations in receiver functions (e.g. [Zhu and Kanamori, 2000](#)) can be re-formulated as a minimum misfit problem and be generalized to multi-layered models. First tests indicate that, e.g., *SciPy*'s `dual_annealing()` function can find a minimum misfit model from teleseismic receiver functions for the thickness, V_S , and V_P/V_S of three layers representative for the continental crust and subducting slab of the Cascadia subduction zone within a few hours. Automatic phase labels (Figures 2 and 5) can help to identify more multiples in complex receiver functions and facilitate a more thorough understanding of the scattered wave field.

Anisotropy is currently parameterized as a single parameter, ani (Equation 1). Internally, *Raysum* handles

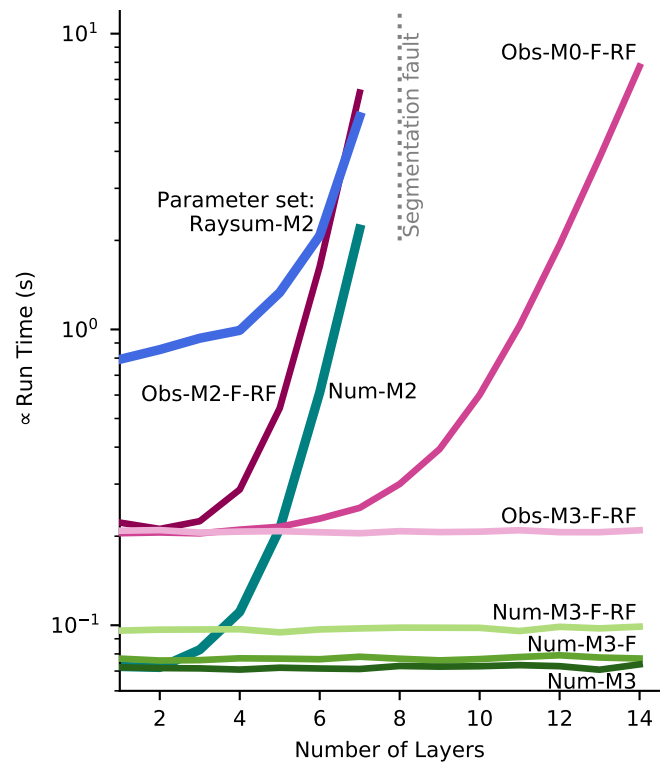


Figure 6 Runtime of *Raysum* and different configurations of *PyRaysum* as a function of numbers of layers in the model. The parameter sets correspond to the following configurations: *Raysum*: Call the *Raysum* binary `seis-spread` from the command line; Parse program in- and output through files. *Obs*: execute `prs.run` and use *Result* class methods for post-processing (Listing 6). *Num*: execute `fraysum.run_bare()` and use *NumPy* array-based post-processing functions (Listing 7). M0, M2, M3: `mults` set to 0, 2, or 3. F: filter. RF: compute receiver functions.

anisotropy in its most general form using the Christoffel equation. This in principle allows to explore other theoretical crystal symmetry classes (e.g. general hexagonal, orthorhombic), as well as anisotropy predicted and measured for specific minerals and rocks (e.g. [Brownlee et al., 2017](#)), which can be implemented through a new definition and internal handling of the *Model* class.

7 Conclusion

PyRaysum is a modern and fast incarnation of *Raysum* ([Frederiksen and Bostock, 2000](#)), the popular algorithm to compute seismograms that result from the plane wave propagation through dipping, anisotropic, layered media. New features include bypassing hard disk read-write operations, automatic labeling of seismic phases, easy definition of explicit phase lists, inclusion of equivalent phases, *ObsPy* integration, efficient receiver function post processing, and interactive manipulation of subsurface models. With these improvements, *PyRaysum* makes it possible to play with receiver functions in a simple and efficient Python environment, as well as to invert for subsurface properties using state-of-the-art inverse modeling algorithms.

ACKNOWLEDGMENTS

The authors thank Andrew Frederiksen for extensive discussion, and for his continued work on *Raysum*; and Michael Bostock for discussion. First and foremost, please cite their work (Frederiksen and Bostock, 2000) when using *PyRaysum*. The comments of two anonymous reviewers helped to improve the manuscript and the initial major release of *PyRaysum*. WB was located on the traditional, ancestral, and unceded territories of the x^wməθk^wəyəm Musqueam People while performing this research. PA acknowledges and respects that his workplace stands on unceded Algonquin territory. This work is funded by the German Research Foundation, grant BL 1758/1-1, and by the Natural Science and Engineering Research Council of Canada, Discovery grant RGPIN-2018-03752. *PyRaysum* relies on open-source software, namely *ObsPy* (Krischer et al., 2015), *NumPy* (Harris et al., 2020), and *SciPy* (Virtanen et al., 2020). Figures were created with *Matplotlib* (Hunter, 2007).

Code availability

PyRaysum is open-source software and is under active development on *GitHub* (<https://github.com/paudetseis/PyRaysum>, last accessed January 2023). A snapshot of the most recent version 1.0.0 is hosted on zenodo (Audet and Bloch, 2022). The full documentation is included with the current snapshot and online at <https://paudetseis.github.io/PyRaysum/index.html>. *Raysum* is available at <https://home.cc.umanitoba.ca/~frederik/Software/>.

References

- Audet, P. and Bloch, W. *PyRaysum*: Software for modeling ray-theoretical body-wave propagation. Dec. 2022. doi: 10.5281/zenodo.7468301.
- Audet, P. and Bürgmann, R. Possible control of subduction zone slow-earthquake periodicity by silica enrichment. *Nature*, 510 (7505):389–392, jun 2014. doi: 10.1038/nature13391.
- Audet, P., Thomson, C., Bostock, M., and Eulenfeld, T. Telewavesim: Python software for teleseismic body wave modeling. *Journal of Open Source Software*, 4(44):1818, dec 2019. doi: 10.21105/joss.01818.
- Brownlee, S. J., Schulte-Pelkum, V., Raju, A., Mahan, K., Condit, C., and Orlandini, O. F. Characteristics of deep crustal seismic anisotropy from a compilation of rock elasticity tensors and their expression in receiver functions. *Tectonics*, 36(9): 1835–1857, sep 2017. doi: 10.1002/2017tc004625.
- Cassidy, J. F. and Ellis, R. M. S-wave velocity structure of the Northern Cascadia Subduction Zone. *Journal of Geophysical Research: Solid Earth*, 98(B3):4407–4421, mar 1993. doi: 10.1029/92jb02696.
- Frederiksen, A. W. and Bostock, M. G. Modelling teleseismic waves in dipping anisotropic structures. *Geophysical Journal International*, 141(2):401–412, may 2000. doi: 10.1046/j.1365-246x.2000.00090.x.
- Harris, C. R., Millman, K. J., van der Walt, S. J., Gommers, R., Virtanen, P., Cournapeau, D., Wieser, E., Taylor, J., Berg, S., Smith, N. J., Kern, R., Picus, M., Hoyer, S., van Kerkwijk, M. H., Brett, M., Haldane, A., del Río, J. F., Wiebe, M., Peterson, P., Gérard-Marchant, P., Sheppard, K., Reddy, T., Weckesser, W., Abbasi, H., Gohlke, C., and Oliphant, T. E. Array programming with NumPy.

- Nature*, 585(7825):357–362, Sept. 2020. doi: 10.1038/s41586-020-2649-2.
- Hunter, J. D. Matplotlib: A 2D graphics environment. *Computing in Science & Engineering*, 9(3):90–95, 2007. doi: 10.1109/MCSE.2007.55.
- Kennett, B. *Seismic Wave Propagation in Stratified Media*. ANU Press, 2009. doi: 10.26530/oapen_459524.
- Kennett, B. L. N. The Removal of Free Surface Interactions From Three-Component Seismograms. *Geophysical Journal International*, 104(1):153–154, jan 1991. doi: 10.1111/j.1365-246x.1991.tb02501.x.
- Krischer, L., Megies, T., Barsch, R., Beyreuther, M., Lecocq, T., Caudron, C., and Wassermann, J. ObsPy: a bridge for seismology into the scientific Python ecosystem. *Computational Science & Discovery*, 8(1):014003, may 2015. doi: 10.1088/1749-4699/8/1/014003.
- Kumar, P., Yuan, X., Kumar, M. R., Kind, R., Li, X., and Chadha, R. K. The rapid drift of the Indian tectonic plate. *Nature*, 449(7164): 894–897, oct 2007. doi: 10.1038/nature06214.
- Levin, V. and Park, J. P-SH conversions in a flat-layered medium with anisotropy of arbitrary orientation. *Geophysical Journal International*, 131(2):253–266, nov 1997. doi: 10.1111/j.1365-246x.1997.tb01220.x.
- Lombardi, D., Braunmiller, J., Kissling, E., and Giardini, D. Moho depth and Poisson's ratio in the Western-Central Alps from receiver functions. *Geophysical Journal International*, 173(1): 249–264, apr 2008. doi: 10.1111/j.1365-246x.2007.03706.x.
- Nicholson, T., Bostock, M., and Cassidy, J. F. New constraints on subduction zone structure in northern Cascadia. *Geophysical Journal International*, 161(3):849–859, jun 2005. doi: 10.1111/j.1365-246x.2005.02605.x.
- Porter, R., Zandt, G., and McQuarrie, N. Pervasive lower-crustal seismic anisotropy in Southern California: Evidence for underplated schists and active tectonics. *Lithosphere*, 3(3):201–220, jun 2011. doi: 10.1130/l126.1.
- Saul, J., Kumar, M. R., and Sarkar, D. Lithospheric and upper mantle structure of the Indian Shield, from teleseismic receiver functions. *Geophysical Research Letters*, 27(16):2357–2360, aug 2000. doi: 10.1029/1999gl011128.
- Schneider, F., Yuan, X., Schurr, B., Mechie, J., Sippl, C., Haberland, C., Minaev, V., Oimahmadov, I., Gadoev, M., Radjabov, N., Abdybachaev, U., Orunbaev, S., and Negmatullaev, S. Seismic imaging of subducting continental lower crust beneath the Pamir. *Earth and Planetary Science Letters*, 375:101–112, aug 2013. doi: 10.1016/j.epsl.2013.05.015.
- Schulte-Pelkum, V., Monsalve, G., Sheehan, A., Pandey, M. R., Sapkota, S., Bilham, R., and Wu, F. Imaging the Indian subcontinent beneath the Himalaya. *Nature*, 435(7046):1222–1225, jun 2005. doi: 10.1038/nature03678.
- Selway, K., Ford, H., and Kelemen, P. The seismic mid-lithosphere discontinuity. *Earth and Planetary Science Letters*, 414:45–57, mar 2015. doi: 10.1016/j.epsl.2014.12.029.
- Sherrington, H. F., Zandt, G., and Frederiksen, A. Crustal fabric in the Tibetan Plateau based on waveform inversions for seismic anisotropy parameters. *Journal of Geophysical Research: Solid Earth*, 109(B2), feb 2004. doi: 10.1029/2002jb002345.
- Sodoudi, F., Yuan, X., Kind, R., Heit, B., and Sadidkhouy, A. Evidence for a missing crustal root and a thin lithosphere beneath the Central Alborz by receiver function studies. *Geophysical Journal International*, 177(2):733–742, may 2009. doi: 10.1111/j.1365-246x.2009.04115.x.
- Thomson, C. Modelling surface waves in anisotropic structures I. Theory. *Physics of the Earth and Planetary Interiors*, 103(3-4):

195–206, nov 1997. doi: 10.1016/s0031-9201(97)00033-2.

Virtanen, P., Gommers, R., Oliphant, T. E., Haberland, M., Reddy, T., Cournapeau, D., Burovski, E., Peterson, P., Weckesser, W., Bright, J., van der Walt, S. J., Brett, M., Wilson, J., Millman, K. J., Mayorov, N., Nelson, A. R. J., Jones, E., Kern, R., Larson, E., Carey, C. J., Polat, İ., Feng, Y., Moore, E. W., VanderPlas, J., Laxalde, D., Perktold, J., Cimrman, R., Henriksen, I., Quintero, E. A., Harris, C. R., Archibald, A. M., Ribeiro, A. H., Pedregosa, F., van Mulbregt, P., and SciPy 1.0 Contributors. SciPy 1.0: Fundamental Algorithms for Scientific Computing in Python. *Nature Methods*, 17:261–272, 2020. doi: 10.1038/s41592-019-0686-2.

Zhu, L. and Kanamori, H. Moho depth variation in southern California from teleseismic receiver functions. *Journal of Geophysical Research: Solid Earth*, 105(B2):2969–2980, feb 2000. doi: 10.1029/1999jb900322.

A Synthetic seismograms for cross validation

Listing 5 Code to generate *Telewavesim* seimograms for validation (Figure 5). Assumes definitions of Listings 1 and 3

```
from telewavesim import utils as tws

baz = 90 # Back-azimuth
slow = 0.06 # Slowness
npts = 4500 # Samples
dt = 0.01 # Sampling Interval
anid = {1: "iso", 0: "tri"} # Anisotropy ID

# Isotropic 1-layer model
tmodi = tws.Model(
    mod1["thickn"] * 1e-3,
    mod1["rho"],
    mod1["vp"] * 1e-3,
    mod1["vs"] * 1e-3,
)

twi = tws.run_plane(
    tmodi, slow, npts, dt, baz
)

# Anisotropic 2-layer model
tmoda = tws.Model(
    anim["thickn"] * 1e-3,
    anim["rho"],
    anim["vp"] * 1e-3,
    anim["vs"] * 1e-3,
    [anid[f] for f in anim["flag"]],
    anim["ani"],
    anim["trend"],
    anim["plunge"],
)

# Run Telewavesim
twa = tws.run_plane(
    tmoda, slow, npts, dt, baz
)
```

B Performance of *ObsPy*-based post-processing

Listing 6 Template for *ObsPy*-based receiver function computation and post processing. Assumes definitions of Listing 1. For performance testing, `Control.mults` was chosen as described in Section 5.

```
ctrl6 = Control(mults=0) # See Section 5
for _ in range(13):
    print(len(mod1), "layers", end="... ")
    res6 = run(mod1, geom1, ctrl6)
    res6.calculate_rfs()
    res6.filter(
        "rfs",
        "bandpass",
        freqmin=0.05,
        freqmax=0.5,
        zerophase=True,
        corners=2,
    )
    print("Done!")
    # Split topmost layer in two
    mod1.split_layer(0)
```

C Performance of *NumPy*-based post-processing

Listing 7 The three *NumPy*-based performance test cases spelled out for the 1-layer example of Listing 1.

```
from pyraysum import frs
from fraysum import run_bare
cases = ["Num-M3-F-RF", "Num-M3-F", "Num-M3"]

fmin = 0.05
fmax = 0.5 # Filter corners in Hz
ctrl1.set_phaselist(["1P0P", "1P0S"])
ctrl1.rot = "PVH" # P-V-H coordinates
rfarray = frs.make_array(geom1, ctrl1)




for case in cases:
    array = run_bare(
        *mod1.parameters,
        *geom1.parameters,
        *ctrl1.parameters,
    )

    if case == "Num-M3-F-RF":
        frs.filtered_rf_array(
            array,
            rfarray,
            geom1.ntr,
            ctrl1.npts,
            ctrl1.dt,
            fmin,
            fmax,
        )

    if case == "Num-M3-F":
        frs.filtered_array(
            array,
            rfarray,
            geom1.ntr,
            ctrl1.npts,
            ctrl1.dt,
            fmin,
            fmax,
        )
```

The article *PyRaysum: Software for Modeling Ray-theoretical Plane Body-wave Propagation in Dipping Anisotropic Media* © 2023 by Wasja Bloch is licensed under CC BY 4.0.

Ocean Surface Gravity Wave Excitation of Flexural Gravity and Extensional Lamb Waves in Ice Shelves

L.S. Abrahams  * ^{1,2}, J.E. Mierzejewski ^{1,3}, E.M. Dunham  ^{1,4}, P.D. Bromirski  ⁵

¹Department of Geophysics, Stanford University, Stanford, CA, USA, ²Now at Lawrence Livermore National Laboratory, Livermore, CA, USA, ³Now at California Polytechnic State University, San Luis Obispo, CA, USA, ⁴Institute of Computational and Mathematical Engineering, Stanford University, Stanford, CA, USA, ⁵Scripps Institution of Oceanography, University of California San Diego, La Jolla, California, USA

Author contributions: *Conceptualization:* L.S. Abrahams, E.M. Dunham. *Software:* L.S. Abrahams, E.M. Dunham. *Validation:* L.S. Abrahams, E.M. Dunham. *Formal Analysis:* L.S. Abrahams, E.M. Dunham, P.D. Bromirski. *Investigation:* L.S. Abrahams, J.E. Mierzejewski, E.M. Dunham. *Writing - original draft:* L.S. Abrahams, E.M. Dunham. *Writing - Review & Editing:* L.S. Abrahams, J.E. Mierzejewski, E.M. Dunham, P.D. Bromirski. *Visualization:* L.S. Abrahams, J.E. Mierzejewski, P.D. Bromirski. *Supervision:* L.S. Abrahams, E.M. Dunham. *Project administration:* E.M. Dunham. *Funding acquisition:* L.S. Abrahams, E.M. Dunham.

Abstract Flexure and extension of ice shelves in response to incident ocean surface gravity waves have been linked to iceberg calving, rift growth, and even disintegration of ice shelves. Most modeling studies utilize a plate bending model for the ice, focusing exclusively on flexural gravity waves. Ross Ice Shelf seismic data show not only flexural gravity waves, with dominantly vertical displacements, but also extensional Lamb waves, which propagate much faster with dominantly horizontal displacements. Our objective is to model the full-wave response of ice shelves, including ocean compressibility, ice elasticity, and gravity. Our model is a 2D vertical cross-section of the ice shelf and sub-shelf ocean cavity. We quantify the frequency-dependent excitation of flexural gravity and extensional Lamb waves and provide a quantitative theory for extensional Lamb wave generation by the horizontal force imparted by pressure changes on the vertical ice shelf edge exerted by gravity waves. Our model predicts a horizontal to vertical displacement ratio that increases with decreasing frequency, with ratio equal to unity at ~ 0.001 Hz. Furthermore, in the very long period band (< 0.003 Hz), tilt from flexural gravity waves provides an order of magnitude larger contribution to seismometer horizontal components than horizontal displacements from extensional Lamb waves.

Non-technical summary In the past three decades, we have seen ice shelves catastrophically weaken and break apart. In some cases, large calving events or ice shelf disintegration is correlated with the arrival of ocean waves and tsunamis. This has prompted the deployment of seismometers on ice shelves to study the ice shelf response to ocean wave impacts. Ocean waves convert to several other wave modes in the ice shelf and ocean layer beneath the ice shelf. In our study, we present computer simulations of the ocean and ice shelf system to quantify the wave motions within and on the surface of the ice shelf, thereby permitting comparison to seismic data. Our results help guide interpretation of seismic data and in understanding which wave modes are most likely to contribute to calving and fracture of ice shelves.

1 Introduction

Ice shelf stability and strength play an important role in understanding and predicting sea level rise (Bromwich and Nicolas, 2010). Ice shelves buttress ice sheets and following ice shelf collapse, ice streams have been observed to accelerate (Dupont and Alley, 2005; Pritchard et al., 2012). In the past three decades, we have seen ice shelves catastrophically weaken and break apart (Rott et al., 1996; De Angelis and Skvarca, 2003; Scambos et al., 2004; Brunt et al., 2011; Banwell et al., 2017; Massom et al., 2018). As the climate continues to warm, thinning and collapse of ice shelves is likely to occur at a more rapid rate.

Weakening of ice shelves has been associated with wave-induced flexure (Holdsworth and Glynn, 1978) as well as basal and surface melting (Paolo et al., 2015).

Basal melting is facilitated through influx (into the sub-ice shelf cavity) of warm seasonal sea water and circumpolar deep water (Walker et al., 2008; Rignot et al., 2013). During the summer months, surface melting increases, creating supraglacial lakes, further thinning the ice shelves and possibly contributing to hydro-fracturing into the ice shelf (Banwell et al., 2013).

Melting and thinning weaken ice shelves, but what creates fractures and finally triggers the collapse of ice shelves is poorly determined. Possible processes include ocean surface gravity wave forcing (Holdsworth and Glynn, 1978; Bromirski et al., 2010; Brunt et al., 2011; Banwell et al., 2017; Massom et al., 2018). Incident ocean waves are partially transmitted into the ice shelf as flexural gravity waves (similar to ocean surface gravity waves but with additional inertia and elastic resistance to bending from the ice) and other elastic waves bearing more similarity to traditional seismic waves. The ability of waves to transmit through the ice

Production Editor:
Gareth Funning
Handling Editor:
Paula Koelemeijer
Copy & Layout Editor:
Kirsty Bayliss

Received:
23rd August 2022
Accepted:
16th February 2023
Published:
15th March 2023

*Corresponding author: labrahams813@gmail.com

shelf and the magnitude of wave-induced stresses depend on the ice shelf structure (ice thickness, elastic moduli, density), depth of water in the sub-shelf cavity, and the properties of the incident wave (frequency, incidence angle, amplitude). Incident waves include ocean swell, storm-generated infragravity waves, tides, and tsunamis (MacAyeal et al., 2006). Low frequency waves penetrate the sub-shelf cavities more efficiently, causing flexure (Sergienko, 2013). This flexural stress can open cracks, drive rift growth, and initiate collapse events. Bromirski et al. (2010) concluded that both of the breakup events on the Wilkins Ice shelf in 2008 matched with arrivals of infragravity waves from large storm events on the Patagonian coast. Brunt et al. (2011) suggested that tsunami arrivals from the 2011 Tohoku-Oki, Japan, earthquake caused a massive calving event on the Sulzberger Ice Shelf. Massom et al. (2018) linked storm-generated swell to calving and break-up of the Larsen A and B and Wilkins ice shelves. Icequake activity near the front of the Ross Ice Shelf is also correlated with ocean wave arrivals (Chen et al., 2019; Aster et al., 2021), though other factors such as tidal and thermal stresses contribute as well (Olinger et al., 2019). Flexural gravity waves are also excited by abrupt rift opening and can be used to track and monitor the expansion of rifts (Olinger et al., 2022).

Most models of the wave response of ice shelves have focused exclusively on the flexural response. However, the Ross Ice Shelf data shows other wave modes, including the fundamental mode extensional Lamb wave that propagates close to the plane stress P-wave speed of ice and has dominantly horizontal displacements (Bromirski et al., 2017; Chen et al., 2018, 2019). These observations motivate us to examine how incident ocean waves convert to flexural gravity and extensional Lamb waves. Chen et al. (2018) suggest that wave-induced pressure changes on the shelf front, which exert a net horizontal force on the ice shelf, are responsible for excitation of extensional Lamb wave. We confirm this hypothesis with our modeling.

Before introducing our model, we remark on the many studies that have focused on the flexural gravity wave response of ice shelves and sea ice. Most work utilizes a bending plate model to describe the ice response, recognizing that horizontal wavelengths are much larger than ice thickness at frequencies of interest. The frequency-domain reflection/transmission problem of gravity waves in open water coupled to flexural gravity waves in ice-covered water was solved by Fox and Squire (1990, 1991). The earlier history of the field is reviewed by Squire et al. (1995); Squire (2007). While much of this work focused on sea ice, attention has shifted recently to ice shelves (Sergienko, 2010, 2013). Lipovsky (2018) provides a methodology to estimate wave-induced bending stresses from measured ice shelf motions. Finite element (Ilyas et al., 2018; Sergienko, 2017) and finite difference (Mattsson et al., 2018) methods can be used to solve to the potential flow problem in sub-shelf cavity. These studies show how the shallow water approximation breaks down at swell frequencies (0.03-0.1 Hz) (Kalyanaraman et al., 2019) and how ice shelves affect the shoaling process as waves

advance into shallower water (Meylan et al., 2021). Solution of the full elasticity problem in the ice shelf can be used to determine the validity of the plate approximation (Sergienko, 2010, 2017; Kalyanaraman et al., 2020). While most efforts focus on 2D vertical cross-section models, some 3D or 2D map-view models have been developed to account for the complex geometries and variable ice thickness and water depth of real ice shelves (Sergienko, 2017; Tazhimbetov et al., 2022). However, use of a bending plate model for the ice shelf precludes study of extensional Lamb waves and other ice shelf wave modes.

Our objective is to model the full-wave response of ice shelves, including ocean compressibility, ice elasticity and inertia, and gravity. We do this for a 2D vertical cross-section of the ice shelf and sub-shelf ocean cavity, coupled to an open-water region. The ice and ocean obey the elastic and acoustic wave equations, respectively, and gravity is added using an extension of the fully coupled method introduced by Lotto and Dunham (2015). This allows us to model extensional Lamb waves in addition to flexural gravity waves. A similar model was utilized by Kalyanaraman et al. (2020) to study wave reflection/transmission and resonance modes of finite length ice shelves. They note the existence of extensional wave resonance modes, but do not perform a systematic investigation of extensional Lamb wave excitation by incident surface gravity waves. This is the primary focus of our study and we anticipate results to be of use when interpreting data from ice shelves and understanding which wave modes might contribute to fracture and calving.

Our paper is organized as follows. We begin with a statement of the model (governing equations and boundary/interface conditions) and review of relevant wave modes for open water and ice-covered water, in the frequency domain, in section 2. This provides the mathematical basis for the reflection/transmission analysis that occupies the remainder of the paper. While the reflection/transmission problem is best formulated and analyzed in the frequency domain, we utilize a time-domain finite difference code for wave propagation to perform the required numerical simulations. Thus we must introduce a procedure, described in section 3, to extract frequency-dependent reflection/transmission coefficients from our time-domain simulations. The reflection/transmission coefficients are also defined in this section. We verify this procedure against known results for surface gravity wave propagation across a step change in water depth (section 4). Then we proceed to study wave reflection/transmission from an ice shelf (section 5), which contains the novel contributions of our study.

2 Model and wave modes

We study wave propagation in a 2D vertical cross-section of the ice shelf and sub-shelf ocean cavity, connected to an open-water region (Figure 1a). We use a coordinate system in which x is horizontal and z is vertical, positive up with the sea surface at $z = 0$ and seafloor at $z = -H_1$. An incident surface gravity wave is im-

posed in the open-water region ($x < 0$) and arrives at the ice shelf edge ($x = 0$), where it is both reflected and transmitted into the ice shelf and sub-shelf cavity. In the open water ($x < 0$) the water depth is H_1 . For $x > 0$, an ice shelf of thickness H_i floats on the water. Given the ice and water densities, ρ_i and ρ_w , respectively, hydrostatic balance requires the water depth in the sub-shelf cavity to be $H_2 = H_1 - (\rho_i/\rho_w)H_i$. The top of the ice shelf is located at $z = (1 - \rho_i/\rho_w)H_i$. The ice-water interface is located $z = -(\rho_i/\rho_w)H_i$ and the sub-shelf ocean cavity extends to $z = -H_1$. When deriving dispersion relations involving the ice, it is convenient to introduce the half-thickness $h = H_i/2$.

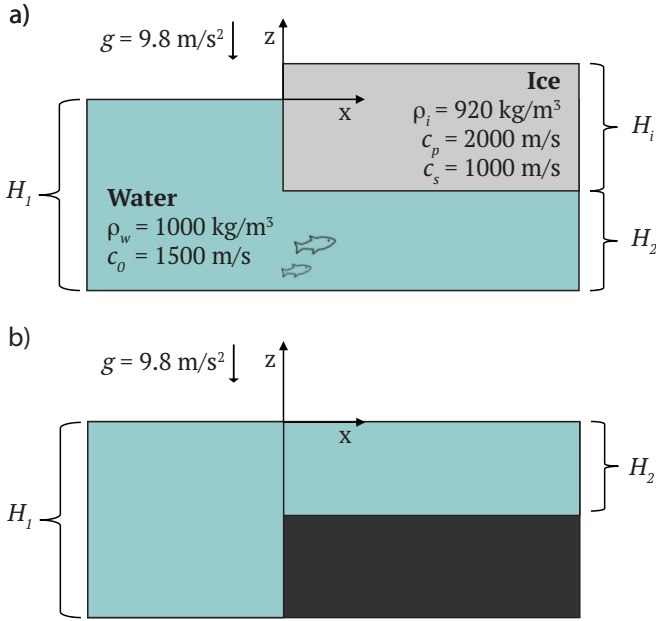


Figure 1 a) An incident surface gravity wave, propagating to the right, reaches the ice shelf edge at $x = 0$, creating reflected surface gravity waves and transmitted flexural gravity and extensional Lamb waves. The ice shelf is of thickness H_i and the ocean is of depth H_1 in open water and H_2 beneath the shelf. b) Step change in water depth at $x = 0$ that causes reflection and transmission of surface gravity waves, used to verify our procedure for calculating frequency-dependent reflection/transmission coefficients from time-domain simulations.

The ice and compressible ocean obey the elastic and acoustic wave equations, respectively, and gravity is added using an extension of the method introduced by [Lotto and Dunham \(2015\)](#), which assumes small perturbations about an initial hydrostatic equilibrium state in the water.

The governing equations in the water are

$$\frac{1}{K_w} \frac{\partial p}{\partial t} + \frac{\partial v_x}{\partial x} + \frac{\partial v_z}{\partial z} = 0, \quad (1)$$

obtained by combining the linearized mass balance with a linearized equation of state; and the momentum balance equations,

$$\rho_w \frac{\partial v_x}{\partial t} + \frac{\partial p}{\partial x} = 0, \quad (2)$$

and

$$\rho_w \frac{\partial v_z}{\partial t} + \frac{\partial p}{\partial z} = 0, \quad (3)$$

for particle velocities v_i , pressure perturbation p , bulk modulus K_w , and density ρ_w . The sound speed is $c_0 = \sqrt{K_w/\rho_w}$. Gravity acts as a restoring force, entering the open-water problem only through linearization of the free surface boundary condition,

$$p - \rho_w g \eta = 0, \quad \text{at } x < 0, z = 0, \quad (4)$$

where wave height η is governed by the linearized kinematic condition on the sea surface,

$$\frac{\partial \eta}{\partial t} = v_z, \quad \text{at } x < 0, z = 0. \quad (5)$$

At the bottom of the ocean, we assume a rigid wall condition,

$$v_z = 0, \quad \text{at } z = -H_1. \quad (6)$$

The ice obeys the elastic wave equation for an isotropic solid with spatially uniform material properties:

$$\rho_i \frac{\partial^2 u_x}{\partial t^2} = (\lambda + \mu) \left(\frac{\partial^2 u_x}{\partial x^2} + \frac{\partial^2 u_z}{\partial x \partial z} \right) + \mu \left(\frac{\partial^2 u_x}{\partial x^2} + \frac{\partial^2 u_x}{\partial z^2} \right), \quad (7)$$

$$\rho_i \frac{\partial^2 u_z}{\partial t^2} = (\lambda + \mu) \left(\frac{\partial^2 u_x}{\partial x \partial z} + \frac{\partial^2 u_z}{\partial z^2} \right) + \mu \left(\frac{\partial^2 u_z}{\partial x^2} + \frac{\partial^2 u_z}{\partial z^2} \right), \quad (8)$$

for particle displacements u_i , density ρ , Lamé parameters λ and μ . The associated P- and S-wave speeds are $c_p = \sqrt{(\lambda + 2\mu)/\rho}$ and $c_s = \sqrt{\mu/\rho}$, respectively. The elastic wave equation is derived from the momentum balance equation, Hooke's law,

$$\sigma_{ij} = \lambda \epsilon_{kk} \delta_{ij} + 2\mu \epsilon_{ij}, \quad (9)$$

where δ_{ij} is the Kronecker delta, and the strain-displacement relation,

$$\epsilon_{ij} = \frac{1}{2} \left(\frac{\partial u_i}{\partial x_j} + \frac{\partial u_j}{\partial x_i} \right). \quad (10)$$

The top of the ice is a free surface,

$$\begin{aligned} \sigma_{xz} &= 0, \\ \sigma_{zz} &= 0, \end{aligned} \quad (11)$$

at $z = (1 - \rho_i/\rho_w)H_i$.

At the ice-water interface along the base of the ice shelf, we balance tractions and enforce continuity of normal velocity:

$$\sigma_{xz} = 0, \quad (12)$$

$$-\sigma_{zz} = p - \rho_w g \eta, \quad \partial \eta / \partial t = v_z, \quad (13)$$

$$\partial u_z / \partial t = v_z, \quad \text{at } x > 0, z = -(\rho_i/\rho_w)H_i, \quad (14)$$

where fields on the left side are evaluated at the bottom of the ice and fields on the right side are evaluated at the top of the water. Here the treatment of gravity in the water is identical to that in the open water region, with η again being the vertical displacement at the top of the water. We are therefore accounting for pressure

changes in response to perturbations about the background hydrostatic state in the water, but neglecting prestress within the ice.

Along the submerged portion of the vertical ice shelf edge, we again balance tractions and enforce continuity of normal velocity:

$$\sigma_{xz} = 0, \quad (15)$$

$$-\sigma_{xx} = p, \quad (16)$$

$$\partial u_x / \partial t = v_x, \quad \text{at } x = 0, \quad -(\rho_i / \rho_w) H_i < z < 0. \quad (17)$$

The portion of the shelf edge above water is a free surface:

$$\sigma_{xz} = 0, \quad (18)$$

$$\sigma_{xx} = 0, \quad \text{at } x = 0, \quad 0 < z < (1 - \rho_i / \rho_w) H_i. \quad (19)$$

Our goal is to study the reflection and transmission of incident surface gravity waves. Reflection and transmission coefficients of various wave modes can be defined in terms of the amplitude of propagating plane wave solutions in the frequency domain, which are derived in the following sections. However, we will extract these reflection and transmission coefficients from time-domain simulations using a procedure described subsequently (section 3).

2.1 Wave modes in open water

We first consider the problem of wave propagation in open water. We solve equations (1-3) with boundary conditions (4-6), assuming $e^{i(kx - \omega t)}$ dependence of all fields, where k is the horizontal wavenumber and ω is the angular frequency. For notational simplicity, $e^{i(kx - \omega t)}$ is implied and we denote the water depth as H . The solution for a wave of amplitude A (i.e., $\eta = Ae^{i(kx - \omega t)}$) is

$$p = \frac{A\omega^2 \rho_w}{\kappa \sinh(\kappa H)} \cosh(\kappa(z + H)), \quad (20)$$

$$v_x = Ak\omega \frac{\cosh(\kappa(z + H))}{\kappa \sinh(\kappa H)}, \quad (21)$$

$$v_z = -iA\omega \frac{\sinh(\kappa(z + H))}{\sinh(H\kappa)}, \quad (22)$$

where

$$\kappa = \sqrt{k^2 - \frac{\omega^2}{c_0^2}}, \quad (23)$$

and ω and k are related by the dispersion relation

$$\omega^2 = g\kappa \tanh(H\kappa). \quad (24)$$

The solutions to (24) include surface gravity waves (with slight corrections due to water compressibility) and acoustic waves (with slight corrections due to gravity) and have been discussed in many previous studies (Sells, 1965; Yamamoto, 1982; Lotto and Dunham, 2015). In this study, we are exclusively interested in the surface gravity wave mode.

2.2 Wave modes in ice-covered water

In Appendix A, we solve the corresponding problem in ice-covered water. For notational simplicity, we denote the water layer thickness as H and the ice thickness as $2h$. The dispersion relation is

$$\frac{\omega \rho_w D_0}{\kappa \sinh(\kappa H)} = \frac{2\rho_i c_s^4}{\omega^3 p F}, \quad (25)$$

where

$$D_0 = \cosh(\kappa H) - \frac{g\kappa}{\omega^2} \sinh(\kappa H), \quad (26)$$

$$F = \frac{\sinh(\alpha h) \sinh(\beta h)}{D_S} + \frac{\cosh(\alpha h) \cosh(\beta h)}{D_A}, \quad (27)$$

$$D_S = 4k^2 \alpha \beta \sinh(\alpha h) \cosh(\beta h) - (k^2 + \beta^2)^2 \cosh(\alpha h) \sinh(\beta h) \quad (28)$$

$$D_A = 4k^2 \alpha \beta \cosh(\alpha h) \sinh(\beta h) - (k^2 + \beta^2)^2 \sinh(\alpha h) \cosh(\beta h), \quad (29)$$

with

$$\alpha = \sqrt{k^2 - \omega^2 / c_p^2}, \quad (30)$$

$$\beta = \sqrt{k^2 - \omega^2 / c_s^2}. \quad (31)$$

Note that $D_0 = 0$ provides the dispersion relation for surface gravity waves in open water, given previously as (24). Similarly, $D_S = 0$ and $D_A = 0$ provide the dispersion relations for symmetric and antisymmetric modes of an elastic layer bounded by free surfaces.

Next we examine limits appropriate for long-wavelength extensional Lamb wave and flexural gravity wave modes. For the fundamental symmetric mode (extensional Lamb wave), assume $kh \ll 1$, such that $\alpha h \ll 1$ and $\beta h \ll 1$. In this limit,

$$D_S \approx -\frac{\omega^2 \beta h}{c_s^4} (\omega^2 - k^2 c_{ps}^2), \quad (32)$$

where the plane stress P-wave speed c_{ps} is defined via

$$c_{ps}^2 = 4c_s^2 \left(1 - \frac{c_s^2}{c_p^2}\right). \quad (33)$$

Thus for an elastic plate bounded by free surfaces, solutions of $D_S = 0$, in this long-wavelength limit, describe nondispersive extensional Lamb waves propagating at c_{ps} .

For the fundamental antisymmetric mode (flexural wave), in addition to $kh \ll 1$, $\alpha h \ll 1$, and $qh \ll 1$, we also assume $\omega / kc_p \ll 1$ and $\omega / kc_s \ll 1$ (phase velocity less than both the P- and S-wave speeds). In this limit, the dispersion relation for flexural waves in an elastic plate bounded by free surfaces, $D_A = 0$, can be written as

$$\omega^2 \approx \frac{4}{3} c_s^2 \left(1 - \frac{c_s^2}{c_p^2}\right) h^2 k^4, \quad (34)$$

or equivalently

$$\omega^2 = \frac{B}{m}k^4, \quad (35)$$

where

$$B = \frac{2Eh^3}{3(1-\nu^2)}, \quad (36)$$

$$m = 2h\rho_i,$$

are the bending stiffness B (written in terms of Young's modulus E and Poisson ratio ν) and the ice mass per horizontal unit area m . Note that

$$\frac{B}{m} = \frac{4}{3}c_s^2 \left(1 - \frac{c_s^2}{c_p^2}\right) h^2. \quad (37)$$

The approximate dispersion relation (35) matches that of flexural waves obeying the Euler-Bernoulli plate model,

$$-m\omega^2 w + B \frac{d^4 w}{dx^4} = 0, \quad (38)$$

where w is the vertical displacement (assumed to be uniform with depth).

Continuing with these approximations (which restricts focus to the flexural wave), but now accounting for the interaction of the ice shelf and water to study flexural gravity waves, we write (27) as

$$F \approx -\frac{c_s^4}{kh\omega^2 \left(\omega^2 - \frac{B}{m}k^4\right)}, \quad (39)$$

such that the dispersion relation (25) becomes

$$\frac{i\omega\rho_w \left[\cosh(kH) - \frac{gk}{\omega^2} \sinh(kH) \right]}{k \sinh(kH)} = \frac{m\omega^2 - Bk^4}{i\omega}, \quad (40)$$

or equivalently,

$$\frac{\rho_w\omega^2}{k \tanh(kH)} = Bk^4 + \rho_w g - m\omega^2. \quad (41)$$

This can be solved for ω as

$$\omega^2 = \frac{\rho_w g + Bk^4}{\rho_w/k \tanh(kH) + m}, \quad (42)$$

matching expressions given in many previous studies on flexural gravity waves (Ewing and Crary, 1934; Fox and Squire, 1990; Squire et al., 1995; Squire, 2007), thereby confirming the consistency of our model with known solutions in this limit.

Figure 2 shows the phase velocity ($c = \omega/k$) and group velocity ($U = d\omega/dk$) for the surface gravity wave, extensional Lamb wave, and flexural gravity wave modes. Parameter values are given in Table 1 and we use the open-water depth $H = H_1$ for the surface gravity wave and the sub-shelf depth $H = H_2$ for the extensional Lamb wave and flexural gravity wave solutions. We focus on frequencies up to 0.02 Hz, corresponding to the very long period (< 0.003 Hz) and infragravity (0.003 – 0.02 Hz) bands. We do not consider higher frequency swell in this study.

Surface gravity waves are normally dispersed, with phase and group velocity reaching a maximum wave

speed of \sqrt{gH} in the long wavelength limit (figure 2a). Extensional Lamb waves exhibit no significant dispersion over the frequency band of interest (figure 2b). In addition to gravity, the elastic restoring force causes the flexural gravity waves to propagate faster than surface gravity waves, and shorter wavelengths propagate faster than longer wavelengths. Therefore, flexural gravity waves are anomalously dispersed, with phase and group velocity reaching a minimum wave speed of \sqrt{gH} in the long wavelength limit (figure 2c). Additionally plotted in figure 2c are the group and phase velocity for the flexural gravity wave using the plate approximation (42), verifying the validity of the plate model at the frequencies of interest. Beamforming and seismic modeling for the Ross Ice Shelf indicate that the dominant flexural gravity wave energy travels at phase speeds of about 70 m/s, consistent with the long wavelength limit (Bromirski et al., 2017).

Finally, we remark that while our model results for the ice shelf response are discussed primarily in terms of wave amplitude (specifically, displacements of the ice surface), the horizontal normal stress σ_{xx} is also of interest because this stress component acts to open and close vertical fractures and rifts. The stresses can be calculated immediately from the surface displacements using the frequency-domain transfer functions given by Lipovsky (2018). For flexural gravity waves, which carry the largest stresses, the stress σ_{xx} can be obtained from the vertical displacement w , in the long wavelength plate theory limit, as (Timoshenko and Goodier, 1970)

$$\sigma_{xx} \approx -\frac{6Bk^2}{H_i^2}w. \quad (43)$$

3 Procedure to extract reflection and transmission coefficients from time-domain simulations

In this section we describe a procedure to extract frequency-dependent reflection and transmission coefficients from our time-domain simulations. The procedure will utilize Fourier transforms in both space and time with the following notation:

$$\tilde{f}(k, t) = \int_{-\infty}^{\infty} f(x, t) e^{-ikx} dx, \quad (44)$$

$$f(x, t) = \frac{1}{2\pi} \int_{-\infty}^{\infty} \tilde{f}(k, t) e^{ikx} dk,$$

$$\hat{f}(x, \omega) = \int_{-\infty}^{\infty} f(x, t) e^{i\omega t} dt, \quad (45)$$

$$f(x, t) = \frac{1}{2\pi} \int_{-\infty}^{\infty} \hat{f}(x, \omega) e^{-i\omega t} d\omega.$$

3.1 Surface gravity wave reflection/transmission for a step change in water depth

We begin with the simpler problem of surface gravity wave reflection/transmission from a step change in water depth. There is no ice shelf in this problem. Let H_1 and H_2 be the water depths in $x < 0$ and $x > 0$,

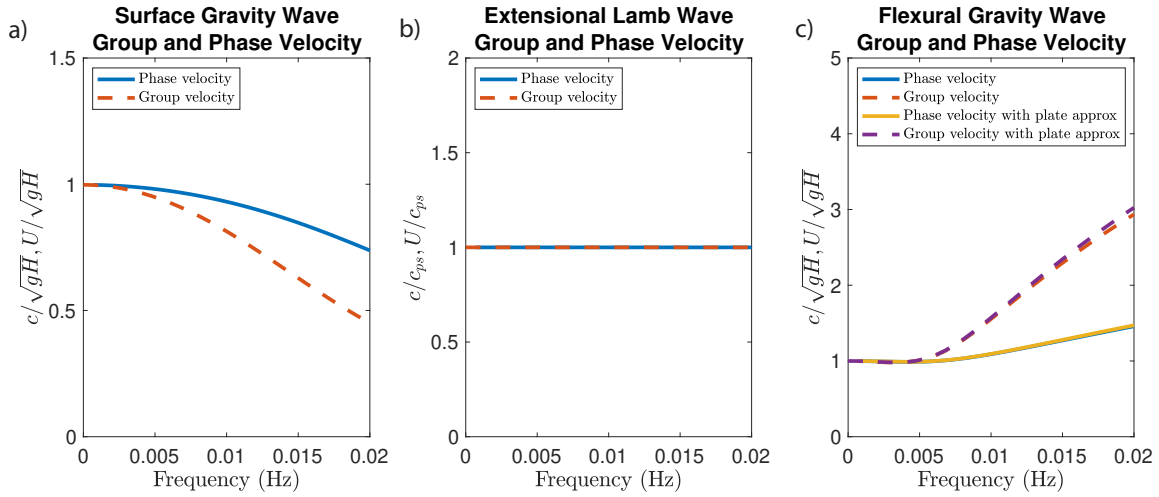


Figure 2 Group and phase velocity for the surface gravity wave, extensional Lamb wave, and flexural gravity wave.

respectively (Figure 1b). The problem is posed in the frequency domain. Define k_1 and k_2 as the wavenumbers of the surface gravity wave mode in $x < 0$ and $x > 0$, respectively, obtained by solving the open-water dispersion relation (24). The wavefield solution in the frequency domain, for an incident wave of spectral amplitude $A(\omega)$, is given by

$$\hat{\eta}(x, \omega) = \begin{cases} A(\omega) [e^{ik_1x} + R(\omega)e^{-ik_1x}] + \text{other modes}, & x < 0, \\ A(\omega)T(\omega)e^{ik_2x} + \text{other modes}, & x > 0, \end{cases} \quad (46)$$

where R and T are the frequency-dependent reflection and transmission coefficients, respectively, for the propagating surface gravity wave mode. In addition, it is well known that except in the shallow water limit, there are additional evanescent surface gravity wave mode solutions to (24), which are confined to the vicinity of the step change in water depth at $x = 0$ (Newman, 1965; Miles, 1967; Dingemans, 1997). These modes can be safely ignored at locations x sufficiently removed from $x = 0$. Furthermore, because we account for water compressibility, there are also acoustic modes. The acoustic modes exist as propagating waves only above some cut-off frequency (approximately $c_0/4H$ for the first mode, or 0.375 Hz for $H = 1000$ m), which is much higher than the frequencies of interest to us. Thus these modes are also evanescent and can be neglected in the following procedure to determine R and T .

Our goal now is to set up a problem in the time domain from which we can extract R and T . To do this, we set initial conditions at $t = 0$ corresponding to a broadband incident wave packet propagating only in the $+x$ direction. Define $\eta(x, 0) = \eta_0(x)$ and its spatial Fourier transform $\tilde{\eta}_0(k)$. The wavefield at some later time t , $\tilde{\eta}(k, t)$, is obtained by multiplying $\tilde{\eta}_0(k)$ by the phase factor $e^{-i\omega_1 t}$, where $\omega_1 = \omega_1(k)$ is obtained from solving the dispersion relation (24) for the surface gravity wave mode in water of depth H_1 . We select the sign of ω_1 such that $\omega_1/k > 0$ so that the wave propagates in the $+x$ direction.

Next we switch between ω and k Fourier transforms using a change of variable based on the dispersion relation. Note that $d\omega = Udk$, where U is the group velocity, which can be viewed as either a function of k or ω , as desired, provided that these are evaluated using the solution to the dispersion relation corresponding to the desired surface gravity wave mode. This procedure is illustrated for the incident wave:

$$\eta^I(x, t) = \frac{1}{2\pi} \int \tilde{\eta}_0(k) e^{i(kx - \omega_1 t)} dk \quad (47)$$

$$= \frac{1}{2\pi} \int \frac{\tilde{\eta}_0(k_1)}{U(k_1)} e^{i(k_1 x - \omega t)} d\omega, \quad (48)$$

where $k_1 = k_1(\omega)$ is evaluated for the surface gravity wave mode in water of depth H_1 . It follows that

$$\hat{\eta}^I(x, \omega) = \int \eta^I(x, t) e^{i\omega t} dt \quad (49)$$

$$= \frac{\tilde{\eta}_0(k_1)}{U(k_1)} e^{ik_1 x}, \quad (50)$$

from which we identify the spectral amplitude of the incident wave in (46) as

$$A(\omega) = \tilde{\eta}_0(k_1)/U(k_1). \quad (51)$$

Initial conditions on pressure and particle velocity are obtained by evaluating (20)-(22) times the surface displacement spectral amplitude $A(\omega)$.

To solve for the reflection coefficient R from our time-domain simulation, we Fourier transform the time series of η at some point $x < 0$ to obtain $\hat{\eta}(x, \omega)$. Then solve (46), neglecting the evanescent surface gravity and acoustic modes, to obtain

$$R(\omega) = \left[\frac{\hat{\eta}(x, \omega)}{A(\omega)} - e^{ik_1 x} \right] e^{ik_1 x}. \quad (52)$$

The procedure can be simplified even further by selecting the x location to be to the left of the initial wave packet, so that only the reflected wave contributes to the time series. In this case, the incident wave in (52), namely the $-e^{ik_1 x}$ term in brackets, can be ignored.

Extracting the transmission coefficient is similar. We select some point $x > 0$ sufficiently far from $x = 0$, extract the time series of η , and Fourier transform it in time to obtain $\hat{\eta}(x, \omega)$. Neglecting evanescent surface gravity and acoustic modes, we solve (46) for the transmission coefficient

$$T(\omega) = \frac{\hat{\eta}(x, \omega)}{A(\omega)} e^{-ik_2x}. \quad (53)$$

While the procedure above is stated for a single x , in our implementation we average the resulting R and T over multiple x , which we find improves the accuracy at high frequencies. With a grid spacing of 200 m, R was averaged over $x = -100$ km to -50 km and T was averaged over $x = -100$ km to -50 km.

The procedure above does require neglecting evanescent surface gravity and acoustic wave modes, which might introduce a small error in the calculated R and T . This error could be eliminated using a more sophisticated procedure that isolates a specific wave mode. For example, it is well known that the eigenfunctions of wave modes in layered media obey orthogonality conditions (Aki and Richards, 2002). The orthogonality conditions require evaluation of integrals of particle velocity and stress fields over depth z at fixed x . We defer this extension to future work.

3.2 Reflection/transmission with an ice shelf

The procedure for extracting reflection/transmission coefficients for the ice shelf problem (Figure 1a) is more complex, as we are interested in multiple wave modes, not all of which are well expressed in the water surface vertical displacement η . Furthermore, we note that seismometers placed on the ice shelf surface are the primary means of measuring wave motions. Thus we define $u(x, t)$ and $w(x, t)$ as the horizontal and vertical displacements of the top surface of the ice shelf.

The incident and reflected wavefield in the open-water region ($x < 0$) is identical to that in (46). The surface displacements of the transmitted wavefield can be written as

$$\hat{u}(x, \omega) = A(\omega) [T_{x,f}(\omega)e^{ik_fx} + T_{x,e}(\omega)e^{ik_ex}] + \text{other modes}, \quad (54)$$

$$\hat{w}(x, \omega) = A(\omega) [T_{z,f}(\omega)e^{ik_fx} + T_{z,e}(\omega)e^{ik_ex}] + \text{other modes}, \quad (55)$$

where the subscript x or z on the transmission coefficients T refers to the displacement direction and the subscripts f and e refer to the flexural gravity and extensional Lamb wave modes, respectively. The wavenumbers k_f and k_e are obtained from the flexural gravity and extensional Lamb wave solutions of the dispersion equation (25). We note that the ratios $T_{x,f}/T_{z,f}$ and $T_{x,e}/T_{z,e}$ are independent of the reflection/transmission process and can be determined from the eigenfunctions given in Appendix A. Thus we need only consider one displacement direction when extracting transmission coefficients for each wave mode. Because flexural gravity waves have dominantly vertical particle motions, we focus on $T_{f,z}$. Similarly, because extensional

Lamb waves have dominantly horizontal particle motions, we focus on $T_{e,x}$.

The procedure for extracting the reflection coefficient of surface gravity waves is identical to the previous problem. To extract transmission coefficients, we record ice surface displacement time series u and w at some $x > 0$ that is sufficiently far from the ice shelf edge. We then exploit the vastly different phase and group velocities of the flexural gravity and extensional Lamb wave modes by windowing the appropriate wave arrivals in the time series. We then Fourier transform these windowed time series in time and evaluate

$$T_{z,f}(\omega) = \frac{\hat{w}(x, \omega)}{A(\omega)} e^{-ik_fx}, \quad (56)$$

$$T_{x,e}(\omega) = \frac{\hat{u}(x, \omega)}{A(\omega)} e^{-ik_ex}. \quad (57)$$

3.3 Numerical simulations

In this study we utilize the finite difference code FDMAP (Dunham et al., 2011; Kozdon et al., 2012, 2013) that couples an acoustic ocean in the presence of gravity to an elastodynamic solid. We employ a Cartesian mesh with uniform (but different) grid spacings in the x and z directions. The method uses sixth-order central differences in space in the interior (with reduced order near boundaries and interfaces) and a third-order explicit Runge-Kutta method for time-stepping. Gravity is accounted for using the method in Lotto and Dunham (2015), for both the open-water region and at the top of the sub-shelf water cavity.

We examine two model geometries. For the open ocean with a floating ice shelf and subshelf cavity problem setup (Figure 1a), the domain extends from $x = -100$ km to $x = 300$ km with the ice shelf edge located at $x = 0$. In the x -direction the grid spacing is 200 m. In the z -direction the domain is divided into 3 blocks. From the seafloor, $z = -H_1 = -1$ km, to the depth of the ice-water interface, $z = -(\rho_i/\rho_w)H_i = -0.368$ km, the grid spacing in the z -direction is 13.45 m (48 grid points). From the depth of the ice-water interface, $z = -(\rho_i/\rho_w)H_i = -0.368$ km, to the open-water free surface $z = 0$, the grid spacing in the z -direction is 5.84 m (64 grid points). From the open-water free surface $z = 0$ to the top of the ice shelf, $z = (1 - \rho_i/\rho_w)H_i = 0.032$ km, the grid spacing in the z -direction is 2.29 m (14 grid points). Characteristic-based absorbing boundary conditions (Kozdon et al., 2012, 2013) are used on the left and right sides of the domain. The simulation runs for a total of 1700 s with time steps of 0.000615 s.

For the step change in water depth problem setup, figure 1b, the domain extends from $x = -400$ km to $x = 400$ km with the step changing occurring at $x = 0$. In the x -direction the grid spacing is 200 m. In this setup $H_1 = 1$ km and $H_2 = 0.25$ km with 10 m grid spacing in the z -direction. The simulation runs for a total of 8000 s with time step of 0.003333 s.

Table 1 Parameter values for dispersion analysis and simulations.

parameter	symbol	value
Density in ocean	ρ_w	1000 kg/m ³
Sound speed in ocean	c_0	1500 m/s
Density in ice	ρ_i	920 kg/m ³
P-wave speed in ice	c_p	2000 m/s
S-wave speed in ice	c_s	1000 m/s
Gravity	g	9.8 m/s ²
Open water ocean depth	H_1	1000 m
Sub-shelf ocean cavity	H_2	632 m
Ice thickness	H_i	400 m

4 Reflection and transmission coefficients for a step change in water depth

Before proceeding to the ice shelf reflection/transmission problem, we verify our model and procedure for extracting R and T on a problem with a known solution. Specifically, we consider a step change in water depth, from H_1 to H_2 at $x = 0$ (Figure 1b).

The reflection/transmission coefficients in the linear long wave (LLW, $k_1 H_1 \ll 1$ and $k_2 H_2 \ll 1$) limit are well known (Lamb, 1905):

$$R_{LLW} = \frac{\sqrt{H_1} - \sqrt{H_2}}{\sqrt{H_1} + \sqrt{H_2}}, \quad (58)$$

and the transmission coefficient is

$$T_{LLW} = \frac{2\sqrt{H_1}}{\sqrt{H_1} + \sqrt{H_2}}. \quad (59)$$

These values are the anticipated limits for R and T in the low frequency limit.

Exact closed form expressions for R and T are not available outside the LLW limit, and instead the problem must be solved numerically or using approximations (Newman, 1965; Miles, 1967; Dingemans, 1997). However, in the high frequency limit, surface gravity waves will be confined to the water surface and will not sense the change in water depth. Hence the high frequency limits are $R \rightarrow 0$, $T \rightarrow 1$.

4.1 Simulation results

Our initial vertical sea surface displacement is a Gaussian,

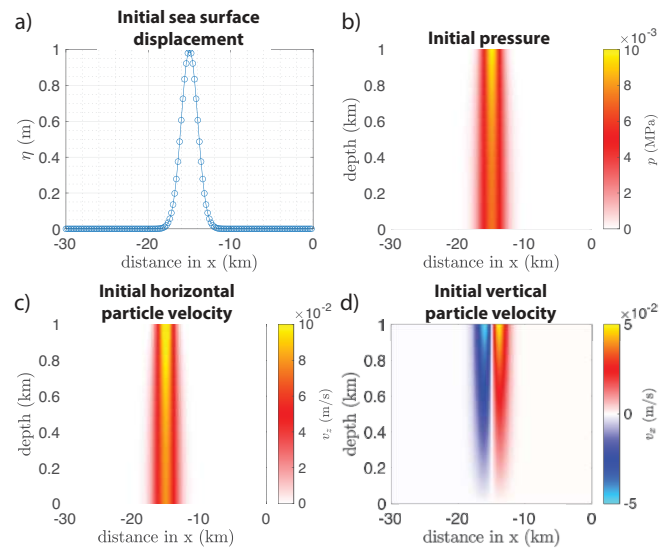
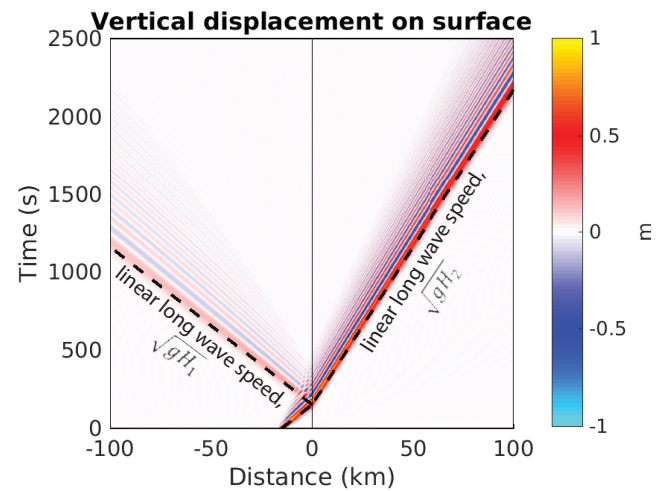
$$\eta_0(x) = A_0 \exp\left(\frac{-(x - x_0)^2}{2\sigma^2}\right), \quad (60)$$

where $A_0 = 1$ m is the amplitude, x_0 is the center of the Gaussian and σ is the width of the Gaussian. We set $x_0 = -15$ km and $\sigma = 1$ km, which provides a wave packet that includes dispersive surface gravity waves at frequencies above the LLW limit. We use the eigenmode solution and Fourier transforms in the x direction (using FFTs on the simulation grid) to determine the pressure and particle velocities in the water corresponding to a wave packet propagating in the $+x$ direction with surface amplitude (60). The initial conditions

are shown in figure 3 and time-domain simulation results are shown in figure 4. Normal dispersion is visible at high frequencies. Because $H_2 < H_1$, the reflection coefficient is positive and the transmission coefficient is greater than unity.

4.2 Reflection and transmission coefficients

From the simulation data, we extract the simulation reflection and transmission coefficients using (52) and (53), respectively. Results are shown in figure 5. The reflection and transmission coefficients match the LLW solutions, given in (58) and (59), in the low frequency limit, but differ at high frequency as seen in previous studies (Newman, 1965; Miles, 1967; Dingemans, 1997).


Figure 3 Simulation initial conditions: a) sea surface displacement, b) pressure, c) horizontal particle velocity, d) vertical particle velocity.

Figure 4 Simulation results for the step change in water depth problem, showing vertical displacement on the surface ($z = 0$) through time.

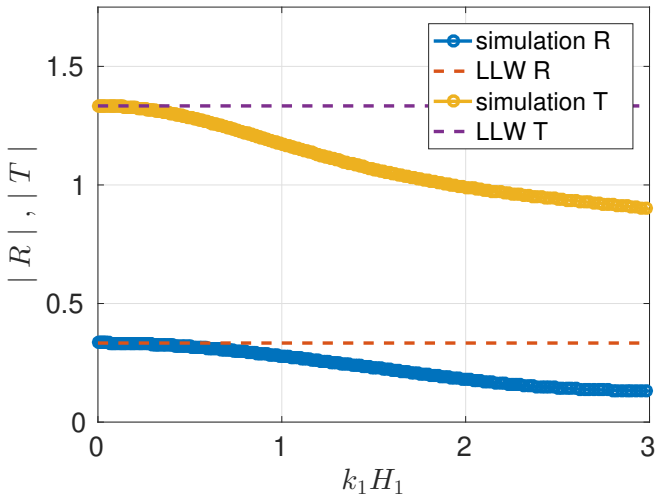


Figure 5 Reflection and transmission coefficients for the step change in water depth problem, which approach the linear long wave (LLW) solution in the low frequency limit.

5 Reflection and transmission coefficients for ice-covered water

Having verified our procedure for determining reflection and transmission coefficients from time-domain simulations, we now turn to the problem of wave interaction with floating ice shelves (Figure 1a).

5.1 Simulation results

We use the same initial conditions for the wave packet as used in the step change in depth problem. Incident surface gravity waves in the open water impact the ice shelf, exciting both flexural gravity and extensional Lamb waves. The flexural gravity waves are dominantly expressed in the vertical components (figure 6) and extensional Lamb waves are dominantly expressed in the horizontal component (figure 7). We also show the horizontal normal stress σ_{xx} in figure 8. The largest stresses are carried by flexural gravity waves, not extensional Lamb waves. Because these waves are in the long wavelength limit where plate theory is valid, equation (43) could also have been used to calculate stresses from flexural gravity waves at the ice shelf surface, after Fourier transforming the simulation results.

5.2 Reflection and transmission coefficients

Following the procedure described in section 3.2, we calculate reflection and transmission coefficients. These propagating wave reflection/transmission results are only valid away from the ice shelf edge, where additional evanescent modes contribute to the motions. Results are shown in Figure 9. We begin by explaining the reflection and transmission of surface gravity and flexural gravity waves (Figure 9a), both quantified in terms of the vertical displacement amplitude on the water or ice surface. At low frequencies, the results match expectations from linear long wave theory without ice, illustrating that the additional inertia and elastic resistance to flexure of the ice are negligible; because $H_2 < H_1$, the transmission coefficient is greater than unity ($T > 1$) in

the low-frequency limit. As frequency increases, R and T both decrease, as seen for the step change in depth problem without ice (Figure 5). The decrease of R for this problem arises from the shorter wavelength waves, which involve motions of the water at depths of order the wavelength, becoming less sensitive to the water depth. In the high frequency limit, the waves simply propagate across the step without reflection. In contrast, for the ice shelf problem, the reflection coefficient begins increasing around 0.01 Hz as the stiffness and inertia of the ice shelf begin to impede wave transmission. The anticipated high frequency limit for R is unity, meaning that surface gravity waves are fully reflected.

Next we examine transmission of extensional Lamb waves, which we quantify in terms of the horizontal displacement amplitude on the ice surface (Figure 9c,d). The transmission coefficient increases as frequency decreases, passing through unity around 0.001 Hz. Transmission coefficients larger than unity indicate that horizontal displacements of the ice surface carried by extensional Lamb waves exceed vertical displacements of the incident gravity waves. In the low frequency limit, T diverges as ω^{-1} , a behavior that we explain in the next section.

5.3 Mechanism for extensional Lamb wave excitation

In this section we provide a quantitative theory for the excitation of extensional Lamb waves by incident surface gravity waves. The incident waves cause pressure changes in the water column and these pressure changes exert a horizontal force on the submerged portion of the ice shelf edge. This excites extensional Lamb waves. This conceptual mechanism was suggested by Chen et al. (2018), which we extend quantitatively as follows.

Consider an incident, time-harmonic surface gravity wave of amplitude A . The wave amplitude at the ice shelf edge differs from A because of the superposition of incident and reflected waves. By neglecting evanescent modes, we approximate the amplitude at the edge as $(1 + R)A$, where R is the frequency-dependent surface gravity wave reflection coefficient. Next we estimate the pressure change in the water column associated with the surface gravity waves as $p = \rho_w g(1 + R)IA$, where

$$I(\omega) = \frac{\rho_w}{\rho_i H_i} \int_{-(\rho_i/\rho_w)H_i}^0 \frac{\cosh(k(z + H_1))}{\cosh(kH_1)} dz, \quad (61)$$

is the normalized integral of the depth-dependent pressure changes from the eigenmode solution given in Appendix A and k is the wavenumber of surface gravity waves at angular frequency ω . The normalization is chosen so that $I \rightarrow 1$ in the low frequency limit ($kH_i \ll 1$) where pressure changes are approximately uniform over the submerged portion of the shelf front. We find that $I \approx 1$ over frequencies of interest in this study. This pressure change gives rise to a net horizontal force

$$\begin{aligned} F &= p \frac{\rho_i}{\rho_w} H_i \\ &= \rho_i g(1 + R)IAH_i. \end{aligned} \quad (62)$$

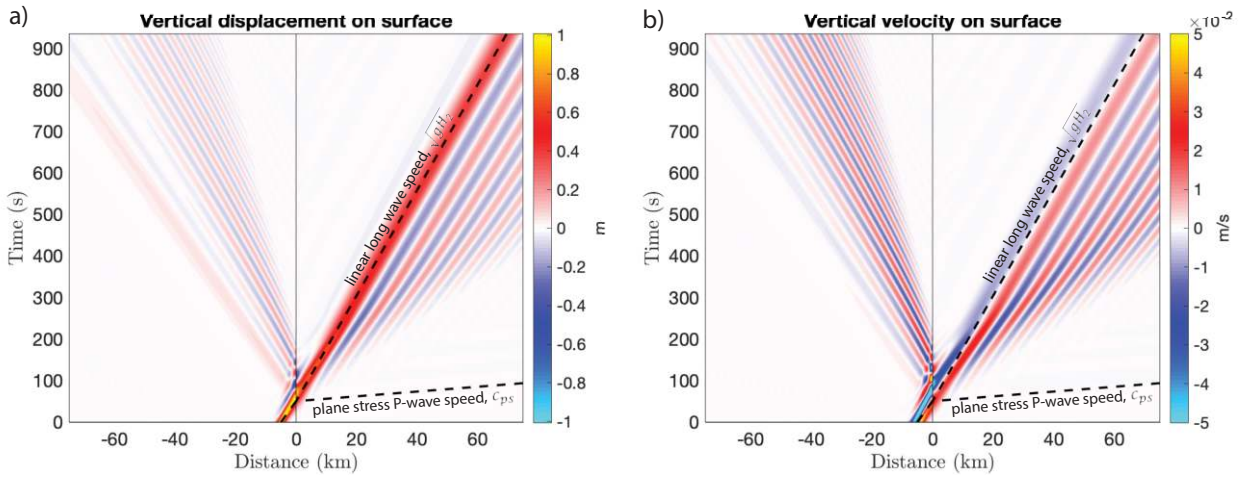


Figure 6 (a) Vertical displacement and (b) vertical velocity on the open-water and ice surface. Surface gravity waves in the open-water region are normally dispersed with the longest wavelengths traveling at the linear long wave speed $\sqrt{gH_1}$. The ice shelf response is dominated by anomalously dispersed flexural gravity waves, with the longest wavelengths traveling at the linear long wave speed $\sqrt{gH_2}$.

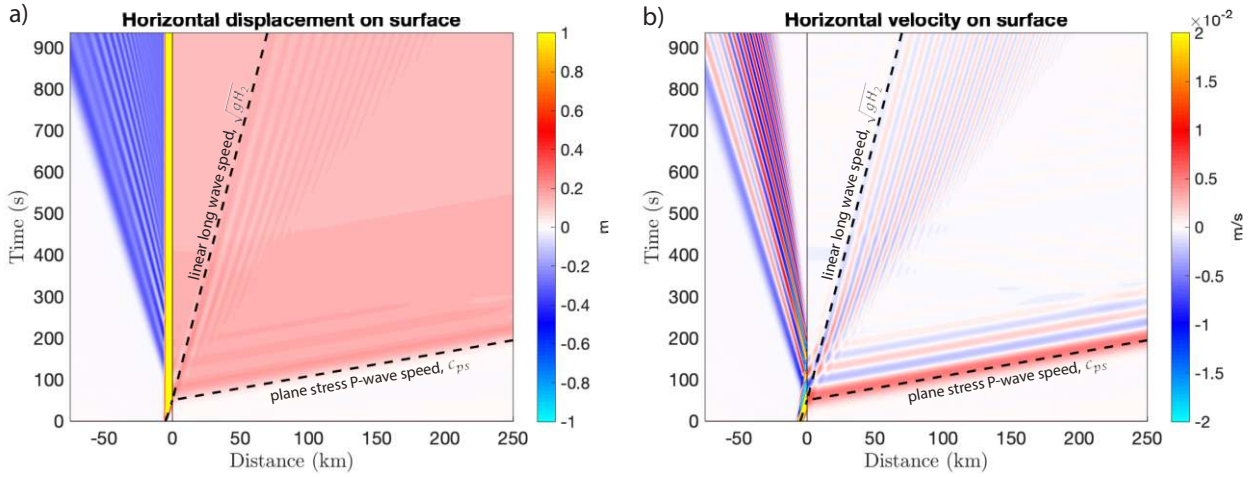


Figure 7 (a) Horizontal displacement and (b) horizontal velocity on the open-water and ice surface. In addition to surface gravity waves in the open-water region and flexural gravity waves in the ice-covered water, we also see extensional Lamb waves. These have minimal dispersion, dominantly horizontal particle motions, and propagate around the plane stress P-wave speed of ice.

Next we assume that this force generates an effectively 1D extensional Lamb wave with depth-independent normal stress σ_{xx} and horizontal particle velocity v_x . The depth-independence of these fields holds asymptotically in the limit of horizontal wavelengths greatly exceeding ice thickness, as evident from the eigenfunctions in Appendix A. This limit is well justified for frequencies of interest. The stress and particle velocity are related by the extensional Lamb wave impedance: $-\sigma_{xx} = \rho_i c_{ps} v_x$, where we have assumed that the phase velocity is approximately c_{ps} (Figure 2b). Force balance requires $F = -\sigma_{xx} H_i$, such that $-\sigma_{xx} = \rho_i g(1 + R)IA$. Inserting this into the impedance relation, we obtain $v_x = (g/c_{ps})(1 + R)IA$. Finally, using $v_x = -i\omega u_x$, we obtain the extensional Lamb wave transmission coefficient

(defined as the ratio u_x/A)

$$T_{x,e}(\omega) = \frac{ig[1 + R(\omega)]I(\omega)}{\omega c_{ps}}. \quad (63)$$

This prediction, using the $R(\omega)$ derived from the simulations, is plotted in Figure 9c,d. There is excellent agreement with the simulation-derived $T_{x,e}(\omega)$. We note that in the low frequency limit (i.e., very long period band), where the ice has negligible effect on gravity wave propagation except by modifying the water depth, we can approximate $R(\omega) \approx R_{LLW}$, which is independent of frequency, and $I(\omega) \approx 1$. This reveals the $T_{x,e} \propto \omega^{-1}$ divergence seen in our simulation results (Figure 9c,d).

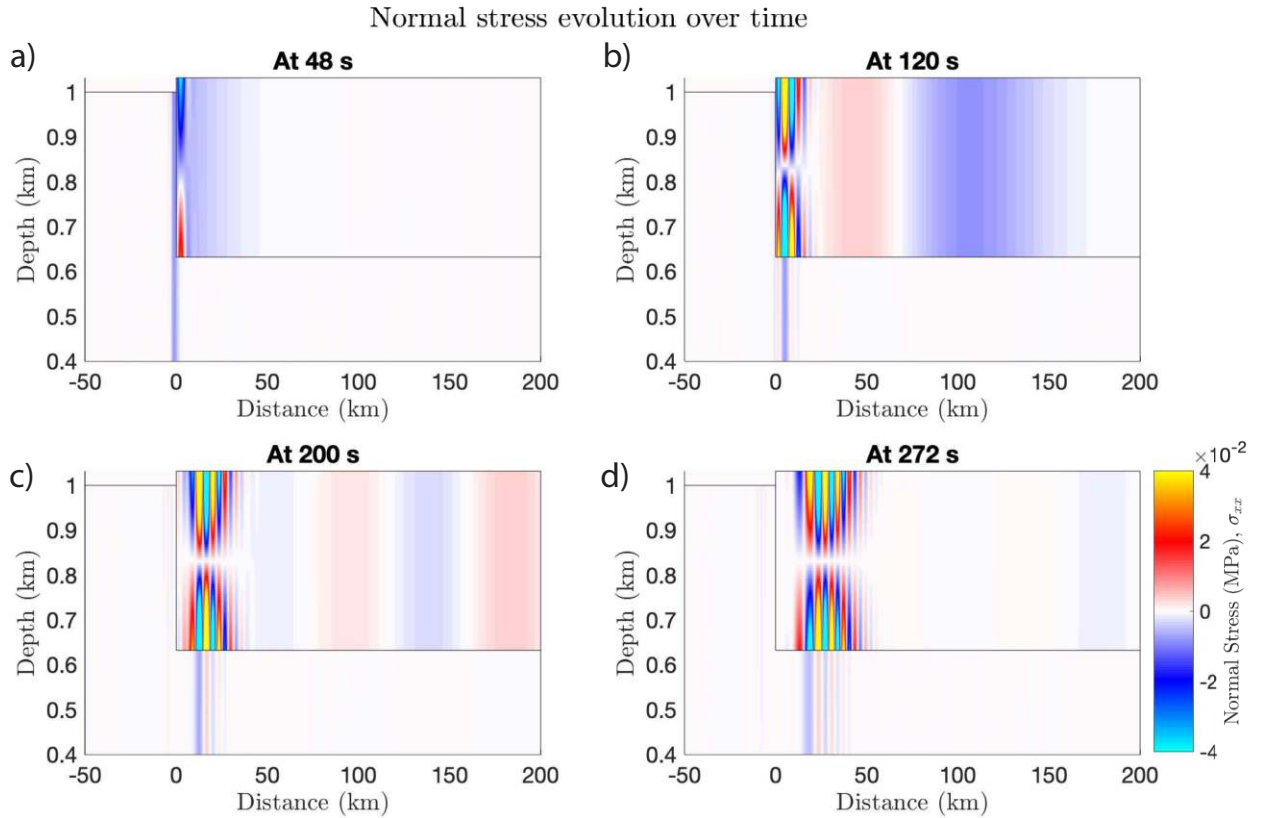


Figure 8 Tensile and compressional horizontal normal stresses (σ_{xx}) in the ice and minus pressure ($-p$) in the water, highlight the propagating long wavelength extensional Lamb waves and shorter wavelength flexural gravity waves. The extensional Lamb wave exhibits symmetric stressing about the centerline of the ice shelf, whereas the flexural gravity wave exhibits antisymmetric stressing. The largest stress changes are carried by the flexural gravity waves.

5.4 Tilt contribution to horizontal seismometer measurements

Our theory and simulation results provide a prediction of both horizontal and vertical displacements of the ice shelf surface, which can be compared to seismic observations. Here we combine previous results to predict the frequency-dependent ratio of horizontal to vertical displacements. We assume that horizontal displacements are dominated by extensional Lamb waves and that vertical displacements are dominated by flexural gravity waves. The predicted displacement ratio is therefore approximated as $|u_x|/|u_z| \approx |T_{x,e}(\omega)|/|T_{z,f}(\omega)|$. We focus on the low frequency limit where the ice has minimal influence on flexural gravity waves, except by reducing the water depth, so that $T_{z,f}(\omega)$ can be approximated as the LLW transmission coefficient (59). Similarly, the surface gravity wave reflection coefficient can be approximated using (58). Then, using these results in (63), and noting that for the LLW problem $1 + R_{LLW} = T_{LLW}$, we find the predicted horizontal-to-vertical displacement ratio

$$\frac{|u_x|}{|u_z|} \approx \frac{g}{\omega c_{ps}} \approx \frac{1 \text{ mHz}}{f}, \quad (64)$$

with the latter expression using the value of c_{ps} for our simulation parameters. Thus vertical displacements are predicted to be larger than horizontal displacements

for frequencies greater than ~ 1 mHz, whereas horizontal displacements will be larger for lower frequencies.

This prediction is in apparent contradiction to observations, which can be found in power spectral density plots for horizontal and vertical seismometer data in Figure 3 of Bromirski et al. (2017). The observations show larger horizontal motions not just in the very long period band but also in the infragravity band. There are several possible explanations for this discrepancy. First, there could be some additional extensional Lamb wave source that is unaccounted for in our model. Turbulent drag along the base of the ice shelf during wave motions in the sub-shelf cavity would provide an additional horizontal force that would excite extensional Lamb waves. Drag of this form is widely used in shallow water wave modeling, with basal shear stress (drag) being proportional to the square of horizontal velocity. Given that this is a nonlinear forcing mechanism, frequency-dependent excitation of extensional waves cannot be quantified without detailed modeling of the broadband wavefield. We defer this to future work. Another hypothesis is that the horizontal seismometer components are not only measuring horizontal displacements, but also include contributions from tilt. Tilt effects are most important at low frequencies, and studies of atmospheric coupling to the solid Earth have identified tilt as important or even dominant at the frequencies of interest to us (Rodgers, 1968; Tanimoto and

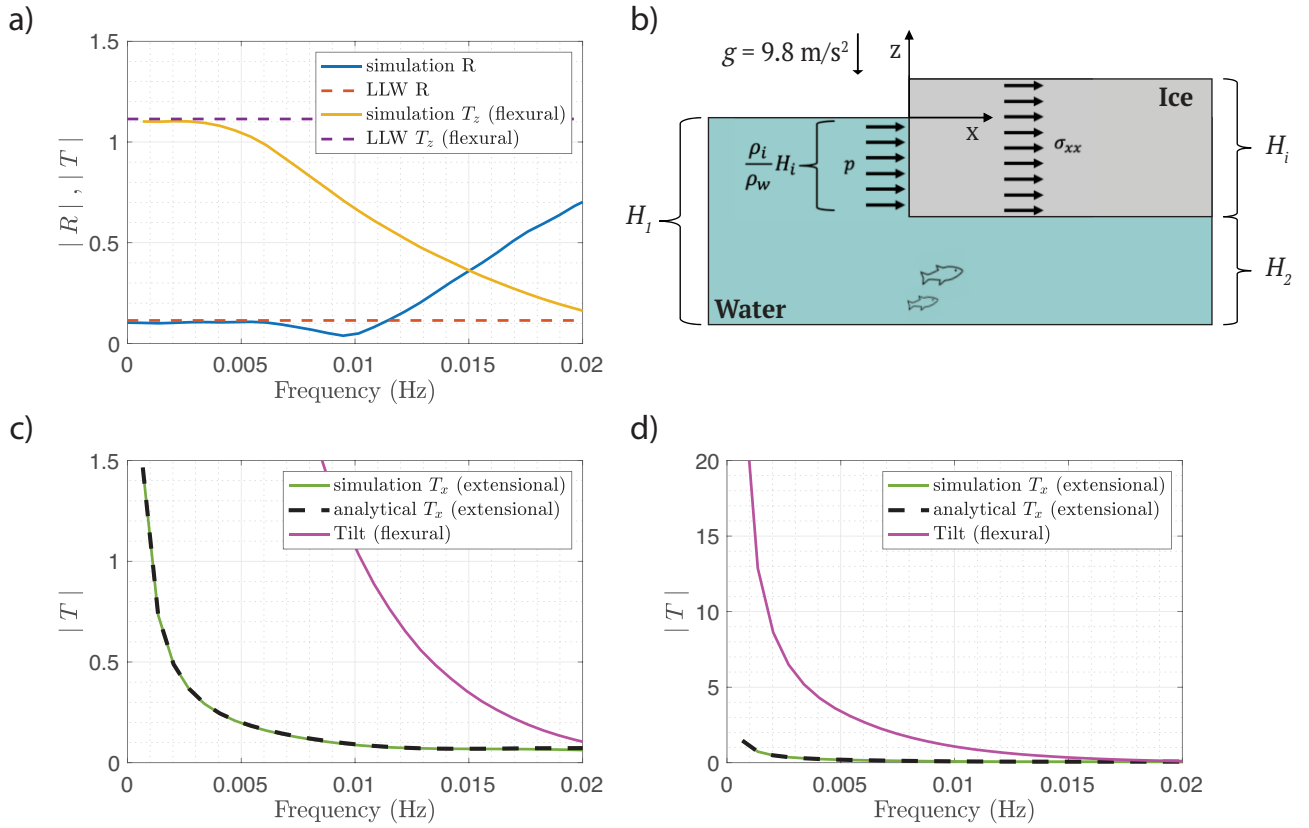


Figure 9 (a) Simulation-derived reflection coefficient (blue) and flexural gravity wave vertical transmission coefficient (yellow) with linear long wave limits for the step depth change problem (red and purple). (b) Diagram illustrating extensional Lamb wave excitation by pressure changes exerted on the ice shelf face by surface gravity waves. (c and d) Simulation-derived extensional Lamb wave horizontal transmission coefficient (green), the analytical prediction for the transmitted extensional wave given in equation (63) (black dashed), and flexural gravity wave tilt contribution to horizontal seismometer measurements given by equation (65) (magenta).

Wang, 2018).

To explore this possibility, we follow Rodgers (1968) by calculating the tilt contribution to horizontal seismometer measurements as

$$\begin{aligned} u_{h,\text{tilt}} &= -\frac{g}{\omega^2} \frac{\partial \hat{w}(x, \omega)}{\partial x} \\ &= -\frac{igk}{\omega^2} \hat{w}, \end{aligned} \quad (65)$$

where the subscript h denotes the seismometer horizontal component and \hat{w} is the vertical displacement of the surface in the frequency domain. The final expression follows by assuming e^{ikx} dependence of the propagating wave, where k is the wavenumber for a given wave mode at angular frequency ω .

We calculate the tilt contribution from both extensional Lamb and flexural gravity waves, taking \hat{w} from our simulations as before, which we normalize by the amplitude of the incident surface gravity wave. We find that the tilt contribution from extensional Lamb waves is negligible in comparison to the actual horizontal displacements carried by these waves. In contrast, the tilt contribution from flexural gravity waves, which is shown in Figure 9c,d, is larger than the horizontal extensional Lamb wave displacements over the

entire frequency band of our study. Specifically, flexural gravity wave tilt is an order of magnitude larger than extensional Lamb wave horizontals at frequencies ~ 0.001 Hz characterizing the very long period band. This ratio decreases toward unity in the infragravity wave band. Thus we conclude that horizontal component seismometers are primarily measuring tilt from flexural gravity waves, especially at low frequencies below 0.0025 Hz.

Additional features of the seismic observations support this idea. Figure 9 of Chen et al. (2018) provides cross-correlation-based seismograms, bandpassed to 0.002-0.004 Hz, showing move-out at the flexural gravity wave speed on both vertical and horizontal components. The beamforming dispersion analysis in their Figure 8 shows larger power on the horizontal component than the vertical component along the flexural gravity wave dispersion curve at frequencies less than 0.02 Hz. This is inconsistent with the expected horizontal to vertical ratio for flexural gravity waves, but at least qualitatively consistent with our results in Figure 9.

To further test the tilt hypothesis, we perform a cross-spectrum analysis at Ross Ice Shelf station DR10 (Figure 10a). Figure 10b and c shows coherence, normalized between 0 and 1, between the two horizontal components and the vertical component. The high coher-

ence between north and vertical components, and low coherence between east and vertical components, is consistent with the primary direction of wave propagation being from the north (ice shelf edge) to the south. The tilt model also predicts a phase shift. Our cross-spectrum analysis uses the opposite sign convention for time Fourier transforms as elsewhere in our study, which reverses the sign of equation (65). After accounting for this, the predicted phase is $\pi/2$, which is consistent with the data below 0.02 Hz (Figure 10d). Therefore we conclude that tilt from flexural gravity waves propagating away from the ice shelf edge provides a significant contribution to the north-south horizontal seismometer measurements at these low frequencies.

6 Conclusion

In this work we have modeled the wave response of the ice shelf and sub-shelf ocean cavity to a surface gravity wave that is incident from open water. This was done using a depth-resolved 2D vertical cross-section model, accounting for full elastodynamics of the ice shelf, in contrast to most prior work that utilizes a bending plate model for the shelf. We extract frequency-dependent reflection and transmission coefficients from our time-domain simulation results, in particular focusing on the amplitude of transmitted flexural gravity and extensional Lamb waves. The incident waves cause pressure changes in the water column at the ice shelf edge, producing a time-varying horizontal force on the submerged portion of the ice shelf edge, which excites extensional Lamb waves. A quantitative version of this theory shows excellent agreement with our simulation results.

Our model also provides a prediction of the horizontal and vertical displacements of the ice shelf surface, which are primarily controlled by extensional Lamb waves and flexural gravity waves, respectively. The vertical is predicted to exceed the horizontal at frequencies greater than ~ 0.001 Hz, which is not seen in seismic data from the Ross Ice Shelf (Bromirski et al., 2017; Chen et al., 2018). We attribute this discrepancy to the expression of tilt from flexural gravity waves on the horizontal seismometer components, which our model predicts will be larger than extensional Lamb wave horizontal displacements at frequencies in the infragravity wave band and lower. We validate this hypothesis by cross-spectrum analysis of the Ross Ice Shelf seismic data. This result implies that extensional Lamb wave amplitudes are most likely smaller than previous studies have suggested. Our modeling suggests that stresses imparted to the ice shelf by incident ocean waves are primarily carried by flexural gravity waves. Even if they play a smaller role in fracture processes than previous thought, extensional Lamb waves are still valuable for constraining the elastic properties of ice (Diez et al., 2016; Chen et al., 2018).

Future extensions of this work are required to explore more realistic geometries, finite-length ice shelves and interaction with grounded ice, and the extension from 2D to 3D with obliquely incident waves. Nonetheless, our work provides an important advance in understand-

ing the wave response of ice shelves to incident ocean waves, a problem receiving growing attention due to the possible role of wave-induced stresses in fracture and calving.

Acknowledgements

This work was supported by the National Science Foundation (OPP-1744759). We thank Brad Lipovsky for pointing out the possible importance of tilt. We also thank handling editor Paula Koelemeijer and two anonymous reviewers for their insightful suggestions. L.S.A. was supported by National Science Foundation Graduate Research Fellowship DGE-1656518, Stanford's Enhancing Diversity in Graduate Education (EDGE) Doctoral Fellowship Program and Diversifying Academia, and Recruiting Excellence (DARE) Doctoral Fellowship Program. J.E.M. was supported by National Science Foundation DGE-1852022 through Stanford's Summer Undergraduate Research in Geoscience and Engineering (SURGE) Program.

Data and code availability

Numerical simulations were performed using FDMAP (<https://bitbucket.org/ericmdunham/fdmap>). Simulation input files and results are available at DOI:10.25740/qy001dt7463 (<https://purl.stanford.edu/qy001dt7463>). The Ross Ice Shelf seismic data are available through the Incorporated Research Institutions for Seismology Data Management Center (IRIS-DMC) under Ross Ice Shelf (RIS) and DRIS network code XH.

References

- Achenbach, J. D. *Wave propagation in elastic solids*. Elsevier, 1973.
- Achenbach, J. D. *Reciprocity in elastodynamics*. Cambridge University Press, 2003.
- Aki, K. and Richards, P. *Quantitative Seismology*. Geology Seismology. University Science Books, 2002.
- Aster, R. C., Lipovsky, B. P., Cole, H. M., Bromirski, P. D., Gerstoft, P., Nyblade, A., Wiens, D. A., and Stephen, R. Swell-triggered seismicity at the near-front damage zone of the Ross Ice Shelf. *Seismological Research Letters*, 92(5):2768–2792, 2021. doi: <https://doi.org/10.1785/0220200478>.
- Banwell, A. F., MacAyeal, D. R., and Sergienko, O. V. Breakup of the Larsen B Ice Shelf triggered by chain reaction drainage of supraglacial lakes. *Geophysical Research Letters*, 40(22): 5872–5876, 2013. doi: <https://doi.org/10.1002/2013GL057694>.
- Banwell, A. F., Willis, I. C., Macdonald, G. J., Goodsell, B., Mayer, D. P., Powell, A., and Macayeal, D. R. Calving and rifting on the McMurdo ice shelf, Antarctica. *Annals of Glaciology*, 58(75pt1): 78–87, 2017. doi: <https://doi.org/10.1017/aog.2017.12>.
- Biot, M. A. The interaction of Rayleigh and Stoneley waves in the ocean bottom. *Bulletin of the Seismological Society of America*, 42(1):81–93, 1952. doi: <https://doi.org/10.1785/BSSA0420010081>.
- Bromirski, P. D., Sergienko, O. V., and MacAyeal, D. R. Transoceanic infragravity waves impacting Antarctic ice shelves. *Geophysical Research Letters*, 37(2), 2010. doi: <https://doi.org/10.1029/2009GL041488>.

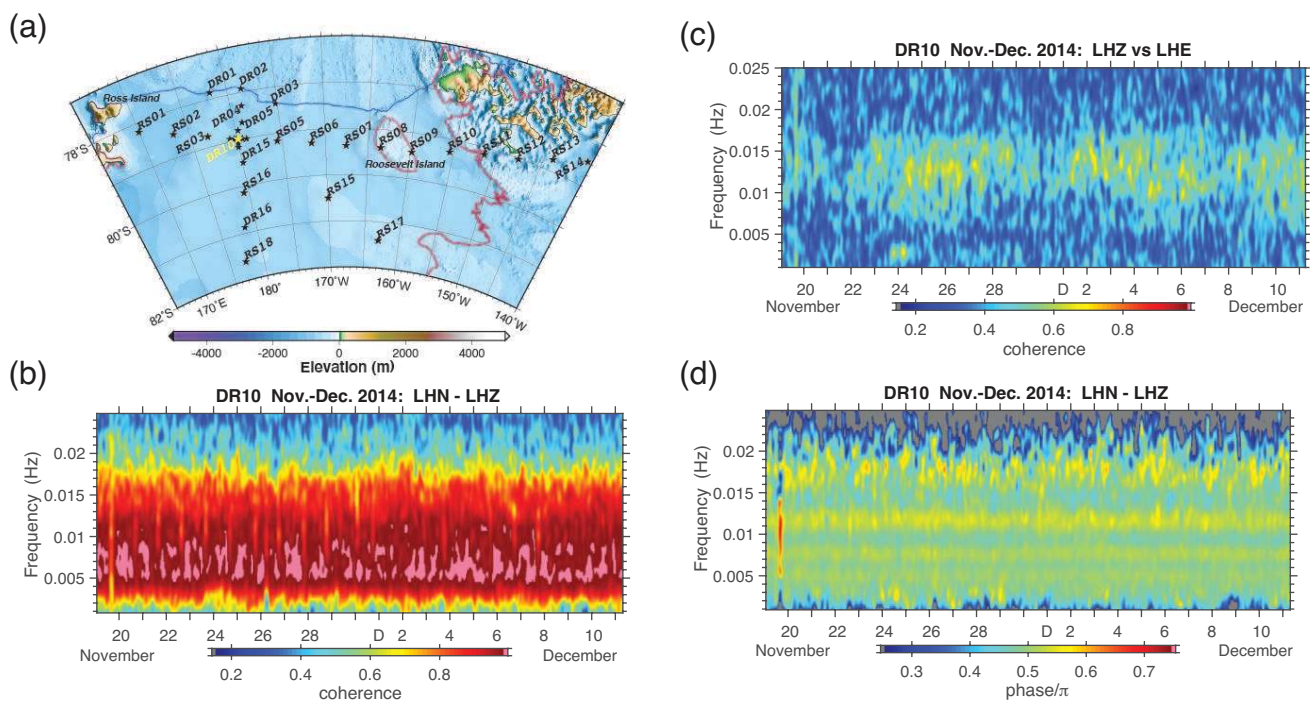


Figure 10 (a) Ross Ice Shelf seismic array, with open water to the north (top). The ice shelf edge and grounding zone are shown as blue and red curves. Cross-spectrum analysis shown in other panels is for station DR10. (b) Coherence between north (LHN) and vertical (LHZ) components. (c) Coherence between east (LHE) and vertical (LHZ) components. (d) Phase between north (LHN) and vertical (LHZ) components, showing agreement with the predicted $\pi/2$ phase for flexural gravity wave tilt dominating the seismometer horizontal records at frequencies less than 0.02 Hz.

Bromirski, P. D., Chen, Z., Stephen, R. A., Gerstoft, P., Arcas, D., Diez, A., Aster, R. C., Wiens, D. A., and Nyblade, A. Tsunami and infragravity waves impacting Antarctic ice shelves. *Journal of Geophysical Research: Oceans*, 122(7):5786–5801, 2017. doi: <https://doi.org/10.1002/2017JC012913>.

Bromwich, D. H. and Nicolas, J. P. Ice-sheet uncertainty. *Nature Geoscience*, 3(9):596–597, 2010. doi: <https://doi.org/10.1038/n-geo946>.

Brunt, K. M., Okal, E. A., and MacAYEAL, D. R. Antarctic ice-shelf calving triggered by the Honshu (Japan) earthquake and tsunami, March 2011. *Journal of Glaciology*, 57(205):785–788, 2011. doi: DOI: <https://doi.org/10.3189/002214311798043681>.

Chen, Z., Bromirski, P. D., Gerstoft, P., Stephen, R. A., Wiens, D. A., Aster, R. C., and Nyblade, A. A. Ocean-excited plate waves in the Ross and Pine Island Glacier ice shelves. *Journal of Glaciology*, 64(247):730–744, 2018. doi: <https://doi.org/10.1017/jog.2018.66>.

Chen, Z., Bromirski, P., Gerstoft, P., Stephen, R., Lee, W. S., Yun, S., Olinger, S., Aster, R., Wiens, D., and Nyblade, A. Ross Ice Shelf icequakes associated with ocean gravity wave activity. *Geophysical Research Letters*, 46(15):8893–8902, 2019. doi: <https://doi.org/10.1029/2019GL084123>.

De Angelis, H. and Skvarca, P. Glacier surge after ice shelf collapse. *Science*, 299(5612):1560–1562, 2003. doi: [10.1126/science.1077987](https://doi.org/10.1126/science.1077987).

Diez, A., Bromirski, P., Gerstoft, P., Stephen, R., Anthony, R., Aster, R., Cai, C., Nyblade, A., and Wiens, D. Ice shelf structure derived from dispersion curve analysis of ambient seismic noise, Ross Ice Shelf, Antarctica. *Geophysical Journal International*, 205(2): 785–795, 2016. doi: [10.1093/gji/ggw036](https://doi.org/10.1093/gji/ggw036).

Dingemans, M. W. *Water wave propagation over uneven bottoms: Part 1 – Linear wave propagation*. World Scientific, 1997.

Dunham, E. M., Belanger, D., Cong, L., and Kozdon, J. E. Earthquake ruptures with strongly rate-weakening friction and off-fault plasticity, Part 1: Planar faults. *Bulletin of the Seismological Society of America*, 101(5):2296–2307, 2011. doi: <https://doi.org/10.1785/0120100075>.

Dupont, T. and Alley, R. Assessment of the importance of ice-shelf buttressing to ice-sheet flow. *Geophysical Research Letters*, 32(4), 2005. doi: <https://doi.org/10.1029/2004GL022024>.

Ewing, M. and Crary, A. Propagation of elastic waves in ice. Part II. *Physics*, 5(7):181–184, 1934.

Fox, C. and Squire, V. A. Reflection and transmission characteristics at the edge of shore fast sea ice. *Journal of Geophysical Research: Oceans*, 95(C7):11629–11639, 1990. doi: <https://doi.org/10.1029/JC095iC07p11629>.

Fox, C. and Squire, V. A. Coupling between the ocean and an ice shelf. *Annals of Glaciology*, 15:101–108, 1991. doi: <https://doi.org/10.3189/1991AoG15-1-101-108>.

Holdsworth, G. and Glynn, J. Iceberg calving from floating glaciers by a vibrating mechanism. *Nature*, 274(5670):464–466, 1978. doi: <https://doi.org/10.1038/274464a0>.

Ilyas, M., Meylan, M. H., Lamichhane, B., and Bennetts, L. G. Time-domain and modal response of ice shelves to wave forcing using the finite element method. *Journal of Fluids and Structures*, 80:113–131, 2018. doi: <https://doi.org/10.1016/j.jfluidstructs.2018.03.010>.

Kalyanaraman, B., Bennetts, L. G., Lamichhane, B., and Meylan, M. H. On the shallow-water limit for modelling ocean-wave induced ice-shelf vibrations. *Wave Motion*, 90:1–16, 2019. doi: <https://doi.org/10.1016/j.wavemoti.2019.04.004>.

Kalyanaraman, B., Meylan, M. H., Bennetts, L. G., and Lamichhane, B. P. A coupled fluid-elasticity model for the wave forcing of an ice-shelf. *Journal of Fluids and Structures*, 97:103074, 2020. doi: <https://doi.org/10.1016/j.jfluidstructs.2020.103074>.

- <https://doi.org/10.1016/j.jfluidstructs.2020.103074>.
- Kozdon, J. E., Dunham, E. M., and Nordström, J. Interaction of waves with frictional interfaces using summation-by-parts difference operators: Weak enforcement of nonlinear boundary conditions. *Journal of Scientific Computing*, 50(2):341–367, 2012. doi: <https://doi.org/10.1007/s10915-011-9485-3>.
- Kozdon, J. E., Dunham, E. M., and Nordström, J. Simulation of dynamic earthquake ruptures in complex geometries using high-order finite difference methods. *Journal of Scientific Computing*, 55(1):92–124, 2013. doi: <https://doi.org/10.1007/s10915-012-9624-5>.
- Kundu, P. K., Cohen, I. M., and Dowling, D. R. *Fluid Mechanics*. Academic Press, 2015.
- Lamb, H. On deep-water waves. *Proceedings of the London Mathematical Society*, 2(1):371–400, 1905.
- Lamb, H. On waves in an elastic plate. *Proceedings of the Royal Society of London. Series A*, 93(648):114–128, 1917. doi: <https://doi.org/10.1098/rspa.1917.0008>.
- Lipovsky, B. P. Ice shelf rift propagation and the mechanics of wave-induced fracture. *Journal of Geophysical Research: Oceans*, 123(6):4014–4033, 2018. doi: <https://doi.org/10.1029/2017JC013664>.
- Lotto, G. C. and Dunham, E. M. High-order finite difference modeling of tsunami generation in a compressible ocean from offshore earthquakes. *Computational Geosciences*, 19(2):327–340, 2015. doi: <https://doi.org/10.1007/s10596-015-9472-0>.
- MacAyeal, D. R., Okal, E. A., Aster, R. C., Bassis, J. N., Brunt, K. M., Cathles, L. M., Drucker, R., Fricker, H. A., Kim, Y.-J., Martin, S., et al. Transoceanic wave propagation links iceberg calving margins of Antarctica with storms in tropics and Northern Hemisphere. *Geophysical Research Letters*, 33(17), 2006. doi: <https://doi.org/10.1029/2006GL027235>.
- Massom, R. A., Scambos, T. A., Bennetts, L. G., Reid, P., Squire, V. A., and Stammerjohn, S. E. Antarctic ice shelf disintegration triggered by sea ice loss and ocean swell. *Nature*, 558(7710):383–389, 2018. doi: <https://doi.org/10.1038/s41586-018-0212-1>.
- Mattsson, K., Dunham, E. M., and Werpers, J. Simulation of acoustic and flexural-gravity waves in ice-covered oceans. *Journal of Computational Physics*, 373:230–252, 2018. doi: <https://doi.org/10.1016/j.jcp.2018.06.060>.
- Meylan, M. H., Ilyas, M., Lamichhane, B. P., and Bennetts, L. G. Swell-induced flexural vibrations of a thickening ice shelf over a shoaling seabed. *Proceedings of the Royal Society A*, 477(2254):20210173, 2021. doi: <https://doi.org/10.1098/rspa.2021.0173>.
- Miles, J. W. Surface-wave scattering matrix for a shelf. *Journal of Fluid Mechanics*, 28(4):755–767, 1967. doi: <https://doi.org/10.1017/S00222112067002423>.
- Newman, J. Propagation of water waves over an infinite step. *Journal of Fluid Mechanics*, 23(2):399–415, 1965. doi: <https://doi.org/10.1017/S00222112065001453>.
- Olinger, S., Lipovsky, B., Wiens, D., Aster, R., Bromirski, P., Chen, Z., Gerstoft, P., Nyblade, A., and Stephen, R. Tidal and thermal stresses drive seismicity along a major Ross Ice Shelf rift. *Geophysical Research Letters*, 46(12):6644–6652, 2019. doi: <https://doi.org/10.1029/2019GL082842>.
- Olinger, S., Lipovsky, B. P., Denolle, M., and Crowell, B. W. Tracking the cracking: a holistic analysis of rapid ice shelf fracture using seismology, geodesy, and satellite imagery on the Pine Island Glacier ice shelf, West Antarctica. *Geophysical Research Letters*, page e2021GL097604, 2022. doi: <https://doi.org/10.1029/2021GL097604>.
- Paolo, F. S., Fricker, H. A., and Padman, L. Volume loss from Antarctic ice shelves is accelerating. *Science*, 348(6232):327–331, 2015. doi: [10.1126/science.aaa0940](https://doi.org/10.1126/science.aaa0940).
- Press, F. and Ewing, M. Propagation of elastic waves in a floating ice sheet. *Eos, Transactions American Geophysical Union*, 32(5):673–678, 1951. doi: <https://doi.org/10.1029/TR032i005p00673>.
- Pritchard, H., Ligtenberg, S. R., Fricker, H. A., Vaughan, D. G., van den Broeke, M. R., and Padman, L. Antarctic ice-sheet loss driven by basal melting of ice shelves. *Nature*, 484(7395):502–505, 2012. doi: <https://doi.org/10.1038/nature10968>.
- Rignot, E., Jacobs, S., Mouginot, J., and Scheuchl, B. Ice-shelf melting around Antarctica. *Science*, 341(6143):266–270, 2013. doi: [10.1126/science.1235798](https://doi.org/10.1126/science.1235798).
- Rodgers, P. The response of the horizontal pendulum seismometer to Rayleigh and Love waves, tilt, and free oscillations of the Earth. *Bulletin of the Seismological Society of America*, 58(5):1385–1406, 1968. doi: <https://doi.org/10.1785/BSSA0580051385>.
- Rott, H., Skvarca, P., and Nagler, T. Rapid collapse of northern Larsen ice shelf, Antarctica. *Science*, 271(5250):788–792, 1996. doi: [10.1126/science.271.5250.788](https://doi.org/10.1126/science.271.5250.788).
- Scambos, T. A., Bohlander, J., Shuman, C. A., and Skvarca, P. Glacier acceleration and thinning after ice shelf collapse in the Larsen B embayment, Antarctica. *Geophysical Research Letters*, 31(18), 2004. doi: [10.1029/2004GL020670](https://doi.org/10.1029/2004GL020670).
- Sells, C. L. The effect of a sudden change of shape of the bottom of a slightly compressible ocean. *Philosophical Transactions of the Royal Society of London. Series A*, 258(1092):495–528, 1965. doi: <https://doi.org/10.1098/rsta.1965.0049>.
- Sergienko, O. V. Elastic response of floating glacier ice to impact of long-period ocean waves. *Journal of Geophysical Research: Earth Surface*, 115(F4), 2010. doi: <https://doi.org/10.1029/2010JF001721>.
- Sergienko, O. V. Normal modes of a coupled ice-shelf/sub-ice-shelf cavity system. *Journal of Glaciology*, 59(213):76–80, 2013. doi: <https://doi.org/10.3189/2013JoG12J096>.
- Sergienko, O. V. Behavior of flexural gravity waves on ice shelves: Application to the Ross Ice Shelf. *Journal of Geophysical Research: Oceans*, 122(8):6147–6164, 2017. doi: <https://doi.org/10.1002/2017JC012947>.
- Squire, V. A. Of ocean waves and sea-ice revisited. *Cold Regions Science and Technology*, 49(2):110–133, 2007. doi: <https://doi.org/10.1016/j.coldregions.2007.04.007>.
- Squire, V. A., Dugan, J. P., Wadhams, P., Rottier, P. J., and Liu, A. K. Of ocean waves and sea ice. *Annual Review of Fluid Mechanics*, 27(1):115–168, 1995. doi: <https://doi.org/10.1146/annurev.fl.27.010195.000555>.
- Tanimoto, T. and Wang, J. Low-frequency seismic noise characteristics from the analysis of co-located seismic and pressure data. *Journal of Geophysical Research: Solid Earth*, 123(7):5853–5885, 2018. doi: <https://doi.org/10.1029/2018JB015519>.
- Tazhimbetov, N., Almquist, M., Werpers, J., and Dunham, E. Simulation of flexural-gravity wave propagation for elastic plates in shallow water using energy-stable finite difference method with weakly enforced boundary and interface conditions. *Available at SSRN 4147169*, 2022. doi: [http://dx.doi.org/10.2139/ssrn.4147169](https://dx.doi.org/10.2139/ssrn.4147169).
- Timoshenko, S. P. and Goodier, J. N. *Theory of Elasticity*. McGraw Hill, 1970.
- Walker, R., Dupont, T., Parizek, B., and Alley, R. Effects of basal-melting distribution on the retreat of ice-shelf grounding lines. *Geophysical Research Letters*, 35(17), 2008. doi: <https://doi.org/10.1029/2008GL034947>.
- Yamamoto, T. Gravity waves and acoustic waves generated by

submarine earthquakes. *International Journal of Soil Dynamics and Earthquake Engineering*, 1(2):75–82, 1982. doi: [https://doi.org/10.1016/0261-7277\(82\)90016-X](https://doi.org/10.1016/0261-7277(82)90016-X).

A Wave modes in ice-covered water

In this appendix, we seek $e^{i(kx-\omega t)}$ solutions for an elastic ice shelf over an acoustic ocean with gravity. This problem was solved by [Press and Ewing \(1951\)](#) for infinitely deep water and by [Lipovsky \(2018\)](#) for finite depth (but incompressible) water. For simplicity we do not use the hat notation for frequency-domain fields that is used in the main text. The solution is developed by solving for the response in the ice and water, separately, to an imposed pressure P on the side bounding the ice-water interface. For the ice, this means $-\sigma_{zz} = P$, and for the water, this means $p - \rho_w g \eta = P$. This response includes the vertical velocity v_z at the same location, which defines the impedances of the ice and water layers, Z_i and Z_w , defined as P/v_z . Enforcing interface conditions (12)-(14) is equivalent to matching impedance: $Z_w = Z_i$, a convenient procedure used by [Biot \(1952\)](#) for a related problem. For notational convenience, the $e^{i(kx-\omega t)}$ term is implied, and we denote the water depth as H and ice thickness as $2h$. Furthermore, we place $z = 0$ at different locations when deriving the water and ice response to simplify the solution.

A.1 Impedance of acoustic ocean with gravity

The general solution in the water, with $z = 0$ being the water surface, is ([Kundu et al., 2015](#))

$$p = A \sinh(\kappa z) + B \cosh(\kappa z), \quad (66)$$

$$v_x = \frac{k}{\rho_w \omega} [A \sinh(\kappa z) + B \cosh(\kappa z)], \quad (67)$$

$$v_z = \frac{\kappa}{i \rho_w \omega} [A \cosh(\kappa z) + B \sinh(\kappa z)], \quad (68)$$

$$\eta = A \frac{\kappa}{\rho_w \omega^2}, \quad (69)$$

where $\kappa = \sqrt{k^2 - \omega^2/c_0^2}$ and the coefficients A and B are to be determined. Setting $v_z = 0$ on $z = -H$ gives

$$A \cosh(\kappa H) - B \sinh(\kappa H) = 0. \quad (70)$$

Next we enforce $p - \rho_w g \eta = P$ on $z = 0$ to obtain

$$-\frac{g\kappa}{\omega^2} A + B = P. \quad (71)$$

It follows that

$$A = \frac{\sinh(\kappa H)}{D_0} P, \quad (72)$$

$$B = \frac{\cosh(\kappa H)}{D_0} P, \quad (73)$$

$$D_0 = \cosh(\kappa H) - \frac{g\kappa}{\omega^2} \sinh(\kappa H), \quad (74)$$

where $D_0 = 0$ is the dispersion relation for wave modes in an ocean with a free surface on top. The impedance is

$$Z_w = \frac{i\omega\rho_w D_0}{\kappa \sinh(\kappa H)}. \quad (75)$$

A.2 Impedance of elastic ice shelf

Next we solve for the response of an elastic ice shelf of thickness $2h$. It is convenient to set $z = 0$ along the centerline with boundary conditions enforced at $z = \pm h$. The displacements and traction components of stress are

$$u_x = k (A_1 e^{-\alpha z} + A_2 e^{\alpha z}) + i\beta (B_1 e^{-\beta z} - B_2 e^{\beta z}), \quad (76)$$

$$u_z = i\alpha (A_1 e^{-\alpha z} - A_2 e^{\alpha z}) - k (B_1 e^{-\beta z} + B_2 e^{\beta z}), \quad (77)$$

$$\sigma_{xz}/\mu = -2k\alpha (A_1 e^{-\alpha z} - A_2 e^{\alpha z}) - i(k^2 + \beta^2) (B_1 e^{-\beta z} + B_2 e^{\beta z}), \quad (78)$$

$$\sigma_{zz}/\mu = -i(k^2 + \beta^2) (A_1 e^{-\alpha z} + A_2 e^{\alpha z}) + 2k\beta (B_1 e^{-\beta z} - B_2 e^{\beta z}), \quad (79)$$

for coefficients A_i, B_i and

$$\alpha = \sqrt{k^2 - \omega^2/c_p^2} \quad (80)$$

$$\beta = \sqrt{k^2 - \omega^2/c_s^2}. \quad (81)$$

Note that symmetric modes will have $A_1 - A_2 = 0$ and $B_1 + B_2 = 0$, whereas antisymmetric modes will have $A_1 + A_2 = 0$ and $B_1 - B_2 = 0$.

Next we enforce $\sigma_{xz} = 0$ on $z = \pm h$, $\sigma_{zz} = 0$ on $z = h$, and $\sigma_{zz} = -P$ on $z = -h$:

$$-2k\alpha (A_1 e^{-\alpha h} - A_2 e^{\alpha h}) - i(k^2 + \beta^2) (B_1 e^{-\beta h} + B_2 e^{\beta h}) = 0, \quad (82)$$

$$-2k\alpha (A_1 e^{\alpha h} - A_2 e^{-\alpha h}) - i(k^2 + \beta^2) (B_1 e^{\beta h} + B_2 e^{-\beta h}) = 0, \quad (83)$$

$$-i(k^2 + \beta^2) (A_1 e^{-\alpha h} + A_2 e^{\alpha h}) + 2k\beta (B_1 e^{-\beta h} - B_2 e^{\beta h}) = 0, \quad (84)$$

$$-i(k^2 + \beta^2) (A_1 e^{\alpha h} + A_2 e^{-\alpha h}) + 2k\beta (B_1 e^{\beta h} - B_2 e^{-\beta h}) = -\frac{P}{\mu}. \quad (85)$$

Then form linear combinations of the resulting equations to highlight excitation of symmetric and antisymmetric modes. Symmetric modes are determined by

$$-2k\alpha \sinh(\alpha h)(A_1 + A_2) - i(k^2 + \beta^2) \sinh(\beta h)(B_1 - B_2) = 0, \quad (86)$$

$$-i(k^2 + \beta^2) \cosh(\alpha h)(A_1 + A_2) + 2k\beta \cosh(\beta h)(B_1 - B_2) = -\frac{P}{2\mu}, \quad (87)$$

and antisymmetric modes by

$$\begin{aligned} & -2k\alpha \cosh(\alpha h)(A_1 - A_2) \\ & - i(k^2 + \beta^2) \cosh(\beta h)(B_1 + B_2) = 0, \end{aligned} \quad (88)$$

$$\begin{aligned} & -i(k^2 + \beta^2) \sinh(\alpha h)(A_1 - A_2) \\ & + 2k\beta \sinh(\beta h)(B_1 + B_2) = -\frac{P}{2\mu}. \end{aligned} \quad (89)$$

The determinants of the coefficient matrices provide the dispersion relations for symmetric ($D_S = 0$) and antisymmetric ($D_A = 0$) modes of an elastic layer bounded by free surfaces:

$$\begin{aligned} D_S &= 4k^2\alpha\beta \sinh(\alpha h) \cosh(\beta h) \\ & - (k^2 + \beta^2)^2 \cosh(\alpha h) \sinh(\beta h), \end{aligned} \quad (90)$$

$$\begin{aligned} D_A &= 4k^2\alpha\beta \cosh(\alpha h) \sinh(\beta h) \\ & - (k^2 + \beta^2)^2 \sinh(\alpha h) \cosh(\beta h). \end{aligned} \quad (91)$$

The dispersion relations $D_S = 0$ and $D_A = 0$ are more often written as (e.g., Lamb, 1917; Achenbach, 1973, 2003)

$$\frac{\tanh(\beta h)}{\tanh(\alpha h)} = \frac{4k^2\alpha\beta}{(k^2 + \beta^2)^2} \text{(symmetric)}, \quad (92)$$

$$\frac{\tanh(\beta h)}{\tanh(\alpha h)} = \frac{(k^2 + \beta^2)^2}{4k^2\alpha\beta} \text{(antisymmetric)}. \quad (93)$$

The coefficients are given by

$$A_1 + A_2 = \frac{i(k^2 + \beta^2) \sinh(\beta h)}{D_S} \frac{P}{2\mu}, \quad (94)$$

$$B_1 - B_2 = -\frac{2k\alpha \sinh(\alpha h)}{D_S} \frac{P}{2\mu}, \quad (95)$$

$$A_1 - A_2 = \frac{i(k^2 + \beta^2) \cosh(\beta h)}{D_A} \frac{P}{2\mu}, \quad (96)$$

$$B_1 + B_2 = -\frac{2k\alpha \cosh(\alpha h)}{D_A} \frac{P}{2\mu}, \quad (97)$$

and hence,

$$A_1 = i(k^2 + \beta^2) \left[\frac{\sinh(\beta h)}{D_S} + \frac{\cosh(\beta h)}{D_A} \right] \frac{P}{4\mu}, \quad (98)$$

$$A_2 = i(k^2 + \beta^2) \left[\frac{\sinh(\beta h)}{D_S} - \frac{\cosh(\beta h)}{D_A} \right] \frac{P}{4\mu}, \quad (99)$$

$$B_1 = -2k\alpha \left[\frac{\sinh(\alpha h)}{D_S} + \frac{\cosh(\alpha h)}{D_A} \right] \frac{P}{4\mu}, \quad (100)$$

$$B_2 = -2k\alpha \left[-\frac{\sinh(\alpha h)}{D_S} + \frac{\cosh(\alpha h)}{D_A} \right] \frac{P}{4\mu}. \quad (101)$$

Next we calculate impedance of the ice as $Z_i = P/v_z$, where $v_z = -i\omega u_z$ is evaluated at $z = -h$:

$$Z_i = \frac{2i\rho_i c_s^4}{\omega^3 \alpha F}, \quad (102)$$

$$F = \frac{\sinh(\alpha h) \sinh(\beta h)}{D_S} + \frac{\cosh(\alpha h) \cosh(\beta h)}{D_A}. \quad (103)$$

A.3 Dispersion relation for coupled ice-water system

The dispersion relation for the coupled system is obtained by matching impedance, $Z_w = Z_i$, yielding

$$\frac{\omega \rho_w D_0}{\kappa \sinh(\kappa H)} = \frac{2\rho_i c_s^4}{\omega^3 \alpha F}. \quad (104)$$

The article *Ocean Surface Gravity Wave Excitation of Flexural Gravity and Extensional Lamb Waves in Ice Shelves* © 2023 by L.S. Abrahams is licensed under CC BY 4.0.

Exploring the Effect of Minimum Magnitude on California Seismic Hazard Models

Molly M. Gallahue* ¹, Leah Salditch ², Madeleine C. Lucas³, James Neely ^{1,4}, Seth Stein ^{1,4}, Norman Abrahamson⁵, Susan E. Hough ⁶

¹Department of Earth and Planetary Sciences, Northwestern University, Evanston, Illinois U.S.A., ²U.S. Geological Survey, Geologic Hazards Science Center, Golden, Colorado, U.S.A., ³Department of Earth and Space Sciences, University of Washington, Seattle, Washington, U.S.A., ⁴Institute for Policy Research, Northwestern University, Evanston, Illinois, U.S.A., ⁵Department of Civil and Environmental Engineering, University of California, Berkeley, California, U.S.A., ⁶U.S. Geological Survey, Earthquake Science Center, Moffett Field, California, U.S.A.

Author contributions: *Conceptualization:* All authors. *Data Curation:* M. Gallahue, L. Salditch, N. Abrahamson, M. Lucas, J. Neely. *Formal Analysis:* M. Gallahue, N. Abrahamson. *Funding Acquisition:* N. Abrahamson, S. Stein, S. Hough. *Investigation:* M. Gallahue, N. Abrahamson, S. Stein, S. Hough. *Methodology:* N. Abrahamson. *Resources:* L. Salditch. *Validation:* M. Gallahue, N. Abrahamson. *Visualization:* M. Gallahue, N. Abrahamson, S. Stein, S. Hough. *Writing – original draft:* M. Gallahue. *Writing – review & editing:* M. Gallahue, S. Stein, S. Hough, L. Salditch.

Abstract A recent topic of interest is the performance of probabilistic seismic hazard maps relative to historically observed shaking. Past studies in several areas have documented an apparent discrepancy between seismic hazard map predictions and historically observed shaking. To explore whether this discrepancy arises because of incompleteness in historical intensity catalogs, we consider maps and historical intensities from California. Current probabilistic seismic hazard maps for California appear to predict stronger short period shaking than historical maxima captured by the California Historical Intensity Mapping Project (CHIMP) dataset between 1857 and 2019. We estimate that CHIMP has a magnitude completeness between M_6 and 6.6, whereas California hazard maps assume a minimum magnitude (M_{Min}) of 5. Disaggregating the maps shows that earthquakes smaller than M_6 and 6.6 respectively contribute about 25% and 45% of hazard across California. Increasing the hazard map's M_{Min} to 6 and 6.6 respectively reduces the discrepancy between predicted and observed shaking by approximately 10–20% and 30–35%. These reductions are not enough to bring the maps and data in alignment. Thus, M_{Min} inconsistencies contribute to, but are not the sole cause of, the discrepancy between predicted and historically observed shaking. These results may be generally applicable to maps elsewhere, although M_{Min} will vary for different historical datasets.

Production Editor:
Gareth Funning
Handling Editor:
Vitor Silva
Copy & Layout Editor:
Théa Ragon

Reviewed by:
Jonathan Griffin,
anonymous reviewer

Received:
August 22, 2022
Accepted:
April 21, 2023
Published:
June 23, 2023

1 Introduction

Probabilistic seismic hazard analyses (PSHA) forecast the probability, p , that during t years of observations shaking at a site will exceed the value shown in a model with a τ -year return period, assumed to be described by a negative exponential distribution,

$$p = 1 - \exp\left(\frac{-t}{\tau}\right) \quad (1)$$

(Cornell, 1968; Field, 2008). Assuming the same behavior over time as over space (the ergodic assumption), p also gives the fraction of sites where observed shaking is expected to exceed the mapped value for any map return period and duration of observations. As the ratio of the observation time to the return period increases, p should also increase because an increasing fraction of the area will have experienced larger earthquakes and thus higher shaking.

This approach, which was introduced by Ward (1995) and used in subsequent analyses (e.g., Albarello and D'Amico, 2008; Fujiwara et al., 2009; Miyazawa and Mori, 2009; Stirling and Gerstenberger, 2010; Nekrasova

et al., 2014; Tasan et al., 2014; Mak and Schorlemmer, 2016a) considers many sites to avoid the constraint that large ground motions at any given site are rare. At any one site, the annual rate of exceedance is $1/\tau$. PSHA models and corresponding maps are based on assumptions about the rates, spatial distribution, and sizes of potential future earthquakes, and ground-motion models (GMMs) that predict the resulting shaking.

Because PSHA maps are critical for earthquake hazard assessment and risk mitigation, assessing how well PSHA models and maps forecast observed shaking is important. The problem is challenging both because of limitations in the available data and because of conceptual issues regarding the assessment of probabilistic forecast performance (Marzocchi and Jordan, 2014; Stein et al., 2015; Wang, 2015; Vanneste et al., 2018; Brooks et al., 2019; Gneiting and Katzfuss, 2014). In particular, shaking data recorded after a PSHA model was made typically span a time period (t) that is extremely short compared to the return period of the hazard map (τ) (e.g., 475 or 2475 years). Hence most post-PSHA model shaking datasets do not fully include the moderately large and large earthquakes that often control hazard for an area. One approach to address this problem is retrospective assessment, or hind-

*Corresponding author: mollygallahue2023@u.northwestern.edu

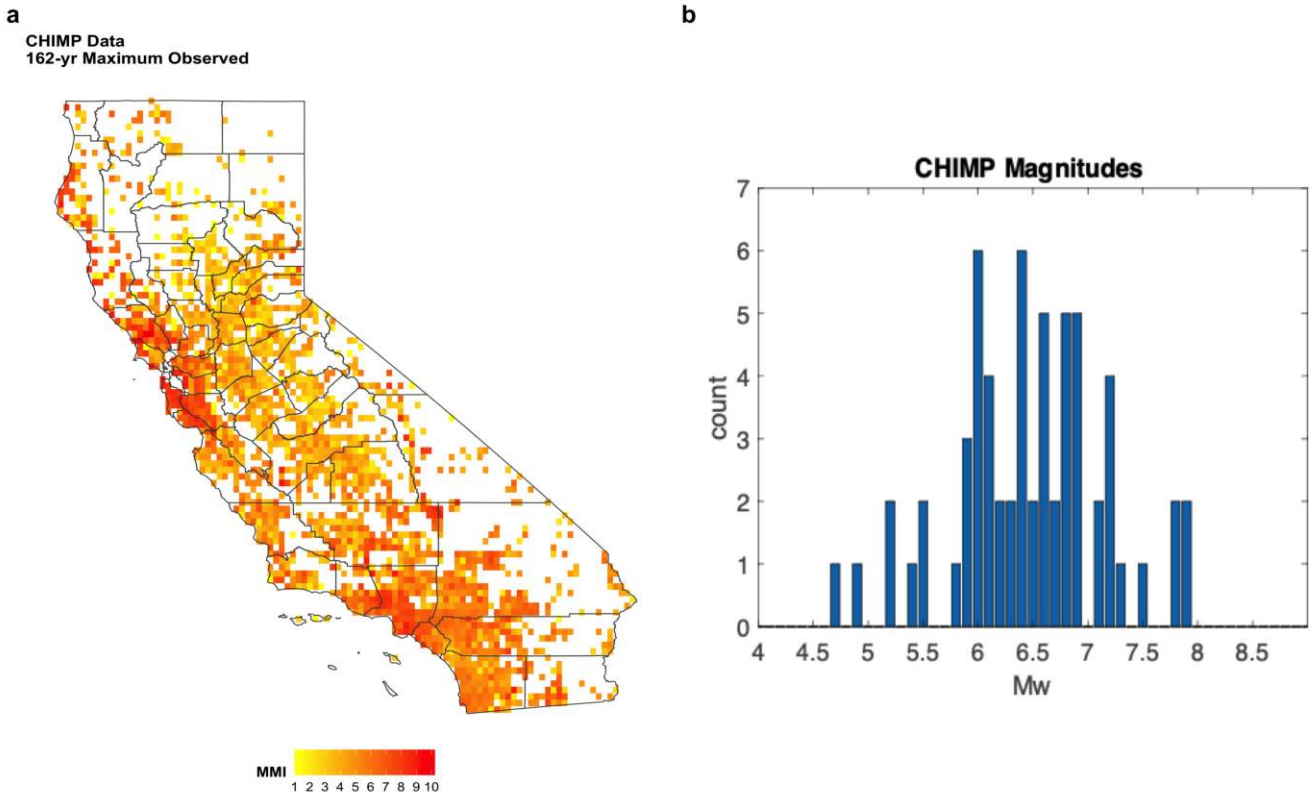


Figure 1 (a) Maximum observed intensity data in 10 × 10 km grid cells from CHIMP (Salditch et al., 2020). (b) Histogram of the magnitudes of the 62 earthquakes included in CHIMP.

casting, which uses compilations of historical shaking data spanning hundreds of years (Stirling and Petersen, 2006; Nekrasova et al., 2014; Mak et al., 2014; Stein et al., 2015; Brooks et al., 2016, 2017, 2018), or in some cases, smaller datasets of instrumental ground-motion data (Stirling and Gerstenberger, 2010; Mak and Schorlemmer, 2016b). The method is similar to that used by meteorologists to improve weather forecasts (Stein et al., 2015).

PSHA maps have recently been compared to historical datasets for several countries. Comparisons of mean hazard maps with catalogs of historical data for Italy, Japan, and California, (USA) have all shown that maps appear to overpredict shaking relative to historical datasets (Stein et al., 2015; Brooks et al., 2016; Salditch et al., 2020). Comparisons for France and Nepal yield similar results (Drouet et al., 2020; Salditch, 2021). Similar studies using ShakeMap data for Australia also demonstrate that the models appear to predict higher shaking than observed in the last 50 years (Allen et al., 2023). Thus, a similar discrepancy arises in different regions for shaking datasets and hazard maps developed by different groups and approaches. Although some studies have found that hazard maps are consistent, or even underpredict, relative to historical datasets (e.g., Rey et al., 2018; Griffin et al., 2019), these studies consider the largest intensities, above which observed data are considered complete. In doing so, these studies exclude regions where observed intensities are significantly less than those predicted, which is where the discrepancy arises. Although a compilation of historically observed shaking may not be complete at the MMI

3 or 4 (say) level, a fair overall comparison of a hazard map should consider grid cells for which one has historically observed maximum intensities. A potential incompleteness bias in historical intensity catalogs is countered by a general reporting bias, whereby severe effects are more likely to be documented than mild or moderate effects (e.g., Hough, 2013). This reporting bias persists with the DYFI system: Mak and Schorlemmer (2016a) showed that, to first order, population density and shaking severity control the likelihood that a DYFI response will be received. Additionally, these studies examine individual sites, which differs from our approach of examining the entire map.

This discrepancy might have several causes, as discussed by Salditch et al. (2020), including that the data may be biased low, the maps may be biased high, or that the misfit may arise purely by chance. One possible cause of the data being biased low is that databases of historically observed shaking may be incomplete for magnitudes that contribute to hazard. To explore this issue, we consider U.S. Geological Survey (USGS) mean probabilistic seismic hazard maps for California and historical observed shaking captured in the California Historical Intensity Mapping Project (CHIMP). The CHIMP catalog is publicly available, and the USGS provides a publicly available tool for disaggregation (<https://earthquake.usgs.gov/hazards/interactive/>), making this study possible.

CHIMP is the first comprehensive compilation of observed seismic intensities from 62 of the largest earthquakes (moment magnitude $M_{4.7-7.9}$; most with $M > 6$) in California over a 162-yr period between 1857 and

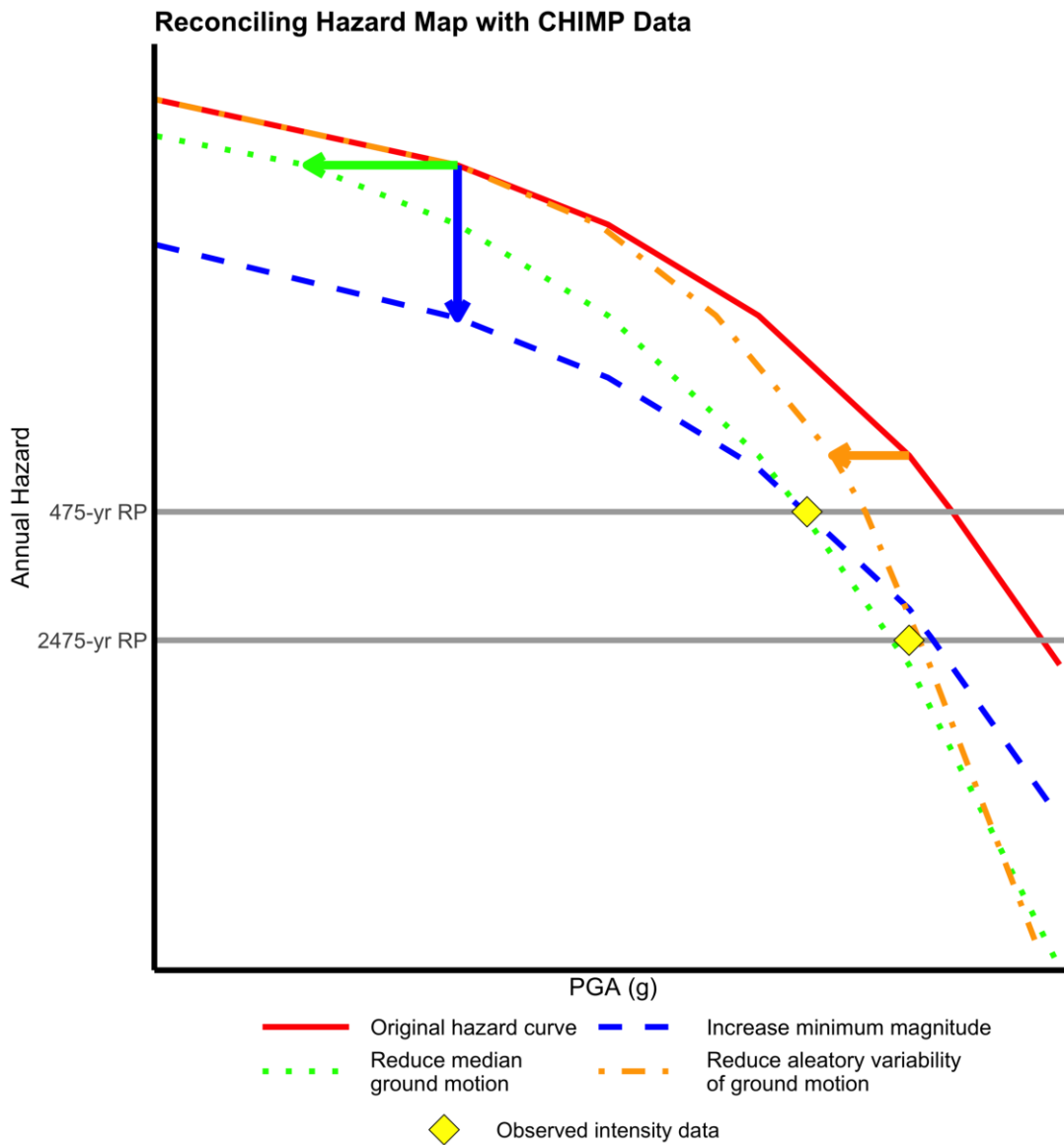


Figure 2 Schematic illustrating three possible adjustments to the hazard model that could make the predicted hazard more consistent with the observed shaking data at a site. Ideally, curves should pass through the yellow diamonds. Curves to the right of the yellow diamonds predict higher shaking than observed in the historical catalog. Arrows show in which direction adjustments change the original hazard curve. 475-yr and 2475-yr return periods (RP) shown.

2019 (Fig. 1b) (Salditch et al., 2020). Intensity values, measured on the Modified Mercalli Intensity (MMI) scale (Wood and Neumann, 1931) were collected from sources including historical newspaper accounts, USGS postcard questionnaires, USGS “Did You Feel It?” (DYFI) program responses, and oral history accounts (Salditch et al., 2020). Assigned intensity values were then aggregated into 10 × 10 km regions, giving the maximum observed intensity in each (Fig. 1a). The nominal uncertainty of each observation is +/- one intensity unit (Salditch et al., 2020), a standard variation between researchers (Hough and Page, 2011; Salditch et al., 2018).

This process is likely to miss shaking due to some smaller historical events for which accounts are limited, and possibly moderate earthquakes outside of California borders that were felt within the state. Salditch et al. (2020) explored CHIMP incompleteness from historical population distributions through interpolated inten-

sities for the three largest earthquakes in California (1857 Fort Tejon, 1872 Owens Valley, and 1906 San Francisco). They showed that results did not change appreciably when more spatially dense intensity values for past large earthquakes were included. Incompleteness of intensity observations at individual points is thus unlikely to account for the discrepancy between maps and observed intensities.

To compare hazard maps with CHIMP, Salditch et al. (2020) converted the 2018 USGS seismic hazard map (Petersen et al., 2020) from peak ground acceleration (PGA) to MMI via Worden et al. (2012) magnitude and distance independent ground-motion intensity conversion equation (GMICE). Here, we use PGA converted to MMI hazard maps for consistency with the Salditch et al. (2020) study.

Equation 1, for $t = 162$ years, predicts that the fraction of sites where observed shaking exceeds the mapped

hazard value should be $p = 0.289$ and 0.063 for 475- and 2475-yr return period maps, respectively. However, the observed fraction of site exceedances, f , calculated by dividing the number of sites where CHIMP data is higher than a 475- and 2475-yr hazard map's prediction by the total number of CHIMP sites, is considerably lower than either p . Salditch et al. (2020) found $f = 0.064$ and 0.006 for the 475- and 2475-yr maps, respectively.

The performance of hazard maps can be quantified using MO , the fractional exceedance metric, which is defined as $|f - p|$ (Stein et al., 2015). Ideally this metric would equal 0, and larger MO s indicate a greater discrepancy between predictions and observations. We also consider the ratio f/p , which can be thought of as a scale factor for the number of earthquakes contributing to hazard that would be needed to align the map predictions and observations. Map “overprediction” arises when $p > f$.

Salditch et al. (2020) found that p is greater than f for the maps with both a 10% probability of exceedance in 50 years (475-yr return period) and a 2% probability of exceedance in 50 years (2475-yr return period), so both overpredict shaking relative to the CHIMP data. This pervasive discrepancy has important implications and calls for detailed investigation.

The overprediction of the shaking data could be influenced by three different factors, shown schematically via the hazard curve for an individual site (Fig. 2) in a hazard map. If the median ground motions as predicted by GMMs were smaller, the hazard curve would shift horizontally, bringing it in closer alignment with observed data. Alternatively, if the assumed hazard model's M_{Min} , the minimum magnitude of earthquakes included in the hazard calculation, were higher, the hazard curve would shift vertically because hazard is reduced due to fewer contributing earthquakes, again bringing it into closer alignment with observed intensities. Lastly, if the aleatory, or random, variability of the ground-motion models were smaller, the hazard distribution would be narrowed, thus steepening the hazard curve. Other effects can also change the hazard curves, but we consider these to be the simplest and thus most likely.

There are several assumptions made when building and testing a hazard map. The comparisons by Salditch et al. (2020) used PSHA maps for a reference site condition, leaving open the possibility that the results might be significantly different if site response were included. Gallahue et al. (2022) showed, however, that incorporating site effects (as predicted by NGA-West2) did not appreciably change high-frequency PSHA maps, and thus that site effects are not a cause of the discrepancy. The weak predicted influence of site response on high-frequency ground motion is due to nonlinear damping at strong shaking levels. Furthermore, comparison of hazard maps (traditionally given in PGA) to observed shaking records (in seismic intensity) requires the use of a GMICE. Salditch et al. (2020) converted PGA hazard maps to intensity using the Worden et al. (2012) GMICE. However, a recent study by Gallahue and Abrahamson (2023) found that the methodology used in the Worden GMICE (and others) leads to overestimated intensities at

PGAs relevant to hazard maps. These biased GMICE will contribute to the observed discrepancy. USGS hazard maps also rely on the mean hazard, but median hazard curves may better align with observed data. Other factors, such as nonergodic ground-motion models used to develop the maps or spatial correlation effects, could also contribute to the discrepancy.

In this paper, we consider whether removing the contribution to seismic hazard from smaller earthquakes (increasing M_{Min} in the hazard maps) to adjust for incompleteness of the CHIMP dataset could contribute to the observed overprediction (Fig. 2). This evaluates the assumption that the minimum magnitudes between maps and data are consistent, or the differences are irrelevant. USGS mean PSHA maps, which we refer to as the reference maps, use a minimum magnitude M_{Min} of 5 in hazard calculations for California (Petersen et al., 2015, 2020). However, the magnitude for completeness is larger for CHIMP. The PSHA maps were also generated using earthquakes within a 100-km zone beyond state borders.

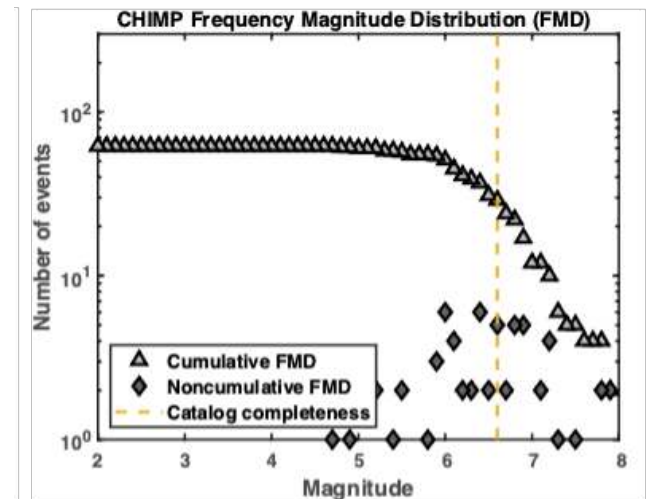


Figure 3 Frequency-magnitude distribution (FMD) of earthquakes in the CHIMP dataset. Estimated catalog completeness level is $M6.6$ (dashed vertical line).

CHIMP considers all earthquakes greater than $M6$, and a few smaller ones. Thus, the lowest possible magnitude of completeness of CHIMP is $M6$. Using the maximum curvature method (Mignan and Woessner, 2012) to calculate the CHIMP catalog's completeness, we find the maximum value of the first derivative of the cumulative frequency-magnitude distribution to be $M6.6$ (Fig. 3). Hence CHIMP is complete for $M6.6+$ but includes some smaller events if they were suspected to control the maximum observed intensity at some sites. We further note that evaluations of PSHA maps using CHIMP rely on locations for which historical intensities are available. Catalog completeness will be lowest in sparsely populated regions; i.e., intensity values will tend to be missing in regions where the catalog is least complete. We thus expect that missing moderate earthquakes in sparsely populated regions, including in the 100-km zone outside of California borders, will tend to

not contribute to assessed map performance. We thus assume that the actual magnitude of completeness for CHIMP is somewhere between M_6 and 6.6 and evaluate M_{Min} at these end members. If $M_{Min} = 6$, 51 earthquakes remain in the catalog. If $M_{Min} = 6.6$, 28 earthquakes remain. For completeness, because M_{Min} can be difficult to resolve, we also tested $M_{Min} = 6.8$. These results did not differ from those for $M_{Min} = 6.6$.

2 Disaggregation of hazard for $M > 6$ and $M > 6.6$

We explore the effect of the minimum magnitude using disaggregation, which gives the fractional contribution to the total predicted hazard for a range of magnitudes and distances. Disaggregation results allow the contribution to hazard from varying magnitudes, distances, and epsilons (number of standard deviations above the median ground motion) to be understood (Bazzurro and Cornell, 1999). Effectively, this breaks the hazard map into the input scenarios, and determines the effect of each. From a mathematical basis, the fraction of the hazard from all events with $M \geq 5$ that results from events with $M \geq M_{Min}$ is:

$$\begin{aligned} \text{Haz}_{PGA}(z|M \geq M_{Min}) \\ = \text{Haz}_{PGA}(z|M \geq 5) \text{Disagg}(M \geq M_{Min}|PGA > z) \end{aligned} \tag{2}$$

where z is predicted ground motion (in PGA), $\text{Disagg}(M \geq M_{Min}|PGA > z)$ is the hazard disaggregation assuming a magnitude greater than M_{Min} and PGA greater than z , and $\text{Haz}_{PGA}(z|M \geq M_{Min})$ is the hazard in terms of PGA of z assuming $M \geq 5$. Figure 4, a disaggregation result for one site in California, demonstrates how the removal of magnitudes less than a certain value would reduce the total hazard (rate of exceedance) due to using a larger M_{Min} in the hazard calculations. Excluding M_{5-6} reduces the hazard less than excluding $M_{5-6.6}$ because fewer events are excluded.

We produce approximate hazard maps for $M_{Min} = 6$ and $M_{Min} = 6.6$ using disaggregation results for a grid of locations in California using the USGS Unified Hazard Tool for return periods of 475 years and 2475 years, corresponding to the two maps examined by Salditch et al. (2020). Because disaggregation reports for the 2018 mean hazard model and map were not available in the USGS tool at the time of this analysis, we used the 2014 mean values. Petersen et al. (2020) found that the mean hazard in California stayed consistent between the 2014 model and the 2018 update, so results for 2014 are expected to be comparable to the more recent 2018 models. Additionally, the earthquake catalog and source models for California in both the 2014 and 2018 maps are from the Uniform California Earthquake Rupture Forecast model (UCERF3). Thus, no earthquakes were added or removed from 2014 to 2018, and no substantial changes occurred in California hazard during this time (Petersen et al., 2020, 2021).

We compute the fraction of the hazard due to larger events at each grid site. The disaggregation shows that the average contribution to hazard of $M \geq 6$ events across

Contribution from all sources

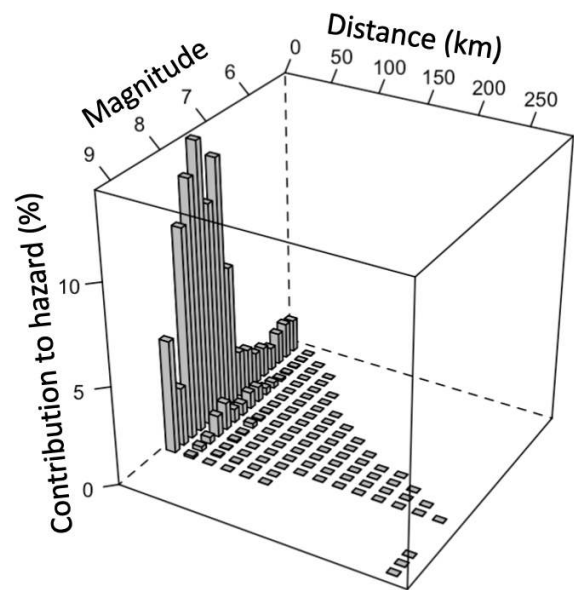


Figure 4 Disaggregation results for a site outside San Francisco. Most of the hazard comes from events with magnitudes greater than ~ 7 and distances < 50 km. If the contribution from smaller magnitude events were removed, the total hazard would decrease.

all sites is $\sim 75\%$ for the 475-yr return period map and $\sim 76\%$ for the 2475-yr return period map. Similarly, the average contribution to hazard of $M \geq 6.6$ events across all sites is smaller, $\sim 53\%$ for the 475-yr return period map and $\sim 55\%$ for the 2475-yr return period map. At each grid site, we reduce the hazard to that excluding $M < 6$ or 6.6 by scaling the hazard curve (Rukstales and Petersen, 2019) by the calculated percent contribution to hazard. Via log-interpolation on the hazard curves, we derive the corresponding decrease in PGA. To scale the hazard maps for the hazard from only $M \geq 6$ or 6.6 events, we adjust the reference hazard map PGA by the PGA percent decrease at the closest grid location (Fig. 5).

The percent decreases in PGA from the reference map to the maps scaled to exclude $M < 6$ or 6.6 are shown in Fig. 6. Excluding the contribution from smaller earthquakes reduces the hazard and thus the corresponding predicted PGA. For 475-yr and 2475-yr return periods, the reduction in the PGA from excluding $M < 6$ events ranges from less than 10% near the major coastal faults to up to 35% in the Sierra foothills. Excluding the contribution from $M < 6.6$ events reduces PGA by up to 65% in the Sierra foothills.

These results show that $M < 6$ events contribute substantially to predicted hazard ($\sim 25\%$), and $M < 6.6$ events contribute even more ($\sim 45\%$). This result is consistent with the result of Minson et al. (2009), that due to the aleatory variability of ground motions and the Gutenberg-Richter distribution of magnitudes (Gutenberg and Richter, 1944), strong short-period shaking is more likely to be generated by more frequent moderate-

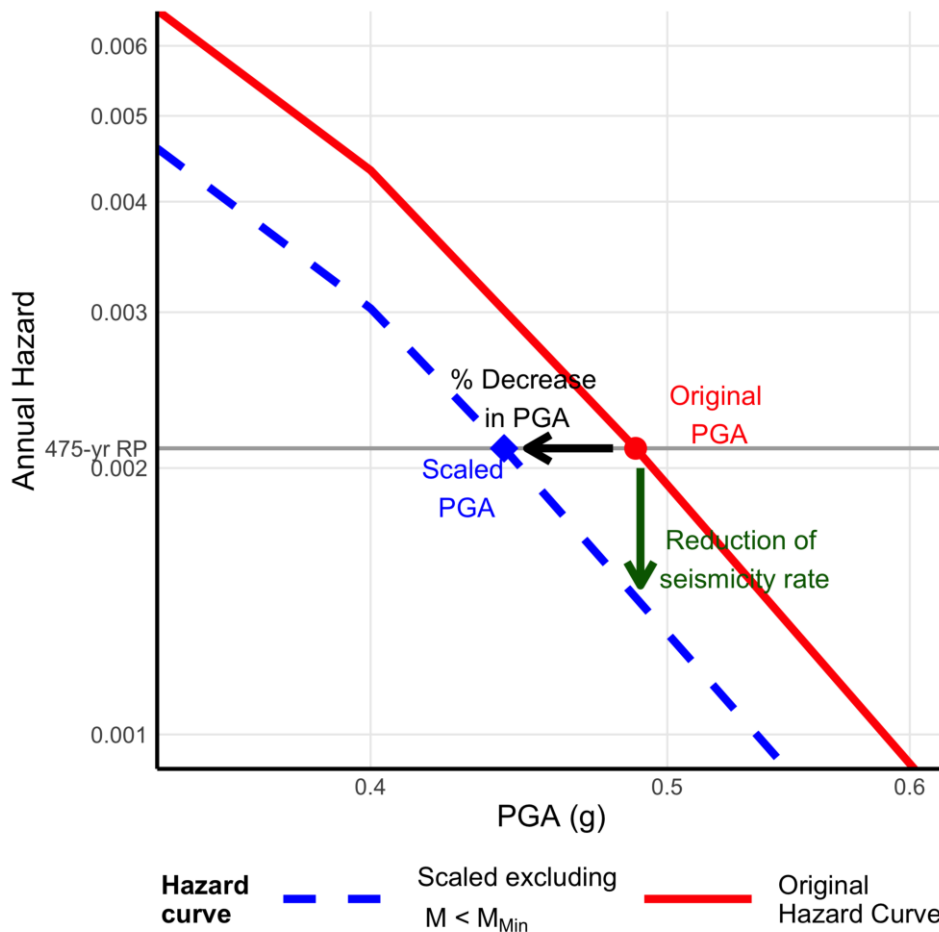


Figure 5 Schematic of decrease in hazard (PGA) with a 475-yr return period (RP) resulting from the hazard curve reduction from increasing M_{Min} .

magnitude earthquakes than by rarer large-magnitude earthquakes. Fig. 6 shows that $M < 6$ and 6.6 events strongly contribute to hazard in some areas. Conceptually, we expect that hazard near major, active faults will be controlled by large earthquakes on those faults. However, away from major faults, hazard will be more controlled by distributed background seismicity, so relatively frequent moderate-magnitude events will contribute more to overall hazard. Figure 7 shows the decrease of the scaled map relative to the reference for all cases, highlighting the MMI reduction from removing the contribution to hazard from smaller earthquakes.

It is worth noting that our described approach produces approximate maps for the given M_{Min} . The approach used here assumes that the relative contributions of the sources to the target exceedance rate does not appreciably change between the original and scaled maps. To completely alter M_{Min} would require changing the minimum magnitude during the calculation of hazard curves that underlie the maps. In doing so, the median and variance of ground motion and the activity rate, all of which influence predictions, would change. As described in Figure 2, changes to the median ground motion shift the hazard curve horizontally, whereas changes to variance would affect the slope of the hazard curve. Changes to the activity rate would shift the hazard curve vertically (Figure 2). However, de-

veloping hazard maps involves extensive computations, so in practice it is often not justifiable to compute hazard models for multiple M_{Min} , as evaluated in this paper.

3 Comparison of $M \geq 6$ Or 6.6 Maps with Historical Intensity Data

Using the metrics from Salditch et al. (2020), we assessed how the hazard maps scaled for $M \geq 6$ or 6.6 perform relative to CHIMP historical intensity data. For this comparison, we edited the CHIMP dataset to include data from only $M \geq 6$ or 6.6 earthquakes, which reduced the number of sites from that shown in Fig. 1a. We only assess hazard map values at the locations in which CHIMP data existed in the $M \geq 6$ or 6.6 sets; thus, the total number of sites evaluated varies between each considered M_{Min} . The $M \geq 6$ or 6.6 scaled PGA map values were converted to MMI via Worden et al. (2012)’s magnitude- and distance- independent equation that does not include aleatory variability.

Comparison of exceedance rates (Fig. 8, 9) shows that the scaled hazard maps excluding $M < 6$ or 6.6 perform better than the reference maps because the lower predicted hazard yields more observed exceedances (Table 1, 2). However, the fractions, f , of sites where the largest shaking exceeds that predicted from either map remain much lower than the predicted fraction, p .

Percent Decrease in PGA Excluding Hazard from $M < M_{Min}$

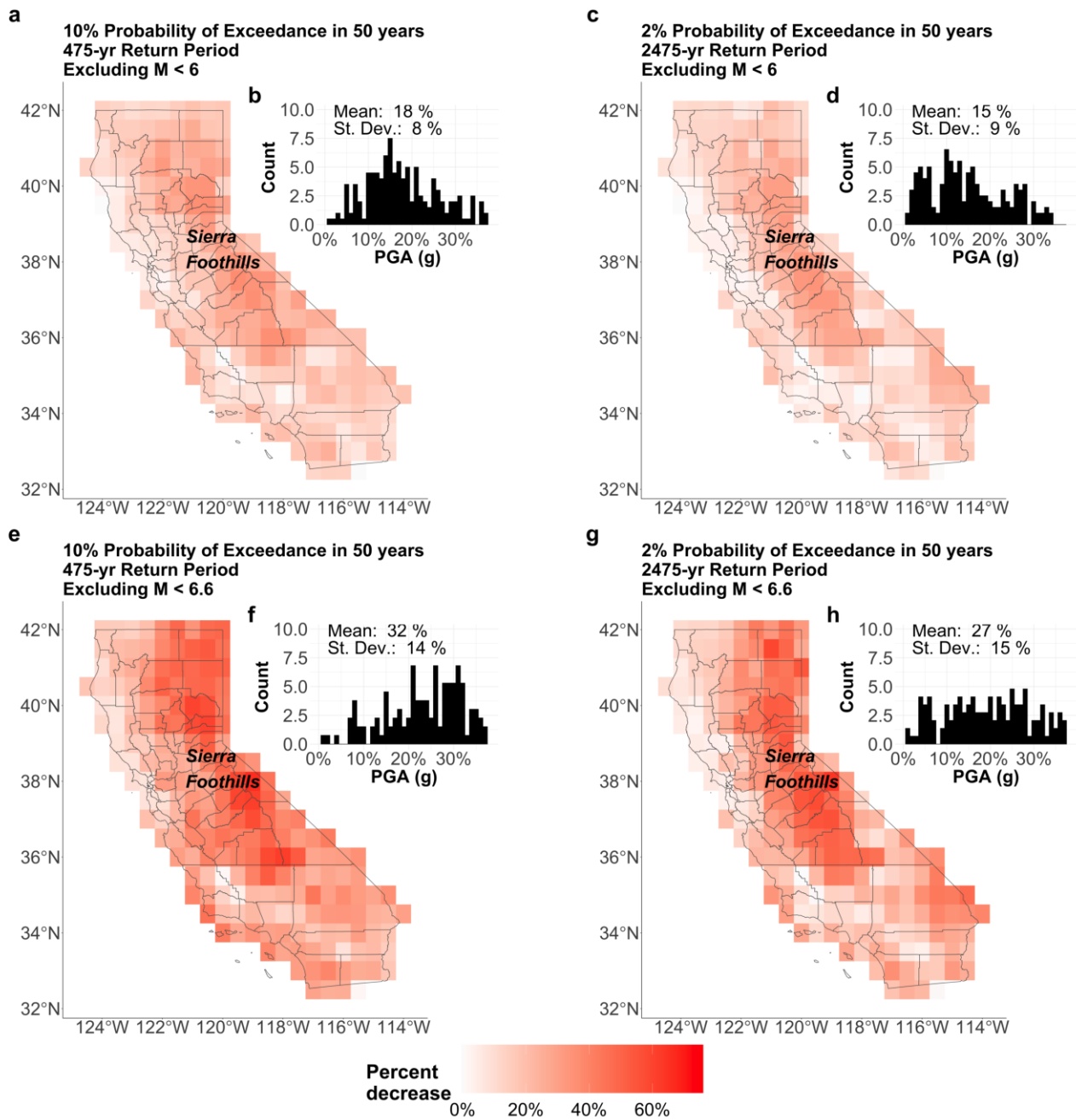


Figure 6 Maps showing percent decreases in PGA. For 10% probability of exceedance in 50 years (475-yr return period) map (a) excludes $M < 6$ earthquakes and (e) excludes $M < 6.6$ earthquakes. For the 2% probability of exceedance in 50 years (2475-yr return period) map (c) excludes $M < 6$ earthquakes and (g) excludes $M < 6.6$ earthquakes. Distributions of the percent decreases for (b), (f) the 475-yr return period and (d), (h) the 2475-yr return period maps. PGA decreases by an average of 18% for the 475-yr return period map and 15% for the 2475-yr return period map when excluding $M < 6$. PGA decreases by an average of 32% for the 475-yr return period map and 27% for the 2475-yr return period map when excluding $M < 6.6$. The most substantial PGA decrease is in the Sierra foothills.

For the 475-yr map with $p = 0.289$ when excluding $M < 6$, f increases from 0.071 (155 exceedances) to 0.107 (234 exceedances) for the scaled map. This represents an increase of ~51%, or 79 sites. Similarly, for the 2475-yr map with $p = 0.063$, f increases from 0.01 (21 exceedances) to 0.016 (35 exceedances), an increase of ~67%, or 14 sites. As a result, M_0 values for the scaled maps were 0.182 and 0.047 for the 10% probability and the 2% probability of exceedance in 50 years maps, lower (showing better fit) than the reference maps' val-

ues of 0.218 and 0.053. The f/p ratios increased from 0.246 and 0.159 for the 475-yr and 2475-yr reference maps to 0.370 and 0.254 for the scaled maps, respectively, indicating improvement in map performance.

Similarly, for the 475-yr map with $p = 0.289$ when excluding $M < 6.6$, f increases from 0.063 (128 exceedances) to 0.139 (283 exceedances) for the scaled map. This represents an increase of ~121%, or 155 sites. For the 2475-yr map with $p = 0.063$, f increases from 0.009 (19 exceedances) to 0.025 (50 exceedances), an increase of

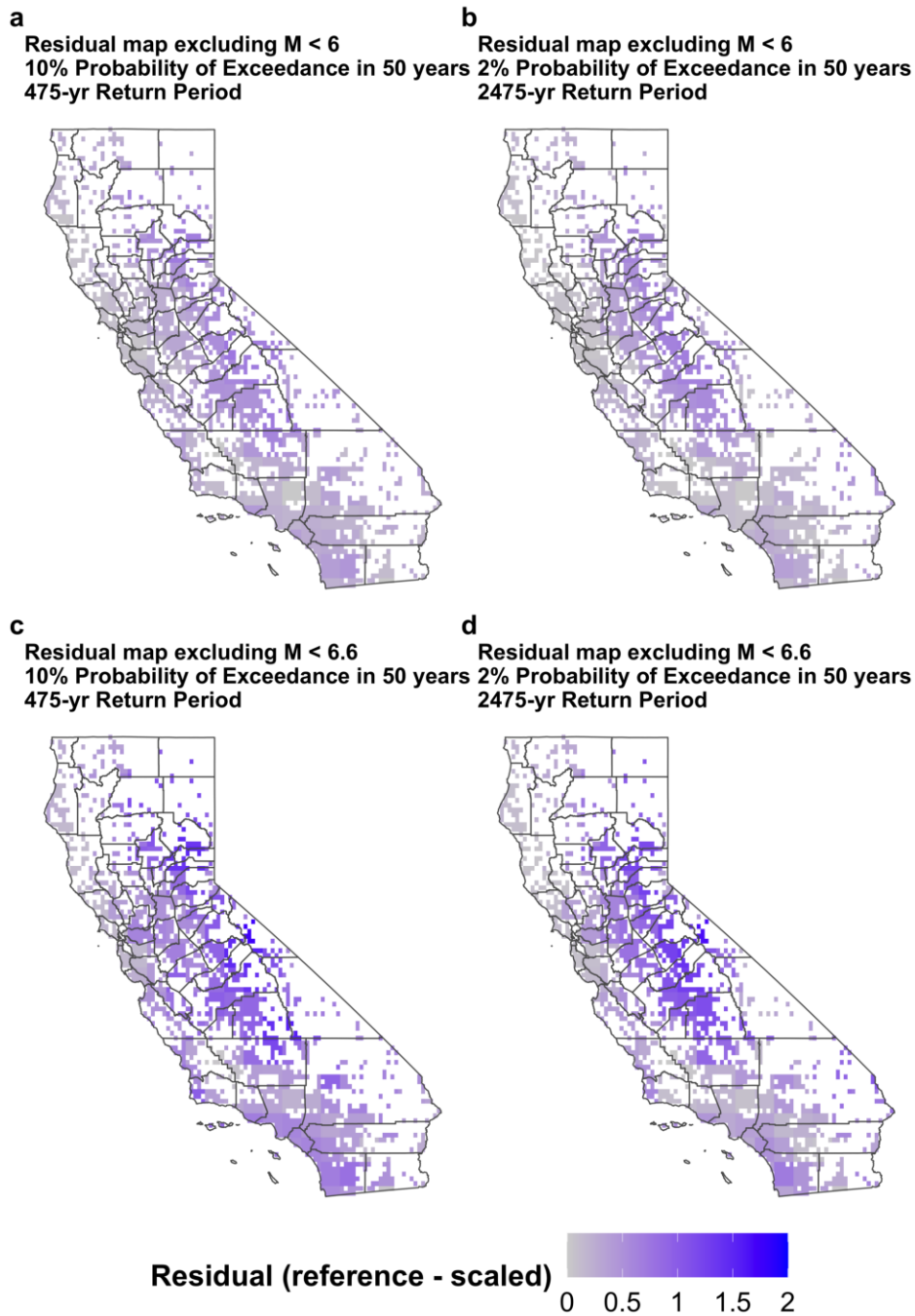


Figure 7 Intensity residuals (reference map intensity minus scaled map intensity) from this study. Scaled map excluding hazard $M < 6$ decreases the 475-yr return period (a) and 2475-yr return period (b) mapped values moderately relative to the reference mapped values. Scaled map excluding hazard $M < 6.6$ decreases the 475-yr return period (c) and 2475-yr return period (d) mapped values even more relative to the reference mapped values.

~178%, or 31 sites. M_0 values for the scaled maps, 0.15 and 0.038 for the 10% probability and the 2% probability of exceedance in 50 years map, were lower (showing better fit) than those for the reference maps, 0.226 and 0.054. Similarly, f/p ratios increased from 0.218 and 0.143 for the 475-yr and 2475-yr reference maps to 0.481 and 0.397 for the scaled maps, respectively, indicating improvement in map performance.

Despite the improvements, the scaled maps still over-predict shaking relative to CHIMP data. We construct 5–95% intervals for the predicted fraction of exceedance to explore if this could be due to chance. We assume the uncertainty in the number of observed ex-

ceedances in 162 years follows a Poisson probability model, such that

$$P(m \leq N) = e^{-\frac{t}{\tau}} \sum_{m=1}^N \frac{(\frac{t}{\tau})^m}{m!} \tag{3}$$

where t is the length of the interval (162 years), τ is approximately the average number of years between each exceedance (equal to $162/N$), N is the predicted number of exceedances, equal to 588 for the 475-yr maps and 128 for the 2475-yr return-period maps. We compute 5% and 95% uncertainty ranges for N by finding $N_{0.05}$ and $N_{0.95}$ such that $P(m \leq N_{0.05})=0.05$ and $P(m \leq N_{0.95})=0.95$.

	Reference map: 475-yr return period	Scaled M6 map: 475-yr return period	Reference map: 2475- yr return period	Scaled M6 map: 2475- yr return period
p	0.289	0.289	0.063	0.063
5-95% range on p	[0.270, 0.308]	[0.270, 0.308]	[0.054, 0.072]	[0.054, 0.072]
f	0.071	0.107	0.01	0.016
Predicted number of exceedances	632	632	138	138
Observed number of exceedances	155	234	21	35
M_0 (ideally 0)	0.218	0.182	0.053	0.047
f/p (ideally 1)	0.246	0.370	0.159	0.254

Table 1 Statistics of comparison of CHIMP data for $M \geq 6$ to both reference and scaled ($M \geq 6$) maps.

	Reference map: 475-yr return period	Scaled M6.6 map: 475- yr return period	Reference map: 2475- yr return period	Scaled M6.6 map: 2475-yr return period
p	0.289	0.289	0.063	0.063
5-95% range on p	[0.270, 0.309]	[0.270, 0.309]	[0.054, 0.072]	[0.054, 0.072]
f	0.063	0.139	0.009	0.025
Predicted number of exceedances	588	588	128	128
Observed number of exceedances	128	283	19	50
M_0 (ideally 0)	0.226	0.15	0.054	0.038
f/p (ideally 1)	0.218	0.481	0.143	0.397

Table 2 Statistics of comparison of CHIMP data for $M \geq 6.6$ to both reference and scaled ($M \geq 6.6$) maps.

Then, $N_{0.05}/2186$ and $N_{0.95}/2186$ are the lower and upper ranges of p , respectively, for the 2186 total sites for $M \geq 6$ comparisons (Fig. 8). Likewise, $N_{0.05}/2033$ and $N_{0.95}/2033$ are the lower and upper ranges of p , respectively, for the 2033 total sites for $M \geq 6.6$ (Fig. 9).

For $M \geq 6$ maps with 2186 sites and predicted exceedances at 632 and 155 sites, the 5–95% uncertainty ranges on p are [0.270, 0.308] and [0.054, 0.072] for the 475-yr and 2475-yr return period maps, respectively. For $M \geq 6.6$ maps with 2033 sites and predicted exceedances at 588 and 128 sites, the 5–95% uncertainty ranges on p are [0.270, 0.309] and [0.054, 0.072] for the 475-yr and 2475-yr return period maps. In all cases, the observed fraction of exceedances, f , for both the reference and scaled maps fall outside the uncertainty ranges of the predicted fraction, p . Thus, we conclude that the observed remaining discrepancy is not due to chance.

4 Discussion

Our results show that the apparent overpredictions of the USGS mean hazard maps relative to the CHIMP dataset cannot be fully explained by increasing M_{Min} to 6 or 6.6 to account for incompleteness of CHIMP. Although removing the contribution to hazard due to $M < 6$ or 6.6 events reduces the overprediction, it does not reduce it enough to fall within 5–95% confidence intervals on the predicted fraction of exceedance for either return period.

It remains possible that the discrepancies between predicted and historically observed ground motions are due to long-term incompleteness of the CHIMP catalog

due to the short length of the historical record. If, however, the inconsistencies between the historical magnitude of completeness and hazard map M_{Min} for California were the only cause of the discrepancy, the number of earthquakes contributing to hazard would need to be reduced by approximately a factor of 4 to align the reference map's (including hazard from $M < 6.6$) observed fraction of exceedance with the 5–95% confidence intervals of the predicted for the 475-yr map (5% interval of f/p for reference maps). Similarly, approximately a factor of 6 reduction would be needed for the 2475-yr map. For the scaled maps excluding the hazard from $M < 6.6$ events, reductions of about a factor of 2 for the 475-yr return period map and for the 2475-yr return period map would be needed to bring the metrics in alignment. Even greater factors would be needed to bring the scaled maps excluding hazards from $M < 6$ maps in alignment. Although Page and Felzer (2015) show that seismicity rate tends to be underestimated from short catalogs, their results indicate it is unlikely that the rate has been underestimated by such large factors. Recent results compiled by the U.S. Geological Survey “Did You Feel It?” system reveal that shaking from M_6 earthquakes is widely felt. For example, the 8 July 2021 M_6 Antelope Valley earthquake, which struck a remote area near the Nevada border, was widely felt throughout north-central California (see Data & Code Availability and Reproducibility).

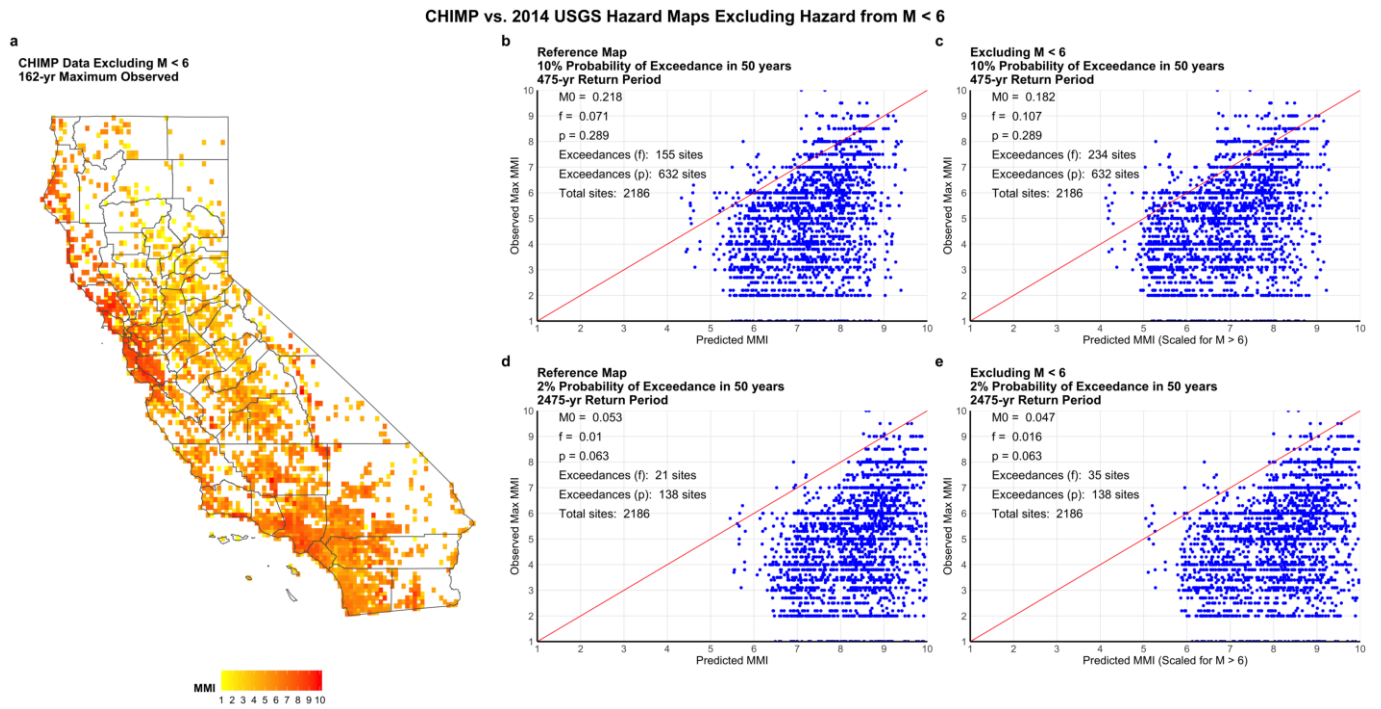


Figure 8 (a) CHIMP data excluding $M < 6$ events. (b–e) Predicted versus observed shaking for the 2014 reference USGS hazard map with 10% probability of exceedance in 50 years (b) and scaled hazard map excluding $M < 6$ (c). (d) and (e) show corresponding results for the map with 2% probability of exceedance in 50. 1:1 line shown in red.

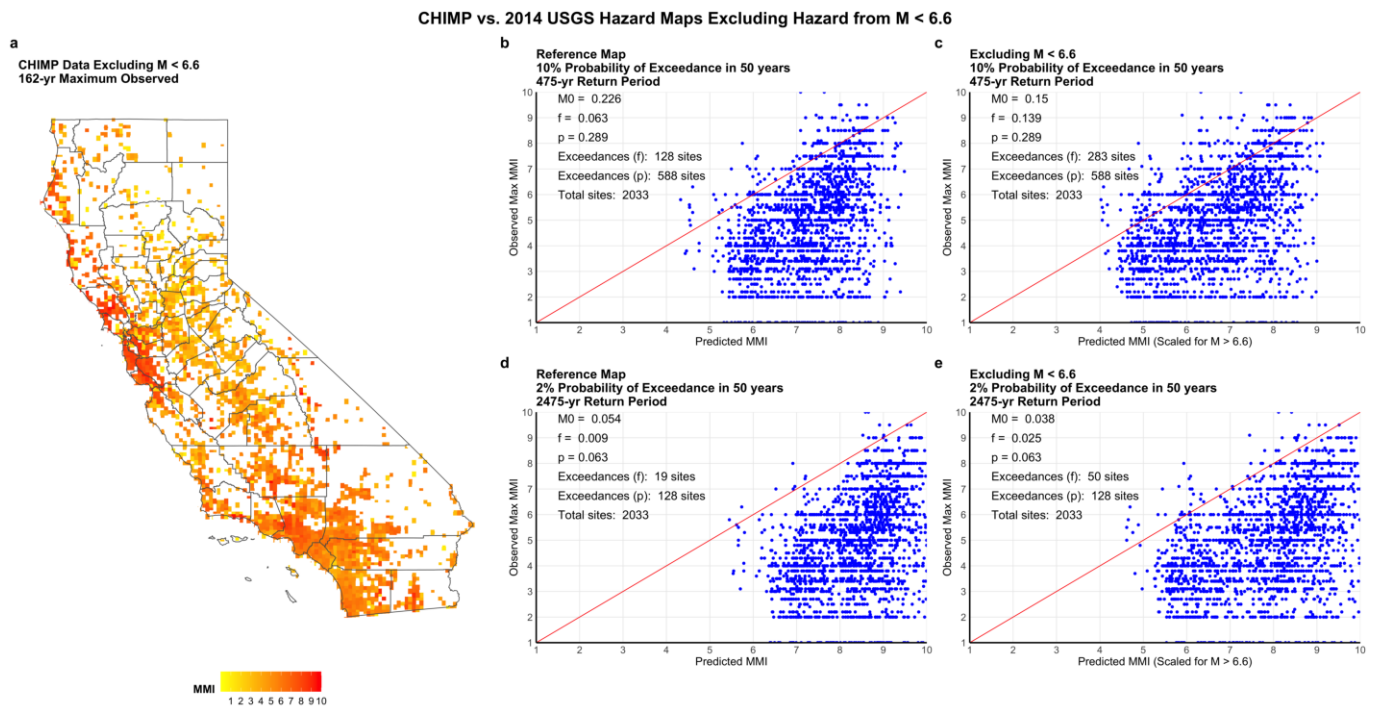


Figure 9 (a) CHIMP data excluding $M < 6.6$ events. b–e) Predicted vs. observed shaking for the 2014 reference USGS hazard map with 10% probability of exceedance in 50 years (b) and scaled hazard map excluding $M < 6.6$ (c). (d) and (e) show corresponding results for the map with 2% probability of exceedance in 50. 1:1 line shown in red.

5 Conclusion

We have considered one possible factor that might explain the discrepancy between predicted shaking in California and the much lower historically observed shaking revealed by the CHIMP dataset (Salditch et al., 2020). Our analysis shows that M_{5-6} earthquakes contribute

approximately 25% of the predicted hazard in California and $M_{5-6.6}$ contribute about 45%, consistent with implications of Minson et al. (2009). Hence, when the hazard maps are scaled to include only the effects of $M > 6$ or 6.6 events, the observed overpredictions lessen. However, this decrease is not large enough that the observed fractional exceedance falls within the 5–95%

confidence interval of that predicted. As such, the discrepancy between predicted and historically observed shaking in California is not due to incompleteness of the CHIMP dataset. These inconsistencies in minimum magnitude contribute to the discrepancy but are less than 30–35% of the discrepancy. Analogous results are expected to arise for discrepancies between maps and historical datasets in other areas when their corresponding M_{Min} s are considered. Future work is planned to focus on other possible effects contributing to the overprediction, including improved conversion equations between PGA and MMI (Gallahue and Abrahamson, 2023), which could lead to improved seismic hazard maps for California and worldwide.

Acknowledgements

The authors thank Andrea Llenos, Jonathan Griffin and an anonymous reviewer for their feedback. This work was partially supported by funding from the PG&E Geosciences Department Long-Term Seismic Program. Portions of this work were also supported by Northwestern University's Institute for Policy Research. Any use of trade, firm, or product names is for descriptive purposes only and does not imply endorsement by the U.S. Government.

Data and code availability

The CHIMP dataset is available as an electronic supplement to Salditch et al. (2020) and at <https://github.com/salditch/CHIMP>. The USGS hazard maps were downloaded from Rukstales and Petersen (2019) at <https://doi.org/10.5066/P9WT5OVB> (last accessed October 2021). The 2014 hazard curves and maps were downloaded from Shumway (2019) at <https://doi.org/10.5066/P9P77LGZ> (last accessed 28 October 2021 and 15 November 2021, respectively). Disaggregation files were downloaded from the Unified Hazard Tool, accessed at <https://earthquake.usgs.gov/hazards/interactive/> from the Dynamic: Conterminous U.S. 2014 (v4.1.4) edition (last accessed 3 November 2021). 2014 USGS hazard maps were downloaded from <https://www.sciencebase.gov/catalog/item/5db9be62e4b06957974eb5ca>, last accessed 15 November 2021. MATLAB scripts for the catalog completeness calculations are from “Basic Statistical Seismology Tutorial” by Brendan Sullivan, modified by Zhigang Peng, were downloaded from http://geophysics.eas.gatech.edu/people/bsullivan/tutorial/StatisticalSeismology.htm#part1_3 (last accessed 21 July 2022). Did You Feel It? results for the 2021 Antelope Valley earthquake can be accessed at <https://earthquake.usgs.gov/earthquakes/eventpage/nc73666231/dyfi/intensity> (last accessed 16 August 2022).

Competing interests

The authors declare no competing interests.



References

- Albarelo, D. and D'Amico, V. Testing probabilistic seismic hazard estimates by comparison with observations: An example in Italy. *Geophysical Journal International*, 175(3), 2008. doi: 10.1111/j.1365-246X.2008.03928.x.
- Allen, T., Ghasemi, H., and Griffin, J. Exploring Australian hazard map exceedance using an Atlas of historical ShakeMaps. *Earthquake Spectra*, 2023.
- Bazzurro, P. and Cornell, A. Disaggregation of seismic hazard. *Bulletin of the Seismological Society of America*, 89(2), 1999. doi: 10.1785/BSSA0890020501.
- Brooks, E., Stein, S., and Spencer, B. Comparing the performance of Japan's earthquake hazard maps to uniform and randomized maps. *Seismological Research Letters*, 87(1), 2016. doi: 10.1785/0220150100.
- Brooks, E., Stein, S., and Spencer, B. Investigating the effects of smoothing on the performance of earthquake hazard maps. *International Journal of Earthquake and Impact Engineering*, 2(2), 2017. doi: 10.1504/IJEIE.2017.10010009.
- Brooks, E., Stein, S., Spencer, B., Salditch, L., Petersen, M., and D.E. M. Assessing earthquake hazard map performance for natural and induced seismicity in the central and eastern United States. *Seismological Research Letters*, 89(1), 2018. doi: 10.1785/0220170124.
- Brooks, E., Neely, J., Stein, S., Spencer, B., and Salditch, L. Assessments of the performance of the 2017 one-year seismic hazard forecast for the Central and Eastern United States via simulated earthquake shaking data. *Seismological Research Letters*, 90(3), 2019. doi: 10.1785/0220190007.
- Cornell, A. Engineering seismic risk analysis. *Bulletin of the Seismological Society of America*, 58(5), 1968. doi: 10.1785/BSSA0580051583.
- Drouet, S., Ameri, G., Le Dortz, K., Secanell, R., and Senfaute, G. A probabilistic seismic hazard map for metropolitan France. *Bulletin of Earthquake Engineering*, 18(3), 2020. doi: 10.1007/s10518-020-00790-7.
- Field, E. Probabilistic seismic hazard analysis: A primer, 2008. https://opensha.org/resources/PSHA_Primer_v2_0.pdf.
- Fujiwara, H., Morikawa, N., Ishikawa, Y., Okumura, T., and J, M. Statistical comparison of national probabilistic seismic hazard maps and frequency of recorded JMA seismic intensities from the K-NET strong-motion observation network in Japan during 1997-2006. *Seismological Research Letters*, 80(3), 2009. doi: 10.1785/gssrl.80.3.458.
- Gallahue, M. and Abrahamson, N. New Methodology for Unbiased Ground-Motion Intensity Conversion Equations (GMICE). *Bulletin of the Seismological Society of America*, 2023. doi: 10.1785/0120220224.
- Gallahue, M., Salditch, L., Lucas, M., Neely, J., Stein, S., Abrahamson, N., Williams, T., and Hough, S. A study on the effect of site response on California seismic hazard map assessment. *Frontiers in Earth Science*, 10, 2022. doi: 10.3389/feart.2022.931340.
- Gneiting, T. and Katzfuss, M. Probabilistic forecasting. *Annual Review of Statistics and Its Application*, 1, 2014. doi: 10.1146/annurev-statistics-062713-085831.
- Griffin, J., Nguyen, N., Cummins, P., and Cipta, A. Historical earthquakes of the eastern Sunda arc: Source mechanisms and intensity-based testing of Indonesia's National Seismic Hazard Assessment. *Bulletin of the Seismological Society of America*, 109(1), 2019.
- Gutenberg, B. and Richter, C. Frequency of earthquakes in California. *Bulletin of the Seismological Society of America*, 34(4), 1944.

- doi: 10.1785/BSSA0340040185.
- Hough, S. Spatial variability of “Did You Feel It?” intensity data: Insights into sampling biases in historical earthquake intensity distributions. *Bulletin of the Seismological Society of America*, 103(5), 2013. doi: 10.1785/0120120285.
- Hough, S. and Page, M. Toward a consistent model for strain accrual and release for the New Madrid Seismic Zone, central United States. *Journal of Geophysical Research*, 116, B03311, 2011. doi: 10.1029/2010JB007783.
- Mak, S. and Schorlemmer, D. What makes people respond to “Did You Feel It?”. *Seismological Research Letters*, 87(1), 2016a. doi: DOI:10.1785.0220150056.
- Mak, S. and Schorlemmer, D. A comparison between the forecast by the U.S. National Seismic Hazard Maps with recent ground-motion records. *Bulletin of the Seismological Society of America*, 106(4), 2016b. doi: 10.1785/0120150323.
- Mak, S., Clements, R., and Schorlemmer, D. The statistical power of testing probabilistic seismic-hazard assessments. *Seismological Research Letters*, 85(4), 2014. doi: 10.1785/0220140012.
- Marzocchi, W. and Jordan, T. Testing for ontological errors in probabilistic forecasting models of natural systems. *Proceedings of the National Academy of Science of the United States of America*, 111(33), 2014. doi: 10.1073/pnas.1410183111.
- Mignan, A. and Woessner, J. Estimating the magnitude of completeness for earthquake catalogs, Community Online Resource for Statistical Seismicity Analysis, 45, 2012.
- Minson, S., Baltay, A., Cochran, E., McBride, S., and Milner, K. Shaking is almost always a surprise: The earthquakes that produce significant ground motion. *Seismological Research Letters*, 92(1), 2009. doi: 10.1785/0220200165.
- Miyazawa, M. and Mori, J. Test of seismic hazard map from 500 years of recorded intensity data in Japan. *Bulletin of the Seismological Society of America*, 99(6), 2009. doi: 10.1785/0120080262.
- Nekrasova, A., Kossobokov, V., Peresanand, A., and Magrin, A. Comparison of NDSHA, PSHA seismic hazard maps and real seismicity for the Italian territory. *Natural Hazards*, 70(1), 2014. doi: 10.1007/s11069-013-0832-6.
- Page, M. and Felzer, K. Southern San Andreas fault seismicity is consistent with the Gutenberg-Richter magnitude-frequency distribution. *Bulletin of the Seismological Society of America*, 105(4), 2015. doi: 10.1785/0120140340.
- Petersen, M., Moschetti, M., Powers, P., Mueller, C., Haller, K., Frankel, A., Zeng, Y., Rezaeian, S., Harmsen, S., Boyd, O., and Field, N. The 2014 United States National Seismic Hazard Model. *Earthquake Spectra*, 31(1), 2015. doi: 10.1193/120814EQS210M.
- Petersen, M., Shumway, A., Powers, P., Mueller, C., Moschetti, M., Frankel, A., Rezaeian, S., McNamara, D., Luco, N., Boyd, O., Rukstales, K., Jaiswal, K., Thompson, E., Hoover, S., Clayton, B., Field, E., and Zeng, Y. The 2018 update of the US National Seismic Hazard Model: Overview of model and implications. *Earthquake Spectra*, 36(1), 2020. doi: 10.1177/8755293019878199.
- Petersen, M., Shumway, A., Powers, P., Mueller, C., Moschetti, M., Frankel, A., Rezaeian, S., McNamara, D., Luco, N., Boyd, O., Rukstales, K., Jaiswal, K., Thompson, E., Hoover, S., Clayton, B., Field, E., and Zeng, Y. The 2018 update of the US National Seismic Hazard Model: Where, why, and how much probabilistic ground motion maps changed. *Earthquake Spectra*, 37(2), 2021. doi: 10.1177/8755293020988016.
- Rey, J., Beauval, C., and Douglas, J. Do French macroseismic intensity observations agree with expectations from the European Seismic Hazard Model 2013? *Journal of Seismology*, 22(3), 2018. doi: 10.1007/210950-017-9724-7.
- Rukstales, K. and Petersen, M. Data release for 2018 update of the U.S. National Seismic Hazard Model, U.S. *Geological Survey data release*, 2019. doi: 10.5066/P9WT50VB.
- Salditch, L. *Investigating Earthquake Recurrence and Hazard Models [Doctorate dissertation]*. Northwestern University, 2021. doi: 10.21985/n2-my3w-v278.
- Salditch, L., Hough, S., Stein, S., Spencer, B., Brooks, E., Neely, J., and Lucas, M. The 1952 Kern County, California earthquake: A case study of issues in the analysis of historical intensity data for estimation of source parameters. *Physics of the Earth and Planetary Interiors*. In, 283, 2018. doi: 10.1016/j.pepi.2018.08.007.
- Salditch, L., Gallahue, M., Lucas, M., Neely, J., Hough, S., and Stein, S. California Historical Intensity Mapping Project (CHIMP): A consistently reinterpreted dataset of seismic intensities for the past 162 yr and implications for seismic hazard maps. *Seismological Research Letters*, 91(5), 2020. doi: 10.1785/0220200065.
- Shumway, A. Data release for the 2014 National Seismic Hazard Model for the conterminous U.S., U.S. *Geological Survey data release*, 2019. doi: 10.5066/P9P77LGGZ.
- Stein, S., Spencer, B., and Brooks, E. Metrics for assessing earthquake hazard map performance. *Bulletin of the Seismological Society of America*, 105(4), 2015. doi: 10.1785/0120140164.
- Stirling, M. and Gerstenberger, M. Ground motion-based testing of seismic hazard models in New Zealand. *Bulletin of the Seismological Society of America*, 100(4), 2010. doi: 10.1785/0120090336.
- Stirling, M. and Petersen, M. Comparison of the historical record of earthquake hazard with seismic-hazard models for New Zealand and the continental United States. *Bulletin of the Seismological Society of America*, 96(6), 2006. doi: 10.1785/0120050176.
- Tasan, H., Beauval, C., Helmstetter, A., Sandikkaya, A., and Guéguen, P. Testing probabilistic seismic hazard estimates against accelerometric data in two countries: France and Turkey. *Geophysical Journal International*, 198(3), 2014. doi: 10.1093/gji/ggu191.
- Vanneste, K., Stein, S., Camelbeeck, T., and Vlemminckx, B. Insights into earthquake hazard maps performance from shaking history simulations. *Scientific Reports*, 8, 2018. doi: 10.1038/s41598-018-20214-6.
- Wang, Z. Predicting or forecasting earthquakes and the resulting ground motion hazards: A dilemma for earth scientists. *Seismological Research Letters*, 86(1), 2015. doi: 10.1785/0220140211.
- Ward, S. Area-based tests of long-term seismic hazard predictions. *Bulletin of the Seismological Society of America*, 85(5), 1995. doi: 10.1785/BSSA0850051285.
- Wood, H. and Neumann, F. Modified Mercalli Intensity scale of 1931. *Bulletin of the Seismological Society of America*, 21(4), 1931. doi: 10.1785/BSSA0210040277.
- Worden, C., Gerstenberger, M., Rhoades, D., and Wald, D. Probabilistic relationships between ground-motion parameters and modified Mercalli intensity in California. *Bulletin of the Seismological Society of America*, 102(1), 2012. doi: 10.1785/0120110156.

The article *Exploring the Effect of Minimum Magnitude on California Seismic Hazard Models* © 2023 by Molly M. Gallahue is licensed under CC BY 4.0.

3D Paleoseismology of the Dog Valley Fault (California, USA) from iOS Lidar and Structure-from-Motion Photogrammetry

Ian K.D. Pierce  *^{1,2}, Richard Koehler ¹

¹Nevada Bureau of Mines and Geology, University of Nevada, Reno, USA, ²Department of Earth Sciences, University of Oxford, Oxford, UK

Author contributions: *Conceptualization:* I. Pierce, R. Koehler. *Data Curation:* I. Pierce. *Formal Analysis:* I. Pierce, R. Koehler. *Funding Acquisition:* I. Pierce, R. Koehler. *Investigation:* I. Pierce, R. Koehler. *Methodology:* I. Pierce, R. Koehler. *Project Administration:* I. Pierce, R. Koehler. *Resources:* I. Pierce, R. Koehler. *Software:* I. Pierce. *Supervision:* R. Koehler. *Validation:* I. Pierce, R. Koehler. *Visualization:* I. Pierce. *Writing – original draft:* I. Pierce. *Writing – review & editing:* I. Pierce, R. Koehler.

Abstract Measuring displacements of buried and faulted strata on strike-slip faults requires detailed 3D trenching excavations. Here we demonstrate a new methodology using co-registered, photorealistic 3D models derived from an iOS-based laser scanner and structure-from-motion photogrammetry to reconstruct stratigraphy and trace a displaced channel sequence across the Dog Valley fault in the northern Walker Lane. We present new geomorphic mapping observations and trenching results. Lidar data reveal a east-northeast striking fault trace that extends about ~25 km from just west of the Polaris Fault to the northwest flank of Peavine Mountain. Youthful fault scarps are visible along much of the fault. Clear lateral displacements are largely absent along the fault; however, right-stepping fault strands, sidehill benches, linear valleys and ridges, and alternating scarp facing directions are all consistent with left-lateral strike slip displacement. Stratigraphic and structural relations exposed in the Dog Valley fault trench show truncations of bedded fluvial and peat deposits and provide evidence for the occurrence of two Holocene earthquakes: the most recent earthquake postdates ~8 ka, and an earlier earthquake occurred between 8491-8345 cal. ybp. Based on 3D excavations of a channel margin, the most recent earthquake produced 115±30 cm of left-lateral displacement, corresponding with up to a M6.7 earthquake. Similar timing for the most recent earthquake on the Polaris fault which orthogonally intersects the Dog Valley fault may indicate rupture behavior similar to conjugate historic ruptures elsewhere in the Walker Lane.

Non-technical summary Here a new set of 3D imaging techniques is used to produce a 3D model of a series of interconnected trenches excavated across the Dog Valley fault near Lake Tahoe, California. The result allows for the accurate digital measurement of displacement of sediments across the fault. The fault is a left-lateral strike-slip fault in the Walker Lane, a zone of distributed shear that is parallel to the San Andreas fault. The fault intersects a neighboring strike-slip fault at a 90° angle, similar to other faults in the Walker Lane that have ruptured together during the last century.

1 Introduction

Paleoseismic studies of active faults are one of the primary methods for estimating the timing, recurrence, and size of prehistoric earthquakes – critical parameters for seismic hazard assessments (McCalpin, 2009). Typical paleoseismic studies combine shallow subsurface excavations ('paleoseismic trenches') with detailed surficial fault maps. These paleoseismic trenches aim to measure the fault displacement and timing of past fault ruptures. While fault displacement is readily measured from a single trench exposure across a dip-slip fault, an array of multiple trenches ('3D trenching') is required to find traceable subsurface piercing lines across a strike-slip fault (Marco et al., 2005; Rockwell et al., 2009; Hall et al., 1999). The standard method of documenting a series of 3D trenches consists of a plan

view map of the trench excavations and then a series of trench-wall-log diagrams. However, aligning these 2D diagrams so they can be visualized in a 3D space is not a simple task.

In recent years, trench-wall diagrams are increasingly constructed using Structure-from-Motion (SfM) algorithms to produce high-detail orthophoto mosaics of trench walls (Haddad et al., 2012; Bemis et al., 2014; Reitman et al., 2015; Delano et al., 2021). SfM relies on photogrammetric principles and many overlapping photographs taken from different positions to reproduce the 3D geometry and camera locations of a scene. Here we present a novel method that uses an Apple iOS laser scanner and SfM 3D modeling to generate a computer model of oriented and aligned high-resolution trench wall images. These aligned images form a readily viewed, true 3D stratigraphic/structural reconstructed model of a volume of faulted crust. This model can then be used for measuring fault displace-

Production Editor:
Gareth Funning
Handling Editor:
Randolph Williams
Copy & Layout Editor:
Hannah F. Mark

Received:
August 4, 2022
Accepted:
December 10, 2022
Published:
January 12, 2023

*Corresponding author: ian@nevada.unr.edu

ments and exploring the fault and stratigraphic structure, not dissimilar to 3D seismic data.

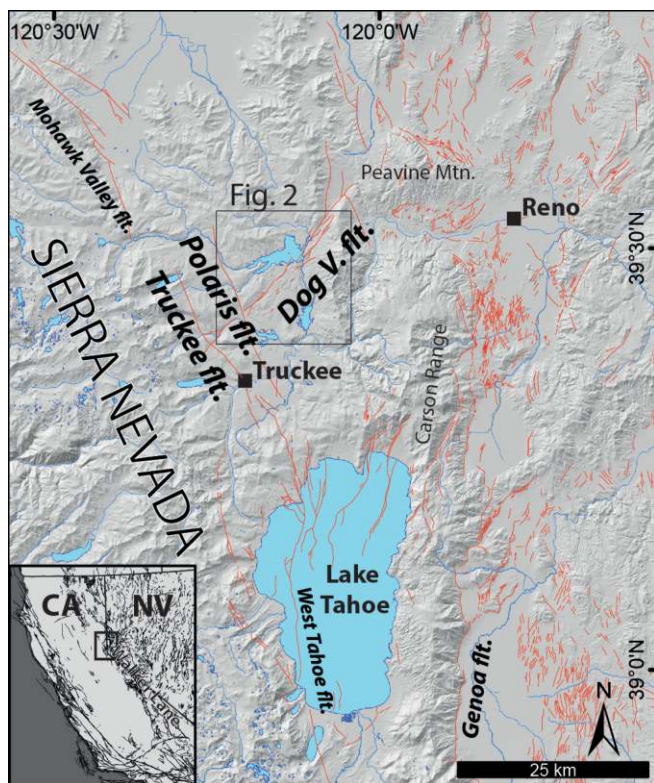


Figure 1 Overview map of the Truckee Basin and surrounding region. Faults (abbreviated *flt.*) in red modified after the USGS Quaternary Fault and Fold Database (U.S.G.S., 2020) to reflect our updated mapping in the Truckee and Tahoe basins. Inset map shows the location with respect to California and Nevada and regional active faults.

We demonstrate the value of this method by employing it in a paleoseismic trench study of the Dog Valley fault within the Walker Lane tectonic province in northeastern California (Figure 1). The Walker Lane is characterized by a complex network of faults including range-front normal faults and conjugate right- and left-lateral strike-slip faults (Wesnousky, 2005). A number of historical earthquakes in the Walker Lane have been associated with conjugate or cross-fault ruptures (Smith and Priestley, 2000; Hatch-Ibarra et al., 2022; Barnhart et al., 2019). However, paleoseismic records in the Walker Lane are insufficient to evaluate how common these types of ruptures are along major faults. Analysis of static stress changes associated with the 2019 Ridgecrest earthquake sequence indicate that the M6.4 earthquake promoted slip in the M7.1 earthquake and triggered creep on the adjacent Garlock fault (Barnhart et al., 2019). Thus, the possibility that earthquakes might promote rupture on intersecting and/or other nearby faults has implications for future seismic hazards in the region.

Based on evaluation of our 3D trench model and field observations, we assess the earthquake history of the Dog Valley fault and estimate the displacement associated with the most recent seismic event. Additionally, we describe the geomorphic expression and length of the Dog Valley fault based on assessment of lidar hill-

shades and field reconnaissance. We then discuss the geometric and paleoseismic relationship of the Dog Valley fault with the intersecting Polaris fault and their significance in the context of conjugate strike-slip faulting and seismic hazards in the Walker Lane fault system. We conclude with a discussion of the utility of this methodology in comparison to alternative methods.

2 Geologic Setting

The Dog Valley fault is within the northern Walker Lane belt in northeast California and extends for ~25 km from north of Truckee, California to the north flank of Peavine Mountain near Reno, Nevada (Figures 1 and 2). The Walker Lane belt is a 100-km-wide zone of distributed faulting following the eastern margin of the Sierra Nevada mountains from ~35°–41°N latitude. The northern Walker Lane accommodates 10–15% (5–7 mm/yr) of the northwest oriented dextral shear between the Pacific and North American plates, with 2–3 mm/yr concentrated along its western margin, spanning the Truckee basin (Bormann et al., 2013, 2016; Pierce et al., 2021; Hammond et al., 2011).

The Truckee basin is the northernmost of a series of left-stepping en echelon basins that extend along the east side of the Sierra Nevada and accommodate dextral shear through a combination of oblique range-front normal faulting, vertical axis block rotations, and discrete strike-slip faulting (Pierce et al., 2021). Within the Truckee basin, this deformation is accommodated by the northwest-striking right-lateral Polaris fault (Hunter et al., 2011), the normal-oblique Truckee fault, and the conjugate northeast-striking left-lateral Dog Valley fault. The Polaris fault has produced Holocene earthquakes and has a minimum right-lateral slip rate of ~0.4 mm/yr (Hunter et al., 2011). A paleoseismic study by Melody et al. (2012) constrained the timing of the most recent Holocene earthquake on the Polaris fault to <7000 yr B.P., based on displacement of the Tsoyawata (Mazama) tephra. The Polaris fault intersects the western end of the Dog Valley fault with a nearly orthogonal geometry (Figure 2). The Truckee fault zone is mapped on the west side of the basin by Olig et al. (2005), but is not the subject of any other known published studies. The Truckee fault zone dextrally and vertically (down to the east) offsets late Pleistocene glacial deposits, suggesting it is an oblique right-lateral normal fault (Olig et al., 2005). Other nearby regional faults include the Mohawk Valley fault to the north (Gold et al., 2014) and West Tahoe fault to the south (Kent et al., 2005; Brothers et al., 2009; Dingler et al., 2009; Pierce et al., 2017) (Figure 1). The faults in the basin have generated several strong historical earthquakes (1966 M6.6 and two ~M6 earthquakes in 1914 and 1948; Olig et al., 2005) and numerous smaller earthquakes (e.g. 2021 M4.7), and pose a significant surface fault rupture and strong ground motion hazard to several water storage dams in the region and the communities of Truckee, California and Reno, Nevada.

Olig et al. (2005) is the most comprehensive study to date of the Dog Valley fault. In that study they report that the Dog Valley fault has produced 3.6–4.0 km

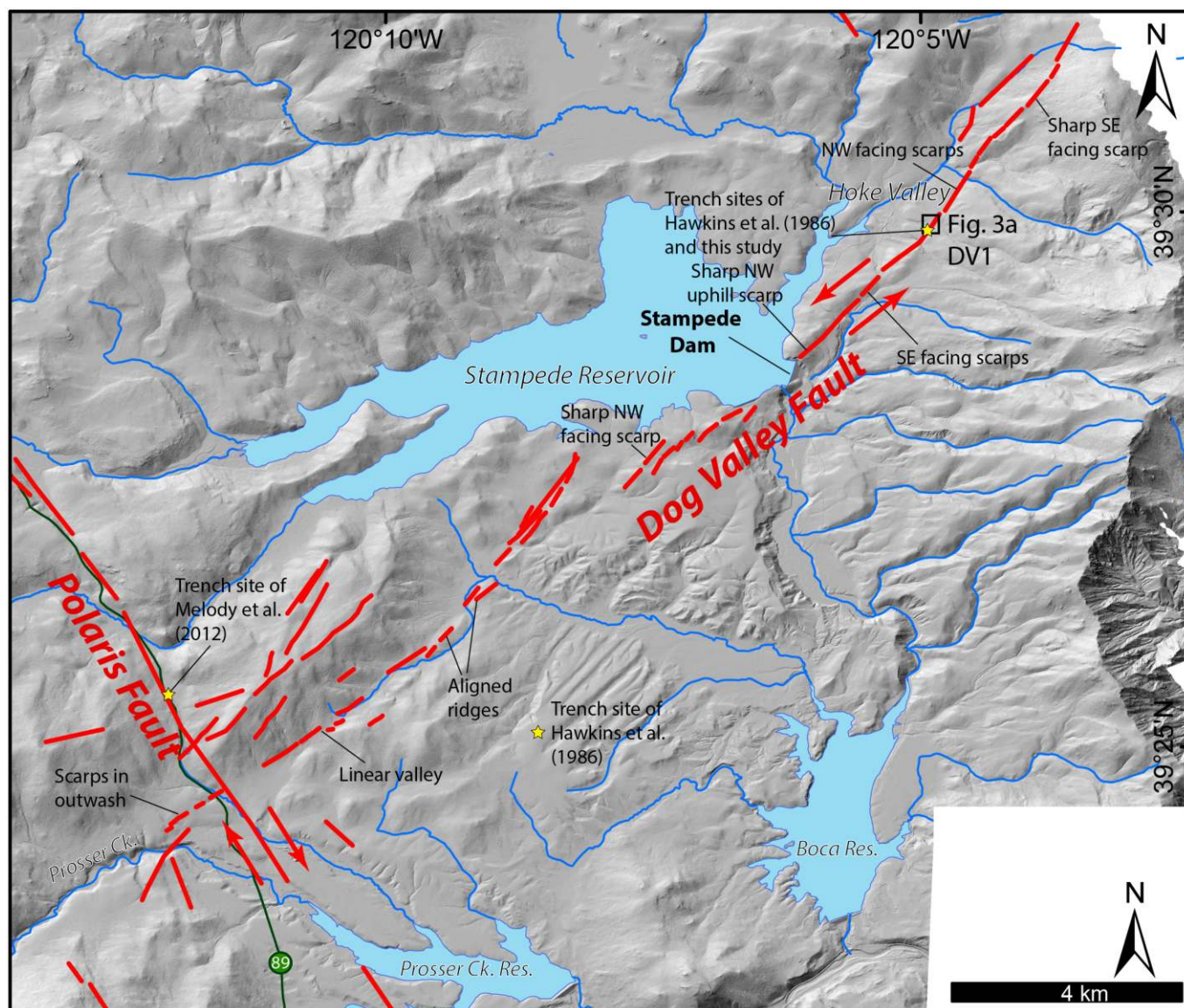


Figure 2 Overview map of the left-lateral Dog Valley fault on a lidar hillshade basemap. Youthful fault traces are mapped in red. Previous paleoseismic trench sites marked with yellow stars. The surface trace of the Dog Valley fault intersects the Polariss fault at a near-orthogonal angle. The trench site for this study is located in Hoke Valley along the northeast portion of the fault.

of cumulative left-lateral offset since ~ 3 Ma. This implies an average long term left-lateral slip rate of ~ 1.3 mm/yr. They also describe a change of scarp morphology from prominent, primarily northwest-facing scarps along the northeastern portion of the fault zone to alternating facing and more subdued and scattered lineaments to the southwest. Along the fault trace they detail a number of features suggestive of strike-slip motion including side-hill benches, ridge-crest saddles, aligned linear drainages, and reversals in scarp directions.

The Dog Valley fault is reported to have been responsible for the 1966 M6.0 Truckee earthquake (Reed, 2014). However, features attributed to surface rupture during this earthquake are scattered and discontinuous. These features are more likely a result of shaking and may be considered lateral spreads in unconsolidated alluvial deposits, rather than surface rupture along the principle fault trace (Olig et al., 2005). Relocated hypocenters show that the Dog Valley fault forms a distinct lin-

ement of ongoing seismic activity (Reed, 2014). The fault is absent from the geologic map of the Independence Lake and Hobart Mills quadrangles (Sylvester and Raines, 2013).

Hawkins et al. (1986) excavated two paleoseismic trenches across scarps thought to be associated with the Dog Valley fault (Figure 2). The first trench was excavated in Hoke Valley, adjacent to the site excavated in this study. The second trench was excavated across a linear drainage north of Prosser Creek Reservoir thought to be the surface expression of the fault responsible for the 1966 earthquake. Neither trench identified any evidence of late Quaternary fault rupture. Hawkins et al. (1986) may not have identified the fault in their Hoke Valley trench because of the amount of water flooding the trench.

3 Methods

3.1 Fault Mapping

We mapped tectonic geomorphic features and fault traces along the length of the Dog Valley fault based on interpretation of lidar hillshade maps and field reconnaissance. The main trace of the Dog Valley fault is visible in the 2014 Tahoe National Forest lidar imagery (OpenTopography, 2017). Mapping along the Dog Valley fault indicates that it is characterized by right-stepping en echelon fault strands expressed as subdued geomorphic features including both northwest- and southeast-facing scarps, closed depressions, aligned linear ridges, springs, and sidehill benches (Figure 2).

The northeastern-most part of the fault cuts across the northwestern flank of Peavine Mountain near Reno, Nevada (Figure 1). Southwest from Peavine Mountain the fault forms a sharp sidehill bench and aligned ridge before entering Hoke Valley (Figure 2). In Hoke Valley, a series of springs and 1-2 m high northwest facing scarps along the base of the range front that bounds the southeastern margin of the valley mark the location of the fault. At the southwest margin of Hoke Valley, the fault cuts across topography forming a series of linear ridges, sidehill benches, and both northwest- and southeast-facing scarps before approaching the Stampede Dam.

The lidar data reveal that the trace of the Dog Valley fault extends through the Stampede Dam (Figure 2). Our field observations indicate that strands of the Dog Valley fault offset Miocene andesite flow breccias and tuff breccias exposed in a roadcut immediately northeast of the dam, and a sharp uphill facing fault scarp extends across a bench on the hillside above this roadcut.

Southwest of Stampede Dam, the fault is clearly expressed by sharp scarps and linear ridges that extend along right-stepping en-echelon strands. The fault then continues along a linear ridge and valley; however, in this area tectonic geomorphic features become less pronounced and we were unable to precisely locate the fault in the field. Just west of the Polaris fault and Highway 89, the fault appears to terminate, forming a subtle southeast facing scarp in glacial outwash deposits along Prosser Creek.

3.2 Trenching Excavation

A series of interconnected 3D paleoseismic trenches (site DV1) were excavated on the southeast margin of Hoke Valley, approximately 3 km northeast of Stampede Reservoir where the Dog Valley fault forms a 2-m-high northwest facing scarp across the mouth of a small alluvial valley (Figures 2, 3a). An apparent left deflection of an ephemeral stream channel adjacent to the trench occurs across the fault at this site.

In total, 16 exposures were imaged, covering a volume roughly 2 m across the fault zone, 4.5 m along the fault, and 2 m deep (Figure 3c). The across fault exposures are labeled from northeast to southwest A01-A14, while the fault parallel exposures are labeled P1 and P2. Initially, a single 11 m long, 80 cm wide, 2 m deep, vertical walled excavation was produced perpendicular to the fault scarp. Both walls of this excavation

(A07 and A08) were carefully cleaned, examined, and described using standard paleoseismic methods (Figure 4). Both walls were then imaged using the methodology described in the following section. After this initial excavation, approximately 2 m of the northeast wall of the trench, centered on the fault zone, was expanded ~20 cm, parallel to the initial excavation. This new exposure (A06) was then cleaned and imaged. This process was repeated for a total of 6 new exposures of the northeast wall (A01-A06), extending 1.5 m northeastward along strike. This process of progressively expanding this cross fault trench produced a fault-parallel exposure on the southeast side of the fault (P2). Next, a second fault parallel trench was excavated (P1), extending from approximately 1 m northwest of the fault exposed on the original southwest wall, for 2.75 m to the southwest. From the southwest end of this fault-parallel exposure, 6 more 2-m-wide cross fault exposures were created (A09-A14), working from southwest to northeast back towards the original southwest trench wall. Finally, cleaning the orthogonal southeast margin of these exposures extended P1 by 2.5-m to the southwest. Orthoimages of each exposure are provided in Figure 5 and in a repository, see the data availability statement for details.

3.3 Trench Wall Imaging

Prior to imaging each trench exposure, the trench walls were cleaned using scraping tools and colored flags were nailed to the walls to mark prominent stratigraphic layers. In most exposures, a short level string line was installed between two nails for referencing. The trench walls were then photographed using a Google Pixel 2 cell phone camera fixed to a 1.5 m long extension pole and a Bluetooth remote shutter trigger. Photographs were taken in portrait orientation, orthogonally to the wall, and approximately 1 m away from the trench wall. Photographs were taken in a 'lawn-mower' pattern, with first a descending vertical column of overlapping photos, then a short (~0.5 m) lateral step, then an ascending vertical column of overlapping photos, then a short step, and so on, until the entire trench wall was photographed. Photos were uploaded to a laptop in the field and processed into an orthoimage using the Agisoft Metashape photogrammetry software (Agisoft LLC, 2022). It is important to field check image processing as, for unknown reasons, a set of photos may fail to properly align and may need to be re-photographed. After ensuring that an orthoimage could successfully be produced, the trench wall was lidar scanned using the SiteScape app on a 2020 Apple iPad Pro in 'high detail' mode. Lidar scanning followed a similar acquisition methodology as the photography, consisting of slowly following a 'lawn mower' pattern orthogonal to the trench wall until the entire wall was covered. In addition to just the wall of interest, each lidar scan also covered parts of the trench network that were not modified during progressive excavations.

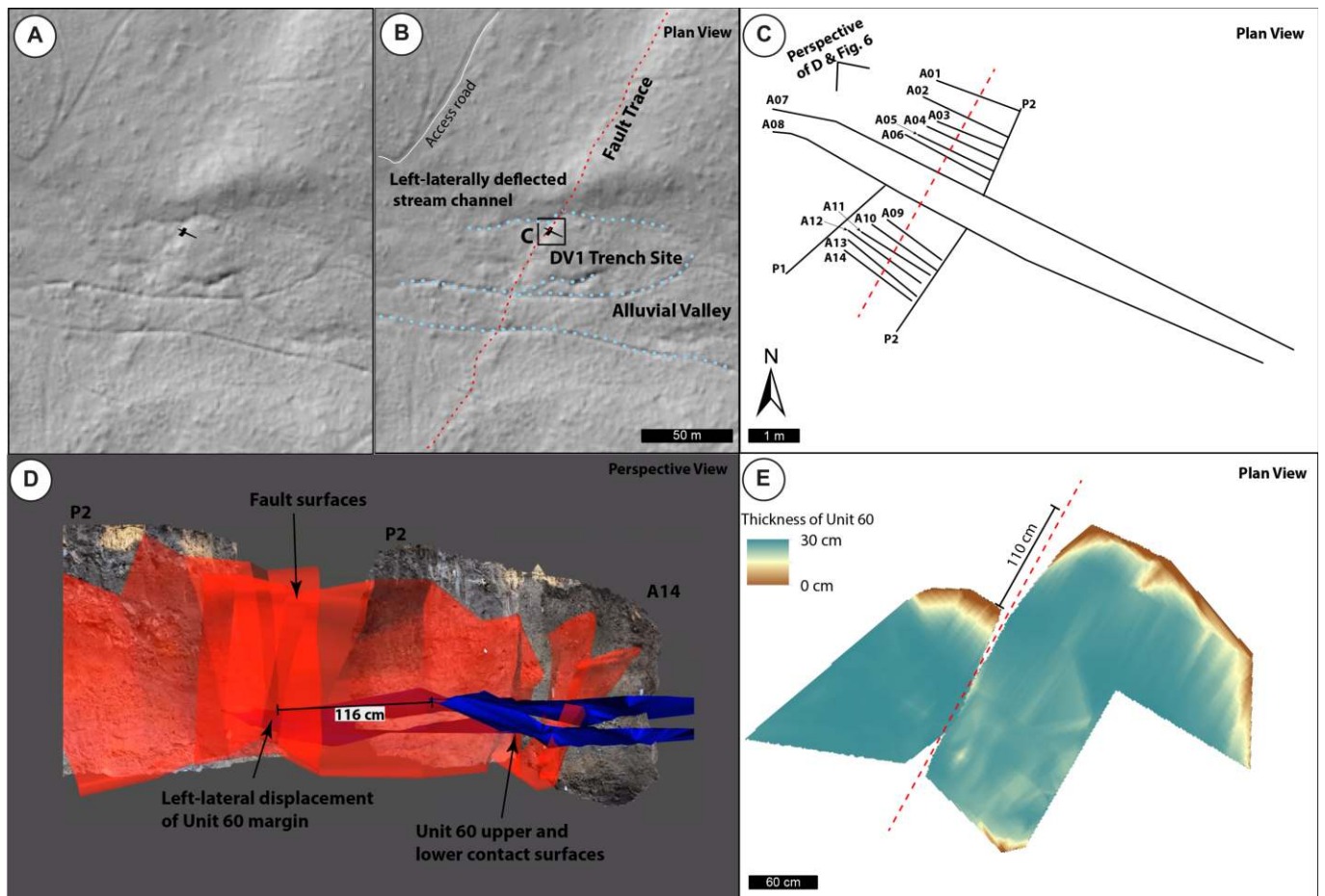


Figure 3 (A) Lidar hillshade and (B) interpreted hillshade of DV1 trench site in Hoke Valley. Dashed red line is fault and dashed blue lines are channels. Note the left-lateral offset of a small channel at this site. (C) plan view map of trench excavation network. Each line shows the location of the trench walls imaged and reproduced in Figures 4-7. The view orientation of (D) and Figure 6 is indicated with brackets. (D) oblique 3D model of stratigraphic reconstruction of Unit 60 (blue) and faults (red). The 116 cm offset of the margin of the Unit 60 channel is shown. (E) Plan view isopach map of Unit 60 showing 110 cm left lateral offset of the channel margin.

3.4 3D Model Construction

For clarity, prior to describing the construction of the 3D model of DV1, we first define and describe the different categories of 3D data we use. A point cloud consists of many individual points that each have an x, y, and z coordinate, and each point may have a photo-based visual color or other data such as reflection intensity. Common point cloud formats include .laz, .las, and .xyz. In contrast, a 3D surface model is typically a triangulated or polygonised surface composed of many connected polygons that together form the surface of a 3D object. 3D surface models can be constructed from a point cloud using a meshing algorithm. 3D models are often textured with photo images to look realistic. Common 3D file formats include .obj, .stl, .3ds, and .glTF. Both point clouds and surface models are different than ‘2.5D’ raster formats common to geospatial software such as digital elevation models (DEMs) or orthoimages/orthophoto mosaics (e.g. .tif, .jpg, etc.). These ‘2.5D’ raster formats are 2-dimensional grids where each grid cell contains data (such as photo-color, elevation, etc.).

In this study we do not attempt to formally assess the accuracy of the iOS laser scanner, but others’ work

shows that its accuracy decreases with increasing size of the object or scene being scanned (Luetzenburg et al., 2021). Luetzenburg et al. (2021) compared an iOS survey of a 130-m-long by 10-m-high sea cliff to a georeferenced SfM survey and found a mean error of 11 cm, while for smaller objects (~50 cm/site) errors were <1 cm, with a minimum size threshold of ~15 cm before accuracy decreases. Our own informal testing of the iOS lidar found that measurements of distances ranging from ~1-3 m made in lidar scans were generally within ~2 cm of those made by hand with a tape measure. While in this study we use a 2020 iPad Pro due to its comparative low cost and ease of use, other close-range handheld laser scanners may be suitable for this workflow. Ideally the scanner used should capture photo RGB values of points (or create photo-textured 3D surface models); otherwise, control points will need to be targets that sufficiently contrast in intensity to be identifiable. Finally, data from whichever scanner or app is used should be readily exportable in a common 3D format.

At the time of the field study, the SiteScape app was the only iOS app that we were aware of that could create a photo-colored point cloud. Since this work was completed, other apps have been developed that can create

more realistic looking photo-textured 3D models (Luetzenburg et al., 2021). With any of these iOS lidar apps (or with other laser scanning systems) this same workflow should be applicable.

First, using the freely available software CloudCompare (GPL Software, 2022), all 3D iOS scans (in this case we use point clouds, but 3D surface models work too) are aligned into a common reference frame (Figure 6b). In our case the reference frame is arbitrary (i.e., local coordinates in meters), but one could align the local reference frame to a global reference frame using control points surveyed with a differential GPS (dGPS). Alignment between iOS scans is achieved by finding unchanged areas within the excavation network that have common reference points that can be identified across multiple excavation models. Ideally these reference points are high contrast flags placed on stable areas of the trench walls. A minimum of 3 points must be identified to translate and rotate a model into alignment, but typically 15-30 points were used. Points should be distributed throughout the space for best results.

Next, using Agisoft Metashape, photos of each trench wall are processed into photo-textured 3D surface models (not 2D orthophoto mosaics; Figure 6c). These are then cropped to only contain the area of interest and then imported into the model in CloudCompare (here using .obj format). Each of these photo-textured 3D models is then warped, scaled, rotated, and fit to the corresponding lidar trench scan (point clouds), using a similar method of identifying common reference points between the lidar scan and the photo-textured 3D surface model. The photo-textured 3D models are used as they are much higher resolution than can be produced using the currently available iOS laser scanning apps. The result is a correctly-scaled high-detail 3D model of all of the trench exposures, where different exposures can be turned on and off and measurements can be made. The result has the added advantage of being insensitive to irregular trench wall surfaces. Curving, sloping, benched, or other non-planar trench walls are not forced to be flat as they would be with a more traditional orthoimage representation.

3.5 3D Stratigraphic-Structural Interpretation

We used three different methods for structural analysis, with the goal of measuring displacement of units across the fault zone. First, 2D stratigraphic models (logs) of each exposure are developed with key units correlated between different exposures (Figure 4). In each exposure, contacts appear as lines on the trench wall. Using CloudCompare, a series of points representing each contact-line are manually extracted from each exposure, independently on each side of the fault. For example, if a given contact is visible in 8 exposures, and on both sides of the fault zone, 16 sets of points would be extracted. The extracted points for each contact of interest on every exposure are then merged into a point cloud, resulting in two point clouds representing each contact surface (one on each side of the fault). The same process is repeated for the fault surfaces. These

point clouds are then used to build 3D surfaces represented by Triangular Irregular Networks (TINs). Once TINs representing contact surfaces are created, two different methods can be used to determine a fault offset. First, if two contact surfaces intersect, this intersection may form a piercing line that can be traced to a piercing point on the fault surface, on either side of the fault, and then an offset measured between these two piercing points (Figure 3d). For the second method, the thickness of a unit between two contact surfaces can be plotted in plan view as an isopach map, and the offset in thickness can be measured across the fault (Figure 3e). The isopach map in Figure 3e was created by using the TIN to raster tool in ArcGIS for two contact-surfaces that bound a unit and then differencing the resulting rasters.

A third, less precise method is also used to estimate fault offset. Each photo-textured 3D model can be cut along the fault zone into two models. One side of the fault in one model is then compared to the other side of the fault in other models to find the qualitatively best matching stratigraphy (Figure 7). This effectively serves to 'backslip' the fault. When a fit is determined, the distance between matching contacts can be measured in the 3D space, again resulting in a slip vector. While this method is less precise, it serves as a useful validation and check on the prior methods.

4 Paleoseismic Results

The trench exposed a sequence of low energy interbedded fluvial overbank sands, silts, and peats (buried soils), with cobble and gravel lenses, and a 1-2 m thick modern meadow soil (Figure 4). These deposits are faulted by a steeply dipping narrow fault zone that reaches nearly to the ground surface. In each exposure, 1-3 main splays of this fault are visible in an ~20 cm wide zone that generally spread upwards forming a weak flower structure. There is negligible vertical deformation across this fault, but in some exposures the strata on the southeast side of the fault either warp slightly down (A11-A14) or slightly up (A04-A08). Strata are mismatched across the fault in most exposures. In the logs, we focus on a clearly traceable sequence of interbedded sand and silty peat layers that can be traced through exposures A04-A14 and P1 and P2. From top to bottom these sand beds are mapped as Unit 50, 60, and 70, and a mottled silt unit 80. Exposure P2 contains a clear sand dike extending from Unit 50 to the modern soil, likely a result of coseismic liquefaction (Figure 4).

In most exposures there is only evidence for the most recent earthquake (E1), based on the primary fault zone that extends to the soil. This event also produced the sand dike in P2. The northeast upper margin of the Unit 50, 60, and 70 sandy channel beds form piercing lines that can be traced across the fault zone (Figure 6). Figure 3e shows an isopach map of Unit 60. These units are left-laterally offset across the fault zone. Left lateral displacements measured from the isopach method (Figure 3e) and 3D piercing point reconstruction method (Figure 3d) of the northeast margin of Unit 60 are 110 and 116 cm, respectively. Using the visual back slip method described above produces slip estimates be-

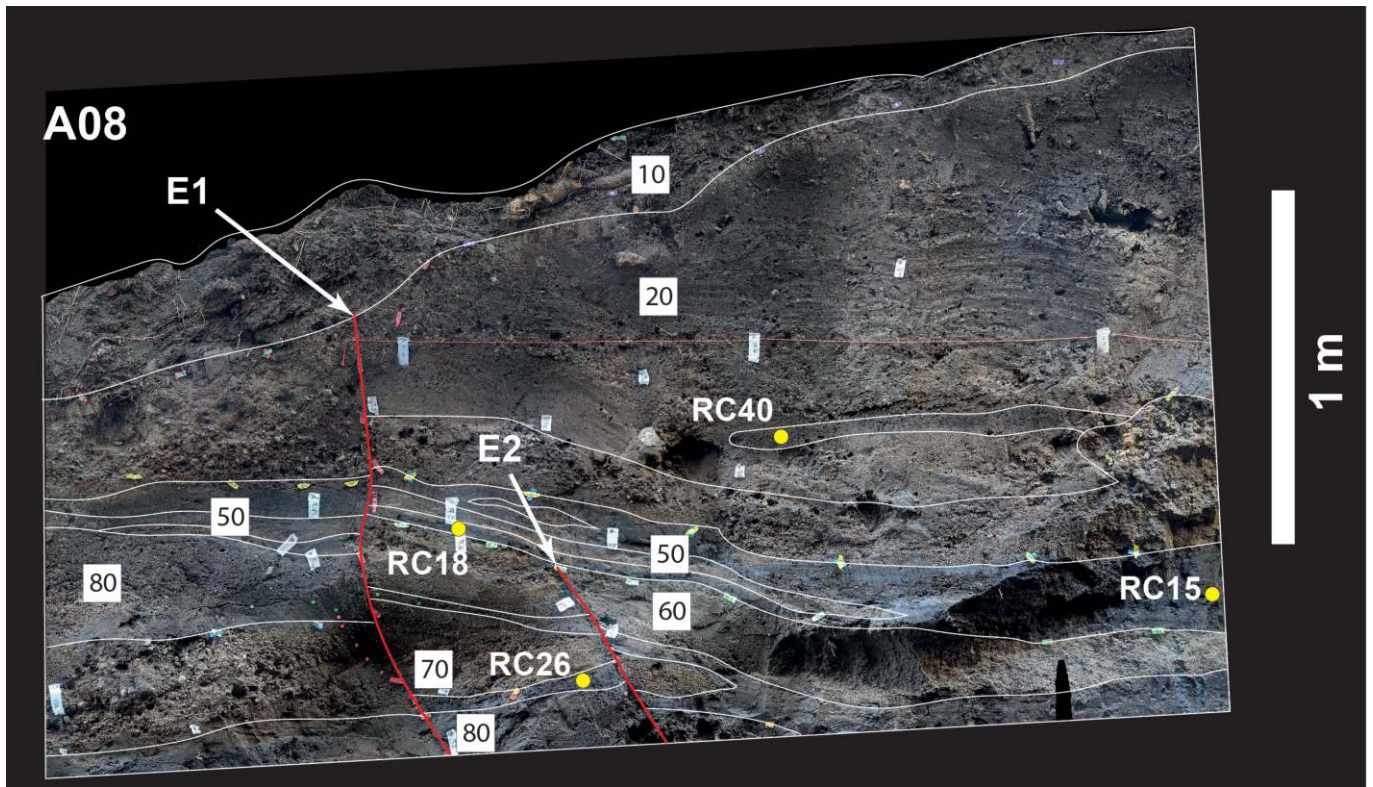


Figure 4 Annotated trench orthoimage showing unit contacts (white lines), radiocarbon samples (yellow dots), and faults (red lines). Upward terminations of events E1 and E2 are indicated with white arrows. See Table 1 for radiocarbon ages and Table 2 for unit descriptions.

tween 88-145 cm (Figure 7). The total range of left-lateral displacement from these various methods is 115 ± 30 cm. We estimate this uncertainty based on the total range of measurements. This uncertainty seems reasonable as it approximates the limit of our fault-parallel resolution based on the average spacing between adjacent excavations.

Evidence for an earlier earthquake (E2) consists of a single upward terminating fault strand in each of exposures A08 and A11-A14 (Figure 5). These fault strands terminate in Unit 60 in A08 and below Unit 70 in A11-A14. In exposure A08, the fault strand is buried by Unit 50. Strata below Unit 60 do not match as well across the fault when visually back-slipped (Figure 7), consistent with increased displacement from an earlier event.

4.1 Event Timing

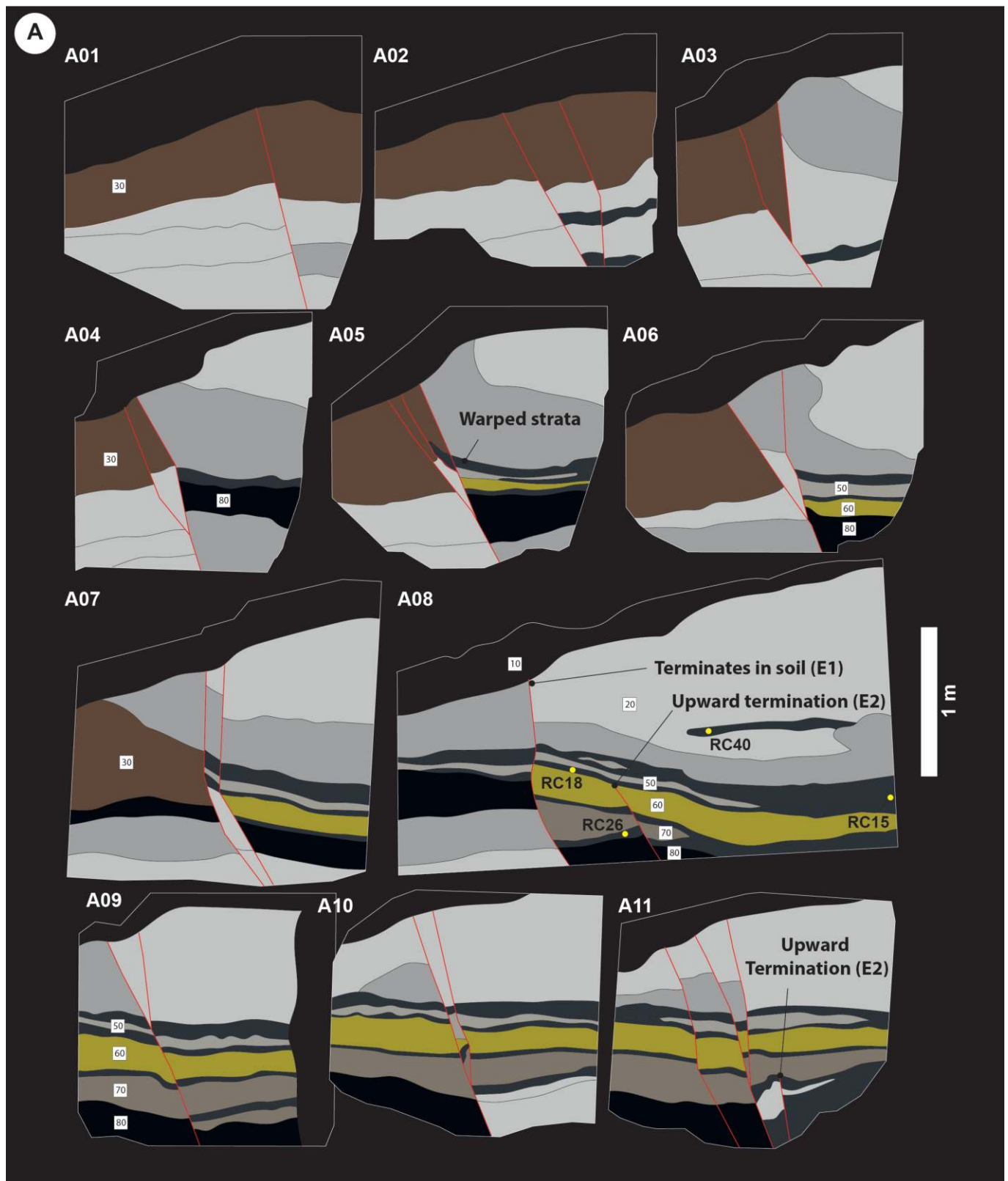
Radiocarbon dating was used to determine the ages of 5 total samples of peat, charcoal, and wood extracted from trench walls A08 and P1. Samples were processed and analyzed at Beta Analytic laboratories. Resulting ages are listed in Table 1. OxCal v4.4 (Bronk Ramsey, 1995) calibrated ages range from 8998-8031 cal. ybp. Sample RC18 is slightly out of stratigraphic order so is discarded from the following analysis. Ages RC43 (P1) and RC26 (A08) predate the older event E2, based on the upward terminating fault in Unit 60 which is buried by Unit 50 in exposure A08. Samples RC15 and RC40 (A08) are younger than E2 and predate the most recent event, E1. No radiocarbon samples postdate E1. By calibrating the ages of these samples we build a sequence model in

OxCal using the stratigraphic positions of the samples and event horizons to determine the timing of these two earthquakes. The resulting limits on event timing are E1: younger than 8051 cal. ybp, and E2: between 8491-8345 cal. ybp (Figure 8). Approximately 1 meter of fine-grained sediment (Unit 20) buries the layer that contains sample RC40 and was faulted in earthquake E1. Given the distribution of ages and the thin peat soils in the lower part of the exposure, sedimentation rates at the site were relatively high in the early Holocene, likely a reflection of the unvegetated post-glacial landscape. As the landscape stabilized in the mid-Holocene, sedimentation rates slowed resulting in the accumulation of Unit 20. We could not definitively track the upward termination of the fault or the sand dike in P2 into the weak late Holocene soil that developed into Unit 20 (Unit 10). These observations suggest that E1 may have occurred within the several thousand years after 8310-8031 cal. Ybp.

4.2 Paleoseismicity magnitude estimated

If the full mapped 25 km fault length (L) ruptured with 115 ± 30 cm of displacement (D) and a 17 km fault width (W) (assuming a vertical fault and 17 km seismogenic thickness from Ruhl et al. (2020)) the moment magnitude can be calculated using the following equation (Hanks and Kanamori, 1979):

$$M_w = \frac{2}{3} \log(3 \times 10^{11} \times L \times W \times D) - 10.73 \quad (1)$$

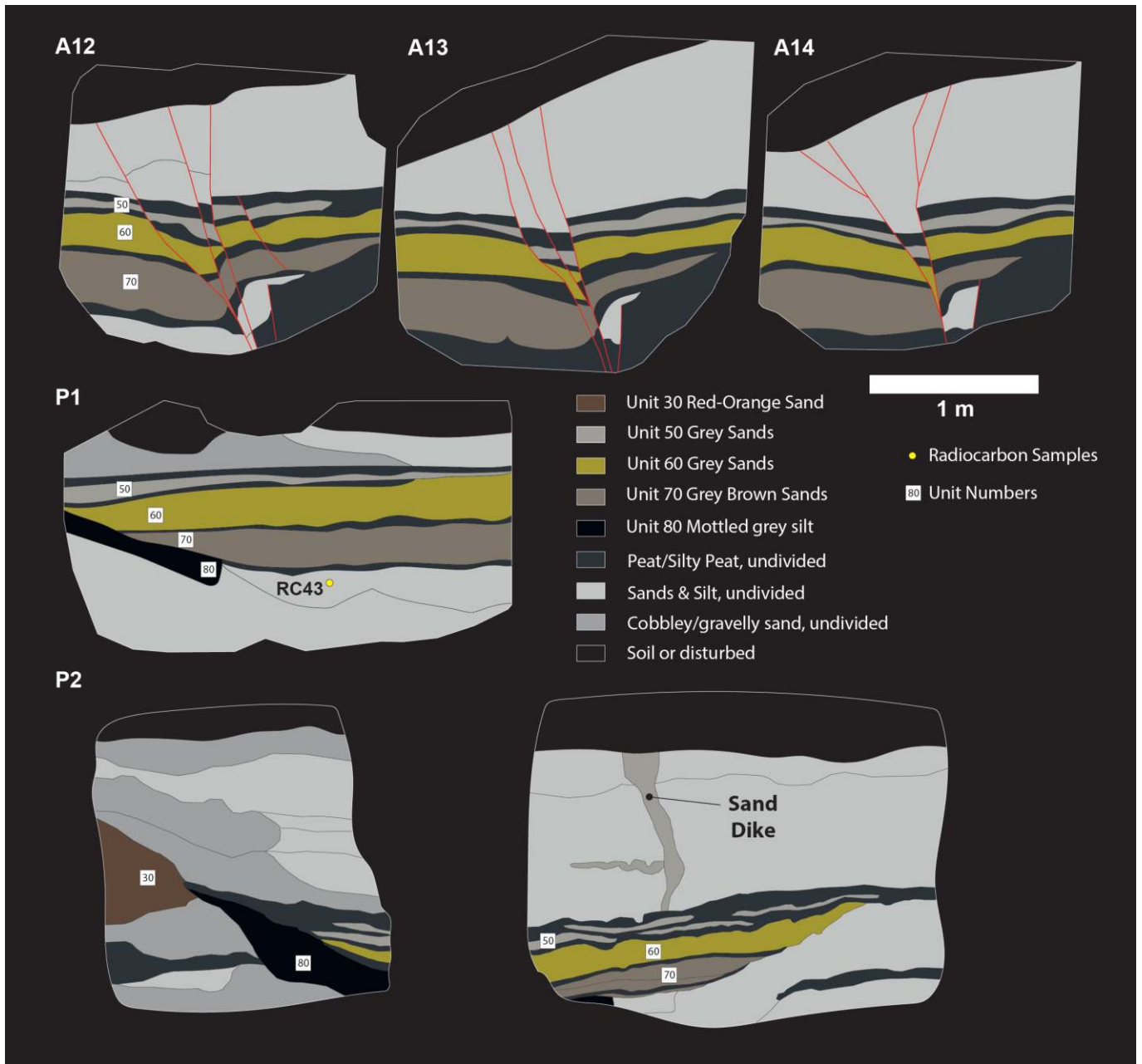


The resulting magnitude is $M_w 6.7 \pm 0.1$. Both this magnitude estimate and the measured geologic slip are similar to those estimated from empirical relations of average displacement-fault length and magnitude-fault length, based on other strike-slip earthquakes and assuming a 25 km rupture length (Wesnousky, 2008).

5 Discussion

5.1 Tectonic Role of the Dog Valley Fault and Conjugate Faulting in the Walker Lane

One of the defining characteristics of the Walker Lane and Eastern California Shear Zone is the presence of conjugate right- and left-lateral faults (Wesnousky, 2005). The Dog Valley fault lies north of the Carson domain in the Walker Lane, a region comprised of a se-



ries of east-dipping normal fault bounded basins that are oriented oblique to the overall northwest structural grain of the Walker Lane (Wesnousky et al., 2012; Pierce et al., 2021). Many of these north-striking normal fault bound basins are paired with an east- or northeast-striking left-lateral strike-slip fault (Li et al., 2017), and several contain northwest-striking strike-slip faults (Pierce et al., 2021). This network of faults works together to accommodate the ~5-7 mm/yr of northwest directed dextral shear in the Carson domain (Pierce et al., 2021).

The Dog Valley fault and the Polaris/Truckee faults share a similar geometric relationship to these other paired faults and may serve a similar role in the accommodation of northwest directed dextral shear. Our fault mapping indicates that the left-lateral Dog Valley fault zone intersects the northwest-striking right-lateral Polaris fault at a nearly orthogonal angle (Figure 2). Our interpretation of trench DV1 along the Dog Valley fault indicates the occurrence of at least one earthquake that

occurred after 8051 cal. ybp that was associated with 115 ± 30 cm of left-lateral displacement, and a prior event that occurred between 8491-8345 cal. ybp. Comparing this result to previously reported earthquake timing data from the conjugate Polaris fault indicates that the most recent earthquake along both faults post-dates ~7-8 ka (Melody et al., 2012). Thus, the geometric and paleoseismic relations indicate that the two faults may be kinematically linked and that ruptures along each fault could occur over a short period of time and possibly contemporaneously in a conjugate earthquake sequence.

Multiple historical earthquakes in Southern California, the Eastern California Shear Zone, and the Walker Lane provide examples of conjugate faults rupturing either simultaneously or closely spaced in time (minutes to decades). These include, in southern California, the 1987 Superstition Hills earthquake sequence (M_s 6.2 and M_s 6.6) and the M_w 6.4 Big Bear earthquake (Jones and Hough, 1995; Hudnut et al., 1989). In the Walker

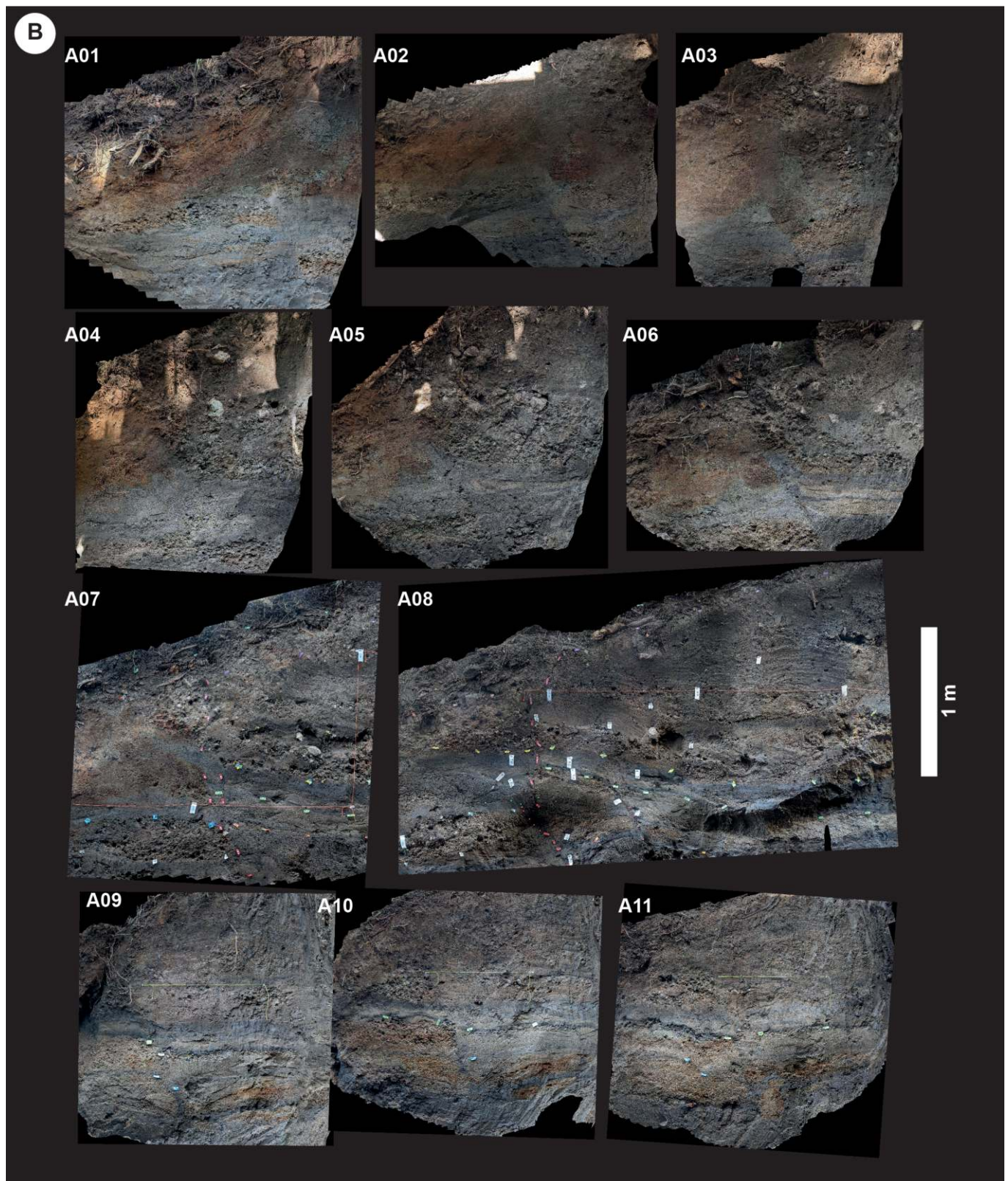


Figure 5 (A) Interpreted trench logs. Faults in red, radiocarbon samples yellow dots. (B) Trench orthophotos. Evidence of the most recent event (E1) consists of a clear fault that extends into the modern soil and a sand dike in slice P2. The earlier event (E2) is evident by an upward terminating fault strand in slices A08 and A11-14.

Lane, conjugate earthquakes include the 1986 Chalfant earthquake (M_w 6.3 and M_w 5.7), the 2015 Nine-Mile Ranch (three M_w 5.4-5.6 events), and the 2019 Ridgecrest earthquake (M_w 6.4 and M_w 7.1) sequences (dePolo and Ramelli, 1987; Smith and Priestley, 2000; Hatch-Ibarra et al., 2022; Barnhart et al., 2019). As observed from

surface ruptures, moment tensor solutions, and focal mechanisms, all of these examples involved rupture on intersecting conjugate northeast- and northwest-striking faults or fault planes.

Aside from the Big Bear earthquake, in each of these examples, the east or northeast-striking left-lateral

Sample Name	Material	D14C	$\delta^{13}C$	Radiocarbon Age (ybp)	Calibrated Age ^a (cal ybp)	OxCal Modeled Age ^b (cal ybp)
RC15	Detrital charcoal	-610.30 ± 1.46 ‰	-26.2 ‰	7570 ± 30	8417-8343	8414-8223
RC18	Charred material from peat	-630.15 ± 1.38 ‰	-23.3 ‰	7990 ± 30	8998-8655 (94.2%) 8665-8655 (1.2%)	-
RC26	Plant material from peat	-616.08 ± 1.43 ‰	-28.7 ‰	7690 ± 30	8543-8411	8544-8413
RC40	Organic sediment from peat*	-599.98 ± 1.49 ‰	-24.7 ‰	7360 ± 30	8310-8031 (11.4%) 8212-8031 (84.1%)	8309-8031
RC43	Wood	-613.68 ± 1.44 ‰	-26.8 ‰	7640 ± 30	8520-8376 (8.3%) 8485-8376 (87.1%)	8522-8389

Samples analyzed by AMS at Beta Analytic Testing Laboratory, Miami, Florida, USA

All samples pretreated with acid/alkali/acid washes unless otherwise noted

*Treated with acid washes only

^aIndependently OxCal calibrated ages using the IntCal 20 curve

^bAges modeled in stratigraphic sequence using OxCal as described in text

Table 1 Radiocarbon lab results and modeled ages for samples from the DV1 trench.

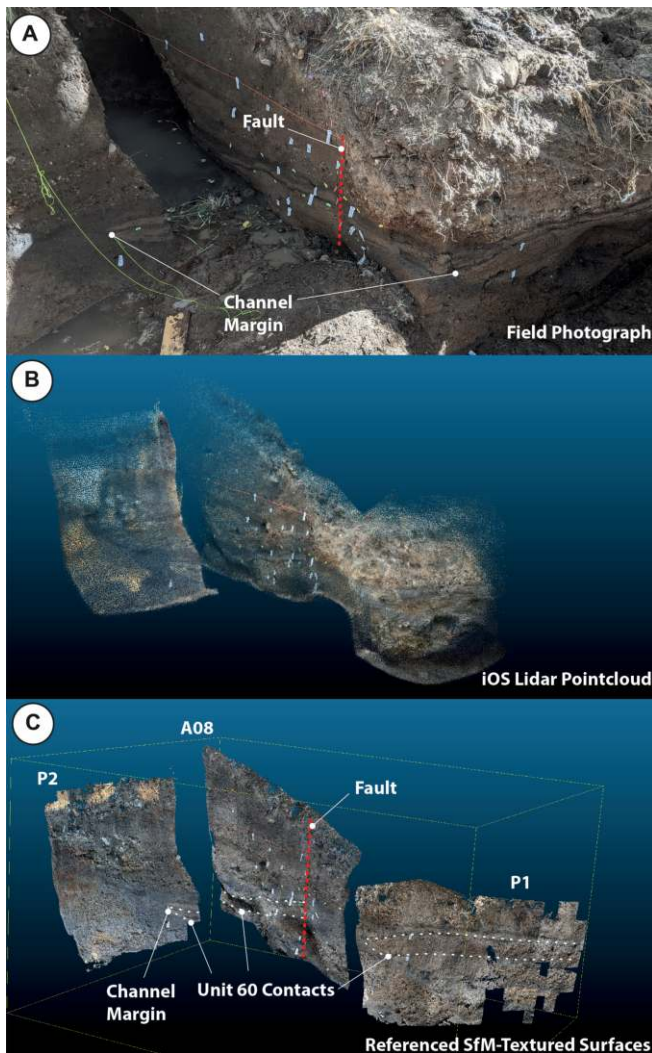


Figure 6 Images showing how the iOS Pointcloud (B) and SfM-textured surfaces (C) are combined to reconstruct the original trench in photo in (A). Note the prominent channel margin sequence (Unit 60) that is displaced across the fault

right-lateral fault ruptures. Each of these examples of ruptures either forms an ‘L’ pattern or ‘T’ pattern in map view, with either one or both faults terminating at or within a few kilometers of the intersection point, and none form a ‘X’ pattern, with both ruptures continuing far beyond the intersection. The Superstition Hills and Nine-Mile Ranch sequences all have an ‘L’ pattern. The Big Bear, Ridgecrest, and Chalfant sequences each have a ‘T’ pattern, and in these examples, the fault that crosses the intersection (the top of the ‘T’) is the northwest-striking right-lateral fault. The Dog Valley and Polaris faults form a ‘T’ pattern with scarps of the Dog Valley fault extending for a few hundred meters southwest of the intersection and 25 km to the northeast (Figure 2). The Polaris fault extends ~14 km north and south from its intersection with the Dog Valley fault. This geometric relationship is similar to other historic ruptures in the Walker Lane, as well as the patterns associated with the 1968-1997 Dasht-e-Bayaz and 2010–2011 Rigan, Iran earthquake sequences (Walker et al., 2011, 2013; Rezapour and Mohsenpur, 2013; Barnhart et al., 2013), providing additional support to the possibility that they may rupture in a conjugate sequence.

Barnhart et al. (2019) indicated that Coulomb stress changes associated with the Ridgecrest earthquakes promoted creep on the nearby Garlock fault. Their analysis indicates that surface creep was induced over distances of ~20-25 km and may have encouraged a future rupture of M_w 6.7-7.0. Although the Coulomb stress changes from a potential Dog Valley/Polaris fault rupture have not been investigated, their potential influence on the nearby Truckee, Mohawk Valley, and West Tahoe faults should be considered in future seismic hazards assessments.

Together, these observations show that conjugate fault ruptures may pose an underappreciated hazard in the Walker Lane and elsewhere. Further modeling and geologic studies should be developed to explore the past rupture histories on conjugate faults, the relative magnitude of contemporaneous ruptures, their influence on

fault ruptures preceded the north or northwest-striking

Unit #	Lower Contact	Upper Contact	Grain Size	Color	Description
10	Wavy/ gradual	n/a	Silt & sand	Gray/ brown	Surface soil, A-Bw horizon. Meadow environment w/ grass and many roots.
20	Sharp, wavy	Wavy/ gradual	Sandy silt to clay-silt w/ gravel	Brown with weak orange mottling	Generally massive. Crude defined layers. Contains channel stringers of gravelly sand. Stringers of gravel have rounded pebbles up to 3 cm. Some crude layers of darker organic material.
30	Sharp	Gradational	Gravelly sandy silt	Red/rusty orange & gray mottled	Massive gravels up to 4 mm. Subtle discontinuous gravel bedding near the base.
50	Sharp/ interbedded	Sharp, wavy	Peat, Silt & clay w/ interbedded sand lenses	Black	Very sticky, very dark black, decomposed organics rich, super soft. From top to bottom, organic silt, interbedded clean sand, prominent organic silt at base. Sand interbed: gray/brown, clean sand. Single grain structure, mostly medium grained sand. Forms small lenses within 50.
60	Wavy/sharp	Wavy/sharp	Medium sand	Gray	Bedded sand with coarse grained single grain sand to fine grained silty sand. Also contains centimeter thick organic silts in discontinuous lenses.
70	Wavy/sharp	Wavy/sharp	Medium sand	Gray	Bedded sand with coarse grained single grain sand to fine grained silty sand. Also contains centimeter thick organic silts in discontinuous lenses.
80	-	Sharp	Peat	Black	Very sticky, very dark black, decomposed organics rich, super soft.

Table 2 Unit descriptions for stratigraphic deposits exposed in the trench.

the occurrence of earthquakes on nearby faults, and their impact on seismic hazard assessments.

5.2 Assessment of utility of iOS scanning method and comparison to prior methods

Properly scaling and referencing a SfM model into real-world units and coordinates requires that either the precise camera locations or the precise locations of control points in the scene be known. Without control points or camera locations, SfM models may appear accurate to the eye, but will be in arbitrary units and can suffer from bowl effects. Bowl effects are common artifacts towards the edges of SfM models where the model gradually warps towards the direction of the cameras, forming an overall concave shape (e.g., Jaud et al., 2019). In an SfM model of a trench, this often results in the ends of the trench warping towards the viewer. A bowl effect is evident in the trench model in Figure 4C of Delano et al. (2021), where the two ends of the trench have greater errors than the center when compared to the model referenced to a total station survey. Bowl effects can be particularly pronounced in very long shallow

trenches and can be problematic as they cause the geometry of the trench (and thus photo projections) to be warped when projecting the SfM model onto a flat surface for creation of a 2D orthophoto mosaic.

Prior methods of accurately scaling photomosaics of paleoseismic trenches using SfM have relied on control points surveyed with either a total station or dGPS (Reitman et al., 2015) or by placing printed scale bars throughout the trench exposure (e.g., Delano et al., 2021). The total station and dGPS methods are time-consuming and require expensive instruments, and in the case of dGPS, may not produce the necessary accuracy in a forested or urban environment. The scale bar method, while cost-effective and quick for a single trench exposure, does not produce a model in a reference frame that can readily be combined with other exposures (critical for 3D trenching), nor are scale bars able to independently correct bowl effects.

The methods presented in this manuscript build on those of Reitman et al. (2015) by substituting the dGPS or total station for the more readily available, easy to use, and cheap iOS (or other) laser scanner. Our method quickly surveys dozens of control points without the

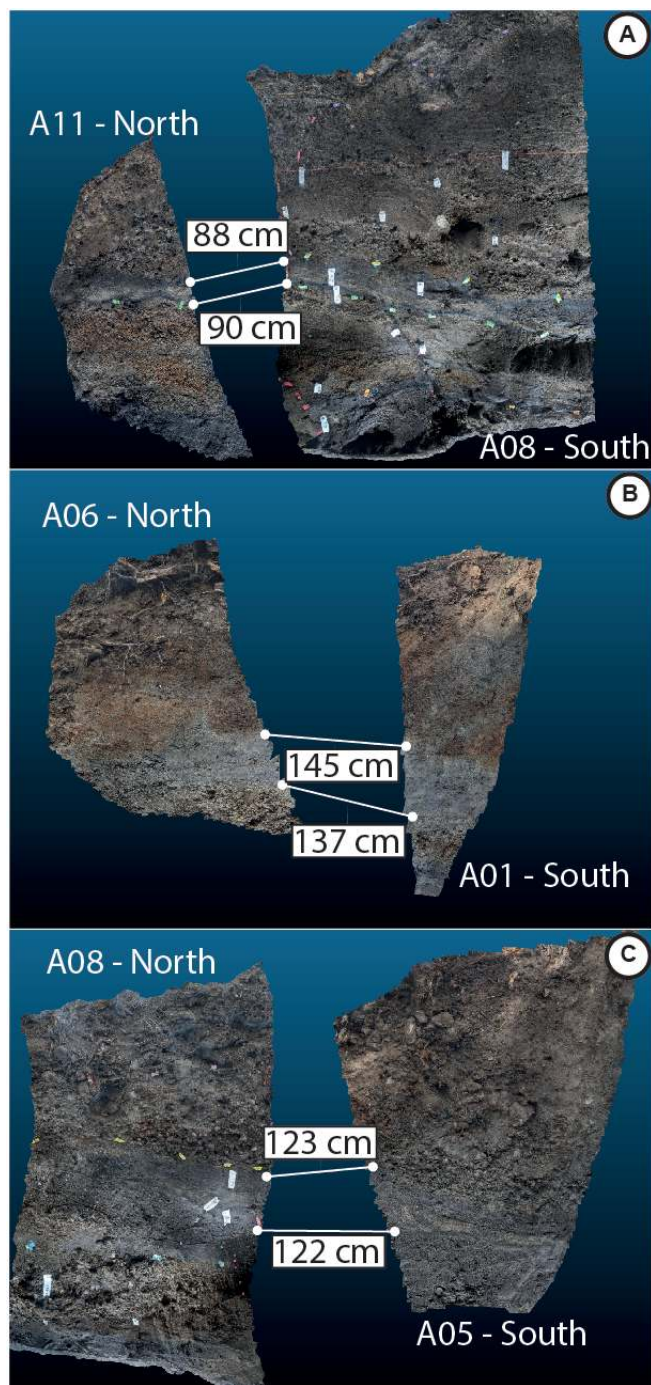


Figure 7 Oblique 3D views showing manual offset estimation via trench slices that have been cut along the fault and are effectively ‘backslipped’ to find the best matching strata. Measurements indicated are the distances between the two matching contacts on opposite sides of the fault, which is an estimate for the displacement.

need for expensive and cumbersome equipment. The resulting iOS scans can be quickly field-verified on the collecting device and then imported and used to produce control points directly in SfM software (e.g. Agisoft Metashape). We also build on a method suggested by Bemis et al. (2014), of collocating 3D trench models into a single digital reference frame. This method places models of progressively excavated 3D paleoseismic trenches into a single 3D model, moving beyond more traditional 2D trench analysis.

Our results show that 3D paleoseismic trenching is greatly enhanced using these surveying methods and 3D software to constrain and model the geometry and orientations of a number of trench slices in a rapid, portable, and cost-effective way. Compared to a single trench, having multiple exposures allowed for the calculation of a robust single event fault displacement and increased confidence in a multiple-event interpretation. Visualization of the resulting 3D trench is greatly improved using modern 3D structural analysis software instead of more traditional pseudo-3D methods using 2D images. This method also more readily allows others to review the trench results in a high detail, realistic format.

6 Conclusions

Here we developed improved methods of 3D paleoseismic trench scanning, logging, and visualization. These cost-effective methods use an iOS laser scanner to establish control points between progressive 3D trenching excavations. Collocating these models into a single reference frame allows for improved visualization and more robust estimates of strike-slip fault displacement. The iOS scanner is useful not only for 3D trenches, but also for accurately scaling models of single trenches and for mitigating bowl effects. We used these methods to determine that a left-lateral offset of 115 ± 30 cm occurred during a single earthquake after 8051 cal. ybp on the Dog Valley fault in northeast California. Based on the length of the fault and estimated offset it is inferred that this event may have had a magnitude of $M_w 6.7 \pm 0.1$. The penultimate earthquake on the Dog Valley fault occurred between 8491-8345 cal. ybp. While the broad range of ages allows that the Dog Valley fault may have contemporaneously ruptured with the Polaris fault, further investigation is required to determine if there is any possible triggering relationship with the conjugate & intersecting right-lateral Polaris fault.

Acknowledgements

We are grateful for discussions in the field with C., D., & O. Madugo, T. Dawson, G. Seitz, J. Zachariassen, S. Wesnousky, J. Bormann, J. McNeil, K. Adams, and K. Knudsen, and advice from R. Arrowsmith in reconstructing the trench model. We are grateful to editor Randolph Williams, and reviews from Sean Bemis and one anonymous reviewer that greatly improved the manuscript. Thanks to R. Hutchinson and J. Cañas of Tahoe National Forest for assisting in permitting access. Research supported by U.S. Geological Survey (G20AP00055). Any use of trade, firm, or product names is for descriptive purposes only and does not imply endorsement by the U.S. Government. Ian Pierce is supported by the Leverhulme Trust project ‘EROICA’.

Data and code availability

All data used in this study are publicly available and listed below.

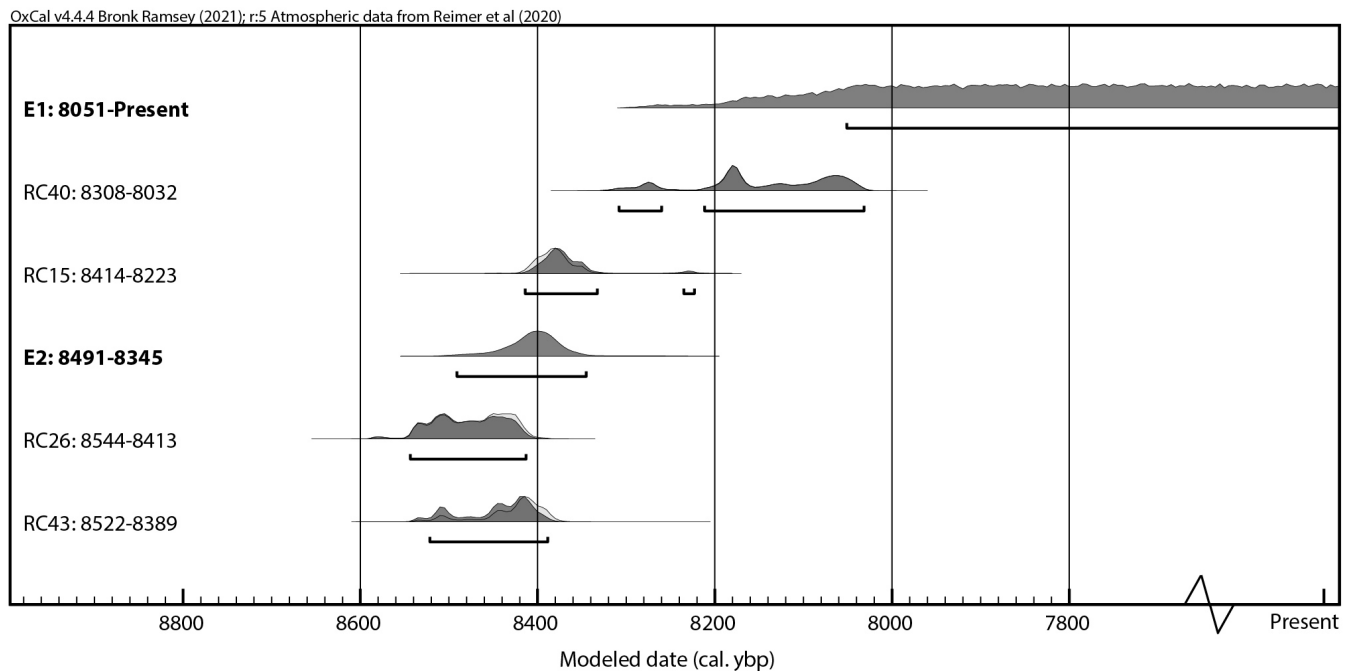


Figure 8 OxCal sequence model of radiocarbon ages showing event horizons. Events E1 and E2 occurred after 8051 and from 8491-8345 cal. ybp, respectively.

Mapped traces from this study of the Dog Valley fault in shapefile format are available here: <https://doi.org/10.5281/zenodo.6986415>

Orthoimages of the trench walls are available here: <https://doi.org/10.5281/zenodo.6986465>

3D Surface textures of trench walls are available here: <https://doi.org/10.5281/zenodo.7341261>

OxCal sequence model code is listed in the supplementary material.

Airborne lidar data used in the study are freely available from opentopography.org: <https://doi.org/10.5069/G9V122Q1>

Competing interests

The authors have no competing interests.

References

- Agisoft LLC. Agisoft Metashape Professional, 2022.
- Barnhart, W., Lohman, R., and Mellors, R. Active accommodation of plate convergence in Southern Iran: Earthquake locations, triggered aseismic slip, and regional strain rates: SOUTHERN IRAN ACTIVE DEFORMATION. *Journal of Geophysical Research: Solid Earth*, 118(10):5699–5711, 2013. doi: 10.1002/jgrb.50380.
- Barnhart, W., Hayes, G., and Gold, R. The July 2019 Ridgecrest, California Earthquake Sequence: Kinematics of Slip and Stressing in Cross-Fault Ruptures. *Geophysical Research Letters*, 2019. doi: 10.1029/2019GL084741.
- Bemis, S., Mickelthwaite, S., Turner, D., James, M. R., Akciz, S., Thiele, S. T., and Bangash, H. A. Ground-based and UAV-Based photogrammetry: A multi-scale, high-resolution mapping tool for structural geology and paleoseismology. *Journal of Structural Geology*, 69:163–178, 2014. doi: 10.1016/j.jsg.2014.10.007.
- Bormann, J., Hammond, W., Kreemer, C., Blewitt, G., and Jha, S. A Synoptic Model of Fault Slip Rates in the Eastern California Shear Zone and Walker Lane from GPS Velocities for Seismic Hazard Studies. In *2013 Seismological Society of America Annual Meeting*, page 323, Salt Lake City, UT, 2013. Seismological Research Letters.
- Bormann, J., Hammond, W. C., Kreemer, C., and Blewitt, G. Accommodation of missing shear strain in the Central Walker Lane, western North America: Constraints from dense GPS measurements. *Earth and Planetary Science Letters*, 440:169–177, 2016. doi: 10.1016/j.epsl.2016.01.015.
- Bronk Ramsey, C. Radiocarbon Calibration and Analysis of Stratigraphy: The OxCal Program. *Radiocarbon*, 37(2):425–430, 1995. doi: 10.1017/S0033822200030903.
- Brothers, D., Kent, G., Driscoll, N., Smith, S., Karlin, R., Dingler, J., Harding, A., Seitz, G., and Babcock, J. New Constraints on Deformation, Slip Rate, and Timing of the Most Recent Earthquake on the West Tahoe-Dollar Point Fault, Lake Tahoe Basin, California. *Bulletin of the Seismological Society of America*, 99(2A):499–519, 2009. doi: 10.1785/0120080135.
- Delano, J., Briggs, R., DuRoss, C., and Gold, R. Quick and Dirty (and Accurate) 3D Paleoseismic Trench Models Using Coded Scale Bars. 2021. doi: 10.1785/0220200246.
- dePolo, C. and Ramelli, A. Preliminary report on surface fractures along the White Mountains fault zone associated with the July 1986 Chalfant Valley earthquake sequence. *Bulletin of the Seismological Society of America*, 77(1):290–296, 1987. doi: 10.1785/BSSA0770010290.
- Dingler, J., Kent, G., Driscoll, N., Babcock, J., Harding, A., Seitz, G., Karlin, B., and Goldman, C. A high-resolution seismic CHIRP investigation of active normal faulting across Lake Tahoe Basin, California-Nevada. *GSA Bulletin*, 121(7/8):1089–1107, 2009. doi: 10.1130/B26244.1.
- Gold, R., Briggs, R., Personius, S., Crone, A., Mahan, S., and Angster, S. Latest Quaternary paleoseismology and evidence of distributed dextral shear along the Mohawk Valley fault zone, northern Walker Lane, California: Paleoseismology Mohawk Valley fault zone. *Journal of Geophysical Research: Solid Earth*, 119(6):5014–5032, 2014. doi: 10.1002/2014JB010987.

- GPL Software. CloudCompare, 2022.
- Haddad, D., Akciz, S., Arrowsmith, J., Rhodes, D., Oldow, J., Zielke, O., Toke, N., A.G., H., Mauer, J., and Shilpakar, P. Applications of airborne and terrestrial laser scanning to paleoseismology. *Geosphere*, 8(4):771–786, 2012. doi: 10.1130/GES00701.1.
- Hall, N., Wright, R., and Clahan, K. Paleoseismic studies of the San Francisco Peninsula segment of the San Andreas Fault zone near Woodside, California. *Journal of Geophysical Research: Solid Earth*, 104(B10):23215–23236, 1999. doi: 10.1029/1999JB900157.
- Hammond, W., Blewitt, G., and Kreemer, C. Block modeling of crustal deformation of the northern Walker Lane and Basin and Range from GPS velocities. *Journal of Geophysical Research*, 116 (B4), 2011. doi: 10.1029/2010JB007817.
- Hanks, T. and Kanamori, H. A moment magnitude scale. *Journal of Geophysical Research: Solid Earth*, 84(B5):2348–2350, 1979. doi: 10.1029/JB084iB05p02348.
- Hatch-Ibarra, R., Abercrombie, R., Ruhl, C., Smith, K., Hammond, W., and Pierce, I. The 2016 Nine Mile Ranch Earthquakes: Hazard and Tectonic Implications of Orthogonal Conjugate Faulting in the Walker Lane. *Bulletin of the Seismological Society of America*, 112, 2022. doi: 10.1785/0120210149.
- Hawkins, F., LaForge, R., and Hansen, R. Seismotectonic Study of the Truckee/Lake Tahoe Area Northeastern Sierra Nevada, California for Stampede, Prosser Creek, Boca, and Lake Tahoe Dams. *Seismotectonic Report*, (85-4):237, 1986.
- Hudnut, K., Seeber, L., and Pacheco, J. Cross-fault triggering in the November 1987 Superstition Hills Earthquake Sequence, southern California. *Geophysical Research Letters*, 16(2):199–202, 1989. doi: 10.1029/GL016i002p00199.
- Hunter, L., Howle, J., Rose, R., and Bawden, G. LiDAR-Assisted Identification of an Active Fault near Truckee, California. *Bulletin of the Seismological Society of America*, 101(3):1162–1181, 2011. doi: 10.1785/0120090261.
- Jaud, M., Passot, S., Allemand, P., Le Dantec, N., Grandjean, P., and Delacourt, C. Suggestions to Limit Geometric Distortions in the Reconstruction of Linear Coastal Landforms by SfM Photogrammetry with PhotoScan® and MicMac® for UAV Surveys with Restricted GCPs Pattern. *Drones*, 3(1):2, 2019. doi: 10.3390/drones3010002.
- Jones, L. and Hough, S. Analysis of broadband records from the. *Bulletin of the Seismological Society of America*, 85(3):688–704, 1995. doi: 10.1785/BSSA0850030688.
- Kent, G., J.M., B., Driscoll, N., Harding, A., Dingler, J., Seitz, G., Gardner, J., Mayer, L., Goldman, C., Heyvaert, A., Richards, R., Karlin, R., Morgna, C., Gayes, P., and Owen, L. 60 k.y. record of extension across the western boundary of the Basin and Range province: Estimate of slip rates from offset shoreline terraces and a catastrophic slide beneath Lake Tahoe. *Geology*, 33(5): 365–368, 2005. doi: 10.1130/G21230.1.
- Li, X., Huang, W., Pierce, I., S.J., A., and Wesnousky, S. Characterizing the Quaternary expression of active faulting along the Olinghouse, Carson, and Wabuska lineaments of the Walker Lane. *Geosphere*, 13(6):2119–2136, 2017. doi: 10.1130/GES01483.1.
- Luetzenburg, G., Kroon, A., and Bjørk, A. Evaluation of the Apple iPhone 12 Pro LiDAR for an Application in Geosciences. *Scientific Reports*, 11(1):22221, 2021. doi: 10.1038/s41598-021-01763-9.
- Marco, S., Rockwell, T., Heimann, A., Frieslander, U., and Agnon, A. Late Holocene activity of the Dead Sea Transform revealed in 3D palaeoseismic trenches on the Jordan Gorge segment. *Earth and Planetary Science Letters*, 234(1–2):189–205, 2005. doi: 10.1016/j.epsl.2005.01.017.
- McCalpin, J. *Paleoseismology*. Academic Press, 2nd edn edition, 2009.
- Melody, A., Whitney, B., and Slack, C. Late Pleistocene and Holocene Faulting in the Western Truckee Basin North of Truckee, California. *Bulletin of the Seismological Society of America*, 102(5):2219–2224, 2012. doi: 10.1785/0120110260.
- Olig, S., Sawyer, T., Wright, D., Terra, F., and Anderson, L. Preliminary seismic source characterization of faults near Stampede and Prosser Creek dams-Washoe Project and Boca dam-Truckee Storage Project, northern Sierra Nevada. 2005.
- OpenTopography. 2014 USFS Tahoe National Forest Lidar, 2017.
- Pierce, I., Wesnousky, S., and Owen, L. Terrestrial cosmogenic surface exposure dating of moraines at Lake Tahoe in the Sierra Nevada of California and slip rate estimate for the West Tahoe Fault. *Geomorphology*, 298:63–71, 2017. doi: 10.1016/j.geomorph.2017.09.030.
- Pierce, I., Wesnousky, S., Owen, L., Bormann, J., Li, X., and Caffee, M. Accommodation of Plate Motion in an Incipient Strike-Slip System: The Central Walker Lane. *Tectonics*, 40(2), 2021. doi: 10.1029/2019TC005612.
- Reed, T. *Spatial Correlation of Earthquakes with Two Known and Two Suspected Seismogenic Faults, North Tahoe-Truckee Area, California*. Master's Thesis. Baylor University, 2014.
- Reitman, N., Bennett, S., Gold, R., Briigs, R., and DuRoss, C. High-Resolution Trench Photomosaics from Image-Based Modeling: Workflow and Error Analysis. *Bulletin of the Seismological Society of America*, 105(5):2354–2366, 2015. doi: 10.1785/0120150041.
- Rezapour, M. and Mohsenpur, A. The 2010 Mw 6.5 Rigan, Iran, Earthquake Aftershock Sequence. *Bulletin of the Seismological Society of America*, 103(3):1793–1800, 2013. doi: 10.1785/0120120288.
- Rockwell, T., Ragona, D., Seitz, G., Langridge, R., Aksoy, M., Ucarus, G., Ferry, M., Meltzner, A., Klinger, Y., Meghraoui, M., Satir, D., Barka, A., and B., A. Palaeoseismology of the North Anatolian Fault near the Marmara Sea: implications for fault segmentation and seismic hazard. *Geological Society, London, Special Publications*, 316(1):31–54, 2009. doi: 10.1144/SP316.3.
- Ruhl, C., Abercrombie, R., Hatch, R., and Smith, K. Seismogenic Depth Variation across the Transtensional Northern Walker Lane. *Geophysics [preprint]*, 2020. doi: 10.1002/es-soar.10504612.1.
- Smith, K. and Priestley, K. Faulting in the 1986 Chalfant, California, Sequence: Local Tectonics and Earthquake Source Parameters. *Bulletin of the Seismological Society of America*, 90(4):813–831, 2000. doi: 10.1785/0119990129.
- Sylvester, A. and Raines, G. *Geology of the Independence Lake and Hobart Mills Quadrangles, Truckee, California*, 2013.
- U.S.G.S. U.S. Geological Survey Quaternary fault and fold database for the United States, 2020.
- Walker, R., Bergman, E., Szeliga, W., and Fielding, E. Insights into the 1968–1997 Dasht-e-Bayaz and Zirkuh earthquake sequences, eastern Iran, from calibrated relocations, InSAR and high-resolution satellite imagery: Dasht-e-Bayaz and Zirkuh earthquake sequences. *Geophysical Journal International*, 187 (3):1577–1603, 2011. doi: 10.1111/j.1365-246X.2011.05213.x.
- Walker, R., Bergman, E., Elliot, J., Fielding, E., Ghods, A.-R., Ghoraishi, M., Jackson, J., Nazari, H., Nemati, M., Oveisi, B., Talebia, M., and Walters, R. The 2010–2011 South Rigan (Baluchestan) earthquake sequence and its implications for distributed deformation and earthquake hazard in southeast Iran. *Geophysical Journal International*, 193(1):349–374, 2013. doi: 10.1093/gji/ggs109.
- Wesnousky, S. Active faulting in the Walker Lane. *Tectonics*, 24(3):



35, 2005. doi: 10.1029/2004TC001645.

Wesnousky, S. Displacement and Geometrical Characteristics of Earthquake Surface Ruptures: Issues and Implications for Seismic-Hazard Analysis and the Process of Earthquake Rupture. *Bulletin of the Seismological Society of America*, 98(4): 1609–1632, 2008. doi: 10.1785/0120070111.

Wesnousky, S., Bormann, J., Kreemer, C., Hammond, W., and Brune, J. Neotectonics, geodesy, and seismic hazard in the Northern Walker Lane of Western North America: Thirty kilometers of crustal shear and no strike-slip? *Earth and Planetary Science Letters*, 329–330:133–140, 2012. doi: 10.1016/j.epsl.2012.02.018.

The article *3D Paleoseismology of the Dog Valley Fault (California, USA) from iOS Lidar and Structure-from-Motion Photogrammetry* © 2023 by Ian K.D. Pierce is licensed under CC BY 4.0.

Imaging the Western Edge of the Aegean Shear Zone: The South Evia 2022-2023 Seismic Sequence

Christos P. Evangelidis  * ¹, Ioannis Fountoulakis  ^{1,2}

¹Institute of Geodynamics, National Observatory of Athens, Athens, Greece, ²Department of Geology, University of Patras, Patras, Greece

Author contributions: *Conceptualization:* C.P.Evangelidis. *Methodology:* I.Fountoulakis. *Software:* I.Fountoulakis. *Formal Analysis:* I.Fountoulakis, C.P.Evangelidis. *Writing - original draft:* C.P.Evangelidis. *Writing - Review & Editing:* C.P.Evangelidis, I.Fountoulakis. *Visualization:* C.P.Evangelidis. *Supervision:* C.P.Evangelidis.

Abstract This report presents the 2022-2023 South Evia island seismic sequence, in the western Aegean sea. An automated workflow, undergoing testing for efficient observatory monitoring in the wake of dense aftershock sequences, was employed to enhance the seismic catalog. It includes a deep-learning phase picker, absolute and relative hypocenter relocation, and moment tensor automatic calculations. The relocated catalog reveals a concentration of earthquake epicenters in a narrow NW-SE zone, with sinistral strike-slip fault movement. The findings of the study indicate the occurrence of an asymmetric rupture within conjugate fault structures in the western Aegean region. These fault structures, although not necessarily both active, play a significant role in marking the transition from dextral (SW-NE) to sinistral (NW-SE) strike-slip ruptures, connecting the Aegean shear zone with normal faulting in mainland Greece. The South Evia 2022-2023 seismic sequence has revealed the activation of this NW-SE strike-slip structure, contrary to previous assumptions of low seismicity in the region. The study highlights the importance of reassessing seismic hazard maps and considering the potential activation of similar zones further south in the future. It also emphasizes the need for the expansion and the densification of seismic networks within the Aegean.

Non-technical summary This report presents a study on the seismic activity that occurred in the South Evia island region of the western Aegean Sea from 2022 to 2023. In order to analyze the earthquake data, a range of advanced automatic techniques, including state-of-the-art machine learning methods, were employed and tested for rapid observatory monitoring after significant aftershock sequences. The study's findings show that earthquake epicenters are concentrated in a narrow zone running from northwest to southeast. The movement along these faults suggests a horizontal left-lateral strike-slip motion. Asymmetric rupture occurring within interconnected fault structures in the western Aegean region plays a significant role in the transition from right-lateral strike-slip fault motion (southwest to northeast) to left-lateral strike-slip (northwest to southeast). The South Evia 2022-2023 seismic sequence shows the activation of a fault structure with northwest-to-southeast strike-slip horizontal motion, contradicting previous assumptions of low seismicity in the area. The study emphasizes the need to reevaluate seismic hazard maps in the region and consider the possibility of similar fault zones being activated further south in the future. It also emphasizes the need to expand the coverage of the seismic networks in the Aegean.

Introduction

The occurrence of two moderate events on the eastern shores of Evia Island in central Greece on November 29, 2022 (moment magnitude (M_w) 4.6 04:32 UTC and M_w 4.8 20:06 UTC), resulted in unrest among the civilian population in the Athens metropolitan area, situated around 50 km to the east. A series of minor pre-shocks was initiated a month before. The moment tensors (MTs) for the mainshocks provided by the National Observatory of Athens (NOA) revealed strike-slip focal mechanisms with either NW-SE or SW-NE strikes. As of June 2023, microearthquake activity persists, including an event of M_w 4.5 that took place on April 22, 2023.

The northern and central parts of the Aegean Sea are dominated by strike-slip zones that reflect the east-

ward shear transmitted from major and minor branches of the North Anatolian Fault (NAT) (e.g. Barbot and Weiss, 2021). These right-lateral strike-slip zones continue westward and end near the primarily E-W oriented normal faulting system, which governs the Greek mainland. It seems that the strike-slip faulting extends as far as Evia Island, but it does not traverse through central Greece (Fig.1). To date, no active faults on the surface have been identified in the southern part of Evia Island (Ganas et al., 2013). Moreover, the Greek Database of Seismogenic Sources (GreDaSS) does not report the existence of seismogenic faults in this area (Caputo and Pavlides, 2013). According to the routine seismic catalogs provided by NOA, the studied region exhibits relatively limited background seismicity compared to other areas in Greece. As a result, this region has been considered to have relatively lower seismic

Production Editor:
Kiran Kumar Thingbaijam
Handling Editor:
Ryo Okuwaki
Copy & Layout Editor:
Oliver Lamb

Signed reviewer(s):
Tiegian Hobbs

Received:
June 7, 2023
Accepted:
June 29, 2023
Published:
July 8, 2023

*Corresponding author: cevan@noa.gr

hazard compared to other regions of mainland Greece (Danciu et al., 2021).

In this report, we image the earthquake activity in the area by utilizing automated techniques to significantly enhance the NOA seismic catalog and image the details of the ruptured faults. We produce a new seismic catalog by deploying a deep-learning phase picker (Mousavi et al., 2020), a rapid arrival earthquake association (Zhang et al., 2019), an absolute location (Klein, 2002), and a relative relocation method (Trugman and Shearer, 2017). We also calculate as many as possible MTs solutions using *Gisola*, an automated regional moment tensor determination tool (Triantafyllis et al., 2021). This seismic monitoring workflow was first implemented by Fountoulakis et al. (2023), after the Mw 7.0 earthquake that occurred in Samos in 2020. Our primary objective is to establish this procedure as an operational system at NOA for analyzing dense aftershock sequences captured by numerous permanent and temporary seismic stations.

Event detection and location

Continuous seismic records from broadband seismic stations located up to 110 km from the main events epicenters were used for the period between October 2022 and April 2023 (Fig. 1). The installation of additional stations from the temporary network 1Y (Wolfgang Friederich et al., 2022), part of the AdriaArray experiment, improved significantly the seismic monitoring capacity in the area.

Using the EQTransformer signal detector (Mousavi et al., 2020), a deep-learning-based system that uses an attention mechanism to detect seismic signals and identify primary and secondary seismic arrivals, we identify earthquake signals and pick P and S seismic wave onsets. The independently identified arrivals are associated with seismic events using the REAL associator and initial locator (Zhang et al., 2019). It deploys a 3D grid around the station with the first recorded P arrival and searches for possible earthquake locations by counting other seismic arrivals within a time window based on theoretical traveltimes. To assure high-quality events, we required event identification with at least *four* P and S phases each. The local P-wave velocity model by Konstantinou et al. (2020) with $V_p/V_s=1.73$ was employed for the theoretical traveltime calculations.

We locate the associated events with the HYPOINVERSE code (Klein, 2002). Low-quality events with azimuthal gaps $> 280^\circ$, average root-mean-square (RMS) residuals > 0.5 sec, and horizontal/vertical error > 0.5 km were discarded from the catalog, leaving 5838 well-located events. We further improve the earthquake locations using the GrowClust code (Trugman and Shearer, 2017), which incorporates techniques for hierarchical clustering and relocation based on waveform cross-correlation (WCC) values. We cross-correlate waveforms for event pairs that appear in common stations. To ensure high relocation precision, we consider only event pairs with 0.65 average minimum WCC values and a minimum of three phases with WCC values > 0.65 . From the 5838 events in the input catalog, 1893

events were successfully relocated and clustered. The exclusive utilization of WCC relocation was driven by the objective of focusing specifically on events that were effectively located. This deliberate choice enabled the precise mapping of the activated fault structures within the designated study area, as depicted in Fig. 2. GrowClust utilizes the bootstrap method to assess formal uncertainties by resampling the input WCC data. This iterative process generates a perturbed set of event locations that is specific to each bootstrap iteration. To calculate the relative relocation uncertainties, bootstrapping was employed with 30 resamplings of the input WCC data, resulting in mean horizontal and vertical errors of approximately 500 m and 450 m, respectively. For the detected and relocated final catalogs, the local magnitudes (M_L) were calculated using the local magnitude scale of Scordilis et al. (2016).

To precisely pinpoint the hypocenters of the three greatest events, we relied mostly on the manual seismic phases provided by NOA and the NonLinLoc location code (Lomax et al., 2000). Here, we do not perform GrowClust relocation because the waveforms from these larger events do not correlate well with those from the other smaller events. NonLinLoc was chosen due to its ability to account for the non-linear nature of the problem, allowing for a solid uncertainty analysis and providing a probability density function, resulting in a more comprehensive representation of the error volume. Hypocenter solutions of these events are presented in Table S1.

The magnitude characteristics of the catalog were additionally examined by analyzing the Frequency-Magnitude distribution. To estimate the magnitude of completeness (M_c) and the corresponding b-values, we employed the Maximum Curvature method proposed by Wiemer and Wyss (2000). As shown in Figure 3 and Table S2, there is a reduction of M_c for the WCC catalog (M_c 1.4) compared to the manually compiled institutional NOA catalog (M_c 1.8) and a significant increase in the detectability levels just by employing automated signal detector and associator routines without WCC (M_c 0.9).

Moment tensor (MT) solutions for the major events of the sequence were obtained using *Gisola* (Triantafyllis et al., 2021). Table S3 lists those events with reliable solutions.

Results and Discussion

The relocated catalog reveals a concentration of epicenters aligned in a narrow NW-SE zone, spanning approximately 5 to 6 kilometers in length (Fig. 2a). This alignment corresponds to the predominant NW-trending sinistral strike-slip fault plane in most calculated MTs, oriented approximately 130° N. When examining a vertical cross-section along the strike, it becomes evident that the majority of events are clustered offshore, specifically within a 3 km long segment (Fig. 2b). Most of these events are confined between 8 to 12 km depth (Fig. 2b). Additionally, a lateral migration of events is observed, originating from the foreshocks (Figure S1). This migration, at an approximate

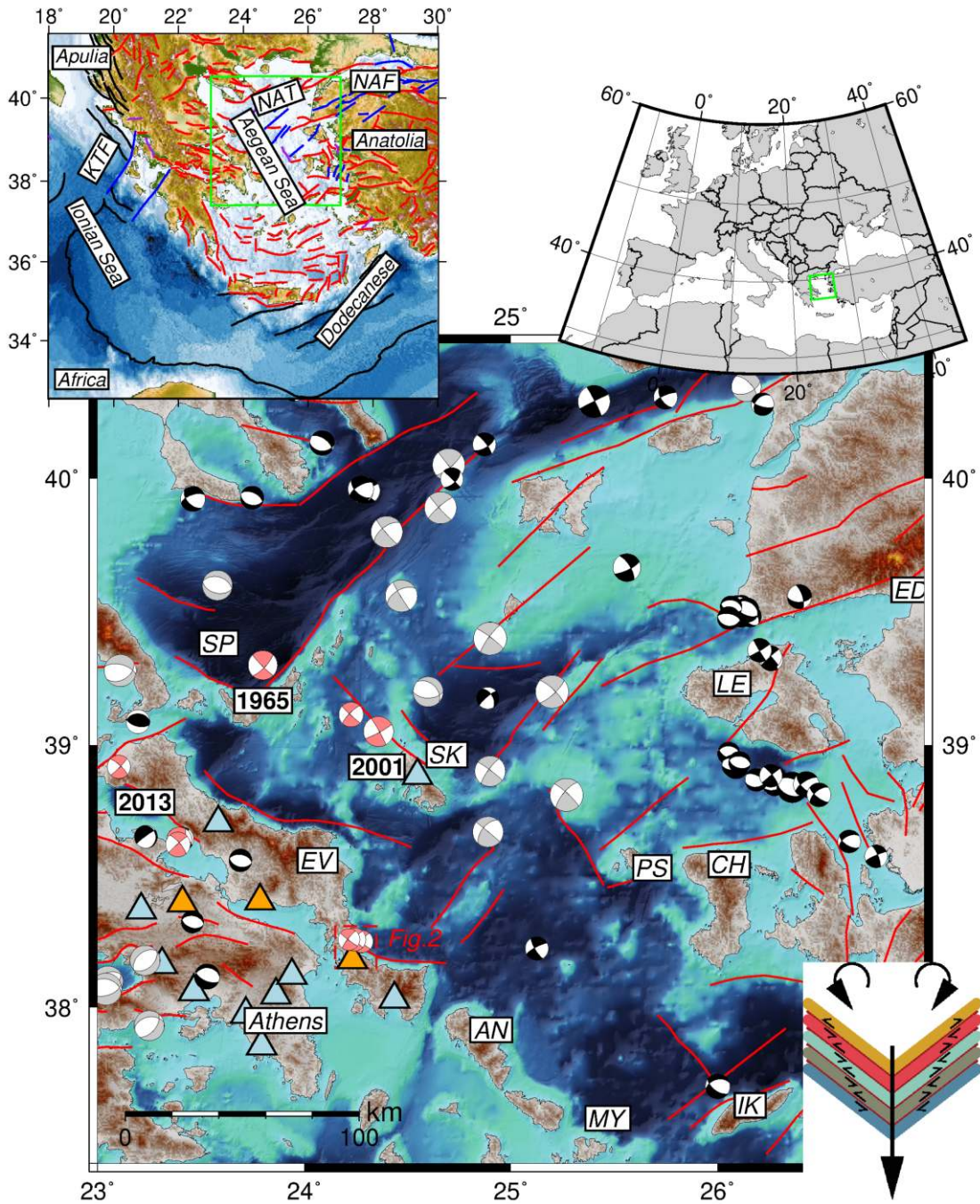


Figure 1 North and central Aegean map. NOA focal mechanisms for earthquakes greater than Mw 4.5 from 2012 onwards are plotted in black (Triantafyllis et al., 2021). Focal mechanisms for events greater than Mw 6 between 1967 and 2012 are plotted in gray, derived from the Centroid Moment Tensor (CMT) catalog (Dziewonski et al., 1981) and other local studies (Kiratzi et al., 1991; Taymaz et al., 1991; Konstantinou et al., 2010). The light red symbols show focal mechanisms obtained by this study and others (Roumelioti et al., 2003; Ganas et al., 2005; Kiratzi, 2014). Fault traces from the GEM Global Active Faults Database (Styron and Pagani, 2020) are plotted in red. Permanent stations used in this study from HL (National Observatory of Athens, Institute of Geodynamics, Athens, 1975) and HA (University of Athens, 2008) seismic networks are shown in blue triangles. Temporary stations from seismic network 1Y (Wolfgang Friederich et al., 2022) are shown in orange triangles. AN: Andros Island, CH: Chios island, ED: Edremit, EV: Evia island, IK: Icaria island, LE: Lesbos island, MY: Mykonos basin, PS: Psara island, SK: Skyros basin, SP: Sporades basin. Top left inset map: A general map view of the Hellenic subduction zone where the African plate subducts beneath the Aegean area, bounded by the dextral North Anatolian Fault (NAF) and North Aegean Trough (NAT) in the northeast and the Kefalonia Transform Fault (KTF) in the west. Traces of normal, dextral strike-slip, sinistral strike-slip, and reverse faults from the GEM database are plotted in red, blue, purple, and black, respectively. The green box outline marks the north and central Aegean area shown in the main figure. Top right inset: A general map view of Europe. The green box outline is similar to the other inset. Lower right inset sketch: a graphical illustration based on Yaltırak et al. (2012) for the broken slab model proposed by Taymaz et al. (1991) depicts the transition from dextral strike-slip systems in the east to sinistral ones in the west.

rate of 50 m/day, ultimately leads up to the date of the two main events on November 29, 2022. Interestingly, a comparable migration speed of 70 m/day was identified during the Thiva 2020-2021 earthquake sequence, occurring just 80 km to the northwest. In that case, the migration was attributed to the diffusion of pore-fluid pressure on a normal fault (Kaviris et al., 2022). As the rupture zone transitions towards onshore regions in the northwest, there is a decrease in the number of relocated events. These remaining events that are observed in onshore regions tend to occur at greater depths, typically ranging from 10 to 12 km. A vertical cross-section perpendicular to the 130° strike images the existence of a fault zone oriented in a NW-SE direction with a steep SW dip (Fig. 2c). The MT of the largest event shows a fault dip that is parallel to the aftershock lineations observed on the eastern fault (Fig. S2). The clustered lineations observed in Figures 2 and S2 indicate the presence of another fault running parallel to the west.

A noticeable cluster of seismic activity is observed in the northwest region, near Zarakes village, which is distinct from the main rupture zone (Fig. 2). This particular cluster is separated from the main rupture zone by a higher topographic relief zone that spans approximately 3 km in length. The abundance of seismic activity in this elevated area suggests two possible scenarios. Firstly, there could be a separate secondary fault within the NW-SE strike-slip fault zone. Alternatively, it could indicate a larger fault zone that fractures into segments, with an unbroken section in the middle.

The analysis of the relocated catalog reveals the presence of numerous offshore events that exhibit a general SW-NE direction. However, due to the limited availability of seismic stations in the eastern offshore region, most of the eastward events have not been relocated using WCC techniques. As a result, SW-NE alignments are not as clearly defined in the relocated catalog. If some SW-NE lineations were more clearly evident, they could potentially be associated with the dextral strike observed in most calculated MTs, which is approximately 220° . However, based on the available MTs and the WCC relocations, there is no conclusive evidence of any significant event occurring along a right-lateral offshore fault (Fig. 2). Therefore, the relocation of this earthquake sequence suggests an asymmetric rupture taking place within a steep NW-SE fault zone, which persists for at least 6 months. It also emphasizes the need for better coverage of seismic stations to overcome this limitation and obtain a more complete picture of the seismic activity, particularly in offshore regions in the Aegean. This consideration is crucial for improving our understanding of fault structures and earthquake mechanisms in the study area.

As the Hellenic subduction zone is rolling back towards the southwest, a pair of opposite rotations occur. Dextrally rotated blocks are observed between the Kefalonia Transform Fault (KTF) and the western edge of the Aegean Sea across Skyros, Evia, etc (Fig. 1). Conversely, on the other side of the Aegean, the southeast Dodecanese islands, Crete, and southwestern Turkey blocks undergo sinistral rotation (e.g. Martin, 2007). In the middle, the Aegean microplate is constrained by two

rigid indentors, the Anatolia (eastern end) and the Apulia (western end) platforms (e.g. Wallace et al., 2009). The proposed model, referred to as the “dual indenter” model, describes the opposing rotation of mainland Greece in a dextral-clockwise direction and Anatolia in a sinistral-anticlockwise direction. This concept bears resemblance to the pinned, broken slat model introduced Taymaz et al. (1991), as well as the “double saloon door” concept put forth by Martin (2007). Considering that the kinematics of the northern and central Aegean can be described from the broken slat model of Taymaz et al. (1991), where a right-hand margin of parallel slats has rotated more than the left, there are points of abrupt change in slip vector, the breakpoints on the slats, that produce conjugate strike-slip fault structures (Fig. 1). Distinct conjugate areas can be identified from north to south based on focal mechanisms. These structures may not exhibit similar seismic activity in terms of temporal occurrence and density. Instead, they serve as indicators of the transition from predominantly dextral to sinistral strike-slip motions. Such areas include the region between Skopelos and Alonissos islands in the Sporades basin, marking the termination of the Northern Aegean Trough (Fig. 1). Another area is found near the Skyros basin, signifying the end of the Skyros-Edremit Trough. Additionally, the South Evia area, the region focused on in this study, lies at the termination of another branch of the Lesvos-Edremit fault system (Fig. 1). Further south, the extension of the Chios-Psara fault system suggests a potential conjugate fault structure between Evia and Andros islands (Fig. 1). Additionally, if the extension of the Ikaria faults, which currently lacks any recorded MTs, exhibits a similar sense of motion, it could potentially indicate the presence of a similar geological structure within the Mykonos basin (Fig. 1).

The existence of these fault structures in the western Aegean that marks the transition from SW-NE dextral strike-slip ruptures to NW-SE sinistral strike-slip ruptures links the Aegean shear zone with the normal faulting in the mainland (Kiratzi, 2014). The first well-documented occurrence of left-lateral strike-slip motions can be traced back to the 2001 Skyros earthquake (Roumelioti et al., 2003; Ganas et al., 2005). Several preceding significant earthquakes, such as the 1965 event in the Sporades basin (Fig. 1), may be also associated with left-lateral strike-slip motions (Kiratzi, 2014). Furthermore, a small seismic sequence on the western shores of northern Evia, which occurred in November 2013, offered supplementary evidence for left-lateral strike-slip motions (Kiratzi, 2014).

The South Evia 2022-2023 sequence has emerged as the southernmost observed area where strike-slip NW-SE faults have been activated. This finding contradicts previous assumptions regarding the relatively low seismicity in the region east of the Athens metropolis. It also implies the potential activation in the future of similar zones, either between Evia and Andros islands or even between Tinos and Mykonos islands in the south (Fig. 1). Consequently, seismic hazard maps for the area need to be reassessed to incorporate this new information and ensure precise evaluations of seismic risk.

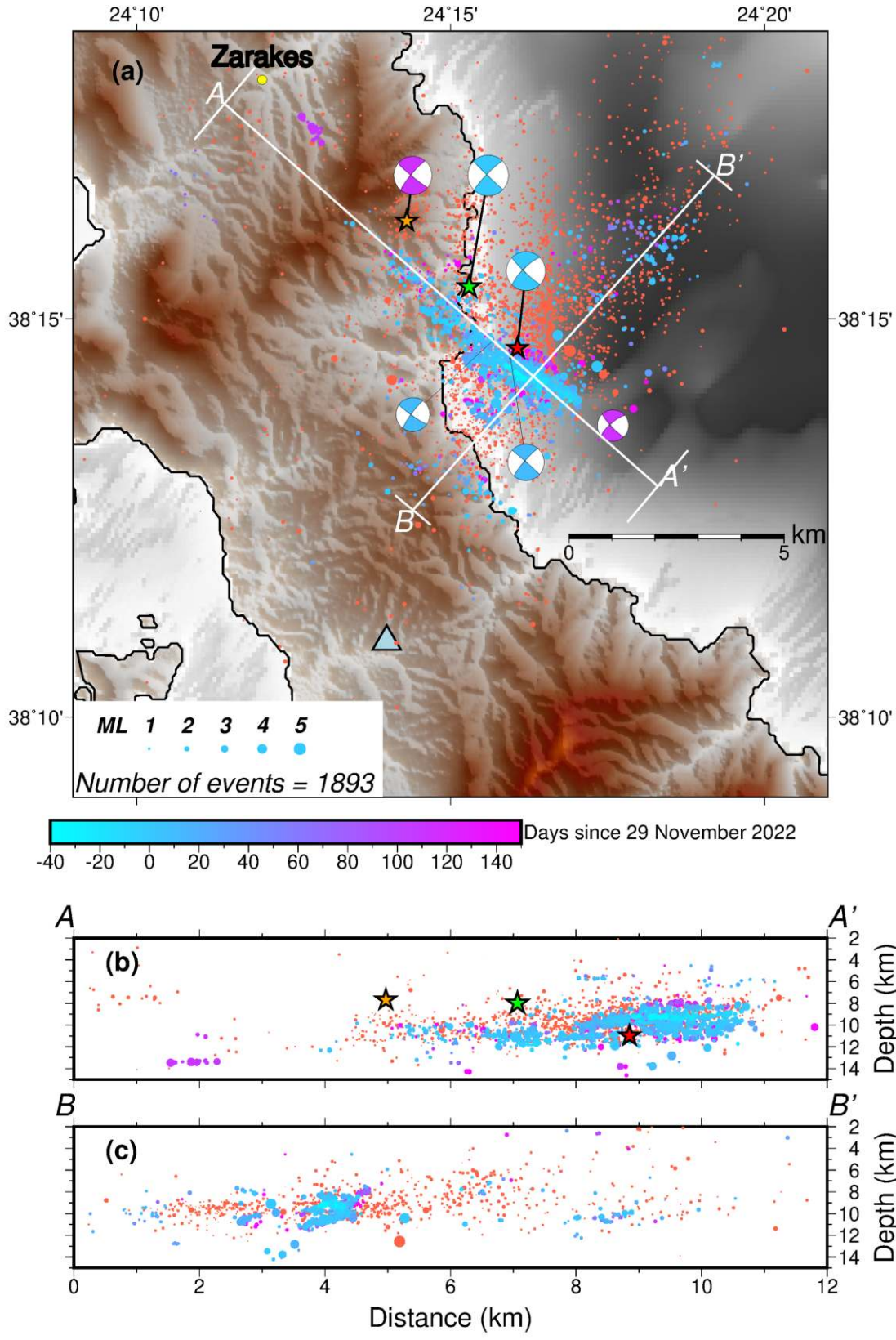


Figure 2 (a) Relocated 2022-2023 earthquake sequence colored based on days since November 29th, 2022, sized proportionally to their local magnitude. Hypocenters in light red are those detected events not relocated with WCC. Moment tensor solutions are colored similarly to the hypocenters. Red and green stars indicate the location of the two largest events of the sequence on the 29th of November 2022. The orange star marks the Mw 4.5 aftershock on April 22, 2023 (b) NW-SE vertical cross-section along fault strike. (c) SW-NE vertical cross-section with orthogonal orientation to the strike of the main fault. The width of the cross-sections are 2 km and 1 km, respectively. Hypocenter colors in vertical cross-sections are similar to the map view in (a).

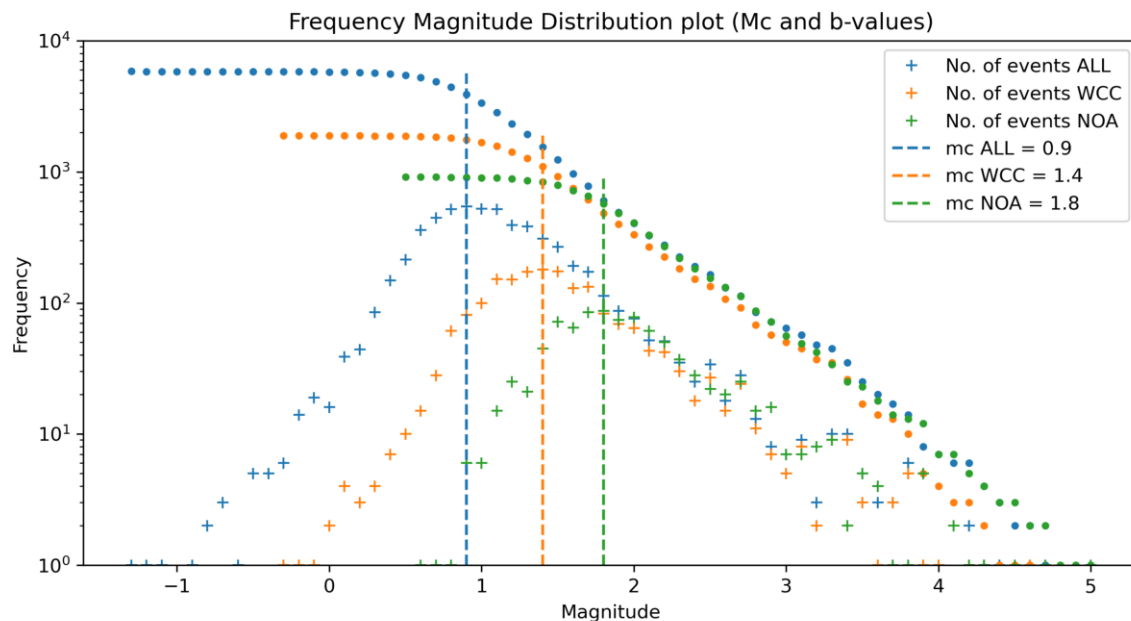


Figure 3 The Frequency-Magnitude distribution (FMD) of the detected (ALL), relocated (WCC), and NOA catalogs with a bin width of 0.1. Colored crosses and circles show the number and the cumulative number of events per magnitude bin, respectively. The magnitudes of completeness (M_c) are estimated using the Maximum Curvature method proposed by [Wiemer and Wyss \(2000\)](#).

Acknowledgements

The GMT mapping software [Wessel and Smith \(1998\)](#) was used for figure preparation. Parts of the analysis were performed using ObsPy ([Beyreuther et al., 2010](#)). We are grateful to the reviewers, Tiegan Hobbs and Ryo Okuwaki, for their valuable feedback and constructive comments. Their input has greatly contributed to the improvement of this manuscript.

Data and code availability

The relocated catalog is available in Zenodo data repository ([Evangelidis and Fountoulakis, 2023](#)). Broad-band seismic records, acquired from the HL ([National Observatory of Athens, Institute of Geodynamics, Athens, 1975](#)), HA ([University of Athens, 2008](#)), HP [University of Patras \(2000\)](#), and 1Y ([Wolfgang Friederich et al., 2022](#)) networks were accessed through the National Observatory of Athens data center node (EIDA@NOA, <http://eida.gein.noa.gr>) ([Evangelidis et al., 2021](#)). Routine seismic catalog locations have been obtained from NOA FDSN event webservice <http://eida.gein.noa.gr/fdsnws/event/1/> and MTs are available at <https://bbnet.gein.noa.gr/HL/seismicity/mts>. For further information regarding the AdriaArray initiative visit https://orfeus.readthedocs.io/en/latest/adria_array_main.html. Bathymetry has been downloaded from EMODnet portal <http://portal.emodnet-bathymetry.eu/gebco-bathymetry-basemap> and GEBCO ([GEBCO Compilation Group, 2023](#)). The land topography data used in this study was obtained from the NASA Shuttle Radar Topography Mission Global dataset, which has a resolution of 1 arc second ([NASA JPL, 2013](#)).

Competing interests

The authors have no competing interests

References

- Barbot, S. and Weiss, J. R. Connecting subduction, extension and shear localization across the Aegean Sea and Anatolia. *Geophysical Journal International*, 226(1):422–445, 02 2021. doi: 10.1093/gji/ggab078.
- Beyreuther, M., Barsch, R., Krischer, L., Megies, T., Behr, Y., and Wassermann, J. ObsPy: A Python Toolbox for Seismology. *Seismological Research Letters*, 81(3):530–533, 05 2010. doi: 10.1785/gssrl.81.3.530.
- Caputo, R. and Pavlides, S. The Greek Database of Seismogenic Sources (GreDaSS), version 2.0.0: A compilation of potential seismogenic sources ($M_w > 5.5$) in the Aegean Region. *GreDaSS*, 2013. doi: 10.15160/unife/gredass/0200.
- Danciu, L., Nandan, S., Reyes, C., Basili, R., Weatherill, G., Beauval, C., Rovida, A., Vilanova, S., Sesetyan, K., Bard, P.-Y., Cotton, F., Wiemer, S., and Giardini, D. The 2020 update of the European Seismic Hazard Model: Model Overview. *European Facilities for Earthquake Hazard and Risk, EFEHR Technical Report 001, v1.0.0*, 2021. doi: 10.12686/a15.
- Dziewonski, A. M., Chou, T.-A., and Woodhouse, J. H. Determination of earthquake source parameters from waveform data for studies of global and regional seismicity. *Journal of Geophysical Research: Solid Earth*, 86(B4):2825–2852, 1981. doi: 10.1029/JB086iB04p02825.
- Evangelidis, C. P. and Fountoulakis, I. Supplementary Dataset for the Report "Imaging the Western Edge of the Aegean Shear Zone: The South Evia 2022-2023 Seismic Sequence". 2023. doi: 10.5281/zenodo.8077688.
- Evangelidis, C. P., Triantafyllis, N., Samios, M., Boukouras, K., Kon-takos, K., Ktenidou, O., Fountoulakis, I., Kalogeras, I., Melis,

- N. S., Galanis, O., Papazachos, C. B., Hatzidimitriou, P., Scordilis, E., Sokos, E., Paraskevopoulos, P., Serpetsidaki, A., Kaviris, G., Kapetanidis, V., Papadimitriou, P., Voulgaris, N., Kassaras, I., Chatzopoulos, G., Makris, I., Vallianatos, F., Kostantinidou, K., Papaioannou, C., Theodoulidis, N., Margaritis, B., Pilidou, S., Dimitriadis, I., Iosif, P., Manakou, M., Roumelioti, Z., Pitolakis, K., Riga, E., Drakatos, G., Kiratzi, A., and Tselentis, G. Seismic Waveform Data from Greece and Cyprus: Integration, Archival, and Open Access. *Seismol. Res. Lett.*, 92(3):1672–1684, 2021. doi: 10.1785/0220200408.
- Fountoulakis, I., Evangelidis, C. P., and Ktenidou, O. Coseismic and Postseismic Imaging of a Composite Fault System: The Samos 2020 Mw 7.0 Sequence. *Bull. Seismol. Soc. Am.*, 03 2023. doi: 10.1785/0120220207.
- Ganas, A., Drakatos, G., Pavlides, S., Stavrakakis, G., Ziazia, M., Sokos, E., and Karastathis, V. The 2001 Mw = 6.4 Skyros earthquake, conjugate strike-slip faulting and spatial variation in stress within the central Aegean Sea. *Journal of Geodynamics*, 39(1):61–77, 2005. doi: 10.1016/j.jog.2004.09.001.
- Ganas, A., Oikonomou, I. A., and Tsimi, C. NOAfaults: a digital database for active faults in Greece. *Bulletin of the Geological Society of Greece*, 47(2):518–530, Jan. 2013. doi: 10.12681/bgsg.11079.
- GEBCO Compilation Group. GEBCO 2023 Grid. *GEBCO 2023 Grid. British Oceanographic Data Centre, National Oceanography Centre, UK*, 2023. doi: 10.5285/f98b053b-0cbc-6c23-e053-6c86abc0af7b.
- Kaviris, G., Kapetanidis, V., Spingos, I., Sakellariou, N., Karakostas, A., Kouskouna, V., Elias, P., Karavias, A., Sakkas, V., Gatsios, T., Kassaras, I., Alexopoulos, J. D., Papadimitriou, P., Voulgaris, N., and Parcharidis, I. Investigation of the Thiva 2020 - 2021 Earthquake Sequence Using Seismological Data and Space Techniques. *Applied Sciences*, 12(5), 2022. doi: 10.3390/app12052630.
- Kiratzi, A., Wagner, G., and Langston, C. Source parameters of some large earthquakes in Northern Aegean determined by body waveform inversion. *Pure and Applied Geophysics*, 135: 515–527, 1991. doi: 10.1007/BF01772403.
- Kiratzi, A. A. *Mechanisms of Earthquakes in Aegean*, pages 1–22. Springer Berlin Heidelberg, Berlin, Heidelberg, 2014. doi: 10.1007/978-3-642-36197-5_99 – 1.
- Klein, F. W. User's guide to HYPOINVERSE-2000: A Fortran program to solve for earthquake locations and magnitudes. *U.S. Geol. Surv. Open-File Rept.*, page 02-171, 2002. doi: 10.3133/ofr02171.
- Konstantinou, K. I., Melis, N. S., and Boukouras, K. Routine Regional Moment Tensor Inversion for Earthquakes in the Greek Region: The National Observatory of Athens (NOA) Database (2001–2006). *Seismological Research Letters*, 81(5):750–760, 09 2010. doi: 10.1785/gssrl.81.5.750.
- Konstantinou, K. I., Mouslopoulou, V., and Saltogianni, V. Seismicity and Active Faulting around the Metropolitan Area of Athens, Greece. *Bull. Seismol. Soc. Am.*, 110(4):1924–1941, 06 2020. doi: 10.1785/0120200039.
- Lomax, A., Virieux, J., Volant, P., and Berge, C. Probabilistic earthquake location in 3D and layered models: Introduction of a Metropolis-Gibbs method and comparison with linear locations. In Thurber, C. H. and Rabinowitz, N., editors, *Advances in Seismic Event Location*, pages 101–134. Kluwer, Amsterdam, 2000. doi: 10.1007/978-94-015-9536-0_5.
- Martin, A. Gondwana breakup via double-saloon-door rifting and seafloor spreading in a backarc basin during subduction rollback. *Tectonophysics*, 445(3):245–272, 2007. doi: 10.1016/j.tecto.2007.08.011.
- Mousavi, M. S., Ellsworth, W. L., Zhu, W., Chuang, L. Y., and Beroza, G. C. Earthquake transformer—an attentive deep-learning model for simultaneous earthquake detection and phase picking. *Nature Communications*, 11:3952, 2020. doi: 10.1038/s41467-020-17591-w.
- NASA JPL. NASA Shuttle Radar Topography Mission Global 1 arc second. *Distributed by NASA EOSDIS Land Processes DAAC*, 2013. doi: 10.5067/MEaSURES/SRTM/SRTMGL1.003.
- National Observatory of Athens, Institute of Geodynamics, Athens. National Observatory of Athens Seismic Network. *International Federation of Digital Seismograph Networks*, 1975. doi: 10.7914/SN/HL.
- Roumelioti, Z., Kiratzi, A., and Melis, N. Relocation of the 26 July 2001 Skyros Island (Greece) earthquake sequence using the double-difference technique. *Physics of the Earth and Planetary Interiors*, 138(3):231–239, 2003. doi: 10.1016/S0031-9201(03)00138-9.
- Scordilis, E. M., Kementzetzidou, D., and Papazachos, B. C. Local magnitude calibration of the Hellenic Unified Seismic Network. *Journal of Seismology*, 20(1):319–332, 2016. doi: 10.1007/s10950-015-9529-5.
- Styron, R. and Pagani, M. The GEM Global Active Faults Database. *Earthquake Spectra*, 36(1_suppl):160–180, 2020. doi: 10.1177/8755293020944182.
- Taymaz, T., Jackson, J., and McKenzie, D. Active tectonics of the north and central Aegean Sea. *Geophysical Journal International*, 106(2):433–490, 1991. doi: 10.1111/j.1365-246X.1991.tb03906.x.
- Triantafyllis, N., Venetis, I. E., Fountoulakis, I., Pikoulis, E., Sokos, E., and Evangelidis, C. P. Gisola: A High-Performance Computing Application for Real-Time Moment Tensor Inversion. *Seismological Research Letters*, 2021. doi: 10.1785/0220210153.
- Trugman, D. T. and Shearer, P. M. GrowClust: A Hierarchical Clustering Algorithm for Relative Earthquake Relocation, with Application to the Spanish Springs and Sheldon, Nevada, Earthquake Sequences. *Seismological Research Letters*, 88(2A):379–391, 2017. doi: 10.1785/0220160188.
- University of Athens. Hellenic Seismological Network, University of Athens, Seismological Laboratory. *International Federation of Digital Seismograph Networks*, 2008. doi: 10.7914/SN/HA.
- University of Patras. University of Patras, Seismological Laboratory. *International Federation of Digital Seismograph Networks*, 2000. doi: 10.7914/SN/HP.
- Wallace, L. M., Ellis, S., and Mann, P. Collisional model for rapid fore-arc block rotations, arc curvature, and episodic back-arc rifting in subduction settings. *Geochemistry, Geophysics, Geosystems*, 10(5), 2009. doi: 10.1029/2008GC002220.
- Wessel, P. and Smith, W. H. New, improved version of Generic Mapping Tools released. *Eos, Transactions American Geophysical Union*, 79(47):579–579, 1998. doi: 10.1029/98EO00426.
- Wiemer, S. and Wyss, M. Minimum Magnitude of Completeness in Earthquake Catalogs: Examples from Alaska, the Western United States, and Japan. *Bulletin of the Seismological Society of America*, 90(4):859–869, 08 2000. doi: 10.1785/0119990114.
- Wolfgang Friederich, Christos Evangelidis, Costas Papazachos, Efthimios Sokos, George Kaviris, and Dragana Cernih. AdriaArray Temporary Network: Greece, North Macedonia. *International Federation of Digital Seismograph Networks*, 2022. doi: 10.7914/y0t2-3b67.
- Yaltırak, C., İşler, E., Aksu, A., and Hiscott, R. Evolution of the Bababurnu Basin and shelf of the Biga Peninsula: Western extension of the middle strand of the North Anatolian Fault Zone, Northeast Aegean Sea, Turkey. *Journal of Asian Earth Sciences*, 57:103–119, 2012. doi: 10.1016/j.jseaes.2012.06.016.

Zhang, M., Ellsworth, W. L., and Beroza, G. C. Rapid Earthquake Association and Location. *Seismological Research Letters*, 90(6): 2276–2284, 2019. doi: 10.1785/0220190052.

The article *Imaging the Western Edge of the Aegean Shear Zone: The South Evia 2022-2023 Seismic Sequence* © 2023 by Christos P. Evangelidis is licensed under CC BY 4.0.

Could planet/sun conjunctions be used to predict large (moment magnitude ≥ 7) earthquakes?

P. Romanet  *1,2

¹Department of Earth Sciences, La Sapienza Università di Roma, Rome, Italy, ²Université Côte d'Azur, IRD, CNRS, Observatoire de la Côte d'Azur, Géoazur, Sophia-Antipolis, France

Author contributions: *Conceptualization:* P. Romanet. *Formal Analysis:* P. Romanet. *Investigation:* P. Romanet. *Methodology:* P. Romanet. *Software:* P. Romanet. *Validation:* P. Romanet. *Visualization:* P. Romanet. *Writing – original draft:* P. Romanet. *Writing – review & editing:* P. Romanet.

Abstract No.

Production Editor:
Kiran Kumar Thingbaijam
Handling Editor:
Ryo Okuwaki
Copy & Layout Editor:
Hannah F. Mark

Reviewed by:
Yen Joe Tan

Received:
March 23, 2023
Accepted:
April 25, 2023
Published:
May 1, 2023

Introduction

Following the recent moment magnitude (Mw) 7.8 and Mw 7.5 Kahramanmaraş, Türkiye, earthquake sequence on 6 February 2023 (U. S. Geological Survey, 2017), an assertion that planet/sun alignments and lunar phases may help to predict an earthquake occurrence became widespread in some news outlets and on social media (Chappell, 2023). In the following, we call this alignment of three celestial bodies a conjunction, although the correct word in astronomy would be a syzygy.

Usually, the assertion that planet/sun alignments and lunar phases may predict an earthquake occurrence is promoted by choosing carefully a period of time at which these alignments occur and showing specific earthquakes that occurred at the same time. Such assertions usually do not mention that these conjunction events do happen extremely frequently, and that most of the time, they are not followed by significant earthquakes. By making a large number of predictions (Garcia, 2017; Service Checknews, 2019), some of them may come true, but that does not mean that the method has any predictive power. The only literature available arguing that conjunctions can be used to predict earthquake occurrence either calls into question fundamental physics without any proof (Omerbashich, 2011; Safronov, 2022), or does not show the background rate of conjunctions (Awadh, 2021). The major logical flaw in these analyses is showing only events that are associated with conjunctions while not paying attention

to the total quantity of conjunctions (see Khalisi, 2021; Zanette, 2011). Indeed, if conjunctions are very common, it is easy to associate them with earthquakes, but it may not help in any way to predict future earthquakes.

The assertion that planet/sun alignment may predict an earthquake can be seen as a more evolved version of the theory that the moon phase has a strong influence on earthquakes. The moon phase theory has been debated for a long time by seismologists (e.g., Schuster, 1897), and the question is still not completely answered yet (Ide et al., 2016; Hough, 2018; Kossobokov and Panza, 2020; Zaccagnino et al., 2022). In some regions, slow-earthquakes like tremors (Nakata et al., 2008; Rubinstein et al., 2008) or low frequency earthquakes (Thomas et al., 2012) are influenced by tides. Depending on the area, the considered period in the seismic cycle (Tanaka, 2010, 2012; Peng et al., 2021), and the focal mechanism (Tsuruoka et al., 1995), the moon phase may have some influence or not. Overall, it seems to have an influence (Yan et al., 2023), at least for some regions/period or time, that may be incorporated in long term probabilistic earthquake forecasting (Ide et al., 2016); however, this effect is too small to be used as a way to predict earthquakes (Witze, 2016). A rigorous attempt to perform short term prediction, with the idea that before a large earthquake, smaller earthquakes would be more tide-sensitive as the crust is approaching critical strength, proved the method to be ineffective for prediction (Hirose et al., 2022).

While for the moon/earth/sun alignments, there exists a physical mechanism by which the stresses are

*Corresponding author: romanet@geoazur.unice.fr

changing in the crust via gravity change which may weakly influence earthquake occurrence (Ide et al., 2016), there is no such mechanism for planets/sun alignments because the electromagnetic and gravity fields due to celestial bodies other than the Sun and moon are usually extremely small when they reach the Earth.

This paper aims to test whether the planet/sun alignment, along with the moon phase, can be used to predict earthquakes. For this purpose, we are systematically comparing the percentage of earthquakes linked with conjunction(s) with the percentage of the time that conjunction(s) are happening over a 69-year period of time using a global catalog of earthquakes. In the future, more detailed analyses can be conducted to examine whether there is an effect of other planets on the occurrence of earthquakes, for example by calculating the gravitational effects on the tractions of differently oriented faults (e.g., Cochran et al., 2004; Ide et al., 2016).

This assertion that planet/sun alignment is strongly promoting earthquakes would be valid only if the rate of earthquakes associated with conjunctions was higher than the conjunction rate. We evaluate the significance of our results by calculating the p-value, making the null hypothesis that earthquakes follow a binomial distribution during the period of our catalog with the probability given by the probability of conjunctions.

Method

We first chose the ISC-GEM catalog (Storchak et al., 2013, 2015; Di Giacomo et al., 2018) and selected earthquakes of $M_w \geq 7$ over the period 1950/01/01-2018/12/31. The reason for starting at the year 1950 is because the catalog starts to be complete for shallow events ($>60\text{km}$) and for $M_w \geq 7$ at years 1918–1939 (Michael, 2014). We chose the 10 years delay as a margin to be sure not to flaw the analysis by missing any $M_w 7$ earthquakes.

To calculate each planet/sun alignment, we took advantage of the Astropy package in python (The Astropy Collaboration et al., 2018, 2022) that allows us to calculate the position of any planets in the solar system, the Sun, and the moon at any time. For each day covering the period of the earthquake catalog, we calculated if there was a conjunction or not. We used the NASA JPL ephemerides model “DE430” (Folkner et al., 2014). We did not take into account leap seconds in the calculation of the day, because the offset is less than a minute for the considered period.

The celestial bodies included are: the Sun, Mercury, Venus, Earth, Mars, Jupiter, Saturn, Uranus, and Neptune.

For each triplet of given three celestial bodies A , B and C in the solar system, we calculated their positions in International Celestial Reference System (ICRS).

We then calculated each vector \vec{AB} , \vec{BC} , \vec{AC} and the associated norms $\|\vec{AB}\|$, $\|\vec{BC}\|$ and $\|\vec{AC}\|$. The vector that has the longest norm shows the greatest distance between two bodies, hence we can find the body that is in the middle. For example, if $\|\vec{AC}\|$ is the greatest distance, we can guess that the celestial body B is in the

middle. Finally, we can calculate the angle between \vec{AB} and \vec{BC} as:

$$\theta = \frac{180}{\pi} \cos^{-1} \left(\frac{\vec{AB} \cdot \vec{BC}}{\|\vec{AB}\| \|\vec{BC}\|} \right), \quad (1)$$

in degrees.

When the angle θ was smaller than a threshold θ_{thr} , we set that there was an alignment of the celestial bodies for the day. In the following paper, we used the threshold $\theta_{\text{thr}} = 3^\circ$ unless stated otherwise.

For the moon phase, we calculated the projection of the moon on the ecliptic plane (the plane that contains the orbital of the Earth). Then, we tried to find if the projection on this plane was in opposition (full Moon) or in conjunction (new Moon) with the Sun from the Earth. A threshold of 6.5° was used, and this threshold is chosen because the average orbital of the moon around the Earth during one day is around 12° .

Results

The results are presented in Table 1 for the threshold $\theta_{\text{thr}} = 3^\circ$. The total time period consists of 25202 days, among which 19565 days are associated with conjunctions, so that 78% of the time, there is at least one conjunction on the day. For the same period, there are 813 earthquakes, among which 640 are associated with conjunctions, so that 79% percent of earthquakes are associated with conjunctions.

We did the same study for earthquakes associated with full or new moon, as well as for earthquakes associated with both full or new moon and at least one conjunction. The percentage of days associated with either full or new moon is 7% (1743/25202), very much the same as the number of earthquakes that happened during full or new moon 7% (58/813). Finally, there are 5% (1349/25202) of days, and 6% (52/813) of earthquakes associated with both full or new moon and at least one conjunction.

We can formulate the null hypothesis that earthquakes follow a binomial law with the probability p given by the number of days that are associated with conjunctions:

$$P[k|n|p] = \binom{n}{k} p^k (1-p)^{n-k}, \quad (2)$$

where P is the probability to observe k earthquakes that are associated with at least one conjunction in the total number of earthquakes n . Because n is large in our sample, we can approximate the binomial distribution by a normal law:

$$P[k|n|p] \approx \frac{e^{-\frac{1}{2} \left(\frac{k-np}{\sqrt{np(1-p)}} \right)^2}}{\sqrt{2\pi np(1-p)}}. \quad (3)$$

Finally, the single-side p-value will be:

$$p_{\text{value}} = \frac{1}{2} - \frac{1}{2} \operatorname{erf} \left(\frac{k-np}{\sqrt{2np(1-p)}} \right), \quad (4)$$

Number of days associated with conjunction(s)	19565/25202 (77.63%)
Number of earthquakes associated with conjunction(s)	640/813 (78.72%) $p_{\text{value}} = 0.23$
Number of days associated with full/new moon	1743/25202 (6.92%)
Number of earthquakes associated with full/new moon	58/813 (7.13%) $p_{\text{value}} = 0.40$
Number of days associated with both full/new moon and conjunction(s)	1349/25202 (5.35%)
Number of earthquakes associated with both full/new moon and conjunction(s)	52/813 (6.40%) $p_{\text{value}} = 0.09$

Table 1 Comparison of the frequency of a particular event (for example a conjunction), and the frequency of an earthquake that can be associated to the event during the period 1950/01/01-2018/12/31. The threshold used here to define a conjunction is $\theta_{\text{thr}} = 3^\circ$. The calculated p-value is one-sided, for the null hypothesis that the earthquakes follow a binomial law with the probability given by the frequency calculated with the number of days.

if $k > np$, where erf is the error function.

The p-value represents the probability of obtaining a value worse than or equal to the calculated value. Usually, a value $p_{\text{value}} < 0.05$ is taken to indicate that we can reject the null hypothesis, meaning that there is only 5% chance that the null hypothesis could be true given the data.

We choose a single-side p-value because this will favor the rejection of the null hypothesis (the single side p-value is lower than the two-side p-value), hence it is providing an initial advantage to the hypothesis that conjunctions are linked to earthquakes. Given that the p-value for earthquakes associated with conjunction(s) is 0.23 (Table 1), we cannot reject the null hypothesis, hence the difference between the observed value of earthquake linked with conjunction(s) and the total number of conjunctions is not significant. The same analysis can be done for earthquakes associated with full/new moon ($p_{\text{value}} = 0.40$, Table 1), or earthquakes that are associated with both full/new moon and at least one conjunction ($p_{\text{value}} = 0.09$, Table 1). In these two cases, the p-value is also high enough ($p_{\text{value}} > 0.05$) that we cannot reject the null hypothesis.

Discussion and conclusion

The frequency of earthquakes associated with conjunction(s) and the frequency of conjunctions are pretty much the same, and the difference is statistically non-significant (all the p-values are larger than 5%). This means that we cannot reject the hypothesis that earthquakes are occurring following a binomial law during the time period of the earthquake catalog.

The fact that the null hypothesis cannot be rejected does not mean that it is the true hypothesis. It just means that given this earthquake catalog, we do not have a scientific basis to reject it.

It is known that earthquakes are not completely random, especially because of aftershocks, and aftershocks have not been removed from the catalog here. However, trying to remove aftershocks and foreshocks does not change the conclusion of the paper (see Supplementary Text and Supplementary Tables S1-S2).

The assertion that earthquakes are linked with conjunctions is unlikely based on our results. For such a strong claim that earthquakes can be predicted using conjunctions and moon phase, because it would have extremely important societal implications, it would need very significant results associated with very low p-value. This is far from being the case here.

We also tried to find if a planet was more often than the others associated with conjunctions (Figure 1). This seems not to be the case because the p-value for every planet (except Neptune) is quite large ($p_{\text{value}} \geq 0.1$). For Neptune, the p-value is small, which means that the probability to observe this result or more extreme results was only 1%. Given the earthquake catalog and the period of time, we cannot statistically rule out that Neptune has some influence. However, it still does not mean that it can be used for earthquake prediction because conjunctions including Neptune are very common and 97% of the time are not followed by a large earthquake (there are 8344 days with at least one conjunction including Neptune, and 266 earthquakes are associated with at least one conjunction including Neptune).

Finally, we tried to see if a conjunction was more often than others associated with earthquake occurrence (Figure 2). The results are less clear, because for a given conjunction, the percentage of one particular conjunction during the whole period is small (<2% for the conjunction that is the most frequent), so that the number of earthquakes sampling this conjunction is also very small. This leads to a large variability. However, we can

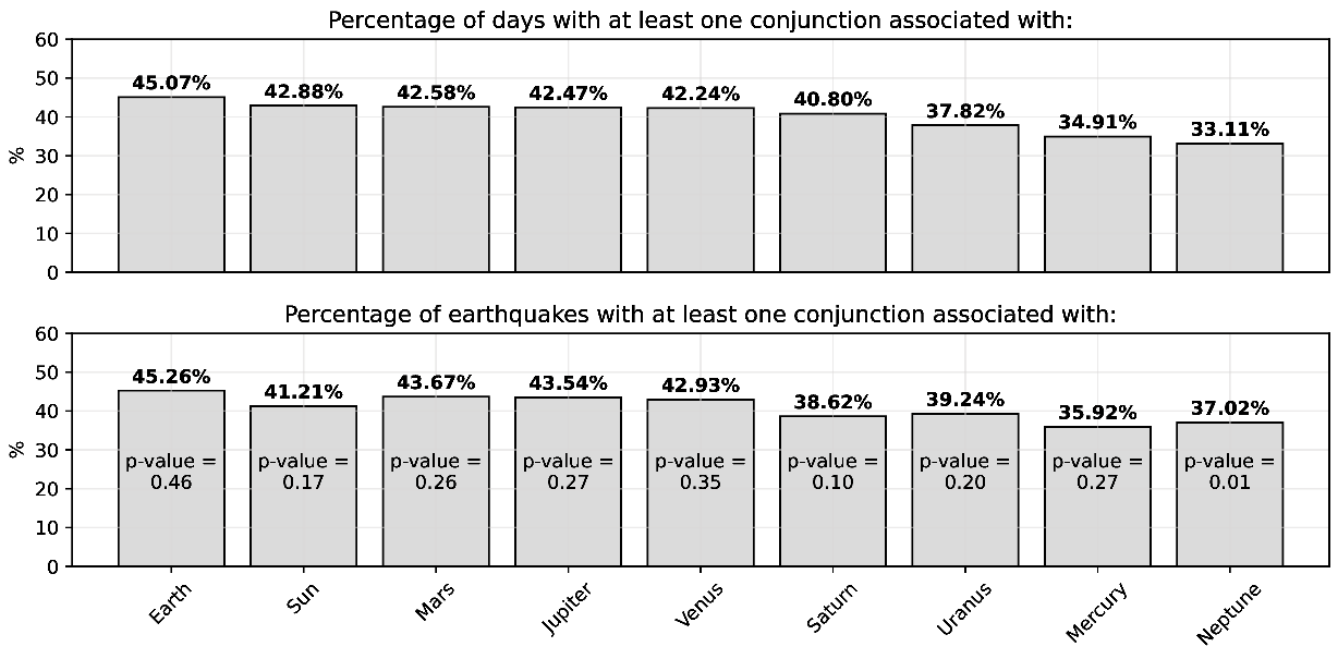


Figure 1 Comparison of the percentage of days involving at least one conjunction associated with a given planet, and the percentage of earthquakes linked with at least one conjunction associated with a given planet. The threshold angle to define a conjunction is $\theta_{thr} = 3^\circ$.

still say that the overall trend is respected, such that the conjunctions that are the most frequent are most often associated with earthquakes.

Changing the threshold for conjunction does not change the results, and the same conclusion can be made. If the threshold angle is too small, we may miss some conjunctions because the orbital plane is not exactly the same for each planet. For example, the results with the threshold of 2° are given in Supplementary Table S3. Reducing the threshold angle mainly reduces the percentage of time conjunctions are happening and reduces in the same way the percentage of earthquakes that are associated with conjunctions.

Persons defending the assertion of planet/sun conjunctions may continue arguing that I still did not look at a particular association of conjunctions, or association with only full moon. This is true. But given the number of possible associations, it is impossible to test them all. Rigorous and scientific tests of any such specific associations are welcomed.

The alignment of three planets/sun is actually something extremely ordinary in the solar system that is happening close to every day (for the threshold 3° , it happens 78% of the time). Finding a conjunction on the day of an earthquake is therefore normal, and if we start looking at time windows including some days before and after an earthquake it becomes even more likely that a conjunction will have occurred. We showed that the percentage of earthquakes associated with at least one conjunction is actually very similar to the percentage of the time where there is at least one conjunction, and that the difference between the two is not statistically significant. Hence, there is no significant effect of planet/sun alignment or moon phase on the occurrence of large earthquakes, and it can certainly not be used to

provide short term prediction of earthquakes.

Acknowledgements

I would like to thank all the seismologists/geologists/scientists that supported me to write this article. I would like to thank the editor Ryo Okuwaki and the reviewer Yen Joe Tan whose comments helped a lot to improve the quality of the paper. Special thanks to Martijn van den Ende and Sylvain Barbot, because I would have never thought about publishing a paper on this topic. I would also like to thank Susan Hough who gave me her blessing to plagiarize her abstract. This research was partially funded by European Research Council (ERC) Starting Grants 101040600 (HYQUAKE).

Data and code availability

The catalog of earthquake is available at the following link: http://www.isc.ac.uk/iscgem/request_catalogue.php

The software used to create the figures and perform the calculation is available on Zenodo (DOI: 10.5281/zenodo.7859401) at the following link: <https://zenodo.org/badge/latestdoi/612635356>. It uses python, with the Astropy package.

Competing interests

The author has no competing interests.

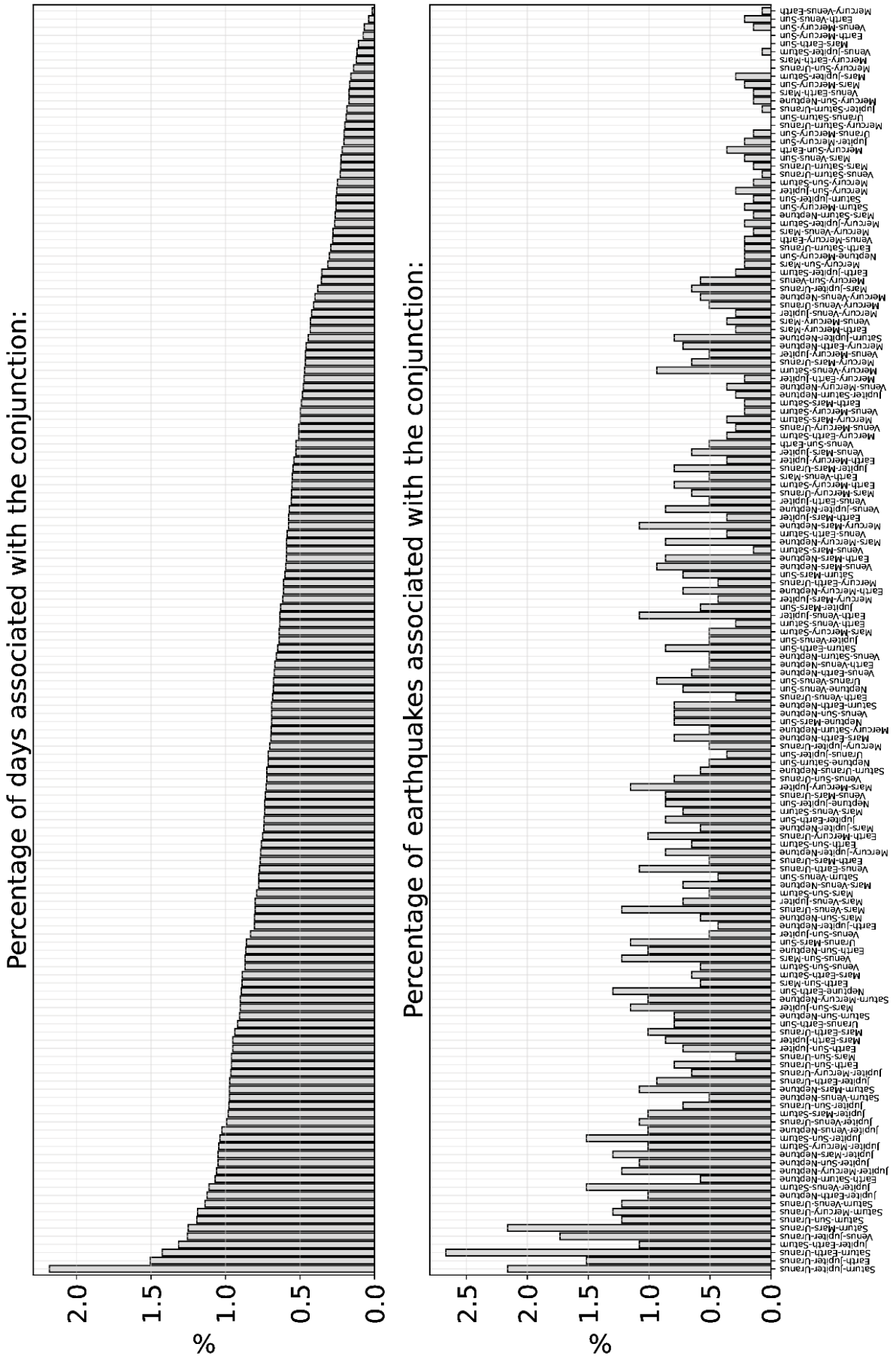


Figure 2 Comparison of the percentage of days that a specific conjunction happens, with the percentage of earthquakes that can be linked with the same specific conjunction. The threshold angle to define a conjunction is $\theta_{thr} = 3^\circ$.

References

- Awadh, S. M. Solar system planetary alignment triggers tides and earthquakes. *Journal of Coastal Conservation*, 25(2):30,, 2021. doi: 10.1007/s11852-021-00822-7.
- Chappell, B. No you can't predict earthquakes, the USGS says, 2023. <https://www.npr.org/2023/02/07/1154893886/earthquake-prediction-turkey-usgs>. last access: 04/24/2023.
- Cochran, E. S., Vidale, J. E., and Tanaka, S. Earth tides can trigger shallow thrust fault earthquakes. *Science*, 306(5699): 1164–1166,, 2004. doi: 10.1126/science.110396.
- Di Giacomo, D., Engdahl, E. R., and Storchak, D. A. The isc-gem earthquake catalogue (1904–2014): status after the extension project. *Earth System Science Data*, 10(4):1877–1899,, 2018. doi: 10.5194/essd-10-1877-2018.
- Folkner, W. M., Williams, J. G., Boggs, D. H., Park, R. S., and Kuchynka, P. The Planetary and Lunar Ephemerides DE430 and DE431. *IPN Progress Report 42-196*, 2014.
- Garcia, A. Dutch Earthquake 'Enthusiast' Claims to Predict Major Tremor, 2017. <https://www.snopes.com/news/2017/03/01/dutch-earthquake-enthusiast-claims-to-predict-major-tremor/>. last access: 04/24/2023.
- Hirose, F., Maeda, K., and Kamigaichi, O. Efficiency of earthquake forecast models based on earth tidal correlation with background seismicity along the Tonga–Kermadec trench. *Earth, Planets and Space*, 74(1):1–11,, 2022. doi: 10.1186/s40623-021-01564-4.
- Hough, S. E. Do large (magnitude8) global earthquakes occur on preferred days of the calendar year or lunar cycle? *Seismol. Res. Lett*, 89(2A):577–581,, 2018. doi: 10.1785/0220170154.
- Ide, S., Yabe, S., and Tanaka, Y. Earthquake potential revealed by tidal influence on earthquake size–frequency statistics. *Nature Geoscience*, 9(11):834–837,, 2016. doi: 10.1038/ngeo2796.
- Khalisi, E. On the erroneous correlation between earthquakes and eclipses. *preprint arXiv:2101.08572*, 2021. doi: 10.48550/arXiv.2101.08572.
- Kossobokov, V. G. and Panza, G. F. A myth of preferred days of strong earthquakes? *Seismol. Res. Lett*, 91(2A):948–955,, 2020. doi: 10.1785/0220190157.
- Michael, A. J. How complete is the isc-gem global earthquake catalog? *Bull. Seism. Soc. Am*, 104(4):1829–1837,, 2014. doi: 10.1785/0120130227.
- Nakata, R., Suda, N., and Tsuruoka, H. Non-volcanic tremor resulting from the combined effect of earth tides and slow slip events. *Nature Geoscience*, 1(10):676–678,, 2008. doi: 10.1038/ngeo288.
- Omerbashich, M. Astronomical alignments as the cause of m6+ seismicity. *preprint arXiv:1104.2036*, 2011. doi: 10.48550/arXiv.1104.2036.
- Peng, G., Lei, X., Wang, G., and Jiang, F. Precursory tidal triggering and b value variation before the 2011 mw 5.1 and 5.0 tengchong, china earthquakes. *Earth Planet. Sci. Lett*, 574:117,167,, 2021. doi: 10.1016/j.epsl.2021.117167.
- Rubinstein, J. L., Rocca, M., Vidale, J. E., Creager, K. C., and Wech, A. G. Tidal modulation of nonvolcanic tremor. *Science*, 319 (5860):186–189, 2008. doi: 10.1126/science.1150558.
- Safronov, A. N. Astronomical triggers as a cause of strong earthquakes. *International Journal of Geosciences*, 13(9):793–829,, 2022. doi: 10.4236/ijg.2022.139040.
- Schuster, A. On lunar and solar periodicities of earthquakes. *Proceedings of the Royal Society of London*, 61(369-377):455–465, 1897. doi: 10.1098/rspl.1897.0060.
- Service Checknews. Non, l'alignement des planètes n'annonce pas un séisme majeur à venir (lien signalé sur facebook), 2019. https://www.liberation.fr/checknews/2019/02/21/non-l-alignement-des-planetes-n-annonce-pas-un-seisme-majeur-a-venir-lien-signalé-sur-facebook_1710551/.
- Storchak, D. A., Di Giacomo, D., Bondar, I., Engdahl, E. R., Harris, J., Lee, W. H., Villasenor, A., and Bormann, P. Public release of the isc-gem global instrumental earthquake catalogue. *Seismol. Res. Lett*, 84(5):810–815, 2013. doi: 10.1785/0220130034.
- Storchak, D. A., Di Giacomo, D., Engdahl, E. R., Harris, J., Bondar, I., Lee, W. H., and Bormann, P. and Villasenor, A. The isc-gem global instrumental earthquake catalogue (1900– 2009): introduction. *Physics of the Earth and Planetary Interiors*, 239:48–63, 2015. doi: 10.1016/j.pepi.2014.06.009.
- Tanaka, S. Tidal triggering of earthquakes precursory to the recent sumatra megathrust earthquakes of 26 december 2004 (mw 9.0) and 12 september 2007 (mw 8.5). *Geophys. Res. Lett*, 37(2), 2010. doi: 10.1029/2009GL041581.
- Tanaka, S. Tidal triggering of earthquakes prior to the 2011 tohoku-oki earthquake (mw 9.1). *Geophys. Res. Lett*, 39(7), 2012. doi: 10.1029/2012GL051179.
- The Astropy Collaboration et al. The astropy project: building an open-science project and status of the v2. 0 core package. *The Astronomical Journal*, 156(3), 2018. doi: 10.3847/1538-3881/aabc4f.
- The Astropy Collaboration et al. The astropy project: sustaining and growing a community-oriented open-source project and the latest major release (v5. 0) of the core package. *The Astrophysical Journal*, 935(2), 2022. doi: 10.3847/1538-4357/ac7c74.
- Thomas, A., Burgmann, R., Shelly, D. R., Beeler, N. M., and Rudolph, M. Tidal triggering of low frequency earthquakes near park-field, california: Implications for fault mechanics within the brittle-ductile transition. *J. Geophys. Res*, 117(B5), 2012. doi: 10.1029/2011JB009036.
- Tsuruoka, H., Ohtake, M., and Sato, H. Statistical test of the tidal triggering of earthquakes: contribution of the ocean tide loading effect. *Geophys. J. Int*, 122(1):183–194, 1995. doi: 10.1111/j.1365-246X.1995.tb03546.x.
- U. S. Geological Survey. Earthquake Hazards Program, 2017, Advanced National Seismic System (ANSS) Comprehensive Catalog of Earthquake Events and Products: Various, 2017.
- Witze, A. Moon's pull can trigger big earthquakes, 2016.
- Yan, R., Chen, X., Sun, H., Xu, J., and Zhou, J. A review of tidal triggering of global earthquakes. *contemporary research in Geodynamics and Earth Tides*, 14(1), 2023. doi: 10.1016/j.geog.2022.06.005.
- Zaccagnino, D., Telesca, L., and Doglioni, C. Correlation between seismic activity and tidal stress perturbations highlights growing instability within the brittle crust. *Scientific Reports*, 12(1), 2022. doi: 10.1038/s41598-022-11328-z.
- Zanette, D. H. Comment on "astronomical alignments as the cause of m6+ seismicity". *preprint arXiv:1109.1240*, 2011. doi: 10.48550/arXiv.1109.1240.

The article *Could planet/sun conjunctions be used to predict large (moment magnitude ≥ 7) earthquakes?* © 2023 by P. Romanet is licensed under CC BY 4.0.

Curated Pacific Northwest AI-ready Seismic Dataset

Yiyu Ni *¹, Alexander R. Hutko ^{1,2}, Francesca Skene ¹, Marine A. Denolle ¹, Stephen D. Malone ^{1,2}, Paul Bodin ^{1,2}, J. Renate Hartog ^{1,2}, Amy K. Wright ^{1,2}

¹Department of Earth and Space Sciences, University of Washington, Seattle, WA, ²Pacific Northwest Seismic Network, Seattle, WA

Author contributions: *Conceptualization:* YN, MD. *Methodology:* YN, MD, AH. *Software:* YN. *Validation:* YN, AW, RH, AH, SM, PB. *Formal analysis:* YN. *Investigation:* YN, MD. *Resources:* MD. *Writing - original draft:* YN. *Writing - review & editing:* YN, MD, AH, RH, AW, SM, FS, PB. *Visualization:* YN, MD. *Supervision:* MD, SM. *Project administration:* MD. *Funding acquisition:* MD, RH.

Abstract The curation of seismic datasets is the cornerstone of seismological research and the starting point of machine-learning applications in seismology. We present a 21-year-long AI-ready dataset of diverse seismic event parameters, instrumentation metadata, and waveforms, as curated by the Pacific Northwest Seismic Network and ourselves. The dataset contains about 190,000 three-component (3C) waveform traces from more than 65,000 earthquake and explosion events, and about 9,200 waveforms from 5,600 exotic events. The magnitude of the events ranges from 0 to 6.4, while the biggest one is 20 December 2022 M6.4 Ferndale Earthquake. We include waveforms from high-gain (EH, BH, and HH channels) and strong-motion (EN channels) seismometers and resample to 100 Hz. We describe the earthquake catalog and the temporal evolution of the data attributes (e.g., event magnitude type, channel type, waveform polarity, and signal-to-noise ratio, phase picks) as the network earthquake monitoring system evolved through time. We propose this AI-ready dataset as a new open-source benchmark dataset.

Non-technical summary AI-ready datasets have been the primary drivers for developing machine learning algorithms. The diversity of the data these models are trained from is a leading factor for model performance and the potential for extrapolation or generalization. This work presents a curated AI-ready dataset of seismic events that were generated and recorded in the Pacific Northwest of the United States. The dataset contains metadata curated by the Pacific Northwest Seismic Network and waveforms from typical earthquakes, but also human-generated quarry blasts and sonic booms, and surface processes such as snow avalanches.

Introduction

The Pacific Northwest (PNW) region of the United States is a dynamic tectonic plate boundary between the North American continental plate and the Juan de Fuca oceanic plate. The active margin between the two plates is a subduction zone that hosts a wide variety of earthquake behaviors: fast and large megathrust earthquakes (Witter et al., 2003), intraslab earthquakes (Gene A. Ichinose, 2004), crustal earthquakes (Gomberg and Bodin, 2021), slow repeating earthquakes (Rogers and Dragert, 2003; Wech and Bartlow, 2014; Bartlow, 2020), tectonic tremor (Wech et al., 2010), and low-frequency events (A.A.Royer and M.G.Bostock, 2014). The PNW has over twenty active volcanoes that have experienced eruptions in the historical record. The PNW has hundreds of glaciers in the Cascades, the Olympic Peninsula, and sitting atop the Cascade Volcanoes. Due to the active tectonics and the particular mid-latitude climate, the PNW also experiences hundreds of landslides every year (Luna and Korup, 2022). Such geohazards generate seismic waves that are well recorded (Allstadt, 2013; Allstadt et al., 2018a; Hibert et al., 2019).

The Pacific Northwest Seismic Network (PNSN) is the

authoritative seismic network in the states of Washington and Oregon as part of the Advanced National Seismic System (ANSS), which is coordinated by the United States Geological Survey (USGS). PNSN started in 1969 with 5 seismometers and has more than 600 active seismic stations as of 1 November 2022. The authoritative boundaries of the seismic network are geographical (see Figure 3), but the Cascadia subduction zone is also active in Northern California and southern British Columbia (Ducellier and Creager, 2022; Dragert et al., 2001). The longevity of the seismic records and the richness of the active geohazards in the PNW form a unique opportunity to explore a vast range of seismic signatures. Comprehensive investigations that relate seismic signature to specific geohazards (Braun et al., 2020; Feng, 2012; Allstadt et al., 2018b; Hibert et al., 2019) benefit from curated datasets.

In recent years, machine learning has increasingly been used for applications in geosciences and seismology in particular. The rise of machine learning, especially deep learning, is largely due to the curation of several computer vision (ImageNet, Deng et al., 2009) and natural language processing (GLUE, Wang et al., 2018) datasets. There is a clear surge of machine-learning workflows in seismological research (Kong et al., 2019; Malfante et al., 2018; Bergen et al., 2019; Mousavi and

Production Editor:
Gareth Funning
Handling Editor:
Yen-Joe Tan
Copy & Layout Editor:
Théa Ragon

Received:
February 8, 2023
Accepted:
April 10, 2023
Published:
May 8, 2023

*Corresponding author: niyiyu@uw.edu

Beroza, 2022) that is driven by the high dimensionality of seismological data, the dramatic growth in data volumes (Hutko et al., 2017), and the effort by the community to curate seismic datasets. There exists today several curated datasets that have become standards for machine-learning seismological research: STEAD—a dataset of local and regional earthquakes and high-frequency noise recorded globally (Stanford Earthquake Dataset, Mousavi et al., 2019), INSTANCE (Italian seismic dataset for machine learning, Michellini et al., 2021), ETHZ (Eidgenössische Technische Hochschule Zürich, Woollam et al., 2022), SCEDC (Southern California Earthquake Data Center, SCEDC, 2013), and Iquique, a data collection of subduction-zone earthquakes and regional recordings (Woollam et al., 2019). These datasets contain earthquake and noise time series recorded by various seismometers. The typical data attributes are basic earthquake source and receiver characteristics, including locations, magnitudes, focal mechanisms, and waveforms. The majority of the earthquake sources in these datasets are of tectonic origins: transform plate boundaries such as in California, subduction zone, and intra-continental crustal earthquakes (Woollam et al., 2019; Michellini et al., 2021). Such datasets are considered “AI-ready” since their data and attributes are packaged in data formats commonly used by the Machine Learning community.

Surface processes may also generate seismic waves. Environmental seismology is a blooming field that utilizes seismic waves to understand surface and environmental processes. There is a body of research done on the seismic signatures of landslides events (Chmiel et al., 2021; Yan et al., 2020; Hibert et al., 2014), avalanche signals (Braun et al., 2020), and debris flows (Chmiel et al., 2021), most of which investigate specific case studies. Catalogs of such events are available in the Incorporated Research Institutions for Seismology (IRIS) Exotic Seismic Event Catalog (ESEC) (e.g., Allstadt et al., 2017; Bahavar et al., 2019; Collins et al., 2022); these refined and ground-truth catalogs only contain a few (~100) events.

Our study provides a novel curated AI-ready dataset of event and waveform data for a diverse range of short-duration seismic sources that include tectonic earthquakes, explosions, surface events such as ice/rock falls and avalanches, sonic booms, and thunderstorms. Not included are phenomena such as non-volcanic tremors or low amplitude low-frequency earthquakes (LFEs). We leverage the 21 years of data curation by the PNSN seismic analysts and researchers to measure the event P- and S-phase arrival times and other attributes. To enable optimal re-usability of our dataset for machine learning studies, we organized the dataset using the SeisBench data format (Woollam et al., 2022) to improve accessibility in the machine learning ecosystem. We acknowledge the accompanying human biases that often pollute AI-ready datasets (Paullada et al., 2021) are well present in our catalog of event and waveform attributes. Some of these identified biases are discussed below and are obvious topics of future investigations.

Data Selection and Preparation

The PNSN has been monitoring the seismicity in the PNW since 1969. However, seismic waveform data from PNSN were recorded on film and paper until 1980, when digital data became available. From 1980 to 2002, event-triggered waveform data (often with a limited duration) were saved, but continuous archiving did not start until 2002. For machine-learning applications, long seismic traces as input data are preferred to allow user flexibility when trimming and shifting the data in future investigations (e.g., data augmentation, Zhu et al., 2020). The data must also have the same dimensions, i.e., the same number of samples. To get waveforms that are long enough (i.e., 150 seconds and longer in this study), we start the curation when continuous data are available from IRIS Data Management Center (DMC) since 2002. The drawback of this choice is that it excludes the largest tectonic earthquakes in the region because they occurred before 2002 (e.g., Nisqually Earthquake of 28 February 2001). In addition, we require that both a P-wave arrival time and an S-wave arrival time information are available for the same station for each event. This requirement removes some of the smaller, older earthquakes for which no S-picks were available. In the context of AI-ready datasets, the associated metadata (labels or attributes) include event-derived parameters, station parameters, and waveform parameters. We use the SeisBench metadata format: Table 2 lists the attributes that we associate with each set of waveforms.

Event Parameters

The detection of new events is both automated and manually reviewed by the regional seismic network staff. The PNSN monitors and reports on the seismicity in the region using data from seismic stations (Figures S1 and S2). A trigger at a station occurs when the short-term-average-long-time-average of the seismic data (STA/LTA, Allen, 1982) exceeds a threshold. When a few stations from a designated geospatial group of seismic stations, called a subnet, experience a trigger, events are automatically saved. The PNSN analysts review all automatically detected events and remove erroneous ones by visual inspection of the event waveforms, a process they refer to as “trigger review”. Teleseisms are also identified but not further processed.

If the waveform has a clear but emergent signal, does not contain distinct P and S arrivals, and the frequency content is relatively low, the PNSN assigns a “surface event” label (su) to the source type. Most surface events are “ice”-quakes or avalanches associated with glaciers in the Cascades and on the volcanoes; however, some may be debris flows or rock falls. Other non-earthquake phenomena occasionally saved by analysts are recordings of sonic booms, thunderstorms, and other “interesting” events. Such waveforms are picked at very few nearby stations (one or two), and we gather the phase pick information in a catalog that we refer to as the “Exotic Event” catalog.

Once the trigger review identifies an event as an actual earthquake, the PNSN analysts further process the data. First, the automated system picks the ar-

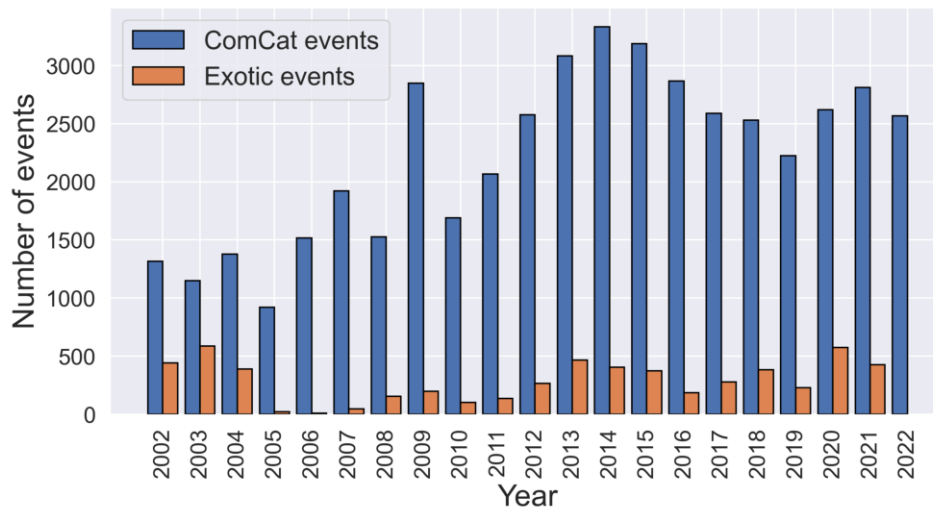


Figure 1 The event counts of ComCat and exotic catalog included in the AI-ready PNW dataset as a function of time.

rival times of seismic phases from the recorded seismograms, which are one of the most important and primary data products extracted from the raw waveforms. The analyst reviews and modifies the picks.

Seismic phase picking is the cornerstone of seismological research. With accurate phase arrival information, the analysts can locate the event and estimate its origin time. At the PNSN, the first P- and S-waves are the phases picked for local and regional events. As a part of the PNSN’s ANSS Quake Monitoring System (AQMS), the network analysts use Jiggle, a graphical user interface in Java to pick arrivals, locate events, and recalculate magnitudes (Hartog et al., 2019). The analysts will manually annotate the arrival time and estimate the uncertainties of their picks. The phase arrivals are only picked on a single component per station, with P-waves usually picked on vertical channels (Z component) and S-waves on horizontal channels (E/N or 1/2 components). When it is clear, the polarity (first motion is up–positive–, or down –negative–) of the P-phase is labeled by the analyst as well. Both acceleration and velocity channels are used for phase picking, although velocity channels are the most commonly used. The PNSN operates sites with both velocity channels (broadband or short-period high-gain seismometers) and acceleration channels (low-gain accelerometers used for “strong motion” seismology). Velocity channels are preferred when both instrument types exist since they usually have a higher signal-to-noise ratio than the strong-motion channel.

Additional earthquake characteristics may be obtained from the phase polarity and amplitudes, such as focal mechanisms and magnitudes. All event parameters are saved in PNSN’s AQMS database, and reasonably well-located earthquakes and explosions are reported to the ANSS Comprehensive Earthquake Catalog (ComCat, Survey, 2017) via USGS Product Distribution Layer (PDL), the software-server infrastructure that all the ANSS regional networks use to distribute earthquake products. It is important to note that the combination of automated tools, which get updated through time, and manual intervention renders the event pa-

rameters not statistically stationary over time.

This study splits the PNW catalog into several datasets: one that has PNSN analyst-verified event attributes that were sent to the USGS, which we refer to as the “ComCat event” dataset, one that we refer to as the “exotic event” dataset and that has remained internal in the PNSN AQMS database, and one that focuses on the 2022 Northern California earthquake sequence. These datasets are packaged in different files because they have different window lengths and data attributes. We collect and organize the data from these. We show in Figure 1 the annual event counts for the two sets of events, ComCat and exotic, that are selected for the curated dataset. The temporal patterns ought not to be interpreted as changes in seismicity rate since there are systematic biases in the detection and labeling of the events through time, whether they are human (analyst) or instrumental (increased instrumental coverage).

ComCat Events

We query the ANSS ComCat and download 65,384 events with magnitudes greater than 0 from 1 January 2002 to 31 December 2022, which we refer to as “ComCat events”. We only select the events from ComCat sent by the PNSN, whose event ID has a “uw” prefix. The event metadata, including phase picks, are downloaded using libcomcat (Hearne and Schovanec, 2020) and stored in the QuakeML format (v1.2, Schorlemmer et al., 2011). The source type of these events are either earthquakes or explosions. The download contains 997,213 associated phase picks. Among these picks, 944,220 were made on velocity channels and only 52,982 (5.3%) on strong-motion channels. For single-channel stations where only the vertical channel (Z) exists (e.g., EHZ), S-waves were also picked only if the onsets were clear. The temporal evolution of the ComCat events reflects a combination of increased coverage and sensitivity of the seismometers. In 2009, a large number of the cataloged events came from an intense swarm of earthquakes at Wooded Island in eastern Washington (Gomberg et al., 2012). As listed in Table 1, the number of events repre-

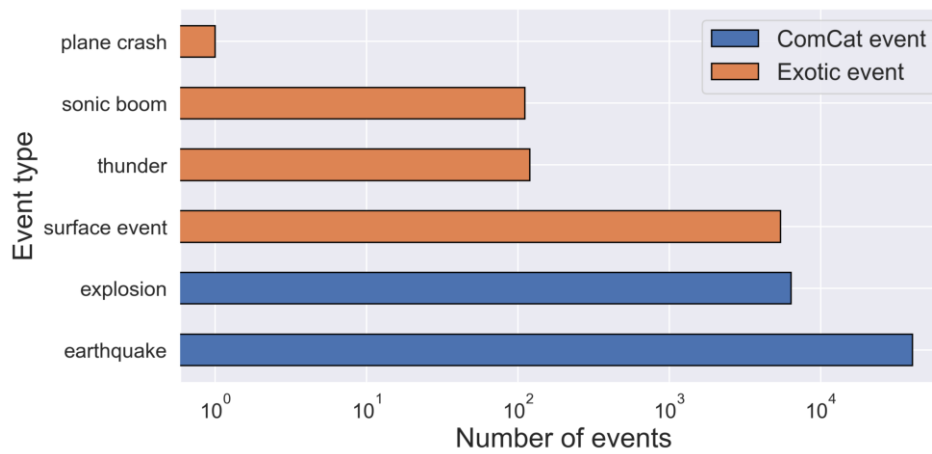


Figure 2 Number of events arranged by event type of the curated ComCat and Exotic event datasets.

sented in our final curated dataset is less than what we originally downloaded due to data selection criteria described in Section .

Exotic Events

We also collect data from 5,657 events cataloged by the PNSN since 2002 that are neither labeled as earthquakes nor explosions. The exotic events are not incorporated in the ANSS ComCat and are only available through the PNSN’s ANSS Earthquake Monitoring System (AQMS) database. In this dataset, we include events that were labeled as “surface event”, “thunder”, “sonic boom”, and unfortunately a “plane crash” (a confirmed event near Whidbey Island, Washington, 3 March 2013). We refer to these events as “exotic events” herein. Figure 2 shows the number of events in each category for our final dataset.

The temporal evolution of the exotic event catalog depends on manual intervention by the analysts. Because non-tectonic earthquakes are not the priority of the PNSN, analysts only pick when time permits. Most of the labeled exotic events, such as surface events, are detected on well-instrumented volcanoes (see Figure S2). The lower event count in the period 2005-2008 coincides with volcanic unrest at Mt. St. Helens, when the network was also desensitized during this period to the events around Mt. St. Helens due to the intense rate of volcano-tectonic seismicity. It is quite possible that other surface events outside of the volcanoes are missing, due to having fewer stations elsewhere.

Most of the exotic events are small in magnitude and seismic amplitude and thus local to a few stations. Due to a lack of additional observation of the events (e.g., a ground truth imagery as done in the ESEC catalog), source characteristics such as the source origin time, location, and magnitude are not provided for these events.

2022 Northern California Ferndale Earthquake Sequence

We also include events associated with the 20 December 2022 M6.4 Ferndale (northern California) Earthquake. This sequence provided us with a rare oppor-

tunity to add labels for moderate-to-large earthquake sizes. These events are outside of the PNSN’s authoritative boundary and, thus are not routinely processed by the network. We select 20 events of $M \geq 3$ reported by the California Integrated Seismic Network (CISN) from that sequence and manually pick 609 P-wave arrivals. Table S1 lists events included in the dataset.

Station Metadata

The station metadata describes the technical information necessary for seismic data processing and tracks the history of any metadata changes. The IRIS DMC stores station metadata as dataless SEED files, but they can be downloaded in the StationXML format from IRIS International Federation of Digital Seismograph Networks Web Service (FDSN-WS, <http://service.iris.edu/fdsnws>). The up-to-date station metadata we use is downloaded using ObsPy (Krischer et al., 2015). These stations are either long-term installations maintained by a seismic network (e.g., UW, University of Washington, 1963) or long-time experiments that lasts several years (e.g., US Transportable Array, FDSN code TA, IRIS Transportable Array, 2003).

Event Waveforms

All digitized data from the PNSN are requested and downloaded through the IRIS FDSN-WS. In total, we download ~70 TB of continuous data in miniSEED from 1 January 2002 to 31 December 2022, which takes 2 months to complete. We first curate waveforms from high-gain velocity seismometers and specific channels from short-period (EH?) and broad-band (either BH? or HH?) seismometers. We do not use the SL? and SH? channels since they are simply derived from EH? channel after low-pass filtering or down-sampling. We also include waveforms from strong-motion EN? stations separately since there are also picks made on these channels by the analysts. We do not correct for instrumental response and do not integrate the acceleration to velocity. All waveforms are resampled to 100 Hz from their original sampling rates, which may be 40 (most BH? channels) or 100 (most EH? and HH? channels).

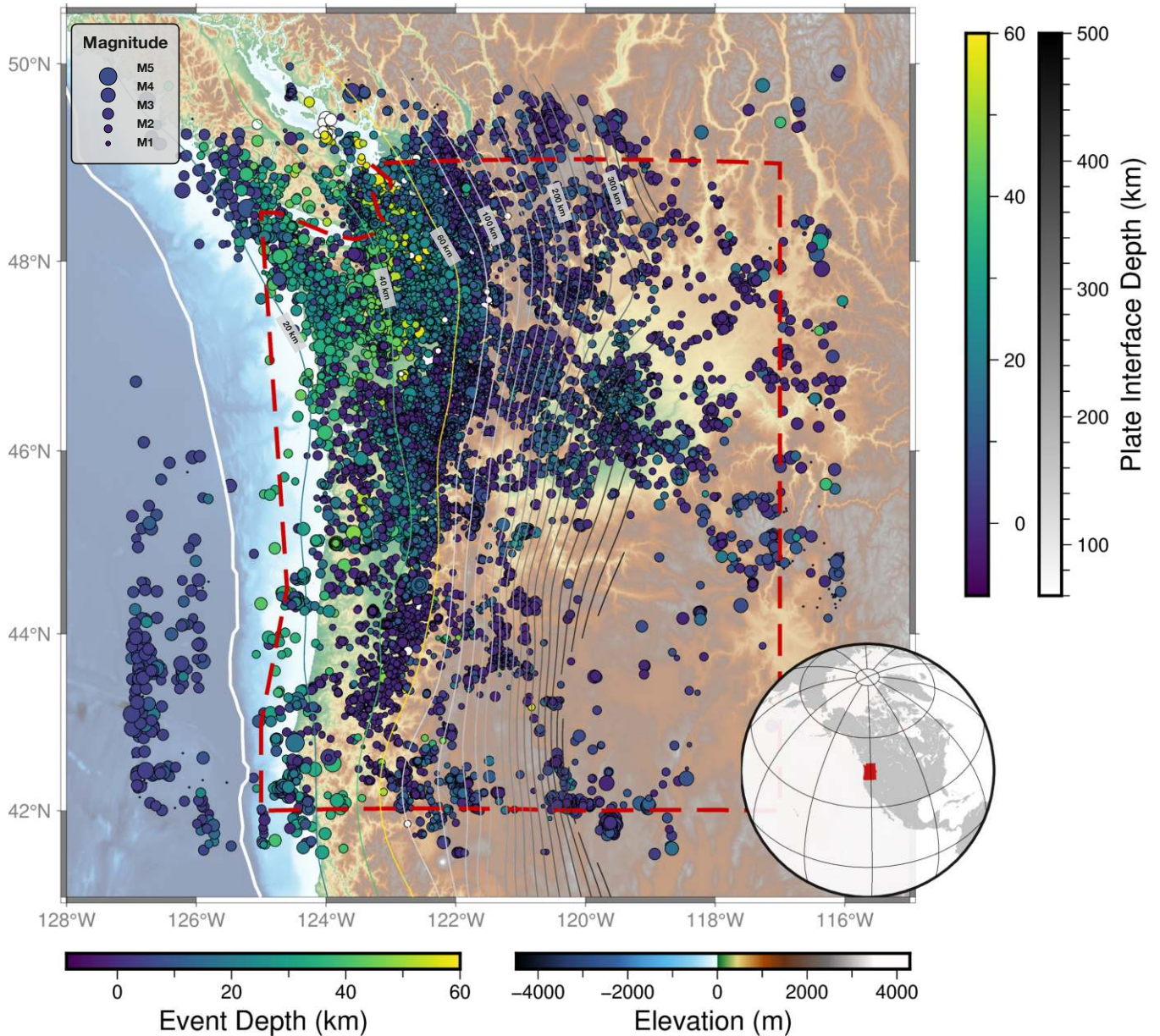


Figure 3 Locations of the events included in the ComCat dataset. The red dashed polygon denotes the authoritative region boundaries of PNSN. The solid lines mark the depth contour of the subduction slab with a 20 km interval Hayes (2018). Some contours are labeled by the slab depth. The plate boundary between Juan de Fuca and North America Plate (plate depth 0 km) is delineated in the white line. Some events are color-coded white because they are deeper than 60 km. These are intermediate-depth earthquakes.

The resampling step is necessary for deep neural networks with fixed input sizes. We keep the data as is, even if it is clipped.

For each ComCat event, we only select the stations where both P- and S-wave are picked. We prepare 150-second data for ComCat events: the window starts 50 seconds before and ends 100 seconds after the source origin time (200 seconds after the origin time for the Northern California earthquake sequence). The same length of traces before this time window is curated as the noise waveforms. The reason for including so much noise window ahead of the origin time is to allow user flexibility when trimming and shifting the data in future investigations. In the ComCat events, less than 1% of the S-wave picks arrive later than 60 seconds after the

origin time. Thus, most S-wave arrivals are included in the time window. Then, we apply a linear detrending. We also resample all waveforms to 100 Hz, which upsamples the broad-band BH? channels. Due to the small inaccuracy (~0.00008%) of the digitizer clock of the analog EHZ stations, the sampling rate at these stations shifts away from strictly 100 Hz. We correct this by resampling to 100 Hz. Gappy traces are discarded. Missing channels, for example, the vertical-component-only instruments (e.g., channel EHZ) are filled with zeroes to keep the consistency of a three-component stream (further detailed below). Picks are only done with data from a single instrument per site, even if a site may have several sensors. Therefore, each “stream” is independent of the other. Examples of earthquake waveforms can be

Magnitude range	Number of included events	Percentage of available events	Number of independent streams
0 - 1	19,735	77.1%	70,168
1 - 2	21,717	79.2%	95,406
2 - 3	4,825	42.8%	21,901
3 - 4	398 (15)	37.9%	2,332 (296)
4 - 5	31 (3)	77.5%	205 (138)
5 - 6	1 (1)	100.0%	4 (86)
6 - 7	0 (1)	N/A	0 (85)
0 - 7	46,707	71.4%	190,016

Table 1 Number of included ComCat events in each magnitude range. The magnitude used here includes duration (Md), local (Ml), and hand (Mh) magnitude. The number of streams includes both velocity and acceleration channels. Also provided is the number of included events as a percentage of downloaded ComCat events. Numbers in the parentheses show the events and streams from the 20 December 2022 Northern California earthquake sequence and are not included in the total number of events/streams.

found in Figure S3 and S4 for the velocity-seismograms and Figure S5 for the acceleration seismograms. Examples of explosion waveforms can be found in Figure S6, S7, and S8.

The PNSN operates seismic stations that are particularly remote. The transfer of data through telemetry sometimes leads to artifacts in the time series. Furthermore, the transition from triggered to continuous data was progressive. Sometimes, both triggered waveforms, which are detrended, and continuous data, which are unprocessed, are sent together: the triggered data overwrites the continuous data, creating a step in the data. These show in both short-period (EH?) and broad-band (BH? and HH?) stations. For example, the time series may contain offsets that could be corrected in the future in the seismic archive at the IRIS DMC (see Figures S9 and S10).

The waveforms extracted for an exotic event are not aligned with the source origin time, which is mostly unknown. Instead, we align the waveforms by the phase picks provided by the analysts. The waveforms start 70 seconds before P-wave picks or 80 seconds before S-wave picks, whichever is available. Most exotic events have no picked S-waves, but if both P- and S-wave picks exist, the P-wave is prioritized to align the time window. The time window is 180 seconds long for all types of exotic events, given the occasional long duration and elongation (e.g., cigar-shaped waveforms, Manconi et al., 2017) of the surface events. We follow the same data-curation process and formats as we process the ComCat events. Examples of surface-event waveforms can be found in Figure S11 and S12. Examples of thunderquakes can be found in Figures S13 and S14. Examples of sonic boom events are found in Figures S15 and S16, and all waveforms from the plane crash event in Figure S17.

We also extract noise-only waveforms. These waveforms are extracted just ahead of the event waveforms. We selected high-gain velocity channels (EH?, HH?, and BH?) using a random selection. To further test if there are hidden events in the noise waveforms, we run the machine learning model (see Section) to test whether events could be detected and only found very few occasions where events may have been present.

We organize the three-component waveforms into NumPy arrays and define a `stream` as a three-

component array (Harris et al., 2020; Krischer et al., 2015). To improve accessibility in the machine-learning ecosystem, we follow the SeisBench data format convention. The metadata is stored in CSV (comma-separated values) files, while all waveforms are stored in the Hierarchical Data Format version 5 (HDF5) format. The signal-to-noise ratios (SNR) are calculated (detailed below) and saved as attributes in the metadata file.

After applying the selection criteria described above, more than 70% of the ComCat events are kept in the dataset. Figure 3 shows the map of the selected events. The datasets cover events within the authoritative boundary of the PNSN, offshore in the Jan de Fuca Ridge, underneath Vancouver Island, and further East in Idaho. We provide an overview of the final number of ComCat waveforms and events in Table 1. The summary compiles the data volume across magnitudes from 0 to 6.4. It is possible that most of the events discarded by the selection had no S-wave picks for clipped waveforms. Our selection criteria also excluded more events before 2010, which we attribute to the much fewer S picks available when the data is clipped or when only vertical-component stations are available.

Machine Learning Phase Picker and Enhanced Earthquake Picks

We provide an alternative catalog of phase picks from the earthquake event catalog as a use-case of the dataset and a research-grade catalog of new picks of P and S waves using Machine Learning (ML). Automating phase picking using deep neural networks has revived the methodological development for picking seismic waves (Mousavi and Beroza, 2022; Münchmeyer et al., 2022).

Here, we use the Earthquake Transformer architecture from Mousavi et al. (2020) and implement phase-picking benchmark tests on the ComCat events. The SeisBench toolbox provides a set of Earthquake Transformer weights for models pre-trained with different datasets. We select all windowed waveforms from HH?, BH? and EH? channels and detrend the waveform. We compare the picks made by these models trained on STEAD, ETHZ, SCEDC, and INSTANCE datasets with the PNSN analyst picks recorded in the ComCat events. We demonstrate their performance by showing the residuals between ComCat picks and ML-predicted picks

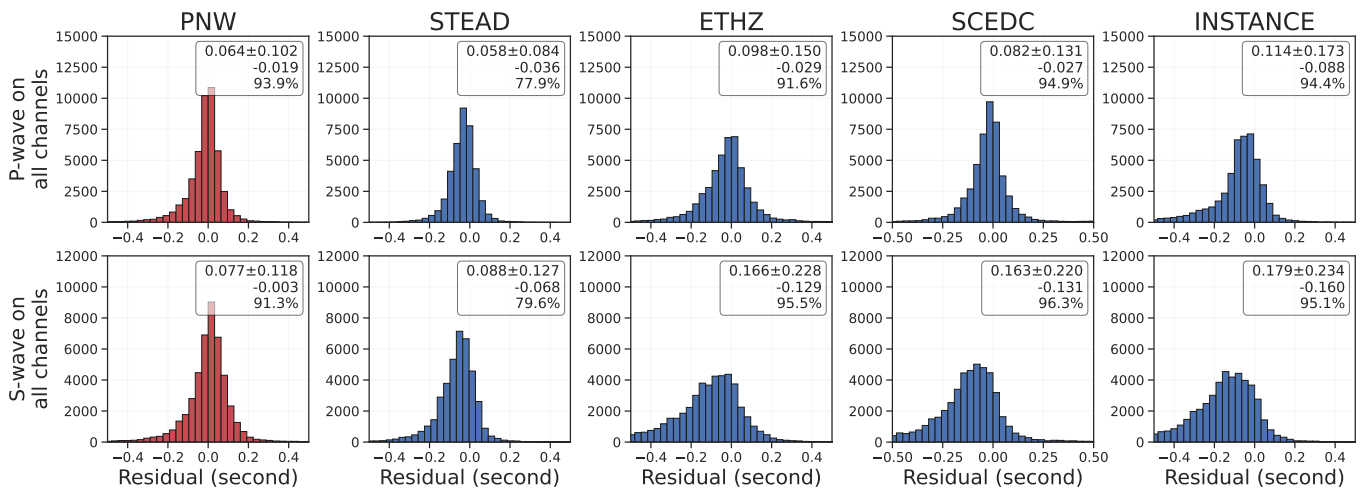


Figure 4 Distributions of P- and S-wave picking residuals ($t_{ML} - t_{PNSN}$) from the benchmark testing on velocity seismograms. The number in the upper right corner of each subplot shows the mean absolute error (MAE), the root-mean-square error (RMSE) as the uncertainties to the MAE, the mean value of the residual, and the picking completeness in percentage concerning the ground truth. The PNW-retrained Earthquake Transformer outperforms the other four pre-trained models from SeisBench (Woollam et al., 2022) in both picking accuracy and detecting completeness.

for P- and S-waves. The performance metrics are the mean absolute error (MAE), the root-mean-square error (RMS) for the phase picking, and the percentage of detected picks relative to ground truth picks.

The input size of the Earthquake Transformer using SeisBench is 3-component, 60 seconds at 100 Hz. The probability threshold for picking is 10%. Figure 4 shows the distributions of the residuals among models and for both P and S wave picks.

The approaches to benchmark the detection and picking performance are i) the seismic network-specific expectations for the manual picking uncertainties and ii) the comparison of bias and variance in the residual distributions relative to other studies (Mousavi et al., 2020; Münchmeyer et al., 2022). We find a general trade-off between detection accuracy (completeness) and phase-pick quality (low errors). The model trained with the STEAD dataset has the best quality in phase picks relative to the (ground truth) analyst’s picks, but it misses more than 20% of the detections. In contrast, the model trained with the SCEDC dataset had the best detectability and only missed about 5% of arrivals for both P- and S-waves, but the picking accuracy, especially that of S-waves, is poor. Both models show negative mean residuals for both P- and S-waves, indicating that the ML picks are always earlier than the manual picks. There is also a similar pattern on the model trained with ETHZ and INSTANCE dataset in Figure 4. The performance trade-off between detection and picking accuracy makes retraining the phase pickers using the PNW data necessary.

Using our curated dataset of ComCat earthquakes and explosions, we retrain the Earthquake Transformer model. Instead of training from scratch (randomly initialized weights), we start the training from the SeisBench-trained model, which used the STEAD dataset, and continue training for additional 100 epochs on our dataset. We note that about 3% of the STEAD data set contains PNSN data, which may be problematic for data leakage. However, the STEAD data is bandpass-

filtered 1-45 Hz, while we do not filter the data. We randomly select 70% of the ComCat dataset for training and use the rest 30% for testing. We use a triangular label with a 10-sample half-width. We use the same loss function that Mousavi et al. (2020) used to train the Earthquake Transformer (a weighted sum of loss from P-, S- and detection branches). We use a small learning rate (1×10^{-4}) with the Adam optimizer (Kingma and Ba, 2014) during the training. Compared with the other pre-trained models, the transfer-learning on the PNW dataset improves the detection accuracy, considerably improves the S-wave picks, and performs as well as the STEAD-trained dataset (see Figure 4). Although not eliminated, the negative mean residuals are reduced after retraining. We also test all these models on strong-motion (acceleration) channels, for which INSTANCE contains the most acceleration waveforms (28.3%). The PNW transfer-learned model outperforms other pre-trained models on strong-motion channels, as shown in Figure S18.

The ability to find more and accurate picks by the retrained Earthquake Transformer makes it possible to create a future Machine-Learning-enhanced earthquake catalog. We revisit waveforms from the ComCat events that included either P or S picks. There are 683,133 P- and 244,431 S-wave picks for 62,054 events from these waveforms. We detect 16,201 (2%) and 207,146 (85%) new arrivals out of 686,748 time windows for P- and S-waves using the refined phase picker. As a crude quality control, we remove the picks where the ratio between the S-travel time and the P-wave travel time exceeds 2.5 or below 1.5. We add these picks with PNSN manual picks as a part of the curated dataset in a separate file. We also use this retrained model to predict the noise waveform and drop those with any prediction greater than 0.1. This step effectively removes unpicked seismic events in the noise waveform.

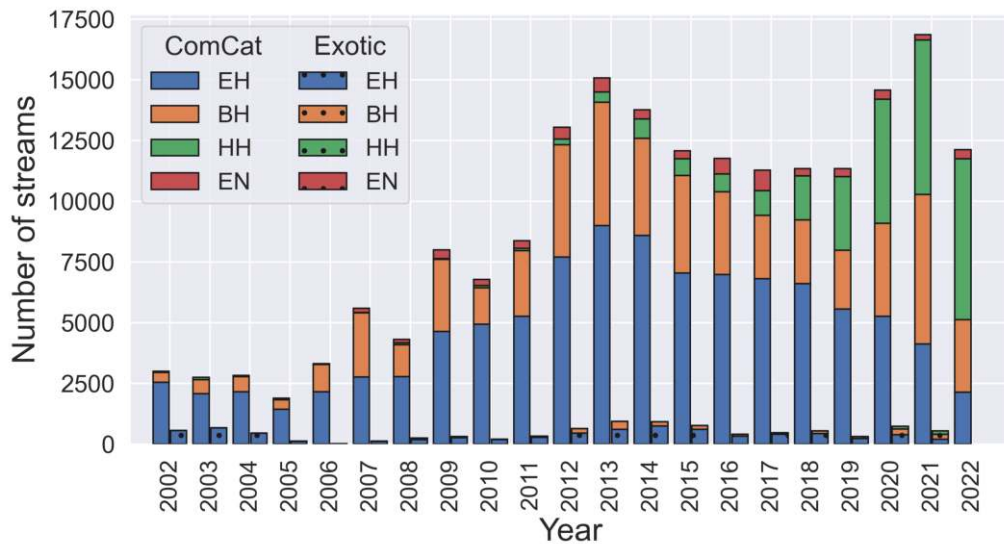


Figure 5 Number of streams from each channel type used in the ComCat and exotic event catalogs through time. Short-period (EH?) and broad-band (BH?) sensors were the predominant channels for both ComCat and exotic datasets before 2012, while the recording at higher sampling rates at broadband sensors (HH?) increasingly has become the standard since then. A limited number of streams from strong-motion accelerometer EN? channels is available in the dataset since 2007.

Description of the AI-ready Dataset

The datasets consist of two files per set, one HDF5 file containing the waveforms and a CSV file with the metadata (attributes).

Waveforms

There are 190,016 and 9,267 three-component streams curated from ComCat and exotic event catalogs, respectively. Figure 5 shows the counts of streams arranged by channel type as a yearly estimate. We store all waveforms in HDF5 files using h5py (Collette et al., 2021) and index them by the trace name in the metadata. The attribute `trace_start_time` in YYYY-MM-DDTHH:MM:SS.SSSZ format describes the UTC time at which the stream begins. Listing 1 illustrates how users can read the waveform data and locate the stream in Python.

Listing 1 Read stream data from SeisBench format waveform file using h5py

```
import h5py
f = h5py.File("/path/to/waveform.hdf5", "r")
trace_name = "bucket1$0,:3,:15001"
bucket, array = trace_name.split('$')
x, y, z = iter([int(i) for i in array.split(',')])
data = f[f'/data/{bucket}'][x, :y, :z]
```

The data is saved as vertical concatenated NumPy arrays of fixed window length (here 150 s), three components. It is distributed over several “buckets” that are “groups” under the HDF5 taxonomy. The trace name (a data attribute saved in the metadata data frame), the index of the data in the bucket, and the index of the first dimension.

Metadata

The metadata describes the waveform data and its attributes and is essential to our dataset. Each stream corresponds to one record (or a row) in the metadata file. We follow SeisBench conventions again. The unit of each attribute is appended as part of the attribute’s name. For example, `source_latitude_deg` indicates the latitude of the source in degrees. A full description of the attributes is listed in Table 2. As many attributes are self-explanatory, we provide more details below.

Station Network Code

Stations selected in both datasets may come from nine different FDSN network codes. These stations are either installed and maintained by PNSN (e.g., UW and UO) or used by PNSN when doing phase picking and events locating (e.g., PB, CC, IU, CN, HW, TA, US). Maps of the stations shown in the dataset show a similar distribution for both ComCat (Figure S1) and exotic events (Figure S2). All stations are in-land stations, and no off-shore stations (e.g., OOI) are used in our dataset. The numbers of streams from each FDSN network and their references are listed in Table 3. PNSN stations contribute more than 85% of streams in the ComCat and Exotic event datasets.

Event ID

An event identifier (ID) is given to each event by the PNSN after the processing is finalized and sent to ANSS through USGS Product Distribution Layer (PDL). The ComCat events contributed by the PNSN have IDs of eight-digit numbers with a “uw” prefix, e.g., “uw10568488”. The event IDs are unique in the catalog. The exotic event IDs are internal to the PNSN AQMS database and cannot be accessed through USGS.

Attribute	Description	Example
event_id	Event identifier	uw10564613
source_origin_time	Source origin time in UTC	2002-10-03T01:56:49.530000
source_latitude_deg	Source latitude in degree	48.553
source_longitude_deg	Source longitude in degree	-122.52
source_type	-	earthquake
source_type_pnsn_label	PNSN AQMS event type	eq
source_depth_km	Source latitude in kilometer	14.907
source_magnitude_preferred	-	2.1
source_magnitude_type_preferred	-	Md
source_magnitude_uncertainty_preferred	-	0.03
source_local/duration/hand_magnitude	MI, Md, and Mh if available	1.32
source_local/duration_magnitude_uncertainty	Magnitude uncertainty if available	0.15
source_depth_uncertainty_km	Source depth uncertainty in kilometer	1.69
source_horizontal_uncertainty_km	Source horizontal uncertainty in kilometer	0.694
station_network_code	FDSN network code	UW
station_code	FDSN station code	GNW
station_location_code	FDSN location code	01
station_channel_code	FDSN channel code (first two digits)	BH
station_latitude_deg	Station latitude in degree	47.5641
station_longitude_deg	Station longitude in degree	-122.825
station_elevation_m	Station elevation in meter	220.0
trace_name	Bucket and array index	bucket1\$0,:3:15001
trace_sampling_rate_hz	All traces resampled to 100 Hz	100
trace_start_time	Trace start time in UTC	2002-10-03T01:55:59.530000Z
trace_P/S_arrival_sample	Closest sample index of arrival	8097
trace_P/S_arrival_uncertainty_s	Picking uncertainty in second	0.02
trace_P/S_onset	P- or S-wave onset	emergent
trace_P_polarity	P-wave arrival polarity	positive
trace_has_offset	Any visible offset in the trace	0 or 1
trace_missing_channel	Number of missing channel of the trace	0, 1, or 2
trace_snr_db	SNR for each component	6.135 3.065 11.766

Table 2 Attributes in the metadata file. Some source attributes are not available for exotic events.

To distinguish them from ComCat events, we add a “pnsn” prefix to their event IDs.

Event Type

When processing a seismic event as the seismic data comes in, the event type is manually specified by the network analysts. For example, the PNSN labels “probable explosion” waveforms that have the characteristics of shallow quarry blasts (strong P waves and location near known quarries). Until the 1990s, the PNSN would confirm these explosions by phone confirmation, though this is no longer routinely done. When sending the finalized event from the AQMS database to the ComCat, PNSN maps and merges several types of events into one: “earthquake”, “slow earthquake”, and “long period volcanic earthquake” are mapped into the “earthquake” category; “explosion”, “shot” and “probable explosion” are merged into the “explosion” category. For simplicity and consistency, we use the event types “earthquake” and “explosion” for the ComCat events, but their original event types are also included for reference in the metadata. Table S2 lists the latest PNSN event-type labels from the PNSN AQMS database.

Source Magnitude and Type

The event size, as represented by the source magnitude, is only available for the ComCat events. All ComCat events included in the dataset have magnitudes less

than seven and greater than zero, as shown in Table 1. The magnitude completeness of the catalog is estimated using the method of [Wiemer and Wyss \(2000\)](#) and found to be around 2 for the years 2019-2022 (Figure S19). The types of magnitudes reported are typical to regional earthquakes that have local seismicity: the local magnitude (MI) and the duration magnitude (Md).

There are three types of magnitude used in the dataset. The PNSN uses a local magnitude (MI, [Richter, 1958](#); [Jennings and Kanamori, 1983](#)) that measures the magnitude of a local earthquake using the average maximum amplitudes of two horizontal seismograms converted to have the Wood-Anderson response, preferably taken from broad-band seismometers, and corrected for the distance between the source and the receiver. Such magnitude is reported by the National Earthquake Information Center (NEIC) for all earthquakes in the US and Canada. The coda duration magnitude Md is calculated based on the duration of shaking measured on the vertical component and could be the only available magnitude product for small events or those not well recorded on well-calibrated stations with horizontal components. Over the course of time, processes to calculate the magnitudes vary because of varied processing routines and analyst interventions.

Until 2012, the PNSN only reported duration magnitude to ComCat for most earthquakes using the algorithm from [Crosson \(1972\)](#), except for a few significant events that were manually changed to the local magni-

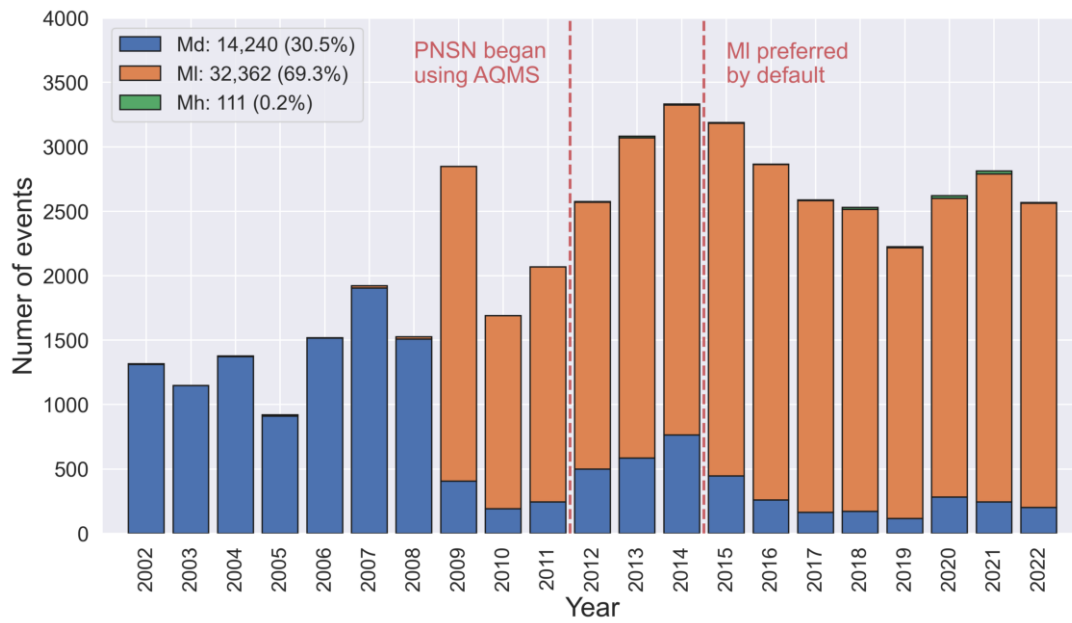


Figure 6 Magnitude types of ComCat events as a function of time. Md and MI denote duration and local magnitudes, respectively. Mh denotes magnitudes manually inserted by the analysts. Before the PNSN began using the ANSS Earthquake Monitoring System (AQMS) in 2012, 483 events had MI estimates, and 46,326 events had Md estimates in the dataset.

tude. The early seismic stations of the PNSN only had vertical components, a small dynamic range, and short-period sensors that would clip even for relatively small magnitude events. It is not possible to obtain a local magnitude from such data. As the network modernized over time, higher dynamic-range three-component sensors were added, and the data quality improved, which allowed PNSN to determine an MI for more events. From 2002 to 2011, 46,326 events had duration magnitude preferred, while only 483 events (average magnitude 2.45) had local magnitude reported as the preferred magnitude type. From 2012 to 2015, the PNSN calculated and reported both duration and local magnitudes, though the local magnitude was still only calculated for larger events. Since 2015, the PNSN has switched from having duration magnitude to the local magnitude as the preferred and default magnitude. 80% of all events included in the ComCat dataset until 2008 have a duration magnitude preferred, after when there were increasingly more MI-preferred magnitudes (Figure 6). While the duration magnitude is still calculated, it is only the preferred magnitude for about 10% of the events each year. From 2002 to 2022, there were also 111 events with an Mh magnitude in the dataset, extracted from the NEIC and manually added by the network analysts. Note that there is no moment magnitude Mw reported in this dataset because the moment magnitude is obtained from low-frequency seismograms, which are often buried in the seismic noise for small earthquakes. Mw magnitude may be included as Mh.

There are potential challenges in interpreting the magnitudes as ground truth labels. Md and MI have known systematic biases that arise from the particularly high near-source scattering of shallow earthquakes or quarry blasts (Koper et al., 2020; Wang et al., 2021). In 2012, the PNSN adopted AQMS, which included a method to measure coda duration that was inconsis-

tent with the previously used method. The PNSN staff did a rough recalibration of their Md relationship to partially account for the systematic difference. However, there is a known inconsistency of the Md magnitudes for the smallest events before 2012 and after 2012. Future efforts must be made to re-calculate the magnitudes more systematically, ideally using consistent methods, throughout the 2002-2022 period.

Table 1 shows the event counts per magnitude bin for this dataset. The largest event in the dataset comes from Mw 6.4 Northern California, 20 December 2022 by the CISM, but this event was outside the PNSN’s authoritative boundaries. Thus, ComCat preferred an origin contributed by CISM. The largest earthquake in this dataset within PNSN’s authoritative boundaries is Md 4.8 Brinnon, Washington, on 25 April 2003 (event ID uw10583988). Relatively small magnitude uncertainty (0.04), depth uncertainty (0.59 km), and horizontal uncertainty (0.347 km) were reported.

Stream Signal-to-Noise Ratio

The signal-to-noise ratio (SNR) is an important factor in measuring the noise level in the traces. Similar to Michelini et al. (2021), we define the noise window as 8 seconds before the P-wave arrival for the ComCat events. To better capture the energy of emergent S-wave onsets, the signal window is defined as 1 second before to 2 seconds after the S-wave arrival. For the exotic event catalog, since P-wave and S-wave arrivals may not be available, the noise window is defined to begin 12 seconds after the beginning of the traces. The signal window is the same as exotic events, P- or S-wave, whichever is available. For each component, the SNR is defined as

$$SNR = 20 \log_{10} \frac{|S_{98}|}{|N_{98}|} \tag{1}$$

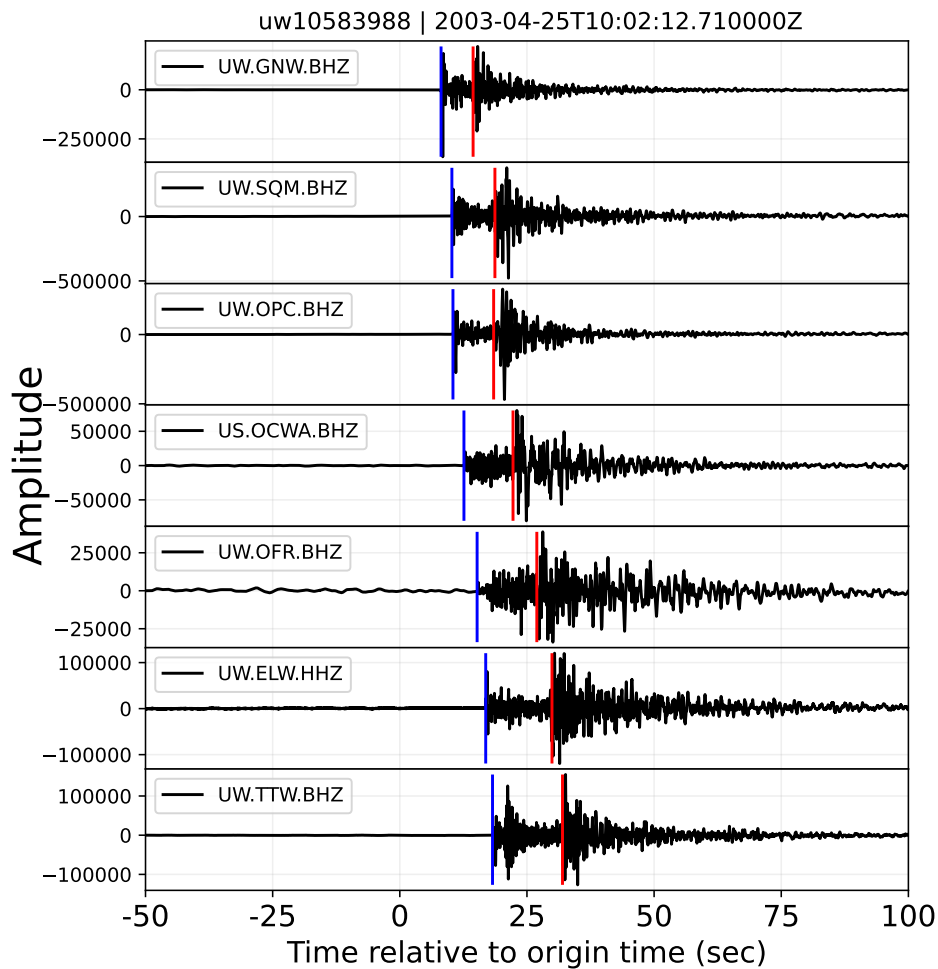


Figure 7 Waveform from event uw10583988 (M4.8 Brinnon, Washington, 25 April 2003) included in the dataset. Only the vertical component is shown. The blue and red vertical lines show P- and S-wave arrival picked, respectively. The amplitude units are in counts.

where $|S_{98}|$ and $|N_{98}|$ are the 98% percentile of the absolute values in the signal and noise window, respectively. When no data is available, e.g., a single-channel station with only the EHZ channel, NaN (not-a-number) is filled as a placeholder in the missing channels. Figure 8 shows the distribution of individual SNRs calculated from the ComCat and exotic event catalogs. The traces with $\text{SNR} > 80 \text{ db}$ (indicating an error in the noise window) or $< -20 \text{ db}$ (indicated too low of a signal) are removed from the dataset.

Uncertainties

The metadata includes four types of uncertainties for the ComCat events. The P- and S-waves arrival uncertainties are estimated at the time of picking. Before the PNSN used AQMS, the uncertainty was directly measured and recorded in the phase data, and a weight was calculated. Using Jiggle from AQMS since 2012, the analysts assign weight as an integer ranging from zero to four to each pick by visually measuring the impulsivity of the arrival. A zero weight indicates the highest accuracy of picks, typically for P-wave arrivals, and has 0.03 seconds of uncertainty. A weight of three indicates a low pick accuracy, typically for S-wave arrival with 0.3 seconds of uncertainty. Phase uncertainties

are used when locating the events, but those with uncertainty weights of four are typically not used in earthquake locations. Before 2012, PNSN used Spong (an adaption of Fasthypo, Herrmann, 1979) as the location engine. This changed to HYPOINVERSE (Klein, 2002) after PNSN started using AQMS and Jiggle.

The origin location (depth and horizontal) uncertainties are the error estimated from the location engine. Figure S28 shows the locations of the events with horizontal uncertainty greater than 20 km. Note the cluster off-shore Oregon that is outside of the PNSN authoritative boundaries. The PNSN has poor location constraints on these events since there are almost no off-shore seismic stations except for the Ocean Observatories Initiative Regional Cable Array (FDSN network code OO, Rutgers University, 2013), which are occasionally picked during PNSN routine data processing. ComCat may not choose these origin products from PNSN as preferred. However, the events with high horizontal uncertainty only make up 0.4% of all ComCat events, and their picks are still accurate enough to be part of the dataset.

We also include the magnitude uncertainties in the metadata. The magnitude is first evaluated on the channel level. For three-component stations, the channel-level local magnitude is calculated only if a P- or S-

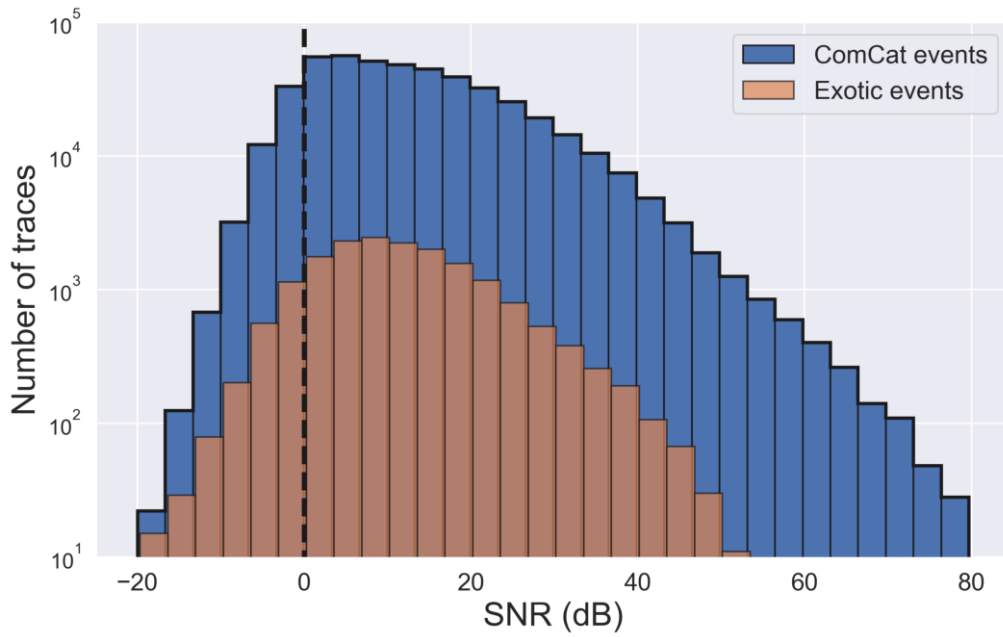


Figure 8 Distribution of signal-to-noise ratios (SNR) of the traces from ComCat and exotic events. SNRs are calculated on each component of the three-component streams.

Network FDSN Code	Number of Streams	Reference
UW*	100,561 5,653 26,716	University of Washington (1963)
PB	41,674 461 11,126	Plate Boundary Observatory Borehole Seismic Network
CC	23,988 3,119 6,784	Cascades Volcano Observatory (2001)
TA	9,912 4 3,012	IRIS Transportable Array (2003)
CN	6,008 2 1,692	Natural Resources Canada (NRCAN Canada) (1975)
US	3,420 0 981	Albuquerque Seismological Laboratory (ASL)/USGS (1990)
UO*	3,593 28 891	University of Oregon (1990)
HW	840 0 252	Hanford Washington Seismic Network
IU	20 0 4	Albuquerque Seismological Laboratory (ASL)/USGS (1988)

Table 3 Description of network FDSN code and their references. Networks annotated by an asterisk mark (*) are maintained by the PNSN. The number of streams shown for each network is from ComCat events, exotic events, and noise, respectively. PB and HW network does not have a registered FDSN network DOI.

wave is picked on one of the components to only select clear signals. Since 2012, a few single-component stations (EHZ) also contribute to the local magnitude and have the same weight as three-component stations. The event magnitude is the median of all channel magnitudes that meet the SNR criteria. The event magnitude uncertainty is the median absolute deviation (MAD) of channel magnitudes used for event magnitude calculation. These uncertainties are calculated for all magnitude types except Mh.

P-wave Polarity

When analysts pick the phase arrivals, Jiggle also automatically measures the first motion of the P-wave picks with weights less than one (e.g., best waveforms), leaving the rests as “undecidable”. The analysts can manually override these polarities if they are confident. Less than 42% of P-waves in this dataset have undecidable polarity information. The P-wave polarity ratio between positive and negative as a function of the year is shown in Figure S20. The sudden switch to a preference to assign or report positive polarities in 2012 highly suggests

that the switch to AQMS and Jiggle in 2012 has affected the PNSN analysts’ output. Until this data collection effort, we were unaware of this fact, and the reason for the abrupt change is unclear.

Conclusion

This work contributes to collecting and curating a seismic dataset for the Pacific Northwest region. The curated dataset is provided with the long-standing work and labeling of the Pacific Northwest Seismic Network analysts and seismologists. We described the temporal and spatial characteristics of the data attributes.

This original contribution focused on preparing the seismic waveforms and PNSN-provided data attributes (phase picks and default source parameters). We picked additional waveforms for the recent 20 December 2022 Northern California earthquake sequence, the largest event recorded recently in proximity to the PNSN authoritative boundaries. We also transfer-learned an established phase picker, the Earthquake Transformer (Mousavi et al., 2020), on the best quality of the PNSN picks and provided additional picks for S waves, which

we provided in this contribution as an alternate catalog of picks.

There remains tremendous work to improve the quality and consistency of the data attributes. We use version control on the curated dataset through GitHub to allow for future development of the data and metadata (Ni, 2023). Examples of future developments may be a refinement of the current attributes or the addition of new labels. In particular, the attribute “magnitude” should be carefully interpreted as 60% of the catalog uses duration magnitude, and 40% of the catalog uses the local magnitude, but both may have biases. Therefore, a follow-up task is to re-calculate these magnitudes using consistent methods. Another avenue for improvement is to re-estimate the polarity of the P and S waves, using the known labels and predicting the “undecided” labels. Furthermore, we have not yet included other types of tectonic events, such as low-frequency earthquakes (Ducellier and Creager, 2022), but these would improve the diversity of events. Finally, an obvious next step will be event classification work that will take the waveforms and predict the event type.

Acknowledgements

Funding was provided by the PNSN (USGS cooperative agreement G20AC00035), the NSF SCOPED award (EAR-2103701), and a fellowship to MD by the David and Lucile Packard Foundation. We thank two anonymous reviewers for their comments and suggestions to improve the manuscripts.

Code and Data Availability

The facilities of IRIS Data Services, and specifically the IRIS Data Management Center, were used for access to waveforms, related metadata, and derived products used in this study. IRIS Data Services are funded through the Seismological Facilities for the Advancement of Geoscience (SAGE) Award of the National Science Foundation under Cooperative Support Agreement EAR-1851048. The earthquake catalog on ComCat contributed by PNSN was downloaded using libcomcat (Hearne and Schovanec, 2020). The Earthquake Transformer implementation is from the SeisBench toolbox (Woollam et al., 2022). All plots are made with Matplotlib (Hunter, 2007) and PyGMT (Uieda et al., 2021). The final datasets and the codes used in this study are available at <https://github.com/niiyiyu/PNW-ML> (Ni, 2023), and we are working to make the dataset available through SeisBench at <https://github.com/seisbench/seisbench>.

References

- A.A.Royer and M.G.Bostock. A comparative study of low frequency earthquake templates in northern Cascadia. *Earth and Planetary Science Letters*, 402:247–256, 2014. doi: 10.1016/j.epsl.2013.08.040.
- Albuquerque Seismological Laboratory (ASL)/USGS. Global Seismograph Network - IRIS/USGS, 1988. <https://www.fdsn.org/networks/detail/IU/>.
- Albuquerque Seismological Laboratory (ASL)/USGS. United States National Seismic Network, 1990. <https://www.fdsn.org/networks/detail/US/>.
- Allen, R. Automatic phase pickers: Their present use and future prospects. *Bulletin of the Seismological Society of America*, 72(6B):S225–S242, 1982. doi: 10.1785/BSSA07206B0225.
- Allstadt, K. Extracting source characteristics and dynamics of the August 2010 Mount Meager landslide from broadband seismograms. *Journal of Geophysical Research: Earth Surface*, 118(3): 1472–1490, 2013. doi: <https://doi.org/10.1002/jgrf.20110>.
- Allstadt, K., McVey, B., and Malone, S. Seismogenic landslides, debris flows, and outburst floods in the western United States and Canada from 1977 to 2017: US Geological Survey data release, 2017.
- Allstadt, K. E., Matoza, R. S., Lockhart, A. B., Moran, S. C., Caplan-Auerbach, J., Haney, M. M., Thelen, W. A., and Malone, S. D. Seismic and acoustic signatures of surficial mass movements at volcanoes. *Journal of Volcanology and Geothermal Research*, 364:76–106, 2018a. doi: <https://doi.org/10.1016/j.jvolgeores.2018.09.007>.
- Allstadt, K. E., Matoza, R. S., Lockhart, A. B., Moran, S. C., Caplan-Auerbach, J., Haney, M. M., Thelen, W. A., and Malone, S. D. Seismic and acoustic signatures of surficial mass movements at volcanoes. *Journal of Volcanology and Geothermal Research*, 364: 76–106, 2018b. doi: 10.1016/j.jvolgeores.2018.09.007.
- Bahavar, M., Allstadt, K. E., Van Fossen, M., Malone, S. D., and Trabant, C. Exotic seismic events catalog (ESEC) data product. *Seismological Research Letters*, 90(3):1355–1363, 2019. doi: 10.1785/0220180402.
- Bartlow, N. M. A long-term view of episodic tremor and slip in Cascadia. *Geophysical Research Letters*, 47(3):e2019GL085303, 2020. doi: 10.1029/2019GL085303.
- Bergen, K. J., Johnson, P. A., de Hoop, M. V., and Beroza, G. C. Machine learning for data-driven discovery in solid Earth geoscience. *Science*, 363(6433):eaau0323, 2019. doi: 10.1126/science.aau0323.
- Braun, T., Frigo, B., Chiaia, B., Bartelt, P., Famiani, D., and Wassermann, J. Seismic signature of the deadly snow avalanche of January 18, 2017, at Rigopiano (Italy). *Scientific reports*, 10(1): 1–10, 2020. doi: 10.1038/s41598-020-75368-z.
- Cascades Volcano Observatory/USGS. Cascade Chain Volcano Monitoring, 2001. <https://www.fdsn.org/networks/detail/CC/>.
- Chmiel, M., Walter, F., Wenner, M., Zhang, Z., McArdell, B. W., and Hibert, C. Machine learning improves debris flow warning. *Geophysical Research Letters*, 48(3):e2020GL090874, 2021. doi: 10.1029/2020GL090874.
- Collette, A., Kluyver, T., Caswell, T. A., Tocknell, J., Kieffer, J., Scopatz, A., Dale, D., Chen, Jelenak, A., payno, juliagarriga, VINCENT, T., Sciarrelli, P., Valls, V., Ghosh, S., Pedersen, U. K., jakirkham, Raspaud, M., Parsons, A., Abbasi, H., Readey, J., Paramonov, A., Chan, L., Solé, V. A., jialin, Danilevski, C., Feng, Y., Vaillant, G. A., Teichmann, M., and Brucher, M. h5py/h5py: 3.2.1. doi: 10.5281/zenodo.4584676.
- Collins, E., Allstadt, K., Groult, C., Hibert, C., Malet, J., Toney, L., and Bessette-Kirton, E. Seismogenic Landslides and other Mass Movements: US Geological Survey data release, 2022.
- Crosson, R. S. Small earthquakes, structure, and tectonics of the Puget Sound region. *Bulletin of the Seismological Society of America*, 62(5):1133–1171, 1972. doi: 10.1785/BSSA0620051133.
- Deng, J., Dong, W., Socher, R., Li, L.-J., Li, K., and Fei-Fei, L. Imagenet: A large-scale hierarchical image database. In *2009 IEEE conference on computer vision and pattern recognition*, pages

- 248–255. Isee, 2009. doi: 10.1109/CVPR.2009.5206848.
- Dragert, H., Wang, K., and James, T. S. A silent slip event on the deeper Cascadia subduction interface. *Science*, 292(5521): 1525–1528, 2001. doi: 10.1126/science.1060152.
- Ducellier, A. and Creager, K. C. An 8-Year-Long Low-Frequency Earthquake Catalog for Southern Cascadia. *Journal of Geophysical Research: Solid Earth*, 127(4):e2021JB022986, 2022. doi: 10.1029/2021JB022986.
- Feng, Z.-y. The seismic signatures of the surge wave from the 2009 Xiaolin landslide-dam breach in Taiwan. *Hydrological Processes*, 26(9):1342–1351, 2012. doi: 10.1002/hyp.8239.
- Gene A. Ichinose, Hong Kie Thio, P. G. S. Rupture process and near-source shaking of the 1965 Seattle-Tacoma and 2001 Nisqually, intraslab earthquakes. *Geophysical Research Letters*, 31(10): 1–4, 2004. doi: 10.1029/2004GL019668.
- Gomberg, J. and Bodin, P. The productivity of Cascadia aftershock sequences. *Bulletin of the Seismological Society of America*, 111(3):1494–1507, 2021. doi: 10.1785/0120200344.
- Gomberg, J., Sherrod, B., Trautman, M., Burns, E., and Snyder, D. Contemporary seismicity in and around the Yakima Fold-and-Thrust belt in eastern Washington. *Bulletin of the Seismological Society of America*, 102(1):309–320, 2012. doi: 10.1785/0120110065.
- Harris, C. R., Millman, K. J., Van Der Walt, S. J., Gommers, R., Virtanen, P., Cournapeau, D., Wieser, E., Taylor, J., Berg, S., Smith, N. J., et al. Array programming with NumPy. *Nature*, 585(7825): 357–362, 2020. doi: 10.1038/s41586-020-2649-2.
- Hartog, J., Friberg, P., Kress, V., Bodin, P., and Bhadha, R. Open-Source ANSS Quake Monitoring System Software. *Seismological Research Letters*, 91:677–686, 2019. doi: 10.1785/0220190219.
- Hayes, G. Slab 2 - A Comprehensive Subduction Zone Geometry Model, 2018. <https://www.sciencebase.gov/catalog/item/5aa1b00ee4b0b1c392e86467>. Type: dataset.
- Hearne, M. and Schovanec, H. E. libcomcat Software Release, 2020. <https://github.com/usgs/libcomcat/>. Medium: Other.
- Herrmann, R. B. FASTHYPO—a hypocenter location program. *Earthquake notes*, 50(2):25–38, 1979. doi: 10.1785/gssrl.50.2.25.
- Hibert, C., Ekström, G., and Stark, C. P. Dynamics of the Bingham Canyon Mine landslides from seismic signal analysis. *Geophysical research letters*, 41(13):4535–4541, 2014. doi: 10.1002/2014GL060592.
- Hibert, C., Michéa, D., Provost, F., Malet, J.-P., and Geertsema, M. Exploration of continuous seismic recordings with a machine learning approach to document 20 yr of landslide activity in Alaska. *Geophysical Journal International*, 219(2):1138–1147, 07 2019. doi: 10.1093/gji/ggz354.
- Hunter, J. D. Matplotlib: A 2D graphics environment. *Computing in science & engineering*, 9(03):90–95, 2007. doi: 10.1109/M-CSE.2007.55.
- Hutko, A. R., Bahavar, M., Trabant, C., Weekly, R. T., Fossen, M. V., and Ahern, T. Data products at the IRIS-DMC: Growth and usage. *Seismological Research Letters*, 88(3):892–903, 2017. doi: 10.1785/0220160190.
- IRIS Transportable Array. USArray Transportable Array, 2003. <https://www.fdsn.org/networks/detail/TA/>.
- Jennings, P. C. and Kanamori, H. Effect of distance on local magnitudes found from strong-motion records. *Bulletin of the Seismological Society of America*, 73(1):265–280, 1983. doi: 10.1785/BSSA0730010265.
- Kingma, D. P. and Ba, J. Adam: A Method for Stochastic Optimization. 2014. doi: 10.48550/ARXIV.1412.6980.
- Klein, F. W. User’s guide to HYPOINVERSE-2000, a Fortran program to solve for earthquake locations and magnitudes. Technical report, US Geological Survey, 2002.
- Kong, Q., Trugman, D. T., Ross, Z. E., Bianco, M. J., Meade, B. J., and Gerstoft, P. Machine learning in seismology: Turning data into insights. *Seismological Research Letters*, 90(1):3–14, 2019. doi: 10.1785/0220180259.
- Koper, K. D., Holt, M. M., Voyles, J. R., Burlacu, R., Pyle, M. L., Wang, R., and Schmandt, B. Discrimination of Small Earthquakes and Buried Single-Fired Chemical Explosions at Local Distances (<150 km) in the Western United States from Comparison of Local Magnitude (ML) and Coda Duration Magnitude (MC). *Bulletin of the Seismological Society of America*, 111(1):558–570, 10 2020. doi: 10.1785/0120200188.
- Krischer, L., Megies, T., Barsch, R., Beyreuther, M., Lecocq, T., Caudron, C., and Wassermann, J. ObsPy: a bridge for seismology into the scientific Python ecosystem. *Computational Science & Discovery*, 8(1):014003, May 2015. doi: 10.1088/1749-4699/8/1/014003.
- Luna, L. V. and Korup, O. Seasonal Landslide Activity Lags Annual Precipitation Pattern in the Pacific Northwest. *Geophysical Research Letters*, 49(18):e2022GL098506, 2022. doi: 10.1029/2022GL098506.
- Malfante, M., Dalla Mura, M., Métaxian, J.-P., Mars, J. I., Macedo, O., and Inza, A. Machine learning for volcano-seismic signals: Challenges and perspectives. *IEEE Signal Processing Magazine*, 35(2):20–30, 2018. doi: 10.1109/MSP.2017.2779166.
- Manconi, A., Gariano, S. L., Coviello, V., and Guzzetti, F. How many rainfall-induced landslides are detectable by a regional seismic monitoring network? In *Workshop on World Landslide Forum*, pages 161–168. Springer, 2017. doi: 10.1007/978-3-319-53487-9_18.
- Michellini, A., Cianetti, S., Gaviano, S., Giunchi, C., Jozinovic, D., and Lauciani, V. INSTANCE - the Italian seismic dataset for machine learning. *Earth System Science Data*, May 2021. doi: 10.5194/essd-2021-164.
- Mousavi, S. M. and Beroza, G. C. Deep-learning seismology. *Science*, 377(6607):eabm4470, 2022. doi: 10.1126/science.abm4470.
- Mousavi, S. M., Sheng, Y., Zhu, W., and Beroza, G. C. STanford Earthquake Dataset (STEAD): A global data set of seismic signals for AI. *IEEE Access*, 7:179464–179476, 2019. doi: 10.1109/ACCESS.2019.2947848.
- Mousavi, S. M., Ellsworth, W. L., Zhu, W., Chuang, L. Y., and Beroza, G. C. Earthquake transformer—an attentive deep-learning model for simultaneous earthquake detection and phase picking. *Nature communications*, 11(1):1–12, 2020. doi: 10.1038/s41467-020-17591-w.
- Münchmeyer, J., Woollam, J., Rietbrock, A., Tilmann, F., Lange, D., Bornstein, T., Diehl, T., Giunchi, C., Haslinger, F., Jozinović, D., et al. Which picker fits my data? A quantitative evaluation of deep learning based seismic pickers. *Journal of Geophysical Research: Solid Earth*, 127(1):e2021JB023499, 2022. doi: 10.1029/2021JB023499.
- Natural Resources Canada (NRCAN Canada). Canadian National Seismograph Network, 1975. <https://www.fdsn.org/networks/detail/CN/>.
- Ni, Y. niyiyu/PNW-ML: PNW-ML Seismic Dataset. doi: 10.5281/zenodo.7627103.
- Paullada, A., Raji, I. D., Bender, E. M., Denton, E., and Hanna, A. Data and its (dis)contents: A survey of dataset development and use in machine learning research. *Patterns*, 2(11):100336, 2021. doi: <https://doi.org/10.1016/j.patter.2021.100336>.
- Richter, C. F. Elementary Seismology. 1958.

- Rogers, G. and Dragert, H. Episodic tremor and slip on the Cascadia subduction zone: The chatter of silent slip. *science*, 300(5627): 1942–1943, 2003. doi: 10.1126/science.1084783.
- Rutgers University. Ocean Observatories Initiative, 2013. <https://www.fdsn.org/networks/detail/OO/>.
- SCEDC. Southern California Earthquake Data Center, 2013. <http://scedc.caltech.edu>. Type: dataset.
- Schorlemmer, D., Euchner, F., Kästli, P., Saul, J., Group, Q. W., et al. QuakeML: status of the XML-based seismological data exchange format. *Annals of Geophysics*, 54(1), 2011. doi: 10.4401/ag-4874.
- Survey, U. S. G. Advanced National Seismic System (ANSS) Comprehensive Catalog. 2017. doi: 10.5066/F7MS3QZH.
- Uieda, L., Tian, D., Leong, W. J., Toney, L., Schlitzer, W., Grund, M., Newton, T., Ziebarth, M., Jones, M., and Wessel, P. PyGMT: A Python interface for the Generic Mapping Tools. doi: 10.5281/zenodo.4522136. The development of PyGMT has been supported by NSF grants OCE-1558403 and EAR-1948603.
- University of Oregon. Pacific Northwest Seismic Network - University of Oregon, 1990. <https://www.fdsn.org/networks/detail/UO/>.
- University of Washington. Pacific Northwest Seismic Network - University of Washington, 1963. <https://www.fdsn.org/networks/detail/UW/>.
- Wang, A., Singh, A., Michael, J., Hill, F., Levy, O., and Bowman, S. R. GLUE: A multi-task benchmark and analysis platform for natural language understanding. *arXiv preprint arXiv:1804.07461*, 2018.
- Wang, R., Schmandt, B., Holt, M., and Koper, K. Advancing Local Distance Discrimination of Explosions and Earthquakes With Joint P/S and ML-MC Classification. *Geophysical Research Letters*, 48(23):e2021GL095721, 2021. doi: 10.1029/2021GL095721.
- Wech, A. G. and Bartlow, N. M. Slip rate and tremor genesis in Cascadia. *Geophysical Research Letters*, 41(2):392–398, 2014. doi: 10.1002/2013GL058607.
- Wech, A. G., Creager, K. C., Houston, H., and Vidale, J. E. An earthquake-like magnitude-frequency distribution of slow slip in northern Cascadia. *Geophysical Research Letters*, 37(22), 2010. doi: 10.1029/2010GL044881.
- Wiemer, S. and Wyss, M. Minimum magnitude of completeness in earthquake catalogs: Examples from Alaska, the western United States, and Japan. *Bulletin of the Seismological Society of America*, 90(4):859–869, 2000. doi: 10.1785/0119990114.
- Witter, R. C., Kelsey, H. M., and Hemphill-Haley, E. Great Cascadia earthquakes and tsunamis of the past 6700 years, Coquille River estuary, southern coastal Oregon. *Geological Society of America Bulletin*, 115(10):1289–1306, 2003. doi: 10.1130/B25189.1.
- Woollam, J., Rietbrock, A., Bueno, A., and De Angelis, S. Convolutional Neural Network for Seismic Phase Classification, Performance Demonstration over a Local Seismic Network. *Seismological Research Letters*, 90(2A):491–502, Mar. 2019. doi: 10.1785/0220180312.
- Woollam, J., Münchmeyer, J., Tilmann, F., Rietbrock, A., Lange, D., Bornstein, T., Diehl, T., Giunchi, C., Haslinger, F., Jozinović, D., et al. SeisBench—A toolbox for machine learning in seismology. *Seismological Society of America*, 93(3):1695–1709, 2022. doi: 10.1785/0220210324.
- Yan, Y., Cui, Y., Tian, X., Hu, S., Guo, J., Wang, Z., Yin, S., and Liao, L. Seismic signal recognition and interpretation of the 2019 “7.23” Shuicheng landslide by seismogram stations. *Landslides*, 17(5): 1191–1206, 2020. doi: 10.1007/s10346-020-01358-x.
- Zhu, W., Mousavi, S. M., and Beroza, G. C. Seismic signal augmentation to improve generalization of deep neural networks. In *Advances in geophysics*, volume 61, pages 151–177. Elsevier, 2020. doi: 10.1016/bs.agph.2020.07.003.

The article *Curated Pacific Northwest AI-ready Seismic Dataset* © 2023 by Yiyu Ni is licensed under CC BY 4.0.

Self-sufficient seismic boxes for monitoring glacier seismology

Ana Nap * ¹, Fabian Walter  ², Martin P. Lüthi  ¹, Adrien Wehrlé  ¹

¹Department of Geography, University of Zürich, Zürich, Switzerland, ²Swiss Federal Institute for Forest, Snow and Landscape Research WSL, Birmersdorf, Switzerland

Author contributions: *Conceptualization:* Ana Nap, Fabian Walter, Martin P. Lüthi. *Formal Analysis:* Ana Nap, Fabian Walter, Adrien Wehrlé. *Writing - Original draft:* Ana Nap. *Visualization:* Ana Nap. *Project administration:* Martin P. Lüthi. *Funding acquisition:* Martin P. Lüthi.

Abstract Glacier seismology is a valuable tool for investigating ice flow dynamics, but sufficient data acquisition in remote and exposed glaciated terrain remains challenging. For data acquisition on a highly crevassed and remote outlet glacier in Greenland we developed self-sufficient and easily deployable seismic stations, "SG-boxes". The SG-boxes contain their own power supply via solar panel, a three-component omni-directional geophone and a GNSS receiver. The SG-boxes can be deployed and retrieved from a hovering helicopter, allowing for deployment in difficult terrain. To assess their performance we conducted a field test comparing the SG-boxes to established on-ice geophone installations at Gornergletscher in Switzerland. Moreover, data from a first SG-box deployment in Greenland were analyzed. The SG-boxes exhibit consistently higher noise levels relative to colocated conventional geophones and a correlation between noise levels, wind and air temperature is found. Despite their noise susceptibility, the SG-boxes detected a total of 13,114 Gornergletscher icequakes over 10 days, which is 30% of the total number of icequakes detected by conventional geophone stations. Hence, even in sub-optimal weather conditions and without additional noise reduction measures, the SG-boxes can provide unique and valuable data from challenging glaciated terrain where no conventional seismic installations are possible.

Non-technical summary Several glacier processes produce seismic signals: small vibrations for example caused by crevasses forming in the ice or the glacier slipping across the bed. These vibrations, called icequakes, give valuable information about glacier flow dynamics and can be measured with seismological sensors at the glacier surface. However, installing seismological sensors on crevassed, exposed and remote glaciated terrain is challenging. Therefore, creative solutions are necessary. For data acquisition on a highly crevassed and remote Greenlandic outlet glacier, we developed self-sufficient and easily deployable seismic stations, "SG-boxes". The SG-boxes receive power via a solar panel, contain a three-component seismic sensor and GNSS receiver for location logging and can be lowered and retrieved from a hovering helicopter. We assessed the SG-boxes performance by comparing them against regular seismic sensors during a 10-day field test on a Swiss glacier. In addition, we analyzed data from a first SG-box deployment in Greenland. We found that the SG-boxes have higher noise levels compared to regular sensors and are especially correlated with increased wind speeds and air temperature. Despite their noise susceptibility, the SG-boxes provide us with unique and valuable data from areas where regular sensor installations are not possible.

Introduction

In recent years glacier seismology has proven to be a valuable tool for investigating short and long term ice flow dynamics (Aster and Winberry, 2017; Podolskiy and Walter, 2016). Glacier seismology provides unique sub-surface information of ice flow and hydraulic processes at a high temporal resolution. These processes include microseismic stick-slip events and stick-slip tremor at the bed enabling us to study basal sliding which is difficult to monitor with other methods (Helmstetter et al., 2015; Rösli et al., 2016a; Guerin et al., 2021). Moreover, fracture icequakes as a result of crevasse formation provide information on stresses at and below the surface (Mikesell et al., 2012; Lind-

ner et al., 2019), changing seismic velocities can be diagnostic for englacial damage (Walter et al., 2015; Sergeant et al., 2020; Chmiel et al., 2021) and glaciohydraulic tremors allow us to study subglacial hydrology (Bartholomäus et al., 2015; Labeledz et al., 2022).

Despite the advantages, seismological measurements on glaciers and ice streams pose logistical and technical challenges, especially at remote and exposed locations such as hanging glaciers in Alpine regions (Faillettaz et al., 2015) and the polar ice sheets in Greenland and Antarctica. Areas of interest are often difficult to access, which demands more creative solutions for seismological data acquisition. Snow-free glacier regions are particularly challenging: as a result of surface melt, installing conventional seismological equipment, such as surface geophones, requires the ability and space

Production Editor:
Gareth Funning
Handling Editor:
Stephen Hicks
Copy & Layout Editor:
Théa Ragon

Received:
September 23, 2022
Accepted:
January 6, 2023
Published:
January 11, 2023

*Corresponding author: ana.nap@geo.uzh.ch

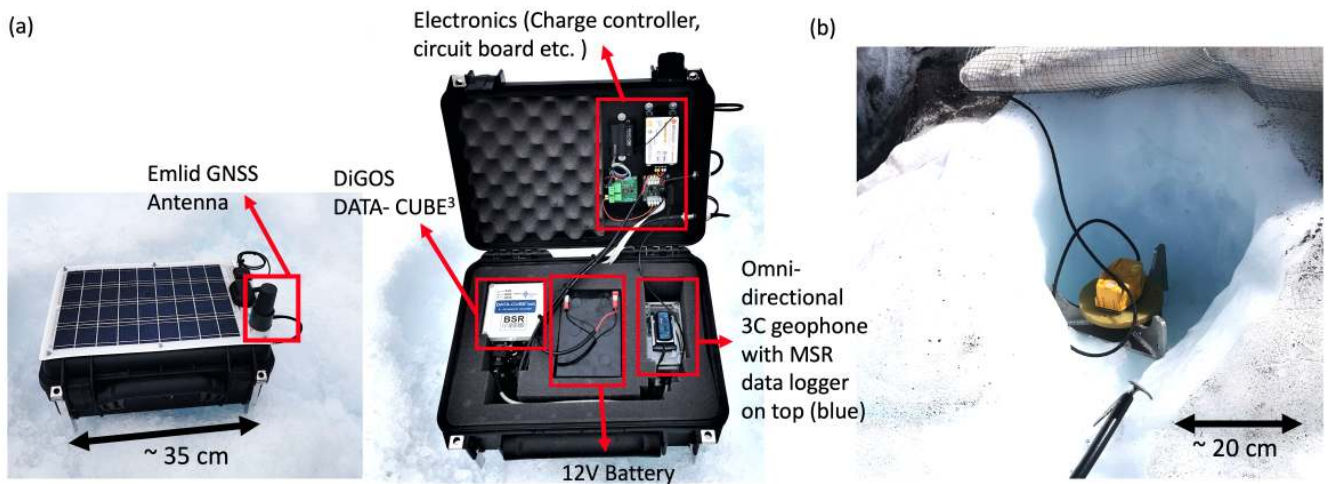


Figure 1 (a) Photos of a SG-box with closed and open lid. The SG-boxes housing is a waterproof PeliTM Protector case. The SG-boxes are equipped with an Emlid Reach M2 GNSS receiver, a 14 Hz three-component omni-directional geophone (SM-6 Omni-Directional by SENSOR Nederland) and a data logger from MSR Electronics GmbH. (b) Photo of a conventional geophone station that was used as reference to compare and validate the SG-boxes. These stations are equipped with a 4.5Hz three component geophone (PE-6/B manufactured by SENSOR Nederland) placed on a metal tripod and sampled with the same type DIGOS Data-CUBE³ as the SG-boxes.

to move around on-ground and/or the need to return every day or every couple of days to re-align the sensors to a horizontal position (Walter et al., 2008; Lindner et al., 2019). A solution to eliminating the requirement of regular maintenance is the use of borehole sensors, which do not demand maintenance visits for up to weeks or months, depending on the depth of the installation and power supply. However, borehole sensors are more costly than surface geophones, take longer to install and can be complicated or even impossible to install in highly crevassed and exposed glaciated terrain. Thus, sufficient data acquisition in these remote areas of interest demand a different approach from conventional surface geophones or borehole sensors.

Here, we present an innovative, easily deployable, self-sufficient seismic recording system designed for use on a remote and difficult to access outlet glacier in Greenland. We describe the design and evaluate the performance of these seismic boxes through a field test on Gornergletscher in Switzerland, as the extreme environment in Greenland complicates comprehensive testing. During the test at Gornergletscher, conventional geophone installations, previously used for on-ice data acquisition (Lindner et al., 2019), were installed as a base-line reference. We compare the conventional geophone data to the data acquired with the seismic boxes and we combine seismological data with weather data to show a critical relation between noise levels and wind. Despite the noise susceptibility, our portable seismic boxes provide valuable measurements in poorly accessible glaciated regions, where typical instrumentation is not possible.

Instrument Design

The main requirements for the instruments are that they are compact, self-sufficient, simple to deploy and

retrieve from a hovering helicopter, require no regular maintenance and can handle tilting caused by surface melt. The outcome was the design of the "SG-boxes", where the "S" stands for seismic and the "G" for GNSS (Global Navigation Satellite System) shown in Figure 1a.

The outside case of the SG-boxes are waterproof PeliTM Protector cases. The SG-boxes contain a self-assembled three-component sensor with three 14 Hz omni-directional geophones (SM-6 Omni-Directional by SENSOR Nederland) fixed directly to the bottom of the box, sampled with a DIGOS Data-CUBE³ digitizer, as well as an Emlid Reach M2 GNSS receiver with the antenna on top of the box lid. The GNSS device is multi-channel (frequencies L1, L2 and L5) and acquires all constellations. The geophone components are placed in the transparent plastic case visible on the right side of the SG-box underneath the blue data logger from MSR Electronics GmbH, that is attached to the top of the plastic geophone case. Every 5 minutes the MSR data logger records the temperature inside the box, the battery voltage and the tilt over three axes allowing for a more detailed analysis of the box performance.

The concept is to place the box directly on top of the ice such that ground movement is conveyed to the geophone inside the box. Omni-directional geophone components are used to ensure that the data are minimally affected by tilt of the box caused by ice melt, snow drift or sliding. The omni-directional geophones are equipped with an internal rotation system that keeps the geophone component at its original orientation, even when tilted. To prevent overall sliding of the SG-boxes on a sloped surface, screw-on metal spikes are attached to the bottom of the box. The GNSS receiver measures the position of the box at 1 Hz, which is a necessity for subsequent data analysis as these boxes are designed for use on fast-flowing (up to 40 m/day) glaciated terrain in Greenland (Joughin et al., 2008). The boxes are self-sufficient in their power supply from a solar panel

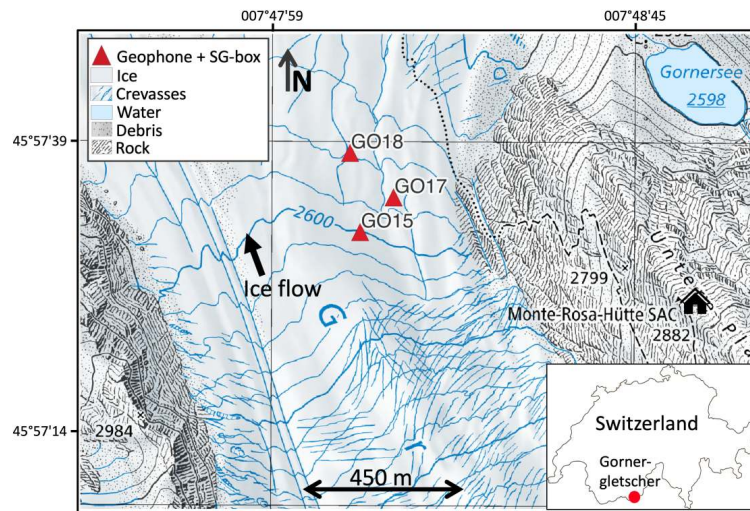


Figure 2 Overview of study site and sensor locations. The red triangles show the sensor locations where regular geophones and SG-boxes were co-located at a maximum of two meters from each other. (Source map: Swisstopo, Swiss Federal Office of Topography). Bottom right corner: Location of test site in Switzerland.

fixed on the box lid and are equipped with a charge control unit which prevents complete drainage of the battery in case of sustained time periods without sufficient solar energy. The SG-boxes can be lowered and recovered from a hovering or touched-down helicopter, either with a rope or by hand, depending on how close the helicopter can approach the surface. Lowering and retrieving the SG-boxes from a hovering helicopter by rope can be achieved by attaching a hook or anchor on a rope to suspension system of wires attached to the top of the box. This suspension system is not shown in Figure 1a, but was tested successfully.

Field test at Gornergletscher

Since extreme polar conditions and poor site access hampered detailed testing in Greenland, we first performed a field test at Gornergletscher in Switzerland in 2021 from the 29th of June until the 15th of July. This allowed us to gain extensive insight into the performance of the SG-boxes via a comparison between data from established installation techniques for on-ice deployment and the SG-boxes. For the validation and comparison of the SG-box data we used three-component geophone stations as shown in Figure 1b. These are 4.5Hz, three-component geophones (PE-6/B manufactured by SENSOR Nederland) previously used in glacier seismology research by Lindner et al. (2019) and sampled with DIGOS Data-CUBE³ digitizers as well, the same digitizer as in the SG-boxes. The regular geophones (Fig. 1b) are henceforth referred to as geophone(s).

The test deployment consisted of an array of 3 geophones arranged with inter station distances of 130-215 m (Fig. 2). As done in previous field campaigns, the geophones were placed in a pit dug into the ice with one melt-water drainage channel and covered with a white fleece tarpaulin to reduce ablation (Figure 1b). These geophone stations require daily or bi-daily additional digging of the pit and re-leveling of the sensors to account for surface melt. The geophones were co-located

with an SG-box (red triangles in Fig. 2), which were placed 1-2 m from the geophone at the ice surface. At GO15 and GO18 the geophones and SG-boxes were co-located for the entire test period and at GO17 only for a total of 10 days. The station names of the geophones are GO15GP, GO17GP and GO18GP and for the SG-boxes GO15SG, GO17SG and GO18SG, respectively. There are no data gaps on any of the stations except for some small (<20 minutes) data gaps in the geophone data during maintenance visits (e.g. changing of batteries or downloading data).

SG-box performance

In the results we focus on the seismological performance of the SG-boxes compared to regular geophones. The GNSS aspect of the SG-boxes to measure glacier flow velocities is of equal value to our research, but the performance of the Emlid GNSS/GPS receivers is already well established and does not need extensive additional analysis. For the sake of giving a complete overview of the SG-boxes performance, information on the GNSS processing and resulting flow speeds is included in the Supplementary Material S1.

Noise characteristics

A main limit on the performance of seismic sensors is (environmental) background noise (McNamara and Buland, 2004). If background noise exceeds or approaches the amplitude of the target signal, data usefulness becomes compromised. Seismic data from high-melt ablation zones contain a wealth of potential noise sources, such as melt-water flow and moulin drainage (Röösli et al., 2016a), rock/ice fall activity (Guillemot et al., 2020), wind (Frankinet et al., 2021; Winter et al., 2021), ice fracturing (Podolskiy and Walter, 2016) and in case of more populated areas also anthropogenic noise (Larose et al., 2015). Given the close proximity of co-located SG-boxes and geophones, we assume that both

sensor types record the same noise signals allowing comparison of their continuous records to evaluate the installation quality. As a result of the manner of installation of the SG-boxes (i.e. loosely placed on the ice surface) we expect them to be particularly sensitive to wind noise and we anticipate a reduced level of ground coupling compared to the geophones.

Probabilistic power spectral density (PPSD)

To estimate noise levels across a range of frequencies we computed PPSDs for both the SG-box and geophone at each station with the ObsPy package (Beyreuther et al., 2010) according to McNamara and Buland (2004). Figure 3a/b display PPSD plots for GO15SG and GO15GP, respectively, and Figure 3c shows the mean PPSD for each sensor.

Across all frequencies the SG-box PPSD in Figure 3a shows a larger variance as well as higher amplitudes than the geophone. The different bands in the PPSD in Figure 3a indicate that noise levels in the SG-box data fluctuate more over time than those of the geophone data. In Figure 3c we see that the mean PPSDs of the SG-boxes are at least 10 dB above the geophones for frequencies up to 50 Hz and up to 20 dB higher for frequencies above 100 Hz.

Background noise, wind and air temperature

A first look at the time series data and spectrograms of the SG-boxes shows that elevated noise levels occur in bounded time periods. During these periods the noise levels of the SG-boxes are up to 40 dB higher than the noise levels of the geophones (Fig. 4). In summer, glacial seismic data often experience heightened noise levels during the day as afternoon air temperatures boost meltwater flow (Canassy et al., 2012; Podolskiy and Walter, 2016; Rössli et al., 2016a; Aster and Winberry, 2017). However, this type of noise usually follows a diurnal rhythm which was not the case for the elevated noise periods of the SG-boxes. In contrast, we found a correlation between the SG-box noise levels and wind speed data from a nearby MeteoSwiss weather station. Considering that the SG-boxes are deployed at the ice surface and the geophones are inside a pit in the ice (Fig. 1) it is consequential that the geophones are more protected against strong winds. A comparison between SG-box data and geophone data during periods of low to no wind (hourly average <5 km/h) and strong wind (hourly average >20 km/h with gusts up to 60 km/h) is shown in Figure 4. During a period of no wind the SG-boxes and geophones contain comparable noise levels and display matching waveform data (Figs. 4a and 4b). For periods with strong wind, where the hourly average is 20 km/h, the SG-boxes experience up to 40 dB higher noise levels compared to no wind (Figs. 4c and 4d). The geophones experience elevated noise levels as well, but only by up to 10 dB.

To quantify and assess temporal variations in noise levels, we computed spectrograms for both the geophones and the SG-boxes across the full test period. The spectrograms were computed in 5.12 s windows with 50% overlap. From the spectrograms we computed 60

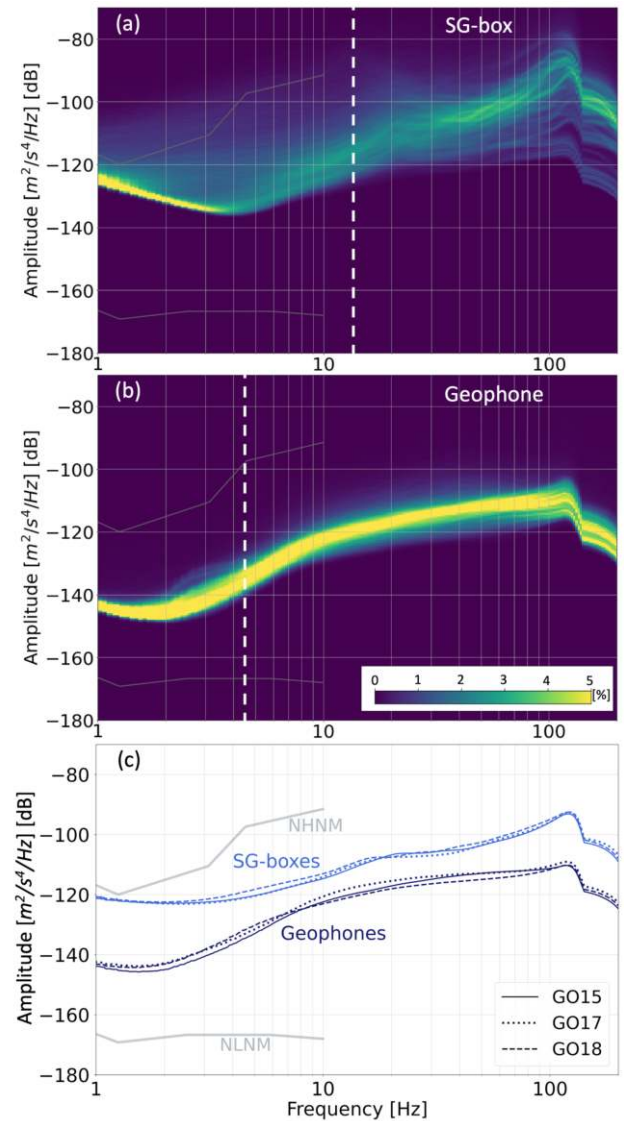


Figure 3 Probabilistic power spectral density (PPSD) of the vertical component at station GO15 for the entire 15 day test period (computed with the ObsPy package (Beyreuther et al., 2010) according to McNamara and Buland (2004)). Grey lines mark the low and high noise models (NLNM and NHNM according to Peterson (1993)) and the vertical white dashed lines indicate the natural frequency of the sensor, 4.5 Hz for the geophones and 14 Hz for the SG-boxes. (a) PPSD GO15SG (b) PPSD GO15GP. (c) Mean PPSD values for all stations (GO15, GO17 and GO18).

minute average power spectral density (PSD) windows in different frequency ranges, 14-30 Hz, 30-100 Hz and 100-190 Hz. Through dividing the average PSDs of the SG-boxes by those of the geophones we obtain a ratio that expresses the noise level of the SG-boxes relative to the geophones for each frequency window. For station GO15 the results of these computations are displayed in Figure 5a and Figure 5b. For station GO17 and GO18 the same results can be found in Fig. S2 and S3. Note that most peaks in Figure 5a and Figure 5b occur during geophone maintenance visits, indicated by the red arrows. When performing maintenance on the stations the sensors were occasionally moved and the pits of the geophones were deepened using an ice-axe, causing

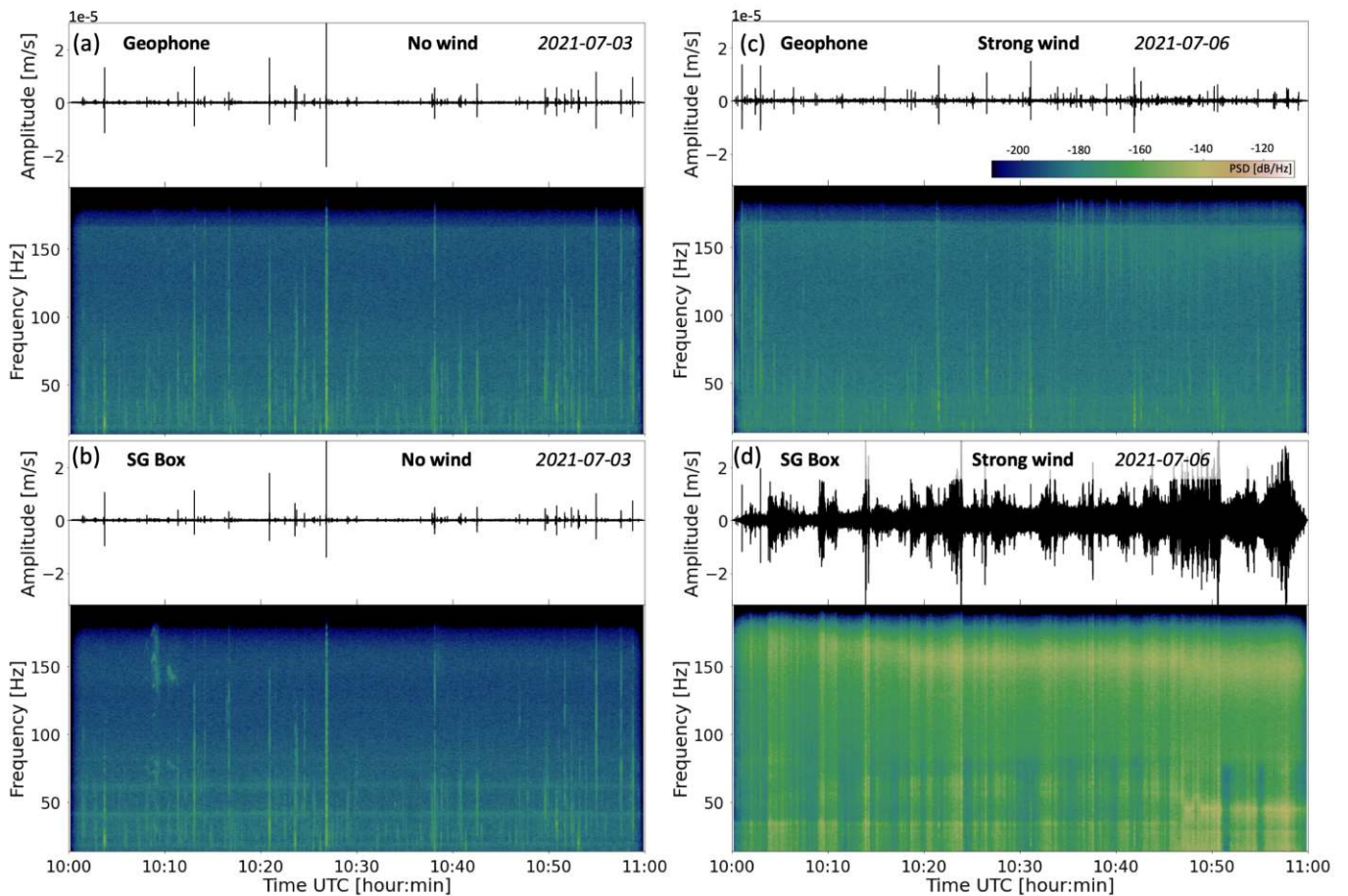


Figure 4 Waveform data and respective spectrograms for times with no wind on July 3rd 2021 (hourly average <5 km/h) and times with strong wind on July 6th 2021 (hourly average >20 km/h with gusts up to 60 km/h) from station GO15. (a) GO15GP data with no wind. (b) GO15SG data with no wind. (c) GO15GP data during strong wind. (d) GO15SG data during strong wind.

high, short duration (<10 minutes) peaks of energy in the data.

Figures 5a/b show that for 70% of the test period the noise level of the SG-box lies above that of the geophone. The high frequency window of 100-190 Hz generally exhibits the highest ratio, a characteristic that can also be seen in the spectrogram of Figure 4d. Figure 5b shows that noise levels can be identical for the SG-box during periods of low wind speed (<5 km/h). Periods of strong wind (hourly average >20km/h and gusts up to 80 km/h) consistently correlate with periods that show elevated noise levels. However, the opposite does not apply: periods of little to no wind do not always correspond to a ratio of one in Figure 5b. For some elevated noise periods during low wind, such as on the 5th and 11th of July, a correlation between elevated noise levels and higher (> 7.5 °C) air temperature can be identified. The above mentioned correlations for station GO15 also apply to stations GO17 and GO18 (Fig. S2 and S3 in the Supplementary Material).

Generally, seismic energy caused by glaciohydraulic processes and surface meltwater flow is concentrated at frequencies below 35 Hz (Bartholomäus et al., 2015; Podolskiy and Walter, 2016; Röögli et al., 2016b; Labeledz et al., 2022) and is therefore not likely to explain the periods of high frequency noise (>100 Hz) during pe-

riods with low wind speeds and high air temperature such as at the start and end of the test period. We also have to consider that the weather data originates from a weather station next to the Monte Rosa Hut, which is 850 m from the deployment and at 450 m higher elevation. Therefore, the wind speed data might not fully represent the situation at the glacier and thus at the sensors. Low wind speeds could be measured at the weather station while strong wind occurred at the glacier, either because of catabatic winds or a more sheltered position of the hut with certain wind directions. We also checked tilt of the SG-box as a possible explanation for elevated noise levels. Figure 5c, displays the tilt of the SG-box on the X, Y and Z component as measured every five minutes by the MSR data logger (see Fig. 1 for the details of the SG-box). The tilt data from Figure 5c shows no correlation with sustained periods of elevated noise for the SG-box as displayed in Figure 5a/b. Only peaks correspond to the moment of changing tilt (e.g. sliding down icy slope). These tilt events account for the peaks in the average PSD that are not caused by maintenance visits.

Waveform quality

Although the noise levels show no correlation with tilt, the waveform quality of the SG-boxes could still be affected. The seismic sensors used for the SG-box are

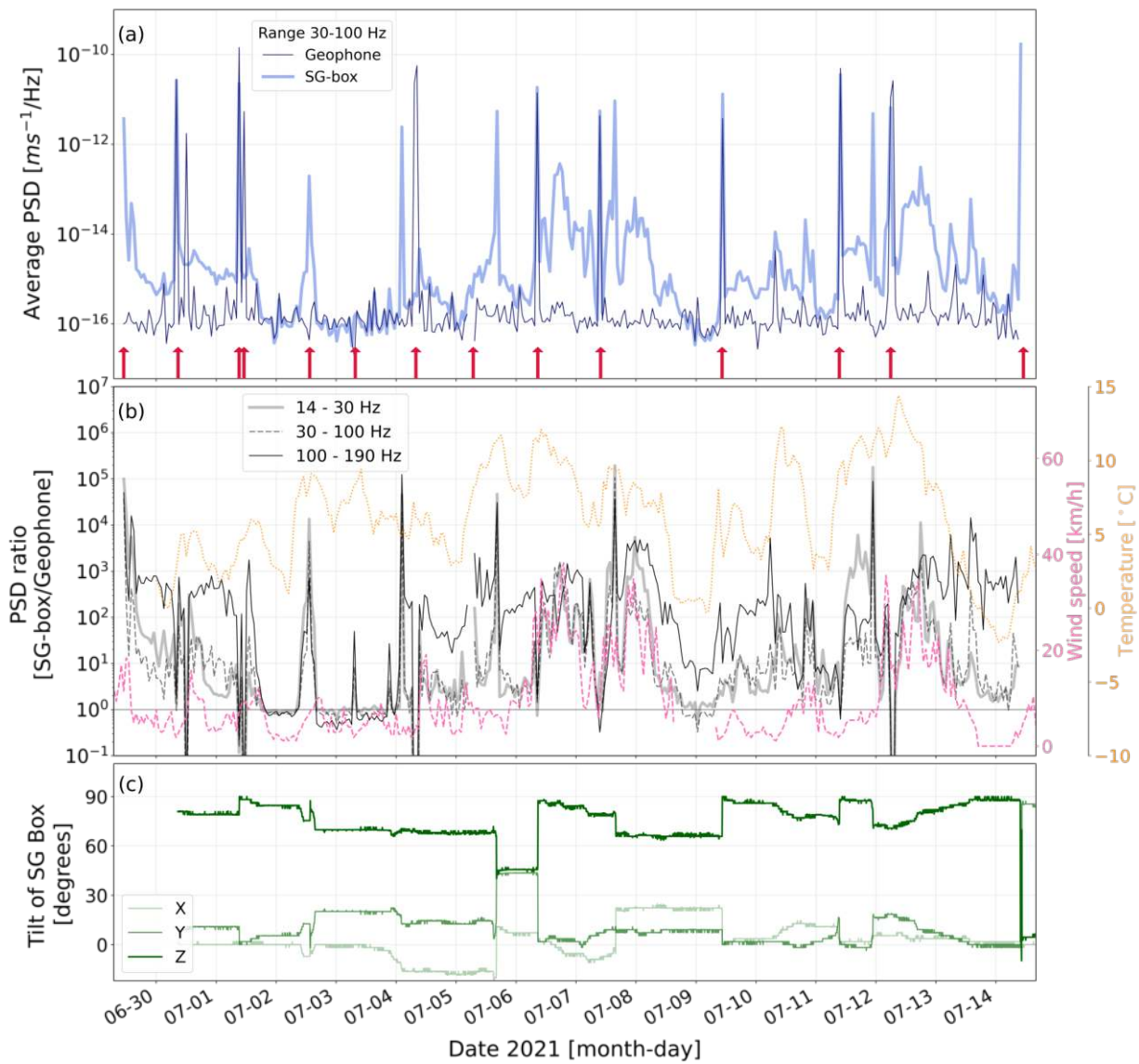


Figure 5 Noise levels and tilt time series of Station GO15. (a) Average power spectral density (PSD) of the SG-box and geophone in a frequency range of 30 to 100 Hz. The average PSD is computed by taking the average value of 60 minute windows in the spectrogram for a defined frequency range. The red arrows indicate the maintenance visit times at the stations. (b) Ratio between average PSD of SG-box and geophone in three frequency windows: 14-30 Hz, 30-100 Hz and 100-190 Hz. Hourly averaged wind speed and hourly averaged temperature measured at the MeteoSwiss weather station at the Monte Rosa Hut are displayed in dashed pink and dotted orange, respectively. A ratio of 1 (i.e. 10^0) corresponds to equal PSD levels of SG-box and geophone. (c) Tilt of three axis of the SG-box measured every 5 minutes by the MSR data logger accelerometer. The SG-box is exactly horizontal when X, Y and Z are 0, 0 and 90 degrees, respectively.

omni-directional, but it remains to be shown if tilting the SG-box from a horizontal position will affect the data quality. Figure 5 shows that prolonged periods of tilt from a horizontal position do not correlate with heightened noise levels of the SG-box. Other than increased noise, reduced waveform accuracy because of tilting is a known problem for seismological sensors in general (Ringler et al., 2015; Faber and Maxwell, 1997). Also coupling and general data fidelity could be affected by sliding of the SG-box.

During the test period, GO15SG experienced an extended period of tilt beyond 45 degrees. This "tilt event" occurred around 16:00 UTC on the 5th of July and the SG-box was re-levelled during a maintenance visit at 9:00 UTC on the 6th of July. The tilt data measured by the

MSR data logger can be found in Figure 5c. Figure 6 shows a photo of the tilted position of the SG-box during the "tilt-event" (taken during the maintenance visit before levelling the SG-box). To assess waveform quality, we cross-checked the waveforms of the SG-box and the geophone for different icequake events before, during and after the "tilt event". In Figure 6 the waveforms of the vertical component for four selected events are found. Identical figures as Figure 6 for the horizontal components are in Fig. S4 and S5.

The waveforms of the SG-box closely resemble those of the geophone, before, during and after the SG-box is tilted (Fig. 6). In the waveform time series a slight difference can be found in the amplitudes of the SG-box and geophone. We assume this difference is caused by

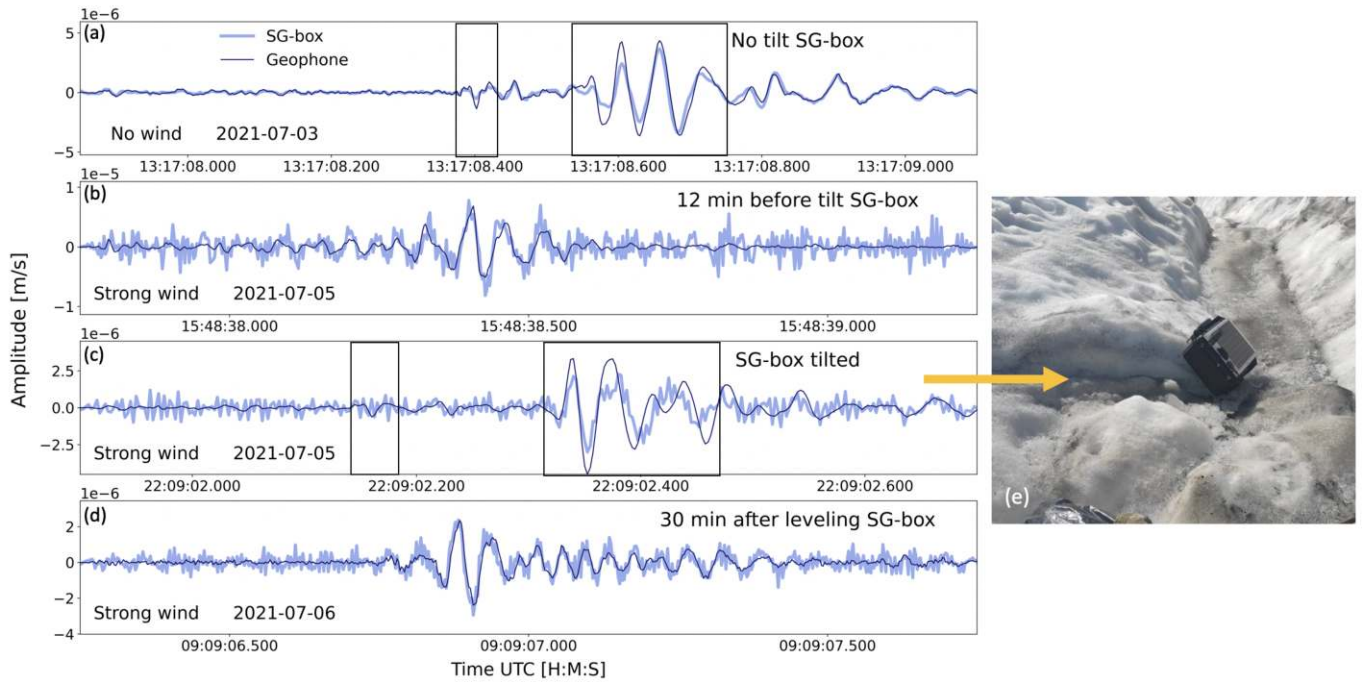


Figure 6 Example of match between SG-box and geophone for selected icequake events before, during and after extreme tilt of SG-box at station GO15. Here the vertical component is shown and the data are bandpass filtered between 14 and 190 Hz. The tilt occurred between approximately 16:00UTC on 2021-07-05 and 09:00UTC the next day. The measured tilt can be found in figure 5. (a) No tilt on 2021-07-03 with no wind. (b) 12 minutes before tilt occurred on 2021-07-05. (c) During tilt of SG-box on 2021-07-05. The amount of tilt the SG-box experienced can be seen in (e), the picture is taken in a horizontal position. (d) 30 minutes after placing the SG-box in a horizontal position again.

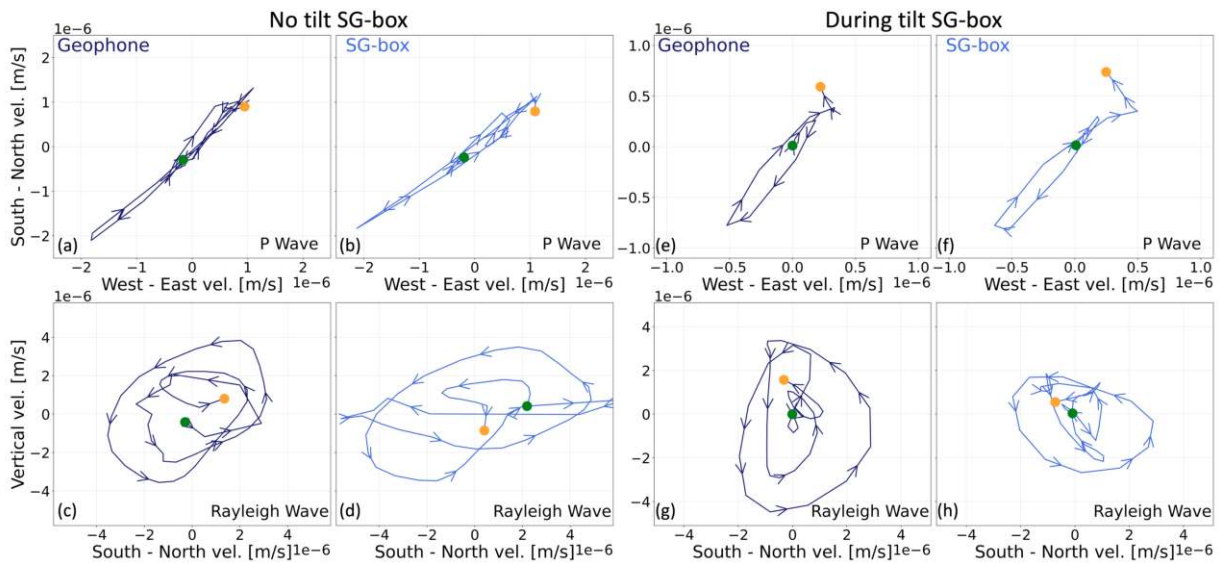


Figure 7 Particle motion of selected events in Fig. 6a and 6c. Green points mark the start of the motion and orange points mark the end. (a, b, c, d) Particle motion in m/s of event depicted in Fig. 6a for the geophone (a and c, dark blue) and SG-box (b and d, light blue) when the SG-box was not tilted. The data are bandpass filtered between 14-150 Hz. The P-wave (a and b) and Rayleigh wave (c and d) correspond to the first and second outlined box in Fig. 6a respectively. (e, f, g, h) Particle motion in m/s of event depicted in Fig. 6c for the geophone (e and g) and SG-box (f and h) when the SG-box was tilted as shown in Fig. 6e. The data are bandpass filtered between 14-100 Hz. The P-wave (e and f) and Rayleigh wave (g and h) correspond to the first and second outlined box in Fig. 6c respectively.

the fact that they are different sensor types and because of a difference in coupling, as the SG-boxes are more loosely placed on the ice than the geophones. Further, a distinct difference between the waveforms of Figure 6b, 6c and 6d is the presence of high frequency noise in

the SG-box data, likely caused by elevated wind speeds during those times (Fig. 4 and 5). The absence of high frequency noise in Figure 6a, when there was low to no wind, supports this assertion. In general, the vertical components are more affected by the high frequency

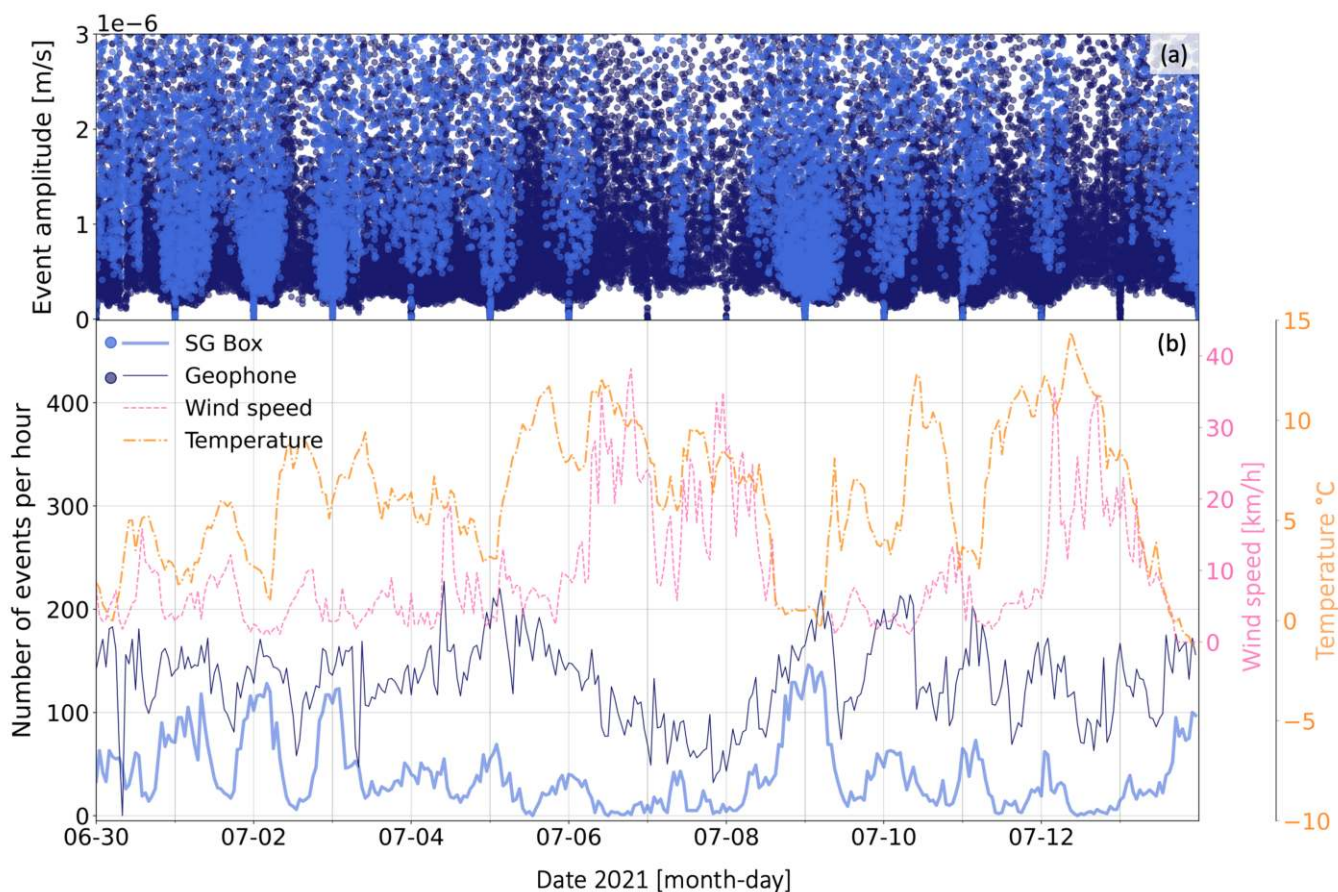


Figure 8 (a) Amplitude of each detected icequake of the SG-boxes (light blue) and geophones (dark blue). The 25% highest amplitudes are left out for clarity. Bottom: Hourly icequake detection with wind speed (dashed pink) and temperature (dotted yellow). (b) Time history of temperature, wind and hourly icequake detections for both the geophones (striped dark blue) and the SG-boxes (solid light blue).

noise than the horizontal components (see Fig. S4 and S5 in the Supplementary Material).

To further assess the quality of the waveform recordings of the SG-box before and during the tilt event we looked at the particle motion of the icequake events from Figure 6a and 6c. These selected events are assumed to be (near) surface events caused by crevasse formation or extension, as they contain clear low frequency (10-50 Hz) Rayleigh waves, compressive P-wave polarity and an estimated back-azimuth towards the S-SW where a large number of crevasses are concentrated (see Fig. 2). Figure 7a - 7d and Figure 7e - 7h show the particle motion for the P- and Rayleigh wave of the events in Figure 6a and 6c respectively. For Figure 7a - 7d the data are bandpass filtered between 14 and 150 Hz and for Figure 7e - 7h between 14 and 100 Hz, to account for the high frequency noise (Fig. 6c) that otherwise superimposes the particle motion. Both events show clear compressional motion in the horizontal plane for the P-waves and retrograde motion in the north-south oriented vertical plane for the Rayleigh waves. Figure 7 shows that even when the SG-box is severely tilted the omni-directional geophones still record the waveforms with good quality.

Event detection

To assess the useful data return further, we compared the SG-boxes and the geophones in terms of icequake event detection. For this comparison the three SG-boxes and the three co-located geophones are treated as two separate triangular arrays.

For icequake event detection we used a classic coincidence short-term/long-term (STA/LTA) trigger from the ObsPy library (Beyreuther et al., 2010) with a coincidence criterion of two out of three sensors. The STA/LTA was performed only on the vertical components that were filtered between 14 and 100 Hz. The STA window was set at 0.1 s and the LTA window at 20 s, the windows were determined in an empirical manner. The algorithm was run separately for the three SG-boxes and the three geophones. To eliminate false picks we performed cross-correlations between the stations within an array when a detection was triggered. By trial-and-error we determined a cross-correlation threshold of 0.5 for an event to be kept. For the geophones this resulted in 44,100 events out of 70,358 that were kept after cross-correlation confirmation and 13,114 out of 47,233 for the SG-boxes. This testifies to a larger number of false detections for the SG-boxes, which is expected considering the fluctuating noise levels which complicate accurate picking with a STA/LTA algorithm. The settings of the cross-correlation threshold also delete a minority of

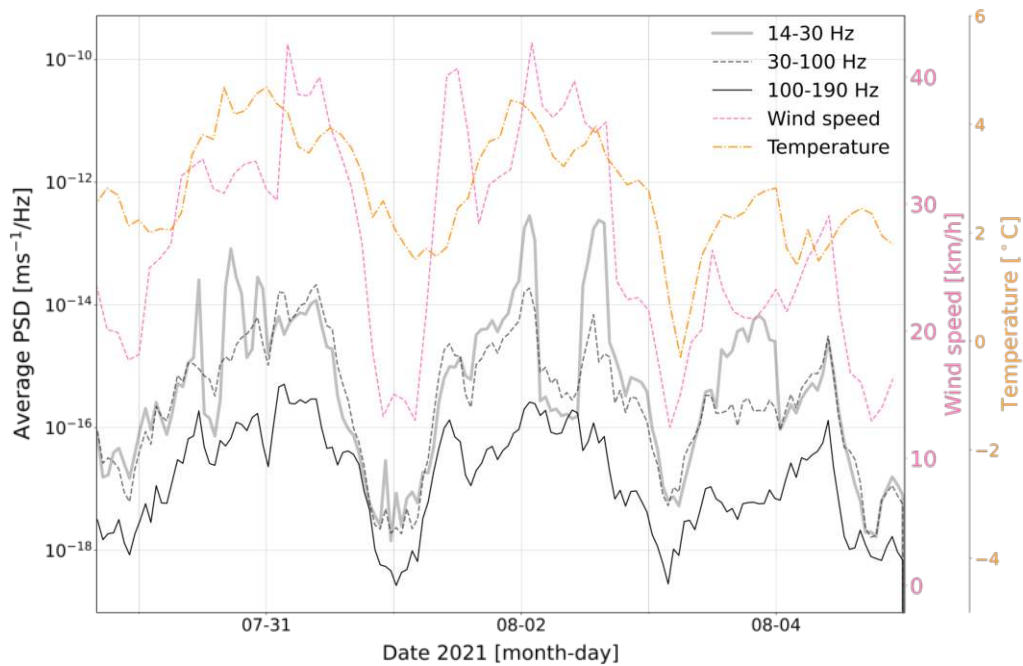


Figure 9 Average PSD of SG-box (grey) installed on Sermeq Kujalleq in Greenland in three frequency windows, 14-30 Hz, 30-100 Hz and 100-190 Hz. Average air temperature and average wind speed (2 hour window averages are transmitted via satellite connection) are plotted on top in dotted orange and striped pink, respectively.

positive picks, but from visual confirmation completely eliminate false positives, which is important for a valid instrument comparison. False positive picks in the SG-box data mainly concentrate in large amplitude noise bursts between 10 s - 10 min in length, where consecutively tens of picks were placed by the STA/LTA algorithm without an actual event being present.

The results show that the geophones consistently detect more events per hour than the SG-boxes (Fig. 8). Specifically, around 30% of events detected on the geophones were detected on the SG-boxes. This is expected considering the elevated noise levels of the SG-boxes compared to the geophones. Additionally, a clear diurnal cycle exists for the detectability of weaker events (Fig. 8). This phenomenon has been described by Walter et al. (2008); Canassy et al. (2012) and Rööslä et al. (2014), who linked daily changes in amplitudes of the weakest detectable events to melt-induced seismic background noise, primarily driven by glaciohydraulic tremor. In our study, both wind speed and air temperature show a link to the number of detected events (Fig. 8). Temperatures above 5 °C and wind speeds above 20 km/h correspond to substantially lower numbers of detected events, especially for the SG-boxes.

Discussion

Compared to the conventional geophones, the SG-boxes are more affected by environmental noise such as wind and air temperature. Nevertheless, the omnidirectional sensors within the SG-box eliminated the effect of tilt on data quality and icequake waveforms show good correlation with geophone records even when the SG-box is tilted beyond 45 degrees from a horizontal position. During the test period at Gorner-

gletscher the SG-boxes were able to detect a total of 13,114 icequakes compared to 44,100 detected by the geophones (i.e. 30%).

Our findings that seismic background noise in SG-box data correlates with wind and air temperature (i.e. increased meltwater flow) are supported by data from a first acquisition with SG-boxes on Sermeq Kujalleq in Kangia (also known as Jakobshavn Isbræ), an outlet glacier on the west coast of Greenland. The boxes were specifically designed for data acquisition on this glacier, as the fast flowing trunk of Sermeq Kujalleq is difficult to access. The first 15 km are extremely crevassed so landing by helicopter is not possible, in the best case a touchdown can be performed, where the helicopter lands lightly on the ice surface but does not turn off the engine. Therefore, regular seismological equipment cannot be installed.

In July/August 2021, six singular SG-boxes at an intersensor distance of approximately 5 km were deployed along the fast ice stream of Sermeq Kujalleq. A deployment map of these SG-boxes and GNSS flow velocity data from two SG-boxes can be found in the Supplementary Material S4. As the SG-boxes were just singular sensor deployments at a relatively large distance from each other, we could not perform the same type of analysis we did for the data from Gornergletscher. Nevertheless, one of the SG-boxes in this deployment was located at 20 m from a weather station, allowing us to compare temperature and wind data to the average PSD of the SG-box, similar to the comparison in Figure 5.

Figure 9 shows a clear correlation between the average PSD and wind and temperature, with average wind speeds above 25 km/h and temperatures above 2 °C corresponding to up to four orders of magnitude higher av-

erage PSD levels. The main difference between the data from Greenland and the data from Gornergletscher is that in Figure 9 the low frequency window (i.e., 14-30 Hz) is consistently higher than the other two frequency windows. An explanation for this could be that the SG-box in Greenland was located close to a sub-glacial or englacial water channel or moulin that would dominate on-ice noise in this frequencies range (Bartholomaeus et al., 2015; Rööslı et al., 2016b; Köpflı et al., 2022; Labedz et al., 2022). The hydrological system on the Greenland icesheet is of a different scale than at an Alpine glacier, such as Gornergletscher. Considering the size of the englacial and subglacial water channels and moulins, it is not unexpected that different frequencies dominate the overall seismic energy (Rööslı et al., 2016b; Podolskiy, 2020).

The fact that the SG-boxes experience higher levels of background noise and are more sensitive to wind than the geophones is not surprising given the manner of deployment: on top of the glacier surface instead of the more protected deployment used for the geophones (Fig. 1). Although the SG-box deployment results in higher noise susceptibility and a reduced level of coupling, the SG-boxes have the advantage of reduced maintenance as well as simple deployment and retrieval. They are suitable for use in remote and exposed areas where deployment of typical instrumentation, such as regular geophones or borehole seismometers, is not possible. The SG-boxes provide unique access to valuable data from these areas. Further, additional measures can be taken to maximize useful data return like placing the SG-boxes in an array to allow for array processing and other advanced filtering techniques to reduce background noise that is uncorrelated between individual stations (Gibbons and Ringdal, 2006; Seydoux et al., 2016).

Summary and Conclusion

We have studied the performance of self-sufficient and easily deployable seismic stations (SG-boxes) for use in remote and hard-to-access glaciated regions such as a highly crevassed outlet glacier in Greenland. By comparing the SG-boxes to regular geophones through a field test at Gornergletscher, Switzerland, we assessed the performance of the boxes. Also, data from a first acquisition with an SG-box in Greenland were analysed. The results from both deployments show that the SG-boxes experience elevated noise levels compared to the regular geophones, especially in the lower frequency range of 14-30 Hz and the higher frequency range of 100-190 Hz. As a clear correlation is found between SG-box noise levels and wind and air temperature data, elevated noise levels are most likely caused by the exposure of the boxes on the glacier surface, in contrast to the more protected deployment of the geophones. Future investigations will benefit from placing the boxes into arrays that allow for array processing to reduce noise and increase signal return. Despite their noise susceptibility, the SG-boxes detected 30% of icequake events compared to conventional geophone installations during a 10 day test period with variable weather. Hence,

even in sub-optimal weather conditions and without additional noise reduction measures the SG-boxes can provide unique and valuable data from poorly accessible glaciated terrain.

Acknowledgements

We want to thank the reviewers for taking the necessary time and effort to review the manuscript. We sincerely appreciate all your valuable comments and suggestions, which helped us in improving the quality of the manuscript. We thank D. Wasser for his expert knowledge and help with designing, building and testing the technical side of the SG-boxes. This research has been supported by the Schweizerischer Nationalfonds zur Förderung der Wissenschaftlichen Forschung grant no. 200020_197015.

Data availability

All data are available at the following link: <https://zenodo.org/record/7516192.Y7wjsSwo9z1> with doi:10.5281/zenodo.7516192.

Competing interests

All authors declare that they have no conflicts of interest.

References

- Aster, R. C. and Winberry, J. P. Glacial seismology. *Reports on Progress in Physics*, 80(12):126801, Nov. 2017. doi: 10.1088/1361-6633/aa8473.
- Bartholomaeus, T. C., Amundson, J. M., Walter, J. I., O'Neel, S., West, M. E., and Larsen, C. F. Subglacial discharge at tidewater glaciers revealed by seismic tremor. *Geophysical Research Letters*, 42(15):6391–6398, 2015. doi: <https://doi.org/10.1002/2015GL064590>.
- Beyreuther, M., Barsch, R., Krischer, L., Megies, T., Behr, Y., and Wassermann, J. ObsPy: A Python toolbox for seismology. *Seismological Research Letters*, 81(3):530–533, 2010. doi: 10.1785/gssrl.81.3.530.
- Canassy, P. D., Faillettaz, J., Walter, F., and Huss, M. Seismic activity and surface motion of a steep temperate glacier: a study on Triftgletscher, Switzerland. *Journal of Glaciology*, 58(209):513–528, 2012. doi: 10.3189/2012JoG11J104.
- Chmiel, M., Walter, F., Preiswerk, L., Funk, M., Meier, L., and Brenner, F. Hanging glacier monitoring with icequake repeaters and seismic coda wave interferometry: a case study of the Eiger hanging glacier. *Natural Hazards and Earth System Sciences*, Sept. 2021. doi: 10.5194/nhess-2021-205.
- Faber, K. and Maxwell, P. W. Geophone spurious frequency: what is it and how does it affect seismic data quality. *Can. J. Explor. Geophys.*, 33(1-2):46–54, 1997.
- Faillettaz, J., Funk, M., and Vincent, C. Avalanching glacier instabilities: Review on processes and early warning perspectives. *Reviews of Geophysics*, 53(2):203–224, 2015. doi: <https://doi.org/10.1002/2014RG000466>.
- Frankinet, B., Lecocq, T., and Camelbeeck, T. Wind-induced seismic noise at the Princess Elisabeth Antarctica Station. *The Cryosphere*, 15(10):5007–5016, Oct. 2021. doi: 10.5194/tc-15-5007-2021.

- Gibbons, S. J. and Ringdal, F. The detection of low magnitude seismic events using array-based waveform correlation. *Geophysical Journal International*, 165(1):149–166, Apr. 2006. doi: 10.1111/j.1365-246X.2006.02865.x.
- Guerin, G., Mordret, A., Rivet, D., Lipovsky, B. P., and Minchew, B. M. Frictional Origin of Slip Events of the Whillans Ice Stream, Antarctica. *Geophysical Research Letters*, 48(11): e2021GL092950, 2021. doi: 10.1029/2021GL092950.
- Guillemot, A., Helmstetter, A., Larose, É., Baillet, L., Garambois, S., Mayoraz, R., and Delaloye, R. Seismic monitoring in the Gugla rock glacier (Switzerland): ambient noise correlation, micro-seismicity and modelling. *Geophysical Journal International*, 221(3):1719–1735, 2020. doi: 10.1093/gji/ggaa097.
- Helmstetter, A., Nicolas, B., Comon, P., and Gay, M. Basal icequakes recorded beneath an Alpine glacier (Glacier d'Argentière, Mont Blanc, France): Evidence for stick-slip motion? *Journal of Geophysical Research: Earth Surface*, 120(3):379–401, 2015. doi: <https://doi.org/10.1002/2014JF003288>.
- Joughin, I., Howat, I. M., Fahnestock, M., Smith, B., Krabill, W., Alley, R. B., Stern, H., and Truffer, M. Continued evolution of Jakobshavn Isbrae following its rapid speedup. *Journal of Geophysical Research: Earth Surface*, 113(F4), 2008. doi: <https://doi.org/10.1029/2008JF001023>.
- Köpfl, M., Gräff, D., Lipovsky, B. P., Selvadurai, P. A., Farinotti, D., and Walter, F. Hydraulic Conditions for Stick-Slip Tremor Beneath an Alpine Glacier. *Geophysical Research Letters*, 49(21):e2022GL100286, 2022. doi: <https://doi.org/10.1029/2022GL100286>.
- Labeledz, C. R., Bartholomäus, T. C., Amundson, J. M., Gimbert, F., Karplus, M. S., Tsai, V. C., and Veitch, S. A. Seismic mapping of subglacial hydrology reveals previously undetected pressurization event. *Journal of Geophysical Research: Earth Surface*, Feb. 2022. doi: 10.1029/2021JF006406.
- Larose, E., Carrière, S., Voisin, C., Bottelin, P., Baillet, L., Guéguen, P., Walter, F., Jongmans, D., Guillier, B., Garambois, S., et al. Environmental seismology: What can we learn on earth surface processes with ambient noise? *Journal of Applied Geophysics*, 116:62–74, 2015. doi: 10.1016/j.jappgeo.2015.02.001.
- Lindner, F., Laske, G., Walter, F., and Doran, A. K. Crevasse-induced Rayleigh-wave azimuthal anisotropy on Glacier de la Plaine Morte, Switzerland. *Annals of Glaciology*, 60(79):96–111, Sept. 2019. doi: 10.1017/aog.2018.25.
- McNamara, D. E. and Buland, R. P. Ambient Noise Levels in the Continental United States. *Bulletin of the Seismological Society of America*, 94(4):1517–1527, Aug. 2004. doi: 10.1785/012003001.
- Mikesell, T., van Wijk, K., Haney, M. M., Bradford, J. H., Marshall, H.-P., and Harper, J. T. Monitoring glacier surface seismicity in time and space using Rayleigh waves. *Journal of Geophysical Research: Earth Surface*, 117(F2), 2012. doi: 10.1029/2011JF002259.
- Peterson, J. R. Observations and modeling of seismic background noise. 1993.
- Podolskiy, E. A. Toward the Acoustic Detection of Two-Phase Flow Patterns and Helmholtz Resonators in Englacial Drainage Systems. *Geophysical Research Letters*, 47(6):e2020GL086951, 2020. doi: <https://doi.org/10.1029/2020GL086951>.
- Podolskiy, E. A. and Walter, F. Cryoseismology. *Reviews of Geophysics*, 54(4):708–758, 2016. doi: 10.1002/2016RG000526.
- Ringler, A. T., Hagerty, M., Holland, J., Gonzales, A., Gee, L. S., Edwards, J., Wilson, D., and Baker, A. M. The data quality analyzer: A quality control program for seismic data. *Computers & Geosciences*, 76:96–111, 2015. doi: 10.1016/j.cageo.2014.12.006.
- Röösli, C., Walter, F., Husen, S., Andrews, L. C., Lüthi, M. P., Catania, G. A., and Kissling, E. Sustained seismic tremors and icequakes detected in the ablation zone of the Greenland ice sheet. *Journal of Glaciology*, 60(221):563–575, 2014. doi: 10.3189/2014JoG13J210.
- Röösli, C., Helmstetter, A., Walter, F., and Kissling, E. Melt-water influences on deep stick-slip icequakes near the base of the Greenland Ice Sheet. *Journal of Geophysical Research: Earth Surface*, 121(2):223–240, 2016a. doi: <https://doi.org/10.1002/2015JF003601>.
- Röösli, C., Walter, F., Ampuero, J.-P., and Kissling, E. Seismic moulin tremor. *Journal of Geophysical Research: Solid Earth*, 121(8):5838–5858, 2016b. doi: 10.1002/2015JB012786.
- Sergeant, A., Chmiel, M., Lindner, F., Walter, F., Roux, P., Chaput, J., Gimbert, F., and Mordret, A. On the Green's function emergence from interferometry of seismic wave fields generated in high-melt glaciers: implications for passive imaging and monitoring. *The Cryosphere*, 14(3):1139–1171, 2020. doi: 10.5194/tc-14-1139-2020.
- Seydoux, L., Shapiro, N., de Rosny, J., Brenguier, F., and Landès, M. Detecting seismic activity with a covariance matrix analysis of data recorded on seismic arrays. *Geophysical Journal International*, 204(3):1430–1442, Mar. 2016. doi: 10.1093/gji/ggv531.
- Walter, F., Deichmann, N., and Funk, M. Basal icequakes during changing subglacial water pressures beneath Gornergletscher, Switzerland. *Journal of Glaciology*, 54(186):511–521, 2008. doi: 10.3189/002214308785837110.
- Walter, F., Roux, P., Röösli, C., Lecoindre, A., Kilb, D., and Roux, P.-F. Using glacier seismicity for phase velocity measurements and Green's function retrieval. *Geophysical Journal International*, 201(3):1722–1737, 2015.
- Winter, K., Lombardi, D., Diaz-Moreno, A., and Bainbridge, R. Monitoring Icequakes in East Antarctica with the Raspberry Shake. *Seismological Research Letters*, Apr. 2021. doi: 10.1785/0220200483.

The article *Self-sufficient seismic boxes for monitoring glacier seismology* © 2023 by Ana Nap is licensed under CC BY 4.0.